volumen 57, número 2, octubre 2021

ISSN en trámite

instituto de astronomía

unam

revista mexicana de astronomía y astrofísica

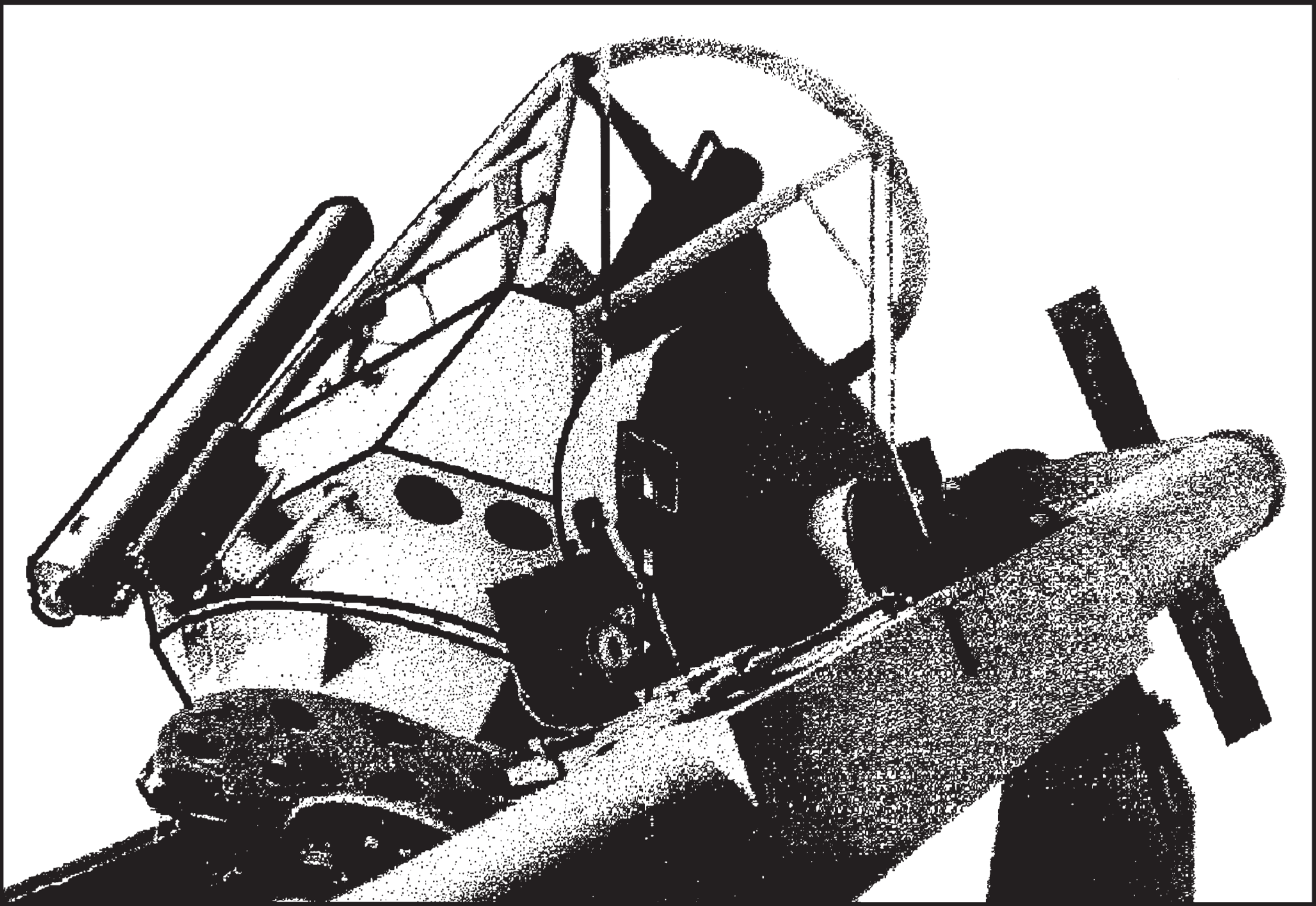

volumen 57
número 2
octubre 2021

revista mexicana de astronomía y astrofísica

Instituto de Astronomía
Universidad Nacional Autónoma de México

revista mexicana de astronomía y astrofísica

Av. Universidad 3000
Col. Universidad Nacional Autónoma de México, C. U.
Alcaldía Coyoacán
04510 Ciudad de México

ISSN en trámite

URL de DOI: https://doi.org/10.22201/ia.01851101p.2021.57.02

rmaa@astro.unam.mx

http://www.astroscu.unam.mx/RMxAA/

La *RMxAA* aparece indexada en Current Contents, Science Citation Index, Astronomy and Astrophysics Abstracts, Physics Briefs, Publicaciones Científicas en América Latina, Astronomy and Astrophysics Monthly Index, PERIODICA, RedALyC, Latindex y SciELO.

Revista Mexicana de Astronomía y Astrofísica, volumen 57, número 2, octubre 2021, es una publicación semestral, editada y distribuida por el Instituto de Astronomía, UNAM, Circuito Exterior, Ciudad Universitaria, 04510, Alcaldía Coyoacán, Ciudad de México, Teléfono: 5556223906, Correo Electrónico: rmaa@astro.unam.mx, ISSN en trámite. Editora responsable: Christine Patricia Allen Armiño. Distribución: Bienes y Servicios del Instituto de Astronomía, UNAM. Impresa por Grupo Edición, S.A. de C.V., Xochicalco 619, Colonia Letrán Valle, 03650, Alcaldía Benito Juárez, Ciudad de México. Fecha de impresión: 27 de septiembre de 2021. Número de ejemplares impresos: 500 en papel Couché de 100 gramos los interiores y en cartulina Couché de 250 gramos los forros. Precio de la publicación: gratuito.

CONTENTS

Revista Mexicana de Astronomía y Astrofísica, **57**, 251–268 (2021)

https://doi.org/10.22201/ia.01851101p.2021.57.02.01

STUDY OF BLAZAR ACTIVITY IN 10 YEAR FERMI-LAT DATA AND IMPLICATIONS FOR TEV NEUTRINO EXPECTATIONS

J. R. Sacahui[1], A. V. Penacchioni[2,8], A. Marinelli[3], A. Sharma[4], M. Castro[5,9], J. M. Osorio[6], and M. A. Morales[7]

Received October 16 2020; accepted March 9 2021

ABSTRACT

Blazars are the most active extragalactic gamma-ray sources. They show sporadic bursts of activity, lasting from hours to months. In this work we present a 10-year analysis of a sample of bright sources detected by Fermi-LAT (100 MeV - 300 GeV). Using 2-week binned light curves (LC) we estimate the duty cycle (DC): fraction of time that the source spends in an active state. The objects show different DC values, with an average of 22.74% and 23.08% when considering (or not) the extragalactic background light (EBL). Additionally, we study the so-called "blazar sequence" trend for the sample of selected blazars in the ten years of data. This analysis constrains a possible counterpart of sub-PeV neutrino emission during the quiescent states, leaving open the possibility to explain the observed IceCube signal during the flaring states.

RESUMEN

Los blazares son las fuentes de rayos gamma más activas. Presentan períodos esporádicos de actividad, con duraciones de horas a meses. En este trabajo presentamos un análisis de una muestra de fuentes brillantes detectadas por Fermi-LAT (100 MeV - 300 GeV) durante una década. Usando curvas de luz con episodios de 2 semanas estimamos el ciclo de actividad (DC): la fracción de tiempo que la fuente pasa en el estado activo. Los objetos presentan diferentes valores del DC, con promedios de 22.74% y 23.08% cuando se considera y no se considera el fondo de luz difusa. Adicionalmente, estudiamos la tendencia conocida como "secuencia de blazares". Este análisis restringe una posible contraparte de neutrinos con energías de sub-PeV durante los estados estacionarios, dejando la posibilidad de explicar las observaciones de IceCube durante los períodos de fase activa.

Key Words: BL Lacertae objects: general — galaxies active — gamma-rays: galaxies — neutrinos

1. INTRODUCTION

Blazars are the most variable and luminous type of active galactic nuclei (AGN). They are among the most powerful emitters in the Universe, and they are thought to be powered by material falling onto a supermassive (10^6 - 10^{10} $M_\odot$) black hole (BH) at the center of the host galaxy through an accretion disc. The strong, non-thermal electromagnetic emission is generally detected in all observable bands, from radio to gamma-rays, and is dominated by a relativistic jet pointing in the direction of the observer (when the jet is not pointing in this direction, they are catalogued as radio galaxies). Blazars thus reveal the energetic processes occurring in the center of active galaxies. The most compelling mechanism

---

[1] Instituto de Investigación en Ciencias Físicas y Matemáticas, USAC, Guatemala.

[2] Instituto de Física de La Plata (IFLP)- CONICET, La Plata, Argentina.

[3] Instituto Nazionale di Fisica Nucleare, Sezione di Napoli, Italy.

[4] Dept. of Physics and Astronomy, Uppsala University, Sweden.

[5] Instituto Nacional de Pesquisas Espaciais (INPE)- Divisão de Astrofísica, Brazil.

[6] Instituto de Astronomía, UNAM, México.

[7] Instituto Balseiro, Universidad Nacional de Cuyo, Argentina.

[8] Dept. of Physics, University of La Plata, Argentina.

[9] Universidade Estadual de Campinas (UNICAMP)- Instituto de Computação, Campinas, Brazil.

for the emission in the range from radio to optical is synchrotron emission, while gamma-rays are produced via inverse Compton (IC) by the same relativistic electrons producing the synchrotron emission (Sikora et al. 1994; Sikora et al. 2009).

Many blazars were first identified as irregular variable stars in our own Galaxy. Their luminosity changes over periods that range from days to years, but without a pattern. With the development of radio astronomy many bright radio sources were discovered, most of them having optical counterparts. This led to the discovery of quasars and blazars in the late 50's. The first redshift measurement was done for Blazar 3C 273 (Schmidt 1963). The Fermi satellite, launched in 2008, paved the way for the beginning of a new blazar era thanks to its Large Area Telescope (LAT), which detects sources in the 0.1 - 300 GeV energy range (Atwood et al. 2009) with much higher sensitivity than its predecessors. Blazars present high variability in this energy range, with periods in which the flux increases considerably (Abdo et al. 2009). Detailed studies of blazar spectra, and in particular their spectral variability (Urry 1996a,b), are fundamental tools to determine the physical processes responsible for particle acceleration and emission in the jet.

Blazars are often divided into two subclasses: BL Lacs (Stickel et al. 1991) and flat spectrum radio quasars (FSRQs) (Angel & Stockman 1980), although up to date there is no complete agreement in the selection criteria. BL Lacs are named after their prototype, BL Lacertae. They are characterized by rapid, large-amplitude flux variability and significant optical polarization. One of their defining features is the weakness or absence of emission lines; therefore, their redshifts can only be determined from features in their host galaxies' spectra. Besides, their spectra are dominated by a relatively featureless non-thermal emission continuum over the entire electromagnetic range. The nearby BL Lacs, which are associated to elliptical galaxies with typical absorption spectra, sometimes have narrow emission lines, while the more distant BL Lacs, whose host galaxies have never been detected, show broad emission lines. All known BL Lacs are associated with core-dominated radio sources.

Another type of source are flat spectrum radio quasars (FSRQ). They are usually more distant, more luminous, and have stronger emission lines than BL Lacs but, due to their similar continuum properties, they are collectively called blazars, together with BL Lacs. There are three suggestions regarding their classification: (i) FSRQ evolve into BL Lacs; (ii) they are different manifestations of the same physical object; and (iii) BL Lacs are gravitationally micro-lensed FSRQ (Urry & Padovani 1995). An example of FSRQ is the source 3C 279 (also known as PKS 1253-05). It presents very high variability in the visible, radio and X-ray bands. It is also one of the brightest sources in the gamma-ray sky monitored by the Fermi Space Telescope.

Blazars have been strong candidate sources of astrophysical neutrinos since 2017, when IceCube reported the first neutrino EHE event (IC-170922A) (Kopper & Blaufuss 2017) with energy ≈ 290 TeV associated with a flare from Blazar TXS 0506+056 (Aartsen et al. 2018). This opened the possibility to establish a link between the neutrino signal and the electromagnetic emission at different energy ranges, which is of key importance in the search for the privileged target of hadronic interaction processes, as well as for a pion decay component at VHE.

However, the blazar contribution to the diffuse astrophysical flux measured by IceCube is still a matter of debate (Aartsen et al. 2017). The diffuse Galactic contribution (Gaggero et al. 2015) is constrained by recent analyses from IceCube and ANTARES (Aartsen et al. 2017a; Albert et al. 2017) to just 8.5% of the full sky measured neutrino flux, and large room remains for other AGNs (Atoyan & Dermer 2001; Padovani et al. 2016; Murase & Waxman 2016) and starburst galaxies (Tamborra et al. 2014; Peretti et al. 2020). In this work we investigate whether the long term observation, which is mainly characterized by the quiescent states, is well described by a leptonic scenario. On the other hand, by concentrating on a possible hadronic component during the flaring states, we remark the importance of the estimation of a DC factor to obtain long term neutrino expectations.

In this paper we analyze a sample of 38 bright blazars: **19** FSRQ and **19** BL Lacs from the Fermi 3FGL catalog (Acero et al. 2015), through 10 years of data (from 2008 to 2018). We made a first selection of the blazars with the highest flux values and, from them, we selected the ones with 'good' LC (not dominated by upper limits). The paper is organized as follows: in § 2 we analyse the LC for each source and identify the active states. Following two different procedures, we distinguish the steady-state phase from the active phase for each of the sources of the sample. In § 3 we calculate the duty cycle (DC) according to the baseline flux obtained with each procedure. In § 4 we discuss a possible negative correlation between the blazar's synchrotron peak frequency and the gamma-ray luminosity. In

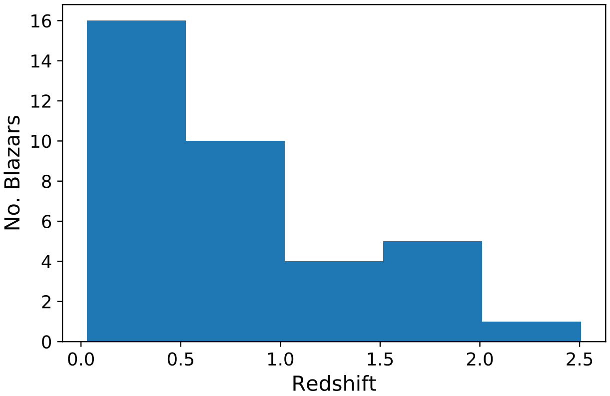

Fig. 1. Redshift distribution of the sample of blazars considered in this work. The color figure can be viewed online.

§ 5 we consider the DC value and the blazar sequence trend from § 4 as useful tools to better understand the physical processes at play in the potential neutrino sources. In § 6 we show our results. Finally, in § 7 we present our discussion and conclusions.

2. DATA ANALYSIS

We selected 38 of the blazars with highest flux values from the Fermi 3FGL catalog (Acero et al. 2015) as listed in Table 1. Among these, there are 2 with no reported redshift. Figure 1 shows the redshift distribution of the sample. The redshift and spectral type of each source were taken from Ackermann et al. (2015). In order to perform the data analysis we made use of the tool *Enrico* (Sanchez & Deil 2013) from the *Fermi Science Tools* (FSSC) software, version v11r5p3[10] (Asercion 2018). The analysis was performed in the energy range of 0.1 - 300 GeV, in a RoI (region of interest) with radius of 20°, considering the isotropic and Galactic diffuse emission components (iso_P8R2_SOURCE_v6_v06.txt and gll_iem_v06.fits[11]) falling within the RoI. For the cases in which we considered the extragalactic background light (EBL) absorption we used the model by Franceschini, Rodighiero, & Vaccari (2008) as reference.

We generated the LC for the 10-year period with two-month, one-month, two-week and one-week time bins. From these, we selected the two-week binning, since it allowed us to see periods of activity with good resolution while minimizing the number of upper limits (UL). Figure 2 shows the LC for the sources 3C 66A, a BL Lac in the Andromeda constellation, and Mkn 421, a BL Lac located in Ursa Major. We consider them as benchmark sources since they have been intensively studied in the last decade, they are relatively nearby sources [($z = 0.444$ (Miller et al. 1978) and $z = 0.03$ (de Vaucouleurs et al. 1991), respectively)] and flux and spectral information is available over the entire electromagnetic spectrum.

3. DUTY CYCLE

The duty cycle is the level of activity of a source. It is obtained by calculating the fraction of time that the source spends in the active phase (or flaring state, with the flux above a given threshold) with respect to the total observation period T_{obs} as a function of the flux:

$$\text{Duty cycle} = \text{DC} = \frac{\sum_{\rm i} {\rm t_i}}{\rm T_{obs}}. \quad (1)$$

Here, t_i is each of the time intervals the source spends in the flaring state (Vercellone et al. 2004). The baseline phase (or steady state) is defined as the fraction of time the flux remains below a given threshold.

In order to separate the active phase from the steady-state phase, we need to define a threshold value for the flux. There are different criteria to do this.

3.1. *Vercellone's Criterion*

Following the work of Vercellone et al. (2004), we define the threshold flux $F_{\rm thr}$ as 1.5 times the average flux of the source:

$$F_{\rm thr} = 1.5\ \overline{F}, \quad (2)$$

(see red-dotted lines in Figure 2). A source is in the active state when the flux of the ith time bin is $> F_{\rm thr}$ and the 1σ uncertainty of the ith time bin is smaller than the difference between the data point and $F_{\rm thr}$ (Jorstad et al. 2001).

The average flux $\overline{F}$ is defined as the weighted mean of all the detections and UL, with weight $w(\sigma) = 1/\sigma$, where σ is the uncertainty of the measurement. In the case of UL, σ is equal to the UL value. $\overline{F}$ can be decomposed into the fluence from the baseline states (flux below $F_{\rm thr}$) and the fluence from the flaring states (flux above $F_{\rm thr}$), respectively:

$$\overline{F} \times T_{\rm obs} = F_{\rm baseline} \times T_{\rm baseline} + \sum_i F_{\rm flare,i}\, t_i. \quad (3)$$

Here, $T_{\rm baseline}$ is the total time the source spends in the baseline state, $F_{\rm baseline}$ is the flux of the baseline state, i.e., the weighted average flux of the non-flaring state (below the threshold $F_{\rm thr}$), $F_{\rm flare,i}$ is the

---

[10] http://fermi.gsfc.nasa.gov/ssc/data/analysis/software.

[11] http://fermi.gsfc.nasa.gov/ssc/data/access/lat/BackgroundModels.html.

TABLE 1

LIST OF OUR SAMPLE OF BLAZARS*

3FGL name	Other name	Classification	Redshift	Spectral Type
J1015.0+4925	1H 1013+498	BL Lac	0.212	PowerLaw
J1229.1+0202	3C 273	FSRQ	0.16	LogParabola
J1256.1-0547	3C 279	FSRQ	0.5362	LogParabola
J2254.0+1608	3C 454.3	FSRQ	0.859	PLExpCutoff
J0222.6+4301	3C 66A	BL Lac	0.444	LogParabola
J1058.5+0133	4C +01.28	BL Lac	0.89	LogParabola
J1224.9+2122	4C +21.35	FSRQ	0.435	LogParabola
J0237.9+2848	4C +28.07	FSRQ	1.206	LogParabola
J1635.2+3809	4C +38.41	FSRQ	1.8139	LogParabola
J0238.6+1636	AO 0235+164	BL Lac	0.94	LogParabola
J1522.1+3144	B2 1520+31	FSRQ	1.4886	LogParabola
J2202.7+4217	BL Lacertae	BL Lac	0.686	LogParabola
J2001.1+4352	MG4 J2001.1+4352	BL Lac	-	PowerLaw
J1104.4+3812	Mkn421	BL Lac	0.031	PowerLaw
J1653.9+3945	Mkn 501	BL Lac	0.0337	PowerLaw
J1555.7+1111	PG 1553+113	BL Lac	0.5	LogParabola
J0428.6-3756	PKS 0426-380	BL Lac	1.111	LogParabola
J0449.4-4350	PKS 0447-439	BL Lac	0.205	PowerLaw
J0457.0-2324	PKS 0454-234	FSRQ	1.003	LogParabola
J0538.8-4405	PKS 0537-441	BL Lac	0.892	LogParabola
J0730.2-1141	PKS 0727-11	FSRQ	1.591	LogParabola
J0808.2-0751	PKS 0805-07	FSRQ	1.8369	LogParabola
J1246.7-2547	PKS 1244-255	FSRQ	0.638	LogParabola
J1427.0+2347	PKS 1424+240	BL Lac	-	LogParabola
J1504.4+1029	PKS 1502+106	FSRQ	1.8379	LogParabola
J1512.8-0906	PKS 1510-089	FSRQ	0.3599	LogParabola
J1625.7-2527	PKS 1622-253	FSRQ	0.7860	LogParabola
J1833.6-2103	PKS 1830-211	FSRQ	2.507	LogParabola
J2158.8-3013	PKS 2155-304	BL Lac	0.116	LogParabola
J2236.5-1432	PKS 2233-148	BL Lac	0.3250	LogParabola
J2329.3-4955	PKS 2326-502	FSRQ	0.518	LogParabola
J1427.9-4206	PKS B1424-418	FSRQ	1.5220	LogParabola
J1802.6-3940	PMN J1802-3940	FSRQ	1.319	LogParabola
J2345.2-1554	PMN J2345-1555	FRSQ	0.621	LogParabola
J0112.1+2245	S2 0109+22	BL Lac	0.265	LogParabola
J0721.9+7120	S5 0716+71	BL Lac	0.300	LogParabola
J0509.4+0541	TXS 0506+056	BL Lac	0.3365	PowerLaw
J0521.7+2113	TXS 0518+211	BL Lac	0.108	PowerLaw

*The redshift value (z) is indicated when available, and marked with '-' when unknown.

average flux of the ith flare and t_i is the duration of each flare. Note that, for Vercelone's criterion, the value of F_{baseline} is fixed once we fix the value of F_{thr}.

3.2. 3σ *or Tluczykont Criterion*

According to Tluczykont et al. (2010), we organize the data into a flux histogram, as shown in Figure 3. A flux state is defined as the integrated flux value in each time bin, obtained from the source LC. We then organize the data into a flux histogram (flux vs. number of events with that value of the flux) and fit them with the sum of a Gaussian and a Log-Normal distribution[12], $f_G + f_{LN}$. The Gaussian,

$$f_G(\mathrm{x}) = \frac{\mathrm{A_G}}{\sigma_\mathrm{G}\sqrt{2\pi}}\exp\left(\frac{-(\mathrm{x}-\mu_\mathrm{G})^2}{2\,\sigma_\mathrm{G}^2}\right), \qquad (4)$$

represents the baseline state, and the Log-Normal,

$$f_{LN}(\mathrm{x}) = \frac{\mathrm{A_{LN}}}{\mathrm{x}\sigma_\mathrm{LN}\sqrt{2\pi}}\exp\left(\frac{-(\log(\mathrm{x})-\mu_\mathrm{LN})^2}{2\,\sigma_\mathrm{LN}^2}\right), \qquad (5)$$

---

[12] Here, x represents the values of the flux for a given blazar, while $f_G(\mathrm{x})$ and $f_{LN}(\mathrm{x})$ represent the number of occurrences (number of time intervals that have a flux x).

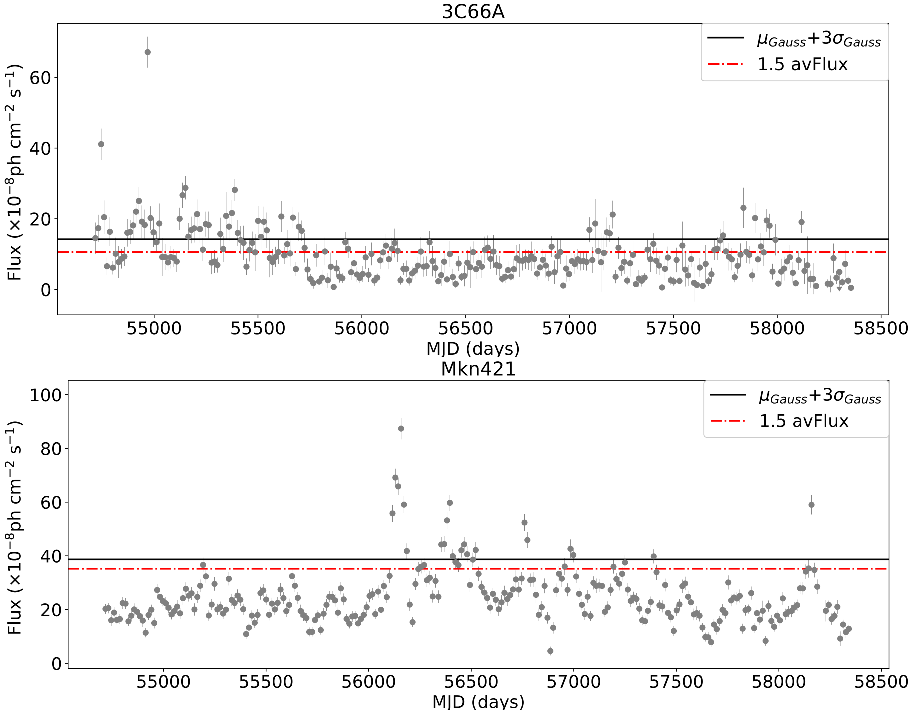

Fig. 2. Flux light curves (considering EBL absorption) for the sources 3C 66A and Mkn 421 using a two-week binning. The red dashed-dotted line and the black solid line are the threshold flux F_{thr} calculated according to Vercellone's criterion and the $\mu_G + 3\sigma$ criterion (Tluczykont). The color figure can be viewed online.

describes the active-state phases. The parameters μ_G, σ_G and A_G are the mean, standard deviation and normalization for the Gaussian distribution, while μ_{LN}, σ_{LN} and A_{LN} are the mean, standard deviation and normalization for the Log-Normal distribution. The parameters of the fits of the entire sample can be found in Appendix A.

According to Tluczykont's criterion, the source threshold flux F_{thr} is a variable in the range from $3\,\sigma_G$ to $\mu_G + 3\,\sigma_G$. We define the flux $F_{baseline}$ as the mean value of all the non-flaring states:

$$F_{baseline} = \frac{\int_0^{F_{thr}} x\, f_G(x)\, dx}{\int_0^{F_{thr}} f_G(x)\, dx}. \tag{6}$$

If the flux is $> F_{\rm thr}$ the source is considered to be in the active phase. We recall that

$$T_{\rm baseline} = T_{\rm obs} - T_{\rm flare}, \tag{7}$$

with $T_{\rm flare} = \sum_i t_i$.

Following the work of Abdo et al. (2014), we calculated the average flare flux

$$\langle F_{flare}\rangle = \frac{\int_{F_{\rm thr}}^{F_{\rm max}} x\, f_{LN}(x)\, dx}{\int_{F_{\rm thr}}^{F_{\rm max}} f_{LN}(x)\, dx} \tag{8}$$

as a function of $F_{\rm thr}$ and $F_{\rm max}$, the maximum flux detected.

In order to obtain the average flux of the flaring states we need to replace F_{flare} by $\langle F_{flare}\rangle$. Substituting these quantities in equation (3) we obtain

$$DC = \frac{T_{\rm flare}}{T_{\rm [obs]}} = \frac{\overline{F} - F_{\rm baseline}}{\langle F_{\rm flare}\rangle - F_{\rm baseline}}. \tag{9}$$

Figure 4 shows the plots of the DC obtained for 3C 66A and Mkn 421. In particular, the value of the DC obtained for Mrk 421 (av DC= 24.7%) is consistent with the results reported by Patricelli et al. (2014) and Abdo et al. (2014) using 3 year Milagro data in the TeV energy range. The DC plots for the whole sample are shown in Appendix B.

The threshold flux calculated for 3C 66A is $F_{\rm thr} = 1.4 \times 10^{-7}$ ph cm^{-2} s^{-1} (Tluczykont criterion, black solid line in Figure 2) and $F_{\rm thr} = 1.06 \times 10^{-7}$ ph cm^{-2} s^{-1} (Vercellone's criterion, red dashed-dotted line in Figure 2). In the case of Mkn 421, $F_{\rm thr} = 3.87 \times 10^{-7}$ ph cm^{-2} s^{-1} (Tluczykont criterion) and $F_{\rm thr} = 3.52 \times 10^{-7}$ ph cm^{-2} s^{-1} (Vercellone's criterion). We recall that these values

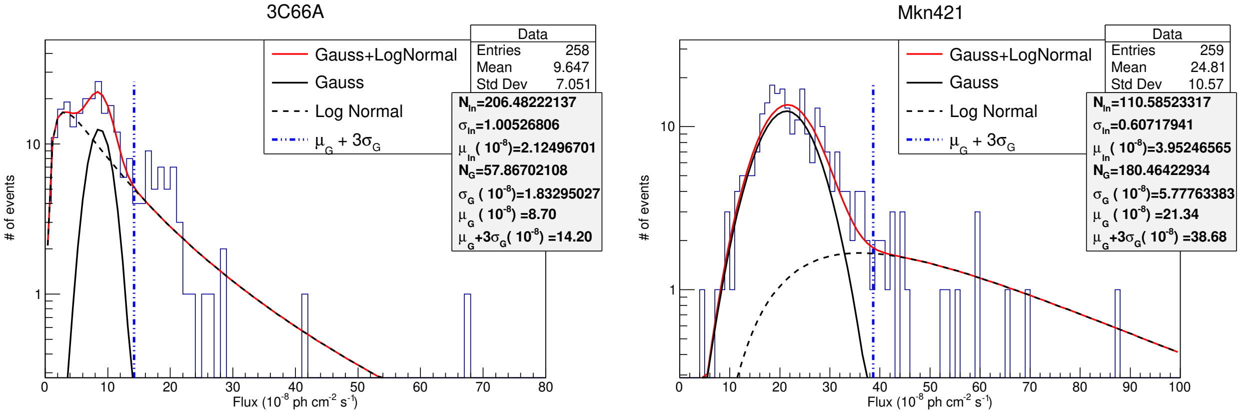

Fig. 3. Flux distribution for the sources 3C 66A and Mkn 421 considering EBL absorption. The black dotted line is the fit with the Log-Normal distribution, the black solid line is the fit with the Gaussian distribution, the red solid line is the fit with the sum of both distributions and the blue dotted line represents the threshold value. The color figure can be viewed online.

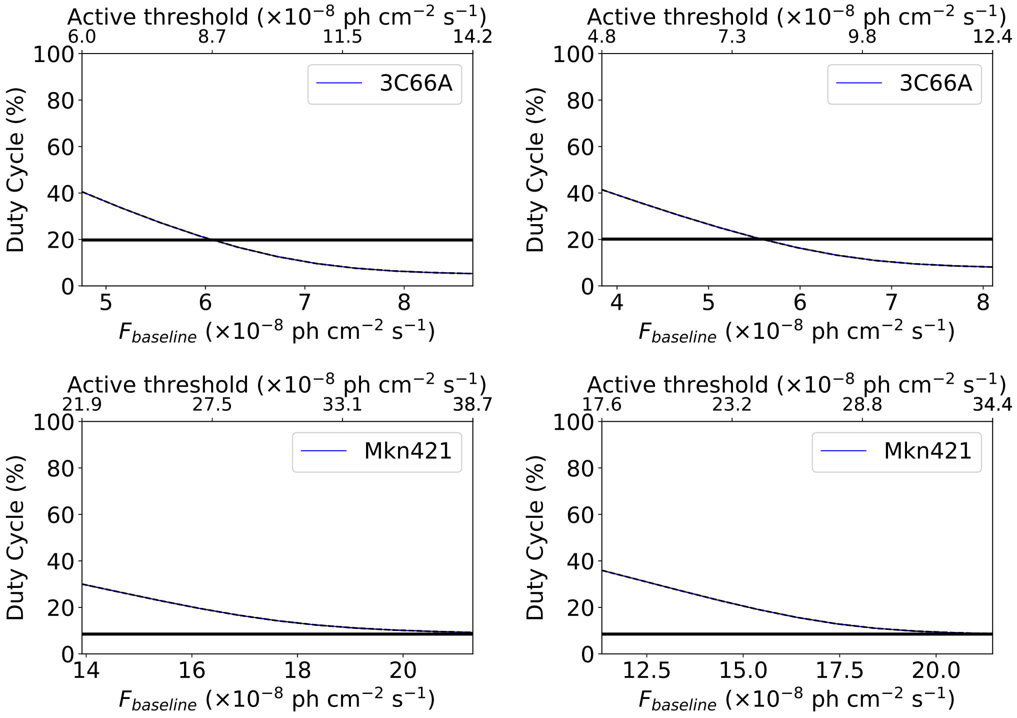

Fig. 4. DC vs. flux with (left panels) and without (right panels) EBL absorption, for 3C 66A (upper panels) and Mkn 421 (lower panels). The blue (black) lines represent the DC range inferred from Tluczykont (Vercellone's) criterion. The color figure can be viewed online.

of $F_{\rm thr}$ have been calculated considering EBL absorption.

4. BLAZAR SEQUENCE

Fossati et al. (1998), Kubo et al. (1998) and Donato et al. (2001) observed a negative correlation between the peak frequency of the synchrotron emission from blazars and their bolometric luminosities (traced through their radio luminosities in their observations). It was named the *observational blazar sequence*, and was thought to be an evidence in favor of leptonic emission from the source. This was later

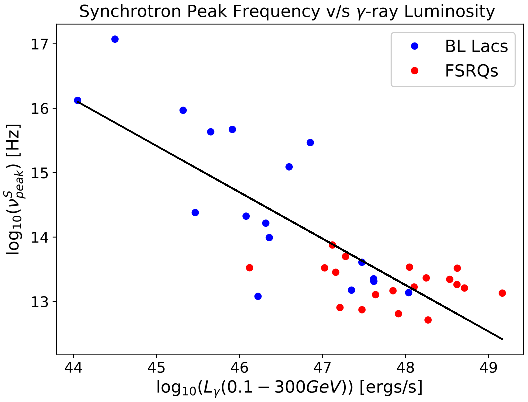

Fig. 5. Correlation between the synchrotron peak frequency and gamma-ray luminosity (0.1 - 300 GeV) for our sample. BL Lacs are shown in blue and FSRQs in red. The black line represents the best fit for the combined sub-sets. The color figure can be viewed online.

revealed to be a result of selection bias, although the existence of a physical blazar sequence (Ghisellini et al. 1998) was explained due to the different cooling experienced by the electrons under different environments in BL Lacs and FSRQs.

In the case of blazars, the gamma-ray luminosity can be a better indicator of the integrated bolometric luminosity than the radio luminosity (Fossati et al. 1998; Wang, Z. et al. 2017). It is thus possible to explore this relationship between the two variables for our sample, using Fermi-LAT data accumulated over 10 years. Figure 5 shows the integrated gamma-ray luminosity (L_γ) in the 0.1 - 300 GeV range, averaged over 10 years of observation, vs. the synchrotron peak frequency (${\nu^s}_{\rm peak}$) for each source. The value of ${\nu^s}_{\rm peak}$ has been obtained from the 3FHL catalog (Ajello et al. 2017) when available. Luminosities have been calculated assuming a ΛCDM Universe with standard cosmological parameters ($H_0 = 67.8$, $\Omega_m = 0.308$, $\Omega_\lambda = 0.692$).

The two sub-samples of BL Lacs and FSRQs show a negative correlation trend, the FSRQs having higher luminosity and lower peak frequency on average as compared to the set of BL Lacs. The combined sample of BL Lacs and FSRQs has a Pearson coefficient of -0.7, with a best-fit slope of -0.72 ± 0.10. This moderate correlation trend can be interpreted in the context of leptonic emission favored in the inner part of the jet, providing information on the sub-PeV neutrino emission from this region (Murase et al. 2014). Other authors (Finke 2013) argue that there is a correlation between Compton dominance and the peak frequency of the synchrotron component, which is also consistent with the blazar sequence.

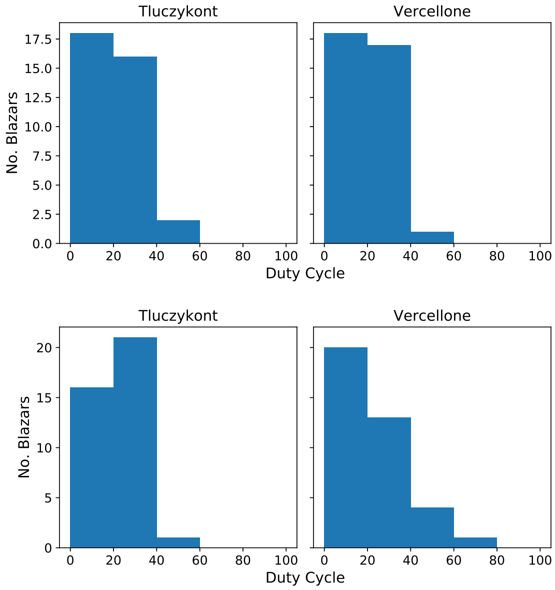

Fig. 6. DC distribution of our samples according to Tluczykont's (left panels) and Vercellone's (right panels) criteria, considering EBL absorption (upper panels) and not considering it (lower panels). The color figure can be viewed online.

5. THE MULTIMESSENGER CASE AND VERY HIGH ENERGY NEUTRINO EMISSION

In this work, two important multimessenger aspects of gamma-ray emission from blazars were analyzed: the DC value and the blazar sequence trend. In particular, they can be used to better understand the physical processes responsible for the gamma-ray emission and to constrain a possible VHE neutrino counterpart. The first parameter represents a duty factor of the blazar activity, and it is considered a crucial factor whenever a long term unblinded analysis is done with a neutrino telescope, taking into account one or more VHE emitting blazars. In particular, under the assumption that the hadronic emission can be amplified during the VHE flaring states, it is worth using this value to set the expected neutrino observations. Figure 6 shows the value of average DCs of the samples obtained with 10 years of Fermi-LAT data. Taking them into account, the known ULs of full-sky neutrino emission expected from blazars can change by a factor > 2. In fact, the full sky upper limit reported by IceCube collaboration for blazars considering the unblinded point-like

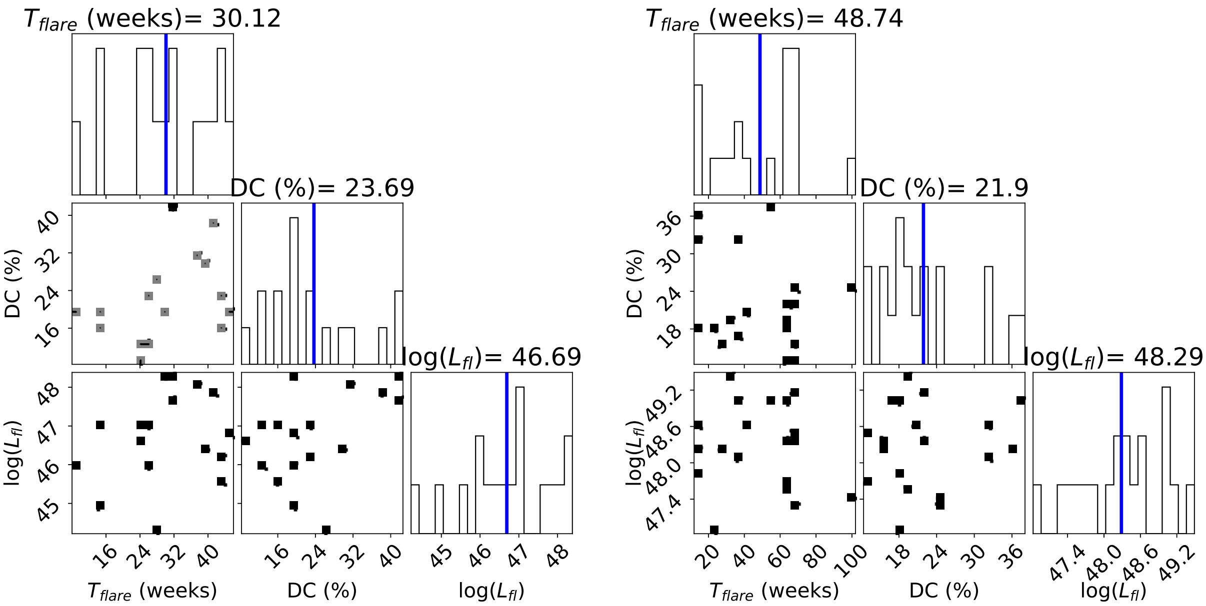

Fig. 7. Relation between flare duration (T_{flare}), duty cycle (DC) and flare luminosity (L_{ff}) for BL Lac type (left panel) and FSRQ type blazars (right panel). The color figure can be viewed online.

searches (Aartsen et al. 2017) does not consider the DC for the weighting factor ($w_{\gamma/\nu}$) when deducing possible neutrino flux from the gamma-ray emission.

In more detail, the contribution to the diffuse astrophysical neutrino flux observed by IceCube (Aartsen et al. 2020, 2016, 2017b) attributed to blazars will decrease from 27% to 7% in Aartsen et al. (2017), for energies $>$ 10 TeV, and from 40-80% to 10-20% in IceCube Collaboration et al. (2018) for energies $>$ 200 TeV, when an average DC of 26% is considered. This decreasing factor on the expected neutrino flux will be quite independent of the blazar gamma-ray luminosity reached during the flaring periods even though the possibility to observe it during such activity period is strictly dependent on that, under the assumption of an amplified hadronic emission of active states.

While the DC can represent a temporal constraint on the hadronic activity from BL Lacs and FSRQs, the blazar sequence trend can constrain the emitting process as well as the energy range of VHE neutrinos produced, limiting the production of sub-PeV neutrinos (Murase et al. 2014) by the interaction of jet accelerated protons with the ambient photon fields. The trend shown in Figure 5 can be explained assuming that a self-synchrotron Compton (SSC) emission scenario takes place in the inner part of the jet. Assuming the results of Murase et al. (2014), Figure 5 favors FSRQs as opposed to BL Lacs as the main candidates for neutrino production in the range 1-100 PeV. Moreover, it is worth highlighting the fact that the blazar sequence reported here takes into account the full Fermi-LAT data set, which is dominated by the quiescent periods and does not exclude a different emission scenario during the flaring periods. If that were the case, Figure 7 shows that we cannot discriminate which class of blazars, BL Lacs or FSRQs, can produce a higher neutrino fluence over a longer observational period.

We searched for possible correlations between these variables. However, no correlation was found. Furthermore, we found no correlation between DC and the source redshift, independently of the criterion used.

6. RESULTS

Tables 2 and 3 show the DC values for all the sources with and without EBL absorption, according to Tluczykonts and Vercellone's criteria. We calculated the DC in the 0.1-300 GeV energy range for $\approx$ 10 years of Fermi-LAT data (2008 - 2018). The table includes: for the Tluczykont criterion, the DC obtained considering the maximum baseline flux (DC$_{bl}$%), the DC obtained assuming 0 as the baseline flux (DC$_0$%), and the average DC for each source (DC$_{av}$%). For Vercellone's criterion, the DC value and its error. The distribution of the values presented in the tables is shown in Figure 6.

TABLE 2

DC VALUES CALCULATED FOR EACH SOURCE CONSIDERING EBL ABSORPTION. FOR OBJECTS WITHOUT A KNOWN REDSHIFT, DC HAS NOT BEEN CALCULATED

Source Name	Tluczykont			Vercellone	
	$DC_{bl}\%$	$DC_0\%$	$DC_{av}\%$	DC %	error DC %
1H 1013+498	8.59	18.18	13.39	5.81	0.01
3C 273	15.73	19.47	17.6	17.05	0.03
3C 279	14.32	15.94	15.13	22.69	0.04
3C 454.3	16.20	16.82	16.51	11.63	0.02
3C 66A	5.29	40.53	22.91	19.77	0.04
4C +01.28	37.12	38.73	37.93	32.56	0.06
4C +21.35	12.06	12.66	12.36	27.31	0.06
4C +28.07	14.47	15.96	15.21	23.05	0.05
4C +38.41	20.47	22.49	21.48	28.96	0.06
AO 0235+164	18.66	20.68	19.67	22.48	0.04
B2 1520+31	29.00	35.86	32.43	21.58	0.05
BL Lacertae	38.86	46.33	42.60	26.36	0.5
MG4 J2001.1+4352	-	-	-	-	-
Mkn 421	9.21	30.01	19.61	8.49	0.02
Mkn 501	15.03	37.15	26.09	7.39	0.01
PG 1553+113	4.11	27.40	15.76	3.46	0.01
PKS 0426-380	40.62	43.57	42.10	25.1	0.05
PKS 0447-439	16.7	29.31	23.01	12.69	0.03
PKS 0454-234	35.2	37.03	36.12	25.49	0.05
PKS 0537-441	29.43	34.52	31.97	26.54	0.05
PKS 0727-11	16.95	23.43	20.19	19.52	0.04
PKS 0805-07	12.75	13.44	13.09	20.08	0.04
PKS 1244-255	20.64	27.46	24.05	18.99	0.04
PKS 1424+240	-	-	-	-	-
PKS 1502+106	35.32	40.84	38.08	23.17	0.05
PKS 1510+089	16.64	20.14	18.39	19.62	0.04
PKS 1622-253	31.86	33.38	32.62	28.4	0.06
PKS 1830-211	16.11	23.56	19.83	12.79	0.03
PKS 2155-304	11.53	20.31	15.92	14.62	0.03
PKS 2233-148	12.25	13.13	12.69	22.83	0.05
PKS 2326-502	14.87	23.12	18.99	41.09	0.08
PKS B1424-418	14.57	21.51	18.04	19.18	0.04
PMN J1802-3940	21.75	22.22	21.98	30.24	0.06
PMN J2345-1555	19.39	28.6	24.00	16.33	0.04
S2 0109+22	2.75	58.24	30.49	25	0.05
S5 0716+71	0.7	15.89	8.3	16.02	0.03
TXS 0506+056	14.16	26.3	20.23	13.51	0.03
TXS 0518+211	13.54	26.41	19.98	13.33	0.03
Mean values	18.24	27.24	22.74	20.09	

Following the Tluczykont criterion, the average DC for the sample when considering EBL absorption (and not) is 22.74% (23.08%). According to Vercellone's criterion we obtained values of 20.09% (22.27%). The blazars PKS 0426-380 and BL Lacertae have the highest DC values (considering EBL absorption), with an average DC of $\approx 42\%$ and 43%, respectively (Tluczykont's criterion). On the other hand, the lowest value of DC obtained corresponds to Blazar S5 0716+71 with a DC_{av} value of $\approx 8\%$ considering EBL absorption (Tluczykont's criterion).

At this point, we must consider the following: choosing a flare flux threshold in terms of the time average flux (Vercellone's criterion) does not allow a direct comparison of DC between sources to be made, because the time average flux is influenced by

TABLE 3

DC VALUES CALCULATED FOR EACH SOURCE WITHOUT EBL ABSORPTION

Source Name	Tluczykont			Vercellone	
	DC_{bl}%	DC_0%	DC_{av}%	DC %	error DC %
1H 1013+498	11.46	40.14	25.80	3.49	0.01
3C 273	16.63	21.03	18.83	16.99	0.03
3C 279	14.04	14.99	14.52	7.72	0.02
3C 454.3	16.2	16.82	16.51	11.63	0.02
3C 66A	8.12	41.42	24.77	20.16	0.04
4C +01.28	31.52	32.12	31.82	32.56	0.07
4C +21.35	15.54	16.70	16.12	4.64	0.01
4C +28.07	19.39	23.24	21.32	23.83	0.05
4C +38.41	12.86	14.93	13.89	4.26	0.01
AO 0235+164	18.37	20.87	19.62	26.25	0.05
B2 1520+31	35.27	43.21	39.24	22.78	0.04
BL Lacertae	41.20	49.60	45.4	26.36	0.05
MG4 J2001.1+4352	7.40	13.24	10.32	13.18	0.03
Mkn 421	8.67	35.93	22.3	8.49	0.02
Mkn 501	12.97	33.92	23.45	6.98	0.01
PG 1553+113	13.52	22.35	17.93	11.58	0.02
PKS 0426-380	37.2	41.14	39.17	53.46	0.1
PKS 0447-439	13.59	27.59	20.59	12.69	0.03
PKS 0454-234	33.71	40.53	37.12	21.24	0.05
PKS 0537-441	28.36	31.41	29.88	55.21	0.1
PKS 0727-11	27.75	37.59	32.67	18.38	0.04
PKS 0805-07	2.32	3.49	2.9	39.15	0.08
PKS 1244-255	11.33	16.95	14.14	62.16	0.1
PKS 1424+240	16.24	25.36	20.80	40.15	0.08
PKS 1502+106	16.34	17.68	17.53	18.08	0.04
PKS 1510+089	13.80	16.10	14.95	15.77	0.03
PKS 1622-253	32.17	33.78	32.98	28	0.06
PKS 1830-211	19.38	25.96	22.67	14.01	0.03
PKS 2155-304	13.44	23.43	18.44	13.46	0.03
PKS 2233-148	17.81	20.03	18.92	21.2	0.04
PKS 2326-502	22.75	24.98	23.87	41.08	0.08
PKS B1424-418	14.31	19.41	16.86	17.83	0.04
PMN J1802-3940	23.82	24.32	24.07	32.13	0.07
PMN J2345-1555	26.37	33.71	29.67	36.54	0.07
S2 0109+22	0.84	53.99	27.41	25	0.05
S5 0716+71	0.70	15.89	8.30	16.02	0.03
TXS 0506+056	19.96	35.59	27.78	10.81	0.02
TXS 0518+211	26.78	42.29	34.54	12.74	0.03
Mean values	18.47	27.67	23.08	22.27	

the level of activity. In the case of a highly active source, the time average flux, and consequently its flare flux threshold, would be much higher than the baseline flux, so the DC only refers to the highest flux states. On the contrary, for a less active source the time average flux is close to the baseline flux, so the DC refers to almost all the flaring states. Since the DC of an active source includes only the highest flux-flaring states, it is possible to obtain a DC value smaller than the one for a less active source and erroneously conclude that the latter is more active than the former. In general, Tluczykont criterion leads to a higher DC average value than Vercellone's criterion.

Figure 7 shows the average DC and flare luminosity (Tluczykont criterion) as a function of the major flare duration, together with flare luminosity vs DC. As seen from the figure, there is no significant difference between the values of DC for BL Lacs and FSRQ. We selected the major flares as the ones presenting the greatest number of consecutive temporal bins with the highest fluence in the 10-year dataset.

7. DISCUSSION AND CONCLUSION

We have presented the results of 10 years of Fermi-LAT data in the energy range of 0.1-300 GeV for a sample of 38 bright blazars following the two criteria presented in § 3. In particular, we have estimated the gamma-ray variability of the BL Lacs and FSRQs present in the sample, as well as the gamma-ray fluence during the activity periods. We have searched for the possible origin of this emission when looking at the entire observation time, dominated by quiescent periods, advocating a more enhanced hadronic component during the flaring periods.

The average DC for the whole sample following Tluczykont's criterion varies in the range [≈8-43]% considering EBL absorption. This implies that blazars present a wide range of activity levels. Ongoing work aims to make a complete spectral analysis of these sources. When correlating the gamma-ray activity to the hadronic emission from the sources, the obtained DC becomes relevant also for the calculation of the expected neutrino signal over a long observational period, as discussed in Marinelli et al. (2019). In particular, the average DC values reported in Figure 7 can be used as a scaling factor for the expected neutrino fluence. It is noteworthy, however, that the variance of the DC inferred considering EBL and not considering it is negligible, which would imply that the DC is not affected by the EBL absorption at these energies and distances. Even though the sample is small, a quick analysis shows that there is no correlation between DC and redshift (nor between DC and luminosity) for this sample of blazars. However, further analysis is required in order to make a stronger statement. Finally, we find that, for this sample, there is no notorious difference between the DC values inferred for FSRQ and BL Lacs (see Figure 7).

JRS acknowledges DIGI-USAC for financial support by Grant 4.8.63.4.44 and DGAPA-UNAM IG101320. **AVP** acknowledges the National Research Council of Argentina (CONICET) by Grant PIP 616, and by the Agencia Nacional de Promoción Científica y Tecnológica (ANPCYT) PICT 140492. **AM** acknowledges Istituto Nazionale di Fisica Nucleare (INFN), Ministero dell' Universitá e della Ricerca (MIUR), PRIN 2017 program (Grant NAT-NET 2017W4HA7S) Italy. **MC** acknowledges Fundação de Ampara à Pesquisa do Estado de São Paulo (FAPESP) for financial support under Grants #2015/25972-0 and #2017/00968-6.

APPENDIX

A. FIT PARAMETERS

TABLE 4

LN+G DISTRIBUTION FIT PARAMETERS. FLUX IS IN UNITS $\times 10^{-8}$

Source name	EBL Correction				No EBL Correction			
	μ_{LN}	σ_{LN}	μ_G	σ_G	μ_{LN}	σ_{LN}	μ_G	σ_G
1H 1013+498	3.43	0.93	4.87	1.83	2.97	1.02	6.31	1.54
3C 273	4.55	1.23	12.99	5.07	4.47	1.18	13.05	4.53
3C 279	6.22	1.49	21.91	11.58	6.33	1.55	15.14	9.96
3C 66A	2.12	1.01	8.70	1.83	2.35	1.1	8.11	1.42
4C +01.28	3.27	1.65	0.96	2.36	3.65	1.12	0.69	3.00
4C +21.35	17.48	4.42	8.25	10.91	10.56	3.77	4.78	1.83
4C +28.07	5.09	1.66	8.83	13.90	5.18	1.81	11.59	7.69
4C +38.41	5.21	1.01	13.70	13.74	4.94	1.72	6.66	2.34
AO 0235+164	5.72	1.93	4.67	2.33	5.91	2.13	5.08	2.36
B2 1520+31	3.58	0.75	9.26	8.03	4.18	0.65	15.03	8.17
BL Lacertae	3.95	1.04	8.58	5.19	3.89	1.05	8.47	4.52
MG4 J2001.1+4352	-	-	-	-	4.52	2.31	4.35	1.92
Mkn421	3.95	0.60	21.34	5.77	4.34	1.13	21.48	4.32
Mkn 501 1	2.58	0.51	6.06	2.16	2.74	0.42	8.13	3.37

TABLE 4. (CONTINUED)

Source name	EBL Correction				No EBL Correction			
	μ_{LN}	σ_{LN}	μ_G	σ_G	μ_{LN}	σ_{LN}	μ_G	σ_G
PG 1553+113	3.17	0.11	12.53	4.13	2.87	0.73	4.99	2.65
PKS 0426-380	3.88	0.78	4.69	7.74	3.84	0.72	6.39	8.16
PKS 0447-439	3.70	0.96	8.60	3.78	3.35	0.91	9.15	4.00
PKS 0454-234	3.81	1.05	2.91	8.15	3.63	0.62	8.65	5.28
PKS 0537-441	4.67	1.45	6.41	2.88	4.60	1.29	5.07	3.14
PKS 0727-11	4.38	1.09	12.44	7.73	4.51	0.69	23.08	12.21
PKS 0805-07	4.46	1.83	1.87	3.78	0.75	1.45	5.01	4.23
PKS 1244-255	4.22	1.12	7.80	3.12	0.60	1.05	7.05	3.26
PKS 1424+240	-	-	-	-	2.69	0.76	5.43	3.53
PKS 1502+106	5.17	1.67	8.73	3.82	5.53	1.83	4.93	1.72
PKS 1510-089	7.14	1.69	37.06	21.16	6.29	1.48	25.86	11.14
PKS 1622-253	0.89	0.22	2.20	1.06	8.59	2.18	23.6	11.85
PKS 1830-211	5.17	0.89	31.88	11.93	4.04	1.26	12.52	3.56
PKS 2155-304	3.37	0.55	8.10	3.70	3.22	0.60	7.82	3.56
PKS 2233-148	4.81	1.98	2.15	1.61	2.74	1.56	2.07	1.73
PKS 2326-502	5.77	1.70	13.35	2.17	19.19	4.81	4.52	1.24
PKS B1424-418	4.32	0.69	31.46	22.91	5.34	0.77	35.14	21.78
PMN J1802-3940	12.08	2.68	13.64	7.35	22.19	4.28	12.65	6.66
PMN J2345-1555	3.32	1.17	5.9	1.8	3.32	1.08	5.32	1.90
S2 0109+22	2.21	1.23	9.38	1.46	2.38	1.25	9.56	1.50
S5 0716+71	3.30	1.56	13.60	6.16	3.3	1.56	13.60	6.17
TXS 0506+056	2.29	0.91	6.60	3.13	2.59	0.78	5.13	1.63
TXS 0518+211	2.63	0.83	11.70	5.97	3.42	0.97	7.71	1.78

B. DUTY CYCLE PLOTS

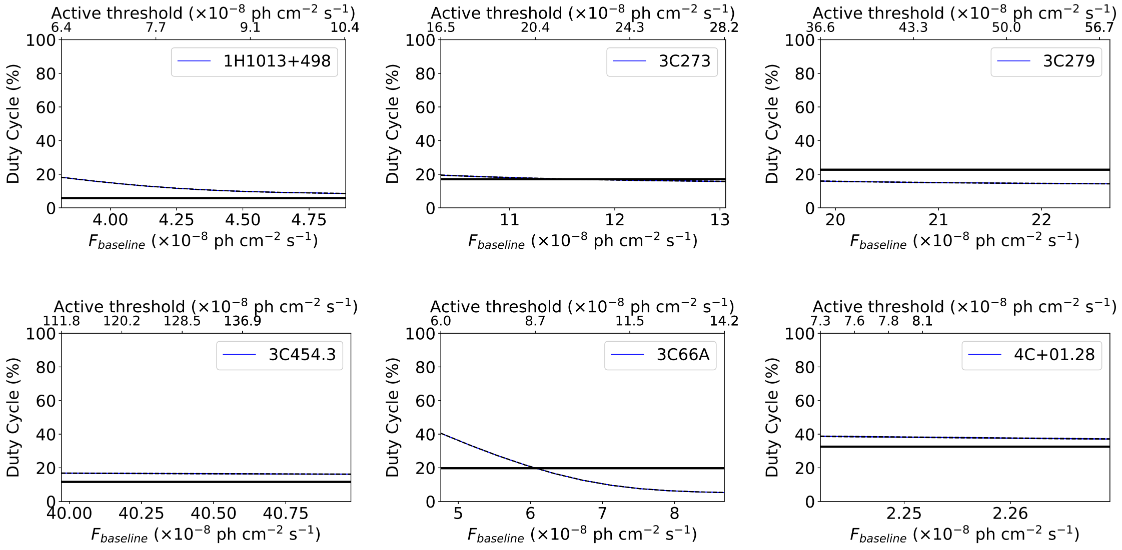

Fig. 8. DC vs. flux conidering EBL absorption. The blue (black) lines represent the DC range inferred from the Tluczykont (Vercellone) criterion. The color figure can be viewed online.

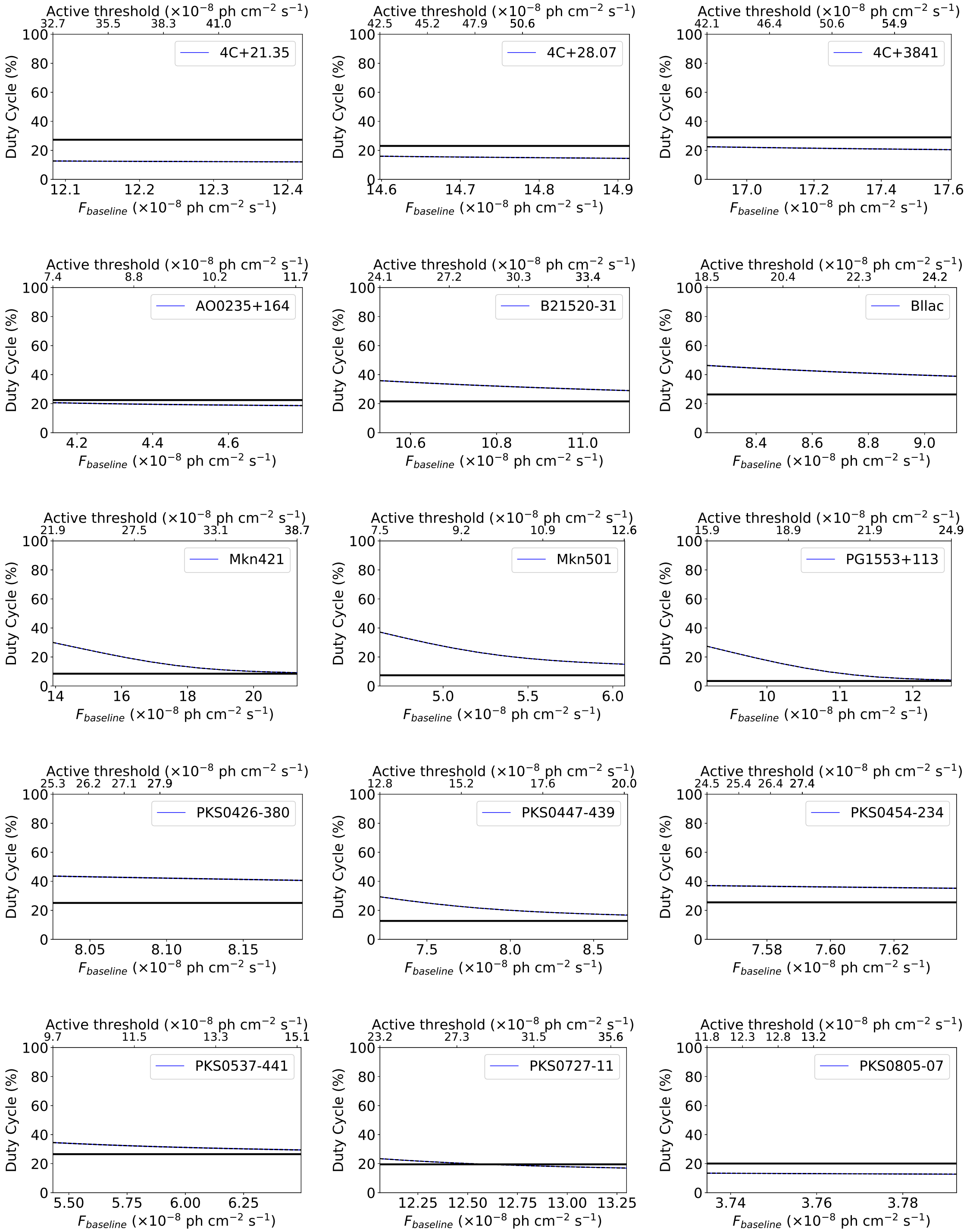

Fig. 8. (Continued)

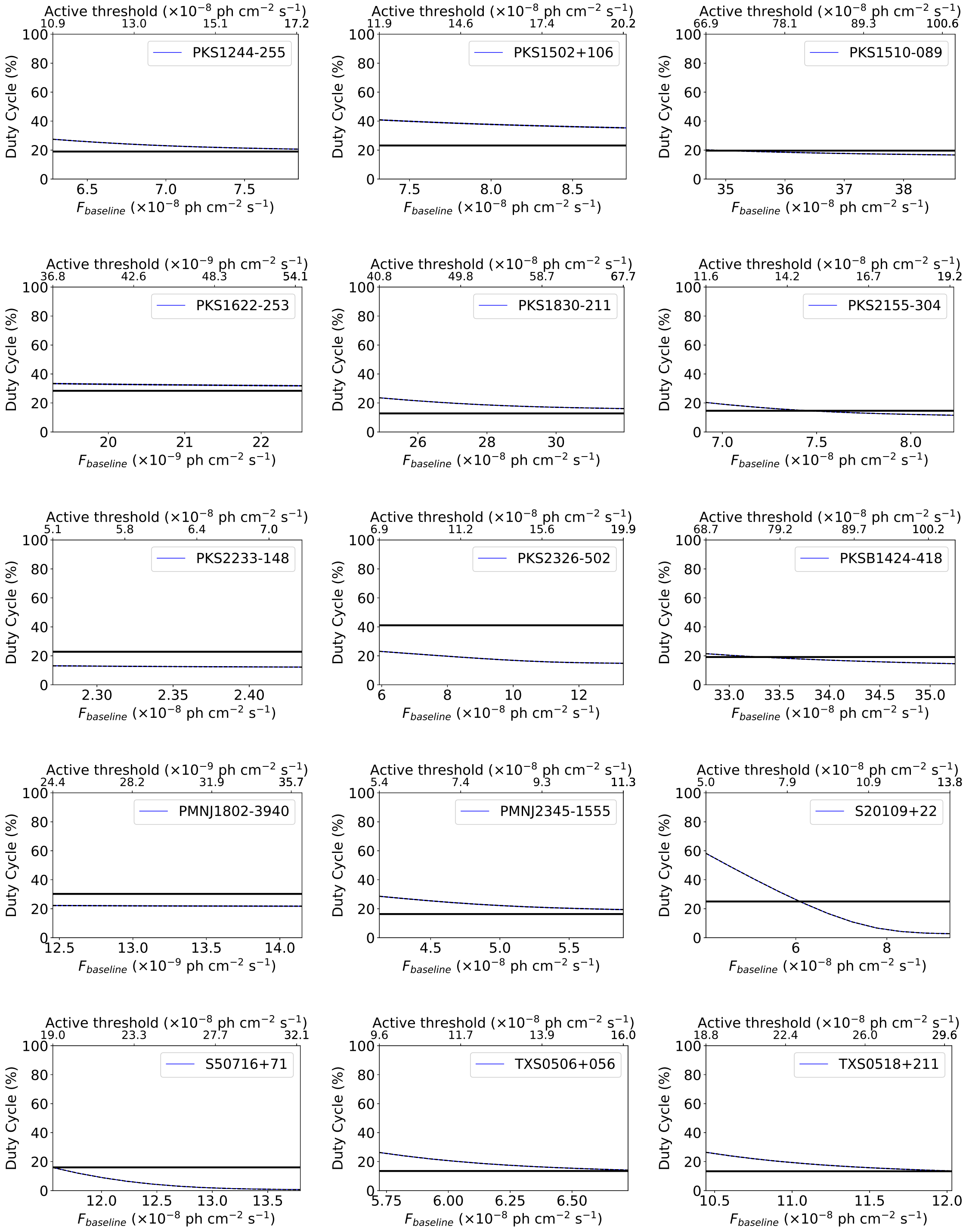

Fig. 8. (Continued)

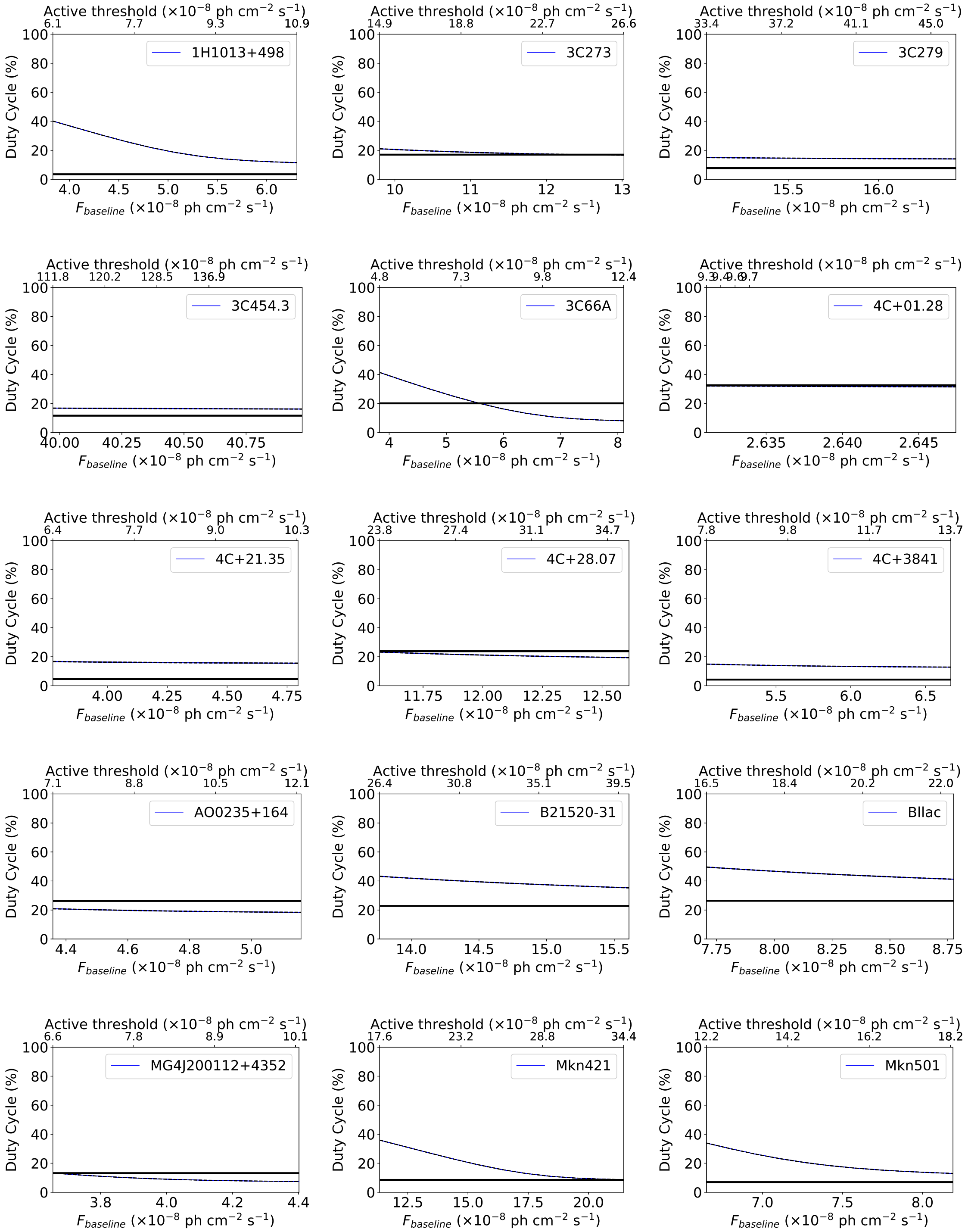

Fig. 9. DC vs. flux for each source of the sample, with no EBL absorption. The blue (black) lines represent the DC range inferred from the Tluczykont (Vercellone) criterion. The color figure can be viewed online.

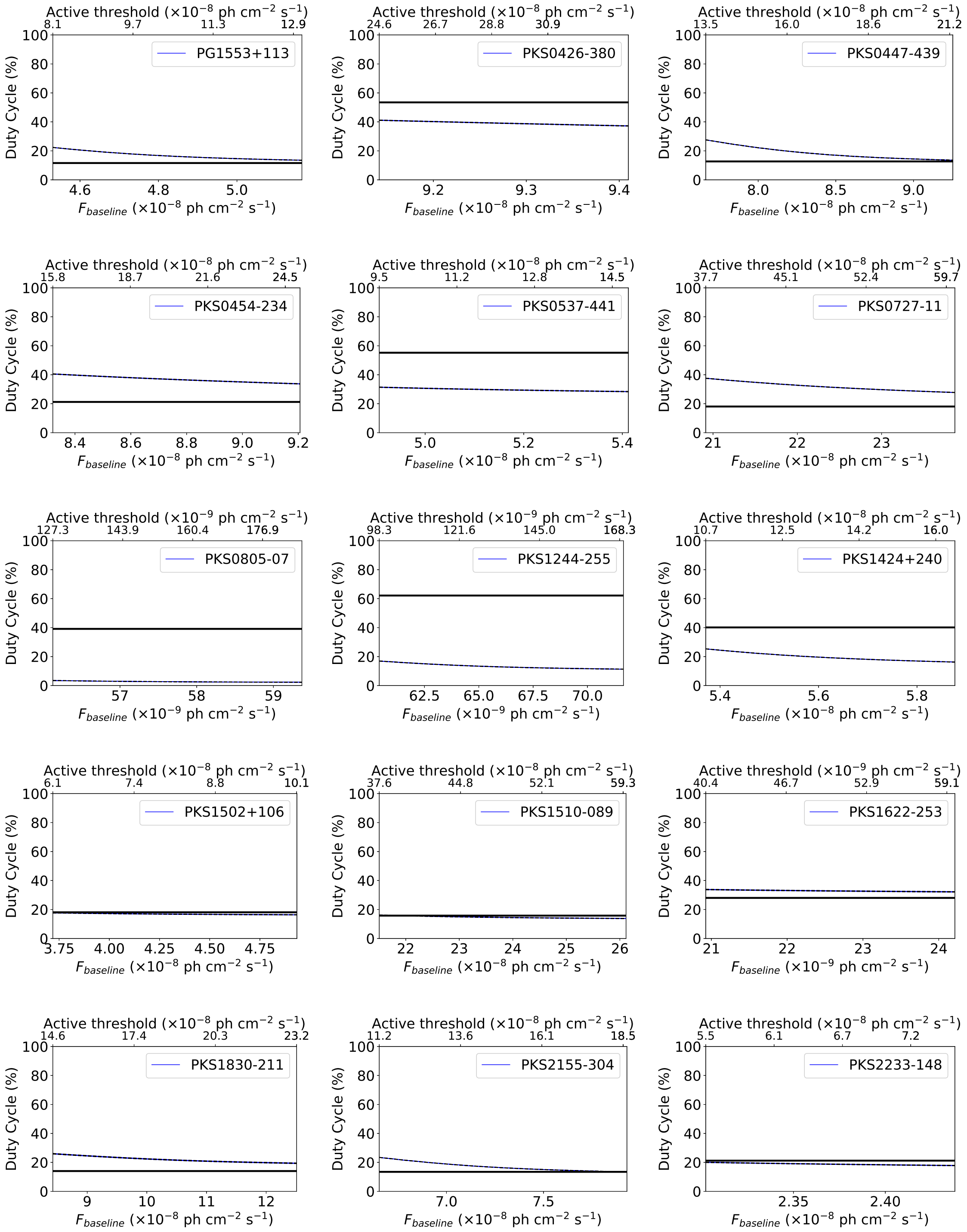

Fig. 9. (Continued)

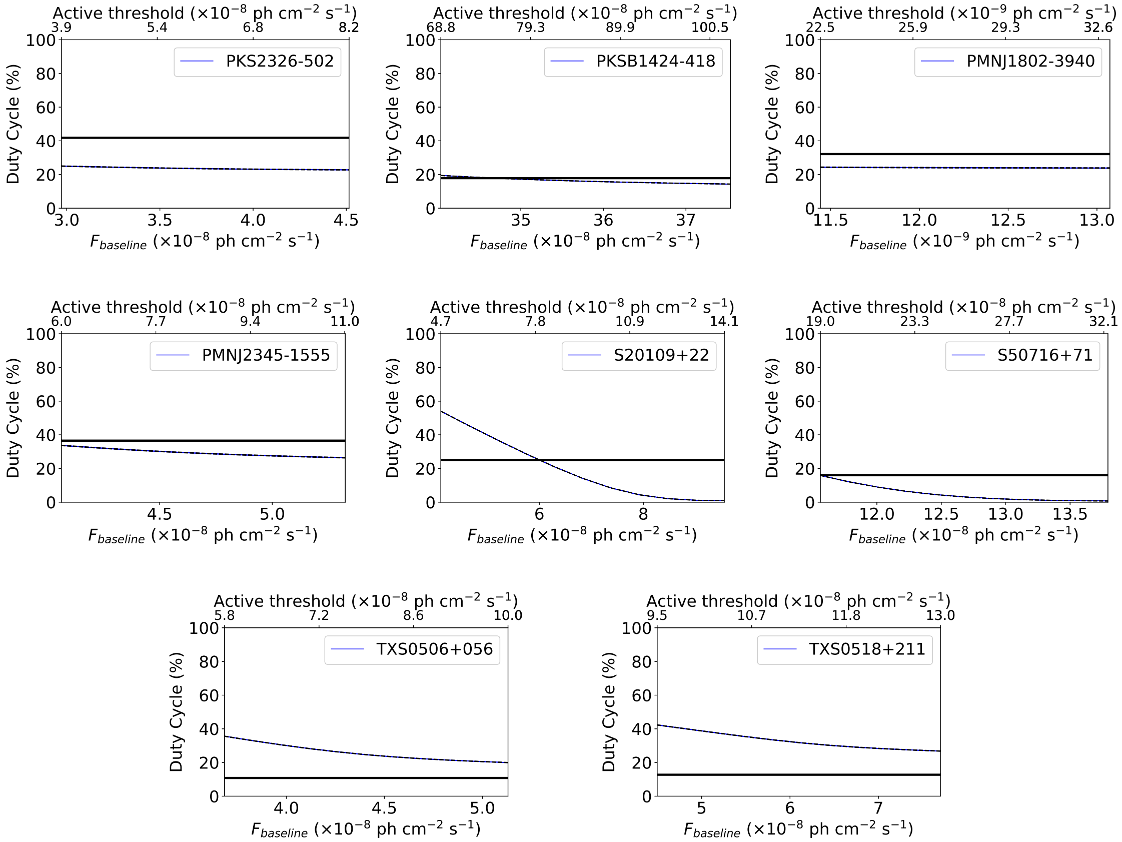

Fig. 9. (Continued)

REFERENCES

Aartsen, M. G., Ackermann, M., Adams, J., et al. 2017, ApJ, 849, 67

Aartsen, M. G., Abraham, K., Ackermann, M., et al. 2017, ApJ, 835, 151

Aartsen, M. G., Ackermann, M., Adams, J., et al. 2018, Sci, 361, 1378

Aartsen, M. G., Ackermann, M., Adams, J., et al. 2020, arXiv:2001.09520

Aartsen, M. G., Abraham, K., Ackermann, M. et al. 2016, ApJ, 833, 3

Aartsen, M. G., Abraham, K., Ackermann, M., et al. 2017, ApJ, 835, 45

Abdo, A. A., Ackermann, M., Ajello, M., et al. 2009, ApJ, 700, 597

Abdo, A. A., Abeysekara, A. U., Allen, B. T., et al. 2014, ApJ, 782, 110

Acero, F., Ackermann, M., Ajello, M., et al. 2015, ApJS, 218, 23

Ackermann, M., Ajello, M., Atwood, W. B., et al. 2015, ApJ, 810, 14

Ajello, M., Atwood, W. B., Baldini, L., et al. 2017, ApJS, 232, 18

Albert, A., André, M., Anghinolfi, M., et al. 2017, PhRvD, 96, 8, 2001

Angel, J. R. P. & Stockman, H. S. 1980, ARA&A, 18, 321

Asercion, J. 2018, AAS, 231, 150.09

Atoyan, A. & Dermer, Ch. D. 2001, PhRvL, 87, 22, 221102

Atwood, W. B., Abdo, A. A., Ackermann, M., et al. 2009, ApJ, 697, 1071

de Vaucouleurs, G., de Vaucouleurs, A., Corwin, H., et al., 1991, Third Reference Catalogue of Bright Galaxies Volume III, (New York, NY: Springer)

Donato, D., Ghisellini, G., Tagliaferri, G., & Fossati, G. 2001, A&A, 375, 739

Finke, J. 2013, in AAS/High Energy Astrophysics Division, 13, 114.01

Fossati, G., Maraschi, L., Celotti, A., Comastri, A., & Ghisellini, G. 1998, MNRAS, 299, 433

Franceschini, A., Rodighiero, G., & Vaccari, M. 2008, A&A, 487, 837

Gaggero, D., Grasso, D., Marinelli, A., Urbano, A., & Valli, M. 2015, ApJ, 815, 25

Ghisellini, G., Celotti, A., Fossati, G., Maraschi, L., & Comastri, A. 1998, MNRAS, 301, 451

IceCube Collaboration, Aartsen, M. G., Ackermann, M., et al. 2018, Sci, 361, 147

Jorstad, S. G., Marscher, A. P., Mattox, J. R., et al. 2001, ApJ, 556, 738

Kopper, C. & Blaufuss, E. 2017, GRB Coordinates Network, Circular Service, No. 21916

Kubo, H., Takahashi, T., Madejski, G., et al. 1998, ApJ, 504, 693

Marinelli, A., Sacahui, J. R., Sharma, A., & Osorio-Archila, M. 2019, arXiv: 1909.13198

Miller, J. S., French, H. B., & Hawley, S. A. 1978, in Pittsburgh Conference on BL Lac Objects, (Pittsburgh, PA: University of Pittsburgh)

Murase, K., Inoue, Y., & Dermer, C. D. 2014, PhRvD, 90, 2

Murase, K. & Waxman, E. 2016, PhRvD, 94, 10

Padovani, P., Resconi, E., Giommi, P., Arsioli, B., & Chang, Y. L. 2016, MNRAS, 457, 3582

Patricelli, B., González, M. M., Fraija, N., & Marinelli, A. 2014, Nuclear Instruments and Methods in Physics Research, 742, 208

Peretti, E., Blasi, P., Aharonian, F., Morlino, G., & Cristofari, P. 2020, MNRAS, 493, 5880

Sanchez, D. A. & Deil, C. 2013, arXiv:1307.4534

Schmidt, M. 1963, Natur, 197, 1040

Sikora, M., Begelman, M. C., & Rees, M. J. 1994, ApJ, 421, 153

Sikora, M., Stawarz, L., Moderski, R., Nalewajko, K., & Madejski, G. M.. 2009, ApJ, 704, 38

Stickel, M., Padovani, P., Urry, C. M., Fried, J. W., & Kuehr, M. 1991, ApJ, 374, 431

Tamborra, I., Ando, S., & Murase, K. 2014, JCAP, 2014, 043

Tluczykont, M., Bernardini, E., Satalecka, K., et al. 2010, A&A, 524, 48

Urry, C. M. 1996a, Probing Blazar Structure Through Multiwavelength Variability, RXTE Proposal

Urry, C. M. 1996b, ASPC, 110, 391

Urry, C. M. & Padovani, P. 1995, PASP, 107, 803

Vercellone, S., Soldi, S., Chen, A. W., & Tavani, M. 2004, MNRAS, 353, 890

Wang, Z., Xue, R., Du, L., et al. 2017, Ap&SS, 362, 191

M. Castro: Instituto Nacional de Pesquisas Espaciais (INPE)- Divisão de Astrofísica, 12227-010, São José dos Campos, São Paulo, Brazil. Universidade Estadual de Campinas (UNICAMP)-Instituto de Computação, 13083-852, Campinas, São Paulo, Brazil (manuel.castro@inpe.br).

A. Marinelli: Instituto Nazionale di Fisica Nucleare, Sezione di Napoli, Complesso Universitario di Monte S. Angelo, Via Cintia ed.G, Napoli, 80126 Italy (antonio.marinelli@na.infn.it).

M. A. Morales: Instituto Balseiro, Universidad Nacional de Cuyo - CNEA, 8400 S. C. Bariloche, Río Negro, Argentina (marco.morales@ib.edu.ar).

J. M. Osorio: Instituto de Astronomía, Universidad National Autónoma de México, México 04510, México (jmosorio@astro.unam.mx).

A. V. Penacchioni: Instituto de Física de La Plata (IFLP)- CONICET, La Plata, Argentina. Dept. of Physics, University of La Plata, c.c. 67, (1900) La Plata, Argentina (la, ana.penacchioni@fisica.unlp.edu.ar).

J. R. Sacahui: Instituto de Investigación en Ciencias Físicas y Matemáticas, ed. T-1, Ciudad Universtiaria, zona 12, Guatemala (jrsacahui@profesor.usac.edu.gt).

A. Sharma: Dept. of Physics and Astronomy, Uppsala University, Box 516, S-75120 Uppsala, Sweden (ankur.sharma@physics.uu.se).

Revista Mexicana de Astronomía y Astrofísica, **57**, 269–277 (2021)

https://doi.org/10.22201/ia.01851101p.2021.57.02.02

VELOCITY SEGREGATION IN A CLUMP-LIKE OUTFLOW WITH A NON-TOP HAT VELOCITY CROSS-SECTION

A. Castellanos-Ramírez[1], A. C. Raga[2], J. Cantó[1], A. Rodríguez-González[2], and L. Hernández-Martínez[3]

Received December 9 2020; accepted March 23 2021

ABSTRACT

High velocity clumps joined to the outflow source by emission with a "Hubble law" ramp of linearly increasing radial velocity vs. distance are observed in some planetary nebulae and in some outflows in star formation regions. We propose a simple model in which a "clump" is ejected from a source over a period τ_0, with a strong axis to edge velocity stratification. This non-top hat cross section results in the production of a highly curved working surface (initially being pushed by the ejected material, and later coasting along due to its inertia). From both analytic models and numerical simulations we find that this working surface has a linear velocity vs. position ramp, and therefore reproduces in a qualitative way the "Hubble law clumps" in planetary nebulae and outflows from young stars.

RESUMEN

Nudos de alta velocidad unidos a la fuente del flujo por una emisión con una rampa de "ley de Hubble" de velocidades radiales con crecimiento lineal en función de la distancia se observan en algunas nebulosas planetarias y en algunos flujos en regiones de formación estelar. Proponemos un modelo simple en el que un "nudo" es expulsado de una fuente en un período τ_0, con una fuerte estratificación de velocidades del eje al borde. Esta estratificación tiene como resultado una superficie de trabajo curvada (inicialmente empujada por el material expulsado, y luego moviéndose bajo su propia inercia). Tanto en los modelos analíticos como en las simulaciones numéricas encontramos que esta superficie de trabajo tiene una dependencia lineal de velocidad vs. posición; por lo tanto, se reproducen cualitativamente los "nudos con ley de Hubble" en nebulosas planetarias y en flujos de estrellas jóvenes.

Key Words: ISM: Herbig-Haro objects — ISM: jets and outflows — planetary nebulae: general — stars: winds, outflows

1. INTRODUCTION

In different stellar outflows, one sometimes finds clump-like flows with an emitting "trail" (linking the clumps to the outflow source) with a "Hubble law" of linearly increasing velocities with distance from the source. This kind of structure is observed in some outflows from young stars (most notably in the Orion BN-KL outflow, see e.g. Allen & Burton (1983), Bally et al. (2017) and Zapata et al. (2011) and in some planetary (PN) and protoplanetary (PPN) nebulae (see, e.g., Alcolea et al. 2001 and Dennis et al. 2008). A second, striking outflow with multiple "Hubble tail clumps" has been recently found by Zapata et al. (2020).

Following the suggestion of Alcolea et al. (2001) that the observed "Hubble law tail" clumps were the result of "velocity sorting" of a sudden ejection with a range of outflow velocities, Raga et al. (2020a,b) developed a model of a "plasmon" resulting from a "single pulse" ejection velocity variability. In this model, an ejection velocity pulse of parabolic (Raga et al. 2020a) or Gaussian (Raga et al. 2020b) time-dependence forms a working surface (the "head" of the plasmon) followed by the material in the low velocity, final wing of the ejection pulse (forming the Hubble law "tail"). These authors called this flow the "head/tail plasmon", adapting the name pro-

---

[1] Instituto de Astronomía, UNAM, México.
[2] Instituto de Ciencias Nucleares, UNAM, México.
[3] Facultad de Ciencias, UNAM, México.

posed by De Young & Axford (1967) for a clump-like outflow.

In the present paper, we study an alternative type of "single pulse outflow" that also produces a structure with a Hubble law of linearly increasing velocities with increasing distances from the outflow source. We propose a cylindrical ejection with:

- a "square pulse" time-dependent ejection velocity, with a sudden "turning on" at an ejection time $\tau = 0$ and a "turning off" at $\tau = \tau_0$,
- a parabolic initial cross section for the ejection velocity (with a peak, on-axis velocity and 0 velocity at the outer edge r_j).

This is in contrast to the single pulse outflows studied by Raga et al. (2020a,b), who proposed parabolic or Gaussian time-dependencies for the velocity and a top-hat cross section ejection for the ejection.

The paper is organized as follows. In § 2, we describe an analytic model, based on the "center of mass" formalism of Cantó et al. (2000), which leads to a simple solution for the motion of the working surface produced by the (non-top hat cross section) ejection pulse. In § 3, we present an axisymmetric numerical simulation (with parameters appropriate for a high velocity knot in a PN), and compare the obtained results with the analytic models. Predictions of position-velocity (PV) diagrams are done from the numerical model. Finally, the results are discussed in § 4.

2. THE ANALYTIC MODEL

2.1. *The Shape of the Working Surface*

Let us consider a hypersonic, cylindrical ejection with a time-dependent, "square pulse" ejection velocity, and a non-top hat cross section. The ejected material will be free-streaming (because the pressure force is negligible) until it reaches a leading working surface (or "head") formed in the interaction between the outflow and the surrounding environment. This situation is shown schematically in Figure 1.

If the material in the working surface is locally well mixed, the center of mass formalism of Cantó et al. (2000) will give the correct position x_{cm} of the working surface for all radii r in the cross section of the outflow. Then,

$$x_{cm}(r,t) = \frac{\int_0^{\tau} \rho_0(r,\tau')u_0(r,\tau')x_j(r,t,\tau')d\tau' + \int_0^{x_{cm}} \rho_a(x)xdx}{\int_0^{\tau} \rho_0(r,\tau')u_0(r,\tau')d\tau' + \int_0^{x_{cm}} \rho_a(x)dx}, \tag{1}$$

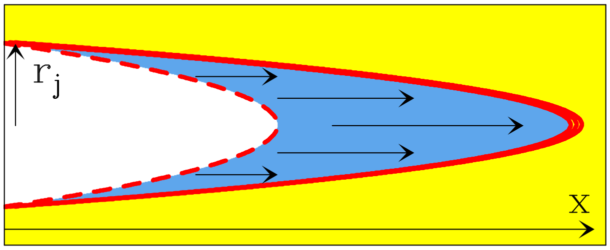

Fig. 1. Schematic diagram showing the interaction of an ejection pulse (of duration τ_0 and initial radius r_j, travelling along the x-direction) with a non-top hat ejection velocity cross section interacting with a uniform environment. The outflow interacts with the environment forming a two-shock, curved working surface (thick, solid red curve). At evolutionary times $t > \tau_0$ the source is no longer ejecting material, and therefore an empty region (limited by the dashed, red curve) is formed close to the outflow source. At large enough times, all of the ejected material will join the working surface, and the empty region will be bounded by the bow shock. The color figure can be viewed online.

where r is the cylindrical radius, x is the distance along the outflow axis, $\rho_a(x)$ is the (possibly position-dependent) ambient density, τ' is the time at which the flow parcels were ejected. $u_0(r,\tau')$ and $\rho_0(r,\tau')$ are the time-dependent velocity and density ejection cross sections (respectively),

$$x_j(r,t,\tau') = (t-\tau')u_0(r,\tau'), \tag{2}$$

is the position that the fluid parcels would have if they were still in the free-flow regime and τ is the time at which the parcels now (i.e., at time t) entering the working surface were ejected. This time τ can be found by appropriately inverting the free-streaming flow relation:

$$\frac{x_{cm}(r,t)}{t-\tau} = u_0(r,\tau). \tag{3}$$

Now, let us assume that we have an ejection pulse with a velocity

$$u_0(r,\tau) = v_0 f(r); \quad 0 \le \tau \le \tau_0, \tag{4}$$

with constant v_0. For $\tau < 0$ and $\tau > \tau_0$ there is no ejection. The function $f(r)$ is the radial profile of the ejection velocity, which we will assume has a peak at $r = 0$ and low velocities at the outer radius r_j of the cylindrical ejection. We will furthermore assume that the ejection density ρ_0 is time independent, and that the outflow moves into a uniform environment of density ρ_a.

We now introduce the ejection velocity given by equation (4) and constant ρ_0 and ρ_a (see above) in equations (1-2) to obtain:

$$\frac{\sigma}{2}x_{cm}^2 + v_0 f(r)\tau x_{cm} + v_0^2 f^2(r)\tau\left(\frac{\tau}{2} - t\right) = 0\,, \quad (5)$$

where

$$\sigma \equiv \frac{\rho_a}{\rho_0} \quad (6)$$

is the environment-to-outflow density ratio. This equation can be inverted to obtain x_{cm} as a function of t and τ:

$$x_{cm} = \frac{v_0 f(r)\tau}{\sigma}\left[\sqrt{1 + \frac{2\sigma}{\tau}\left(t - \frac{\tau}{2}\right)} - 1\right]\,, \quad (7)$$

where τ is the ejection time of the material entering the working surface at an evolutionary time t (see equation 3).

Now, as t grows, the ejection time τ also grows. and eventually reaches τ_0. For $\tau > \tau_0$, all of the ejected material (at a given radius r) has fully entered the working surface, and for larger times the position of the working surface evolves following equation (7) with $\tau = \tau_0$.

It is also possible to obtain x_{cm} fully as a function of evolutionary time t by combining equations (3) and (4) to obtain

$$\tau = t - \frac{x_{cm}}{v_0 f(r)}, \quad (8)$$

valid for $\tau \leq \tau_0$, and substituting this into equation (5). After some manipulation, one obtains:

$$x_{cm} = \frac{v_0 f(r) t}{\sigma^{1/2} + 1}\,, \quad (9)$$

which (not surprisingly) corresponds to the constant velocity motion predicted from a simple "ramp-pressure balance" argument. This solution was derived for the head of a constant velocity, non-top hat cross section jet by Raga et al. (1998).

For $\tau > \tau_0$, the position is given by equation (7) with $\tau = \tau_0$:

$$x_{cm} = \frac{v_0 f(r)\tau_0}{\sigma}\left[\sqrt{1 + \frac{2\sigma}{\tau_0}\left(t - \frac{\tau_0}{2}\right)} - 1\right]\,. \quad (10)$$

The transition between the regimes of equation (9) and (10) occurs at the evolutionary time t_c when the material ejected at τ_0 catches up with the working surface. The position of the last ejected material is:

$$x_0 = (t - \tau_0) v_0 f(r)\,, \quad (11)$$

and it catches up with the working surface when $t = t_c$ and $x_0 = x_{ws}$. We can now use the value of x_{ws} obtained from equations (9) or (10), which when substituted in equation (11) both lead to:

$$t_c = \left(1 + \sigma^{-1/2}\right)\tau_0\,, \quad (12)$$

which is independent of r. Therefore, at a time t_c, the material of the pulse ejected at all radii is fully incorporated into the working surface. At a time t_c, the working surface has a shape:

$$x_c(r) = \frac{v_0 f(r)\tau_0}{\sigma^{1/2}}\,, \quad (13)$$

obtained by combining equations (9) and (12).

2.2. *The Velocity Structure*

The velocity of the material within a fully mixed working surface is directed along the x-axis (see Figure 1). The position-dependent velocity can be straightforwardly obtained by calculating the time-derivative of the $x_{cm}(r, t)$ locus of the working surface (given by equations 9 and 10, depending on the value of t).

For $t \leq t_c$ (see equation 12), from equation (9) we obtain:

$$v_{cm} = \frac{v_0 f(r)}{1 + \sigma^{1/2}} = \frac{x_{cm}}{t}\,. \quad (14)$$

Therefore, the velocity in the curved working surface has a "Hubble law" of linearly increasing velocities as a function of distance along the x-axis, with a slope of $1/t$.

For $t > t_c$ (see equation 12), from equation (10) we obtain:

$$v_{cm} = \frac{v_0 f(r)}{\sqrt{1 + \frac{2\sigma}{\tau_0}\left(t - \frac{\tau_0}{2}\right)}} =$$

$$\frac{\sigma x_{cm}}{\tau_0\sqrt{1 + \frac{2\sigma}{\tau_0}\left(t - \frac{\tau_0}{2}\right)}\left[\sqrt{1 + \frac{2\sigma}{\tau_0}\left(t - \frac{\tau_0}{2}\right)} - 1\right]}\,. \quad (15)$$

Again, the velocity as a function of distance follows a linear, "Hubble law". The slope of this law (see equation 15) is $1/t$ for $t = t_c$, and approaches a value of $1/(2t)$ for $t \gg \tau_0$.

2.3. *Solutions for Different σ Values*

If we choose values for the density ratio $\sigma = \rho_a/\rho_0$, from equations (9-10) we obtain the position x_{ws} and from equations (14-15) the velocity of the working surface on the symmetry axis. The positions and

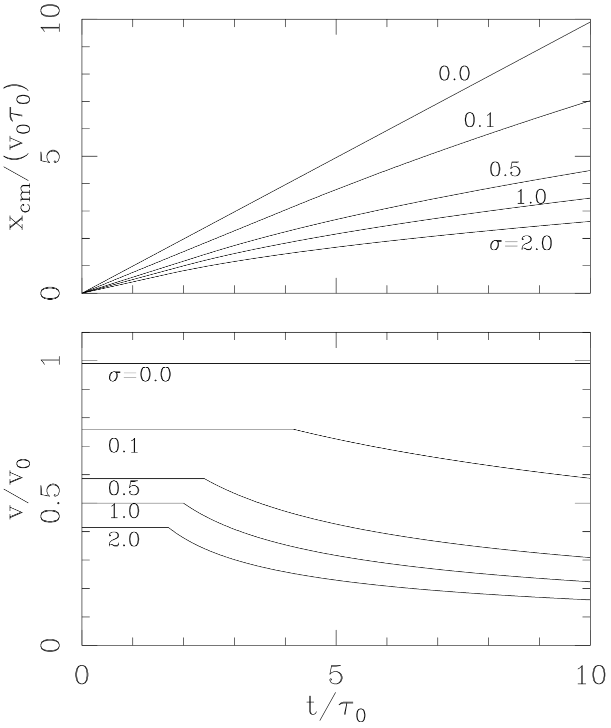

Fig. 2. Position (top) and axial velocity (bottom) of the head of the plasmon as a function of time. The curves are labelled with the values of σ used to calculate the solutions (see equations 9, 10, 14 and 15).

velocities obtained for $\sigma = 0$, 0.1, 0,5, 1.0 and 2.0 are shown in Figure 2.

For $\sigma = 0$ (the "free plasmon") the plasmon head moves at a constant velocity v_0 (see equation 4). For $\sigma > 0$, the working surface moves at a constant velocity (given by equation 14) for $t \leq t_c$ (see equation 12), and has a monotonically decreasing velocity for $t > t_c$. The velocity at all times has lower values for larger σ.

In order to illustrate the shapes that the plasmon (i.e., the working surface) can take, we choose a parabolic ejection velocity cross section (see equation 4):

$$f(r) = 1 - \left(\frac{r}{r_j}\right)^2 , \tag{16}$$

where r_j is the radius of the cylindrical outflow.

In Figure 3, we show the time-evolution of the flow for three different values of the environment-to-ejection density ratio: $\sigma = 0$, 0.1 and 0.5. For $\sigma = 0$, the time at which the ejected material fully enters the working surface is $t_c \to \infty$ (see equation 12). For $\sigma = 0.1$ and 0.5, we obtain $t_c = 4.1\tau_0$ and $2.41\tau_0$, respectively. The shapes shown in Figure 3 were obtained using equation (9) for times $t \leq t_c$ and equation (10) for $t > t_c$ (this case applies only to the $t = 3$ and $4\tau_0$ frames of the $\sigma = 0.5$ case).

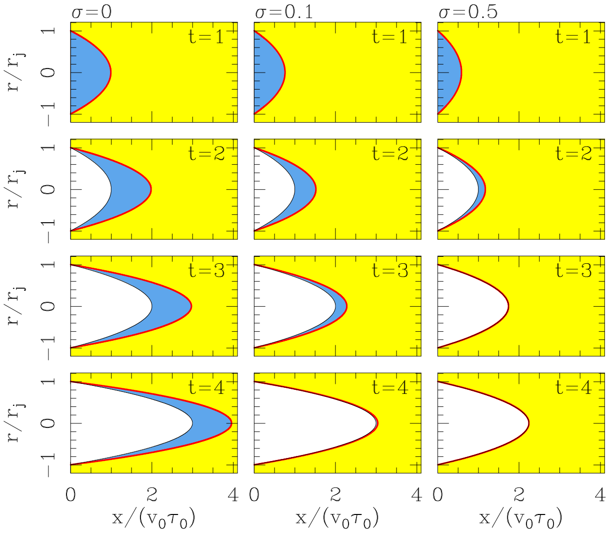

Fig. 3. Solutions for an outflow pulse with a parabolic ejection velocity cross section (see § 2.3). The three columns show the time-evolutions obtained for different values of $\sigma = \rho_a/\rho_0$, and are labelled with the corresponding σ (above the top graphs). The four lines correspond to different evolutionary times: $t = \tau_0$ (top), $2\tau_0$, $3\tau_0$ and $4\tau_0$ (bottom). The working surface is shown with the thick, solid line, and the "empty cavity" region is shaded white. The blue region (not always present) is the ejected material which has still not been incorporated into the working surface. The color figure can be viewed online.

Also shown in Figure 3 is the "empty region" formed for $t > \tau_0$ (i.e., when the ejection has already stopped) close to the outflow source (see equation 11). In the $\sigma = 0$ case, the working surface moves freely, and therefore the ejected material (shown in blue in Figure 3) never catches up with it. In the $\sigma = 0.1$ case, in the $t = 4\tau_0$ frame most of the ejected material has already caught up with the working surface, and in the $\sigma = 0.5$ case in the $t = 3$ and $4\tau_0$ frames (which have $t > t_c$, see above) all of the outflow material is within the working surface, and the "empty region" fills the volume between the outflow source and the working surface.

3. A NUMERICAL SIMULATION

3.1. *Flow Parameters*

In order to illustrate in more detail the full characteristics of the flow, we compute an axisymmetric numerical simulation of the "parabolic cross section plasmon" described in § 2.3 using the WALICXE-2D code (Esquivel et al. 2009). We choose parameters

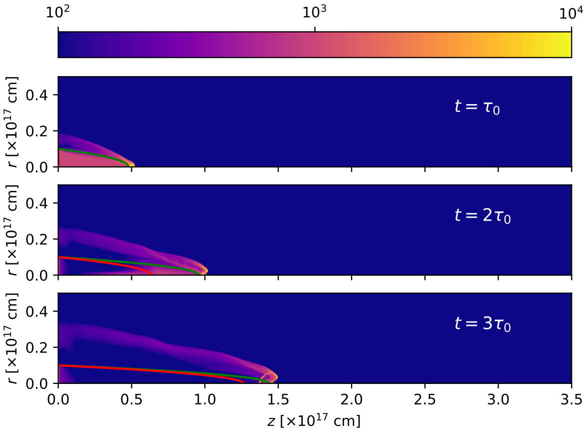

Fig. 4. Number density stratifications obtained from the numerical simulation for times $t = 100$, 200 and 300 yr. The densities are shown with the logarithmic colour scale given by the top bar (in cm^{-3}). The shape of the working surface obtained from the analytic model is shown with the green curve, and the inner limit of the analytic "empty cavity" is shown with the red curve. The distances along and across the outflow axis are given in units of 10^{17} cm. The color figure can be viewed online.

appropriate for a high velocity clump in a PN: an axial velocity with an on-axis value $v_0 = 200$ km s^{-1} (decreasing parabolically to zero at a radius r_j, see equation 16), an initial radius $r_j = 10^{16}$ cm, an ejection atom+ion number density $n_0 = 10^4$ cm^{-3} (independent of radius) and an ambient density $n_a = 100$ cm^{-3}. Initially, both the outflow and the environment have a 10^4 K temperature. The ejection is imposed at $t = 0$ (at the beginning of the simulation) and ends at a time $\tau_0 = 100$ yr. For these parameters, the environment to outflow density ratio has a value $\sigma = 0.1$, and we then expect the ejected material to be fully incorporated into the working surface at a time $t_c = 416.2$ yr (see equation 12).

We assume that all of the flow is photoionized by the central star of the PN. We consider this photoionization in an approximate way by imposing a minimum temperature $T = 10^4$ K and full ionization for Hydrogen throughout the flow. The parametrized cooling function of Biro & Raga (1994) is used for $T > 10^4$ K.

The computational domain has a size of $(35, 8.75) \times 10^{16}$ cm (along and across the outflow axis, respectively), resolved with a 7-level binary adaptive grid with a maximum resolution of 8.54×10^{13} cm. An inflow boundary is applied at $x = 0$ and $r > r_j$ for $t < \tau_0$, a reflection boundary is applied outside the injection region (at $x = 0$) and on the symmetry axis, and a free outflow is imposed in the remaining grid boundaries.

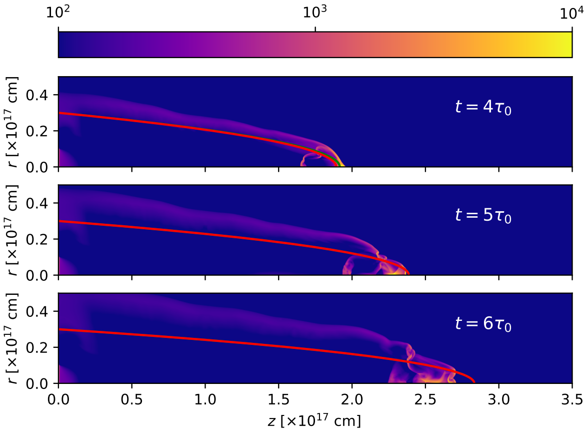

Fig. 5. The same as Figure 4, but for times $t = 400$, 500 and 600 yr. The color figure can be viewed online.

3.2. *Results*

We have run the simulation described in § 3.1 for a total time of 600 yr. Figures 4 and 5 show time-frames (at times $t = 100$, 200, 300, 400, 500 and 600 yr) of the resulting density stratification. In these figures, we show the shape of the working surface (equations 9 and 10). For times $t \leq t_c = 416.2$ yr (see § 3.1), we also show the inner edge of the "empty cavity" of the analytic model (equation 11). For $t > t_c$, all of the region inside the working surface is in the "empty cavity" regime, and for $t \leq \tau_0 = 100$ yr there is no empty region.

It is clear that even though at early times (see the $t = \tau_0$ frame of Figure 4) the working surface of the numerical simulation has a shape that partially agrees with the analytic model, at later times the working surface has bow shock wings which are considerably broader than the analytic prediction (see the remaining frames of Figures 4 and 5). This difference is partly due to the lack of perfect mixing (assumed in the analytic model) between outflow and environment material in the numerical simulation. The other effect that pushes out material sideways from the head of the working surface is the radial gas pressure gradient (also not included in the analytic model). However, the position of leading region of the working surface approximately agrees with the analytic model at all times (see Figures 4 and 5).

We have computed the recombination cascade Hα emission coefficient, and integrated it through lines of sight in order to compute intensity maps.

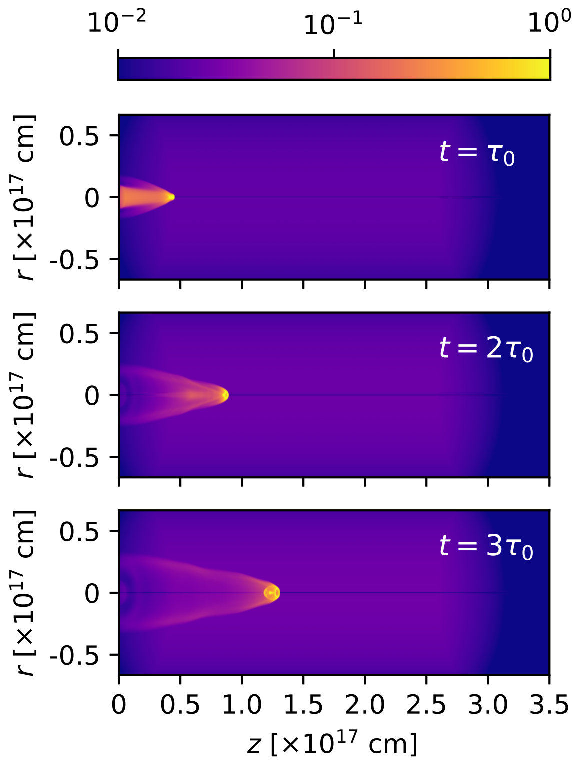

Fig. 6. Hα maps obtained from the numerical simulation for times t = 100, 200 and 300 yr. The maps are computed assuming a 30° angle between the outflow axis and the plane of the sky. The emission (normalized to the peak emission of each map) is shown with the logarithmic colour scale given by the top bar. The distances along and across the outflow axis are given in units of 10^{17} cm. The color figure can be viewed online.

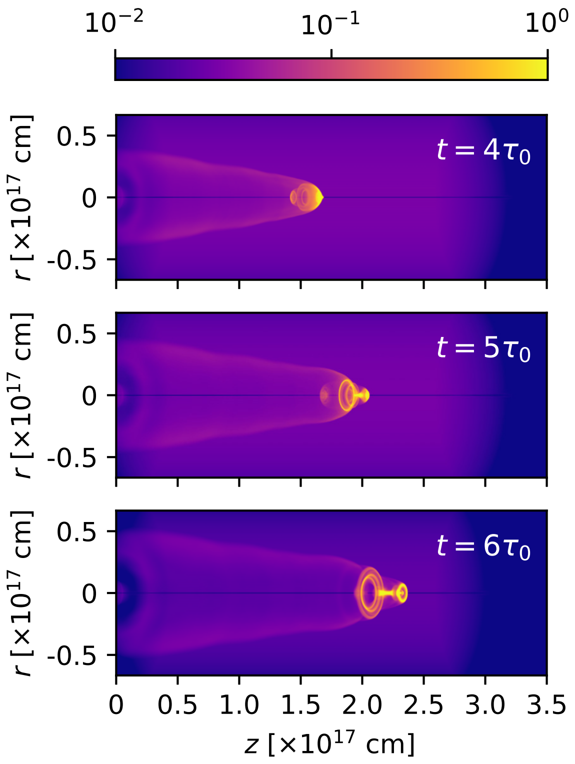

Fig. 7. The same as Figure 6, but for times t = 400, 500 and 600 yr. The color figure can be viewed online.

Figures 6 and 7 show the emission maps computed assuming a 30° angle between the outflow axis and the plane of the sky, for times t = 100, 200, 300, 400, 500 and 600 yr.

From Figures 6 and 7, we see that the earlier maps (the t = 100 and 200 yr, top two frames of Figure 6) show the emission from the ejected material before it reaches the working surface. In all of the later maps, we see a bright, compact component in the leading, on-axis region of the working surface, and the emission of extended bow shock wings trailing this clump.

With the Hα emission coefficient we have also computed predicted position-velocity (PV) diagrams. These PV diagrams correspond to long-slit spectra obtained with a "narrow" spectrograph slit with a full projected width of 2×10^{16} cm straddling the outflow axis (see Figures 8 and 9) and with a "wide" spectrograph slit that includes all of the emission of the bow shock (see Figures 10 and 11), and show the emission as a function of position along the outflow axis and radial velocity (along the line of sight). Figures (8, 9) and (10, 11) show the PV diagrams computed for a 30° orientation of the outflow axis with respect to the plane of the sky, and for times t = 100, 200, 300, 400, 500 and 600 yr.

From these figures it is clear that in all of the PV diagrams we see:

- qualitatively very similar results for slits of different widths (seen comparing Figure 8 to Figure 10, and 9 to 11),
- a bright, compact emission feature at the position and velocity of the on-axis, leading region of the working surface,
- an approximately linear ramp of increasing radial velocities, ending at the position of the leading clump.

Apart from these two components, in the earlier frames (t = 100 and 200 yr, the two top frames of Figure 8) we see the ejected material (at a projected

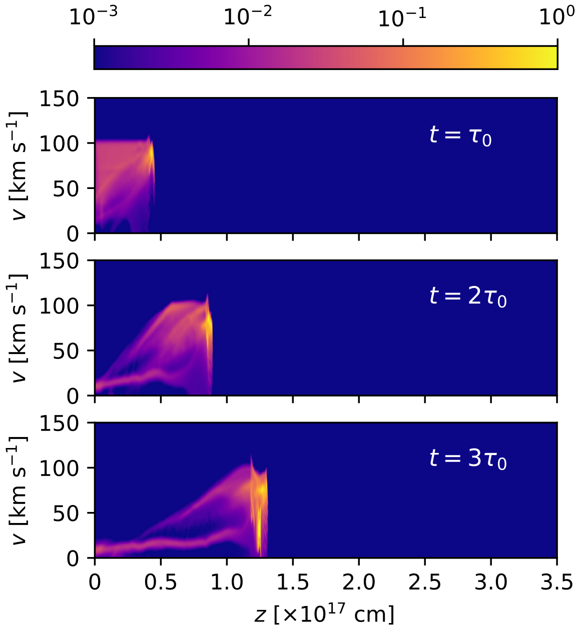

Fig. 8. Hα position-velocity diagrams obtained from the numerical simulation for times t = 100, 200 and 300 yr. These PV diagrams have been calculated assuming that a long spectrograph slit with a projected full width of 2×10^{16} cm straddles the symmetry axis of the flow. The maps are computed assuming a 30° angle between the outflow axis and the plane of the sky. The emission (normalized to the peak emission of each map) is shown with the logarithmic colour scale given by the top bar. The distances along the outflow axis are given in units of 10^{17} cm, and the radial velocities in km s^{-1}. The color figure can be viewed online.

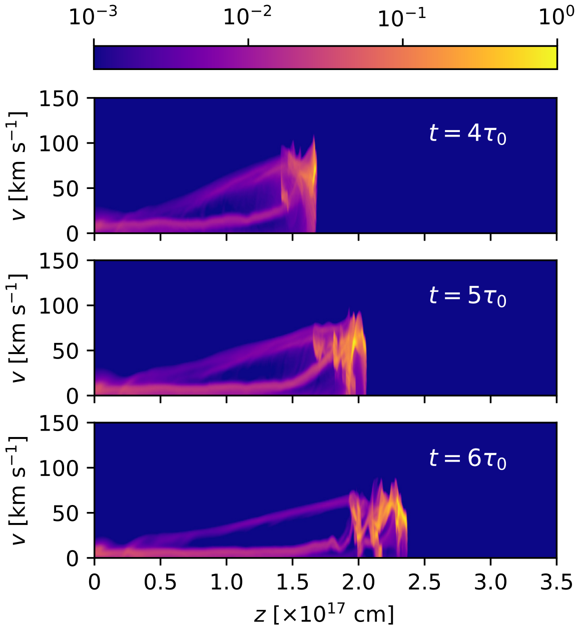

Fig. 9. The same as Figure 8, but for times t = 400, 500 and 600 yr. The color figure can be viewed online.

velocity of 100 km s^{-1}) before it reaches the working surface. This component disappears at later times, since all of the ejected material has then been incorporated into the working surface. Also, at all times we see a low velocity component, which corresponds to environmental material that has been shocked by the far bow shock wings and has not mixed with the rest of the flow.

4. SUMMARY

We have studied the flow resulting from a constant density, collimated, cylindrical non-top hat cross section ejection of material over a finite time τ_0. We first calculate an analytic model (based on the "center of mass formalism" of Cantó et al. 2000) with which we obtain analytic expressions for the time-evolution of the working surface produced by the interaction of the ejection with a uniform environment.

This solution has two regimes:

- a working surface which is being fed by the ejected material (see equation 9). This solution was previously derived by Raga et al. (1998),
- a working surface in which all of the ejected material has already been incorporated (see equation 10).

The transition between the two regimes occurs at the time t_c given by equation (12). For $t < t_c$, the region inside the working surface is partly filled by the ejected material (with an inner cavity with a boundary given by equation 11). For $t > t_c$, the region within the working surface is "empty" (i.e., as in the ballistic analytic model, see Figure 3).

For $t < t_c$, the working surface moves at a constant velocity, and for $t > t_c$ it slows down, more strongly for larger values of the environment-to-ejection density ratio $\sigma = \rho_a/\rho_0$ (see Figure 2). For these two regimes, we find that the material in the working surface has a linear velocity vs. x (the position along the outflow axis) dependence, given by equations (14) and (15).

We also compute an axisymmetric numerical simulation, with conditions appropriate for a high velocity clump in a PN. We find that the density structure

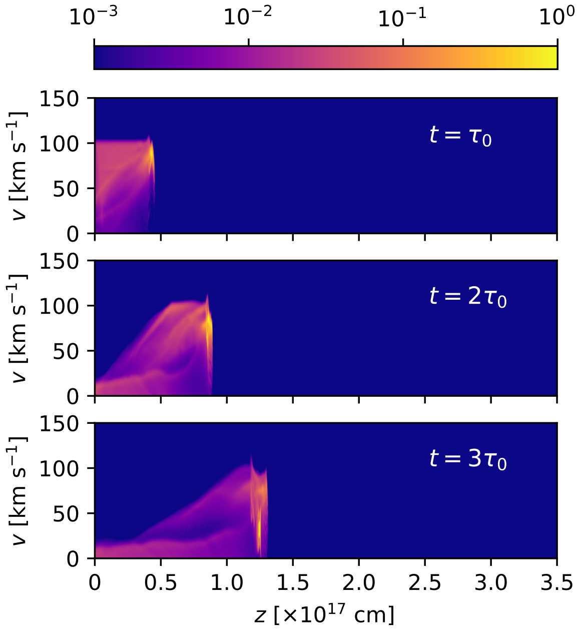

Fig. 10. The same as Figure 8, but with PV diagrams calculated for a wide spectrograph slit that straddles the symmetry axis and includes all of the emitting region of the flow. The color figure can be viewed online.

initially shows a working surface and a low density cavity that agree well with the analytic predictions (see Figure 4). However, at later times the numerical working surface develops bow shock wings that are considerably broader than the ones of the analytic prediction (see Figures 4 and 5). The position of the leading region of the working surface shows a reasonably good agreement with the analytic model for all of the computed times.

From the numerical simulation, we have calculated Hα maps (Figures 6 and 7) and PV diagrams (Figures 8 to 11). We find that the PV diagrams do show the linear radial velocity vs. position “Hubble law” predicted from the analytic models (see Figures 8 and 9).

Therefore, we have found a new way of straightforwardly obtaining clump-like outflows with a “Hubble law” linear radial velocity ramp joining them to the outflow source. This is an alternative scenario to the one of the “single peak radial velocity pulse” model of Raga et al. (2020a,b), which also produces “Hubble law clumps”. Clearly, these two possibilities are useful as guidelines to obtaining detailed models of structures with these characteristics in PN (see, e.g., Dennis et al. 2008) or in outflows in star formation regions (see, e.g., Zapata et al. 2020).

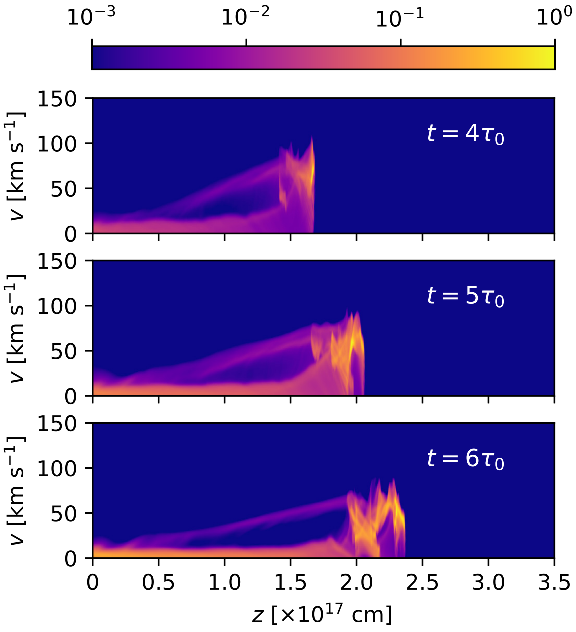

Fig. 11. The same as Figure 9, but with PV diagrams obtained with a wide spectrograph slit that includes all of the emitting region of the flow. The color figure can be viewed online.

We end by noting that the results presented in this paper directly depend on quite arbitrary assumptions of a pulse-like ejection and a non-top hat ejection velocity cross section. Reasonable arguments for these two assumptions can be presented:

- an ejection with a limited duration is partially justified by the observation of clump-like flows in outflows from young and evolved stars, which most likely imply such a time-limited ejection,

- a non-top hat outflow cross section could be the result of a magnetocentrifugal ejection from an accretion disk (which produces higher outflow velocities from the inner regions of the disk), or the result of an initial, turbulent outflow region that generates the centrally peaked velocity profile.

This is by no means a concrete proof that the characteristics that we have assumed for the outflow are correct. This type of uncertainty is present in the vast majority of the jet models in the astrophysical literature, many of which share the assumption of a simple but unlikely “sudden turn-on”, top hat cross section” ejection.

This work was supported by DGAPA (UNAM) Grants IG100218 and IA103121. A.C.R. acknowledges support from a DGAPA-UNAM Postdoctoral Fellowship.

REFERENCES

Alcolea, J., Bujarrabal, V., Sánchez Contreras, C., Neri, R., & Zweigle, J. 2001, A&A, 373, 932

Allen, D. A. & Burton, M. G. 1983, Natur, 363, 54

Bally, J., Ginsburg, A., Arce, H., et al. 2017, ApJ, 837, 60

Biro, S. & Raga, A. C. 1994, ApJ, 434, 221

Cantó, J., Raga, A. C., & D'Alessio, P. 2000, MNRAS, 313, 656

Dennis, T. J., Cunningham, A. J., Frank, A., et al. 2008, ApJ, 679, 1327

De Young, D. S. & Axford, W. I. 1967, Natur, 216, 129

Esquivel, A., Raga, A. C., Cantó, J., & Rodríguez-González, A. 2009, A&A, 507, 855

Raga, A. C., Rodríguez-González, A., Hernández-Martínez, L., Cantó, J., & Castellanos-Ramírez, A. 2020a, MNRAS, 499, 91

Raga, A. C., Cantó, J., Castellanos-Ramírez, A., Rodríguez-González, A., & Hernández-Martínez, L. 2020b, RMxAA, submitted

Raga, A. C., Cantó, J., & Cabrit, S. 1998, A&A, 332, 714

Zapata, L., Ho, P. T. P., Fernández-López, M., et al. 2020, ApJ, 902, 47

Zapata, L. A., Loinard, L., Schmid-Burgk, J., et al. 2011, ApJ, 726, 12

J. Cantó and A. Castellanos-Ramírez: Universidad Nacional Autónoma de México, Instituto Astronomía, Ap. 70-264, CDMX, 04510, México.

L. Hernández-Martínez: Facultad de Ciencias, Universidad Nacional Autónoma de México, Av. Universidad 3000, Circuito Exerior S/N, 04510 CDMX, México.

A. C. Raga and A. Rodríguez-González: Instituto de Ciencias Nucleares, Universidad Nacional Autónoma de México, Ap. 70-543, 04510 CDMX, México (raga@nucleares.unam.mx).

Revista Mexicana de Astronomía y Astrofísica, **57**, 279–295 (2021)

https://doi.org/10.22201/ia.01851101p.2021.57.02.03

ON THE EFFECTS OF SOLAR RADIATION PRESSURE ON THE DEVIATION OF ASTEROIDS

L. O. Marchi[1], D. M. Sanchez[1], F. C. F. Venditti[2], A. F. B A. Prado[3], and A. K. Misra[4]

Received August 17 2020; accepted March 25 2021

ABSTRACT

In this work, we study the effects of solar radiation pressure (SRP) on the problem of changing the orbit of an asteroid to support planetary defense, scientific research, or exploitation of materials. This alternative considers a tethered reflective balloon (or a set of reflective balloons) attached to the asteroid, with a high area-to-mass ratio, to use the SRP to deflect a potentially hazardous asteroid (PHA) or to approximate the target asteroid to Earth. The tether is assumed to be inextensible and massless, and the motion is described only in the orbital plane of the asteroid around the Sun. The model is then used to study the effects that the tether length, the reflectivity coefficient, and the area-to-mass ratio have on the deviation of the trajectory of the asteroid.

RESUMEN

Estudiamos los efectos de la presión de la radiación solar (SRP) sobre el problema de la modificación de la órbita de un asteroide para propósitos de defensa planetaria, investigación científica o explotación de materiales. Consideramos un globo reflector (o un conjunto de ellos) sujeto con una correa al asteroide, con una relación área-masa grande, para utilizar la SRP para desviar a un asteroide potencialmente dañino (PHA), o para aproximar al asteroide a la Tierra. Suponemos que la correa es inextensible y de masa cero. El movimiento se describe sólo en el plano orbital del asteroide en torno al Sol. El modelo se usa para estudiar los efectos de la longitud de la correa, el coeficiente de reflectividad y el cociente área-masa sobre la desviación de la trayectoria del asteroide.

Key Words: balloons — celestial mechanics — minor planets, asteroids: general — minor planets, asteroids: individual: PHAs

1. INTRODUCTION

Although found practically everywhere in the Solar System, the majority of asteroids and comets are concentrated in three locations: the Asteroid Belt, the Kuiper Belt, and the Oort Cloud (Hsieh & Jewitt 2006).

Particularly, potentially hazardous asteroids (PHAs) have become a research topic for several scientists around the world, due to the real possibilities of a future impact with Earth. It is scientifically accepted that, in the past, the extinction of dinosaurs was caused by the impact of an asteroid on the Yucatan Peninsula, in Mexico (Chappell et al. 2013). At least two more events of smaller magnitudes related to the impact of asteroids can be found in Russia: Tunguska, in 1908, and Chelyabinsk, in 2013. There are several studies dedicated to the characterization of these rocky bodies, such as shape, size, spin state, and composition (Ostro et al. 1995; Nolan et al. 2013), which are necessary for remote reconnaissance and space exploration missions, as shown in Bosanac et al. (2015); Liang et al. (2019); Aljbaae et al. (2020). This information is also important to understand the origin and evolution of planetary

---

[1] Division of Space Mechanics and Control - National Institute for Space Research (INPE),CEP 12227-010, São José dos Campos - SP, Brazil.

[2] Arecibo Observatory, University of Central Florida, HC3 BOX 53995, Arecibo, PR, 00612, USA.

[3] Postgraduate Division - National Institute for Space Research (INPE), SP, Brazil. - Volunteer Professor, Academy of Engineering, RUDN University, Moscow, Russia.

[4] Department of Mechanical Engineering - McGill University, QC H3A 0G4, Campus of Montréal, Canada.

systems, since small bodies are considered to be remnants from the formation of the Solar System (Michel et al. 2015).

Over the last decades, there was an increased effort to develop asteroid deflection techniques. These strategies can be classified depending on the characteristics of the asteroid, the mechanism that causes the deflection, and the time available to complete the mission. For example, the change in angular momentum of an asteroid can be performed through the use of kinetic impactors, nuclear interceptors, and mass drivers (Brack & McMahon 2020; Sánchez-Lozano et al. 2020). The first measurement of a kinetic impact experiment is planned for 2022 by NASA's Double Asteroid Redirection Test (DART) mission, whose target will be the binary near-Earth asteroid system Didymos (Cheng et al. 2018).

Low-thrust techniques can also be considered, such as gravity tractors, or passive methods, such as changes on the surface of the asteroid by thermal induction (Bottke Jr et al. 2006; Vasile & Maddock 2010). One example of the latter technique is a study using a tethered system formed by a solar sail attached to an asteroid with a tether of constant length (Gao & Wu 2016). The gravity tractor is a technique that uses the perturbation coming from the mass of the spacecraft that is positioned near the asteroid (Lu & Love 2005). There are also studies of formation flying with solar sails and gravity tractors, which are combined to optimize the deflection (Gong et al. 2009). This is a weak perturbation, so longer times are necessary to change the trajectory of the asteroid. When using this technique, times of the order of hundreds of years need to be considered. An assessment of several deflection mechanisms can be found in Sanchez et al. (2009) and an overview of techniques can be found in Morrison (2019).

Space tethers are long cables with several different proposed applications, such as space elevators (Woo & Misra 2013; Cohen & Misra 2017), tether satellite systems (Misra 2008), debris removal (Aslanov & Yudintsev 2013), electrodynamic tethers for power (Estes et al. 2000), etc., but they are not limited to these applications. They can also be used for the displacement of the center of mass of the PHA, by attaching a long tether and a ballast mass to the asteroid (French & Mazzoleni 2009; Mashayekhi & Misra 2012, 2016). A smaller asteroid may also be used as a ballast mass, or even boulders from the surface of the asteroid (Vil'ke et al. 2013; Venditti et al. 2015, 2018; Marchi et al. 2018; Venditti et al. 2020).

Solar radiation pressure (SRP) can also affect the motion of asteroids indirectly, for example, by placing a solar sail on the asteroid to change its trajectory; it also can be used for asteroid de-spin to optimize the deflection (Dachwald & Wie 2007; Kikuchi & Kawaguchi 2018). In this paper, our main objective is to analyze the influence of the SRP on the dynamics of an asteroid-tether-balloon system by using a reflective balloon (or a set of balloons) with high area-to-mass ratio to increase the acceleration due to SRP, pulling the asteroid outwards of the Sun. The tether used to attach the balloon to the asteroid keeps the balloon away from the asteroid. It is expected that the effect of the SRP will become more evident in regions of closer proximity to the Sun.

The Yarkovsky and YORP effects are thermal radiation driven phenomena. These effects can change the trajectory of small asteroids, depending on their physical properties (Farnocchia et al. 2013; Vokrouhlicky et al. 2015). The smaller the body, the greater will be the orbit perturbation. The SRP overcomes the thermal effects on the asteroid-tether-balloon system; therefore, the thermal contribution is neglected in this work.

The proposed technique adds a new option to the non-disruptive techniques (which do not cause fragmentation) to change the orbit of an asteroid. The main advantage, if compared to other tethered techniques, is that the use of long tethers and large masses (ballast) are not required, as proposed by French & Mazzoleni (2009); Mashayekhi & Misra (2012); Venditti et al. (2020). There is also no fuel consumption involved after the system is built, which is another advantage of the technique suggested here. Another application of this strategy would be to transfer these bodies closer to Earth to explore them scientifically or commercially. An example is the ongoing OSIRIS-REx mission, whose goal is to return a sample from asteroid Bennu (Aslanov & Yudintsev 2013; Vokrouhlicky et al. 2015; Lauretta et al. 2017). A technique to bring asteroids to the proximity of the Earth could help future sample return missions, as well as asteroid mining missions.

In § 2, we present the physical model of balloon-tether-PHA system and the development of the equations of motion. In § 3, the effect of the balloon on the orbit deviation and, consequently, the effect of the SRP, is obtained by making a comparison between the real orbit of the asteroid, i. e., without the balloon, and the orbit of the asteroid with the balloon attached. We performed the simulations considering asteroid Bennu, and also a small fictional asteroid. The root mean square deviation is used to verify the impact of each parameter of the system on the deviation of the asteroid and to obtain empirical equations to relate these parameters. Furthermore, the results show that the SRP allows greater deviations in the trajectory for balloon configurations with a high area-to-mass ratio when compared to the use of the gravity tractor in a period of a century of operation, the usual time considered for gravity tractor techniques. Finally, we conclude (in § 4) that this study contributes not only to the verification and validation of the effect of SRP on asteroid deflection, but also to present general results through simple equations.

2. METHODOLOGY

In this section, we describe the development of the mathematical model of a system consisting of a balloon with a reflective surface and a high area-to-mass ratio, attached to an asteroid with a tether. In the last part of this section, the variables used to layout the results, as well as the scheme of the numerical simulations, are shown. The physical model is two-dimensional and the dynamics of the problem is described in the plane of the orbit of the asteroid around the Sun using the Lagrangian formalism. Due to this first simplification, the model is valid only for asteroids with low orbital inclination. Furthermore, the mass and flexibility of the tether are not considered. Current limitations and constraints on the structural construction of the whole apparatus are not the focus of this work and are not discussed here.

2.1. *Physical Model*

Figure 1 shows the schematic representation of the system, where the two main reference systems are presented. The inertial frame (XY), Sun-centered, is represented by the unit vectors $\hat{e}_1, \hat{e}_2$. The unit vectors $\hat{a}_1, \hat{a}_2$ refer to the rotational frame (xy), with origin at the center of mass of the asteroid. We assume that they are aligned with the asteroid's principal axis of inertia. The letters S, A, B, and P refer to the Sun, the center of mass of the asteroid, the point of attachment of the balloon, and the point of attachment of the tether, respectively.

There is a large number of parameters and variables related to this model: m_A is the mass of the asteroid, A_B/m_B is the area-to-mass ratio of the balloon, M is the mass of the Sun, R_{SA} is the distance between the Sun and the asteroid, R_{PA} is the distance between the center of mass and the point of attachment on the asteroid, R_{AB} is the distance between the center of mass of the asteroid and the balloon, R_{SB} is the distance between the Sun and the balloon, l is the length of the tether, ν is the true anomaly of the asteroid, θ is the rotation angle of the asteroid, α is the angle that the tether makes with AP, ψ is the angle between the perihelion of the Earth and the perihelion of the asteroid, η is the angle between R_{SA} and R_{SB}, ξ is the angle between R_{PA} and the x-axis of the reference system (xy), ϕ is the angle between R_{PA} and R_{AB}, F_{GR} is the gravitational force of attraction of the Sun on the balloon, and F_{PR} is the force applied by the solar radiation on the balloon.

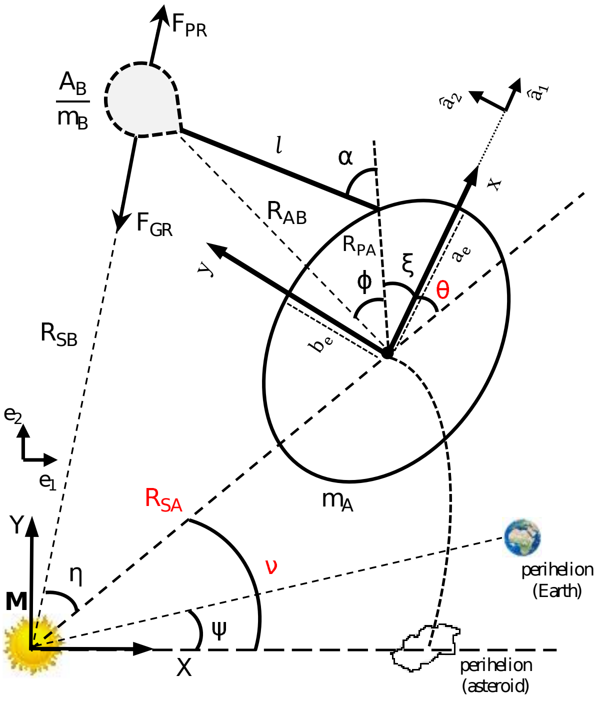

Fig. 1. Schematic representation of the physical model. The color figure can be viewed online.

The angle α is assumed to be constant (the tether has no pendular motion) to keep the position of m_B fixed with respect to m_A. This assumption facilitates the modeling phase because the position of the center of mass of the system does not change with time. In addition, only m_A has a rotation about its own principal axis. In the model adopted, we have three degrees of freedom (or generalized coordinates), which are: R_{SA}, ν and, θ.

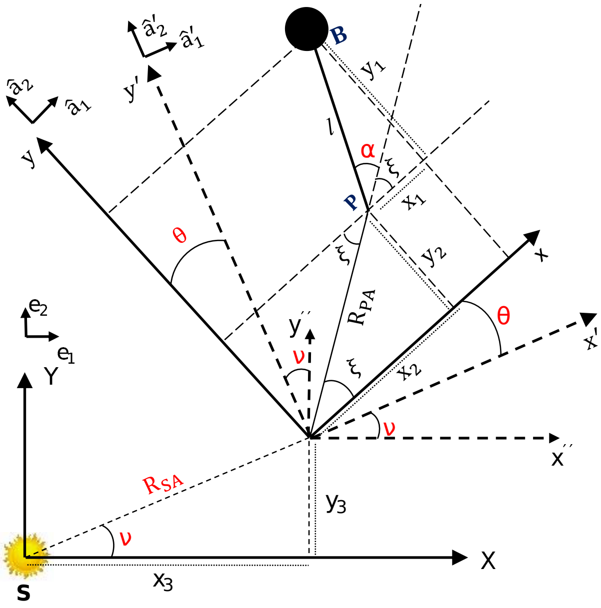

Fig. 2. Geometry used to determine the velocities of the asteroid and the balloon in the inertial coordinate system. The color figure can be viewed online.

2.2. *Mathematical Model*

Figure 2 illustrates the geometry required to determine the velocities of the asteroid and the balloon with respect to the inertial frame (XY). Two intermediate reference frames (x',y') and (x'',y'') are used in the transformation of coordinates of the balloon from the body system (xy) to the inertial system (XY).

The position and velocity vectors of the asteroid's center of mass are represented by equations (1) and (2), and the position and velocity vectors of the balloon are shown in equations (3) and (4). The equations are described in the inertial coordinate system (centered in the Sun):

$$\vec{r}_{A_{XY}} = R_{SA}\cos(\nu)\hat{e}_1 + R_{SA}\sin(\nu)\hat{e}_2, \tag{1}$$

$$\begin{aligned}\vec{v}_{A_{XY}} = \; & [\dot{R}_{SA}\cos(\nu) - R_{SA}\dot{\nu}\sin(\nu)]\hat{e}_1 + \\ & [\dot{R}_{SA}\sin(\nu) + R_{SA}\dot{\nu}\cos(\nu)]\hat{e}_2,\end{aligned} \tag{2}$$

$$\begin{aligned}\vec{r}_{B_{XY}} = & [l\cos(\alpha+\xi+\theta+\nu) + R_{PA}\cos(\xi+\theta+\nu) + \\ & R_{SA}\cos(\nu)]\hat{e}_1 + [l\sin(\alpha+\xi+\theta+\nu) + \\ & R_{PA}\sin(\xi+\theta+\nu) + R_{SA}\sin(\nu)]\hat{e}_2,\end{aligned} \tag{3}$$

$$\begin{aligned}\vec{v}_{B_{XY}} = & [\dot{R}_{SA}\cos(\nu) - R_{SA}\dot{\nu}\sin\nu - \\ & R_{PA}\sin(\xi+\theta+\nu)(\dot{\theta}+\dot{\nu}) - \\ & l\sin(\alpha+\xi+\theta+\nu)(\dot{\theta}+\dot{\nu})]\hat{e}_1 + \\ & [\dot{R}_{SA}\sin(\nu) + R_{SA}\dot{\nu}\cos\nu + \\ & R_{PA}\cos(\xi+\theta+\nu)(\dot{\theta}+\dot{\nu}) + \\ & l\cos(\alpha+\xi+\theta+\nu)(\dot{\theta}+\dot{\nu})]\hat{e}_2.\end{aligned} \tag{4}$$

From equations (2) and (4), we have the following scalar products:

$$\vec{v}_{A_{XY}} \cdot \vec{v}_{A_{XY}} = \dot{R}_{SA}^2 + R_{SA}^2\dot{\nu}^2, \tag{5}$$

$$\begin{aligned}\vec{v}_{B_{XY}} \cdot \vec{v}_{B_{XY}} = & \dot{R}_{SA}^2 + R_{SA}^2\dot{\nu}^2 + l^2(\dot{\theta}+\dot{\nu})^2 + \\ & R_{PA}^2(\dot{\theta}+\dot{\nu})^2 + 2(\dot{\theta}+\dot{\nu})[lR_{PA}(\dot{\theta}+\dot{\nu})\cos(\alpha) + \\ & R_{PA}R_{SA}\dot{\nu}\cos(\xi+\theta) + lR_{SA}\dot{\nu}\cos(\alpha+\xi+\theta) - \\ & \dot{R}_{SA}R_{PA}\sin(\xi+\theta) - l\dot{R}_{SA}\sin(\alpha+\xi+\theta)].\end{aligned} \tag{6}$$

The total translational kinetic energy is composed of two parts, the first one associated with the PHA and the second one with the balloon, according to equation (7).

$$T_{TK} = \frac{1}{2}m_A(\vec{v}_{A_{XY}} \cdot \vec{v}_{A_{XY}}) + \frac{1}{2}m_B(\vec{v}_{B_{XY}} \cdot \vec{v}_{B_{XY}}). \tag{7}$$

We assume that the asteroid rotates and the balloon is static with respect to the asteroid. The coordinate system defined on the asteroid originates from its center of mass and it is aligned with its main axes. In equation (8), we have the total rotational kinetic energy, given by:

$$T_{TR} = \frac{1}{2}I_A(\dot{\theta}+\dot{\nu})^2, \tag{8}$$

where I_A is the moment of inertia with respect to the axis normal to the plane of motion of a homogeneous body resulting from the association of the asteroid, the tether, and the balloon.

Bennu has an oblate spheroidal shape with a prominent equator, frequently called "top-shaped" (Michel et al. 2020). Simulations using the spherical harmonics expansion to consider the asteroid oblateness did not show significant differences when compared to a sphere for this type of configuration (Venditti et al. 2020). Therefore, Bennu was modeled as a sphere with a diameter of 492 m in this paper.[1] Equations 9 show the two formulations that

---

[1] https://ssd.jpl.nasa.gov/sbdb.cgi#top (last access January/2021).

are used to calculate I_A with respect to the center of mass of the asteroid. The first one was used for the asteroid alone, while the second one is an approximation for the asteroid-tether-balloon system. These two formulations are necessary, since the simulations using the asteroid and the simulations using the asteroid-tether-balloon models are made independently of each other.

$$I_A = \begin{cases} \frac{2}{5} m_A R_0^2 \text{ for asteroid (spherical equator)}, \\ \\ \frac{2}{5} m_A R_0^2 + m_B R_{AB}^2 \text{ for asteroid-tether-balloon}, \end{cases} \tag{9}$$

where R_0 is the characteristic length of the asteroid.

Therefore, by replacing equations (5) and (6) in equation (7) and summing the expression obtained with equation (8), we have that the total kinetic energy of the system is given by:

$$\begin{aligned} T_{TOT} = \frac{1}{2}(m_A + m_B)[\dot{R}_{SA}^2 + R_{SA}^2 \dot{\nu}^2] + \\ \frac{1}{2}(\dot{\theta} + \dot{\nu})^2 \Big[m_B(l^2 + R_{PA}^2) + I_A \Big] + \\ m_B(\dot{\theta} + \dot{\nu}) \Big[l R_{PA}(\dot{\theta} + \dot{\nu}) \cos(\alpha) + \\ PAR_{SA}\dot{\nu}\cos(\xi + \theta) + \\ l R_{SA}\dot{\nu}\cos(\alpha + \xi + \theta) - \dot{R}_{SA} R_{PA} \sin(\xi + \theta) - \\ l \dot{R}_{SA} \sin(\alpha + \xi + \theta) \Big]. \end{aligned} \tag{10}$$

The acceleration due to the solar radiation pressure depends on the orientation of the Sun light with respect to the surface of the balloon. However, we consider a simplified model where the SRP is always normal to the surface of the balloon (Farrés 2017). The effect of imperfections and absorptions of photons by the surface of the balloon can be considered in a more realistic model and requires a more detailed study (Deng et al. 2019), which is out of the scope of this work. Thus, the acceleration due to the SRP ($\ddot{\vec{P}}_R$) can be expressed as:

$$\ddot{\vec{P}}_R = -c_r P_{rad} \Big(\frac{A_B}{m_B} \Big) \Big(\frac{au}{|\vec{r}_A - \vec{r}_S|} \Big)^2 \frac{\vec{r}_A - \vec{r}_S}{|\vec{r}_A - \vec{r}_S|}, \tag{11}$$

where c_r is the solar radiation pressure coefficient (considered equal to 2 for maximum reflectivity), P_{rad} is the SRP at an au ($4.56 \times 10^{-6}\,\mathrm{N/m^2}$), where au is the Astronomical Unit (the average distance Sun-Earth, $1.49597870700 \times 10^8$ km), A_B is the projected area in the direction of the Sun, m_B is the mass of the balloon, $\vec{r}_A$ is the position vector of the asteroid, and $\vec{r}_S$ is the position vector of the Sun.

In this study, the phenomenon of occultation of the balloon by the asteroid (shadow) is not considered. The SRP acceleration on the asteroid is also neglected, and only the effects on the balloon are analyzed. Therefore, the absolute value of the solar radiation force can be expressed as (Luo et al. 2009):

$$F_R = c_r P_{rad} A_B \Big(\frac{au}{R_{SB}} \Big)^2, \tag{12}$$

where R_{SB} is the distance between the Sun and the balloon.

According to McInnes (1999), we can interpret β as the ratio between the solar acceleration and the gravitational attraction acting on the balloon, i.e.,

$$\beta = \frac{F_{PR}}{F_{GR}} = \frac{\frac{c_r P_{rad} A_B au^2}{R_{SB}^2}}{\frac{GMm_B}{R_{SB}^2}} = c_r P_{rad} \frac{au^2}{GM} \frac{A_B}{m_B}. \tag{13}$$

Since the SRP is proportional to the inverse square of the distance to the Sun, it is common to write its effect as a correction of the Sun's gravitational attraction (Simmons et al. 1985; McInnes 1999; Zotos 2015). Thus, the resulting force acting on the balloon, written as a function of the parameter β, is:

$$F_{RES} = -\frac{GMm_B}{R_{SB}^2}(1 - \beta). \tag{14}$$

Based on Brouwer & Clemence (1961), we can write the potential energy between the Sun and the asteroid, and the Sun and the balloon, respectively, as:

$$U_{SA} = -\int_{\infty}^{R_{SA}} -\frac{GMm_A}{R_{SA}^2} dR_{SA} = -\frac{GMm_A}{R_{SA}}, \tag{15}$$

$$\begin{aligned} U_{SB} &= -\int_{\infty}^{R_{SB}} -\frac{GMm_B}{R_{SB}^2}(1 - \beta) dR_{SB} \\ &= -\frac{GMm_B}{R_{SB}}(1 - \beta). \end{aligned} \tag{16}$$

The position of the balloon relative to the asteroid is kept fixed. We assume that there is no gravitational potential between these bodies. The distance between the Sun and the balloon (R_{SB}) is determined by applying the cosine law in the triangle (SAB) shown in Figure 1. We assume that the distance between the Sun and the asteroid is much greater than the distance between the balloon and the asteroid ($R_{AB} << R_{SA}$). Then, we can develop

$1/R_{SB}$ in a power series as a function of R_{SA}. Equation (17) shows the result of this series truncated in the second term.

$$\frac{1}{R_{SB}} \approx \frac{1}{R_{SA}} - \frac{R_{AB}}{R_{SA}^2}\cos(\theta + \xi + \varphi). \tag{17}$$

The total gravitational energy of the system is given by the sum of equations (15) and (16), after replacing R_{SB} by equation (17). The final result is shown in equation (18).

$$\begin{gathered} U_{TOT} = -\frac{GM}{R_{SA}}\Big[m_A + m_B(1-\beta)\Big] + \\ m_B(1-\beta)GM\frac{R_{AB}}{R_{SA}^2}\cos(\theta + \xi + \varphi). \end{gathered} \tag{18}$$

Thus, the Lagrangian of the system is obtained by subtracting the kinetic energy from the potential energy. The result is shown in equation (19).

$$\begin{gathered} \mathcal{L} = T_{TOT} - U_{TOT} = +\frac{1}{2}(m_A + m_B)(\dot{R}_{SA}^2 + R_{SA}^2\dot{\nu}^2) \\ +\frac{1}{2}(\dot{\theta} + \dot{\nu})^2[m_B(l^2 + R_{PA}^2) + I_A] \\ +m_B(\dot{\theta} + \dot{\nu})\Big[lR_{PA}(\dot{\theta} + \dot{\nu})\cos(\alpha) \\ +R_{PA}R_{SA}\dot{\nu}\cos(\xi + \theta) + lR_{SA}\dot{\nu}\cos(\alpha + \xi + \theta) \\ -\dot{R}_{SA}R_{PA}\sin(\xi + \theta) - l\dot{R}_{SA}\sin(\alpha + \xi + \theta)] + m_A\frac{GM}{R_{SA}} \\ +m_B(1-\beta)\Big[\frac{GM}{R_{SA}} - GM\frac{R_{AB}}{R_{SA}^2}\cos(\theta + \xi + \varphi)\Big]. \end{gathered} \tag{19}$$

Finally, the second-order differential equations for the generalized coordinates R_{SA}, ν, θ for the asteroid-tether-balloon system are obtained from the Lagrange equations, assuming that the non-conservative forces are zero. The results are shown in equations (20), (21) and (22).

$$\begin{gathered} (m_A + m_B)[\ddot{R}_{SA} - R_{SA}\dot{\nu}^2] \\ +\frac{GM}{R_{SA}^2}\Big[m_A + m_B(1-\beta)\Big(1 - 2\frac{R_{AB}}{R_{SA}}\cos(\theta + \xi + \varphi)\Big)\Big] \\ -m_B\dot{\theta}(\dot{\nu} + \dot{\theta})\Big[R_{PA}\cos(\theta + \xi) + l\cos(\alpha + \theta + \xi)\Big] \\ -m_B\dot{\nu}(\dot{\nu} + \dot{\theta})\Big[R_{PA}\cos(\theta + \xi) + l\cos(\alpha + \theta + \xi)\Big] \\ -m_B(\ddot{\nu} + \ddot{\theta})\Big[R_{PA}\sin(\theta + \xi) + l\sin(\alpha + \xi + \theta)\Big] = 0, \end{gathered} \tag{20}$$

$$\begin{gathered} \ddot{\nu}[m_B(2lR_{PA}\cos(\alpha) + l^2 + R_{PA}^2) \\ +2m_BR_{SA}(l\cos(\alpha + \xi + \theta) + R_{PA}\cos(\xi + \theta)) \\ +(m_A + m_B)R_{SA}^2] + m_B\Big[\ddot{\theta}\Big(lR_{SA}\cos(\alpha + \xi + \theta) \\ +2lR_{PA}\cos(\alpha) + l^2 + R_{PA}^2 + R_{PA}R_{SA}\cos(\xi + \theta)\Big) \\ -\ddot{R}_{SA}\Big(l\sin(\alpha + \xi + \theta) + R_{PA}\sin(\xi + \theta)\Big) \\ -\dot{R}_{SA}\dot{\theta}\Big(l\cos(\alpha + \xi + \theta) + R_{PA}\cos(\xi + \theta)\Big)\Big] \\ +2\dot{\nu}\Big[\dot{R}_{SA}\Big(m_B(l\cos(\alpha + \xi + \theta) \\ +R_{PA}\cos(\xi + \theta)) + (m_A + m_B)R_{SA}\Big) \\ -m_BR_{SA}\dot{\theta}(l\sin(\alpha + \xi + \theta) + R_{PA}\sin(\xi + \theta))\Big] \\ +m_B\dot{\theta}\Big[\dot{R}_{SA}(l\cos(\alpha + \xi + \theta) + R_{PA}\cos(\xi + \theta)) \\ -R_{SA}\dot{\theta}(l\sin(\alpha + \xi + \theta) \\ +R_{PA}\sin(\xi + \theta))\Big] + I_A(\ddot{\theta} + \ddot{\nu}) = 0, \end{gathered} \tag{21}$$

$$\begin{gathered} -m_B\ddot{R}_{SA}(R_{PA}\sin(\xi + \theta) + l\sin(\alpha + \xi + \theta)) \\ +m_B\dot{\nu}\Big[\dot{R}_{SA}(R_{PA}\cos(\xi + \theta) + l\cos(\alpha + \xi + \theta)) \\ -R_{SA}\dot{\theta}(R_{PA}\sin(\xi + \theta) + l\sin(\alpha + \xi + \theta))\Big] + I_A(\ddot{\theta} + \ddot{\nu}) \\ +m_B\Big[-\dot{R}_{SA}\dot{\theta}(R_{PA}\cos(\xi + \theta) + l\cos(\alpha + \xi + \theta)) \\ +\ddot{\theta}(l^2 + R_{PA}^2 + 2lR_{PA}\cos(\alpha)) \\ +\ddot{\nu}(l^2 + R_{PA}^2 + 2lR_{PA}\cos(\alpha) \\ +R_{PA}R_{SA}\cos(\xi + \theta) + lR_{SA}\cos(\alpha + \xi + \theta))\Big] \\ -m_B(\dot{\nu} + \dot{\theta})\Big[-\dot{R}_{SA}R_{PA}\cos(\xi + \theta) \\ -l\dot{R}_{SA}\cos(\alpha + \xi + \theta) \\ -R_{SA}R_{PA}\dot{\nu}\sin(\xi + \theta) - lR_{SA}\dot{\nu}\sin(\alpha + \xi + \theta)\Big] \\ -\frac{GMm_B(1-\beta)R_{AB}\sin(\varphi + \xi + \theta)}{R_{SA}^2} = 0. \end{gathered} \tag{22}$$

2.3. *Main Parameters and Overview of the Simulations*

Recent papers found in the literature use high values of the area-to-mass ratio to study the dynamics of debris in Earth's orbit (Valk & Lamaître 2008; Anselmo & Pardini 2010; Rosengren & Scheeres 2013; Früh & Moriba 2014). The membranes known as "gossamer" can be used to build large thin structures. These structures can be useful in many space applications (Deng et al. 2019). Another example of future missions that will use large structures is to transport telescopes to the stratosphere for scientific

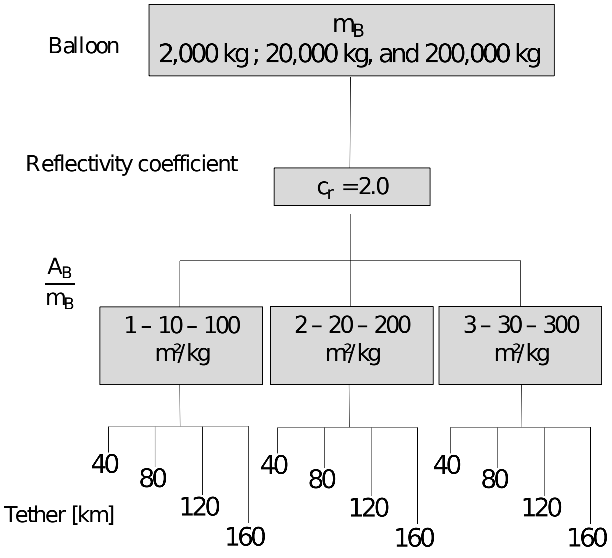

Fig. 3. Overview of the simulations.

purposes.[1] Inspired by these ideas, we use high values of area-to-mass ratio for a different purpose: to maneuver an asteroid. We propose to use a balloon that uses the SRP as a propulsion system and this concept is tested in this work. The effects of the balloon's mass (m_B), the length of the tether (l), and the area-to-mass ratio (A_B/m_B) of the spacecraft are the parameters considered in the analysis, as shown in the flowchart of Figure 3 .

We use two parameters δ and Δ to measure the deviation of the asteroid due to the balloon. These two parameters are, respectively, the distance Earth-asteroid, which is calculated for trajectories with and without the presence of the balloon; and the relative distance between the trajectories with and without the balloon. The latter can be calculated because the equation of motion of the asteroid, considering the balloon, is integrated along with the equation of motion of the asteroid without the balloon, respectively. Then, the trajectory of the asteroid without the balloon can be considered as a reference trajectory. Figure 4 shows the two main deviation parameters. These parameters are also used to assess the efficiency of using a balloon to deflect an asteroid, since the larger the deviation in the trajectory the more efficient is the configuration adopted. Both parameters are calculated using the distance between two points in the Cartesian plane.

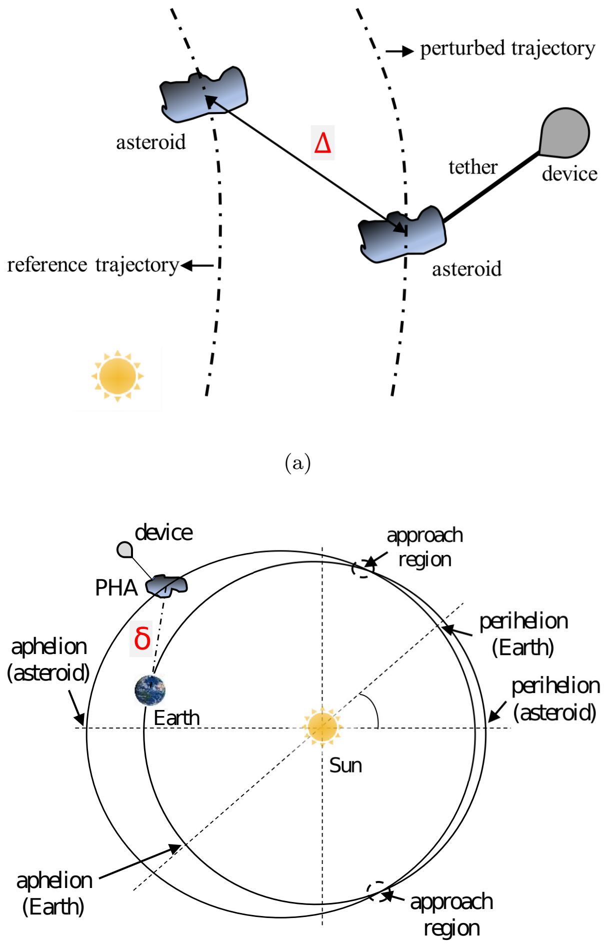

(a)

(b)

Fig. 4. Parameters of deviation between (a) the trajectories of the PHA with the balloon and without the balloon (b) asteroid-tether-balloon system and Earth. The color figure can be viewed online.

The effect of the SRP acting on the system is inserted in the mathematical model through the parameter β. The relation of A_B/m_B with β, for $c_r = 2.0$, is given by [see equation (13)]:

$$\frac{A_B}{m_B} = 684.20\beta \, . \tag{23}$$

3. RESULTS AND ANALYSIS

In this section, we analyze the results obtained from the numerical simulations using the proposed physical model. In § 3.1, the lowest fuel consumption for a transfer between Earth and Bennu is determined for a 20-year interval, from 2020-2040. The relative

---

[1] https://www.nasa.gov/feature/jpl/nasa-mission-will-study-the-cosmos-with-a-stratospheric-balloon (last access January/2021)

TABLE 1

ORBITAL PARAMETERS OF 101955 BENNU AT EPOCH 2455562.5 (2011-JAN-01.0)

Element	Value
a	1.12639 au
e	0.20374
q	0.89689 au
i	6.03493°
Ω	2.06087°
ω	66.22307°
P_B	436.64873 days

distance Δ between the trajectories of the asteroid with the balloon and without the balloon (reference trajectory), and the distance δ, from the PHA to the Earth, are discussed in § 3.2 and § 3.3, respectively.

The root mean square (RMS) is frequently used to calculate experimental errors. However, this method can be used to compare two models, as in Sanchez et al. (2014). Therefore, we calculate the RMS deviation from the orbit with the balloon with respect to the orbit without the balloon. In this case, empirical equations are obtained to relate the tether length and the area-to-mass ratio with the mean deviations (§ 3.4).

3.1. *Determination of the Initial Position of the Bodies*

Numerical simulations were performed for asteroid 101955 Bennu. The main reasons for choosing this asteroid are: (i) it is one of the top PHAs on the Sentry list[1], which monitors objects with the potential of a future impact with the Earth; (ii) it has low orbital inclination (our physical model is two-dimensional); (iii) it is the target of the OSIRIS-REx mission. Table 1 shows the orbital parameters of this body, which are: semi-major axis (a), eccentricity (e), perihelion distance (q), inclination (i), longitude of the ascending node (Ω), argument of perigee (ω), and orbital period (P_B). In addition, Bennu has a mass of 7.8×10^{10} kg, with dimensions 0.565 km × 0.535 km × 0.508 km, and a rotation period of 4.297 h.

The choice of the initial date for the position of the bodies (Bennu and Earth) was obtained through a model based on the patched-conics (Crenshaw 1963; Miele & Wang 1999; Sanchez et al. 2019). The best trajectory is found such that it minimizes the fuel consumption (ΔV) required to transfer a spacecraft from the Earth (circular orbit with 200 km altitude) to the desired body in an given time interval (2020-2040). The initial position of the bodies and the arrival and departure dates of the spacecraft are shown in Figure 5. The duration of the transfer is 353 days, and the consumption required by a bi-impulsive maneuver is $\Delta V_{TOT} = 3.243$ km/s. Notice that the arrival date is very close to the crossing point of the orbits of Bennu and the Earth. This result is expected, because maneuvers for orbital inclination correction are very costly. It was also considered that the tether is fixed to the balloon immediately after the arrival of the spacecraft in Bennu (red trajectory).

TABLE 2

DEFINITION OF LINE OF APSIDES OF EARTH AND BENNU AT INITIAL TIME

Date of departure of the spacecraft	Line of apsides			
	Earth		Bennu	
	$\omega(^\circ)$	$\Omega(^\circ)$	$\omega(^\circ)$	$\Omega(^\circ)$
28 Oct 2035	287.90	175.18	66.46	1.92

Table 2 contains the argument of pericenter (ω) and the longitude of the ascending node (Ω) used to define the position of the Earth's perigee (π_E) and Bennu's perigee (π_B). From this, it was considered that the line of apsides of the orbit of Bennu coincides with the X-axis of the inertial system, which means that the perigee of its orbit is on that axis. The same hypothesis was used to numerically integrate the Earth's orbit. However, for the launch date of the spacecraft (10.28.2035), the phase angle between the line of apsides of Bennu and the Earth is $\psi = 34.69°$. In this way, it is necessary to rotate the Earth coordinates position using the coordinate transformation matrix between the inertial system and the rotational system, centered in the Sun (Vallado 1997).

Finally, Table 3 presents the initial conditions for the simulations.

3.2. *Determination of Distances from the Earth*

In this section, we will discuss the orbit deviation's of the PHA by the balloon connected with the tether, using masses of 2000 kg, 20 000 kg, and 200 000 kg for the balloon. The simulations show that the use of the balloon results in two types of deflections. The first

---

[1] https://cneos.jpl.nasa.gov/sentry/ (last access January/2021)

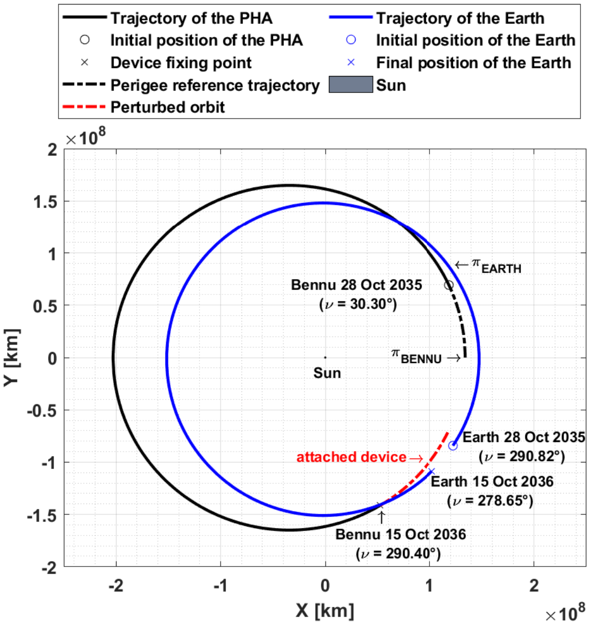

Fig. 5. Initial position of the bodies and the orbital geometry. The color figure can be viewed online.

TABLE 3

INITIAL VALUES OF STATE VARIABLES

Variables	Values
ν [deg]	30.30
R_{SA} [km]	1.374×10^{11}
θ [deg]	0
$\dot{\nu}$ [deg/s]	1.406×10^{-5}
$\dot{R}_{SA}$ [km/s]	2.947×10^{3}
$\dot{\theta}$ [deg/s]	0.0232

one will be called a negative deflection, i.e, Bennu is brought closer to Earth, as observed in Figure 6 at a time of 56.30 years. However, at a time of 122.99 years, the deflection is set to positive, because the use of balloon increases the distance between Bennu and the Earth.

Figure 7 shows the distances from Bennu to Earth in separate graphs, for the two scenarios mentioned above; the cases in which the deviations of the trajectories without balloon (“dashed pink line curves”) and with the balloon, but without taking into account the SRP (“black dashed curves”). The two dashed curves are practically overlapping, since the mass of the balloon is very small compared to Bennu’s mass. Therefore, the center of mass of the system suffers a small displacement and, consequently, the deviations are less significant, in contrast with the results obtained by Venditti et al. (2020), since the ballast is much more massive than the balloon considered in this paper.

For balloons with mass of 2000 kg and 200 000 kg, the same results shown in Figure 7 were obtained. However, they were omitted here. Equation 24 allows us to directly evaluate the deviations between the black dashed curve (without balloon) and the red curves (with balloon),

$$\delta_{NP/P} = \delta_{NP} - \delta_{P}, \qquad (24)$$

where δ_{NP} and δ_{P} refer to the distance between the PHA and the Earth, with and without the attached balloon, respectively.

In Figures 8(a) and 8(c), the deflections were positive, that is, in these cases the use of the balloon decreased the distance between the Earth and the PHA. In contrast, Figures 8(b) and 8(d) show that the deviations are negative, meaning that the PHA’s trajectory is increasing its distance from the Earth. In both cases the ratio A_B/m_B amplifies the magnitude of the deviations. For example, in 56.3 years it is possible to deflect the asteroid by 25 R_{EARTH}, considering a balloon of 200 000 kg and, $A_B/m_B = 300$ m^2/kg.

3.3. *Deviations Due to Orbit Perturbation*

The simulations were made with the four tether lengths presented in Figure 3. However, in this section, only the results for the 40 km tether are shown.

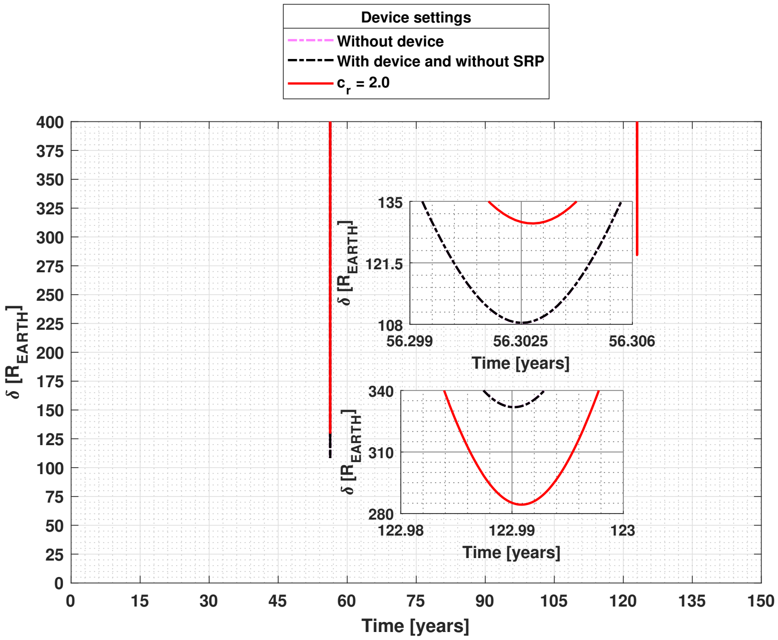

Fig. 6. Bennu-Earth distances for values smaller than 400 R_{EARTH}, for the case of $m_B = 200\,000$ kg and $A_B/m_B = 300$ m^2/kg. The color figure can be viewed online.

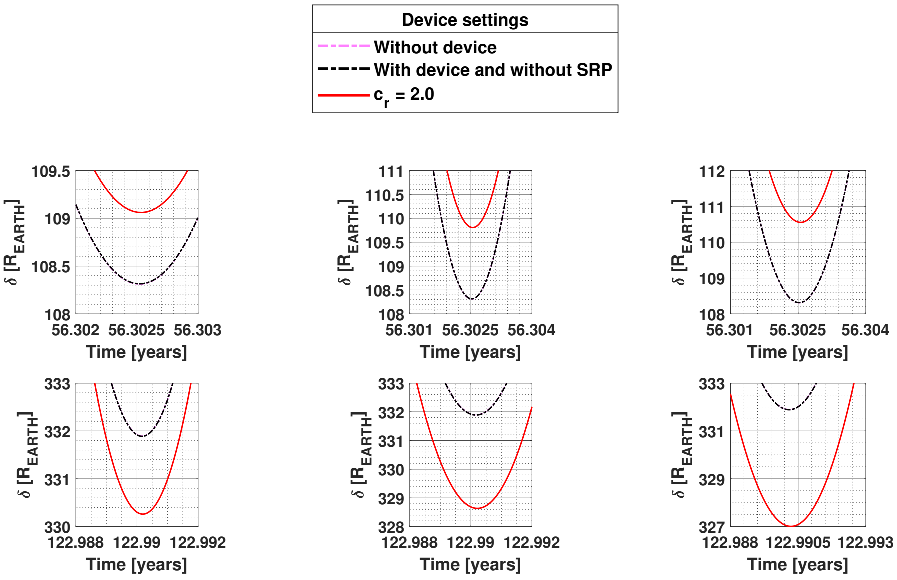

(a) (b) (c)

Fig. 7. Distance between PHA and the Earth in terrestrial radius units considering a balloon with $m_B = 20\,000$ kg for (a): $A_B/m_B = 100$ m^2/kg, (b): $A_B/m_B = 200$ m^2/kg, and (c): $A_B/m_B = 300$ m^2/kg. The color figure can be viewed online.

The effect of the tether length on the deviation is a subject of analysis in § 3.4.

The analysis shown in Figure 9 was made for 150 years and it shows the deviations in the trajectory due to the balloon [see Figure 4(a)], considering a balloon with 20 000 kg. The deviations are proportional to A_B/m_B. Simulations for longer periods of time, and perturbations, such as N-bodies, general

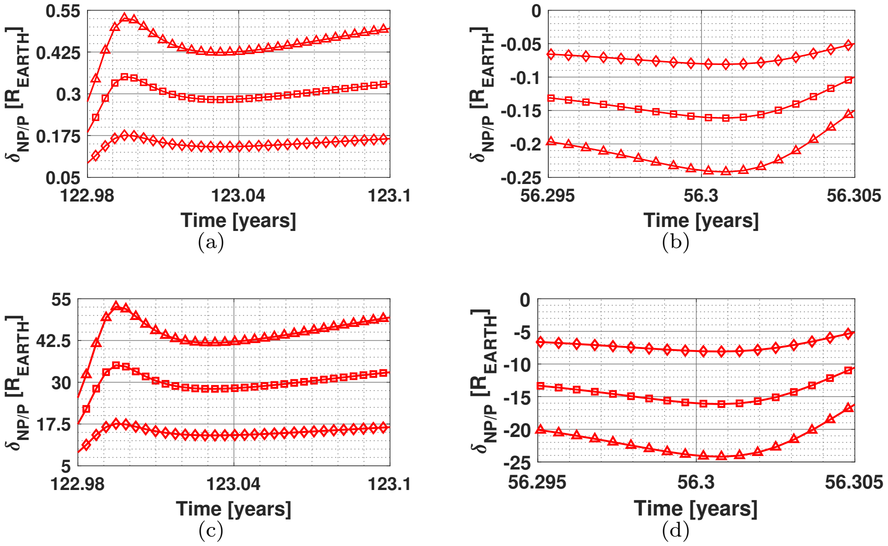

(a) (b)

(c) (d)

Fig. 8. Difference in δ considering a balloon with 2.000 kg, (a) positive deflection, (b) negative deflection; and a balloon with 200 000 kg, (c) positive deflection, and (d) negative deflection. The lines with diamond markings refer to $A_B/m_B = 100$ m^2/kg, square markings to $A_B/m_B = 200$ m^2/kg, and triangle markings to $A_B/m_B = 300$ m^2/kg. The color figure can be viewed online.

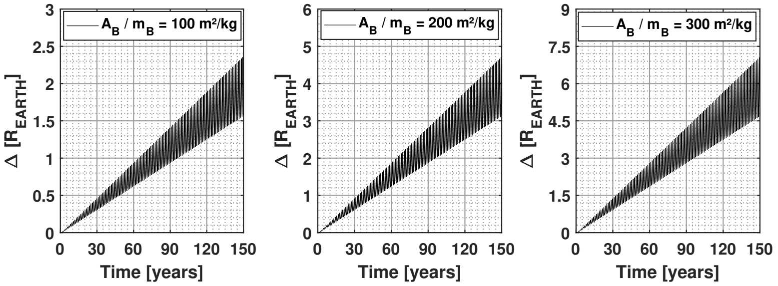

Fig. 9. Deviation between the trajectories of the PHA with and without balloon in terrestrial radius units, considering a 20 000 kg balloon and $l = 40$ km.

relativity, Yarkovsky effect, flattening of planets and moons, among others, should be considered in the physical model, but this is not the main objective of the present paper. Furthermore, the method proposed in this work may be more appropriate when considering warning times of a few decades, as is the case with the gravity tractor method (NTRS 2015).

The results for balloons with masses of 2000 kg and 200 000 kg are shown in Figure 10. In the first year of simulation there is no deviation, because this period refers to the time that the spacecraft travels to Bennu, as can be seen in the magnification of this part of the figure. The magnitude of the deviations when increasing the mass by a factor of 100 is also shown. For example, a less massive balloon generates a deviation of 0.70 R_{EARTH} when A_B/m_B is 300 m^2/kg [see Figure 10(a)], whereas a more massive balloon (one hundred times larger) enables deviations of approximately 70 R_{EARTH} for the same settings [see Figure 10(b)].

3.4. *Effects of the Tether Length: Mean Deviation of the Trajectory*

To summarize the large amount of results and to present them in a clear way, we use the root-mean-square deviation, according to equation 25. Usually, the RMS method is used to calculate the error of an experimental measurement with respect to a reference value, or even to calculate the error of an approximation with respect to a true value of this function (Freedman et al. 2007; Sanchez et al. 2014).

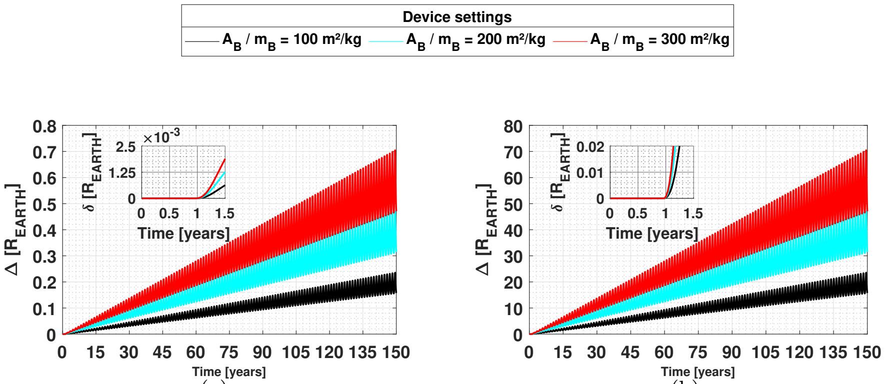

(a) (b)

Fig. 10. Deviations between the trajectories of the PHA with and without the balloon, in terrestrial radius units, for $l = 40$ km, and considering a balloon with (a): 2000 kg, and (b): 200 000 kg. The color figure can be viewed online.

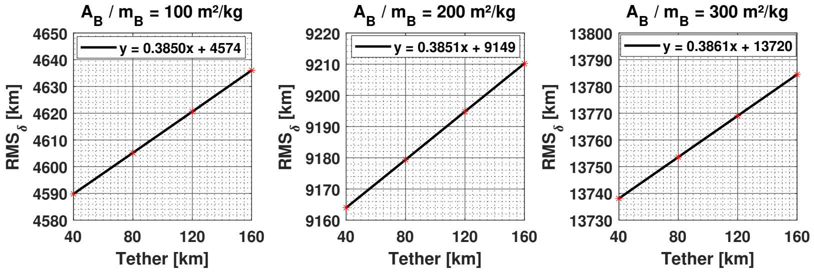

Fig. 11. RMS deviations for δ considering a balloon with a mass of 20 000 kg. The color figure can be viewed online.

However, this method can also be used to compare two sets of values, one used as a reference set and the other one as the "measurement" set. In our case, we used the RMS to compare the trajectory without balloon, which is our reference orbit, with the trajectory generated by the simulation considering the balloon. In this case, this RMS deviation shows the deviation from one trajectory to another. Hence, we need to determine the differences between the reference and perturbed (with balloon) orbits. Particularly in this problem, we define the reference values (y_k) as determined by the Keplerian orbit, and the perturbed values $(\hat{y}_k)$ as those obtained by the perturbed system, with the addition of the tether and the balloon. The total number of points evaluated corresponds to the value of N.

$$RMS_\delta = \frac{1}{N}\sqrt{\sum_{k=1}^{N}(\hat{y}_k - y_k)^2}. \tag{25}$$

The RMS deviation for a balloon with a mass of 20 000 kg is shown in Figure 11. We used the RMS deviation to quantify the effect of the tether length (l) on deviations with the Earth (δ). Using this technique, it is possible to note that the change in RMS_δ is less sensitive to l, considering the values of m_B used. In all cases, we have determined linear equations that relate these two parameters. The residuals between the values calculated with the model and the linear approximation were less than 0.1 km, as seen in Figure 12(a). Figure 12(b) shows the norm of residuals, when is a measurement of the quality of the fit, where a smaller value indicates a better fit.

Table 4 shows the differences with respect to the longest and shortest tether length considered. It can be seen that A_B/m_B has little relevance for each particular analysis of m_B, but the magnitudes of the deviations increase by the same factor (10) as the increase in m_B.

Figure 11 shows the three curves (with their respective equations) obtained by the linear fit. This same procedure was performed for the other two values of m_B used, but the graphs are omitted. The linear coefficient of these equations can be divided by A_B/m_B, such that three linear equations for RMS_δ, as a function of l and A_B/m_B, are obtained. Then, a single general equation was obtained for the calculation of RMS_δ as a function of all the balloon parameters (l, A_B/m_B, and m_B), as given in equa-

TABLE 4

EFFECT OF TETHER LENGTH (l) IN RMS_δ CONSIDERING THREE MASS VALUES (M_B) FOR THE BALLOON

A_B/m_B [m^2/kg]	$RMS_{\delta_{160km}} - RMS_{\delta_{40km}}$ [km]		
	$m_B = 2000$ kg	$m_B = 20\,000$ kg	$m_B = 200\,000$ kg
100	4.658	46.268	462.625
200	4.638	46.249	462.435
300	4.625	46.248	462.284

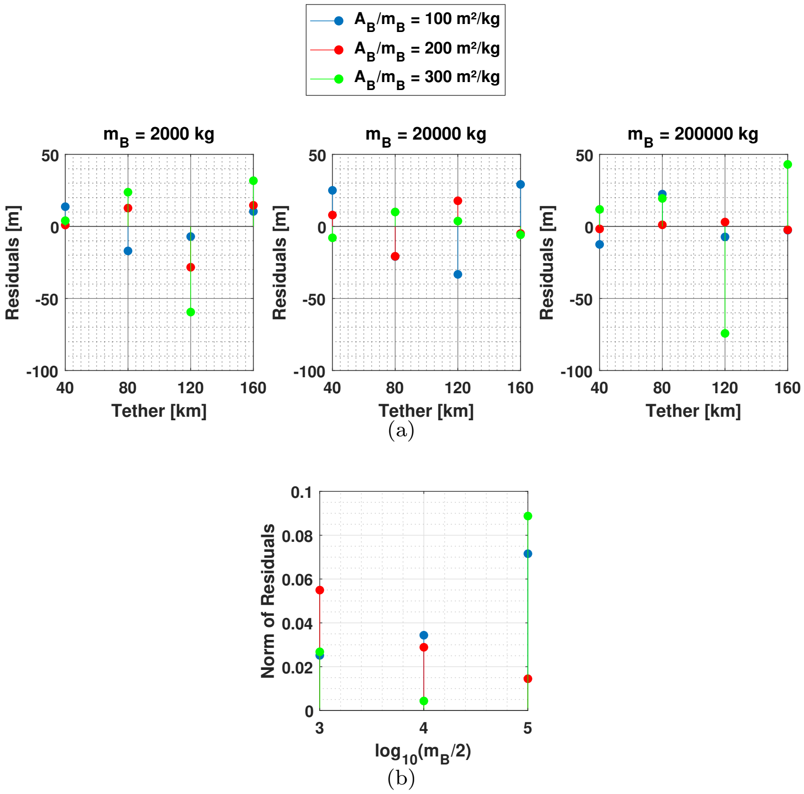

(a)

(b)

Fig. 12. Comparison between the calculated data and the linear fit for $m_B = 2000$ kg, $m_B = 20\,000$ kg, and $m_B = 200\,000$ kg; (a) residuals, (b) norm of residuals. The color figure can be viewed online.

tion (26). The RMS_δ has a linear behavior that is directly proportional to $10^{-5}m_B$. The new coefficients obtained in each step, for the reduction of the equations, were calculated using a simple mean.

$$RMS_\delta = 10^{-5} m_B \Big(1.923l + 222.986 \frac{A_B}{m_B} \Big). \qquad (26)$$

In this empirical equation, it is verified that, for the same value of A_B/m_B, increasing the mass of the balloon (m_B) implies that we must increase the cross section area illuminated by the Sun (A_B), that is, the balloon will have larger physical dimensions.

3.5. *A Particular Case: Deflection of Small Asteroids*

In this section, we will test the concept of transferring a small asteroid, similar to the one in the Chelyabinsk event in 2013, to orbits closer to the Earth, for scientific and space mining purposes. The deviation method we propose provides trajectory approximations in shorter times (18.9 years), because the mass of the asteroid is of the order of 10^6 kg. Moreover, we will also show the case where the asteroid can be deflected farther from the Earth after 56.3 years from the start of the application of the method. The initial condition vector of the asteroid

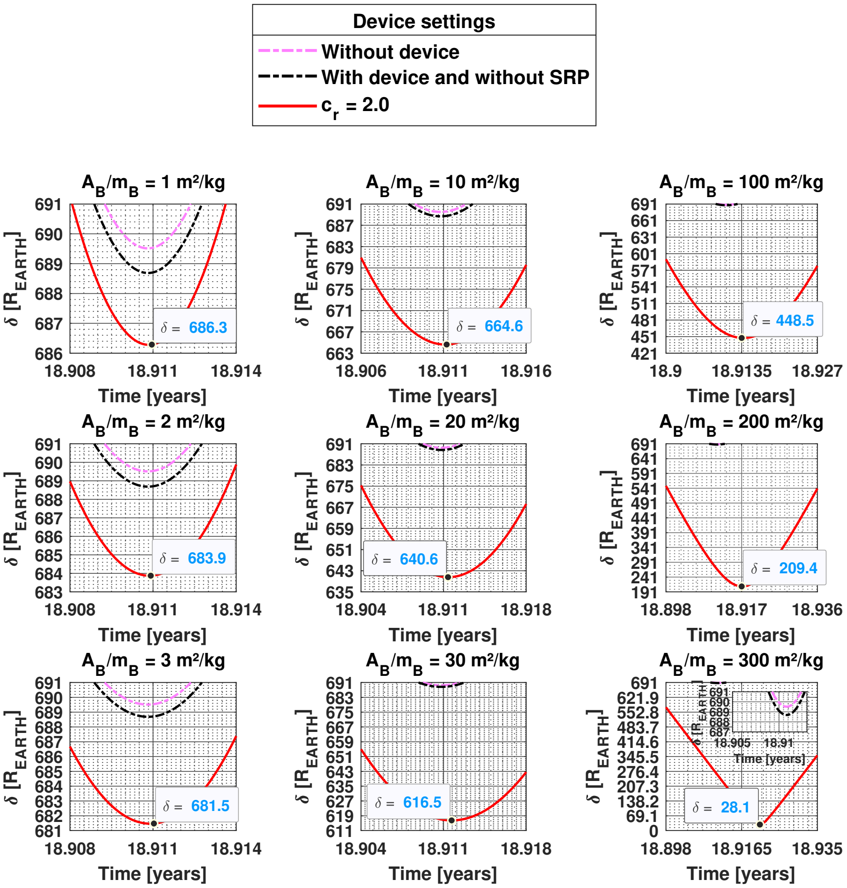

Fig. 13. Distance between a small asteroid and the Earth, in terrestrial radius units, considering a balloon with m_B = 2000 kg and a tether of 40 km, for a period of operation of less than 20 years. The color figure can be viewed online.

considered is shown in Table 3 (§ 3.1), as well as the other parameters.

Figure 13 shows the effects of m_B and A_B/m_B for the situation where the asteroid would be approaching the Earth. In the cases discussed in the previous sections, we had $m_B/m_A = 2.56 \times 10^{-8}$ for $m_B = 2000\,\text{kg}$. However, here we consider $m_B/m_A = 2.56 \times 10^{-4}$. The reduction of this ratio implies that a mass of 2000 kg becomes more effective in changing the trajectory of the asteroid, as expected. This effect causes a deviation of about 0.8 R_{EARTH} in approximately 19 years of simulation and is determined when the magenta and black curves are compared. The lengths of l considered here do not change this deviation beyond about a few hundred kilometers, because the operating time is short and m_B is small. In this way, the center of mass of the system undergoes very small displacements.

We were able to transfer an approaching asteroid from a distance of 689.5 R_{EARTH} to approximately 28 R_{EARTH}, using $A_B/m_B = 300\,\text{m}^2/\text{kg}$. This would bring it closer to Earth by 180 000 km.

TABLE 5

APPROXIMATE VALUES OF δ DUE TO THE CHANGES OF A_B/M_B*

A_B/m_B [m^2/kg]	$d\delta$ [R_{EARTH}]
1 - 2 - 3	2.34
10 - 20 - 30	23.40
100 - 200 - 300	234.00

*For the case of deflection of the trajectory of the asteroid to bring it close to Earth.

Table 5 shows the effects of the balloon parameters on the variation of δ. Note that deviations of more than 200 R_{EARTH} were obtained by using the proposed technique to bring the asteroid closer to the Earth. This shift saves very large amounts of fuel, if these transfers are performed using engines.

TABLE 6

APPROXIMATE VALUES OF δ DUE TO THE CHANGE OF A_B/M_B*

A_B/m_B [m^2/kg]	$d\delta$ [R_{EARTH}]
1 - 2 - 3	7.25
10 - 20 - 30	72.50
100 - 200 - 300	725.00

*For the case of deflection of the trajectory away from Earth.

Figure 14 shows the results for the case where the PHA trajectory is increasing its distance from the Earth. The asteroid approaches 108 R_{EARTH} in natural conditions (black curves) after 56.3 years of simulations. The increase in l at 40 km corresponds to an approximate increase of 2.5 R_{EARTH} in the deviation δ, for any A_B/m_B configuration.

Table 6 shows the approximate values for the variations caused in δ due to changes in the balloon parameters. The deflection is increased by 7.25 R_{EARTH} as A_B/m_B increases by 1 m^2/kg. For example, a balloon with 3 m^2/kg of mass area offers an additional 14.5 R_{EARTH} in δ, when compared to a balloon with 1 m^2/kg. This would be the simplest design and construction out of all the balloon configurations considered, but it is important to see the possibilities of this technique. Deviations of more than 700 R_{EARTH} can be achieved. Of course they depend on high values of the area-to-mass ratio, but our goal is to show the potential of the technique, even if there are technological problems for its applications. Besides, there are also intermediate values that are closer to be technologically viable.

Equation (27) provides approximate values of Δ as a function of the balloon parameters for 50 years of operation. The effect of l is much smaller than the effect of A_B/m_B.

$$\Delta = 0.058l + 6.721\frac{A_B}{m_B}. \qquad (27)$$

Table 7 shows the variations in Δ due to changes in the balloon parameters. Δ is little sensitive to l and is directly proportional to A_B/m_B. There is also a large range of values, of the deviations, from 6.7 R_{EARTH} to near 670 R_{EARTH}.

TABLE 7

APPROXIMATE VALUES OF Δ DUE TO CHANGES OF A_B/M_B

Tether [km]	A_B/m_B [m^2/kg]	$d\Delta$[R_{EARTH}]
	1 - 2 - 3	6.73
40 - 80 - 120 - 160	10 - 20 - 30	67.26
	100 - 200 - 300	672.65

4. CONCLUSION

In this work, the main objective was the investigation of an alternative solution to modify the orbit of an asteroid that poses a risk of collision with Earth, or to bring the asteroid closer for mining purposes or scientific research. The proposed technique suggests the use of one balloon (or several) with a large area-to-mass ratio that is attached to the asteroid with a tether, using the SRP to alter the trajectory of the asteroid. This technique enables the deviation of the whole asteroid, avoiding unpredictable situations caused by fragmentation, as might happen when using other deflection methods, such as the kinetic impact or nuclear explosives.

There are two factors that modify the trajectory of the asteroid. The force coming from the SRP, and the displacement of the center of mass of the system due to the mass of the balloon. The deviations coming from the SRP are much larger and dominate the scenario, because the mass of the balloon is much smaller than the mass of the asteroid. Although it is a technique that takes several years to deliver results, larger deviations can be obtained depending on the configuration of the balloon, when compared to the use of the gravity tractor, which is a technique that also requires a large period of time to be implemented.

In the case that we consider, an asteroid with mass similar to that of (21088) Chelyabinsk, the minimum distance Earth-asteroid was reduced by 1.2 %, 10.6 % and 96 %, when A_B/m_B was 3 m^2/kg, 30 m^2/kg and 300 m^2/kg, respectively. This result was obtained in less than 20 years of operation. In addition, the distance from the asteroid after 56.3 years of operation was 22 times greater when we consider $A_B/m_B = 300\,\mathrm{m}^2$/kg.

On the other side, if the goal is to bring the asteroid closer to Earth for mining or scientific research, a decrease in distance of the order of 700 R_{EARTH} was achieved. Those are important values, because a space mission would require much less fuel to reach the asteroid.

It is noted that the largest deviations are obtained using large values of area-to-mass ratio, which would cause technological problems for the construction of the balloon, but the goal of the present paper

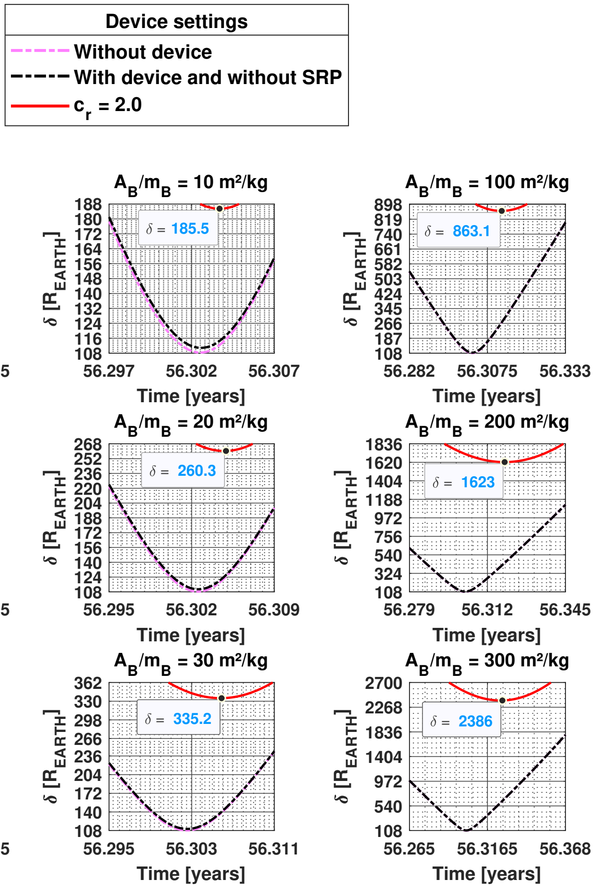

Fig. 14. Distance between a small asteroid and the Earth, in terrestrial radius units, considering a balloon with m_B = 2000 kg and a tether of 40 km, for a period of operation of less than 60 years. The color figure can be viewed online.

is to show the potential of the proposed technique, not taking into account technological problems. Besides, there are also intermediate values of deviations that do not require such large balloons, specially considering the possibility of using several smaller balloons.

Therefore, shorter tethers can be used to attach multiple balloons to the surface of the asteroid, thus constituting large areas for collecting the SRP. This configuration is much more feasible, because it reduces the structural stress in the tether, facilitating the construction of the whole apparatus, which would be fixed on the asteroid. In addition, other cases could be predicted from the empirical equations that relate the main parameters of the model.

The authors wish to express their appreciation for the support provided by grants #140501/2017-7, 301338/2016-7, 406841/2016-0, and 150678/2019-3 from the National Council for Scientific and Technological Development (CNPq) and grants 2016/24561-0 from São Paulo Research Foundation (FAPESP). We also thank the financial support from the National Council for the Improvement of Higher Education (CAPES).

REFERENCES

Aljbaae, S., Prado, A. F. B. A., Sanchez, D. M., & Hussmann, H. 2020, MNRAS, 496, 1645
Anselmo, L. & Pardini, C. 2010, AcAau, 67, 204
Aslanov, V. & Yudintsev, V. 2013, AcAau, 91, 149
Brack, D. N. & McMahon, J. W. 2020, JSpRo, 57, 413
Bosanac, N., Howell, K. C. & Fischbach, E. 2015, CeMDA, 122, 27
Bottke, W. F. Jr., Vokrouhlický, D. P., Rubincam, D. P., & Nesvorný, D. 2006, AREPS, 34, 157
Brouwer, D. & Clemence, G. M. 1997, Methods of Celestial Mechanics, (London, UK: Academic Press)
Chappell, S. P., Abercromby, A. F., & Gernhardt, M. L.2013, AcAu, 89, 166
Cheng, A. F., Rivkin, A. S., Michel, P., et al. 2018, P&SS, 157, 104

Cohen, S. S. & Misra, A. K. 2017, JGCD, 30, 171
Crenshaw, J. W. 1963, AIAA, 1, 2168
Dachwald, B. & Wie, B. 2007, JSpRo, 44, 755
Deng, X., Yixiang, X., & Clarke, C. 2019, Composites Part B: Engineering, 157, 266
Estes, R. D., Johnson, C. L., Lorenzini, E. C, et al. 2000, JSpRo, 37, 205
Farnocchia, D., Chesley, S. R., Chodas, P. W., et al. 2013, Icar, 224, 192
Farrés, A. 2017, AcAau, 137, 78
Freedman, D., Pisani, R., & Purves, R. 2007, Statistics, (4th ed., W. Norton & Company)
French, D. B. & Mazzoleni, A. P. 2009, JSpRo, 46, 645
Früh, C. & Moriba, K. J. 2014, AcAau, 91, 227
Gao, Y. & Wu, J. 2016, AdSpR, 57, 1002
Gong, S., Li, J., & Bao Yin, H. 2009, CeMDA, 105, 159
Hsieh, H. H. & Jewitt, D. 2006, Sci, 312, 561
Kikuchi, S. & Kawaguchi, J. 2018, AcAau, 156, 375
Lauretta, D. S., Balram-Knutson, S. S., Beshore, E., et al. 2017, SSRv, 212, 925
Liang, Y., Gómez, G., Masdemont, J. J., & Xu, M. 2019, JGCD, 42, 2521
Lu, E. T. & Love, S. G. 2005, Natur, 438, 177
Luo, C., Zhen, J. H., & Gao, D. 2009, Chinese J. Astronaut., 30, 2111
Marchi, L. O., Venditti, F. C. F, Misra, A. K., & Prado, A. F. B. A. 2018, Effect of Earth-Moon perturbation on the deflection of tethered asteroid systems, in 69TH INTERNATIONAL ASTRONAUTICAL CONGRESS, Bremen, Germany. International Astronautical Federation
Mashayekhi, M. J. & Misra, A. K. 2012, AcAau, 75, 71
_________. 2016, CeMDA, 125, 363
McInnes, C. R. 1999, Solar Sailing. Technology, dynamics and mission applications (London, UK: Springer)
Michel, P., Ballouz, R. L., Barnouin, O. S., et al. 2020, NatCo, 11, 1
Michel, P., DeMeo, F. E., & Bottke, W. F. 1999, Asteroids IV, (Tuczon, AZ: UAP)
Miele, A. & Wang, T. 1999, AcAau, 45, 119
Misra, A. K. 2008, AcAau, 63, 1169
Morrison, D. 2019, Overview of Active Planetary Defense Methods, Space and Society (Springer, Cham)
Nolan, M. C., Magri, Ch., Howell, E. S., et al. 2013, Icar, 226, 629
NTRS, Enhanced Gravity Tractor Technique for Planetary Defense, 2015
Ostro, S. J., Hudson, R. S., Jurgens, R. F., et al. 1995, Sci, 270, 80
Rosengren, A. J. & Scheeres, D. J. 2013, AdSpR, 52, 1545
Sanchez, P., Colombo, C., Vasile, M., & Radice, G. 2009, JGCD, 32, 121
Sanchez, D. M., Prado, A. F. B., & Yokoyama, T. 2009, AdSpR, 54, 1008
Sanchez, D. M., Sukhanov, A. A., & Prado, A. F. B. A. 2019, RMxAA, 55, 39
Sánchez-Lozano, J. M., Fernández-Martínez, M., Saucedo-Fernández, A. A., & Trigo-Rodríguez, J. M. 2019, AcAau, 176, 383
Simmons, J. F. L., Macdonald, A. J. C, & Brown, J. C. 1985, CeMec, 35, 145
Valk, S. & Lamaître, A. 2008, AdSpR, 42, 1429
Vallado, D. A. & McClain, W. D. 1997, Fundamentals of Astrodynamics and Applications (McGraw-Hill Companies)
Vasile, M. & Maddock, C. A. 2010, CeMDA, 107, 265
Venditti, F. C. F & Misra, A. C. 2015, Deflection of a binary asteroid asteroid system using tethers, in 66TH INTERNATIONAL ASTRONAUTICAL CONGRESS, Jerusalem, Israel. International Astronautical Federation
Venditti, F. C. F, Marchi, L. O., Misra, A. K., et al. 2018, Dynamics of tethered binary asteroid systems, in 49TH LUNAR AND PLANETARY CONFERENCE, The Woodlans, Texas. Lunar and Planetary Institute and NASA
Venditti, F. C. F., Marchi, L. O., Misra, A. K., Sanchez, D. M., & Prado, A. F. B. A. 2020, EPJST, 229, 1463
Vil'ke, V. G., Chumachenko, E. N., Dunham, D. W., & Nazarov, R. R. 2013, CosRe, 51, 315
Vokrouhlický, D., Bottke, W. F, Chesley, S. R., Scheeres, D. J., & Statler, T. S. 2015, in Asteroids IV, ed. P. Michel, F. E. DeMeo, and F. Bottke (Tuczon, AZ: UAP)
Woo, P. & Misra, A. K. 2013, AcAau, 87, 153
Zotos, E. 2015, Ap&SS, 360, 1

L. O. Marchi and D. M. Sanchez: Division of Space Mechanics and Control - National Institute for Space Research (INPE), CEP 12227-010, São José dos Campos - SP, Brazil (marchi.luis@yahoo.com.br).
A. K. Misra: Department of Mechanical Engineering - McGill University, QC H3A 0G4, Campus of Montréal, Canada.
A. F. B. A. Prado: Postgraduate Division - National Institute for Space Research (INPE), CEP 12227-010, São José dos Campos - SP, Brazil. - Volunteer Professor, Academy of Engineering, RUDN University, Miklukho-Maklaya street 6, Moscow, Russia, 117198 (antonio.prado@inpe.br).
F. C. F. Venditti: Arecibo Observatory, University of Central Florida, HC3 BOX 53995, Arecibo, PR, 00612, USA.

Revista Mexicana de Astronomía y Astrofísica, **57**, 297–309 (2021)

https://doi.org/10.22201/ia.01851101p.2021.57.02.04

ESTIMATING THE PROPAGATION OF A UNIFORMLY ACCELERATED JET

J. I. Castorena[1], A. C. Raga[1], A. Esquivel[1], A. Rodríguez-González[1], L. Hernández-Martínez[2], J. Cantó[3], and F. Clever[3]

Received October 13 2020; accepted March 29 2021

ABSTRACT

We study the problem of a Herbig-Haro jet with a uniformly accelerating ejection velocity, travelling into a uniform environment. For the ejection density we consider two cases: a time-independent density, and a time-independent mass loss rate. For these two cases, we obtain analytic solutions for the motion of the jet head using a ram-pressure balance and a center of mass equation of motion. We also compute axisymmetric numerical simulations of the same flow, and compare the time-dependent positions of the leading working surface shocks with the predictions of the two analytic models. We find that if the jet is over-dense and over-pressured (with respect to the environment) during its evolution, a good agreement is obtained with the analytic models, with the flow initially following the center of mass analytic solution, and (for the constant ejection density case) at later times approaching the ram-pressure balance solution.

RESUMEN

Estudiamos el problema de un yet Herbig-Haro uniformemente acelerado, que se mueve a través de un medio homogéneo. Consideramos dos casos para la densidad de expulsión: una densidad independiente del tiempo, y una tasa de pérdida de masa constante. En ambos casos utilizamos los formalismos de equilibrio de presión hidrodinámica y de posición de centro de masa para obtener soluciones analíticas. También realizamos simulaciones numéricas de este flujo, y comparamos la dependencia temporal de la posición de los choques que conforman la superficie de trabajo con las predicciones analíticas. Encontramos que si la densidad y la presión del yet son mayores que los correspondientes valores del medio, durante toda la evolución, entonces se obtiene una buena coincidencia con los modelos analíticos: en un inicio el flujo sigue la solución analítica de centro de masa y en tiempos posteriores se acerca a la solución de equilibrio de presión hidrodinámica.

Key Words: Herbig-Haro objects — ISM: jets and outflows

1. INTRODUCTION

Jets from young stars and their associated Herbig-Haro objects (HH) are now the most studied and best understood of all astrophysical jets. HH jets are collimated bipolar ejections from low, intermediate and sometimes high mass protostars or young stars (see, e.g., the review of Frank et al. 2014). The interaction between HH jets and the surrounding environment generates a main working surface known as the "head". This structure (formed by a bow shock/jet shock pair) is a clear sign of the "turning on" of the jet, which typically occurred at times of $\approx 10^3 \rightarrow 10^4$ yr ago in observed HH jets.

This type of jets also have a structure of emitting knots (some of them resembling the jet head, and others forming aligned chains of more compact emission peaks) in the region between the outflow source and the jet head (see, e.g., Reipurth & Heathcote 1990 and the review of Reipurth & Bally 2001). Several possibilities of how to model these knots have been explored (see, e.g., Raga & Kofman, 1992, and Micono et al. 1998), but presently the favoured explanation is that they are the result of a time-variability in the ejection, which leads to the formation of "internal working surfaces" within the jet

---

[1] Instituto de Ciencias Nucleares, UNAM, México.

[2] Facultad de Ciencias, UNAM, México

[3] Instituto de Astronomía, UNAM, México.

beam (see, e.g., Raga et al 1990). Some of the "classical HH objects" of the catalogue of Herbig (1974) are associated with either jet heads or knots.

A problem that has received little attention is the effect of a "slow turning on" of the outflow on the jet head. As far as we are aware, the only simulations studying the dynamics of the head of a "slow turning on" jet (as opposed to a jet which is instantaneously "switched on" at full velocity) are the ones of Lim et al. (2002). These authors focus their study on the survival of H_2 molecules in the resulting, accelerating jet head, presenting 1D hydrodynamic simulations including an H_2 formation/destruction chemical network.

Of course, there are a number of numerical studies of the ejection of MHD jets from star+accretion disk systems (e.g., Ouyed et al. 2003; Hiromitsu & Shibata 2005; Zanni et al. 2007; Ahmed & Shibata 2008; Romanova et al. 2018), in which a sudden switch on of the jet is definitely not imposed (the "switching on" of the outflow being a result of the simulated accretion+ejection flow). These models produce a highly super-alfvénic leading head that evolves consistently with the computed time-dependence of the ejection.

In the present paper, we revisit the "slow turn on jet" problem. We study the dynamics of the head of a cylindrical jet with a linear ramp of increasing ejection velocity as a function of ejection time. We combine this ejection velocity with two forms for the ejection density variability:

- a constant ejection density,
- a constant mass loss rate (so that the ejection density is proportional to the inverse of the ejection velocity).

We obtain analytical models of this flow by assuming that the material in the jet beam is free streaming (before reaching the jet head), and that the motion of the working surface of the jet head can be described:

- by using a ram-pressure balance condition,
- by assuming that it coincides with the motion of the center of mass of the material that has entered the working surface.

The first of these assumptions (see, e.g., Raga & Cantó 1998) is correct for a "massless" working surface which instantaneously ejects most of the material sideways (into a jet cocoon), while the latter assumption (see Cantó et al. 2000) is appropriate for the "mass conserving" case in which the shocked material mostly stays within the working surface.

We also carry out axisymmetric numerical simulations of the flow, and compare the results with the ram-pressure balance and center of mass analytic models. This is the first time that a comparison between numerical simulations and the two analytic approximations (described above) has been attempted.

The paper is organized as follows. In § 2 we present the center of mass and the ram-pressure balance solutions for a uniformly accelerated jet evolving in a homogeneous interstellar medium. In § 3 we present the axisymmetric numerical simulations. A comparison of the results with the analytic models is done in § 4. A discussion of the results is held in § 5, and concluding remarks are given in § 6.

2. ANALYTIC MODEL

We consider a jet with an ejection velocity of the form

$$u_0(\tau) = \begin{cases} 0\,, & \tau < 0, \\ a\tau\,, & \tau \geq 0, \end{cases} \tag{1}$$

where a is a constant acceleration and τ the ejection time. We assume a cylindrical flow, with a jet cross section σ which is circular and constant. We also assume that the jet moves into an environment of uniform density ρ_a.

We consider two different forms for the ejection density:

1. a constant mass loss rate per unit area $\dot{m}$, such that the ejection density is given by

$$\rho_0(\tau) = \frac{\dot{m}}{u_0(\tau)}, \tag{2}$$

2. a time-independent ejection density,

$$\rho_0 = \text{const.} \tag{3}$$

We assume that the flow in the jet beam is free-streaming, satisfying the condition:

$$u(x,t) = \frac{x}{t-\tau} = u_0(\tau)\,, \tag{4}$$

where $u(x,t)$ is the velocity as a function of distance x from the source at an evolutionary time t and $u_0(\tau)$ is the ejection velocity (at the ejection time $\tau < t$). For an ejection time $\tau < 0$, $x = 0$, i.e., no material is ejected. Also, for a cylindrical, free-streaming flow, the density is given by:

$$\rho(x,t) = \frac{\rho_0\, u_0}{u_0 - (t-\tau)\dot{u}_0}, \tag{5}$$

where $\rho_0(\tau)$ is the ejection density (see equation 2 or 3) and $\dot{u}_0 = du_0/d\tau$ is the derivative of the ejection velocity with respect to the ejection time (for a derivation of this equation, see Raga & Kofman, 1992). The relationship between the evolutionary time t and the ejection time τ can be obtained from equations (1) and (4). Later, in § 2.1, we explicitly show this relationship.

When the flow starts (at $t = 0$), a working surface is formed at $x = 0$. This "jet head" then travels away from the outflow source for increasing times. In order to describe the time evolution of this working surface, we use two analytic approximations:

1. *center of mass*- we assume that the position of the working surface coincides with the center of mass of the ejected, free-streaming material,
2. *ram-pressure balance*- we assume that the motion of the working surface is determined by the jet/environment ram-pressure balance condition.

The first of these approximations is appropriate for a working surface in which the shocked gas mostly remains within the jet head, and the latter approximation is valid for a working surface that ejects most of the matter sideways (into a jet cocoon).

We therefore develop four analytic models, with the two ejection densities and the two analytic approximations described above. The models all share the linearly accelerating ejection velocity given by equation (1).

2.1. *Center of Mass Equation of Motion*

We first consider a "mass conserving" working surface. For this case, we assume that the material going through the bow and jet shocks mostly stays within the working surface, with only a small fraction of this material being ejected sideways into the jet cocoon. The working surface position should then coincide with the center of mass of the free-streaming fluid parcels that have piled up within it. This center of mass position is given by:

$$x_{cm} = \frac{\int x dm}{\int dm}, \tag{6}$$

with the differential element of mass given by:

$$dm = \sigma\, \rho_0(\tau)\, u_0(\tau)\, d\tau + \sigma\, \rho_a(x)\, dx. \tag{7}$$

In this equation, the first term on the right-hand-side corresponds to the ejected material, and the second term to the swept-up, stationary, environment entering the working surface. In equation (7), σ is the jet cross section, $\rho_0(\tau)$ is the ejection density, $u_0(\tau)$ the ejection velocity and $\rho_a(x)$ the (possibly position-dependent) environmental density.

Using equations (4-7) and considering that the ejection time τ' is integrated from 0 to τ, we obtain:

$$x_{cm}\left[\int_0^{\tau} \rho_0(\tau')\, u_0(\tau')\, d\tau' + \int_0^{x_{cm}} \rho_a\, dx\right] = \int_0^{\tau} x_j\, \rho_0(\tau')\, u_0(\tau)\, d\tau' + \int_0^{x_{cm}} x\, \rho_a\, dx, \tag{8}$$

where we have set $\rho_a = const.$, and x_j is the position that the fluid parcels would have if they were still free-streaming:

$$x_j = (t - \tau')\, u_0(\tau'), \tag{9}$$

see equation (4).

Also, from equations (1) and (4) we find:

$$t = \frac{x_{cm}}{a\tau} + \tau. \tag{10}$$

Equation (10) can be inverted to obtain

$$\tau = \frac{1}{2}\left(t + \sqrt{t^2 - \frac{4x_{cm}}{a}}\right). \tag{11}$$

Combining equations (8-10), we obtain:

$$x_{cm}\left[\int_0^{\tau} \rho_0(\tau')\, a\tau'\, d\tau' + \frac{\rho_a\, x_{cm}}{2}\right] = \int_0^{\tau} (t-\tau')a^2\, \tau'^2\, \rho_0(\tau')\, d\tau'. \tag{12}$$

In order to carry out the remaining integrals, we have to specify $\rho_0(\tau')$. We consider two forms for the ejection density (see equation 2).

(a) *Constant mass loss rate.*

Equation (12) takes the form:

$$x_{cm}\left(\dot{m}\tau + \frac{\rho_a\, x_{cm}}{2}\right) = \dot{m}a\tau^2\left(\frac{t}{2} - \frac{\tau}{3}\right). \tag{13}$$

Using equations (10) and (13), we obtain

$$x_{cm}^2 + \frac{\dot{m}\tau}{\rho_a}\, x_{cm} - \frac{\dot{m}a\tau^3}{3\rho_a} = 0, \tag{14}$$

this is a quadratic equation with one positive solution, given by

$$x_{cm}(\tau) = \frac{\dot{m}\tau}{2\rho_a}\left[-1 + \sqrt{1 + \frac{4a\rho_a\tau}{3\dot{m}}}\right]. \tag{15}$$

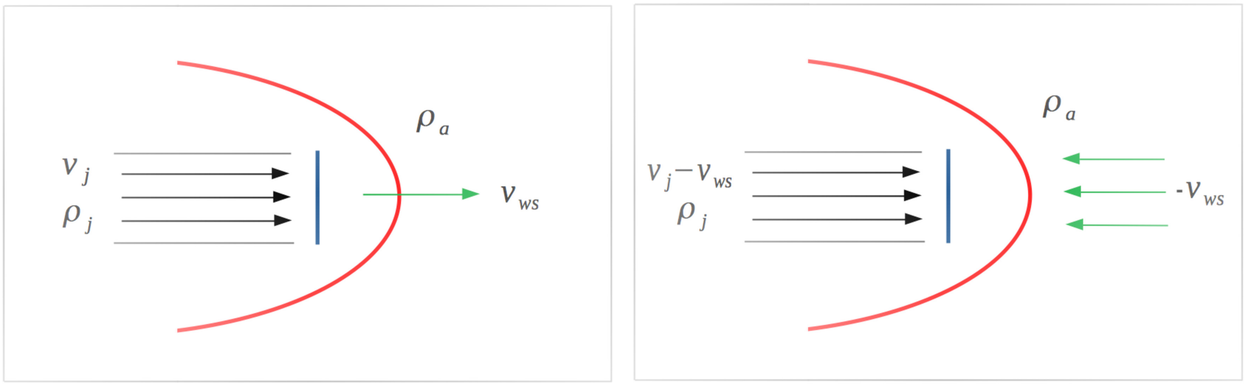

Fig. 1. Jet head working surface in a reference frame at rest with respect to the outflow source (left) and in a reference frame moving along with the working surface (right). The bow shock is shown in red and the jet shock in blue. The color figure can be viewed online.

In the low density limit $\rho_a \to 0$, equation (14) takes a particularly simple form that leads to finding the solution

$$x_{cm} = \frac{a\tau^2}{3}. \tag{16}$$

This solution can also be obtained by carrying out a first-order Taylor series expansion of equation (15).

By substituting equation (11) into (13), we can also obtain x_{cm} as an explicit function of t, giving

$$x_{cm} = \frac{8}{9}x_c\left[\left(1+\frac{3}{4}\frac{t}{t_c}\right)^{3/2} - \left(1+\frac{9}{8}\frac{t}{t_c}\right)\right], \tag{17}$$

with $t_c \equiv \dot{m}/a\rho_a$ and $x_c \equiv \dot{m}^2/a\rho_a^2$.

In the $t \ll t_c$ limit, a second order Taylor series expansion of equation (17) gives:

$$x_{cm} \approx \frac{3}{16}at^2. \tag{18}$$

(b) *Constant ejection density.*

With a constant ρ_0, equation (12) takes the form:

$$x_{cm}\left(\frac{\rho_0\, a\tau^2}{2} + \frac{\rho_a\, x_{cm}}{2}\right) = \rho_0\, a^2\tau^3\left(\frac{t}{3} - \frac{\tau}{4}\right), \tag{19}$$

where t and τ are related through equation (10).

Substituting t as a function of τ we obtain:

$$x_{cm}^2 + \frac{\rho_0\, a\tau^2}{3\rho_a}x_{cm} - \frac{\rho_0\, a^2\tau^4}{6\rho_a} = 0, \tag{20}$$

which has a positive solution

$$x_{cm}(\tau) = \frac{\rho_0\, a\tau^2}{6\rho_a}\left[-1+\sqrt{1+\frac{6\rho_a}{\rho_0}}\right]. \tag{21}$$

In the $\rho_a \to 0$ limit, equation (20) (or, alternatively, equation 21) takes the form

$$x_{cm} = \frac{a\tau^2}{2}, \tag{22}$$

with a quadratic dependency on the ejection time.

We can also find a solution to (19) as a function of evolutionary time t (using equation 11), giving:

$$x_{cm} = \frac{a}{9}\beta_0\left[\frac{\beta_0(\beta_0^2-18)+(\beta_0^2+6)^{3/2}}{(\beta_0^2-2)^2}\right]t^2, \tag{23}$$

where

$$\beta_0 = \sqrt{\frac{\rho_0}{\rho_a}}, \tag{24}$$

and therefore the position x_{cm} has a quadratic dependency on the evolutionary time t.

Equation (23) takes the form of a constant acceleration condition, with the acceleration given by

$$g = \frac{2a}{9}\beta_0\left[\frac{\beta_0(\beta_0^2-18)+(\beta_0^2+6)^{3/2}}{(\beta_0^2-2)^2}\right], \tag{25}$$

which in the $\rho_a \to 0$ low density limit becomes,

$$g \approx \left(\frac{2}{3}\right)^{1/2} a\,\beta_0. \tag{26}$$

2.2. *Ram-Pressure Balance Equation of Motion*

Figure 1 shows a schematic diagram of a jet head propagating through a stationary environment. This leading working surface has a structure consisting of two shocks: an upstream shock known as the jet shock (or Mach disk), which is slowing down the jet material, and a downstream bow shock which is accelerating the surrounding material. The two-shock working surface structure travels away from the outflow source at a velocity v_{ws}.

The right panel of Figure 1 shows the situation seen in a reference frame at motion with the jet head. For a hypersonic flow, the two working surface shocks are strong, so that the post-shock gas pressures are given by:

$$P_{bs} = \frac{2}{\gamma+1}\rho_a v_{ws}^2, \tag{27}$$

for the bow shock, and

$$P_{js} = \frac{2}{\gamma+1}\rho_j \left(v_j - v_{ws}\right)^2, \tag{28}$$

for the jet shock (assuming that the jet and the environment have the same specific heat ratio γ). In this equation, v_j and ρ_j are the velocity (with respect to the outflow source) and the density of the material that is presently entering the jet shock.

If the working surface is moving with a constant velocity the condition

$$P_{bs} = P_{js} \;\Rightarrow\; \rho_a v_{ws}^2 = \rho_j \left(v_j - v_{ws}\right)^2, \tag{29}$$

is satisfied. This is called the *ram-pressure balance* condition. This condition is also valid for a working surface moving with a variable velocity as long as the inertia of the material between the bow shock and the jet shock is negligible, which is the case if most of the material is ejected sideways from the working surface into a jet cocoon.

From equation (29) we find that

$$v_{ws} = \frac{\beta v_j}{1+\beta} \quad , \qquad \text{with} \qquad \beta \equiv \sqrt{\frac{\rho_j}{\rho_a}}. \tag{30}$$

Clearly, the shock velocity associated with the bow shock is $v_{bs} = v_{ws}$ and the shock velocity of the jet shock is:

$$v_{js} = \frac{v_j}{1+\beta}. \tag{31}$$

We now consider the equation of motion $v_{ws} = dx_{ws}/dt$ for the working surface. Setting $v_j = u_0(\tau)$ (i.e., the velocity of the material entering the working surface is equal to the ejection velocity at the corresponding ejection time τ), we then have:

$$\left(1 + \sqrt{\frac{\rho_a}{\rho_j}}\right)\frac{dx_{ws}}{dt} = u_0(\tau). \tag{32}$$

The ejection time τ of the material entering the working surface is obtained from the free-streaming relation

$$x_{ws} = (t-\tau)u_0(\tau),$$

where t is the evolutionary time (see equation 4). Solving for t and differentiating with respect to τ we obtain

$$\frac{dt}{d\tau} = 1 + \frac{1}{u_0}\frac{dx_{ws}}{d\tau} - \frac{x_{ws}}{u_0^2}\frac{du_0}{d\tau}. \tag{33}$$

Combining equations (32) and (33), we obtain:

$$\frac{dx_{ws}}{d\tau}\sqrt{\frac{\rho_a}{\rho_j}} = u_0 - x_{ws}\frac{d\ln u_0}{d\tau}. \tag{34}$$

The density of the jet material entering the working surface is $\rho_j = \rho(x_{ws}, t)$ (see equation 5), which for our chosen ejection velocity variability (see equation 1) becomes:

$$\rho_j = \frac{\rho_0}{1 - \frac{x_{ws}}{a\tau^2}}. \tag{35}$$

Finally, from equations (34) and (35) we obtain:

$$\frac{dx_{ws}}{d\tau} = \sqrt{\frac{\rho_0}{\rho_a}}\, a\tau \sqrt{1 - \frac{x_{ws}}{a\tau^2}}. \tag{36}$$

In order to proceed it is now necessary to specify the form of $\rho_0(\tau)$. We therefore consider the two cases of constant mass loss rate and constant ejection density.

(a) *Constant mass loss rate.*

For $\dot{m} = \text{const.}$ equation (36) takes the form:

$$\frac{dx_{ws}}{d\tau} = \sqrt{\frac{\dot{m}}{\rho_a}\left(a\tau - \frac{x_{ws}}{\tau}\right)}. \tag{37}$$

It is convenient to use the dimensionless variables:

$$\eta = \frac{a\rho_a^2}{\dot{m}^2}x_{ws} \ , \quad y = \frac{a\rho_a}{\dot{m}}\tau. \tag{38}$$

In terms of these variables, equation (37) is

$$\frac{d\eta}{dy} = \sqrt{y - \frac{\eta}{y}}. \tag{39}$$

In Appendix A, it is shown that an approximate analytic solution of equation (39) can be constructed as a non-linear average of a "near" and a "far field" analytic solution (see equations 51 and 52), which in terms of the respective dimensional variables is

$$x_{ws} = \frac{\dot{m}^2}{a\rho_a^2}\left[\left(\frac{a\rho_a}{\dot{m}}\tau\right)^{-\frac{5}{2}} + \left(\frac{3}{2}\right)^{\frac{5}{4}}\left(\frac{a\rho_a}{\dot{m}}\tau\right)^{-\frac{15}{8}}\right]^{-\frac{4}{5}}. \tag{40}$$

(b) *Constant ejection density.*

Setting $\rho_0 = $ const. in (36) and taking the square of the equation, we obtain:

$$\frac{\rho_a}{a\rho_0}\left(\frac{dx_{ws}}{d\tau}\right)^2 + x_{ws} - a\tau^2 = 0. \qquad (41)$$

Proposing a power law solution, we find that

$$x_{ws} = \frac{a\rho_0}{8\rho_a}\left[-1 + \sqrt{1 + \frac{16\rho_a}{\rho_0}}\right]\tau^2. \qquad (42)$$

We therefore find a quadratic dependency on the ejection time.

Using equations (11) and (42) we then obtain:

$$x_{ws} = \frac{8a\beta_0^2\left(-1 + \sqrt{1 + \frac{16}{\beta_0^2}}\right)}{\left[8 + \beta_0^2\left(-1 + \sqrt{1 + \frac{16}{\beta_0^2}}\right)\right]^2}\, t^2, \qquad (43)$$

where β_0 is given by equation (24). This implies a quadratic dependence on the evolutionary time.

In the $\beta_0 \ll 1$ limit, equation (43) becomes

$$x_{ws} \approx \frac{a}{2}\,\beta_0\, t^2, \qquad (44)$$

and the $\beta_0 \gg 1$ limit leads to

$$x_{ws} \approx \frac{a}{4}\, t^2. \qquad (45)$$

3. THE NUMERICAL SIMULATIONS

In order to check our analytical solutions we computed a set of 2D axisymmetric simulations for both the constant mass loss rate and constant ejection density cases. For the simulations we use a code that solves the ideal gas-dynamic (Euler) equations in a fixed two dimensional grid. The code uses a second order Godunov type method with the HLLC (Toro et. al. 1994) approximate Riemann solver, including a linear reconstruction of the primitive variables with the *minmod* slope limiter to avoid spurious oscillations. In order to use cylindrical coordinates, the appropriate geometrical source ($\propto 1/r$) terms are included after each time step in an operator splitting fashion. Additionally, we incorporated the cooling function dependent on density, metallicity and temperature in the energy equation (also as source term) as proposed by Wang et al. (2014), which we compute assuming a solar metallicity.

In order to stabilize the method an artificial diffusion with a (dimensionless) value of 0.01 was added to all of the equations, and a Courant number of 0.2 was used. The code is written in fortran90 and is parallelized with the *Message Passing Interface.* We used a computational grid with a size of 0.05 and 0.2 pc along the r and x directions, respectively. The spatial resolution was ≈ 6.89 au, corresponding to 600×6000 cells along the radial and axial directions.

3.1. *Initial and Boundary Conditions*

We model jets propagating into a uniform, quiescent environment, and consider the values $n_a = 100$ cm^{-3} and $n_a = 5000$ cm^{-3} for the environmental density. For convenience, from now on we will use number density instead of mass density. We consider a mean molecular weight of $\mu = 1.3$. We also consider the cases of jets with a constant mass loss rate and a constant ejection density.

In all simulations, we consider the ejection velocity variability given by equation (1) with $a = 100$ km s^{-1} per millenium $= 3.17 \times 10^{-4}$ cm s^{-2}. An initial jet radius $r_j = 300$ AU (the cross section being $\sigma = \pi r_j^2$) and a temperature $T = 100$ K (for both the jet and the environment) were imposed in all models.

We therefore compute four models, two with constant ejection density (which we label n_{100} and n_{5000}, with the subscript giving the ambient density in cm^{-3}) and two with constant mass loss rate (which we label $\dot{m}_{100}$ and $\dot{m}_{5000}$). For the models $\dot{m}_{100}$ and $\dot{m}_{5000}$ we choose a total mass loss rate $\dot{M} = 2.24 \times 10^{-8}\, M_{\odot}$yr^{-1}, which corresponds to a mass loss rate at the jet source per unit area $\dot{m} = 3.36 \times 10^{-13}$ g cm^{-2} s^{-1}. For the models n_{100} and n_{5000}, we choose a density $n_j = 1.66 \times 10^4$ cm^{-3} (for a gas with 90% H and 10% He). The model parameters are summarized in Table 1.

In the constant mass flux cases, we find a maximum jet density of $n_j = 1.56 \times 10^7$ cm^{-3}, and a minimum jet density of $n_j = 6.24 \times 10^3$ cm^{-3}, corresponding to an ejection time $\tau = 1$ yr, and $\tau = 2500$ yr, respectively.

We should note that the parameters we have chosen are inspired in the characteristics of "classical" HH jets such as HH 34 and HH 111, which have:

- radii $\approx$ 100 AU (Reipurth et al. 2002) and $\approx$ 300 AU (Reipurth et al. 1997), for HH 34 and HH 111, respectively. We chose the larger of these two radii in order to have a better resolution of the jet in our numerical simulations. These jet radii are measured in the "jet knot chain" at distances of $\approx 10''$ (corresponding to $\approx 6 \times 10^{16}$ cm) from the outflow sources, and

TABLE 1

PHYSICAL CONDITIONS FOR THE NUMERICAL SIMULATIONS

	$\dot{M}_j$ ($M_\odot\,\mathrm{yr}^{-1}$)	n_j (cm^{-3})	n_a (cm^{-3})
n_{100}	$1.30 \times 10^{-7*}$	1.66×10^4	100
n_{5000}			5000
$\dot{m}_{100}$	3.35×10^{-7}	$1.55 \times 10^{4*}$	100
$\dot{m}_{5000}$			5000

*These values correspond to an ejection time $\tau = 1000\,\mathrm{yr}$.

not in the considerably broader HH 34S and HH 111V "heads";

- full spatial velocities (i.e., combining radial velocities and proper motions) between 200 and 300 km s^{-1} (Hartigan et al. 2001; Reipurth et al. 2002) and lengths (out to HH 34S and HH 111V) of $\approx 8 \times 10^{17}$ cm. We have then made a choice of $a = 100\,\mathrm{km\,s^{-1}}$ per millenium (see above), which after an evolutionary time of $\approx$ 2500 yr produces a jet head with a position and velocity similar to the ones of HH 34S and HH 111V (see the following section). The simulations are stopped at this time (i.e., at 2500 yr);
- mass loss rates in the $10^{-8} \to 10^{-7}$ $M_\odot$ yr^{-1} range (depending on the emission lines used for deriving this value and on the position along the jets, see Podio et al, 2006). We have therefore chosen densities that produce mass loss rates of this order of magnitude;
- even though the ambient densities in HH 34 and HH 111 are of ≈ 10 cm^{-3} (Raga et al. 1991), we have chosen higher environmental densities (of 100 and 5000 cm^{-3}, see above) in order to have a substantial braking effect and to obtain larger differences between the center of mass and ram-pressure balance solutions.

4. RESULTS

We computed four numerical simulations, two with a constant ejection density (models n_{100} and n_{5000}) and two with a constant mass loss rate (models $\dot{m}_{100}$ and $\dot{m}_{5000}$). The top two (purple background) and bottom two (black background) panels presented in Figure 2 display the numerical density and temperature stratifications at an evolutionary time of 2500 yr for these four models.

Generally, the highest densities and temperatures are found in the on-axis regions of the jet heads. The jet heads of the models with constant ejection density (models n_{100} and n_{5000}) have traveled to distances from the outflow source larger than the ones of constant mass loss rate ($\dot{m}_{100}$ and $\dot{m}_{5000}$). This qualitative difference is due to the fact that in the constant mass loss rate models the injected momentum rate $\dot{M}_j v_j$ scales linearly with v_j (and hence also increases linearly with time, see equation 1), while this scaling is quadratic (with ejection velocity and with time) in the constant ejection density models. This means that the constant ejection density jets have a larger momentum content.

As a result of the lower jet beam density and pressure, the constant mass loss rate models develop an incident/reflected crossing shock structure, which (in the incident shock region) leads to the production of faster off-axis motions in the jet head (see the two bottom panels of Figure 2). This kind of structure is always found in jet simulations with appropriate parameters, i.e. simulations where the jet is under-dense and under-pressured with respect to the environment during its evolution (see, e.g., Raga 1988; Downes & Ray 1999).

The upper left panel of Figure 3 shows the position of the bow shock (dash-dotted blue line) and jet shock (dotted blue line) as a function of time for the $\dot{m}_{100}$ constant mass loss rate model. These positions were obtained by searching for the jumps along the symmetry axis of the pressure stratifications for both the bow shock and jet shock. We compare these shock positions with the analytical solution of the center of mass (dashed green line) and ram-pressure balance (solid red line) analytic models. We find that the position of the bow shock lies close to the prediction from the center of mass analytic model, and the jet shock position lies somewhat below.

The upper right panel of Figure 3 shows the time-dependent position of the jet head for the n_{100} constant ejection density model. For times $<$ 1500 yr, the jet and bow shock positions (obtained from the numerical simulation) quite closely follow the center of mass analytic solution. At larger times, the jet and bow shock positions lie above the center of mass solution, and begin to approach the ram-pressure balance solution. At all times, the positions of the jet and bow shock lie in between the working surface positions predicted by the two analytic models.

The lower left panel of Figure 3 shows the evolution of the jet head for the $\dot{m}_{5000}$ constant mass loss rate model. For this model, the positions of the jet and bow shock initially follow the center of mass analytic solution, but for times $t > 1500$ yr begin to show large deviations, moving more slowly than

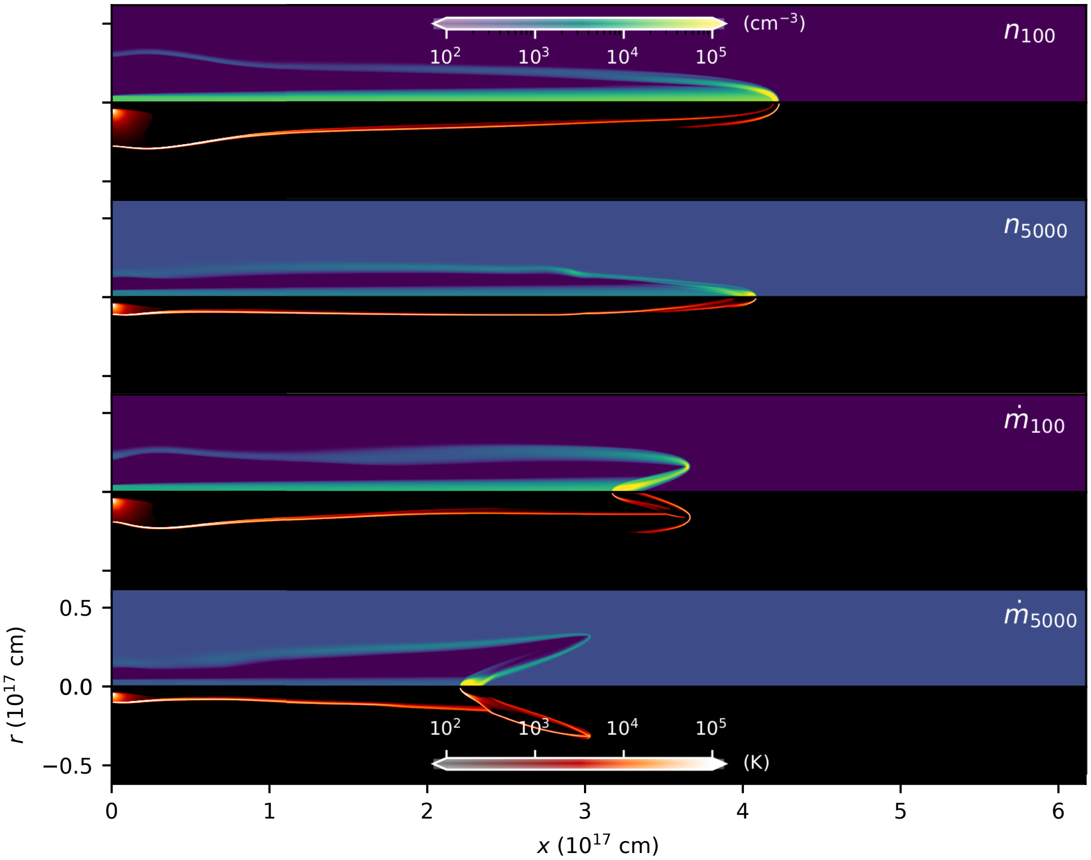

Fig. 2. Numerical density and temperature stratifications obtained from our four models (see the text and Table 1), at an evolutionary time of 2500 years. For each model, we show the number density (top half) and temperature (bottom half) in logarithmic color scales. The axial and radial axes are given in units of 10^{17} cm. In the constant mass loss rate models the jet density and the pressure drop quite considerably, leading to the formation of internal "crossing shocks". The color figure can be viewed online.

the predictions of the two analytic models. These strong deviations are not surprising given the rather extreme departures from a constant cross section, cylindrical jet beam (assumed in the analytic models) found in the numerical simulation (see the bottom panel of Figure 2).

The strong departures from the simple, cylindrical structure assumed in the analytic models occurs because at increasing times the jet density (and pressure) drop quite considerably in this model, leading to the formation of internal "crossing shocks". These shocks then lead to the formation of complex off-axis structures in the jet head (see the two bottom panels of Figure 2).

The lower right panel of Figure 3 shows the dynamics of the jet head for the n_{5000} constant ejection density model. This model shows jet and bow shock positions that initially follow the center of mass analytic model, and at times $t > 1500$ yr tend to approximate the ram-pressure balance model.

Finally, we calculate the relative position differences $\Delta x_a/x_{cm} = x/x_{cm} - 1$, with x_{cm} being the position of the "center of mass jet head" (see equations 17 and 21). The distance from the source x_a corresponds either to the bow shock or jet shock positions (obtained from the numerical simulations), or to the position of the "ram-pressure balance jet head" (see equations 40 and 43). Figure 4 shows the relative position differences (with respect to the center of mass position for the jet head) for all of our computed models. The first thing to note (see the red lines in the two right panels of Figure 4) is that the relative position difference between the center of mass and ram pressure balance solutions does not strongly depend on time for the constant ejection density models (a result that can be seen by comparing equations 21 and 42). This result does not

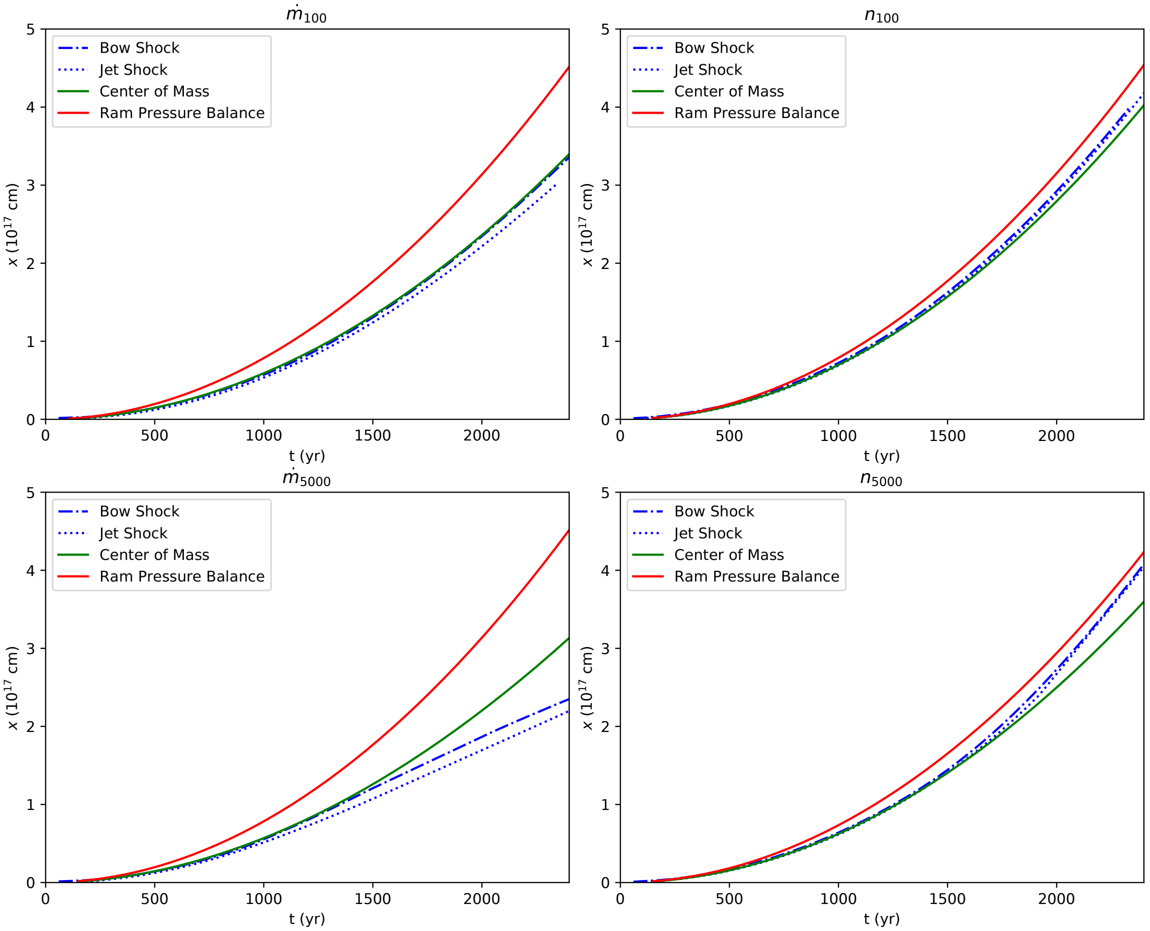

Fig. 3. Position of the jet head as a function of time for the constant mass loss rate models (left panels) and the constant ejection density models (right panels). The red solid line shows the ram-pressure balance solution and the green dashed line shows the center of mass solution. The dash-dotted line shows the bow shock and the dotted line the jet shock positions obtained from the numerical simulations. The color figure can be viewed online.

strictly hold for the constant mass loss rate models (red lines in the left panels of Figure 4).

For the constant mass loss rate models we see that for $t > 550$ yr the bow and jet shock positions remain below the center of mass working surface position, with negative Δx values (see the left panels of Figure 4). For the constant ejection density models (right panels of Figure 4) we see an initial convergence to the center of mass solution of the bow and jet shock positions, and for $t > 1300$ yr we see progressively larger, positive values for $\Delta x/x_{cm}$ (starting to approach the ram-pressure balance working surface position).

5. DISCUSSION

We have presented a first attempt to compare the analytic ram-pressure balance (Raga & Kofman 1992) and center of mass (Cantó et al. 2000) formalisms (for obtaining the motions of working surfaces in variable ejection jets) with axisymmetric numerical simulations. To this effect, we chose the relatively simple problem of the leading head of a jet produced with an ejection velocity that increases linearly with time. We explored the cases of a time-independent mass loss rate (in which the ejection density scales as the inverse of the ejection velocity) and of a constant ejection density. From the simulations we computed the on-axis positions of the jet shock and bow shock, and compared them with the predictions of the analytic models (in which the jet and bow shock are assumed to be spatially coincident).

For three of our four simulations (models n_{100}, n_{5000} and $\dot{m}_{100}$), a good agreement is found between the numerical simulations and the analytic models. In these three models the jet and bow shock positions initially follow the center of mass analytic solution,

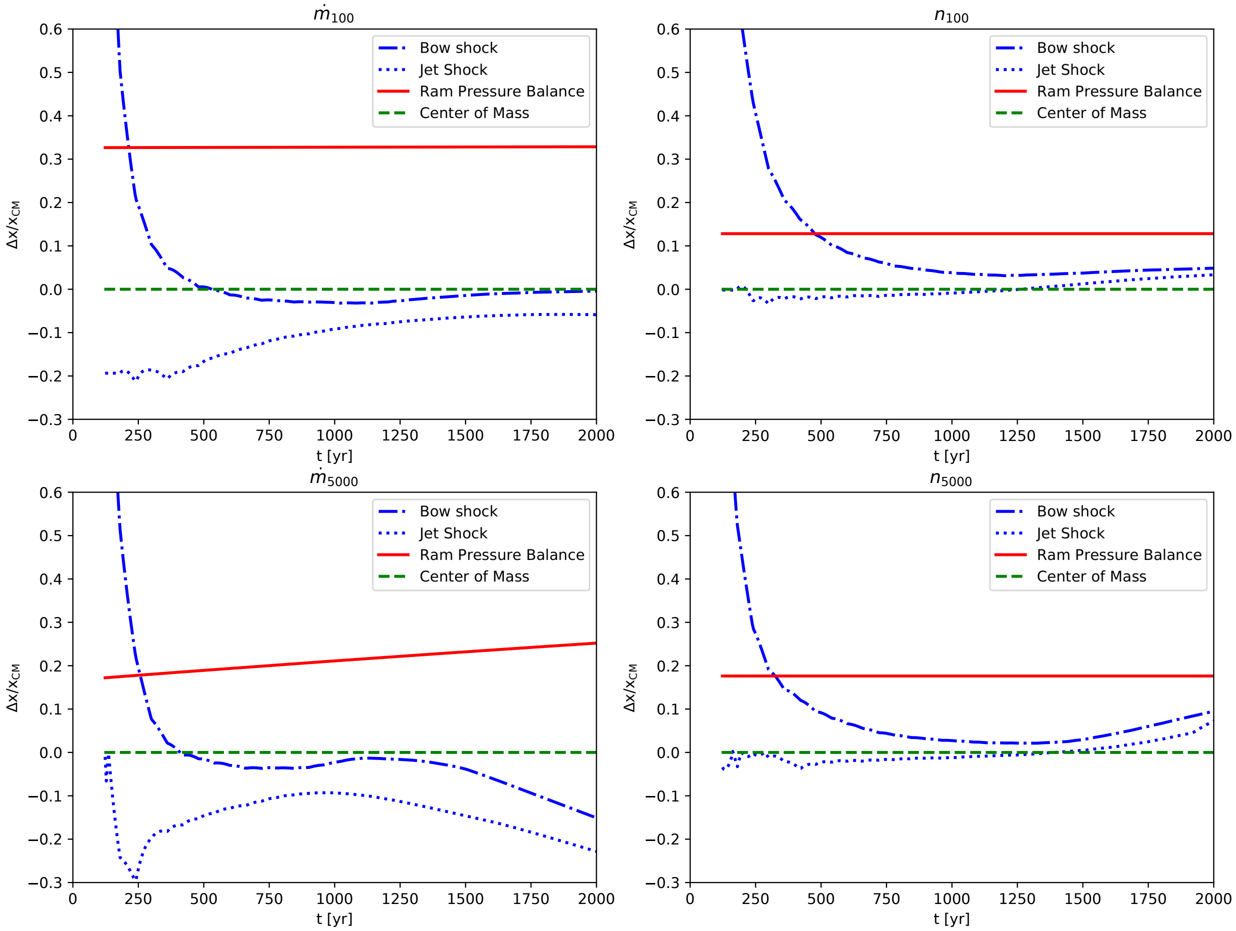

Fig. 4. The relative differences of the ram-pressure balance solution (solid red line), the numerical bow shock (dash-dotted blue line) and jet shock positions (dotted blue line) with respect to the center of mass working surface solution (the dashed, green line showing the $\Delta x/x_{cm} = 0$ line) as a function of time t. The results obtained for our four models (see Table 1) are shown (constant mass loss rate models on the left, and constant ejection density models on the right). The color figure can be viewed online.

and (for two of these models) at later times deviate towards the faster moving, ram-pressure balance analytic model. This result is satisfactory, as one would expect that at early times the shocked jet and environment material will mostly remain within the working surface (as assumed in the center of mass formalism), and that a substantial sideways leakage of material (as assumed in the ram-pressure balance model) should occur at later times. This is discussed in more detail below.

It is clear that right after a working surface is formed, the two associated shocks are very close to each other (with a separation $d \ll r_j$, where r_j is the local jet beam radius). Because the surface $S \approx 2\pi r_j l$ through which the gas exits the working surface is then small ($S \ll \pi r_j^2$), most of the mass going through the shocks remains within the working surface. At later times, the separation between the two shocks increases, and part of the mass processed by the working surface shocks is ejected sideways into a jet cocoon. For a jet with a time-independent ejection velocity, the separation d between the two shocks attains a steady maximum value determined by the balance between the incoming and outflowing mass rates. Such a balance between inflow and outflow from the working surface is also approximately attained in the case of a variable velocity jet, but the resulting shock separation (and also mass within the working surface) still has a (slower) time-dependence.

It is possible to obtain analytic estimates of the separation between the two shocks (and therefore the mass of the gas within the working surface) with different degrees of complexity (and accuracy), following the approaches developed for determining the shock standoff distance in blunt body flows (see, e.g., the book of Hayes & Probstein 2003 and Cantó & Raga 1998). Here, we present a very simple estimate of the mass within a working surface.

In the stationary state (i.e., after the initial regime of growing separation between the two working surface shocks), the mass M_{ws} within the two working surface shocks is:

$$M_{ws} \approx \dot{M}_{in} t_s \,, \tag{46}$$

where $\dot{M}_{in}$ is the mass being fed through the two shocks and t_s is the timescale for sideways leakage of the material. Assuming that the two shocks are highly radiative (with a cooling distance[4] to $\approx 10^3$ K much smaller than the jet radius r_j), this leakage will occur at the post-cooling sound speed $c_0 = \sqrt{5kT/3\mu m_H} \approx 3$ km s^{-1} (for $T = 10^3$ K and $\mu = 1.3$), and we then have

$$t_s = \frac{r_j}{2c_0} \,. \tag{47}$$

Also, the total mass that has been fed into the working surface is

$$M_{in} \approx \dot{M}_{in} t_d \,, \tag{48}$$

where $t_d = x_{ws}/v_{ws}$ is the dynamical timescale (with x_{ws} being the position and v_{ws} the velocity of the working surface).

Combining equations (46-48) we obtain

$$\frac{M_{ws}}{M_{in}} \leq \min\left[1, \frac{r_j}{2x_{ws}}\frac{v_{ws}}{c_0}\right] \,. \tag{49}$$

In this equation, we have considered that the $M_{ws}/M_{in} \leq 1$ condition has to be satisfied (with $M_{ws} = M_{in}$ for the initial, mass conserving regime, and $M_{ws} < M_{in}$ when the sideways ejection from the working surface becomes important), while our analytic estimate can give values > 1 because of its implicit assumption of a balance between the mass rates into and out of the working surface (which is not satisfied in the early evolution of the working surface, as discussed above). Clearly, for the case of an accelerating working surface (as the one that we obtain from our variable ejection models), the derivation of equation (49) should be done evaluating the appropriate integrals (see § 4 of the paper of Lim et al. 2002), but the simple derivation shown above still gives the correct scaling properties.

We now consider that the transition between the mass conserving and efficient mass losing working surface regimes (which can be described with the "center of mass" and "ram-pressure balance" equations of motion, respectively) occurs when $M_{ws}/M_{in} \approx 1/2$ (i.e., that the working surface has lost half of the processed jet material). Therefore, the position x_t of the working surface at which the transition between the center of mass and ram pressure balance regimes occurs can be estimated setting $M_{ws}/M_{in} = 1/2$ in equation (49), which gives:

$$x_t = \frac{v_{ws}}{c_0} r_j \,. \tag{50}$$

Setting $c_0 = 3$ km s^{-1} (see above), $r_j = 300$ au (see § 3) and a velocity $v_{ws} \approx 200$ km s^{-1}, we then obtain $x_t \approx 3 \times 10^{17}$ cm, This is the correct order of magnitude for the location of the transition between the "mass conserving" center of mass and the "efficient mass losing" ram-pressure balance regimes for the working surface found in our n_{100} and n_{5000} numerical simulations (see Figure 3).

To summarize, we find that numerical simulations of a jet with a linearly accelerating ejection velocity vs. time produce a leading head which at early times can be analytically modeled with the center of mass formalism, and (for appropriate flow parameters) at later evolutionary times approaches the ram-pressure balance solutions. The distance from the source at which the transition between these two regimes occurs can be estimated with equation (50). This result holds provided that during its time-evolution the jet does not become under dense/under pressured, in which case strong departures from the analytic solutions are found.

6. CONCLUSIONS

This paper presents a first attempt to compare analytic solutions based on both the "ram-pressure balance" and "center of mass" formalisms with hydrodynamical (axisymmetric) simulations. For this comparison we have studied the case of a linearly increasing ejection velocity as a function of time (and two different forms for the ejection density, see § 2).

This simple ejection variability could apply to the early evolution of an HH outflow, and is relevant for the problem of entrainment of environmental molecular material into the jet head (see Lim et al. 2002) and the potential destruction of molecules by shocks, particularly in the jet head. Since a direct application to the observed, evolved, HH jets is not straightforward, the interest of our work is primarily theoretical.

---

[4] The cooling distance is usually defined as the distance from a plane-parallel shock to the point where the temperature has dropped to a certain value (see for example Hartigan et al., 1987).

While full analytic solutions for different forms of the ejection variability have been found in the past with the "center of mass" formalism (see Cantó et al, 2000 and Cantó & Raga 2003), no solutions (except the trivial one for the constant ejection case) have been found with the "ram-pressure balance" equation of motion for the working surfaces. We were surprised to find that the "linearly accelerating" ejection velocity case does lead to a full, analytic ram-pressure balance solution for the case of a constant ejection density (though we managed to find only an approximate analytic solution for the constant mass loss rate case). This result implies that ram-pressure balance analytic solutions might also exist for other ejection velocity/density variability combinations.

Comparing the center of mass and the ram-pressure balance solutions with axisymmetric numerical simulations (with the same parameters) we find that for the case of over-dense jets (with higher densities in the jet side of the leading working surface) the numerical results initially follow the center of mass solution, and at later times approach the ram-pressure balance analytic solution. This result shows a satisfying consistency between the analytic approaches and the numerical solutions with the full (axisymmetric) hydrodynamic equations. Not unexpectedly, we do not find a good agreement between the analytic and numerical results for cases in which the jet density drops to values lower than the environmental density, as the jet beam then develops internal shocks (in the numerical solutions) that affect the motion of the leading working surface.

Clearly, it would be interesting to extend this comparison between numerical simulations and analytic solutions of variable jets to the case of jets with "internal working surfaces" within their beams. This problem, which would clearly have much more direct applications to observed HH jets, is left for a future study.

ARa and JC acknowledge support from the DGAPA-UNAM Grant IG100218. We thank an anonymous referee for helpful comments which lead (among other things) to many of the issues discussed in § 5.

APPENDIX

In § 2.1 we established that for a constant mass loss rate the ram-pressure balance assumption leads to equation (37). In terms of dimensionless variables (see equation 38) the equation of motion takes the form presented in (39). By integrating it numerically we obtain the $\eta(y)$ dependency shown the top frame of Figure 5.

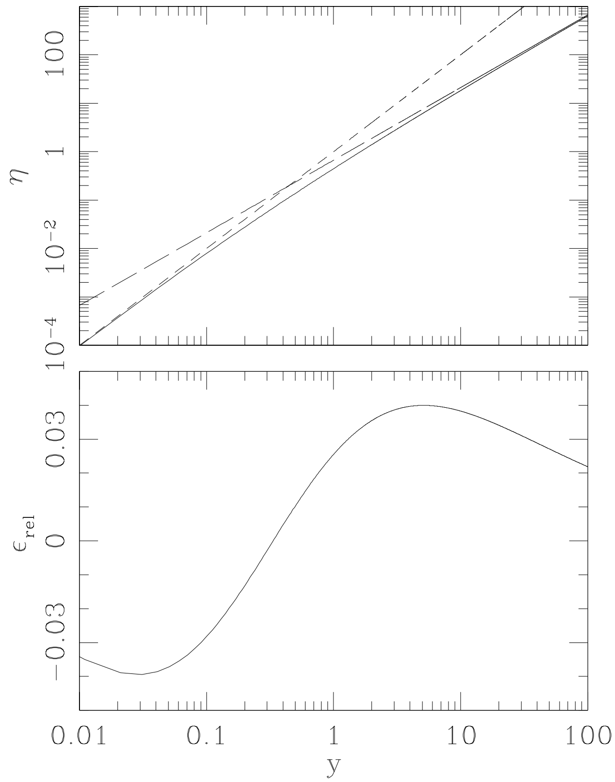

Fig. 5. Top frame: the exact (i.e., numerical) solution of equation (39) (solid curve), the "near" (short dashes) and the "far field" (long dashes) analytic solutions given by equation (51). Bottom frame: relative deviation of the approximate solution of equation (52) with respect to the "exact" (numerical) solution of equation (39).

This figure also shows the"near" and "far field" solutions

$$\eta_n(y) = y^2\ , \qquad \eta_f(y) = \frac{2}{3}y^{3/2}, \tag{51}$$

which correspond to the $y \to 0$ (near) and $y \gg 1$ (far) limits, respectively. These two solutions can be obtained straightforwardly taking the appropriate limits in equation (39).

Since the solutions in (51) represent two regimes with analytical integrals, a non-linear average between this approximations is computed:

$$\eta^{(a)} = \left(\eta_n^{-5/4} + \eta_f^{-5/4}\right)^{-4/5}\ , \tag{52}$$

to obtain an approximation to the full $\eta(y)$ solution. This average has a relative error $\epsilon_{rel} = \eta^{(a)}/\eta - 1 < 0.04$ with respect to the "exact" solution $\eta(y)$ (obtained by numerical integration of equation 39), and is therefore a reasonable analytical approximation of the solution. The dependency of ϵ_{rel} on y is shown in the bottom panel of Figure 5.

Another approximation to the numerical $\eta(y)$ solution is

$$\eta^{(b)} = \frac{2y}{9}\left(-1+\sqrt{1+9y}\right), \tag{53}$$

which coincides with the exact solution in the $y \to 0$ and $y \to \infty$ limits, and has a maximum relative deviation of ≈ 0.09. This approximation has a functional form similar to the solution for the constant mass loss rate case obtained with the "center of mass formalism" (see equation 15).

REFERENCES

Ahmed, I. & Shibata, K. 2008, PASJ, 60, 871

Cantó, J., Raga, A.C., & D'Alessio, P. 2000, MNRAS, 313, 656

Cantó, J. & Raga, A. C. 1998, MNRAS, 297, 383

_________. 2003, RMxAA, 39, 261

Downes, T. P. & Ray, T. P. 1999, A&A, 345, 977

Frank, A., Ray, T. P., Cabrit, S., et al. 2014, in Protostars and Planets VI, ed. H. Beuther, R. S. Klessen, C. P. Dullemond, and T. Henning (Tucson, AZ: UAP), 451

Hartigan, P., Morse, J. A., Reipurth, B., Heathcote, S., & Bally, J. 2001, ApJ, 559, 157

Hartigan, P., Raymond, J., & Hartmann, L. 1987, ApJ, 316, 323

Hayes, W. D. & Probstein, R. F. 2003, Hypersonic Inviscid Flow (Mineola, NY: Dover)

Heathcote, S. & Reipurth, B. 1990, AJ, 104, 2193

Herbig, G. 1974, LicOB, 658, 1

Hiromitsu, K. & Shibata, K. 2005, ApJ, 634, 879

Lim, A. J., Raga, A. C., Rawlings, J. M. C., & Williams, D. A. 2002, MNRAS, 335, 817

Micono, M., Massaglia, S., Bodo, G., Rossi, P., & Ferrari, A. 1998, A&A, 333, 1001

Ouyed, R., Clarke, D. A., & Pudritz, R. E. 2003, ApJ, 582, 292

Podio, L., Bacciotti, F., Nisini, B., et al. A&A, 456, 189

Raga, A. C. 1988, ApJ, 335, 820

Raga, A. C., Cantó, J., Binette, L., & Calvet, N. 1990, ApJ, 364, 601

Raga, A. C. & Binette, L. 1991, RMxAA, 22, 265

Raga, A. C. & Cantó, J. 1998, RMxAA, 34, 73

Raga, A. C. & Kofman, L. 1992, ApJ, 386, 222

Reipurth, B. 1991, ESOC, 33, 247

Reipurth, B. & Bally, J. 2001, ARA&A, 39, 403

Reipurth, B. & Heathcote, S. 1990, A&A, 229, 527

_________. 1991, A&A, 246, 511

Reipurth, B., Hartigan, P., Heathcote, S., Morse, J. A., & Bally, J. 1997, AJ, 114, 757

Reipurth, B., Heathcote, S., Morse, J., Hartigan, P., & Bally, J. 2002, AJ, 123, 362

Romanova, M. M., Blinova, A. A., Ustyugova, G. V., Koldoba, A. V., & Lovelace, R. V. E. 2018, NewA, 62, 94

Toro, E. F., Spruce, M., & Speares, W. 1994, ShWav, 4, 25

Wang, Y., Ferland, G. J., Lykins, M. L., et al. 2014, MNRAS, 440, 3100

Zanni, C., Ferrari, A., Rosner, R., Bodo, G., & Massaglia, S. 2007, A&A, 469, 811

J. Cantó and F. Clever: Instituto de Astronomía, Universidad Nacional Autónoma de México, Apdo. Postal 70-264, 04510, CDMX, México (mclever@astro.unam.mx).

J. I. Castorena: Instituto de Ciencias Nucleares, Universidad Nacional Autónoma de México, Apdo. Postal 70-543, 04510, CDMX, México (jicastorena@correo.nucleares.unam.mx).

A. Esquivel, A. C. Raga, and A. Rodríguez-González: Instituto de Ciencias Nucleares, Universidad Nacional Autónoma de México, Apdo. Postal 70-543, 04510, CDMX, México (raga, ary, esquivel@nucleares.unam.mx).

L. Hernández-Martínez: Facultad de Ciencias, Universidad Nacional Autónoma de México, Av. Universidad 3000, Circuito Exterior S/N, Delegación Coyoacán, C.P. 04510, Ciudad Universitaria, CDMX, México (lilihe@ciencias.unam.mx).

Revista Mexicana de Astronomía y Astrofísica, **57**, 311–319 (2021)

https://doi.org/10.22201/ia.01851101p.2021.57.02.05

LOCATION AND STABILITY OF THE TRIANGULAR POINTS IN THE TRIAXIAL ELLIPTIC RESTRICTED THREE-BODY PROBLEM

M. Radwan[1] and Nihad. S. Abd El Motelp[2]

Received February 4 2021; accepted April 12 2021

ABSTRACT

The main goal of the present paper is to evaluate the perturbed locations and investigate the linear stability of the triangular points. We studied the problem in the elliptic restricted three body problem frame of work. The problem is generalized in the sense that the two primaries are considered as triaxial bodies. It was found that the locations of these points are affected by the triaxiality coefficients of the primaries and the eccentricity of orbits. Also, the stability regions depend on the involved perturbations. We also studied the periodic orbits in the vicinity of the triangular points.

RESUMEN

Nuestro objetvo principal es determinar las ubicaciones perturbadas e investigar la estabilidad lineal de los puntos triangulares. Realizamos nuestro estudio en el marco del problema elíptico restringido de tres cuerpos. Generalizamos el problema considerando a los dos cuerpos primarios como cuerpos triaxiales. Encontramos que la ubicación de los puntos triangulares se ve afectada por los coeficientes de triaxialidad de los cuerpos primarios y por la excentricidad de las órbitas. También notamos que las regiones de estabilidad dependen de las perturbaciones inducidas y estudiamos las órbitas periódicas en la vecindad de los puntos triangulares.

Key Words: celestial mechanics — gravitation — methods: analytical — methods: numerical — planets and satellites: dynamical evolution and stability

1. INTRODUCTION

The restricted three-body problem (R3BP) is the most significant problem in celestial mechanics. This due to its wide applications in space dynamics and solar system dynamics. The knowledge of the R3BP is crucial in almost all space applications. We can define this problem as a dynamical system in which an infinitesimal body moves in the gravitational field of two massive bodies (primaries). The two primaries move about their common centre of mass in either circular or elliptic orbits, which leads to the famous circular or elliptic restricted problems, respectively (Musielak & Quarles 2014). In the elliptic restricted three-body problem, ER3BP, it is assumed that the smaller primary moves around the more massive one in an elliptical orbit. The influence of the infinitesimal mass on the motion of the primaries is negligible. This significantly simplified model has more applications in space dynamics than the more general problem.

Despite the fact that the RTBP is not integrable, five specified solutions in the rotating frame are known. These solutions correspond to equilibrium positions. Three of these equilibrium points, known as collinear points, are located on the line joining the two massive primaries in the rotating reference frame. The remaining two points, called triangular points, form equilateral triangles with the massive primaries. The determination of the location of these libration points is of great interest for different space applications (Abd El-Salam 2019). In general the equilateral equilibrium points are conditionally stable, while the collinear libration points are usually unstable (Singh & Tyokyaa 2016).

Most of the celestial bodies are of irregular nature and cannot be assumed to be spherical in the RTBP, because their stability of movement is influenced by their shape. The planets of the solar system and

---

[1] Astronomy; Space Science and Metreology Department, Faculty of Science, Cairo University, 12613 Giza, Egypt.

[2] Astronomy Department, National Research Institute of Astronomy and Geophysics (NRIAG), 11421 Helwan, Cairo, Egypt.

their satellites are assumed as extended bodies and cannot be regarded as spheres. Furthermore, the effect of eccentricity on the orbits is significant. Hence, in order to achieve an acceptable accuracy, we have to take into account that the orbits of most celestial bodies are elliptic rather than circular (Singh & Tyokyaa 2016).

From the theory of small oscillations around the triangular points two types of periodic orbits can be obtained; short-period orbits with periods approximately the same as the orbital period of the primaries, and long-period orbits with periods many times that of the primaries. The importance of investigating these periodic orbits lies in their frequent appearance in nature; they provide us with important information about orbital resonances, spin orbits and are also useful to approximate quasi-periodic trajectories (Abouelmagd (2013), Mittal et al. (2009), Kumar & Sharma (2020), Ahmed et al. (2020)).

A number of studies have been performed on the equilateral triangular points of the restricted three-body problem. Singh & Begha (2011) investigated the existence of periodic orbits about the triangular points, namely L_4 and L_5, in the RTBP when the primaries are considered as triaxial and oblate spheroid bodies, besides perturbations due to Coriolis and centrifugal forces. The authors found that long and short periodic orbits exist around these points, and that their eccentricities and periods are influenced by the involved perturbations. Singh & Umar (2012) studied the stability of triangular points in the ER3BP, when both oblate primaries emit light energy. The locations of L_4 and L_5 are shifted away from the line joining the two primaries, as compared to the classical case. The stability region decreases or increases with variations in eccentricity, oblateness and radiation pressure. Naryan & Usha (2014) investigated the stability of infinitesimal motions around the equilateral points. They considered the more massive primary as a radiant source and the less massive one as a triaxial body. Zahra et al. (2016), Zahra et al. (2017) studied the locations and linear stability of the triangular points under the effects of oblateness and triaxiality of the primaries, plus small relativistic perturbations. They found that the locations of the triangular points are affected by the considered perturbations. Numerical explorations were carried out to show the effect of perturbations on the position and stability. Singh & Tyokyaa (2016) investigated the positions and stability of the libration points when both primaries are taken as oblate spheroids with oblateness up to the fourth zonal harmonic J_4. They found that both harmonic coefficients J_2 and J_4, eccentricity and semi-major axis have destabilizing tendencies and as a result the size of the region of stability decreases with an increase in the parameters involved.

Recently, Hadia et al. (2019) studied analytically the existence and the linear stability of the libration points assuming the primaries as triaxial bodies and the Euler angles as specified values. The authors proved that the positions and the stability of the triangular points change according to the effect of the triaxiality of the primaries. Furthermore, they presented the solution of long and short periodic orbits for a stable motion. Cárcamo-Díaz et al. (2020) revisited the circular spatial restricted problem. The authors presented some new results in the light of the concept of Lie stability. This paper studies the positions and stability of the well-known triangular points, in the elliptic restricted problem frame of work. The triaxiality of the primary bodies is taken into consideration. In addition, we study the periodic orbits around the triangular points. To examine the present problem we carry out several numerical explorations.

2. DYNAMICAL MODEL

Let m_1, m_2 and m_3 be the masses of the primary, secondary, and the third infinitesimal body, respectively. The third body moves under the effect of the triaxial primaries, but it does not affect their motion. The two primaries move around their common centre of mass in elliptic orbits. We consider a rotating coordinate system (x, y, z) with origin at the centre of mass of the primaries. The primaries are permanently located on the x-axis, which is the line joining them. When investigating the restricted three-body problem it is better to choose a system of normalized units. So, we assume that the distance between the primaries is unity and we choose also the unit of time to make the gravitational constant unity. The total mass of the primaries is considered as 1, i.e. $m_1 + m_2 = 1$. In this normalized system we adopt $\mu = \dfrac{m_2}{m_1 + m_2}$ as a dimensionless mass parameter. According to the above considerations, the equations of motion of the third infinitesimal body moving under the effect of the triaxial primaries located at $(\mu, 0)$, $(1-\mu, 0)$ are given by (Ahmed et al. 2020)

$$\ddot{x} - 2\,n\,\dot{y} = \frac{\partial U}{\partial x}, \qquad \ddot{y} + 2\,n\,\dot{x} = \frac{\partial U}{\partial y}, \tag{1}$$

with

$$U = \frac{n^2}{2}\ \left[(1-\mu)\ r_1^2 + \mu\, r_2^2\right] + \frac{(1-\mu)}{r_1} + \frac{\mu}{r_2} + \frac{(1-\mu)\ (2\,\sigma_1-\sigma_2)}{2\,r_1^3} - \frac{3\ (1-\mu)\ (\sigma_1-\sigma_2)\ y^2}{2\,r_1^5} + \frac{\mu\ (2\,\gamma_1-\gamma_2)}{2\,r_2^3} - \frac{3\,\mu\ (\gamma_1-\gamma_2)\ y^2}{2\,r_2^5}. \tag{2}$$

$$\begin{aligned} r_1 &= \sqrt{(x+\mu)^2+y^2},\\ r_2 &= \sqrt{(x+\mu-1)^2+y^2}, \end{aligned} \tag{3}$$

$$n = \frac{1}{a\,(1-e^2)}\left\{1+\frac{3}{2}\left[(2\sigma_1-\sigma_2)+(2\gamma_1-\gamma_2)\right]\right\}. \tag{4}$$

Here, U is the restricted three-body potential; n is the mean motion of the primaries; r_1 and r_2 are the distances of the infinitesimal mass from the primaries; σ_1, σ_2 and γ_1, γ_2 are the triaxiality coefficients of the bigger and smaller primaries, respectively.

3. LOCATIONS OF THE TRIANGULAR POINTS

The libration points represent stationary solutions of the restricted three-body problem. The positions of these points can be obtained by setting all components of the relative velocity and acceleration equal to zero, i.e. we found them by setting $\dot{x} = \dot{y} = 0 = \ddot{x} = \ddot{y}$. Consequently, the locations of these points can be found by solving simultaneously the nonlinear equations $U_x = U_y = 0$, and $y \neq 0$. Setting

$$\begin{aligned} A_\gamma &= \gamma_1-\gamma_2, & A_\sigma &= \sigma_1-\sigma_2,\\ A_\alpha &= 2\,\gamma_1-\gamma_2, & A_\beta &= 2\,\sigma_1-\sigma_2, \end{aligned}$$

we have

$$\begin{aligned} U_x =& -\mu\ (-1+x+\mu)\left[\frac{1}{r_2^3}+\frac{3}{2\,r_2^5}\,A_\alpha-\frac{15\,y^2}{2\,r_2^7}\,A_\gamma\right]\\ &+\frac{x}{a\ (1-e^2)}+(1-\mu)\ (x+\mu)\left[\frac{1}{r_1^3}-\frac{3}{2\,r_1^5}\,A_\beta\right.\\ &\left.+\frac{3}{2\,a\ (1-e^2)}\ (A_\alpha+A_\beta)-\frac{15\,y^2}{2\,r_1^7}\,A_\sigma\right], \end{aligned} \tag{5}$$

$$\begin{aligned} U_y = -y\Bigg\{&\frac{\mu}{r_2^3}+\frac{1-\mu}{r_1^3}+\frac{3\mu}{2r_2^5}A_\alpha+\frac{3\,(1-\mu)}{2r_1^5}A_\beta-\\ &\frac{1}{a\ (1-e^2)}\left[1+\frac{3}{2}\,(A_\alpha+A_\beta)\right]-\\ &\frac{15\,y^2}{2}\left[\frac{\mu\,A_\gamma}{r_2^7}+\frac{(1-\mu)}{r_1^7}\,A_\sigma\right]-\\ &\frac{3\,\mu}{r_2^5}\,A_\gamma+\frac{3\ (1-\mu)}{r_1^5}\,A_\sigma\Bigg\}, \end{aligned} \tag{6}$$

Ignoring the triaxiality perturbations due to the primary bodies yields the equilateral solution of the classical restricted three-body problem i.e. $r_1 = r_2 = 1$. Then, it may be reasonable to consider that the locations of these points are the same as given by classical problem, but perturbed by small terms, i.e.

$$r_i = 1+\delta_i, \qquad \delta_i << 1, \qquad (i=1,2)\,. \tag{7}$$

Substituting this assumption (7) into (3), solving for x and y and retaining terms up to the first order in the small quantities δ_i we get:

$$\begin{aligned} x &= \frac{1}{2}\left(2\,\delta_1-2\,\delta_2-2\,\mu+1\right),\\ y &= \pm\frac{1}{2}\sqrt{(3+4\ (\delta_1+\delta_2))}. \end{aligned} \tag{8}$$

Substituting the values of r_1, r_2, x and y into equations (5) and (6) and ignoring the terms higher than order one in δ_i we obtain the following two simultaneous equations in δ_1 and δ_2.

$$A_1+A_2\delta_1+A_3\delta_2=0, \qquad B_1+B_2\delta_1+B_3\delta_2=0. \tag{9}$$

The corresponding solution is:

$$\delta_1 = -\frac{A_3\,B_1-A_1\,B_3}{A_3\,B_2-A_2\,B_3}, \qquad A_3\,B_2-A_2\,B_3\neq 0, \tag{10}$$

$$\delta_2 = -\frac{-A_2\,B_1+A_1\,B_2}{A_3\,B_2-A_2\,B_3}, \qquad A_3\,B_2-A_2\,B_3\neq 0, \tag{11}$$

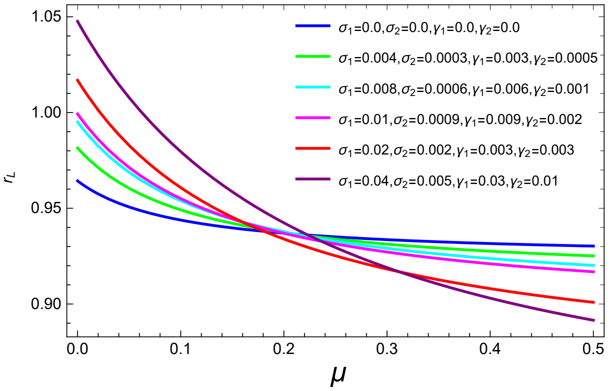

Fig. 1. The locations of $L_{4,5}$ with different triaxiality coefficients and eccentricity $e = 0.2$. The color figure can be viewed online.

where:

$$A_1 = -\frac{1}{2} + \mu + \frac{3}{4}\left(\mu\, A_\alpha - A_\beta + \mu\, A_\beta\right) + \frac{3}{4\,a\,(1-e^2)}\left(A_\alpha + A_\beta\right) + \frac{3}{2\,a\,(1-e^2)}\left(1 - \mu\,(2 + 3\,A_\alpha + 3\,A_\beta)\right) + \frac{45}{16}\left(-\mu\,(A_\gamma + A_\sigma) + A_\sigma\right), \tag{12}$$

$$A_2 = \frac{1}{2} - \frac{1}{a\,(1-e^2)}\left(1 + \frac{3}{2}\,(A_\alpha + A_\beta)\right) + \frac{3}{2}\left(1 - \mu A_\alpha + \frac{3}{2}(1-\mu)A_\beta - \frac{55}{8}(1-\mu)A_\sigma + \frac{5}{4}\mu A_\gamma\right), \tag{13}$$

$$A_3 = 1 + \frac{3}{2}\,A_\beta + \frac{1}{a\,(1-e^2)}\left(1 + \frac{3}{2}\,(A_\alpha + A_\beta)\right) - \frac{15}{8}\,A_\sigma - \frac{3}{2}\,\mu\left(1 + \frac{3}{2}A_\alpha + A_\beta - \frac{55}{8} - \frac{5}{4}\,A_\sigma\right), \tag{14}$$

$$B_1 = -\frac{\sqrt{3}}{2}\left\{1 - \frac{1}{a\,(1-e^2)}\left[1 + \frac{3}{2}\left(A_\alpha + A_\beta\right)\right] - \frac{3}{2}\left[A_\beta - \frac{7}{4}A_\sigma + \mu\left(A_\alpha - A_\beta - \frac{7}{4}A_\gamma + \frac{7}{4}A_\sigma\right)\right]\right\}, \tag{15}$$

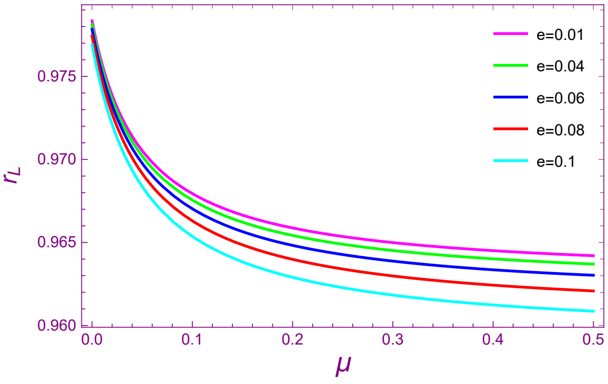

Fig. 2. The locations of $L_{4,5}$ with different eccentricities and triaxiality coefficients $\sigma_1 = 0.0002$, $\sigma_2 = 0.0005$, $\gamma_1 = 0.003$ and $\gamma_2 = 0.002$. The color figure can be viewed online.

$$B_2 = \frac{7}{2\sqrt{3}} + \frac{1}{\sqrt{3}a\,(1-e^2)}\left[1 + \frac{3}{2}\left(A_\alpha + A_\beta\right)\right] + \frac{\sqrt{3}}{2}\left[\frac{13}{2}\,A_\beta - \frac{121}{8}\,A_\sigma - \mu\left(3 + A_\alpha + \frac{13}{2}\,A_\beta - \frac{37}{4}\,A_\gamma - \frac{121}{8}A_\sigma\right)\right], \tag{16}$$

$$B_3 = -\frac{1}{\sqrt{3}}\left(1 + \frac{1}{a\,(-1+e^2)}\right) + \frac{3\sqrt{3}}{2}\left[\frac{37}{4}\,A_\sigma - \frac{A_\beta}{3} + \mu\left(1 + \frac{13}{2}\,A_\alpha + A_\beta - \frac{121}{8}\,A_\gamma - \frac{37}{4}\,A_\sigma\right) - \frac{(A_\alpha + A_\beta)}{a\,(-1+e^2)}\right]. \tag{17}$$

4. GRAPHICAL REPRESENTATIONS (LOCATION)

In Figures 1-2 we plot the locations $r_{L_{4,5}}$ of the triangular points in the elliptic restricted three body problem, taking into consideration triaxiality and eccentricity effects. Figure 1 represents the variation of $r_{4,5}$ against the mass ratio μ. The calculations are carried out for several dynamical models with different coefficients γ_i and σ_i; and constant eccentricity of the orbit of the primary $e = 0.2$. As is clear from the figure, the locations begin to decrease sharply until we reach the value $\mu \approx 0.15$, then they decrease slowly. We also observe that the variation in the locations $r_{L_{4,5}}$ is small, because the triaxiality coefficients are very small. Figure 2 depicts the variation of $r_{L_{4,5}}$ against the mass ratio μ with constant triaxiality coefficients. We applied our case study to a range of eccentricities; the eccentricity e takes the values $0.01, 0.04, 0.06, 0.08$ and 0.1. We notice that the change in the curves is nearly the same for all considered cases. This is because the chosen values of e are small. The dynamics is approximately the same but with different sizes of the perturbations. We expect that the larger the eccentricity the larger will be the perturbation in the positions of the triangular points.

5. STABILITY OF THE TRIANGULAR POINTS

The dynamical models which describe the restricted problem are very difficult. The great complexity of these models leads us to focus our attention on linearized dynamics, because in this case we obtain simplified mathematical expressions that could be handled easily. The location of the third body is displaced little from the equilibrium point due to the considered perturbations. If the resultant motion of this body is a rapid departure from this point, we call such a position of equilibrium point an unstable one; if the body just oscillates about the point, it is said to be a stable position (Abd El-Salam 2019). To examine the possible motion of the infinitesimal body in the proximity of the triangular points, the equations of motion should be linearized. Let the position of the triangular points be $(x_\circ,y_\circ)$ and let the third body be displaced to the point $(x_\circ+\xi,\ y_\circ+\eta)$, where ξ and η are small displacement in $(x_\circ, y_\circ)$, so that the linearized equations can be written as:

$$\begin{aligned} \ddot{\xi} - 2\,n\,\dot{\eta} &= \frac{1}{a\,(1-e^2)}\left(U_{xx}^{L_{4,5}}\,\xi + U_{xy}^{L_{4,5}}\,\eta\right), \\ \ddot{\eta} - 2\,n\,\dot{\xi} &= \frac{1}{a\,(1-e^2)}\left(U_{yy}^{L_{4,5}}\,\eta + U_{xy}^{L_{4,5}}\,\xi\right). \end{aligned} \tag{18}$$

Here $U_{xx}^{L_{4,5}}$ denotes the second derivative of U with respect to x computed at the stationary solution and the rest of the derivatives are defined similarly. The characteristic equation corresponding to equation (18) may be written as

$$\begin{aligned} \lambda^4 + \left(4n^2 - U_{xx}^{L_{4,5}} - U_{yy}^{L_{4,5}}\right)\lambda^2 + \\ U_{xx}^{L_{4,5}} U_{yy}^{L_{4,5}} - \left(U_{xy}^{L_{4,5}}\right)^2 = 0, \end{aligned} \tag{19}$$

which may be written in the form

$$\lambda^4 + U_{L_i}\,\lambda^2 + \nu_{L_i} = 0, \tag{20}$$

with

$$\begin{aligned} U_{L_i} &= \left(4\,n^2 - U_{xx}^{L_{4,5}} - U_{yy}^{L_{4,5}}\right), \\ \nu_{L_i} &= U_{xx}^{L_{4,5}}\,U_{yy}^{L_{4,5}} - \left(U_{xy}^{L_{4,5}}\right)^2. \end{aligned} \tag{21}$$

The roots of equation (21) are

$$\lambda_{1,2} = \pm\frac{\sqrt{-U_{L_i} - \sqrt{U_{L_i}^2 - 4\,\nu_{L_i}}}}{\sqrt{2}}, \tag{22}$$

and

$$\lambda_{3,4} = \pm\frac{\sqrt{-U_{L_i} + \sqrt{U_{L_i}^2 - 4\,\nu_{L_i}}}}{\sqrt{2}}. \tag{23}$$

The possible solutions for equation (19) will determine the stability of the equilibrium points. We have three possibilities: asymptotically stable, when all the solutions are real and negative; unstable, when at least one of the solutions is positive and real; and finally, the stable case when all solutions are purely imaginary (Szebehely 1967). We will focus our attention only on the case with oscillatory stable solutions about the triangular points. To investigate the stability/instability we first compute the partial derivatives required for equations (22) and (23) as

$$\begin{aligned} U_{xx} = \frac{1}{a\,(1-e^2)}&\left[1 + \frac{3}{2}\,(A_\alpha + A_\beta)\right] + \\ &\mu\left\{\frac{3\,(\mu+x-1)^2}{r_2^5} - \frac{1}{r_2^3} + \right. \\ &\frac{3}{2}A_\alpha\left[\frac{5\,(\mu+x-1)^2}{r_2^7} - \frac{1}{r_2^5}\right] - \\ &\left.\frac{15}{2}y^2 A_\gamma\left[\frac{7}{r_2^9}\,(\mu+x-1)^2 - \frac{1}{r_2^7}\right]\right\} + \\ &(1-\mu)\left\{\frac{3}{2}\,A_\beta\left[\frac{5\,(\mu+x)^2}{r_1^7} - \frac{1}{r_1^5}\right] + \right. \\ &\left.\left[\frac{3\,(\mu+x)^2}{r_1^5} - \frac{1}{r_1^3}\right] - \frac{15}{2}y^2 A_\sigma\left[\frac{7\,(\mu+x)^2}{r_1^9} - \frac{1}{r_1^7}\right]\right\}, \end{aligned} \tag{24}$$

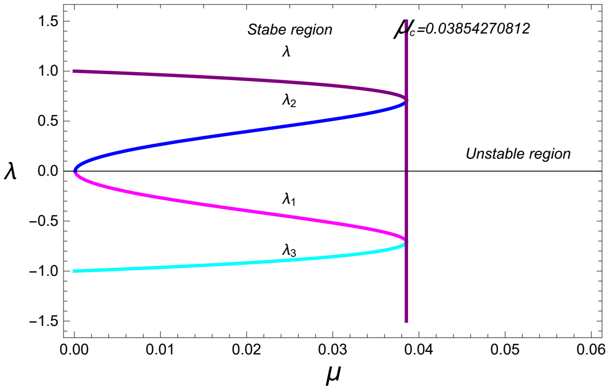

Fig. 3. The imaginary part of the eigenvalues versus the mass parameter in the classical case, $\sigma_i = \gamma_i = 0$. The color figure can be viewed online.

$$U_{yy} = \frac{1}{a\ (1-e^2)}\ \left[1+\frac{3}{2}\left(A_\alpha+A_\beta\right)\right]+$$
$$\mu\left\{3A_\gamma\left[\frac{10y^2}{r_2^7}-\frac{5y^2}{2}\left(\frac{7y^2}{r_2^9}-\frac{1}{r_2^7}\right)-\frac{1}{r_2^5}\right]\right\}+$$
$$(1-\mu)\left\{\frac{3\ y^2}{r_1^5}-\frac{1}{r_1^3}+\frac{3}{2}\left(\frac{5\ y^2}{r_1^7}-\frac{1}{r_1^5}\right)A_\beta-\right.$$
$$3\ A_\sigma\ \left[\frac{1}{r_1^5}+5\ y^2\left(\frac{-2}{r_1^7}+\frac{7\ y^2}{2\ r_1^9}-\frac{1}{2\ r_1^7}\right)\right]+$$
$$\left.\frac{3\ A_\alpha}{2}\ \left(\frac{5\ y^2}{r_2^7}-\frac{1}{r_2^5}\right)+\frac{3\ y^2}{r_2^5}-\frac{1}{r_2^3}\right\}, \tag{25}$$

$$U_{xy} = y\left\{\mu\ (\mu+x-1)\ \left[-\frac{105\ y^2 A_\gamma}{2\ r_2^9}+\frac{15\ A_\alpha}{2\ r_2^7}+\right.\right.$$
$$\left.\frac{15\ A_\gamma}{r_2^7}+\frac{3}{r_2^5}\right]+y\ (1-\mu)\ (\mu+x)\ \left[\frac{3}{r_1^5}-\right.$$
$$\left.\left.\frac{105\ y^2\ A_\sigma}{2\ r_1^9}+\frac{15\ A_\beta}{2\ r_1^7}+\frac{15\ A_\sigma}{r_1^7}\right]\right\}. \tag{26}$$

6. GRAPHICAL REPRESENTATIONS (STABILITY)

Figures 3-5 illustrate the stability regions taking into consideration the triaxiality coefficients and the eccentricity of the orbits. Figure 3 represents the classical case i.e. when $\sigma_i = 0$, $\gamma_i = 0$ and $e = 0$ as well. Figure 4 depicts the stability regions for dynamical systems with different triaxiality coefficients, while Figure 5 shows these regions for different eccentricities and constant coefficients. We can see from Figure 4 that each stability region is characterized by different values of the triaxiality coefficients. The size of the regions is not much different from that of the classical case; this because the perturbation due to the triaxiality coefficients is small. In Figure 5 the effect of different eccentricities on the size of the regions is obvious. Comparing with previous work e.g. Abd El-Salam (2015), we found that the size of the regions is slightly different from that found in the quoted paper due to the perturbations considered in each case. We expect that as the eccentricity increases the stability regions will be de-

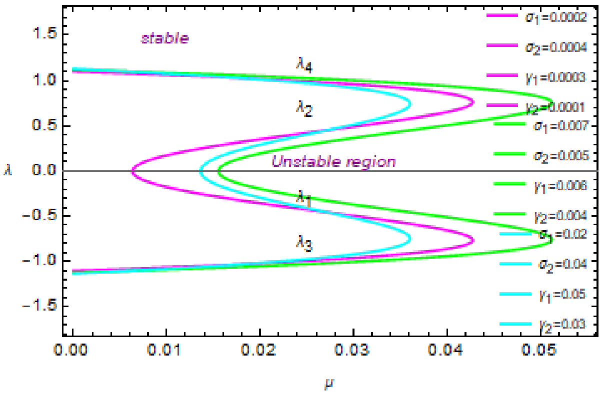

Fig. 4. The imaginary part of the eigenvalues versus the mass parameter with eccentricity $e = 0.01$ and different triaxial parameters. The color figure can be viewed online.

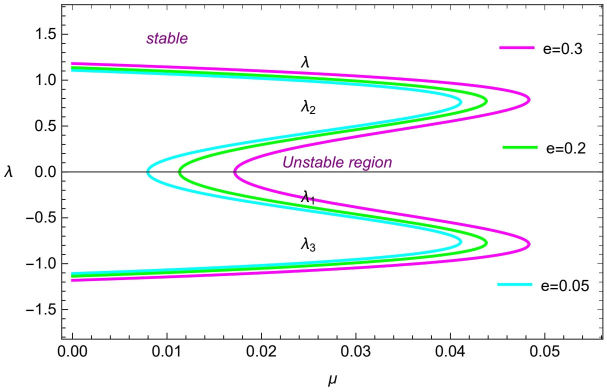

Fig. 5. The imaginary part of the eigenvalues versus the mass parameter with different eccentricities and triaxial parameters, $\sigma_1 = 0.001$, $\sigma_2 = 0.004$, $\gamma_1 = 0.003$ and $\gamma_2 = 0.002$. The color figure can be viewed online.

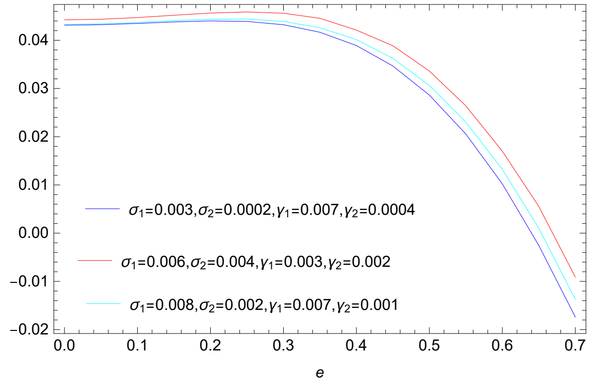

Fig. 6. The critical mass ratio versus eccentricity for different values of the triaxial parameters. The color figure can be viewed online.

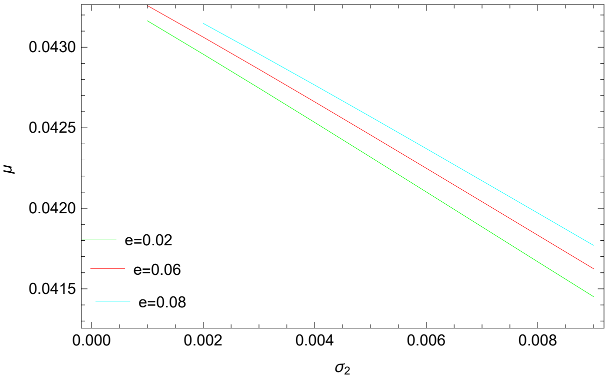

Fig. 7. The critical mass ratio versus triaxial parameter σ_2, for different values of the eccentricity. The color figure can be viewed online.

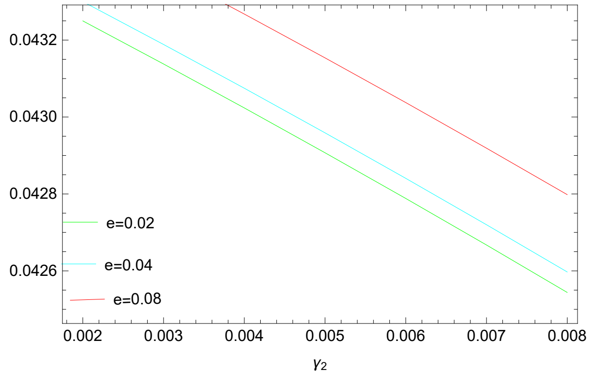

Fig. 8. The critical mass ratio versus triaxial parameter γ_2, for different values of the eccentricity. The color figure can be viewed online.

TABLE 1

VALUES OF THE CRITICAL MASS RATIO FOR DIFFERENT DYNAMICAL MODELS

σ_1	σ_2	γ_1	γ_2	e	a	μ_c
0	0	0	0	0	1	0.0385209
0.006	0.0004	0.03	0.002	0.2	0.92	0.0443621
0.006	0.0004	0.03	0.002	0.4	0.92	0.0401412
0.006	0.0004	0.03	0.002	0.6	0.92	0.0132093
0.003	0.0002	0.007	0.0004	0.02	0.92	0.0456447
0.003	0.0002	0.007	0.0004	0.04	0.92	0.0424109
0.003	0.0002	0.007	0.0004	0.07	0.92	0.00909276
0.009	0.002	0.008	0.002	0.02	0.92	0.042956
0.009	0.004	0.008	0.002	0.02	0.92	0.0425331
0.009	0.008	0.008	0.002	0.02	0.92	0.0416678
0.006	0.001	0.008	0.001	0.08	0.92	0.0466464
0.006	0.001	0.008	0.005	0.08	0.92	0.0431538
0.006	0.001	0.008	0.008	0.08	0.92	0.0427982

stroyed. Table 1 gives the values of the critical mass for some selected dynamical models. These values are computed under the effect of the included perturbations. We notice from the table that when the triaxiality coefficients (σ_i and γ_i) are equal to zero, μ_c reduces to the critical mass value of the classical restricted problem (see Figure 3). We also notice from Figures 4, 5 that the triaxiality coefficients of the primaries change the range of stability.

In addition, we can also investigate the behavior of the system by plotting the critical mass ratio against the eccentricity for different values of the triaxial parameters σ_i and γ_i. We plot different combinations of triaxial parameters and a stable region is observed. Figure 6 shows that the increase in the eccentricity reduces the region of stability of the infinitesimal body about the triangular points. Figures 7 and 8 represent the variation of the critical mass with the triaxial parameters when the eccentricity is constant. We can see from the two figures that increasing the triaxial parameters results in a destabilizing effect in the system.

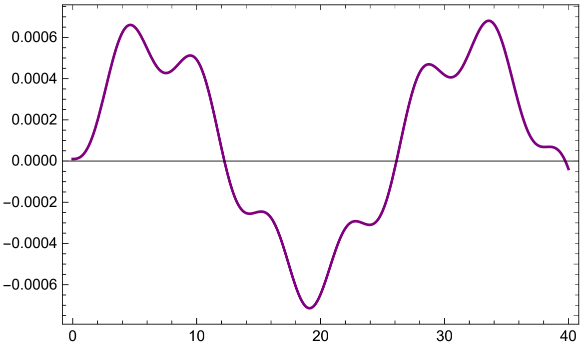

Fig. 9. $x[t]$ as a function of time with triaxiality coefficients $\sigma_1 = 0.007$, $\sigma_2 = 0.002$, $\gamma_1 = 0.005$, $\gamma_2 = 0.002$, $\mu = 0.01$, $e = 0.01$ and $a = 0.92$. The color figure can be viewed online.

7. MOTION IN THE PROXIMITY OF THE TRIANGULAR POINTS

It is known that periodic orbits represent the backbone in the study of dynamical systems in celestial mechanics. Since in the range $0 \leq \mu \leq \mu_c$, the roots of the characteristic polynomial of the present system are purely imaginary, we conclude that the motion around the triangular points L_4 (or L_5) is stable and composed of two harmonic motions. The solutions for the perturbed motion about the triangular point L_4 (in the synodic reference frame) may be written as

$$X[t] = \sum_{j=1}^{4} \alpha_j \, e^{\lambda_j \, t}, \tag{27}$$

$$Y[t] = \sum_{j=1}^{4} \beta_j \, e^{\lambda_j \, t}, \tag{28}$$

where the terms with coefficients α_j and β_j represent the short and long periodic motion. The constants α_j and β_j are not independent. Applying the initial conditions to the solutions of the system these solutions may be written in the form

$$\begin{aligned} X[t] = {} & 5.80204 * 10^{-5} \, \sin(0.241582 \, t) - \\ & 1.31958 * 10^{-5} \, \sin(1.06221 \, t) + \\ & 3.19255 * 10^{-5} \, \cos(0.241582 \, t) - \\ & 2.19255 * 10^{-5} \, \cos(1.06221 \, t). \end{aligned} \tag{29}$$

$$\begin{aligned} Y[t] = {} & 8.06288‘ * 10^{-5} \, \cos(0.241582‘ \, t) - \\ & 7.062876‘ * 10^{-5} \, \cos(1.06221‘ \, t) - \\ & 3.054769‘ * 10^{-5} \, \sin(0.241582‘ \, t) + \\ & 6.9475842 * 10^{-5} \, \sin(1.06221 \, t). \end{aligned} \tag{30}$$

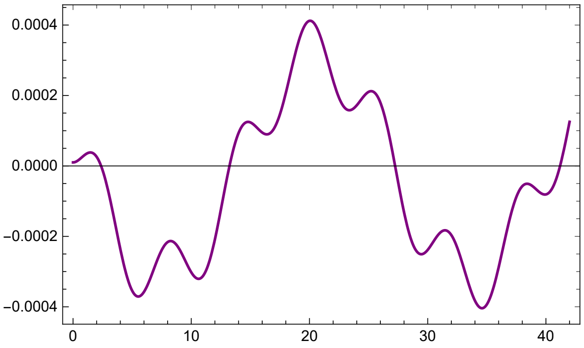

Fig. 10. $y[t]$ as a function of time with triaxiality coefficients $\sigma_1 = 0.007$, $\sigma_2 = 0.002$,$\gamma_1 = 0.005$, $\gamma_2 = 0.002$, $\mu = 0.01$, $e = 0.01$ and $a = 0.92$. The color figure can be viewed online.

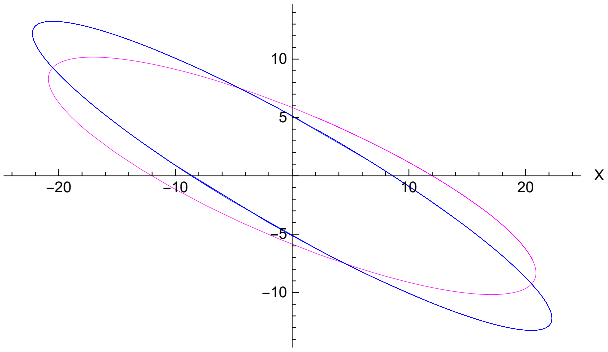

Fig. 11. Comparison between the long period motion in both the classical case (blue curve) and the present dynamical system (magenta curve). The color figure can be viewed online.

We may note from equations (29) and (30) that the solution is of the oscillatory type with fundamental periods of $\frac{2\,\pi}{0.241582‘}$ and $\frac{2\,\pi}{1.06221}$ times the orbital periods of the orbiting body. Hence the body will remain in the proximity of the triangular point L_4 and the motion is stable. These two different types of frequencies in the solution exist due to the fact that the resulting motion of the small body is composed of two types of motion. Firstly, a short-period motion with a period close to the orbital period of the less massive primary, and secondly a superimposed long-period one known as a libration around the point L_4. The two solutions are depicted in Figures 9 and 10. The graph of the trajectory in the vicinity of equilibrium point L_4 is shown in Figures 11 and 12 with magenta color. The graphs contain both the short and the long-period motions. Figure 11 shows a com-

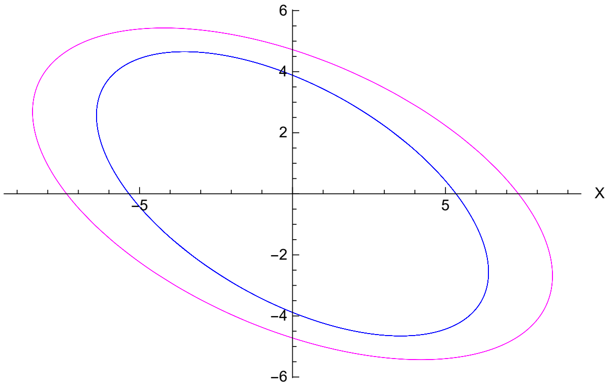

Fig. 12. Comparison between the short period motion in both the classical case (blue) and the present dynamical system (magenta). The color figure can be viewed online.

parison between the long-period motions in both the classical case (blue curve) and the present dynamical system (magenta curve), while Figure 12 shows a comparison between the two systems in the short-period case. It is observed that the trajectories (magenta curve) in both figures are shifted from those of the classical case. This is due to the included perturbations.

8. CONCLUSIONS

We have studied the existence and linear stability of the triangular points in the elliptic restricted three-body problem when the primaries are triaxial bodies. We found that the locations and the linear stability of the triangular points are affected by the triaxiality coefficients of the primaries and the eccentricity of the orbit. We also noticed that the size of the stability regions depends on the triaxiality coefficients and the eccentricity of the orbits. In addition, we studied the periodic orbits in the vicinity of the triangular points. We showed that these orbits are elliptical. Further, we observed that the shape of the periodic orbits changed due to the triaxiality of the primaries and showed a deviation from the classical case.

REFERENCES

Abd El-Salam, F. A., 2015, Ap&SS, 357, 15
__________. 2019, NewA, 68, 25
Abouelmagd, Elbaz I. 2013, EM&P, 110, 143
Ahmed, A. A., Selim, H. H., Kamel, A. K. G., et al. 2020, Applied Mathematics and Nonlinear Sciences, 5, 157
Cárcamo-Díaz, D., Palacián, J. F., Vidal, C., & Yanguas, P. 2020, RCD, 25, 131
Kumar, P. & Sharma, R. K. 2020, Indian Journal of Science and Technology, 13, 32
Mittal, A., Ahmad, I., & Bhatnagar, K. B., 2009, Ap&SS, 323, 65
Musielak, Z. E. & Quarles, B. 2014, RPPh, 77, 6, 065901
Narayan, A. & Usha, T. 2014, Ap&SS, 351, 135
Selim, H. H., Guirao, J. L. G., & Abouelmagd, E. I. 2019, Discrete & Continuous Dynamical Systems-S, 12, 703
Singh, J. & Begha, J. M. 2011, Ap&SS, 332, 319
Singh, J. & Umar, A. 2012, AJ, 143, 109
Singh, J. & Tyokyaa, R. K. 2016, EPJP, 131, 365
Szebehely, V. G. 1967, Theory of orbits. The restricted problem of three bodies (New York, NY: Academic Press)
Zahra, K., Radwan, M., & Awad, M. E. 2016, Nonlinear Analysis and Differential Equations, 4, 609
Zahra, K., Awad, Z., Dwidar, H. R., & Radwan, M. 2017, SerAJ, 195, 47

Nihad S. Abd El Motelp: Astronomy; Astronomy Department, National Research Institute of Astronomy and Geophysics (NRIAG), 11421 Helwan, Cairo, Egypt (nihad.saad@nriag.sci.eg).
M. Radwan: Astronomy; Space Science and Metreology Department, Faculty of Science, Cairo University, 12613 Giza, Egypt (mradwan@sci.cu.edu.eg).

Revista Mexicana de Astronomía y Astrofísica, **57**, 321–334 (2021)

https://doi.org/10.22201/ia.01851101p.2021.57.02.06

A STUDY OF THE SECULAR VARIATION OF THE HIGH-AMPLITUDE DELTA SCUTI STAR AD CMi[1]

J. H. Peña[2,3,4], D. S. Piña[2,4], H. Huepa[3], S. B. Juárez[4], C. Villarreal[4], J. Guillén[4], A. A. Soni[2,4], A. Rentería[2,3,4], J. M. Donaire[5], R. R. Muñoz[5], T. Benadalid[5], J. D. Paredes[6], E. D. Orozco[4], I. Soberanes[4], H. Posadas[4], C. Castro[4], J. Briones[4], M. Romero[4], F. Martinez[4], A. L. Zuñiga[4], J. L. Carrillo[4], B. Chávez[4], D. Navez[4], and C. García[4]

Received June 1 2020; accepted April 20 2021

ABSTRACT

We determine the nature of the Delta Scuti star AD CMi and its physical parameters from newly determined times of maximum light and other times from the literature, as well as from $uvby-\beta$ photoelectric photometry.

RESUMEN

A partir de los recién determinados tiempos de máximo en fotometría de la estrella Delta Scuti AD CMi y una recopilación de tiempos de máximo de la literatura, así como datos con fotométria $uvby-\beta$ hemos determinado la naturaleza de esta estrella y sus parámetros físicos.

Key Words: asteroseismology — stars: fundamental parameters — stars: variables: Scuti

1. INTRODUCTION

The study of δ Scuti stars has undergone many changes since its inception. Soon after the pioneering works of Eggen (1957) and Millis (1966, 1968), systematic studies like those of Breger (1979) and the early considerations about the nature of their variability by the French group led by Le Contel et al. (1974), as well as the later coordinated longitudinal campaigns designed to discover the true nature of the pulsational variability, altered the nature of our knowledge of these stars. During these years some researchers such as Zessewitch (1950) and Abhyankar (1959), among others, recognized the value of using the old data sets which provided, as in the present study, time bases of fifty years or more leading to more precise interpretations of the variability. However, the attainable limits of ground-based observations were finally reached and efforts were made to study these variables from space.

As Garrido and Poretti (2004) pointed out, teams dedicated to δ Scuti stars have begun changing their observational strategies. After the Canadian satellite MOST was successfully launched to study asteroseismology from space, other missions were designed to determine adequate frequency resolutions. This satellite, and COROT, were the first to study δ Scuti stars from space. CoRoT (Convection, Rotations, and Planetary Transits), led by the CNES in association with French laboratories with large international participation, was a satellite built to study the internal structure of stars and to detect extrasolar planets. It continuously observed star fields in the Milky Way for periods of up to 6 months. Over the course of 2,729 days, CoRoT collected some 160,000 light curves showing variations of star brightness over time. This mission ended in June 2014.

There have been several other space projects. One of the most important was that of NASA's Kepler satellite, which was launched on March 6, 2009 with the primary mission of searching for exoplanets via planetary transits using high-precision, long time-series CCD photometry with a secondary mission of studying stellar variability (Guzik et al., 2019). In 2013 the K2 mission was developed to ob-

---

[1] Based on observations collected at the Tonantzintla and San Pedro Mártir Observatories, México.

[2] Instituto de Astronomía, Universidad Nacional Autónoma de México, Cd. México.

[3] Observatorio Astronómico Nacional, Tonantzintla Puebla, México.

[4] Facultad de Ciencias, Universidad Nacional Autónoma de México.

[5] Universidad Mayor de San Andrés, La Paz, Bolivia.

[6] Universidad Central de Venezuela, Venezuela.

serve 19 new fields along the ecliptic plane. δ Scuti variables have been included in these campaigns since they are a promising type of star for research using pulsations to infer interior structure and, as a result, to test the input of physics and methods of solar and stellar modelling. Multiple papers have utilized the Kepler data, and as Guzik et al. (2019) pointed out, the lists of candidate stars observed for these data could be used to discover targets for asteroseismic research.

Recent studies of δ Scuti stars using data from the Kepler mission include Bowman and Kurtz (2018) who demonstrated that an ensemble-based approach using space photometry from the Kepler mission was not only possible, but it was also valuable as a method to identify stars for mode identification and asteroseismic modelling. This work was extended by Antoci et al. (2019) for hot young δ Scuti stars which were missing in the Kepler mission data set.

Kepler's database, combined with other satellite results such as Gaia DR2 that provided the parallaxes, has served to derive precise luminosities (Murphy et al., 2019) for stars in and around the δ Scuti instability strip for a sample of over 15 000 A and F stars with δ and non δ Sctuti stars. Murphy et al., (2019) determined a new empirical instability strip based on the observed pulsator fraction that is systematically hotter than the theoretical strips. Ziaali et al. (2019) examined the period-luminosity (P-L) relation for δ Sctuti stars with the same Gaia DR2 parallaxes for the sample of Rodriguez et al. (2000) as well as 1124 stars observed by the Kepler mission and determined absolute magnitudes. Barcelo Forteza et al. (2020) remarked that thanks to the high-precision photometric data legacy from space telescopes, like CoRoT and Kepler, the scientific community was able to detect and characterize the power spectra of hundreds of thousands of stars. Thanks to long-duration high-cadence TESS light curves, they could analyze more than two thousand δ Scuti classical pulsators and proposed the frequency at maximum power as a proper seismic index, since it is directly related to the intrinsic temperature, mass and radius of the star.

Extending the study of large satellite data sets, Jayasinghe et al. (2020) characterized an all-sky catalogue of 8400 δ Scuti variables in ASAS-SN, which included 3300 new discoveries and combined with the Gaia DR2 derived period-luminosity relationships for both the fundamental mode and overtone pulsators. The determined results are indicative of a Galactocentric radial metallicity gradient. In their sample, Jayasinghe et al. (2020) identified two new δ Scuti eclipsing binaries, ASASSN-V J071855.62-434247.3 and ASASSN-V J170344.20-615941.2 with short orbital periods of 2.6096 and 2.5347 d, respectively. Regarding particular stars, Handler et al. (2020) carried out a study of a close binary system, HD 74423, discovered by TESS. They claim that it might be the prototype of a new class of obliquely pulsating stars in which the interactions of stellar pulsations and tidal distortion can be studied.

In the present paper we utilize both the observations of the AD CMi star obtained decades ago to determine its secular behavior as well as $uvby-\beta$ to determine its physical parameters. The HADS star AD CMi has the following characteristics: right ascension and declination of 07:52:47.18, +01:35:50.50 (epoch 2000), magnitude of 9.38, a spectral type of F0IV, a period of $0.12297443\,d$ (2.9 hr) and an amplitude of variation of 0.3 mag. All these features make it an easy target for the small telescopes provided with CCD cameras that are used in our astronomical courses.

With respect to the background of the star, according to Anderson and McNamara (1960) AD CMi was discovered by Hoffmeister (1934) and Zessewitch (1950) who described it as an eclipsing variable of Algol type, with a period of 1.276 d. Abhyankar (1959) determined that AD CMi was an intrinsic variable with a period of only 3 h. From their analysis they found the following ephemerides for this star: $Hel.max. = JD2436601.8228 + 0.122972E$. Breger (1975) carried out an extensive study of AD CMi with $uvby-\beta$ photometry. He determined a Wesselink radius of $3R_{\odot}$ which leads to a Population I mass. He stated that except for the large amplitude, the star is virtually indistinguishable from a normal δ Scuti variable. Dean et al. (1977) considered AD CMi to be an RR Lyrae star and reported V and $V-I$ photometry from one night. Later, in 1983, Balona and Stobie reported simultaneous $BVRI$ photometry and photoelectric radial velocities of several dwarf Cepheids, AD CMi among them, but no conclusions were reached. It was Rodríguez and the Spanish group who conducted several studies of this star. The first (Rodriguez et al., 1988) used $uvby-\beta$ photometry and proposed the possibility of a quadratic ephemerides. They derived physical parameters of $T_e = 7550\,K$, $\log g = 3.83$ and $M_V = 1.68\,\mathrm{mag}$. Through the Wesselink method they derived a radius of $2.77\,R_{\odot}$ and a mass of $1.9\,M_{\odot}$. In a later paper (Rodríguez et al., 1990) they proposed a period change slightly different from that determined independently by Jiang (1987).

The last comprehensive study of AD CMi was done by Khokhuntod et al. (2007). With observations carried out in 2005 and 2006, they analyzed the pulsation of the star with the derived multiple frequencies fitted to their data. Besides the dominant frequency and its harmonics, one low frequency ($2.27402\,c/d$) was discovered which, they stated, provided a reasonable interpretation for the long-noticed luminosity variation at maximum and minimum light. The results provided the updated value of period of $0.122974478\,d$, and seemed to support the model of a combination of the evolutionary effect and light-time effect of a binary system. Now, with an extended time basis of more than twelve years we can verify and refine their findings.

In order to carry out an analysis to determine the physical parameters, $uvby-\beta$ photoelectric photometry can be considered. These include several sources starting with the observations of Epstein & Abraham de Epstein (1973), Rodríguez (1988) and the observations presented in this paper carried out in 2013, 2014, 2016, 2017, 2018 and 2019, and summarized in Table 1.

2. OBSERVATIONS

Although some of the times of maximum light of this star have been reported elsewhere (Peña et al., 2017), we here present new times of maxima and the detailed procedure followed to acquire the data. The observations were done at both the Observatorio Astronómico Nacional of San Pedro Mártir (SPM) and that of Tonantzintla (TNT), in México. Table 1 presents the log of observations, as well as the new times of maximum light.

2.1. *Data Acquisition and Reduction at Tonantzintla*

Three 10-inch Meade telescopes were utilized at the TNT Observatory and are denoted by $m1$, $m2$ and me. These telescopes were equipped with CCD cameras and the observations were done using V and G filters. During all the observational nights this procedure was followed: the integration time was 1 min and there were around 11,000 counts, enough to secure high precision. The reduction work was done with AstroImageJ (Collins & Kielkopf (2012)). This software is relatively easy to use and, besides being free, it works satisfactorily on the most common computing platforms. With the CCD photometry two reference stars were utilized whenever possible in a differential photometry mode. The results were obtained from the difference $V_{\text{variable}} - V_{\text{reference}}$ and the scatter calculated from the difference $V_{\text{reference1}} - V_{\text{reference2}}$. Light curves were also obtained. In order to calculate the times of maximum light a program that considers the derivative function was used. A fifth polynomial was adjusted between the selected points in order to enclose the point of maximum light. On applying the derivative, as a criterion, the roots were determined in such a way that an f adjustment function was found, so that in the open selected interval, the derivative equal to zero was a minimum (if it was convex) or maximum (if it was concave) relative to f. The new times of maximum light are listed in Table 1. In this table, in Column 1 the date of observation is listed, in Column 2 the observers/reducers; in Column 3 the obtained number of points during the night, and in Column 4 the time span of the observations. Column 5 specifies the number of maxima for that night; Column 6 the time of maximum in HJD-2400000; and Column 7 the telescope utilized (*m1*, *m2* and *me* stand for small 10" Meade telescopes, whereas 84 describes the telescope at the SPM observatory); Column 8 describes the filter utilized (V in the UBV system and G for the GRB filter system, whereas in the $uvby-\beta$ we utilized only the y filter transformed into Olsen's (1983) photoelectric photometry system. Finally, the last two Columns 9 and 10 specify the CCD camera and the observatories, Tonantzintla (TNT) and San Pedro Mártir (SPM).

2.2. *Data Acquisition and Reduction at SPM*

As was stated in Peña et al. (2016) reporting on BO Lyn, the observational pattern as well as the reduction procedure have been employed at the SPM Observatory since 1986 and, hence, have been described many times. A detailed description of the methodology can be found in Peña et al. (2007).

The star AD CMi was observed in $uvby-\beta$ photometry over various seasons: November, 2013; January, December, 2016 and 2017. The first one covered six nights, whereas the second one three nights in January and seven in December, 2016. AD CMi was observed on only one night in the 2017 December season.

Over the nights of observation of the AD CMi star the following procedure was used: Each measurement consisted of at least five ten-second integrations of the star and three ten-second integrations of the sky simultaneously for the $uvby$ filters, and almost simultaneously for the narrow and wide filters that define Hβ.

TABLE 1

LOG OF OBSERVING SEASONS AND NEW TIMES OF MAXIMA OF AD CMI

Date yr/mo/day	Observers/reducers	Npoints	Time span (day)	Nmax	Tmax 2400000+	Telescope	Filters	Camera	Observatory
13/02/0910	cvr/cvr	202	0.13	1	56333.8206	m1	G	ST8	TNT
13/02/2223	aas/arl	226	0.12	1	56346.7301	m1	wo	ST8	TNT
13/11/1718	cvr/jhp	20	0.09	1	56613.9390	84	$uvby-\beta$	spectr	SPM
14/04/0506	AOA14/cgs	99	0.08	1	56753.6540	m2	wo	ST8300	TNT
16/01/1213	aas,jg/jhp	48	0.01	1	57400.8690	84	$uvby-\beta$	spectr	SPM
16/01/2122	ESAOBELA16/cgs	148	0.20	1	57409.8501	m1	G	ST8	TNT
16/01/2122	ESAOBELA16/cgs	179	0.15	1	57409.8501	m2	V	1001	TNT
16/01/2223	ESAOBELA16/dsp	112	0.16	0		m2	V	ST8	TNT
16/02/1112	dsp/dsp	130	0.14	1	57430.7541	m2	V	1001	TNT
16/02/1213	AOA16/dsp	80	0.06	0		me	V	1001	TNT
16/03/1112	AOA16/dsp	167	0.15	1	57459.6543	m1	V	1001	TNT
16/03/1213	AOA16/dsp	103	0.12	0		m1	V	1001	TNT
16/12/1314	dsp/dsp	42	0.11	0		84	$uvby-\beta$	spectr	SPM
17/01/1415	ESAOBELA17/dsp	144	0.12	1	57768.8131	m1	V	1001	TNT
18/01/1112	ESAOBELA18/dsp	80	0.09	0		me	V	1001	TNT
18/01/1213	ESAOBELA18/dsp	133	0.07	0		me	V	1001	TNT
18/01/2122	ESAOBELA18/dsp	137	0.12	0		me	V	1001	TNT
18/03/0304	AOA18/dsp	157	0.15	1	58181.7596	m1	V	1001	TNT
18/03/1718	AOA18/dsp	129	0.13	1	58195.7759	m1	V	1001	TNT
19/01/1516	ESAOBELA19/hh	97	0.15	1	58499.8951	m2	V	ST8	TNT
19/01/1819	ESAOBELA19/hh	205	0.16	1	58502.8419	m2	V	ST8	TNT
19/01/2122	ESAOBELA19/hh	141	0.19	1	58505.9170	m2	V	ST8	TNT
19/01/2223	ESAOBELA19/hh	186	0.21	2	58506.7780 58506.9044	m2	V	ST8	TNT
19/02/0102	jgt/jgt	228	0.27	2	58516.7387 58516.8638	m2	wo	8300	TNT
19/03/0102	AOA19/arl	47	0.04	0		m1	V	1001	TNT
19/03/1516	AOA19/arl	32	0.02	0		me	V	1001	TNT
19/03/1617	AOA19/arl	187	0.14	1	58559.7805	me	V	1001	TNT

Notes: jhp, J. H. Peña; dsp, D. S. Piña; arl, A. Rentería; jgt, J. Guillén; cvr, C. Villarreal; cgs: C. García; hh, H. Huepa AOA14: N. Ordoñez, S. Mafla, W. Fajardo, M. Rojas, I. Cruz, O. Martinez, E. Rojas, J. Rosales, W. Fajardo, A. Garcia & W. Fuentes; ESAOBELA16: A. Rodríguez, V. Valera, A. Escobar, M. Agudelo, A.Osorto, J. Aguilar, R. Arango, C. Rojas, J. Gómez, J. Osorio, & M. Chacón,; AOA16: Juarez, K. Lozano, K., Padilla, A., Santillan, P. and Velazquez R., ESAOBELA17: Ramirez, C., Rodriguez, M, Vargas, S., Castellon, C., Salgado, R., Mata, J., de la Fuente, D., Santa Cruz, R., Gonzalez, L., Chipana, K.; ESAOBELA18: Calle, C., Huanca, E., Uchima, J., Ramírez, R., Funes, R., Martinez, J., Mejía, R., Sarmiento, Y., Cruz, M., Meza, E., Alvarado, N., Huaman, V. & Ochoa, G.; AOA18: A. L. Zuñiga, J. L. Carrillo, S. B. Juárez, B. Chávez & D. Navez; ESAOBELA19: A. Belen Blanco, T. Benadalid, J. M. Donaire, M. Quiroz-Rojas, P. Escobar, M. Mireles, R. Mejía, A. León, C. Zelada, J. Ng, A. Arcila, L. E. Salazar, P. Escobar & M. M. Mireles; AOA19: I. Soberanes, H. Posadas, C. Castro, J. Briones & M. Romero.

The details of the second season are described in Peña et al. (2019), whereas for the 2013 season the transformation coefficients of that night are listed in Table 2. In the 2016 season three nights were lost due to bad weather.

What must be emphasized here are the transformation coefficients for the observed seasons (Table 2) and the season errors which were evaluated using the observed standard stars. These uncertainties were calculated through the differences in magnitude and colors for (V, $b{-}y$, m_1, c_1 and Hβ) which are (0.0870, 0.0065, 0.0085, 0.0212, 0.0179); (0.054, 0.012, 0.019, 0.025, 0.012) and (0.032, 0.010,0.011,0.013, 0.012) for the 2013 and both the 2016 and 2017 seasons, respectively, for a total of 94 points in $uvby$ and 68 points in Hβ, which provide a numerical evaluation of our uncertainties. We must call attention to the bad quality of the December 2016 season. However, since the effects of the clouds compensate each other, the color indexes gave reasonable values, whereas the V showed significant larger scatter and, will not be taken into account. The obtained data will be sent to the archives and are available upon request.

3. PERIOD DETERMINATION

To determine the period behavior of AD CMi the following three methods were employed: (1) Time series analyses of different data sets. (2) Period determination through O−C differences minimization

TABLE 2

MEAN VALUES AND STANDARD DEVIATIONS $<\sigma>$ OF THE TRANSFORMATION COEFFICIENTS OBTAINED FOR THE SEASONS

Season	B	D	F	J	H	I	L
2013 Nov	0.027	0.973	1.034	0.034	1.022	0.146	-1.495
$<\sigma>$	0.029	0.010	0.004	0.014	0.031	0.028	0.015
2016 Jan	0.031	1.008	1.031	-0.004	1.015	0.159	-1.362
$<\sigma>$	0.028	0.003	0.015	0.015	0.005	0.004	0.060
2016 Dec	0.134	0.993	1.024	0.043	1.025	0.101	
$<\sigma>$	0.243	0.009	0.065	0.055	0.009	0.026	
2017 Dec	0.016	1.013	1.002	0.023	1.032	0.131	-1.314
$<\sigma>$	0.084	0.047	0.040	0.035	0.015	0.029	0.100

(PDDM), and (3) O−C differences calculated utilizing a compiled collection of times of maximum light.

The previously determined ephemerides equations, as well as the newly determined ones are listed in Table 3.

3.1. *Time Series*

As a first method to determine the period, we used a time series method which is commonly utilized in the δ Scuti star community: Period04 (Lenz & Breger, 2005). There are several data sets which can be analyzed with this code:

i) The combined data in $uvby-\beta$ of Rodriguez et al. (1988) and the present paper's data.

In this case, we were fortunate enough that AD CMi had been observed in 1984 by Rodriguez et al. (1988) with a spectrophotometer similar to that of the SPM observatory, so a time series analysis was possible using their data along with the observations reported in the present paper. The initial time is $HJD\,2445766.3497$ and the end time $HJD\,2457400.9452$, with a total of 339 data points. The time span covered is then 11634.5955 d or 31.8 yr which is 94684 cycles, an enormous gap during which no observations were made of this system. To combine both seasons we first had to level them. Rodriguez et al. (1988) published their result in differential magnitudes relative to the $BD+2^{\circ}1804$ star. We observed this star both in 2017 (once) and 2018 (three times) and found that its photometric values were 8.181 ± 0.010 in V; 0.335 ± 0.003 in $(b-y)$; 0.155 ± 0.005 in m_1 and 0.347 ± 0.006 for c_1. The uncertainties are the standard deviation of the four measurements. The details of the accuracy of each season can be found in Peña et al. (2019). The analysis of these data gave the results listed in Table 4 (Set 1), with a zero point of 8.6046, and residuals of 0.014532.

ii) To this data set we added that of Epstein & Abraham de Epstein (1973) (Set 2). They observed this star in 1973 and considered it to be an RR Lyra star. A few points in each of the four consecutive reported nights comprise the data sample of only fifteen data points. This enlarges the times basis from $HJD2441010.6949$, their first reported point, to $HJD2457400.9452$, our last observed point, a difference of $16390\,d$ (44.9 yr) equal to 133388 cycles. However, the gaps between the sets are enormous.

iii) To fill these gaps we considered the ASAS data (Pojmanski et al. 2005), because this sample contains 464 points over a time span of 907 days in the years from 2002 to 2005. The V magnitude sample was increased with the values of Dean et al. (1977), Epstein et al. (1973), Balona & Stobie (1983), and Kilambi & Rahman (1993). Therefore, we compiled 1300 points in this final data set. The photometry presented by Kilambi & Rahman (1993) lists differential magnitudes referred to $HD\,64561$ star, with a magnitude of 8.20 ± 0.02.

The analysis of Period04 is presented in Figure 1. At the top is the periodogram of the original data and at the bottom, that of the residuals after the produced frequency was subtracted. Table 4 summarizes these results (set 3).

The results of utilizing Period04 gave as the first frequency $8.13830066\,c/d$ with an amplitude of 0.1409 and a phase of 0.1759. Evaluating the residuals we obtained the following numerical values: 16.254, 0.02898 and 0.4234 respectively. Fitting the data to these values gave as residuals a frequency of $0.0025\,c/d$ with an amplitude of 0.2881 and a phase of 0.1689. These values correspond to a period of $0.12287577\,d$ for the first frequency and to $0.061523\,d$. Given the numerical frequency values the results of Period04 gave f and $2f$, or a value close to it ($16.276\,c/d$). When a *phase vs. magnitude* plot

TABLE 3

LOG OF EFEMERIDES EQUATIONS

Reference	T_0	Period	A	β
Abhyankar59	2436601.8228	0.122972		
Anderson60	2436601.8228	0.122974		
Breger75	2442429.4582	0.12297443		
Rodriguez88	2436601.8226	0.12297431	1.9×10^{-12}	
Rodriguez90	2436601.8225	0.12297426	2.7×10^{-12}	
Yang92	2436601.8224	0.12297429	2.19×10^{-12}	
Burchi93	2447506.5815	0.122974448		
Kim94	2442429.4582	0.12297455		
Fu96	2436601.8203	0.12297446		4.6×10^{-13}
Fu2000	2436601.8203	0.122974463		3.50×10^{-13}
Hurta2007	2436601.82736	0.12297451		
Pongsak2007	2436601.8219	0.122974478		
PP time series	2436601.8186	0.122974518		
PP PDDM	2458559.7805	0.122974511		

$T = T_0 + PE + AE^2$ $\qquad$ $T = T_0 + PE + \frac{\beta}{2}E^2$

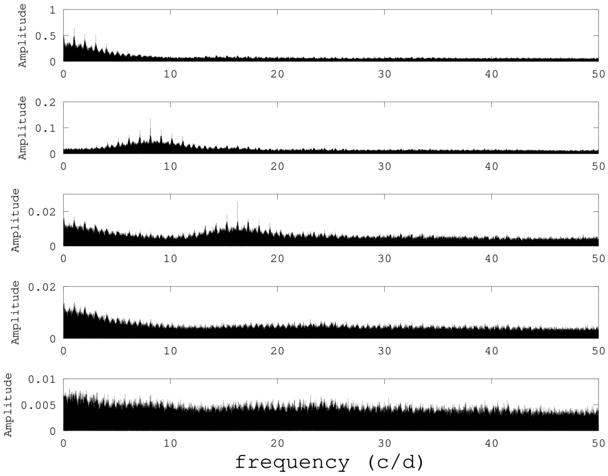

Fig. 1. The analysis of Period04 is presented. Descending, the periodogram of the window function and subsequently each maxima is presented. At the bottom, the residuals after the three frequencies have been subtracted. Emphasis should be made on the Y-axis scale.

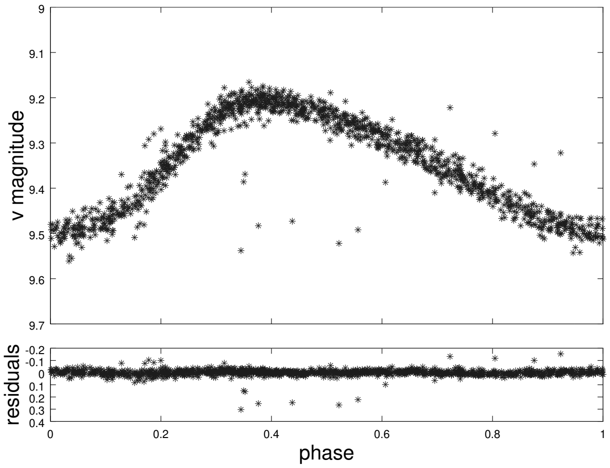

Fig. 2. Top: Phase diagram after the analysis of Period04 using frequency F1 set 3 of Table 4. Bottom: The residuals after the three frequencies have been subtracted.

was constructed, the phasing shows the correctness of the determined period (Figure 2).

3.2. *Period Determination Through* O−C *Differences Minimization (PDDM)*

We employed another method based on the concept of the minimization of the chord length linking all the points in the O−C diagram for different values of changing periods, looking for the best period which corresponds to the minimum chord length (see the case of KZ Hya, Peña et al. 2018).

A set of 94 times of maxima was considered for this analysis. Taking this into consideration, we used the determined period value in § 3.1 and the standard deviation of those consecutive differences to keep an interval span in which the period is located; those values are 0.1230 ± 0.0002 d. Maintaining a period precision of a billionth and taking the interval span period into consideration, 500,000 periods were used to perform this method. The T_0 used to calcu-

TABLE 4

OUTPUT OF PERIOD04 CALCULATED WITH THE V MAGNITUDE OF SEVERAL DATA SETS

Considered data	Nr.	Frequency	Amplitude	Phase	Residuals
Set 1	F1	8.13821236	0.145219814	0.2134	0.0281
	F2	16.2544156	0.0281107579	0.2715	0.0199
	F3	0.00249795	0.754162399	0.9004	0.01453
Set 2	F1	8.13830066	0.140946042	0.1759	0.036
	F2	16.245476	0.0289895308	0.4235	0.028
	F3	0.00256016	0.28816242	0.1689	0.229
Set 3	F1	8.13176594	0.140564142	0.0110	0.3364
	F2	16.2635352	0.0262466142	0.5018	0.0282
	F3	1.0705324	0.0121627692	0.4000	0.0266

Notes: Set 1: Rodriguez et al. (1988) and the present paper's $uvby-\beta$. Set 2: Adds *uvby* of Epstein and Abraham de Epstein (1973). Set 3: All data listed in Table 3.

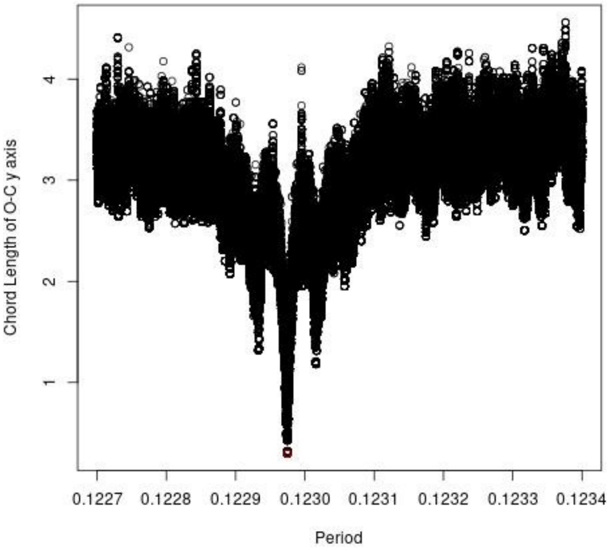

Fig. 3. Period determination through an O−C difference minimization.

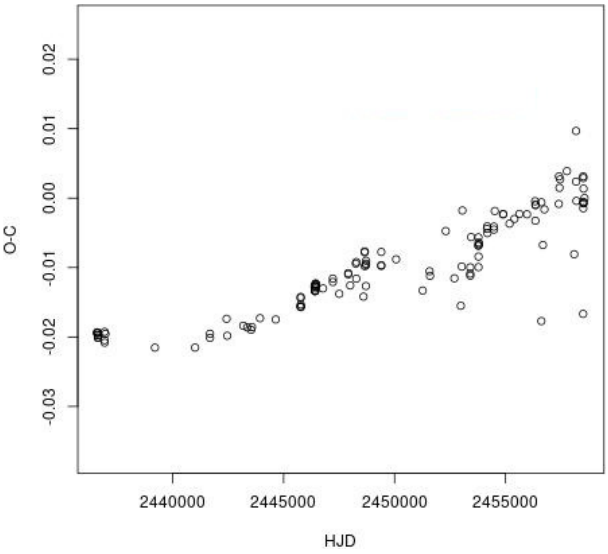

Fig. 4. O−C residuals after the adjustment to the obtained period.

late the O−C diagrams was 2458559.7805. Then the best period is the one with the smallest chord length and it is shown in Figure 3.

The ephemerides equation is then:

$$T_{max} = 2458559.7805 + 0.122974391 \times E.$$

As we can see in Figure 4, the plot shows a slope and marginally a sinusoidal behavior which can be related to the light-travel time effect (LTTE), revealing the possible presence of a second body. This visualization is later confirmed (Figure 5).

Then, we adjusted a sinusoidal function to the O−C diagram performing a fit using Levenberg-Marquardt Algorithm. We then used a combination of the chord length minimization and the non-linear fit for a sinusoidal function, taking the periods with the minimum chord length and, as a second criterion, the RMS error of the non-linear fitting.

The fitting equation for the O−C diagram is

$$O - C = Z + A\sin(2\pi(\Omega E + \Phi))$$

and the continuous line in Figure 6 shows the sinusoidal fit over the O−C diagram with a new period.

The sinusoidal function parameters are listed in Table 5. Accordingly, the period of the sinusoidal behavior is 10,247.8759 days or 28.1 years.

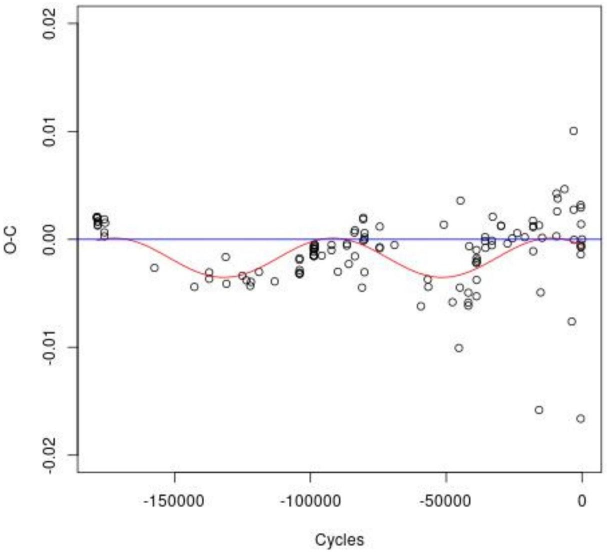

Fig. 5. O−C diagram with the sinusoidal function fit obtained by the PDDM method.

TABLE 5

EQUATION PARAMETERS FOR THE SINUSOIDAL FIT

	Value
Z	-1.709×10^{-3}
Ω	1.243×10^{-5}
A	-1.817×10^{-3}
Φ	8.905×10^{-1}
RSS residuals	1.186×10^{-3}

The ephemerides equation determined by this method is:

$$T_{max} = 2458559.7805 + 0.122974511 \times E.$$

The goodness of the model is determined by the RSS residuals listed in Table 3.

3.3. *O−C and Mass Determination*

Before calculating the coefficients of the ephemerides equation, we reviewed the existing literature related to AD CMi. Several authors have conducted studies on the O−C behavior of these particular objects and, in this preliminary stage, we took the existing updated list of times of maxima from the literature, plus the data that we acquired. We built the O−C diagram with the obtained period values from Period04 (set 3).

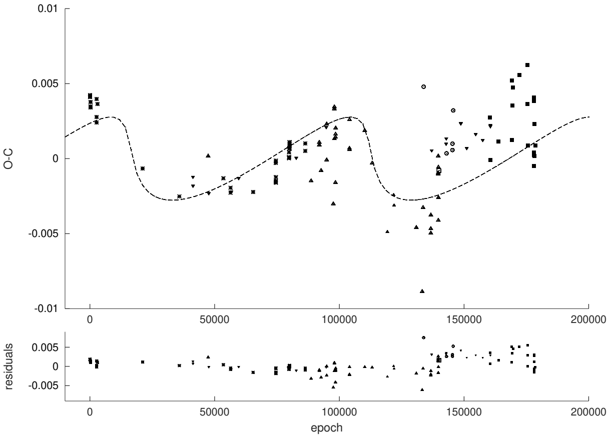

Fig. 6. Upper: O−C diagram and fit to the equation 4. Lower: residual of the fit.

The O−C diagram (Figure 6) shows a variation and a cyclic pattern with no quadratic component. Hence our solution is of the form:

$$\mathrm{O} - \mathrm{C} = T_0 + PE + \tau \tag{1}$$

where τ is the equation given by Irvin (1952)

$$\tau = \frac{K}{\sqrt{1-e^2\cos^2\omega}}\left[\frac{1-e^2}{1+e\cos\nu}\sin(\nu+\omega) + e\sin\omega\right], \tag{2}$$

$$K = \frac{1}{2}\left(\tau_{max} - \tau_{min}\right) = \frac{a\sin i\sqrt{1-e^2\cos^2\omega}}{c}. \tag{3}$$

The fit (Figure 6) was done by least squares with the Levenberg-Marquard algorithm, using the relation provided by Li & Qian (2010) in their equation 3:

$$\begin{aligned} A'\left[\frac{1-e^2}{1+e\cos\nu}\sin(\nu+\omega) + e\sin\omega\right] &= \\ A'\left[\sqrt{1-e^2}\sin E^*\cos\omega + \cos E^*\sin\omega\right]&, \end{aligned} \tag{4}$$

where $A' = \frac{A\sin i}{c}$ is the projection of the semi-major axis and c is the speed of light. Kepler's equation provides the relationship between the mean anomaly (M) and the anomalous eccentricity (E^*)

$$M = E^* - eE^*, \tag{5}$$

with

$$M = \frac{2\pi}{P_{orb}}\left(P \times E - T\right), \tag{6}$$

where e, ω, P_{orb}, T, P and E are: the eccentricity, the periastron longitude, the orbital period, the time

TABLE 6

ORBITAL PARAMETERS

Parameter	value
e	0.80
ω (deg)	170
$A \sin i$ (AU)	0.78
P_{orb} (yr)	32.33

of periastron passage, the period of pulsation of AD CMi ($P = 0.122974518$) and the epoch, respectively.

Since equation 5 is trascendental, the solutions for E^* are obtained through Bessel series

$$E^* = M + \sum_{n=1}^{\infty} \frac{2}{n} J_n(ne) \sin(nM), \tag{7}$$

where

$$J_n(ne) = \sum_{k=0}^{\infty} (-1)^k \frac{1}{k!\Gamma(n+k+1)} \left(\frac{ne}{2}\right)^{n+2k}. \tag{8}$$

The obtained orbital parameters with the fit are presented in Table 6 and have been used to build the plot of Figure 6.

The mass function is given by Fu et al. (2008) with $P_{orb} = 32.33$ (yr).

$$f(m) = \frac{(A \sin i)^3}{P_{orb}^2} = 0.0004525. \tag{9}$$

To calculate the mass of the companion, the solution of the following function was evaluated for m_2:

$$f(m) = \frac{(m_2 \sin i)^3}{(m_1 + m_2)^2}, \tag{10}$$

for a mass of $m_1 = 1.93 M_\odot$ obtained by McNamara (1997). A mass was calculated for several inclination angles as shown in Table 7, where the minimum mass that can be obtained for the companion star is $0.12 M_\odot$ (Figure 7).

Pongsak Khokhuntod et al. (2007) stated that the binary orbit has a period of 27.2 ± 0.5 years, with an eccentricity of 0.8 ± 0.1. However, since there is a big gap between the first 12 data points and the rest, and the bulk of the data spans only one cycle, this result should not be considered to be an accurate solution of the orbital parameters.

However, this is a plausible solution because it diminishes the dispersion, as can be see in the residuals in Figure 6. From the data shown in Table 7 and represented in Figure 7 we can consider the mass determination of the companion as a function of this angle since we cannot determine the inclination angle. If we do so, the probability that the companion is an M type star is 75%. The minimum mass is discarded because in our light curves there is no evidence of eclipses. Of course, more observations are needed to corroborate this result

TABLE 7

ORBITAL SEMI-MAJOR AXIS AND COMPANION'S MASS AS A FUNCTION OF ANGLE

$i(deg)$	A (AU)	$m_2(M_\odot)$
5	8.93975	2.30637
15	3.01040	0.54239
25	1.84362	0.31112
35	1.35840	0.22320
45	1.10188	0.17854
55	0.95116	0.15286
65	0.85969	0.13748
75	0.80663	0.12863
85	0.78212	0.12456

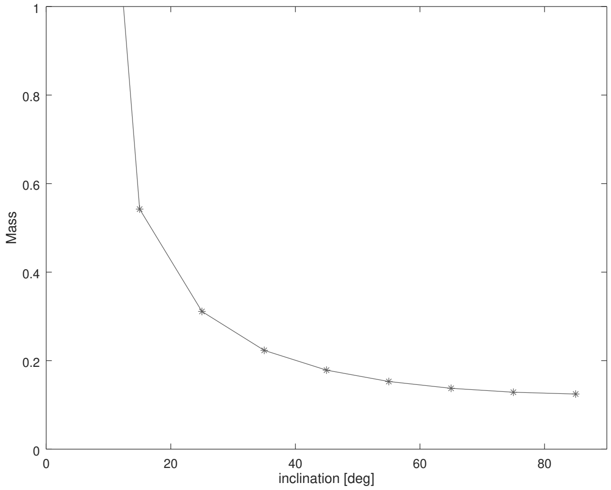

Fig. 7. Mass as a function of angle.

3.4. *Period Determination Conclusions*

Despite having been determined to be a variable star many years ago, the nature of this star has been variously described, from a binary star to a pulsating star, as well as an RR Lyrae and, finally a δ Scuti star. Since then, more information has been gathered but no period analysis was done. In the present paper, different approaches were utilized to determine the stability of the pulsation. With respect to its period determination and interpretation, it has varied from a periodic star to a quadratic fit which should be interpreted as a changing period.

The first method used to determine the periodic content utilized a time series analysis of different data sets. The first set is that of the V filter of the photometry of Rodriguez et al. (1988) and that of the V filter of the $uvby-\beta$ photometry of the present paper. The time span covered for all the data is 17084 d or 47 years, which in cycles is 138926. The second method we used was PDDM which gives a first approximation to the period of a binary system. Finally, in the third method we utilized O−C analyses via the LTTE.

The amazing result is that the $uvby-\beta$ photoelectric photometry adjusts to a phase both in magnitude and color indexes with the properly determined frequency.

In conclusion, there was a systematic improvement of the period, but not only that: Yang et al. (1992) postulated that the quadratic fit was much better, so the period was considered to be increasing at a rate of ($1.3 \pm 0.07 \times 10^{-8}$ days/year) although they could not fit the curve well with the observations from 1985 and 1986.

They suggested that more observations were urgently needed to clarify the true situation of the period variation. It is just now that these observations and analysis have been done with congruent results.

Data from other independent sources, such as the Kepler field or TESS, would have been very useful but, unfortunately, the star was not observed by either.

4. PHYSICAL PARAMETERS

Determination of the physical parameters of a star is possible if a comparison of theoretical models, such as those of Lester, Gray & Kurucz (1986), (hereinafter LGK86), is made. The $uvby-\beta$ unreddened color indexes are used because the $uvby-\beta$ photometric system has the advantage that reddening and unreddened colors can be determined from the photometry, the proper calibrations depending on the spectral type of the considered object. Nissen's (1988) procedure is applicable for A and F type stars and Shobbrook's (1984) for earlier spectral types. Hence, accurate determination of the spectral type is crucial.

According to Houk and Swift (1999) as reported in Simbad, AD CMi has a spectral type of F0IV/V. To corroborate this, we fixed its position in the unreddened color diagram $[m_1]$ vs. $[c_1]$ that was established for the open cluster Alpha Per (Peña et al. 2006) for which the unreddened color indexes were compared to the spectroscopically determined spectral types from several sources. In all cases the photometrically determined spectral types coincided with those determined spectroscopically, assuring us of the goodness of the method. We applied these calibrations to the $uvby-\beta$ photometry obtained (Table 8) for AD CMi corroborating first that the known spectral type of AD CMi was correct (Figure 8). To further check our results using $uvby-\beta$ photometry, we calculated the unreddened indexes $[m_1]$ $[c_1]$ from the other two sources, that of Epstein et al. (1973) and of Rodriguez et al. (1988). This latter reference reported the photometry of AD CMi differentially with respect to the star HD 63776 which was measured during two different years 2017 (once) and 2018 (three points) and obtained the following values for V, $(b-y)_1$, m_1, and c_1 (8.181 ± 0.010, 0.335 ± 0.003, 0.155 ± 0.005, 0.347 ± 0.006) respectively which immediately allowed us to calculate the $uvby-\beta$ values for AD CMi in the 1988 season. In all three cases with $uvby-\beta$ photometry, the location of AD CMi is in the same position, making its spectral type determination unquestionable. In view of this, the prescription to determine the reddening is that of Nissen (1988).

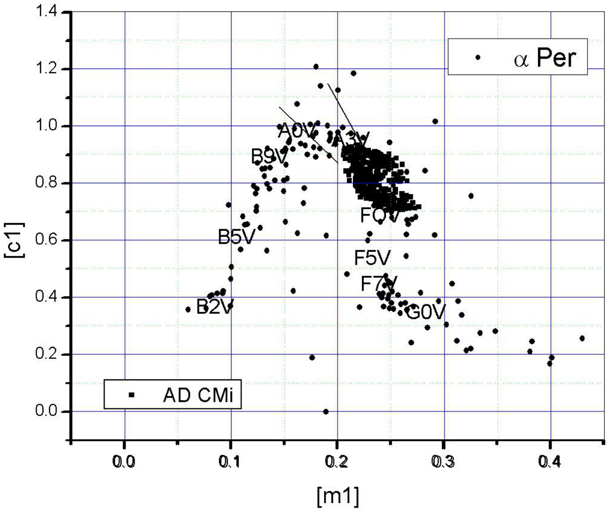

Fig. 8. Position of AD CMi in the unreddened indexes of Alpha Per from all sources with $uvby-\beta$ photometry.

We determined the unreddened indexes of AD CMi which were measured over three different seasons at SPM: 2013, 2016 and 2017. The spectral types we determined were A and F, not late enough to calculate the metallicity.

TABLE 8

AVERAGED MAGNITUDES, COLOR INDEXES AND β WITH THEIR UNCERTAINTIES IN PHASE BINS AS A FUNCTION OF PHASE

Phase	V	$(b-y)$	m_1	c_1	β	σ V	σ $(b-y)$	σ m_1	σ c_1	σ β	N
0.00	9.208	0.152	0.179	0.936	2.792	0.012	0.007	0.013	0.018	0.014	15
0.05	9.221	0.155	0.179	0.933	2.776	0.012	0.009	0.021	0.021	0.012	12
0.10	9.245	0.165	0.175	0.918	2.774	0.011	0.009	0.019	0.024	0.016	17
0.15	9.269	0.169	0.182	0.884	2.778	0.013	0.005	0.014	0.022	0.015	9
0.20	9.299	0.176	0.175	0.883	2.759	0.009	0.010	0.019	0.026	0.015	14
0.25	9.322	0.188	0.169	0.866	2.749	0.017	0.008	0.010	0.021	0.014	16
0.30	9.361	0.192	0.171	0.845	2.752	0.018	0.006	0.018	0.026	0.011	16
0.35	9.399	0.201	0.175	0.820	2.740	0.019	0.011	0.022	0.027	0.017	21
0.40	9.430	0.210	0.171	0.810	2.735	0.019	0.004	0.014	0.021	0.019	13
0.45	9.447	0.216	0.171	0.796	2.726	0.033	0.005	0.012	0.024	0.019	16
0.50	9.480	0.215	0.176	0.786	2.718	0.016	0.005	0.014	0.017	0.007	12
0.55	9.493	0.218	0.174	0.777	2.719	0.015	0.007	0.012	0.014	0.017	11
0.60	9.481	0.214	0.180	0.777	2.725	0.019	0.007	0.017	0.023	0.020	13
0.65	9.460	0.210	0.177	0.783	2.736	0.022	0.008	0.015	0.016	0.009	13
0.70	9.438	0.194	0.187	0.776	2.743	0.025	0.011	0.022	0.026	0.026	9
0.75	9.372	0.189	0.175	0.806	2.751	0.021	0.007	0.015	0.020	0.019	11
0.80	9.314	0.178	0.175	0.832	2.760	0.025	0.009	0.012	0.028	0.014	22
0.85	9.241	0.163	0.176	0.872	2.784	0.021	0.009	0.017	0.036	0.014	26
0.90	9.209	0.151	0.187	0.895	2.792	0.015	0.008	0.017	0.030	0.020	35
0.95	9.203	0.145	0.187	0.925	2.796	0.014	0.008	0.016	0.020	0.017	33

We relied on $uvby-\beta$ photometry again to determine the metallicity. We followed a prescription proposed by Meakes et al. (1991) for short period Population II Cepheids from $uvby-\beta$ photometry. LGK86 calculated grids for stellar atmospheres for G, F, A, B and O stars for different values of [Fe/H] (-3.0, -2.5, -2.0, -1.5,-1.0, -0.5, 0.0, 0.5 and 1.0) in a temperature range from 5500 up to 50 000 K. The surface gravities vary approximately from the main sequence values to the limit of the radiation pressure in 0.5 intervals in $\log g$.

We built a $(b-y)_0$ vs. m_0 diagram for all reported metallicities (Figure 9). A surface gravity of 4 which would be the case for a δ Scuti star, was assumed for all. Then we plotted the unreddened data points of AD CMi onto this diagram. As can be seen in Figure 9, this star has a metallicity close to a 0.0, solar composition. As a corollary, we determined the effective temperature in the range of variation (7500, 8200K). This is the metallicity chosen for the comparison with the LGK86 models.

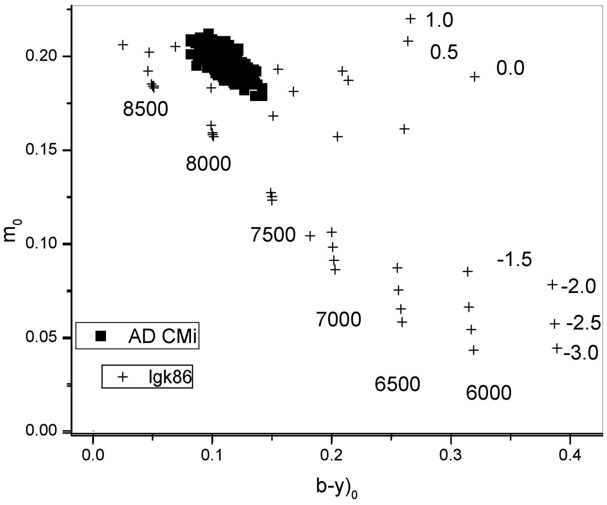

Fig. 9. Position of AD CMi for several metallicities for models with log g equal 4.0.

4.1. *Calibration Utilizing all the Available $uvby-\beta$ Observations*

To diminish the large scatter in the magnitude and photometric indexes, we averaged the entire set with available $uvby-\beta$ photometry: SPM over three seasons: 2013, 2016 and 2017 (the data will be sent upon request), along with those of Epstein et al. (1973) and of Rodriguez et al. (1988,) covering a time span of 12314 days, or 100135 cycles in phase bins of 0.05

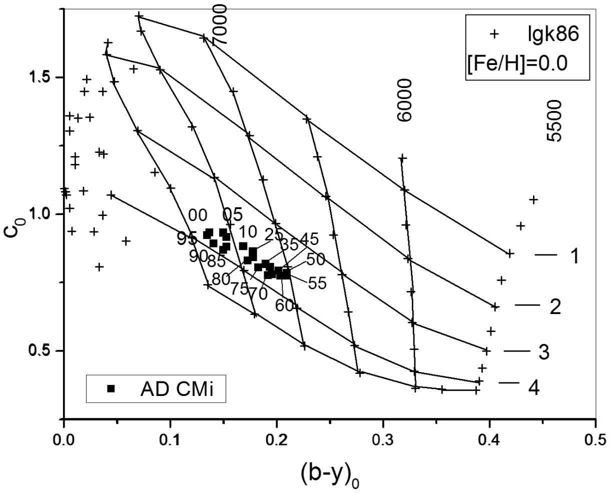

Fig. 10. Position of the unreddened color indexes of AD CMi in the theoretical models of LGK86. Phase is indicated in integers.

intervals, utilizing the epoch of Kilambi & Rahman (1993) and the frequency determined in this paper. Given the large number of points in the whole sample (509) we cleaned the data deleting points that were notoriously out of the trend. The reduced sample includes 333 data points.

The averaged points are presented in Table (8), (Column 1 phase; Column 2 magnitude; subsequent columns list $(b-y)$, m_1, c_1, next column presents values of Hβ). The standard deviation for each bin is presented in the subsequent columns. The last column presents the number of entries on average.

We applied Nissen's prescription to the averaged values and determined the reddening, the unreddened indexes $(b-y)_0$, m_0,c_0, as well as the absolute magnitude, and distance for each phase point. Mean values were calculated for $E(b-y)$ for two cases: (i) the whole data sample and (ii) in phase limits between 0.3 and 0.8, which is customary for pulsating stars to avoid the maximum. It gave, for the whole cycle, values of 0.010 ± 0.010; whereas for the previously mentioned phase limits we obtained, 0.010 ± 0.005. The distance, for the same limits, was 370 ± 38 pc and 369 ± 36 pc, respectively. The uncertainty is merely the standard deviation. The procedure to determine the physical parameters has been reported elsewhere (Peña et al., 2016). The metallicity values are the same in both cases [Fe/H] of 0.13 ± 0.013.

The physical parameters determination was performed by Rodriguez et al. (1988) through $uvby-\beta$ photoelectric photometry. We have utilized the same procedure (see for example Peña & Martinez; 2014; Peña & Sareyan, 2006).

They derived an $E(b\text{-}y)$ of 0.017 ± 0.007 and $T_e(K)$ of 7550 ± 190 and $\log g$ (dex) of 3.83 ± 0.06. The values we obtained are presented below and the results are equal, since the same $uvby-\beta$ photometry was considered and the same analysis was done, though thirty years later with an extended time basis. A comparison between the photometric, the unreddened indexes c_0 and $(b-y)_0$ obtained for the star with the models allowed us to determine the effective temperature T_e and the surface gravity $\log g$ (Figure 10). Table 9 lists these values. Column 1 shows the phase, Columns 2 the reddening; Columns 3 to 5 the unreddened indexes and β. Figure 10 shows the position of the unreddened color indexes of AD CMi in the theoretical models of LGK86. Phase is indicated as integers. Subsequent columns present the unreddened magnitude, the absolute magnitude, the distance modulus, the distance in parsecs and the effective temperature from the LGK86 plot. Column 12 lists the effective temperature obtained from the theoretical relation reported by Rodriguez (1989) based on a relation from Petersen & Jorgensen (1972, hereinafter P&J72) $Te = 6850 + 1250 \times (\beta - 2.684)/0.144$ for each value and averaged in the corresponding phase bin. In the final column the surface gravity $\log g$ from the plot is presented.

4.2. *Physical Parameters. Conclusions*

One of the major contributions of the present paper is the analysis of $uvby-\beta$ photoelectric photometry with an extended time basis. From the $uvby-\beta$ photometry we have obtained basically the same results as Rodriguez et al. (1988) but with a time span extended thirty years. This has proven the stability of the star.

5. CONCLUSIONS

New observations in $uvby-\beta$ and CCD photometry were carried out at the San Pedro Mártir and Tonantzintla observatories, respectively, on the δ Scuti star AD CMi.

With respect to the study of the period stability of the star, we have corroborated what Yang et al. (1992) postulated: that a quadratic fit was much better, so that the period was considered to be increasing at a rate of $(1.3 \pm 0.07) \times 10^{-8}$ days/year, although they could not fit the curve well with the observations in 1985 and 1986. We have accomplished this fit with our results.

TABLE 9

$E(B-Y)$, COLOR INDEXES, DISTANCE, EFFECTIVE TEMPERATURE AND LOG G IN EACH BIN AS A FUNCTION OF PHASE

Phase	$E(b-y)$	$(b-y)_0$	m_0	c_0	β	V	Mv	DM	Dst pc	Te LGK86	Te P&J72	$\log g$
0.01	0.015	0.137	0.184	0.933	2.792	9.14	1.24	7.9	381	7700	7788	3.75
0.05	0.005	0.150	0.181	0.932	2.776	9.20	1.02	8.2	432	7600	7649	3.6
0.10	0.012	0.153	0.179	0.916	2.774	9.19	1.13	8.1	410	7600	7631	3.7
0.15	0.016	0.153	0.187	0.881	2.778	9.20	1.49	7.7	348	7600	7666	3.8
0.20	0.007	0.169	0.177	0.882	2.759	9.27	1.22	8.1	407	7400	7501	3.6
0.25	0.010	0.178	0.172	0.864	2.749	9.28	1.23	8.1	407	7300	7414	3.6
0.30	0.014	0.178	0.175	0.842	2.752	9.30	1.46	7.8	369	7400	7440	3.6
0.35	0.011	0.190	0.178	0.818	2.740	9.35	1.52	7.8	368	7200	7336	3.6
0.40	0.016	0.194	0.176	0.807	2.735	9.36	1.49	7.9	375	7200	7293	3.6
0.45	0.014	0.202	0.175	0.793	2.726	9.38	1.41	8.0	394	7200	7215	3.5
0.50	0.005	0.210	0.177	0.785	2.718	9.46	1.30	8.2	429	7100	7145	3.5
0.55	0.008	0.210	0.177	0.775	2.719	9.46	1.41	8.1	407	7100	7154	3.5
0.60	0.010	0.204	0.183	0.775	2.725	9.44	1.55	7.9	377	7100	7206	3.5
0.65	0.014	0.196	0.181	0.780	2.736	9.40	1.76	7.6	338	7200	7301	3.6
0.70	0.002	0.192	0.188	0.776	2.743	9.43	1.96	7.5	312	7200	7362	3.8
0.75	0.006	0.183	0.177	0.805	2.751	9.34	1.80	7.5	323	7300	7432	3.8
0.80	0.005	0.173	0.177	0.831	2.760	9.29	1.69	7.6	331	7400	7510	3.8
0.85	0.013	0.150	0.180	0.869	2.784	9.18	1.69	7.5	315	7700	7718	3.9
0.90	0.010	0.141	0.190	0.893	2.792	9.17	1.61	7.6	325	7700	7788	3.9
0.95	0.010	0.135	0.190	0.923	2.796	9.16	1.40	7.8	357	7800	7822	3.8
Average	0.010							7.8	370	7390	7468	3.7
σ	0.010							0.2	38	234	220	0.8
Average	0.010							7.8	369	7200	7288	3.6
σ	0.005							0.2	37	106	94	0.1

These new $uvby-\beta$ data, combined with the previous data from Epstein et al. (1973) and Rodriguez et el. (1988), comprising a time span of 133,388 days served to determine the reddening as well as the unreddened indexes utilizing Nissen's (1988) calibrations. Metallicity values were calculated for only two points when the star passed through spectral class F, and these were also inferred from $uvby-\beta$ photoelectric photometry plotting the unreddened values of $(b-y)_0$ and m_0 on the grids determined from the models of LGK86 for different metallicities for values of surface gravity equal 4. These comparisons served to discriminate among the theoretical models that have been developed by LGK86 for the most adequate metallicity value. Once this was established, the proper model of LGK86 provided the physical characteristics of the star, $\log T_e$ and the surface gravity log g. The effective temperature was also calculated through the theoretical relation (P&J72). The numerical values obtained by both methods gave similar results within the error bars, and gave a good idea of the behavior of the star.

In the present study we have demonstrated that AD CMi is pulsating with one stable varying period whose O−C residuals show a sinusoidal pattern compatible with a light-travel time effect. It is interesting to mention that in the excellent discussion of Templeton (2005), he states that: "In all cases except SZ Lyn, the period of the purported binarity is close to that of the duration of the (O−C) measurements, making it difficult to prove that the signal is truly sinusoidal. A sinusoidal interpretation is only reliable when multiple cycles are recorded, as in SZ Lyn. While the binary hypothesis is certainly possible in most of these cases, conclusive proof will not be available for years or even decades to come."

We would like to thank the staff of the OAN at SPM and Tonantzintla for their assistance in securing the observations. Thanks to J. P. Ñauñay, of the Yachay Tech. University, Ecuador for obtaining some times of maximum light. This work was partially supported by the OAD of the IAU (ESAOBEL), PAPIIT IN106615, IG100620 and PAPIME PE113016. Proofreading was done by J. Miller. C. Guzmán, and F. Ruiz assisted us in the computing. Thanks to B. Juárez for the bibliographic help. All the students thank the IA for allotting the telescope time. Special thanks to A. Pani for the observations and discussions. We acknowledge the comments and suggestions of an anonymous referee that improved this paper. We have made use of the Simbad databases operated at CDS, Strasbourg, France; NASA ADS Astronomy Query Form.

REFERENCES

Abhyankar, K. D. 1959, ApJ, 130, 834
Anderson, L. R. & McNamara, D. H. 1960, PASP, 72, 506
Antoci, V., Cunha, M. S., Bowman, D. M., et al. 2019, MNRAS, 490, 4040
Balona, L. A. & Stobie, R. S. 1983, SAAOC, 7, 19
Barceló Forteza, S., Moya, A., Barrado, D., et al. 2020, A&A, 638, 59
Bowman, D. M. & Kurtz, D. W. 2018, MNRAS, 476, 3169
Collins, K. A., Kielopf, J. F., & Stassun, K. G. 2012, AstroImage: Processing and Photometric Extraction for Ultra-precise Astronomical Light Curves, arXiv:1601.02622
Dean, J. F., Cousins, A. W. J., Bywater, R. A., & Warren, P. R. 1977, MmRAS, 83, 69
Eggen, O. J. 1957, AJ, 62, 14
Epstein, I. & de Epstein, A. E. A. 1973, AJ, 78, 83
Garrido, R. & Poretti, E. 2004, ASPC, 310, 560
Guzik, J. A., Garcia, J. A., & Jackiewicz, J. 2019, FrASS, 6, 40
Handler, G., Kurta, D. W., Rappaport, S. A., et al. 2020, NatAs, 4, 684
Hoffmeister, C. 1934, AN, 253, 195
Houk, N. & Swift, C. 1999, MSS, 5
Jayasinghe, T., Stanek, K. Z., Kochanek, C. S., et al. 2020, MNRAS, 493, 4186
Khokhuntod, P., Fu, J.-N., Boonyatar, Ch., et al. 2007, ChJAA, 7, 421
Kilambi, G. C. & Rahman, A. 1993, BASI, 21, 47
Le Contel, J. M., Valtier, J. C., Sareyan, J. P., Baglin, A., & Zribi, G. 1974, A&AS, 15, 115
Lenz, P. & Breger, M. 2005, CoAst, 146, 53
Lester, J. B., Gray, R. O., & Kurucz, R. I. 1986, ApJ, 61, 509
McNamara, D. 1997, PASP, 109, 1221
Meakes, M., Wallerstein, G., & Opalko, J. F. 1991, AJ, 101, 1795
Millis, R. L. 1966, IBVS, 137
_________. 1968, An Investigation of the Delta Scuti Stars. PhD. Thesis. The University of Wisconsin-Madison
Murphy, S. J., Hey, D., Van Reeth, T., & Bedding, T. R. 2019, MNRAS, 485, 2380
Nissen, P. E. 1988, A&A, 199, 146
Olsen, E. H. 1983, A&AS, 54, 55
Peña, J. H. & Sareyan, J.-P. 2006, RMxAA, 42, 179
Peña, J. H., Sareyan, J.-P., Cervantes-Sodi, B., et al. 2007, RMxAA, 43, 217
Peña, J. H. & Martínez, A. 2014, RMxAA, 50, 119
Peña, J. H., Piña D. S., Rentería, A., et al. 2018, RMxAA, 54, 85
Peña, J. H., Calderón, J., & Piña, D. S. 2019, RMxAA, 55, 203
Petersen, J. O. & Jørgensen, H. E. 1972, A&A, 17, 367
Pojmanski, G., Pilecki, B., & Szczygiel, D. 2005, AcA, 55, 275
Rodríguez, E., Rolland, A., & López de Coca, P. 1988, RMxAA, 16, 7
_________. 1990, IBVS, 3427, 1
Rodríguez, E., López-Gonzalez, M. J., & López de Coca, P. 2000, ASPC, 210, 499
Shobbrook, R. R. 1984, MNRAS, 211, 659
Templeton, M. R. 2005, JAVSO, 34, 1
Zessewitch, B. P. 1950, Astro. Circ. USSR, 100, 18
Ziaali, E., Bedding, T. R., Murphy, S. J., Van Reeth, T., & Hey, D. R. 2019, MNRAS, 486, 4348

J. M. Donaire, R. R. Muñoz, and T. Benadalid: Universidad Mayor de San Andrés, La Paz, Bolivia.
H. Huepa, J. H. Peña, and A. Rentería: Observatorio Astronómico Nacional, Tonantzintla Puebla, México. J. Briones, J. L. Carrillo, C. Castro, B. Chávez, C. García, J. Guillén, S. B. Juárez, F. Martinez, D. Navez, E. D. Orozco, J. H. Peña, D. S. Piña, H. Posadas, A. Rentería, M. Romero, I. Soberanes, A. A. Soni, C. Villarreal, and A. L. Zuñiga: Facultad de Ciencias, Universidad Nacional Autónoma de México.
J. D. Paredes: Universidad Central de Venezuela, Venezuela.
J. H. Peña, D. S. Piña, A. Rentería, and A. A. Soni: Instituto de Astronomía, Universidad Nacional Autónoma de México, Apdo. Postal 70-264, Cd. de México (jhpena@astro.unam.mx).

Revista Mexicana de Astronomía y Astrofísica, **57**, 335–349 (2021)

https://doi.org/10.22201/ia.01851101p.2021.57.02.07

THE CHALLENGES OF MODELLING THE ACTIVITIES OCCURRING ON ECLIPSING BINARIES V1130 CYG AND V461 LYR

E. Yoldaş and H. A. Dal

Department of Astronomy and Space Sciences, University of Ege, Bornova, 35100 İzmir, Turkey.

Received July 19 2020; accepted May 6 2021

ABSTRACT

We present the findings for the magnetic activities seen on V1130 Cyg and V461 Lyr. In the case of V1130 Cyg, the secondary component's temperature was found to be 3891±50 K, while the mass ratio was computed as 0.689±0.001, and the orbital inclination as 90°.00±0°.01. The temperature of V461 Lyr's secondary component was found to be 4206±50 K, and the mass ratio was calculated as 0.999±0.001 with 89°.58±0°.01 of orbital inclination. The analyses exhibit the effects of the stellar spots on the light curves. The models indicate that there are two types of flares in the case of V1130 Cyg, and three types of flares for V461 Lyr. The Plateau parameters have been found as 2.1997 s for Group 1 and 1.0068 s for Group 2 in the case of V1130 Lyr. They have been computed as 1.9015 s for Group 1, 2.7943 s for Group 2, and 3.4324 s for Group 3 of V461 Lyr.

RESUMEN

Presentamos algunos hallazgos sobre la actividad magnética en V1130 Cyg y V461 Lyr. Para V1130 Cyg encontramos que la temperatura de la componente secundaria es 3891±50 K, el cociente de masas es 0.689±0.001 y la inclinación orbital es 90°.00±0°.01. Determinamos que la temperatura de la secundaria de V461 Lyr es 4206±50 K, el cociente de masas es 0.999±0.001 y la inclinación orbital es 89°.58±0°.01. Los análisis muestran los efectos de las manchas estelares en las curvas de luz. Los modelos indican que hay dos tipos de ráfagas en V1130 Cyg, y tres tipos de ráfagas en V461 Lyr. Los parámetros del "plateau" que encontramos son 2.1997 s para el Grupo 1 y 1.0068 s para el Grupo 2 en el caso de V1130 Lyr, así como 1.9015 s para el Grupo 1, 2.7943 s para el Grupo 2, y 3.4324 s para el Grupo 3 de V461 Lyr.

Key Words: methods: data analysis — stars: binaries: eclipsing — stars: flare — stars: individual: V1130 Cyg, V461 Lyr — techniques: photometric

1. INTRODUCTION

The number of cool spots observed on the solar photosphere fluctuates for the decades of a cycle period. Schwabe (1844) stated the average cycle length as about 11 years. The patterns based on the magnetic field are observed in the case of the late-type stars as well as the solar case (Kron 1950). In the case of the solar analogues, some long-term variations have been discovered from the long-term observations of the Ca II H (λ3968 Å) and K (λ3933 Å) emission lines, as it is in the solar case (Wilson 1978). Considering the solar-stellar relations found by comprehensive studies, the examination of long-term activity cycles leads us to understand how their dynamos work (Baliunas et al. 1995; Rempel 2008).

Flare activity was detected in the sun by Carrington (1859) and Hodgson (1859) for the first time. Flare activity on WX UMa was reported in 1940 (van Maanen 1940), which may be the earliest known stellar flare. The stars exhibiting flare activity are now called UV Ceti type stars (or flare stars). UV Ceti type stars are young stars that have just come to the main sequence. Numerous red dwarf stars in both open clusters and association exhibit flare activity (Mirzoian 1990; Pigatto 1990). A decrease in the number of the flare stars is observed with the increase in the age of the cluster, as an expected result of the Skumanich Law (Skumanich 1972; Marcy & Chen 1992; Pettersen 1991; Stauffer 1991).

Activity level rises with increasing rotational speed, which causes mass loss to increase. The studies indicate that the solar mass loss is about $2 \times 10^{-14} M_{\odot}$ per year (Gershberg 2005). In the case of UV Ceti stars, the mass loss reaches about $10^{-10} M_{\odot}$ per year due to the flare activity. High-level mass losses of these stars explain how they lose most of their angular momentum at the beginning of the main sequence stage (Marcy & Chen 1992). Apart from the mass loss, there are also remarkable energy differences between the solar and stellar flares. The energy level can easily reach from 10^{30} erg to 10^{32} erg during the solar two-ribbon flares (Gershberg 2005; Benz 2008; Emslie et al. 2012). In the case of RS CVn binaries, it can be about 10^{31} erg (Haisch et al. 1991). However, Mathioudakis et al. (1992) found that the flare energies vary in the range of 1-180×10^{33} erg for II Peg, which is an RS CVn star. On the other hand, long-term observations demonstrated that the energy level can easily reach from 10^{28} erg to 10^{34} erg for dMe stars (Gershberg 2005), and also 10^{36} erg in the case of the magnetically active members of a young open cluster like Pleiades (Gershberg & Shakhovskaia 1983). The flare energy values are different from those measured in the solar case. Despite all available situations, the flare events observed in these stars are generally explained by the same physical mechanism as with the solar flares.

To understand the whole flare process in detail, one should compare the flares detected from different types of stars. In this respect, there are several studies in the literature. Some of them have been concentrated on the flare frequencies. For example, Ishida et al. (1991) have described two different flare frequencies as the flare frequencies N_1, which is the flare number per hour, and N_2, which is flare energy emitted to space per second. Leto et al. (1997) have demonstrated that the flare frequency of EV Lac varies from one observing season to the next. However, some other studies have concentrated on the flare energy level or limits. In the early 1970s, Gershberg (1972) described the flare energy spectrum, which depends on the distribution of flare cumulative frequency. The distribution of flare cumulative frequency is almost the most studied examination technique in the literature, even today. Indeed, one can see it in several studies such as Ramsay & Doyle (2015); Davenport (2016); Maehara (2017); Davenport et al. (2019); Tu et al. (2020). Another study has recently been conducted by Dal & Evren (2010, 2011), developing a model based on fitting the distributions of flare equivalent duration versus flare total times in the logarithmic scale, which is called the One Phase Exponential Association (hereafter OPEA) model.

In this study, the results found for the flare and spot activities of V1130 Cyg (KIC 4660977) and V461 Lyr (KIC 6205460) will be presented, which depend on the findings of their OPEA Models with model parameters and stellar spot migrations. V1130 Cyg was classified as a variable star by Miller (1966) for the first time. The V-band brightness has been given as $12^{m}.560$, while infrared JHK have been given as $11^{m}.124$, $10^{m}.764$, $10^{m}.657$, respectively (Zacharias et al. 2005). In the literature, the spectral types of its components have been given as F7 + K0 IV with orbital period (P) of 0.5625613 day (Svechnikov & Kuznetsova 1990). The temperatures of the components have been computed as $T_1 = 5587$ K and $T_2 = 6621$ K (Armstrong et al. 2014). According to Mathur et al. (2017), the temperature of target is $T_{eff} = 5674K$ with $\log\ g = 3.942$ cm/s^2. They estimated the radius and mass of the target as $1.754 R_{\odot}$ and $0.984 M_{\odot}$ at a distance of 512.130 pc. V461 Lyr was discovered by Bonnie Buratti in 1973 and the system was classified as a variable star by Dexter (1974). The V-band and infrared JHK brightnesses have been given as $13^{m}.190$, $10^{m}.952$, $10^{m}.392$, $10^{m}.267$ in the NOMAD catalogue, respectively (Zacharias et al. 2005). The orbital period (P) of the system, which has a spectral type G9 (Qian et al. 2018), is 3.722831 days (Watson et al. 2006). Mathur et al. (2017) give physical parameters of the target as $T_{eff} = 5425$ K, $\log\ g = 3.678$ cm/s^2, $R = 2.592 R_{\odot}$, $M = 1.166 M_{\odot}$ at a distance of 656.895 pc.

2. DATA AND ANALYSES

The Kepler Mission was devoted to find exo-planets. Indeed, more than 150000 targets were observed (Borucki et al. 2010; Koch et al. 2010; Caldwell et al. 2010). These observations are the most sensitive observations ever made (Jenkins et al. 2010a,b). In the mission, many variables such as eclipsing binaries, chromospheric active or pulsating stars, have been discovered apart from numerous exo-planets (Slawson et al. 2011; Matijevič et al. 2012). There are several spotted and flaring targets among newly discovered eclipsing binaries (Balona 2015). The targets' data analysed in this study have been taken from the Kepler Database (Slawson et al. 2011; Matijevič et al. 2012). From the database, all available de-trended short cadence (hereafter SC) and de-trended

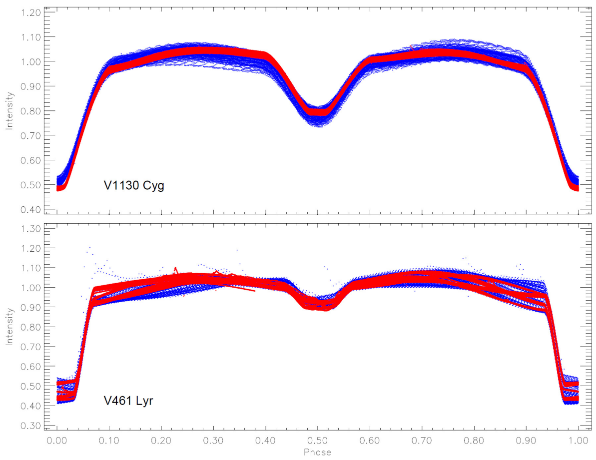

Fig. 1. The light curves of the system are presented. The light curve of V1130 Cyg is shown in the upper panel, that of V461 Lyr in the bottom panel. In both panels, the LC data light curve is plotted as filled blue circles, the SC data light curve as filled red circles. The color figure can be viewed online.

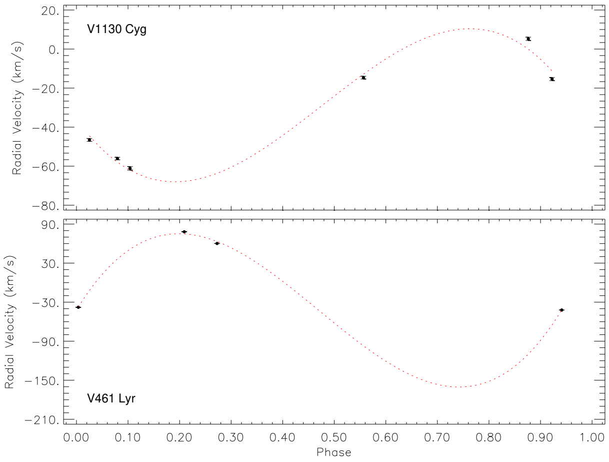

Fig. 2. The radial velocity curves obtained by the Sloan 2.5 m Telescope (Gunn et al. 2006; Ahumada et al. 2019) for both targets. In panels, observations are represented by filled circles with their error bars, while the estimated curves are shown with red-dotted lines. The color figure can be viewed online.

long cadence (hereafter LC) data have been taken. The light curves of the targets are shown in Figure 1 for both SC and LC data in different colors.

Several spectra have been taken for both targets at the same time, and their data have been provided in the Sloan Digital Sky Surveys (SDSS) archive (Majewski et al. 2017). Both targets have been observed in Apache Point Observatory (APO), using the Sloan 2.5 m Telescope (Gunn et al. 2006). Six spectra have been taken for V1130 Cyg, and four spectra for V461 Lyr. Their data have been released in the database of SDSS IV APOGEE 2 Data Release 16 (DR16) (Ahumada et al. 2019). Although available spectral data do not cover all phases of the targets sufficiently to calculate the radial velocity curve amplitude, considering their orbital periods, the available data suffice to indicate that both targets should be binary stars as it is seen from Figure 2. Using a Python script, depending on the method in the Spectroscopic Binary Solver software (Johnson 2004), we have tried to estimate possible radial velocity curves for the targets over the available data to just make an impression, depending on the fixed orbital periods. In the figure, the observations have been shown by filled circles with their error bars, while the estimated radial velocities are presented by red-dotted lines. According to these estimates, the semi-amplitude (K1) of radial velocity has been found to be about 39.19 km/s^{-1} for V1130 Cyg, and about 117.79 km/s^{-1} for V461 Lyr. According to these results, the radial velocity curves of both targets should have been obtained over just one component.

In the study, we have used the Pre-search Data Conditioning Simple Aperture Photometry (PDC-SAP) data (Smith et al. 2012; Stumpe et al. 2012) in both SC and LC format for the period $(O-C)$ analyses. For the light curve analyses, we have used LC data for both systems. In the analyses of stellar spot activity, we have used both SC and LC data in a suitable format for V1130 Cyg, while we have used LC data for V461 Lyr. The estimations over the available spectra of the targets have been considered for the light curve analyses, and also for the discussion of the nature of the systems in the last section.

2.1. *Orbital Period Variation*

The minima times have been computed from the public SC and LC data taken from the Kepler Database (Slawson et al. 2011; Matijevič et al. 2012) without applying any correction to the observations. In the case of V1130 Cyg, 3249 minima times have been computed from the LC data, while 220 minima times have been obtained from the SC data. In the case of V461 Lyr, 716 minima times have been computed from LC data, and 75 minima from the SC data. We have computed the $(O-C)_I$ differences, between the observed minima times and the computed ones. We have obtained the $(O-C)_I$ differences for all minima times for both systems. From

TABLE 1

ALL THE MINIMA TIMES AND THEIR RESIDUALS FOR V1130 CYG AND V461 LYR

HJD (+24 00000)	E	Type	$(O-CI)$ (day)	$(O-CII)$ (day)
V1130 Cyg				
54953.77285	-0.50	II	0.0025	0.00263
54954.05240	0.00	I	0.0007	0.00089
54954.33091	0.50	II	-0.0020	-0.00187
54954.61010	1.00	I	-0.0041	-0.00397
54954.89837	1.50	II	0.0029	0.00303
54955.17831	2.00	I	0.0015	0.00169
54955.45665	2.50	II	-0.0014	-0.00126
54955.73540	3.00	I	-0.0039	-0.00378
54956.02374	3.50	II	0.0031	0.00328
54956.30492	4.00	I	0.0030	0.00317
V461 Lyr				
54956.46324	0.00	I	0.0080	-0.01903
54958.31067	0.50	II	-0.0060	-0.03299
54962.03404	1.50	II	-0.0054	-0.03241
54965.75160	2.50	II	-0.0107	-0.03764
54969.47630	3.50	II	-0.0088	-0.03573
54973.19484	4.50	II	-0.0131	-0.03998
54976.91960	5.50	II	-0.0112	-0.03802
54980.64768	6.50	II	-0.0060	-0.03272
54984.36835	7.50	II	-0.0081	-0.03484
54988.08618	8.50	II	-0.0131	-0.03981

the data sets of $(O-C)_I$ differences, we have extracted all the minima with large error, due to the flare frequencies. We recognized that the purified $(O-C)_I$ differences exhibited a linear trend. To remove these trends, we applied a linear corrections to all minima time residuals using equation (1) for V1130 Cyg and equation (2) for V461 Lyr:

$$JD\ (Hel.) = 24\ 54954.051501(1) + 0^d.562560(1) \times E, \tag{1}$$

$$JD(Hel.) = 24\ 54956.482260(6) + 3^d.722791(3) \times E. \tag{2}$$

After these linear corrections, we have obtained $(O-C)_{II}$ residuals, taking the differences between linear fits and the $(O-C)_I$ values. All obtained minima times, their $(O-C)_I$ differences and $(O-C)_{II}$ residuals are tabulated in Table 1. When the $(O-C)_{II}$ residuals are plotted versus time, it is seen that the residuals exhibit some systematic variation with time, as shown in Figure 3. In the case of V1130 Cyg, the stellar spot activity occurring on the active component leads the $(O-C)_{II}$ residuals of both the primary and secondary minima to vary synchronously, but in opposite directions, due to the effects presented by Tran et al. (2013) and Balaji et al. (2015). However, it can be seen from the bottom panel of Figure 3 that the secondary minima times are much more affected by spot activity due to their shallower amplitude.

2.2. *Light Curve Analyses*

To detect the absolute light variation of each flare, all the variations such as geometrical effects and sinusoidal variation at out-of-eclipses need to be modelled. To this end, we firstly conducted light curve analyses for both systems. As a first step, we removed the flares from the total light variations, as well as the scattering observations caused by technical problems. Then, for both systems, we chose several consecutive cycles, that were least affected by the spot activity. Lastly, we computed averaged light curves to obtain the data set for the analyses, using the data of these cycles.

We have used the PHOEBE V.0.32 software (Prša & Zwitter 2005), which depends on the Wilson-Devinney Code (Wilson & Devinney 1971; Wilson 1990), to analyse the light curve. We have tried to model the light curve separately by using three modes, such as Mode 2 (detached system), Mode 4 (semi-detached system with the primary component filling its Roche-Lobe), and Mode 5 (semi-detached system with the secondary component filling its Roche-Lobe). Astrophysically acceptable solutions have been found in the analyses with Mode 2 for both systems.

In the light curve analyses, the sinusoidal variations seen at out-of-eclipses have been modelled by two cool spots for the chosen data set. In the analyses, although the third body parameter has been taken as a free parameter, it has been seen that there is no excess of total light due to any third body. The parameters resulting from the light curve analyses are listed in Table 2, while the solutions are shown with the averaged observing data in Figure 4.

2.3. *Rotational Modulation and Stellar Spot Activity*

In the systems' light curves, careful examination of the light variations at out-of-eclipses indicates some wave-like sinusoidal variations. Considering both the surface temperature of the components and available flare activities, these wave-like sinusoidal variations must be a stellar rotational modulation caused by the stellar cool spots. It is seen that the minima times of the sinusoidal variations vary when these

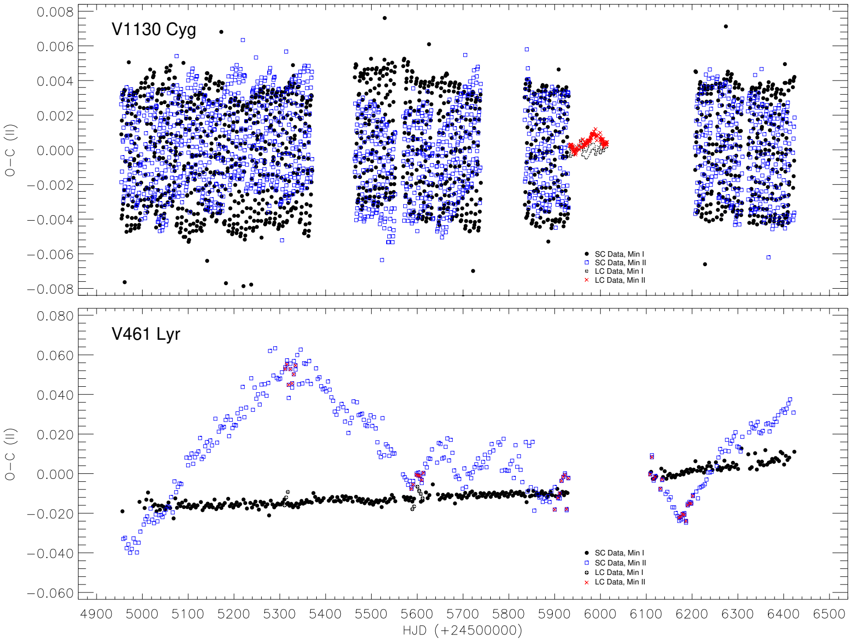

Fig. 3. The variations of $(O-CII)$ residuals obtained by the linear corrections are shown for V1130 Cyg and V461 Lyr, analysing their LC and SC data. The meaning of the symbols is shown in each panel. The color figure can be viewed online.

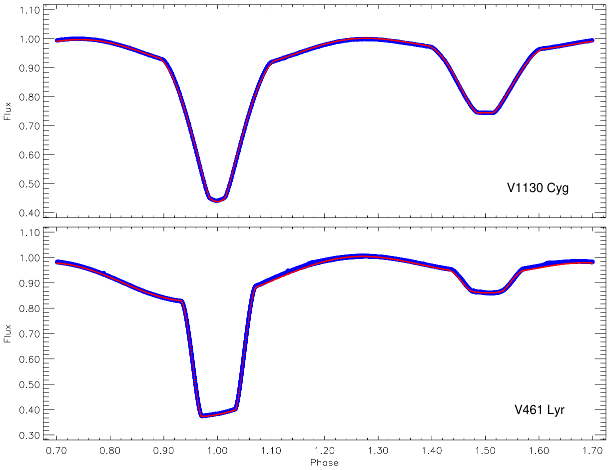

Fig. 4. The observed light curves and the synthetic light curve solutions are plotted versus orbital period phases for both V1130 Cyg (upper panel) and V461 Lyr (bottom panel). In the panels, the filled blue circles represent the observations for both systems, while the red lines represent the synthetic curves. The color figure can be viewed online.

variations are examined cycle by cycle. This indicates that the active regions exhibit rapid migration on the components' surfaces. Since it is not possible to model the whole light curves in one step, the data were separated into subsets, considering the shape

TABLE 2

SOLUTION PARAMETERS FOR V1130 CYG AND V461 LYR*

Parameter	V1130 Cyg	V461 Lyr
q	0.685±0.001	0.999±0.001
$i(^{\circ})$	90.00±0.01	89.58±0.01
$T_1(K)$	6530 (fixed)	5774 (fixed)
$T_2(K)$	3891±50	4206±50
Ω_1	0.357±0.003	0.970±0.003
Ω_2	0.376±0.003	0.428±0.003
L_1/L_T	0.811±0.002	0.455±0.002
L_2/L_T	0.188±0.002	0.546±0.002
g_1, g_2	0.32, 0.32 (fixed)	0.32, 0.32 (fixed)
A_1, A_2	0.50, 0.50 (fixed)	0.50, 0.50 (fixed)
$x_{1,bol}, x_{2,bol}$	0.64, 0.70 (fixed)	0.64, 0.664 (fixed)
x_1, x_2	0.616, 0.616 (fixed)	0.758, 0.751 (fixed)
$< r_1 >$	0.3628±0.0012	0.1551±0.0002
$< r_2 >$	0.2708±0.0021	0.3171±0.0014
$Co-Lat^{(rad)}_{SpotI}$	1.135±0.003	1.135±0.003
$Long^{(rad)}_{SpotI}$	2.880±0.003	3.526±0.003
$R^{(rad)}_{SpotI}$	0.611±0.001	0.698±0.001
T_{fSpotI}	0.900±0.001	0.900±0.001
$Co-Lat^{(rad)}_{SpotII}$	1.135±0.003	1.135±0.003
$Long^{(rad)}_{SpotII}$	0.524±0.003	6.248±0.003
$R^{(rad)}_{SpotII}$	0.436±0.001	0.436±0.001
$T_{fSpotII}$	1.100±0.001	0.970±0.001

*Found from the light curve analyses.

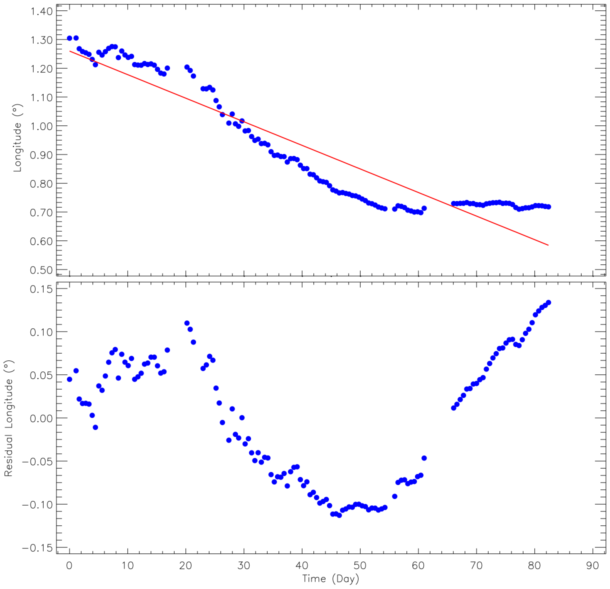

Fig. 5. In the upper panel, the longitudinal variation (filled blue circles) of the stellar cool spot and its linear model for the stellar spots of V1130 Cyg are demonstrated. In the bottom panel, the residuals taken from the linear model are shown. The color figure can be viewed online.

structures as minima phases, minima, and maxima levels of the consecutive light curves.

In the case of V1130 Cyg, the residuals of the long cadence data have been separated into 30 subsets as described above, which are modelled one by one. In the case of V461 Lyr, the residuals of long cadence data have been modelled in two groups; the deep and shallow minima. In these analyses, the sinusoidal variations have been modelled by using the least squares method to determine their minima times. Then, using these minima times, we have found the migrations of wave-like variation toward the earlier phases in the light curves for both systems.

In the case of V1130 Cyg, examination of the migrations indicates that the active component has one spotted area migrating longitudinally on the stellar surface with a period of 0.33388 years (121.951 d). In the case of V641 Lyr, the analyses have demonstrated that both components have two spotted areas on their surfaces. Two spotted areas on one component migrate with periods of 11.577 and 10.585 years. On the other component, two other spotted areas migrate with periods of 11.807 and 12.836 years. The migrations of all these spots are shown in Figures 5 and 6.

2.4. *Stellar Flare Activity*

To understand the nature of the flare activity and its behaviour on the components, all the variations except the flares in the light curves have been removed. Furthermore, the scattering points due to technical reasons have also been removed from the data.

To determine parameters such as the flare start-end points and the flare equivalent durations, it is necessary to determine the quiescent level of the systems. The sinusoidal light-variations at out-of-eclipses have been modelled by Fourier series. Using these synthetic models, the quiescent level for each flare has been defined. Using the available data in the Kepler Database, 94 flares from V1130 Cyg and 254 flares from V461 Lyr have been detected. The parameters have been calculated for each flare. Two flare examples and their quiescent levels identified by Fourier analysis are shown in Figure 7.

After determining the flare start and end times, the flare parameters such as flare maximum time, equivalent duration (P), flare rise (T_r) and decay (T_d) times, flare total time (T_t) and flare amplitude were calculated for each flare. All these parameters are tabulated in Table 3. The time error has been about $\pm 10^{-8}$ day for the observation times given in the Kepler Database (Jenkins et al. 2010a,b). Therefore, the error values of the flare time scales have been about ± 0.0001 day (± 8.64 s). The error values of the computed flare equivalent durations are given in the table for each listed flare. In general, the minimum error value has been found to be ± 0.001 s for both targets. The maximum error values have been found to be ± 1.006 s for V461 Lyr and ± 1.030 s for V1130 Cyg. At this point, it should be noted that equivalent durations of all flares have been calculated by equation (3) defined by Gershberg (1972):

$$P = \int [(I_{flare} - I_0)/I_0]\, dt, \qquad (3)$$

where P is the flare equivalent duration in seconds, the I_{flare} is the flux at the flare moment, and I_0 is the quiescent level flux of the system calculated by the Fourier series at out-of-eclipses. Considering the reasons explained by Dal & Evren (2010, 2011), the flare energies have not been calculated. The equivalent duration parameter has been used instead of the flare energy parameter in the subsequent models.

The distributions of flare equivalent durations on a logarithmic scale versus flare total durations have been modelled by the One Phase Exponential Association (hereafter OPEA) defined by equation (4) (Motulsky 2007; Spanier & Oldham 1987). The SPSS V17.0 (Green et al. 1996) and GraphPad Prism

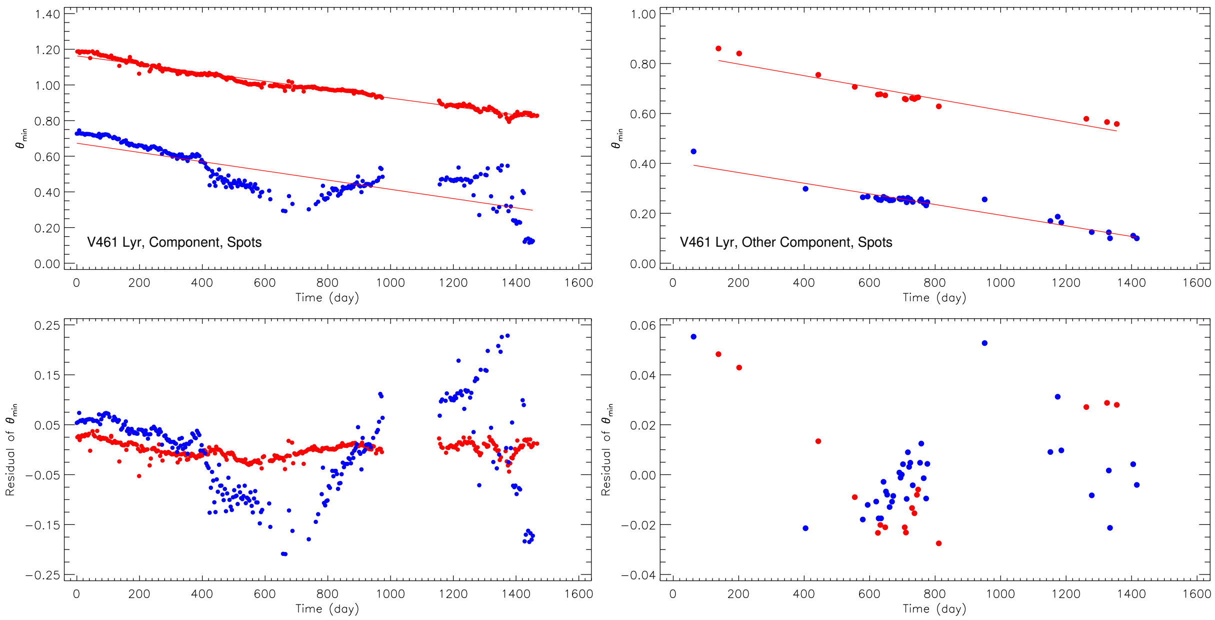

Fig. 6. In the upper left panel, the longitudinal variation of spotted areas on the chromospheric active component of V461 Lyr is shown, while the variation of residuals obtained from the models is exhibited in the lower left panel. In the figure, filled red circles represent the first spot, and filled blue circles the second one. In the upper right panel, the longitudinal variation of the spotted areas on the other component is shown versus time. In the lower right panel, the residuals obtained from the models are shown. The filled blue circles represent the first and the red circles the second spot. The color figure can be viewed online.

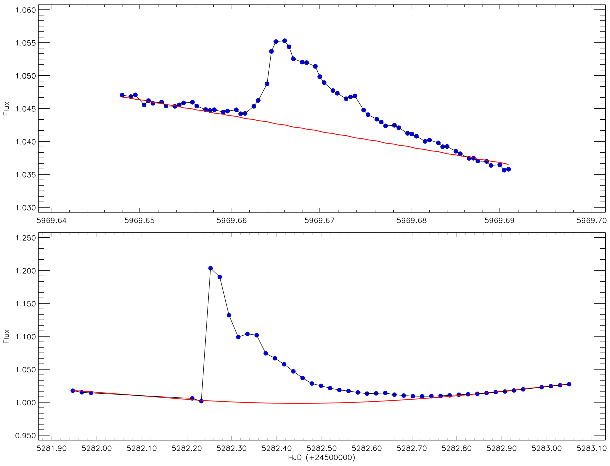

Fig. 7. The flare examples detected from V1130 Cyg (top panel) and V461 Lyr (bottom panel) are shown. In the panels, the filled circles show the observations, while the red lines show the quiescent level defined by Fourier analysis for each light curve part of the targets. The color figure can be viewed online.

V5.02 (Dawson & Trapp 2004) softwares have been used to derive the models, following the method of Dal & Evren (2010, 2011):

$$y \;=\; y_0 \,+\, (Plateau \,-\, y_0) \,\times\, (1 \,-\, e^{-k \,\times\, x}), \quad (4)$$

where the parameter y is the flare equivalent duration on the logarithmic scale, while the parameter x is the flare total duration, according to the definition of Dal & Evren (2010). The parameter y_0 is the flare-equivalent duration on the logarithmic scale for the least total duration. In other words, the parameter y_0 is the least equivalent duration occurring in a flare. It is an important point that the parameter y_0 does not depend only on the flare mechanism occurring in the star, but also on the sensitivity of the optical system used for the observations. The parameter *Plateau* is the upper limit for the flare equivalent duration on the logarithmic scale. Dal & Evren (2011) defined the *Plateau* value as the saturation level for a star in the observing band. Using the least-squares method, the OPEA models have been derived for the distributions of flare equivalent durations on the logarithmic scale versus the flare total durations.

However, when we compared the distributions of the flare equivalent durations versus the flare total time on a logarithmic scale, we noticed that one fit cannot model the distributions. Since some flares are remarkably scattered out of the 95% confidence intervals of the model fits derived from overall flares for each target, we have tried to model separately

TABLE 3

PARAMETERS CALCULATED FOR EACH FLARE FOR V1130 CYG AND V461 LYR[*]

Flare Time (+2400000)	P (s)	T_r (s)	T_d (s)	T_t (s)	Amplitude (Intensity)
			V1130 Cyg		
55933.033204	2.871±0.027	647.313120	706.166208	1353.479328	0.004747
55933.093141	0.772±0.006	647.304480	58.853952	706.158432	0.001733
55933.305644	0.928±0.006	353.096928	1000.391904	1353.488832	0.001241
55933.402359	0.375±0.004	294.224832	294.242976	588.467808	0.001498
55933.843711	5.487±0.090	470.769408	2177.338751	2648.108160	0.002957
55933.877766	0.878±0.006	588.476448	706.159296	1294.635744	0.002133
55934.114788	0.621±0.005	882.702144	176.535072	1059.237216	0.001674
55934.154291	0.381±0.004	294.242976	470.769408	765.012384	0.001469
55935.054703	2.688±0.024	176.543712	1824.259968	2000.803680	0.005598
55935.314883	0.051±0.001	58.853952	58.836672	117.690624	0.000856
			V461 Lyr		
54962.714192	26.897±0.003	5296.624128	15889.872384	21186.496512	0.002636
54962.918537	2.003±0.001	1765.540800	3531.083328	5296.624128	0.000497
54973.871418	29.043±0.004	3531.065184	14124.295296	17655.360479	0.004381
54974.096197	21.781±0.003	5296.610304	10593.221472	15889.831776	0.002037
54979.552190	7.268±0.001	1765.525248	7062.134688	8827.659936	0.001591
54981.820410	732.250±0.536	3531.055680	52965.879264	56496.934945	0.005567
54983.250817	12.554±.002	3531.053952	7062.126048	10593.180000	0.002931
55018.928916	203.042±0.052	5296.501440	30013.447104	35309.948544	0.018895
55022.872672	24.872±0.003	1765.493280	14123.942784	15889.436064	0.003486
55026.060364	424.376±0.207	38840.757120	22951.355616	61792.112736	0.012320

[*] Obtained from the analysis of data from the Kepler satellite. In the table the error of each equivalent duration (P) is listed, while the error of the flare time scales is given in the text. The rest of the list can be found in the online archive of the journal.

these scattered flares. In the analyses, we have tried first to derive just one OPEA model for all the flares, but both the correlation coefficient squared (R^2) and the probability value $p-value$, which is an indicator of the sensitivity of the model, indicate that a single model cannot be derived for the flares in the case of each target. The tests done by using the least-squares method in the SPSS V17.0 and GraphPad Prism V5.02 programs have shown that the flares should be classified in two groups in the case of V1130 Cyg and in three groups in the case of V461 Lyr. The models obtained in this way are shown in Figure 8, while the parameters of each OPEA model are listed in Table 4. The *span* value listed in the table is the difference between $Plateau$ and y_0 values. The $half-life$ value is half of the first x value, in which the model reaches the $Plateau$ value. In other words, it is half of the minimum flare total time, which is enough for the maximum flare energy to occur in the flare mechanism.

For each group, the distribution model of the flare equivalent durations versus the flare total time has been tested using three different methods such as the D'Agostino-Pearson normality test, the Shapiro-Wilk normality test, and the Kolmogorov-Smirnov test (D'Agostino & Stephens 1986). The $p - value$ values have been computed, following these methods. According to the results, the distribution of flare equivalent durations versus the flare total time cannot be modelled by any other function apart from the OPEA function. The $p-values$ have been found to be < 0.001 in the methods as listed in Table 4.

To check whether the separations seen in the OPEA models are the real situation, or not, we have computed the flare cumulative frequency distributions depending on each different energy limit (Gershberg 1972) for each group. To reveal the flare energy character of a star, Gershberg (1972) defined the flare cumulative frequency distribution, separately calculated for each different energy limit.

TABLE 4

THE OPEA PARAMETERS OBTAINED BY USING THE LEAST SQUARES METHOD

V461 Lyr	Group 1	Group 2	Group 3
Best-fit values			
Y_0	-0.8112±0.2493	0.0082±0.1226	-0.0972±0.3168
$Plateau$	1.9015±0.2565	2.7943±0.1676	3.4324±0.1755
$Half-life$	15004.2	16767.6	10118.60
$Span$	2.7127±0.2157	2.7860±0.1270	3.5296±0.2743
95% Confidence			
Y_0	-1.3257 to -0.2968	-0.2321 to 0.2486	-0.7581 to 0.5637
$Plateau$	1.3720 to 2.4310	2.4658 to 3.1228	3.0664 to 3.7985
$Half-life$	9640.85 to 33817.20	13042.70 to 23470.50	7329.38 to 16334.90
$Span$	2.2675 to 3.1579	2.5370 to 3.0350	2.9574 to 4.1018
R^2	0.87	0.74	0.91
$p-value1$	0.0091	> 0.0001	0.0036
$p-value2$	0.013	0.005	0.0061
$p-value3$	> 0.10	0.0158	0.0038

V1130 Cyg	Group 1	Group 2	-
Best-fit values			
Y_0	-0.9133±0.0664	-1.0765±0.0828	-
$Plateau$	2.1997±0.3495	1.00676±0.1023	-
$Half-life$	1456.51	1226.07	-
$Span$	3.1130±0.3173	2.0833±0.0891	-
95% Confidence			
Y_0	-1.0497 to -0.7770	-1.2421 to -0.9109	-
$Plateau$	1.4825 to 2.9168	0.8022 to 1.2113	-
$Half-life$	1031.79 to 2475.54	978.88 to 1640.26	-
$Span$	2.4619 to 3.7641	1.9051 to 2.2614	-
R^2	0.96	0.91	-
$p-value_1$	0.0001	0.2982	-
$p-value_2$	0.0040	0.2183	-
$p-value_3$	> 0.1000	> 0.1000	-

However, the flare equivalent durations have been used instead of the flare energy to compute the flare cumulative frequencies in this study, because of the reasons stated above. The obtained flare cumulative frequency distributions are shown for V1130 Cyg in Figure 9 and V461 Lyr in Figure 10. As seen from Figures 9 and 10, the flare cumulative frequencies exhibit the distributions in the form of an exponential function. Indeed, the least-squares method in the GraphPad Prism V5.02 program has indicated that an exponential function seems to be the most suitable function to fit these distributions, and therefore we have modelled all the distributions by exponential functions. The obtained exponential functions are shown by red lines in Figures 9 and 10.

V1130 Cyg has been observed over 23810.584 h in total. The sum of equivalent duration for its 94 flares has been calculated as 267.576 seconds. V461 Lyr has been observed along 3580.667 h in total. The sum of equivalent durations has been calculated as 25831.721 seconds over its 255 flares. Ishida et al. (1991) has defined two different flare frequencies for the flare activity. These frequencies are expressed by equations 5, 6:

$$N_1 = \Sigma n_f \,/\, \Sigma T_t, \tag{5}$$

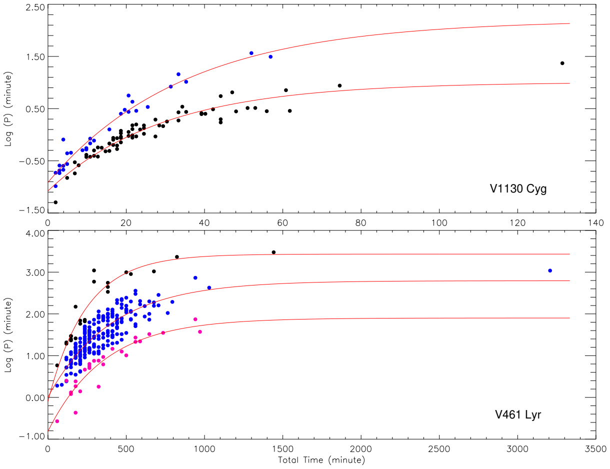

Fig. 8. The OPEA models obtained for 94 flares for V1130 Cyg and 255 flares for V461 Lyr, determined by analysing the observation data available in the Kepler Database. The filled circles in the figure show each flare, while the lines show the OPEA models. In the upper panel, the filled blue circles represent the Group 1 flares, the filled black circles the Group 2 flares. In the bottom panel, the filled black circles represent the Group 3 flares; the filled blue circles the Group 2 flares, and the filled pink circles show the Group 1 flares. The color figure can be viewed online.

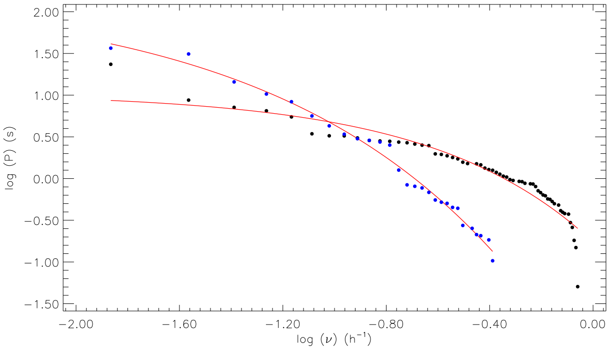

Fig. 9. Cumulative flare frequencies and their models derived for Group 1 (30 flares) and Group 2 (64 flares) obtained from V1130 Cyg observations. The black circles in the figure represent Group 1 and the blue circles represent Group 2. In the figure, the red lines represent the exponential distribution models. The color figure can be viewed online.

$$N_2 \;=\; \Sigma P \;/\; \Sigma T_t. \tag{6}$$

Here, Σn_f is the total number of flares, ΣT_t is the total observation time for each star. ΣP is the sum of the equivalent duration calculated over all the flares. The flare frequencies obtained under these definitions are given in Table 5.

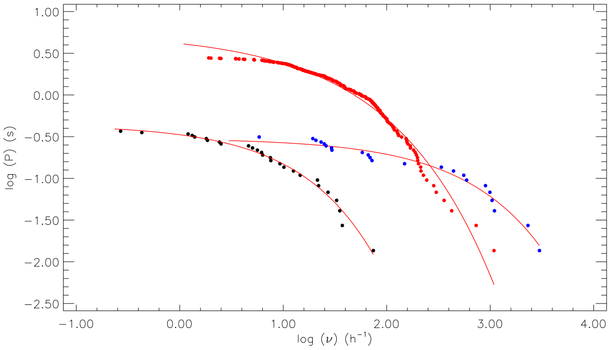

Fig. 10. Cumulative flare frequencies and their models derived for Group 1 (over 27 flares), Group 2 (over 205 flares) and Group 3 (over 23 flares) obtained from V461 Lyr observations. The black circles in the figure represent Group 1, the red ones represent Group 2, the blue circles represent Group 3. In the figure, the red lines represent the exponential distribution models. The color figure can be viewed online.

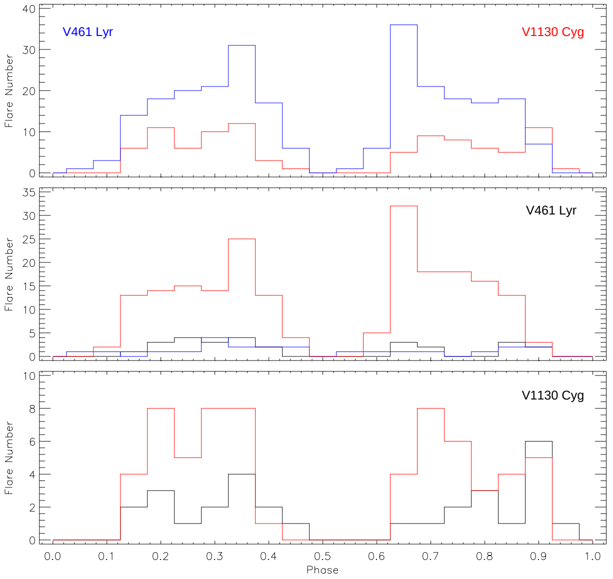

Fig. 11. The distributions of flare total number in each phase interval of 0.05, plotted versus phase for 255 flares detected for V461 Lyr and for 94 flares for V1130 Cyg. In the upper panel the flare phase distributions are shown by a blue line for V461 Lyr and a red line for V1130 Cyg. In the middle and bottom panels, the black lines represent Group 1 flares for both targets, while the red lines show Group 2 flares. In the middle panel, the blue line represents Group 3 flares of V461 Lyr. The color figure can be viewed online.

It is well-known that the flare events are generally random phenomena in the case of UV Ceti type flare stars. To test this situation for both targets, we calculated the phase distribution of the flares,

TABLE 5

FLARE FREQUENCIES COMPUTED FOR BOTH SYSTEMS

Flare Parameters	All	Group 1	Group 2	Group 3
		V461 Lyr		
Total Observation Time (h)	3580.667	3580.667	3580.667	3580.667
Flare Number	255	27	205	23
Total Equ. Dur. (s)	25831.721	352.662	13572.733	11865.771
N_1 (h^{-1})	0.07122	0.00754	0.05725	0.00642
N_2	0.00024	0.00003	0.00105	0.00092
		V1130 Cyg		
Total Observation Time (h)	23810.584	23810.584	23810.584	-
Flare Number	94	30	64	-
Total Equ. Dur. (s)	267.576	133.788	128.561	-
N_1 (h^{-1})	0.00395	0.00126	0.00269	-
N_2	0.00001	0.00001	0.00001	-

depending on the orbital periods of the targets. The total flare numbers were computed in phase intervals of 0.05 for the flares of both targets. Then, we plotted these numbers versus the phase, as seen in Figure 11. We show separately the phase distributions of the flares for each group in the middle and bottom panels of the same figure.

3. RESULTS AND DISCUSSION

Analysis of V1130 Cyg and V461 Lyr data taken from the Kepler Database (Slawson et al. 2011; Matijevič et al. 2012) shows that both systems have high-level chromospheric activity. It is necessary to investigate which components exhibit chromospheric activity in the systems and to determine their activity levels in comparison with similar stars. For this aim, first of all, the physical parameters of the components have to be determined. For both systems, it is seen that various calibrations and approaches to reveal the physical structure of components have been made in the literature, but no complete light curve analysis has been found. Considering the available radial velocity variations of the targets as shown in Figure 2, both targets should be binary stars. As described in § 2, the semi-amplitudes (K1) of the radial velocities have been estimated as at least 39.19 km s^{-1} for V1130 Cyg and 117.79 km s^{-1} for V461 Lyr. These values seem to be enough to support the fact that both targets are the combinations of two stars at least, and not single stars with a planetary system. Therefore, for the first time in the literature, the light curve analyses of the systems have been performed with PHOEBE V.0.32 software, and the parameters obtained in these analyses are listed in Table 2.

The spectral type of V1130 Cyg is given in the literature as F7 + K0 IV (Svechnikov & Kuznetsova 1990). The temperatures of the components are given as $T_1 = 5587$ K and $T_2 = 6621$ K (Armstrong et al. 2014). In the light curve analysis with PHOEBE V.0.32 software, the temperature of the primary component has been taken as 6530 K and that of the secondary as 3891±50 K. The mass ratio (q) of the components has been found to be 0.689±0.001, while the orbital inclination angle (i) of the system has been obtained as 90°.00±0°.01. The mass of the primary component has been found as 1.337 $M_\odot$ and 0.526 $M_\odot$ for the secondary. In addition, the calculated radii have been computed as 1.264 $R_\odot$ for the primary component and 0.611 $R_\odot$ for the secondary. Considering Kepler's 3rd Law, the semi-major axis has been found to be 3.53 $R_\odot$.

The spectral type of V461 Lyr's primary component has been given as G9 (Qian et al. 2018). In the light curve analysis with PHOEBE V.0.32 software, the temperature of the primary component has been taken as 5774 K, and that of the secondary as 4206±50 K. The mass ratio (q) has been found to be 0.999±0.001, while the orbital inclination angle (i) of the system has been obtained as 89°.58±0°.01. The mass of the primary component has been found to be 0.993 $M_\odot$ and 0.612 $M_\odot$ for the secondary component. In addition, the radii have been computed as 1.021 $R_\odot$ for the primary component and 0.677 $R_\odot$

for the other one. Similarly, the semi-major axis has been found to be 11.83 $R_{\odot}$. In the MAST database (Gao et al. 2016), the log g values have been given as 3.678 cm/s^2 for V1130 Cyg and 4.320 cm/s^2 for V461 Lyr. Considering the radii and luminosities obtained in this study together with these log g values, it is seen that the secondary components are more evolved compared to the primary components in both systems.

3249 minima times have been computed from V1130 Cyg's long cadence data and 220 ones from the short cadence data. 716 minima times have been calculated from V461 Lyr's long cadence data and 75 ones from the short cadence data. The $(O-C)_{II}$ residuals shown in Figure 3 have been obtained by applying a linear correction given by equations 1, 2. It is seen that the expected results have been found, according to both Tran et al. (2013) and Balaji et al. (2015), whose studies were concentrated on the magnetic activity effects on the minima times. The primary and secondary minima times are differentiated by the effect of the chromospheric activity of the systems. If one examines the minima times of V461 Lyr, it will be seen that the chromospheric activity mostly affects the variations of the secondary minima. Therefore, the $(O-C)$ analysis is quite difficult for this target. As seen from the $(O-C)_{II}$ residuals shown in the bottom panel of Figure 3, the correction rates have been found to be remarkably different, analysing the primary minima and the secondary minima together. This makes it difficult to understand the nature of the system. At this point, it cannot be said for sure whether the linear trend seen in the primary minima times is caused by an inadequate analysis, or not. It is possible that it can be a small part of a sinusoidal variation due to the effect of cool spots.

V1130 Cyg has been observed over 23810.584 h in total, according to the available data in the Kepler Database, where 94 flares have been obtained in total. When the distribution of flare equivalent durations versus the flare total times on the logarithmic scales was analysed, an interesting fact was noticed. The obtained OPEA model exhibits two different distributions. The flares were divided into two groups: 30 flares in the first group and 64 flares in the second group. Therefore, two separate OPEA models were derived for both groups. When the parameters of the obtained models have been compared with each other, the statistical tests have shown that these two groups are separate and cannot be modelled under a single model. The Plateau values obtained separately from these two groups have been found to be 2.1997 s for Group 1 and 1.0068 s for Group 2. It is seen that there is approximately a two-times difference between these two Plateau values. The situation was encountered for the first time by Kamil & Dal (2017). Considering that the OPEA models derived by the flares come from different components, the temperatures of the components of V1130 Cyg are suitable to exhibit different group flares, according to Dal & Evren (2011).

V461 Lyr was observed over 3580.667 h in total. As a result of the analysis, 255 flares were obtained in total. Then, the OPEA model was derived for these flares. The same interesting situation was also seen in the case of V461 Lyr. The data cannot be represented by one model. The data seem to be best represented by three different models, shown in Figure 8. Therefore, the flares obtained from V461 Lyr were divided into three groups: 27 flares in the first group, 205 flares in the second group, and 23 ones in the third group. Three OPEA models were created for the flares of these groups. The Plateau values were obtained as 1.9015 s for Group 1, 2.7943 s for Group 2, and 3.4324 s for Group 3. The components' temperatures could explain the division into two flare groups. In this case, the systems must have an unseen third component to provide a third group. But there has been no observational information about the third body. Besides, there were no background and foreground stars near the system that could exhibit flare activity to create a third group.

Taking into account the frequency definitions of Gershberg (1972), in the case of V1130 Cyg, the flare frequencies of Group 1 were found to be $N_1 = 0.00126\,\mathrm{h}^{-1}$ and $N_2 = 0.00001$, while $N_1 = 0.00269\,\mathrm{h}^{-1}$ and $N_2 = 0.00001$ for Group 2 flares. From V461 Lyr's flares, the flare frequencies were found as $N_1 = 0.00754\,\mathrm{h}^{-1}$ and $N_2 = 0.00003$ for Group 1 flares, $N_1 = 0.05725\,\mathrm{h}^{-1}$ and $N_2 = 0.00105$ for Group 2 flares, and also $N_1 = 0.00642\,\mathrm{h}^{-1}$ and $N_2 = 0.00092$ for Group 3. In the case of UV Ceti type single stars, the N_1 flare frequency was found to be $N_1 = 1.331\,\mathrm{h}^{-1}$ for AD Leo, $N_1 = 1.056\,\mathrm{h}^{-1}$ for EV Lac. The N_2 flare frequency was found to be $N_2 = 0.088$ for EQ Peg, $N_2 = 0.086$ for AD Leo (Dal & Evren 2011). In the case of eclipsing binaries, with just one component being a chromospherically active star, the flare frequencies have been found to be $N_1 = 0.01735\,\mathrm{h}^{-1}$ and $N_2 = 0.00001$ for KIC 9641031, $N_1 = 0.01351\,\mathrm{h}^{-1}$ and $N_2 = 0.00006$ for KIC 9761199, $N_1 = 0.05087\,\mathrm{h}^{-1}$ and $N_2 = 0.0005$ for KIC 11548140 (Yoldaş & Dal 2016, 2017b,a). As an indicator of flare activity level, one of the most reliable parameters should be the flare frequency if it was determined over long observing durations. In this study, the flare frequencies were computed over 29630.74161 hours, while they were also computed over long observing durations in the cited studies. Consequently, in this study, the flare frequencies are quite suitable to discuss stellar activity levels.

Solving the OPEA models, the Half-life parameter for V1130 Cyg was found to be 1456.515 s for Group 1 flares, 1226.070 s for Group 2 flares. In the case of V461 Lyr, it was found to be 15004.2 s for Group 1, 16767.6 s for Group 2, and 10118.6 for Group 3 s. These values are remarkably higher than the values obtained from classical UV Ceti type stars. For example, they are 433.10 s for DO Cep, 334.30 s for EQ Peg, and 226.30 s for V1005 Ori (Dal & Evren 2011). Similarly, they are 2291.7 s for KIC 9641031, 1014 s for KIC 9761199, 2233.6 s for KIC 11548140 (Yoldaş & Dal 2016, 2017b,a).

The longest rise time (T_r) was found to be 1706.558976 s for Group 1 and 2765.821248 s for Group 2 in the case of V1130 Cyg. The longest rise time was found to be 1765.447488 s for Group 1, 38840.757120 s for Group 2, and 10592.6832 s for Group 3 in the case V461 Lyr. According to some examples from the classical single UV Ceti type stars, the maximum rise times were 2062 s for V1005 Ori, 1967 s for CR Dra (Dal & Evren 2011). It was found to be 1118.099 s for KIC 9761199 (Yoldaş & Dal 2017b), while it was 3942.749 s for KIC 11548140 (Yoldaş & Dal 2017a). In the case of the flares observed in the UV Ceti type single stars, the maximum flare total time was found to be 5236 s for V1005 Ori, and it was 4955 s for CR Dra (Dal & Evren 2011). However, the longest flares obtained in the case of V1130 Cyg were 3413.250144 s for Group 1 and 7885.51805 s for Group 2. The longest flares obtained in the case of V461 Lyr were 58258.0624 s for Group 1, 192431.8967 s for Group 2, and 86506.9597 s for Group 3. The longest flares lasted 5178.87 s for KIC 9641031, 1118.099 s for KIC 9761199 and 22185.361 s for KIC 11548140 (Yoldaş & Dal 2016, 2017b,a). The comparisons show that V1130 Cyg and V461 Lyr have relatively higher chromospheric activity compared to similar systems, although the values are not as high as those obtained in the case of UV Ceti type single stars.

It has been understood from the variations at out-of-eclipses that the systems exhibit cool spot activity as well as flare activity. The reason for these variations is the rapid evolution of stellar cool spots on the stellar surface. The stellar spot activities seen on the chromospherically active components have been analysed by examining the minima phase variations of the sinusoidal variations versus time. As a result of the analysis, it is seen that the active component of V1130 Cyg has a spot migration with a period of 0.33388 years. However, V461 Lyr has four spots on its two active components. The migration periods were found to be 11.58 years and 10.59 years for two spots on the same component. The migration periods of the other two spots on the other component were found to be 11.81 years and 12.84 years.

The observations of the spot groups on the solar surface show that two permanent active longitudes occur between 180 degrees. These effective longitudes are known as Carrington Coordinates and are fixed structures for some authors, while others indicate that the effective longitude rotation speeds are not constant and may be different (Lopez Arroyo 1961; Stanek 1972). Similarly, stellar cool spots detected on the active components of the systems showed migration, but the migration periods were different for each spot. As shown in the lower panels of Figures 5 and 6, some wave-like variations remain after correcting for migration movements with some linear model fits. From the spots seen for the first time to the end of the observation season in the data, it is seen that the migration periods have a great variation, which reveals that differential rotation on the surfaces of the stars is very strong.

Apart from this situation, as shown in Figure 6, there are two pairs of active longitudes on V461 Lyr, and the active longitudes in each pair are located with a longitude interval of 180 degrees. This means that there are four active longitudes positioned with a longitude interval of 90 degrees. According to this scene, an observer can detect some flares from the longitudes at 90 degrees on the stellar surface. In this case, we expect to see an almost homogeneous phase distribution for the flares from V461 Lyr. On the other hand, as shown in Figure 11, the total number of flares detected in each phase interval of 0.05 is increasing toward the phases of 0.35 and 0.65. It seems that the flare numbers start to increase from phase 0.35 and decrease until phase 0.65. However, the flare number drops to nearly zero at phase of 0.50. The active component should be blacked out by the other component in the direction of the observer. Consequently, according to this scenario, the flare frequency varies from one phase interval to the next one; and it reaches a maximum around phase 0.50, where the stellar surface part is positioned toward the other component. Because of the tidal effect, the possibility of flare occurrence on the surface part facing the other components becomes higher than anywhere on the surface, though the flares can occur anywhere on the stellar surface due to the spotted regions in the active longitude.

In the case of V1130 Cyg, the target has just one active longitude where the cool spots occur. As shown in Figure 11, the flare numbers increase at phases 0.20, 0.35, 0.70, and 0.90. Similarly, the flare number decrease to near zero at phase 0.50. This could be caused by the eclipses of the components. V1130 Cyg exhibits a different behaviour from V461 Lyr. The target shows a nearly homogeneous phase distribution for the flares despite the single active longitude.

In the literature there are several studies such as Hawley et al. (2014); Dal & Özdarcan (2018), in which flare frequency variation versus rotational phase is mentioned. Dal & Özdarcan (2018) demonstrated that the flare frequency of KIC 12418816 increases toward phase 0.85. However, Hawley et al. (2014) indicated that the flare frequency of GJ 1243 does not exhibit any clear variation with phase. At this point, it must be noted that GJ 1243 is remarkably one of the most active stars. Indeed, V1130 Cyg exhibits 94 flares over 29630.742 hours of observing patrol, while V461 Lyr exhibits 255 flares in total. However, Davenport et al. (2014) detected over 6100 individual flare events from GJ 1243 in 7665.6 hours (about 11 months). GJ 1243 is a single M dwarf, most probably a fully convective star; and its whole surface must be fully covered with magnetic lines. As a result, as in the case of UV Ceti type flare stars, the flare time distribution does not exhibit any correlation with the rotation period in the case of GJ 1243, unlike both V461 Lyr and V1130 Cyg.

Apart from the phase distributions of total flare numbers in each phase interval of 0.05, we also examined the phase distributions of each flare group for both systems. One expects that the flares in each group come from different sources due to the different mechanisms working on the stellar surfaces. In this case, it is expected that the flare phase distributions should be maximum around the different phases. However, the distributions shown in Figure 11 indicate that all groups have a maximum around the same phases. This reveals that even if the sources or the mechanisms of each flare group are different from each other, the locations of each flare group on the stellar surface are roughly the same.

We thank the referee for useful comments that contributed to the improvement of the paper. We also wish to thank the Turkish Scientific and Technical Research Council (TÜBİTAK) for supporting this work through Grant No. 116F213.

REFERENCES

Ahumada, R., Allende Prieto, C., Almeida, A., et al. 2019, arXiv:1912.02905

Armstrong, D. J., Gómez-Maqueo, Ch. Y., Faedi, F., & Pollacco, D. 2014, MNRAS, 437, 3473

Balaji, B., Croll, B., Levine, A. M., & Rappaport, S. 2015, MNRAS, 448, 429

Baliunas, S. L., Donahue, R. A., Soon, W. H., et al. 1995, ApJ, 438, 269

Balona, L. A. 2015, MNRAS, 447, 2714

Benz, A. O. 2008, LRSP, 5, 1

Borucki, W. J., Koch, D., Basri, G., et al. 2010, Sci, 327, 977

Caldwell, D. A., Kolodziejczak, J. J., Van Cleve, J. E., et al. 2010, ApJ, 713, 92

Carrington, R. C. 1859, MNRAS, 20, 13

D'Agostino, R. B. & Stephens, M. A. 1986, Goodness-of-fit techniques (New York, NY: Dekker)

Dal, H. A. & Evren, S. 2010, AJ, 140, 483

_________. 2011, AJ, 141, 33

Dal, H. A. & Özdarcan, O. 2018, MNRAS, 474, 326

Davenport, J. R. A. 2016, ApJ, 829, 23

Davenport, J. R. A., Covey, K. R., Clarke, R. W., et al. 2019, ApJ, 871, 241

Davenport, J. R. A., Hawley, S. L., Hebb, L., et al. 2014, ApJ, 797, 122

Dawson, B. & Trapp, R. 2004, Basic & Clinical Biostatistics 4/E, Lange Basic Science (McGraw-Hill Education)

Dexter, L. 1974, JAAVSO, 3, 59

Emslie, A. G., Dennis, B. R., Shih, A. Y., et al. 2012, ApJ, 759, 71

Gao, Q., Xin, Y., Liu, J.-F., Zhang, X.-B., & Gao, S. 2016, ApJS, 224, 37

Gershberg, R. E. 1972, Ap&SS, 19, 75

_________. 2005, Solar-Type Activity in Main-Sequence Stars (Berlin, Heidelberg: Springer)

Gershberg, R. E. & Shakhovskaia, N. I. 1983, Ap&SS, 95, 235

Green, S. B., Salkind, N. J., & Jones, T. M. 1996, Using SPSS for Windows; Analyzing and Understanding Data, (1st ed., NJ, USA: Prentice Hall PTR)

Gunn, J. E., Siegmund, W. A., Mannery, E. J., et al. 2006, AJ, 131, 2332

Haisch, B., Strong, K. T., & Rodono, M. 1991, ARA&A, 29, 275

Hawley, S. L., Davenport, J. R. A., Kowalski, A. F., et al. 2014, ApJ, 797, 121

Hodgson, R. 1859, MNRAS, 20, 15

Ishida, K., Ichimura, K., Shimizu, Y., & Mahasenaputra. 1991, Ap&SS, 182, 227

Jenkins, J. M., Caldwell, D. A., Chandrasekaran, H., et al. 2010a, ApJ, 713, 87

Jenkins, J. M., Chandrasekaran, H., McCauliff, S. D., et al. 2010b, SPIE, 7740
Johnson, D. O. 2004, JAD, 10, 3
Kamil, C. & Dal, H. A. 2017, PASA, 34, 29
Koch, D. G., Borucki, W. J., Basri, G., et al. 2010, ApJ, 713, 79
Kron, G. E. 1950, AJ, 55, 69
Leto, G., Pagano, I., Buemi, C. S., & Rodono, M. 1997, A&A, 327, 1114
Lopez Arroyo, M. 1961, Obs, 81, 205
Maehara, H. 2017, IAUS 328, Living Around Active Stars, ed. D. Nandy, A. Valio, & P. Petit, 22
Majewski, S. R., Schiavon, R. P., Frinchaboy, P. M., et al. 2017, AJ, 154, 94
Marcy, G. W. & Chen, G. H. 1992, ApJ, 390, 550
Mathioudakis, M., Doyle, J. G., Avgoloupis, V., Mavridis, L. N., & Seiradakis, J. H. 1992, MNRAS, 255, 48
Mathur, S., Huber, D., Batalha, N. M., et al. 2017, ApJS, 229, 30
Matijevič, G., Prša, A., Orosz, J. A., et al. 2012, AJ, 143, 123
Miller, W. J. 1966, RA, 7, 217
Mirzoian, L. V. 1990, IAUS 137, Flare Stars in Star Clusters, Associations and the Solar Vicinity, ed. L. V. Mirzoian, B. R. Pettersen, & M. K. Tsvetkov (Boston, MA: Kluwer Academic), 1
Motulsky, H. 2007, GraphPad Software, 31, 39
Pettersen, B. R. 1991, MmSAI, 62, 217
Pigatto, L. 1990, IAUS 137, Flare Stars in Star Clusters, Associations, and the Solar Vicinity, ed. L. V. Mirzoyan, B. R. Pettersen, & M. K. Tsvetkov (Boston, MA: Kluwer Academic), 117
Prša, A. & Zwitter, T. 2005, ApJ, 628, 426
Qian, S. -B., Zhang, J., He, J. -J., et al. 2018, ApJS, 235, 5
Ramsay, G. & Doyle, J. G. 2015, MNRAS, 449, 3015
Rempel, M. 2008, JPhCS, 118, 012032
Schwabe, H. 1844, AN, 21, 233
Skumanich, A. 1972, ApJ, 171, 565
Slawson, R. W., Prša, A., Welsh, W. F., et al. 2011, AJ, 142, 160
Smith, J. C., Stumpe, M. C., Van Cleve, J. E., et al. 2012, PASP, 124, 1000
Spanier, J. & Oldham, K. B. 1987, An Atlas of Functions (Bristol, PA: Taylor & Francis/Hemisphere)
Stanek, W. 1972, SoPh, 27, 89
Stauffer, J. R. 1991, ASIC 340, Angular Momentum Evolution of Young Stars, ed. S. Catalano & J. R. Stauffer (Boston, MA: Kluwer Academic Publishers)
Stumpe, M. C., Smith, J. C., Van Cleve, J. E., et al. 2012, PASP, 124, 985
Svechnikov, M. A. & Kuznetsova, E. F. 1990, Katalog priblizhennykh fotometricheskikh i absoliutnykh elementov zatmennykh peremennykh zvezd (Izd-vo Ural'skogo universiteta)
Tran, K., Levine, A., Rappaport, S., et al. 2013, ApJ, 774, 81
Tu, Z.-L., Yang, M., Zhang, Z. J., & Wang, F. Y. 2020, ApJ, 890, 46
van Maanen, A. 1940, ApJ, 91, 503
Watson, C. L., Henden, A. A., & Price, A. 2006, ASS, 25, 47
Wilson, O. C. 1978, ApJ, 226, 379
Wilson, R. E. 1990, ApJ, 356, 613
Wilson, R. E. & Devinney, E. J. 1971, ApJ, 166, 605
Yoldaş, E. & Dal, H. A. 2016, PASA, 33, 16
_________. 2017a, PASA, 34, 60
_________. 2017b, RMxAA, 53, 67
Zacharias, N., Monet, D. G., Levine, S. E., et al. 2005, VizieR Online Data Catalog: I/297

H. A. Dal and E. Yoldaş: Department of Astronomy and Space Sciences, University of Ege, Bornova, 35100 İzmir, Turkey (ezgiyoldas@gmail.com).

Revista Mexicana de Astronomía y Astrofísica, **57**, 351–361 (2021)

https://doi.org/10.22201/ia.01851101p.2021.57.02.08

CHROMOSPHERIC ACTIVITY NATURE OF KIC 6044064

E. Yoldaş

Department of Astronomy and Space Sciences, University of Ege, Bornova, 35100 İzmir, Turkey.

Received September 10 2020; accepted May 27 2021

ABSTRACT

This study presents results obtained from the data of KIC 6044064 (KOI 6652). KIC 6044064 was observed by the Kepler Mission for a total of 1384.254 days. 525 minima times were determined, 264 of which were primary minima and the rest were secondary minima. The OPEA model was derived and its parameters were obtained. On the secondary component, there are two different spot bands latitudinally outstretched, consisting of three spots located with a phase interval of 0.33. The average migration period was found to be 623.063 ± 4.870 days (1.71 ± 0.01 years) for the first spot group, while it was 1125.514 ± 7.305 days (3.08 ± 0.02 years) for the second group. The spectral types of the components seem to be G7V + K9V. Their masses and radii were determined to be $0.86 M_{\odot}$ and $0.89 R_{\odot}$ for the primary component and $0.54 M_{\odot}$ and $0.62 R_{\odot}$ for the secondary component.

RESUMEN

Presentamos resultados obtenidos con los datos de KIC 6044064 (KOI 6652) que fue observada por la misión Kepler durante un total de 1384.254 días. Se determinaron 525 tiempos de mínimo, de los cuales 264 fueron mínimos primarios y el resto ssecundarios. Se obtuvo el modelo OPEA y sus parámetros. En la componente secundaria se encuentran dos bandas distintas de manchas extendidas en latitud, con tres manchas ubicadas a 0.33 de intervalo de fase. Se determinó un período promedio de migración de 623.063 ± 4.870 días (1.71 ± 0.01 años) para el primer grupo de manchas, y de 1125.514 ± 7.305 días (3.08 ± 0.02 años)para el segundo grupo. Los tipos espectrales de las componentes son G7V + K9V. Se obtuvieron valores para las masas y radios de las componentes de $0.86 M_{\odot}$ y $0.89 R_{\odot}$ para la primaria, y de $0.54 M_{\odot}$ y $0.62 R_{\odot}$ para la secundaria.

Key Words: binaries: eclipsing — methods: data analysis — stars: flare — stars: individual: KIC 6044064 — techniques: photometric

1. INTRODUCTION

Chromospheric activity is an interaction between the magnetic field and the plasma. Solar spots and flares are well-known examples of this phenomenon. The oldest records of sunspots are found in Chinese records dating back 2000 years (Clark & Stephenson 1978; Wittmann & Xu 1987). For the first time in the literature, Kron (1950) discovered that UV Ceti stars also exhibit spot activity. Kron (1950) detected the sinus-like variations in the light curve of an eclipsing binary YY Gem, and then Kunkel (1975) called this event the BY Dra Syndrome, in which the variation is caused by a heterogeneous temperature distribution on the stellar surface.

Berdyugina & Usoskin (2003) found on the solar surface two active longitudes separated by 180°, and found that these longitudes are semi-stable. According to some authors, such as Lopez Arroyo (1961); Stanek (1972); Bogart (1982), these active longitudes vary versus the time. The dominant active longitude also varies in time; this phenomenon is called Flip-Flop event. These events are very important to understand the north-south asymmetry that the stellar magnetic topology exhibits. In these events, the angular velocity is an important parameter because this parameter determines the rotational velocities of the latitudes where the spots or groups of spots are seen.

A flare event is a consequence of magnetic reconnection in the outer convective envelope of the star (Pettersen 1989). Flare activity was first detected on the solar surface by Carrington (1859) and Hodgson (1859). UV Ceti is the first star on which flare activity was detected. According to Skumanich's law, the younger stars have a higher rotational velocity, which causes the activity level to increase (Skumanich 1972; Marcy & Chen 1992). This is the reason why the dwarfs found in open clusters mostly show flare activity (Mirzoian 1990; Pigatto 1990). This is also the reason why the number of UV Ceti type stars decreases with increasing cluster age (Marcy & Chen 1992; Pettersen 1991; Stauffer 1991).

The mass loss rate increases with increasing flare activity level. The solar mass-loss rate is known to be 2×10^{-14} $M_{\odot}$ per year due to the flare activity (Gershberg 2005). In the case of UV Ceti-type stars, it reaches almost 10^{-10} $M_{\odot}$ per year due to the higher flare activity level. The higher mass-loss rate explains why these stars lose most of their total angular momentum in the earliest main sequence stages (Marcy & Chen 1992). Although it is a well-known phenomenon that stellar evolution is absolutely affected by the high mass loss due to flare activity, flare events are not yet fully explained.

Among the parameters of flares, energy is an important one. There is a marked difference between the flare energies obtained from stars of different spectral types. The energies measured from two-ribbon flares generally have a level between 10^{30} and 10^{31} ergs (Gershberg 2005; Benz 2008). RS CVn binaries have many flares with an energy level of 10^{31} erg (Haisch et al. 1991). According to the long-term observations, the energies of the flares detected from dMe stars range from 10^{28} to 10^{34} erg (Gershberg 2005). The flare energies measured from the members of the Pleiades cluster and Orion Association can reach 10^{36} erg (Gershberg & Shakhovskaia 1983). Although the observations show that there are significant differences between solar and stellar flares when it comes to mass-loss ratio or flare energy levels, stellar flare events are still explained by the solar flare processes. In the studies such as Aschwanden et al. (2017); Gershberg (2005) and Hudson & Khan (1996), it is argued that magnetic reconnection processes are the dominant energy source in flare events.

In this study, both flare and spot activities of KOI 6652 (KIC 6044064) are examined. The results are compared with the chromospheric activity behaviour of UV Ceti-type stars.

The JHK brightnesses of the system are given as $13^{m}.485$, $12^{m}.976$, $12^{m}.853$ in the 2MASS All-Sky Survey Catalogue, respectively (Cutri et al. 2003). A detailed light curve analysis of the system cannot be found in the literature. However, the temperatures of the components were estimated by Kjurkchieva et al. (2017) to be 5095 K for the primary component and 3032 K for the secondary component. In the same study, the mass ratio (q) of the system was estimated as 0.4138. Examination of the light curves obtained from the Kepler observations revealed that the orbital period of the system is 5.063157 days. The mass and radius for the target are given as $0.71 M_{\odot}$ and $0.68 R_{\odot}$, respectively (Morton et al. 2016). The radius is given by Zhang & Showman (2018) as $4.151 R_{\odot}$ at the distance of 3186.626 pc. Davenport (2016) first noticed that the target exhibits flare activity. In this study, we analysed the light curve of the system and derived its synthetic curve. Considering the obtained synthetic curve, we have tried to detect the flare activity present.

2. DATA AND ANALYSES

The Kepler Space Telescope, which has observed more than 150,000 sources, was launched for the discovery of exoplanets (Borucki et al. 2010; Koch et al. 2010; Caldwell et al. 2010). The Kepler observations are the most sensitive photometric data ever obtained (Jenkins et al. 2010a,b). In addition to exoplanets, many variable stars have also been discovered (Slawson et al. 2011; Matijevič et al. 2012). There are many single and binary stars exhibiting spot and flare activity among them (Balona 2015). For the target, photometric data were taken from the Kepler Database (Slawson et al. 2011; Matijevič et al. 2012).

Long cadence (hereafter LC) data were used in all analyses. KIC 6044064 was observed for 1384.254 days, from JD 2454964.512414 to JD 2456424.001369, with some technical interruptions. After removing observations with large errors due to the technical problems, the phases were calculated using the ephemerides from the Kepler Mission database. The data were arranged into appropriate formats for the analysis of different variations such as flare activity, spot activity and $(O-C)$ variations. All the available long cadence data of KIC 6044064 are shown in Figure 1.

2.1. *Orbital Period Variation*

The minima times of the system were obtained without correction from the LC data. The minima times

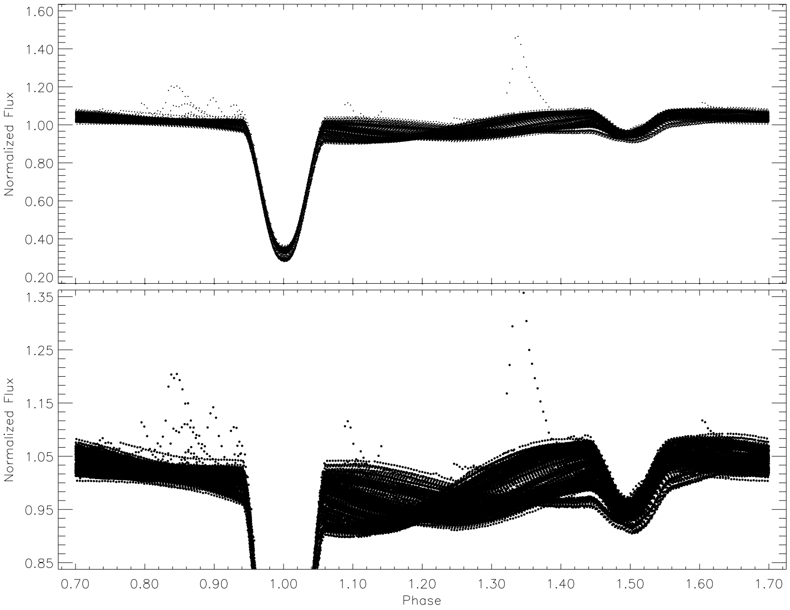

Fig. 1. The light variation obtained from the long cadence data taken from the Kepler database is plotted versus the phase depending on the orbital period.

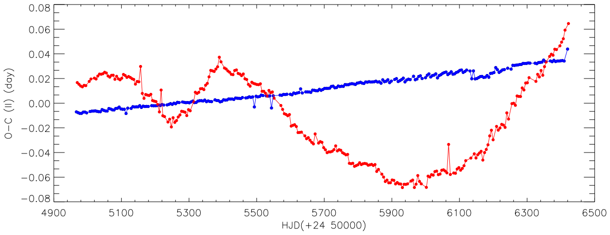

Fig. 2. The variations of $(O-C)_{II}$ residuals obtained after a linear correction are shown. The filled blue dots represent the $(O-C)_{II}$ residuals computed from the primary minima times, while the filled red dots show those computed from secondary minima times. The color figure can be viewed online.

were calculated using a script depending on the method described by Kwee & van Woerden (1956). Each minimum in the light curves was fitted separately using the high-order spline functions. Using these fits, a total of 525 minima times were obtained. 264 of them were computed from the primary minima, while 261 of them were calculated from the secondary minima. The deviations between observed and calculated minima times were calculated as $(O-C)$ differences. We show these differences by the term of $(O-C)_I$. We noticed that the $(O-C)$ differences show a linear trend due to the incorrect orbital period, which needs to be adjusted. Using the least squares method, we modelled the distribution of the $(O-C)$ differences versus the observation time. To remove the linear trend of the distribution, a linear correction given by Equation (1) was applied to the $(O-C)$ distribution.

$$JD\ (Hel.) = 24\,549666.71483(2) + 5^{d}.0630559(2) \times E, \tag{1}$$

where the term HJD (Hel.) is the Heliocentric Julian Day, while the first term on the right side of the equation is the epoch, and the second term is the orbital period of the system. The number in parenthesis seen in the equation is the error of each term on the right side. The parameter E is the cycle number.

In the last step we computed the deviations between the linear fit and the $(O-C)_I$ differences; we call these the secondary residuals $(O-C)_{II}$. In Figure 2, an interesting variation is seen in the plane of $(O-C)_{II}$ versus time. The $(O-C)_{II}$ residuals vary in time, but in different directions. The $(O-C)_{II}$ residuals of the primary minima still vary in a linear trend, while those of the secondary minima vary in a sinusoidal form. As indicated by Tran et al. (2013) and Balaji et al. (2015), the secondary minima are strongly affected by the position of the spotted area and its movement on the component, while the residuals of the primary minima are not affected as much.

2.2. *Light Curve Analyses*

To obtain an acceptable solution from the light curve analyses of the LC data, the distortion caused by

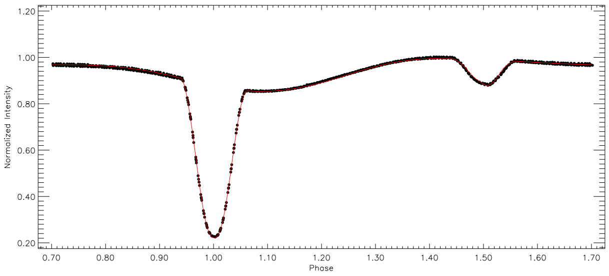

Fig. 3. The light curve obtained by using the data averaged with the interval of 0.005 and the synthetic light curve are shown. In the figure, the filled circles represent the observations, while the red line represents the synthetic light curve. The color figure can be viewed online.

the flare activity was removed from the light curve. Finding two consecutive cycles that were least affected by the sinusoidal variation, we averaged their data with a phase interval of 0.005. Using the PHOEBE V.0.32 software (Prša & Zwitter 2005), the light curve analysis was performed for these average data, shown by the filled black circles in Figure 3. The method used in the PHOEBE V.0.32 software is based on the 2015 version of Wilson-Devinney Code (Wilson & Van Hamme 2014). Several modes were first tried in the light curve analysis. The astrophysical and statistically acceptable solution was obtained in the detached mode, known as Mode 2.

There are several studies in the literature on the components of KIC 6044064. The temperatures of the primary and secondary components were given as 5095 K and 3032 K by Kjurkchieva et al. (2017), respectively. However, the initial analyses did not yield a statistically acceptable solution by taking these values. Because of this, using the calibrations given by Tokunaga (2000), we calculated the de-reddened colours from the infrared $(H-K)$ and $(J-H)$ color indexes given by Cutri et al. (2003) and then we calculated the temperature as 5375 K from these values. In the light curve analysis, the temperature of the secondary component was taken as a free parameter, while the temperature of the primary component was taken as 5375 K. The values for the albedos (A_1, A_2) and the gravity darkening coefficients (g_1, g_2) were determined according to convective stars for both components (Lucy 1967; Ruciński 1969). In addition, the linear limb-darkening coefficients (x_1, x_2) were taken from van Hamme (1993). The dimensionless potentials (Ω_1, Ω_2), the luminosity fraction of the primary component (L_1), and the inclination (i) of the system were taken as adjustable parameters. The synthetic curve obtained from the light curve analysis is shown in Figure 3, while the solution parameters are tabulated in Table 1. The parameters T_1 and T_2 are the temperatures, while r_1 and r_2 are the fractional radii of the components. The parameters $Co-Lat$, $Long$, R_{spot}, T_{spot} are the latitude, longitude, radius and temperature for each spot on the active component, respectively. The secondary component should be the active component, considering the temperatures of the components.

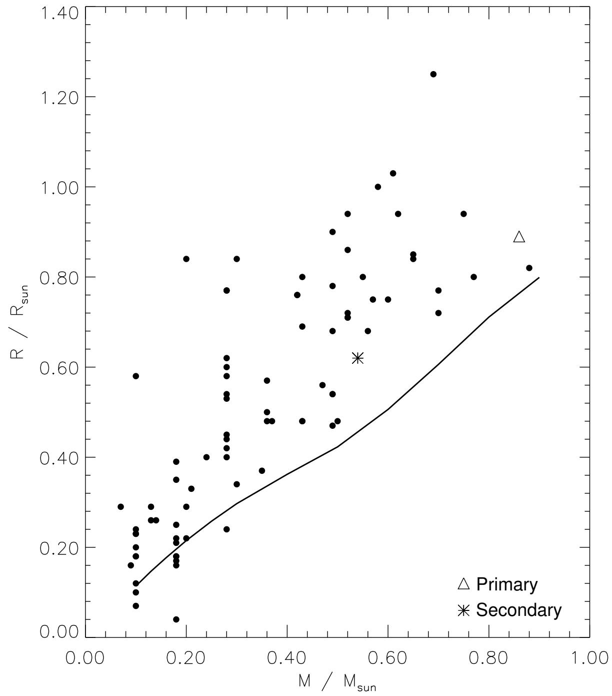

Fig. 4. The positions of the components are shown among UV Ceti type stars in the plane of mass-radius. The filled circles represent the target's analogues listed by Gershberg et al. (1999). The open triangle represents the primary component of KIC 6044064, while the asterisk shows the secondary component. The theoretical ZAMS model developed by Siess et al. (2000) is shown by the line.

Using the calibrations given by Tokunaga (2000), the spectral types of the components were determined as G7V + K9V. Using the same calibrations, the mass of the primary component was determined as 0.86 $M_\odot$ and that of the secondary as 0.54 $M_\odot$. Using Kepler's third law, the semi-major axis of the system was estimated to be $a = 13.88R_\odot$. Considering the estimated semi-major axis, the radii were obtained as $0.89R_\odot$ for the primary component and $0.62R_\odot$ for the secondary from their fractional radii.

Considering the variation at out-of-eclipses, we notice that the system exhibits chromospheric activity. At this point, we compare the system with its analogues listed in the Gershberg et al. (1999) cat-

TABLE 1

THE PARAMETERS OBTAINED FROM THE LIGHT CURVE ANALYSIS

Parameter	Value
q	0.948±0.005
$i(^{\circ})$	83.04±0.03
$T_1(K)$	5375 (fixed)
$T_2(K)$	3951±50
Ω_1	0.813±0.014
Ω_2	0.486±0.018
L_1/L_T	0.694±0.0010
L_2/L_T	0.306 (fixed)
g_1, g_2	0.32, 0.32 (fixed)
A_1, A_2	0.50, 0.50 (fixed)
$x_{1,bol}\ , x_{2,bol}$	0.61, 0.61 (fixed)
x_1, x_2	0.736, 0.736 (fixed)
$< r_1 >$	0.5585±0.0003
$< r_2 >$	0.2515±0.0013
$Co-Lat^{(rad)}_{SpotI}$	1.186(fixed)
$Long^{(rad)}_{SpotI}$	2.513(fixed)
$R^{(rad)}_{SpotI}$	0.611(fixed)
$T_{f\,SpotI}$	0.550 (fixed)
$Co-Lat^{(rad)}_{SpotII}$	1.196 (fixed)
$Long^{(rad)}_{SpotII}$	0.297 (fixed)
$R^{(rad)}_{SpotII}$	0.122 (fixed)
$T_{f\,SpotII}$	1.350 (fixed)

alogue in the mass-radius plane, shown in Figure 4. The filled circles in the figure represent well-known active stars listed in the catalogue, while the line represents the zero-age main sequence (ZAMS) taken from Siess et al. (2000).

2.3. *Rotational Modulation and Stellar Spot Activity*

It was seen that there is a remarkable sinusoidal variation excluding the flares at out-of-eclipses. Considering both the dominant flare activity and the components' temperatures, it is clear that this variation should be a rotational modulation effect caused by the stellar spots. Examination of the consecutive cycles in the light curves, their minimum location, and level change over a few cycles, shows that the spotted area must evolve rapidly and move on the active component. Therefore, it is not possible to model all the light variation at once. For this reason, the data were split into several sets, considering the spot minimum phases with their levels for the consecutive cycles. Consequently, the entire LC data were divided into 11 subsets and modelled with two sinus waves. In this calculation, a Python script based on the Fourier method is used, and an example model is shown in Figure 5.

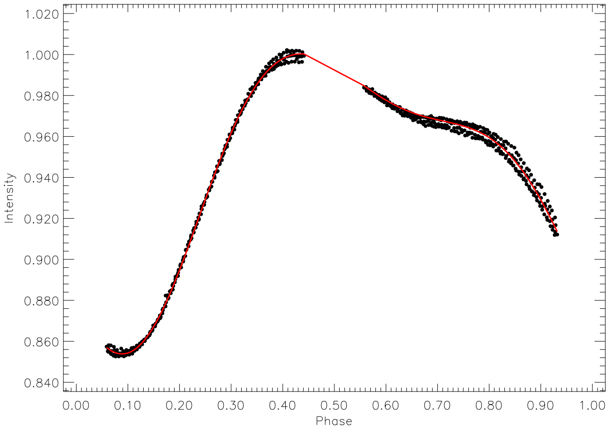

Fig. 5. The sinusoidal variation at out-of-eclipse between JD 2454982.188225 and JD 2454971.419273 is shown. In the figure, the black dots represent the observations, while the red line shows the model obtained by using the Fourier Method. The color figure can be viewed online.

The minima phases of the first sinusoidal variation show a temporal migration towards the early phases, while the minima phases of the second sinusoidal variation migrate in the same direction, but twice as fast as the previous one. This means that, at first sight, there are two spotted regions. However, we have noticed an interesting phenomenon that both the first and second sinusoidal variations should be caused by three separate spots in each area. Each of them separates into at least three spots because their minimum phases are separated into three parts by a phase interval of 0.33. These two distinct groups of spots and their migrations over time are shown in Figure 6.

As a result of the linear models created by the regression calculations with the least squares method, the spot migration periods of the first group were found to be 600.796±3.653 days (1.66±0.01 year), 657.726±3.653 days (1.80±0.01 year) and 610.665±7.305 days (1.67±0.02 year) from phase of 0.00 to 1.00, respectively. The spot migration periods of the second group were calculated as 1134.754±7.305 days (3.11±0.02 year), 1135.787±10.957 days (3.11±0.03 year) and 1106.286±7.305 days (3.03±0.02 year).

2.4. *Flare Activity and OPEA Model*

To study the flare behaviour of the system, all the variations apart from the flares are removed from the light curve. For this aim, we have used the synthetic curves derived by the light curve analysis for the geometrical effects and by the Fourier method for the sinusoidal variations.

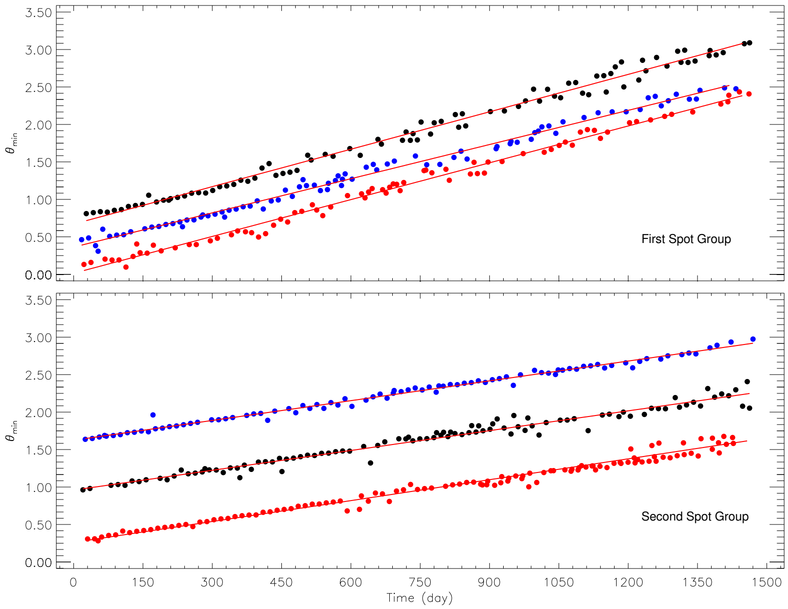

Fig. 6. The longitudinal spot migrations of the first group and their models are shown versus time in the upper panel, while they are shown for the second group in the lower panel. The filled black circles represent the first spot of both groups, the filled blue circles represent the second spot, while the filled red circles represent the third spot of the groups. The color figure can be viewed online.

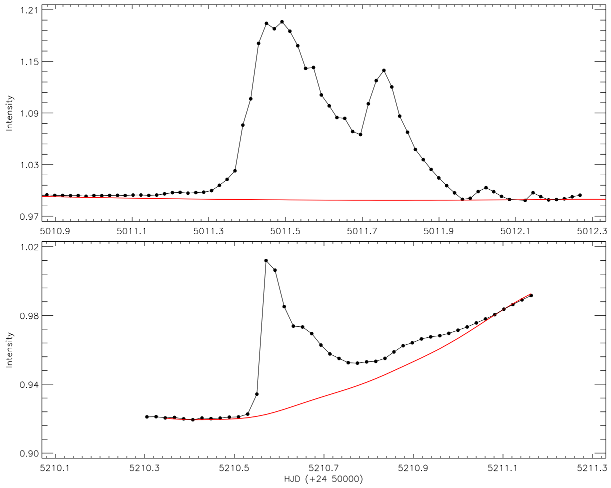

Fig. 7. Two flare examples detected from the target are shown. In the figure, the filled black circles show the observations, while the red lines show the quiescent levels defined by the Fourier method. The color figure can be viewed online.

In order to calculate the flare parameters, first of all, the flare beginning and end times need to be determined. Two examples are shown with their quiescent levels defined by the synthetic curves in Figure 7. In total, 44 flares with their parameters were determined. In the calculation, the equivalent durations were calculated using equation (2) defined by Gershberg (1972):

$$P = \int [(I_{flare} - I_0)/I_0]dt, \tag{2}$$

where P is the flare equivalent duration in seconds, I_{flare} is the flux at the moment of the flare, and I_0 is the quiescent flux of the system calculated by the Fourier method. As explained by Dal & Evren (2010, 2011), the term L in the flare energy calculation ($E = L \times P$) causes an incorrect decomposition of the stars in the plane $(B - V)$ - $\log(P_u)$ when comparing the flares of stars from different spectral types. For this reason, we do not calculate the flare energies, and the equivalent duration parameter is used for the analyses or comparisons.

Examining the relationships between the flare parameters, it is seen that the flare equivalent durations as a rule are distributed as a function of the total flare time. Following Dal & Evren (2010, 2011), regressions in SPSS V17.0 (Green et al. 1996) and GraphPad Prism V5.02 (Dawson & Trapp 2004) software were used to try to find the best function to model the distribution of flare equivalent durations via the flare total time on a logarithmic scale. In this step, the regression calculations showed that the best model is an exponential function known as the One Phase Exponential Association (hereafter

TABLE 2

PARAMETERS DERIVED FROM THE OPEA MODEL*

Parameter	Values	95 % Confidence Intervals
y_0	0.958951	0.447653 to 1.47025
$Plateau$	3.9833	3.33968 to 4.62692
K	0.00002272	0.00001006 to 0.00003537
Tau	44022.7	28272.0 to 99399.2
$Half - time$	30514.2	19596.6 to 68898.3
$Span$	3.02435	2.53178 to 3.51692
R^2	-	0.85

*Using the least squares method.

OPEA) function. The OPEA is a special function with term *Plateau* defined by Equation (3) (Motulsky 2007; Spanier & Oldham 1987):

$$y = y_0 + (Plateau - y_0) \times (1 - e^{-k \times x}), \quad (3)$$

where the term y is the equivalent duration in the logarithmic scale; k is a constant and x is the total flare time, while y_0 is the theoretical flare equivalent duration obtained for the minimum total flare time (Dal & Evren 2011). The term *Plateau* defines the upper limit for the equivalent duration obtained from a given star. It means that the *Plateau* parameter gives a certain information about the maximum flare energy level of that star. In fact, the *Plateau* is the maximum equivalent duration. For this reason, the *Plateau* parameter is defined as the saturation level for the flare activity in the observed wavelength range for this particular target (Dal & Evren 2011). In order to derive the synthetic curve of the best model, we used the program GraphPad Prism V5.02, in which we used the least squares method for the non-linear regression calculations.

The obtained model is shown in Figure 8. The calculated model parameters are listed in Table 2. The *span* value listed in the table is the difference between *Plateau* and y_0 values. The $half-life$ value is half of the first x value at which the maximum flare equivalent duration is reached. In other words, it is half of the total flare time at which the first highest flare energy is seen.

KIC 6044064 was observed for a total of 1384.254 days (33222.09917 hours). From these observations, 44 flares were detected. The phases of 44 flares were calculated depending on the orbital period of the system, and the flare phase distribution of 44 flares is shown in Figure 9. The sum of equivalent durations is 35519.622 seconds over all flares. Two separate flare frequencies, N_1 and N_2, have been defined in the literature by Ishida et al. (1991). These frequencies are given by equations (4, 5):

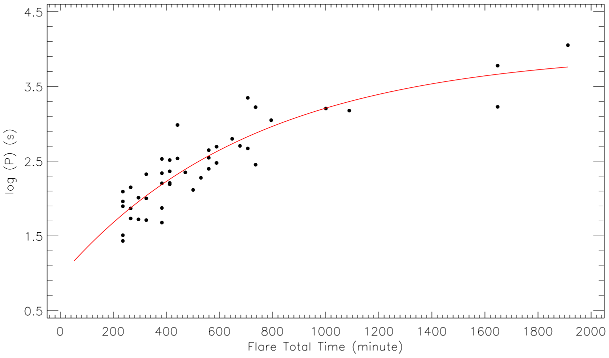

Fig. 8. The OPEA model obtained for 44 flares is shown. In the figure, the filled circles represent the log(P) values computed from the observed flares, while the red line shows the derived OPEA model. The color figure can be viewed online.

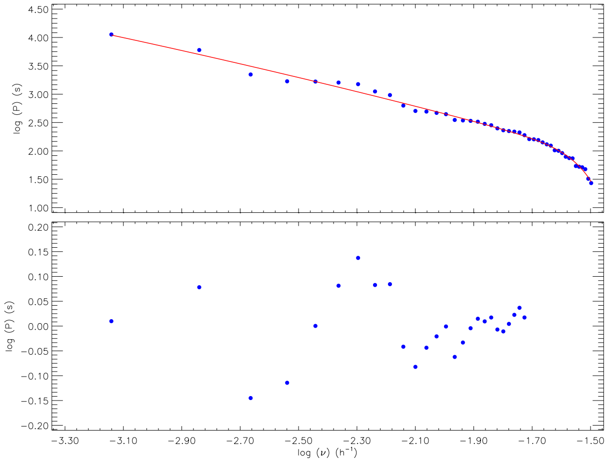

Fig. 9. The flare cumulative frequency distribution and its the exponential model derived for 44 flares are shown in the upper panel, while the residuals are shown in the bottom panel. The color figure can be viewed online.

$$N_1 = \Sigma n_f \;/\; \Sigma T_t, \quad (4)$$

$$N_2 = \Sigma P \;/\; \Sigma T_t, \quad (5)$$

where Σn_f is the total number of flares, and ΣT_t is defined as the total observation time. ΣP is the sum of the equivalent duration over all flares. According to these definitions, the frequencies were found to be N_1 =0.00132 h^{-1} and N_2 =0.00030.

We also computed the flare cumulative frequency distributions depending on each different energy limit. Gershberg (1972) defined the flare cumulative frequency distribution calculated separately for

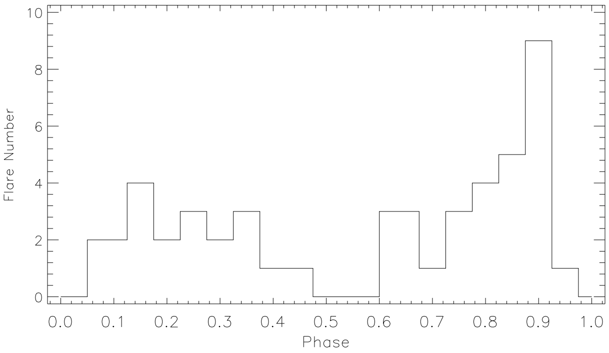

Fig. 10. The distribution of the flare total number obtained in the phase intervals of 0.05 is shown versus the phase.

each different energy limit to reveal the character of the flare energy for given a star. Because of the above reasons, the flare equivalent durations is also used instead of the flare energy to compute the flare cumulative frequencies in this study. The obtained flare cumulative frequency distributions are shown in Figure 9. As can be seen in the figure, the flare cumulative frequencies exhibit a distribution in the form of an exponential function. In fact, the least squares method showed that an exponential function seems to be the most appropriate function to fit these distributions; hence we modelled the distributions with the exponential function. The obtained exponential functions are represented by the red line in Figure 9.

The standard models show that the flare energies emerge in the magnetic loops where the spots are located (Gershberg 2005; Benz 2008) at their foot points. Therefore, both the cool spots and the flares are expected to have the same phase distribution. To compare the phase distributions of these two activity structures obtained from KIC 6044064, the phase of each flare was calculated depending on the orbital period, then we obtained the total number of flares in each 0.05 phase interval. Their variation is shown in Figure 10.

3. RESULTS AND DISCUSSION

3.1. *Orbital Period Variation*

The $(O-C)_{II}$ residuals seem to vary in different ways. According to Tran et al. (2013) and Balaji et al. (2015), magnetic activity causes an affect on the variations of the minima times. The trends of primary and secondary minima time variations are expected to separate from each other due to the chromospheric activity. In the case of KIC 6044064, this effect reveals itself on the time variation of the secondary minima. The residuals of the secondary minima times exhibit a sinusoidal variation around zero with a large amplitude, although the primary minima times still show a linear trend. The linear corrections could not reduce the trend of the primary minimum residuals to zero, since the $(O-C)_I$ trend of the secondary minima times has a larger slope than that of the primary minima. It is more likely that the $(O-C)_{II}$ residuals of the primary minima should be a small part of a sinusoidal long-term oscillation due to the chromospheric activity.

3.2. *Classification*

The temperature of the primary component was found to be 5375 K, and that of the secondary was 3951 K. Thus, their spectral types were determined as G7V + K9V depending on the JHK brightness. Considering the temperatures and the estimated masses, we compared the system with its analogues. For this aim, we compared the components with other young flare stars on the mass-radius plane, which can be seen in Figure 4. It is expected that the flaring young stars listed by Gershberg et al. (1999) should be close to the ZAMS modelled by Siess et al. (2000). However, these stars appear to be somewhat evolved out of the main sequence, according to their positions on the mass-radius plane. It is possible that their calculated radii could be too large due to the high level chromospheric activity effects. Both the positions of the components in the mass-radius plane and the observed flare and spot activities indicate that KIC 6044064 should be an eclipsing binary system of the BY Dra type.

Both flare and stellar spot activities make it one of the stars having a high level of activity. The target has several rapidly evolving spots located on three active longitudes, which are separated from each other by 120 degrees inside two latitude bands.

In addition, the flare parameters are much higher than those obtained from all other chromospheric active stars. For example, KOI 6652 has a higher activity level than YY Gem, which has the same physical properties as KOI 6652 (Kochukhov & Shulyak 2019).

3.3. *Spots*

Indeed, KIC 6044064 has a high level of chromospheric activity. Apart from the flare activity, a sinusoidal variation is seen with a rapidly changing asymmetry at out-of-eclipses. This variation is caused by the evolving cool spots as well as their rapid longitudinal migration. There are two active longitudes on the solar surface, known as Carrington Coordinates, with a separation of 180° from each other. According to Bonomo & Lanza (2012), there are several active longitudes where stellar spots are formed. According to some authors, the active longitudes are stable structures with a constant rotational velocity relative to each other, although some authors claim that the active longitudes cannot have a constant rotational velocity, but have different rotational velocities relative to each other (Richardson 1947; Lopez Arroyo 1961; Stanek 1972; Bogart 1982). In the case of KIC 6044064, there are two different spot groups consisting of three spots located with a phase interval of 0.33 relative to each other. The phase interval of 0.33 corresponds to a longitude difference of 120°. Both spotted areas on the stellar surface show migration in the same direction, but with different velocities. It is noteworthy here that each spot in a spot group shows the same longitudinal motion with a longitude interval of 120° at the same velocity. In particular, all three spots in the second group move at exactly the same velocity, so that their longitudinal positions on the stellar surface do not change at all relative to each other. For this reason, the slopes of the linear models of their longitudinal migrations have almost the same value up to the 4th digit.

As a result, the average migration period was found to be 623.063±4.870 days (1.71±0.01 year) for the first spot group, while it was 1125.514±7.305 days (3.08±0.02 year) for the second group. The values of the migration periods indicate that KIC 6044064 is generally a solar analogue. This is because the period of each group is in agreement with the periods between 1.5-3.0 years found for the active longitude migrations of the solar spots (Berdyugina & Usoskin 2003). The existence of fixed migrations and the migration period values can help us to configure the stellar surface. It is clear that both groups of spots should be located in the latitudes above the stellar co-rotation latitude, assuming that KIC 6044064 exhibits the standard differential rotation. The spots are located at a latitude where the rotation velocity is lower than the mean stellar rotation velocity, hence the minima of the sinusoidal variations migrate toward the increasing phases in the light curves. Moreover, the fact that the spots in each group move as if they were locked to each other indicates that the spots in each group should be located at nearly the same latitude. All these situations give the impression that there must be two spot-belts in two upper latitudes. The spotted regions should surround the stellar surface at two different latitudes above the co-rotation latitude, and different regions of the belts appear more active than other parts. Taking into account the average longitudinal migration periods, the trend of which is shown in the bottom panel of Figure 6, the second spot belt should be at higher latitudes. However, it should be noted here that these spot belts may not be located on the same component. This is because both components are most likely candidates for exhibiting chromospheric activity.

3.4. *Flares*

There should be three active longitudes on the secondary component, and the active longitudes are located with a longitude interval of 120 degrees. According to this scenario, it is possible that an observer can detect some flares from the longitudes per 120 degrees on the surface of the secondary component. In this case, we expect a nearly homogeneous phase distribution for the flares coming from the target. On the other hand, as can be seen in Figure 10, the total number of flares detected in each phase interval of 0.05 increases towards phases 0.15 and 0.85. The flare number starts to increase after phase 0.70 and decreases before phase 0.40. However, at phase 0.00, the flare number suddenly drops to almost zero. It is possible that during the primary minima, the active component is eclipsed by the other component towards the observer. Consequently, the flare frequency varies from one phase interval to the next; and it must reach a maximum between phases 0.85-0.15. Because of tidal effects, the flare occurring possibility on the surface facing the other component becomes higher than anywhere else on the surface, although the flares can occur anywhere on the stellar surface.

The *Plateau* value was determined to be 3.983 s over 44 flares detected from KIC 6044064. This value is so high that the secondary component must be compared with similar close binaries exhibiting flare activity. In this regard, we compared its flare nature with those obtained from KIC 9641031, KIC 9761199, KIC 11548140, KIC 12004834 (Yoldaş & Dal 2016, 2017b,a, 2019). This value was found to be 1.232 s for KIC 9641031, 1.951 s for KIC 9761199, 2.312 s for KIC 11548140 and 2.093 s for KIC 12004834. The plateau values of KIC 6044064 are much higher than those of its analogues. For this reason, it should be much more appropriate to compare the target with UV Ceti type single stars, which exhibit flare activity with high frequency and high energy level. Therefore, we compared the secondary component with EV Lac. The plateau value of EV Lac is 3.014 s (Dal & Evren 2011). It is clear that the plateau value of KIC 6044064 is also higher than that obtained from EV Lac, which is known to be one of the most active UV Ceti-type stars. This means that KIC 6044064 has a remarkably high level of magnetic activity, which makes the system an important target to understand the magnetic activity behaviour in binary systems.

According to the longitudinal migration behaviour, the secondary component should have a Solar-like nature. On the other hand, if we consider the flare phase distribution together with its computed plateau value, the tidal effect between the components should have a dominant effect on the magnetic activity of the target. The flare frequency distribution versus phase is effected by both the tidal effect and the overall flare power. In fact, its plateau value is much higher than the values obtained from any other single or binary targets.

Dal & Evren (2010, 2011); Dal (2012); Yoldaş & Dal (2016, 2017b,a, 2019); Dal (2020) discuss that the plateau parameter depends on both the magnetic field strength and the electron density. Thus, considering this target having the highest plateau parameter among its analogues, KIC 6044064 should have the highest magnetic field strength or/and the highest electron density. This situation should be a consequence of its binary nature under a strong tidal effect.

Apart from the plateau value, the half-life parameter was found to be 30514.2 s. This value is almost 70 times greater than the values obtained for single flare stars, while it is about 13 times greater than the value obtained for binary systems containing a dMe-type component. The half-life parameter is 433.10 s for DO Cep, 334.30 s for EQ Peg, and 226.30 s for V1005 Ori (Dal & Evren 2011). Similarly, it is 2291.7 s for KIC 9641031, 1014 s for KIC 9761199, and 2233.6 s for KIC 1548140. For the flare time scales, the longest observed flare of KIC 11548140 has a total flare time of 22185.361 s, while it is 114760.368 s for KIC 6044064. The flare time scale values are an indicator of the length of the magnetic loop. In this case, the magnetic loop length of KIC 6044064 is remarkably larger than that of all other targets (Dal 2012, 2020). This situation should also be an indicator of the tidal interaction between its components, making the target an important laboratory for researchers modeling the magnetic interaction of binary systems.

3.5. *Summary*

As a result, KIC 6044064 appears to be a BY Dra binary whose components should be cool main sequence stars with the potential to exhibit chromospheric activity. Incidentally, the spot distributions and their movements are quite remarkable. Considering the longitudinal spot migration behaviour, the target appears to be a solar analogue. In this case, it should not be a young star like the pre-main sequence stars. Therefore, the target is expected to have a stable activity cycle like the Sun. To determine whether it has a stable cycle or not, more observations are needed. For this reason, the target appears to be one of the important systems that should be included in the long-term photometric or high-resolution spectral observation patrol.

REFERENCES

Aschwanden, M. J., Caspi, A., Cohen, C. M. S., et al. 2017, ApJ, 836, 17

Balaji, B., Croll, B., Levine, A. M., & Rappaport, S. 2015, MNRAS, 448, 429

Balona, L. A. 2015, MNRAS, 447, 2714

Benz, A. O. 2008, LRSP, 5, 1

Berdyugina, S. V. & Usoskin, I. G. 2003, A&A, 405, 1121

Bogart, R. S. 1982, SoPh, 76, 155

Bonomo, A. S. & Lanza, A. F. 2012, A&A, 547, 37

Borucki, W. J., Koch, D., Basri, G., et al. 2010, Sci, 327, 977

Caldwell, D. A., Kolodziejczak, J. J., Van Cleve, J. E., et al. 2010, ApJ, 713, 92

Carrington, R. C. 1859, MNRAS, 20, 13

Clark, D. H. & Stephenson, F. R. 1978, QJRAS, 19, 387

Cutri, R. M., Skrutskie, M. F., van Dyk, S., et al. 2003, VizieR Online Data Catalog: II/246

Dal, H. A. 2012, PASJ, 64, 82

_________. 2020, MNRAS, 495, 4529

Dal, H. A. & Evren, S. 2010, AJ, 140, 483

_________. 2011, AJ, 141, 33

Dawson, B. & Trapp, R. 2004, Basic & Clinical Biostatistics 4/E, Lange Basic Science (McGraw-Hill Education)

Gershberg, R. E. 1972, Ap&SS, 19, 75

_________. 2005, Solar-Type Activity in Main-Sequence Stars (Berlin, Heidelberg: Springer)

Gershberg, R. E., Katsova, M. M., Lovkaya, M. N., Terebizh, A. V., & Shakhovskaya, N. I. 1999, A&AS, 139, 555

Gershberg, R. E. & Shakhovskaia, N. I. 1983, Ap&SS, 95, 235

Green, S. B., Salkind, N. J., & Jones, T. M. 1996, Using SPSS for Windows; Analyzing and Understanding Data, (1st. ed.; NJ, USA: Prentice Hall PTR)

Haisch, B., Strong, K. T., & Rodono, M. 1991, ARA&A, 29, 275

Hodgson, R. 1859, MNRAS, 20, 15

Hudson, H. S. & Khan, J. I. 1996, ASPC, 111, 135
Ishida, K., Ichimura, K., Shimizu, Y., & Mahasenaputra. 1991, Ap&SS, 182, 227
Jenkins, J. M., Caldwell, D. A., Chandrasekaran, H., et al. 2010a, ApJ, 713, 87
Jenkins, J. M., Chandrasekaran, H., McCauliff, S. D., et al. 2010b, SPIE, 7740
Kjurkchieva, D., Vasileva, D., & Atanasova, T. 2017, AJ, 154, 105
Koch, D. G., Borucki, W. J., Basri, G., et al. 2010, ApJ, 713, 79
Kochukhov, O. & Shulyak, D. 2019, ApJ, 873, 69
Kron, G. E. 1950, AJ, 55, 69
Kunkel, W. E. 1975, IAUS, 67, 15
Kwee, K. K. & van Woerden, H. 1956, BAN, 12, 327
Lopez Arroyo, M. 1961, Obs, 81, 205
Lucy, L. B. 1967, ZA, 65, 89
Marcy, G. W. & Chen, G. H. 1992, ApJ, 390, 550
Matijevič, G., Prša, A., Orosz, J. A., et al. 2012, AJ, 143, 123
Mirzoian, L. V. 1990, IAUS, 137, Flare Stars in Star Clusters, ed. L. V. Mirzoyan, B. R. Pettersen, & M. K. Tsvetkov, (Boston, MA: Kluwer Academic), 1
Morton, T. D., Bryson, S. T., Coughlin, J. L., et al. 2016, ApJ, 822, 86
Motulsky, H. 2007, GraphPad Software, 31, 39
Pettersen, B. R. 1989, SoPh, 121, 299
_________. 1991, MmSAI, 62, 217
Pigatto, L. 1990, IAUS, 137, Flare Stars in Star Clusters, and the Solar Vicinity, ed. L. V. Mirzoian, B. R. Pettersen, & M. K. Tsvetkov (Boston, MA: Kluwer Academic), 117
Prša, A. & Zwitter, T. 2005, ApJ, 628, 426
Richardson, R. S. 1947, PA, 55, 120
Ruciński, S. M. 1969, AcA, 19, 245
Siess, L., Dufour, E., & Forestini, M. 2000, A&A, 358, 593
Skumanich, A. 1972, ApJ, 171, 565
Slawson, R. W., Prša, A., Welsh, W. F., et al. 2011, AJ, 142, 160
Spanier, J. & Oldham, K. B. 1987, An Atlas of Functions (Bristol, PA: Taylor & Francis/Hemisphere)
Stanek, W. 1972, SoPh, 27, 89
Stauffer, J. R. 1991, ASIC 340, Angular Momentum Evolution of Young Stars, ed. S. Catalano & J. R. Stauffer, (Boston, MA: Kluwer Academic Publishers), 117
Tokunaga, A. T. 2000, in Allen's astrophysical quantities (4th. ed.; New York, NY: AIP Press; Springer), 143
Tran, K., Levine, A., Rappaport, S., et al. 2013, ApJ, 774, 81
van Hamme, W. 1993, AJ, 106, 2096
Wilson, R. E. & Van Hamme, W. 2014, ApJ, 780, 151
Wittmann, A. D. & Xu, Z. T. 1987, A&AS, 70, 83
Yoldaş, E. & Dal, H. A. 2016, PASA, 33, 16
_________. 2017a, PASA, 34, 60
_________. 2017b, RMxAA, 53, 67
_________. 2019, RMxAA, 55, 73
Zhang, X. & Showman, A. P. 2018, ApJ, 866, 2

E. Yoldaş: Department of Astronomy and Space Sciences, University of Ege, Bornova, 35100 İzmir, Turkey (ezgiyoldas@gmail.com).

Revista Mexicana de Astronomía y Astrofísica, **57**, 363–379 (2021)

https://doi.org/10.22201/ia.01851101p.2021.57.02.09

THE FIRST DETAILED ANALYSIS ON THE ASTROPHYSICAL PROPERTIES OF THE ECCENTRIC BINARY V990 HER

E. Kiran[1], V. Bakiş[1], H. Bakiş[1], and Ö. L. Değirmenci[2]

Received February 11 2021; accepted June 7 2021

ABSTRACT

We present accurate physical parameters of the eccentric binary system V990 Her which has an orbital period of $P = 8.193315 \pm 0.000003$ days using its photometric and spectroscopic data. The physical parameters of the components were derived as $T_{\rm eff1}= 8000 \pm 200$ K, $T_{\rm eff2}= 7570 \pm 200$ K, $M_1 = 2.01 \pm 0.07\ M_\odot$, $M_2 = 1.83 \pm 0.03\ M_\odot$, $R_1 = 2.22 \pm 0.02\ R_\odot$, $R_2 = 2.12 \pm 0.01\ R_\odot$, $\log(L_1/L_\odot) = 1.25 \pm 0.04$, $\log(L_2/L_\odot) = 1.12 \pm 0.05$. Our findings revealed that both components are slightly evolved from the zero-age main sequence with an age of 6.3×10^8 years. We estimated an apsidal motion with a period of $U = 14683 \pm 2936$ years in the system and the internal structure constants of the components were derived for the first time.

RESUMEN

Presentamos parámetros físicos precisos para la binaria excéntrica V990 Her, cuyo período es $P = 8.193315 \pm 0.000003$ días, mediante datos fotométricos y espectroscópicos. Para los parámetros físicos de las componentes obtuvimos los siguientes valores: $T_{\rm eff1}{=}8000 \pm 200$ K, $T_{\rm eff2}= 7570 \pm 200$ K, $M_1 = 2.01 \pm 0.07\ M_\odot$, $M_2 = 1.83 \pm 0.03\ M_\odot$, $R_1 = 2.22 \pm 0.02\ R_\odot$, $R_2 = 2.12 \pm 0.01\ R_\odot$, $\log(L_1/L_\odot) = 1.25 \pm 0.04$, $\log(L_2/L_\odot) = 1.12 \pm 0.05$. Nuestras soluciones revelan que ambas componentes han evolucionado de la secuencia principal de edad cero, y que tienen edades de 6.3×10^8 años. Estimamos que el movimiento absidal del sistema tiene un período de $U = 14683 \pm 2936$ y obtenemos por primera vez las constantes de la estructura interna de las componentes.

Key Words: binaries: eclipsing — stars: individual: V990 Her — techniques: photometric — techniques: spectroscopic

1. INTRODUCTION

Apsidal motion in detached eclipsing binaries with eccentric orbits is one of the methods used to examine the effects of the tidal distortion on the dynamical evolution of the binary and to test stellar evolution models. Orbital elements and absolute parameters of the components of such systems are required to estimate the internal structure constants (ISCs) of the components which are tests of stellar evolutionary models. Based on this motivation, we have examined the V990 Her binary system, which has not been studied in detail before.

V990 Her (HD169888, GSC 01581 01786)($\alpha_{2000} = 18^{\rm h}25^{\rm m}56^{\rm s}.71$, $\delta_{2000} = 21^\circ 36' 21''.34$) is an early type (A0, Cannon & Pickering, 1993) eclipsing binary system, which was classified as an Algol type by Kazarovets et al. (1999). Later the system was listed in the eccentric eclipsing binary systems catalogue published by Otero et al. (2006) reporting the light elements as $T_0(HJD) = 2448048.755$, $P = 8^d.19329$. McDonald et al. (2012) reported the effective temperature $T_{\rm eff} = 7514$ K and luminosity $L = 27.45 L_\odot$ of the system. The binary type of the system is given as detached main sequence system (DM) by Avvakumova et al. (2013).

In the following section (§2), we present information about the photometric and spectroscopic observations and reduction procedures of the data used in our analysis of the V990 Her system. The analysis of the data is given in § 3. In § 4 and § 5 we present the results and the discussion.

---

[1] Department of Space Sciences and Technologies, Faculty of Science, Akdeniz University, 07058, Antalya, Turkey.

[2] Department of Astronomy and Space Sciences, Faculty of Science, Ege University, 35100, Bornova - İzmir, Turkey.

2. OBSERVATIONS AND DATA REDUCTION

2.1. *Photometric Data*

In this study, both new observational and survey data (available to the public) were used for the photometric analysis.

Time series photometric observations of V990 Her were made between 2018-2019 using the 0.6 m automated telescope (T60) of the TÜBİTAK National Observatory (TUG), which is equipped with a 2048×2048 pixels FLI ProLine 3041–UV CCD camera with a pixel size of $15\times15\,\mu\text{m}^2$. The Akdeniz University 0.25 m telescope (AUT25) which is equipped with a 2184×1472 pixels QSI632ws CCD camera with a pixel size of 6.8 μ was also used. Magnitudes of the system in different passbands were extracted from the reduced **Bessel** VRI photometric frames with the PHOT package in IRAF[3].

Additional photometric data of the system have been collected from four sources, the Hipparcos and Tycho Catalogues (Esa 1997), the All Sky Automated Survey (ASAS-3) (Pojmanski & Maciejewski 2004) Database, the Multi-site All-Sky CAmeRA (MASCARA) (Talens et al. 2017) Survey and the QuickLook Pipeline (QLP) light curves (LCs) observed by the Transiting Exoplanet Survey Satellite (TESS) and produced by the MIT QuickLook Pipeline (QLP) (Huang et al. 2020). To obtain the times of minima to be used in the $O-C$ analysis in § 3.1 we used the MASCARA LCs published by Burggraaff et al. (2018) and the TESS QLP LCs (Sector 26) which are available at the Mikulski Archive for Space Telescopes (MAST) as a High Level Science Product. The photometric data taken from Hipparcos photometry and ASAS-3 were not sufficient to specify the minimum depth of the system. Therefore, we prefer to use only our T60 and AUT25 photometric data for the LCs analysis (see § 3.3 and § 3.6).

2.2. *Spectroscopic Data*

Spectroscopic data were collected by using the eShel spectrograph, which has a resolving power of 12000 covering the 4045-8100 Å wavelength range in 27 orders that is connected to the 60 cm telescope (UBT60) of Akdeniz University with a 20-m fiber. More information on the UBT60 telescope system is given by Bakış et al. (2020). We collected 29 spectra of V990 Her on different observing nights during June-September 2017 and August-October 2018 seasons (see Table 1). In Table 1, the columns show the order of the observing night, mid-observing time of the spectra in heliocentric Julian date, total exposure time, S/N ratio value around 5500 Å and the orbital phase calculated with the ephemeris of the primary minimum given in equation (1).

IRAF was used for the reduction of the spectroscopic data and for the measurement of the components' radial velocities (RVs). In each observing night, bias, dark frames and flat spectra from a tungsten lamp were obtained for image reduction. Order aperture extractions and elimination of scattered light through the orders were made by using the IRAF ÉCHELLE package. The wavelength calibration was performed with thorium-argon lamp spectra which were taken before and after each object spectrum.

3. ANALYSIS

3.1. *Improved Ephemerides and Apsidal Motion*

Before attempting the photometric and spectroscopic analysis, the available ephemerides of the system given by Otero et al. (2006) were improved. Some photometric minimum data of V990 Her were published by Kreiner (2004), which were used, together with the newly obtained minima times, for the $O-C$ analysis. We measured two secondary and one primary times of minima from the MASCARA LCs and two primary and one secondary times of minima from the TESS QLP LCs. The measured original times of minima in units of BJD from TESS LCs were converted to HJD unit by using online applets[4] (Eastman et al. 2010). Additionally, we obtained three primary and one secondary times of minima during our photometric observations. The Kwee & van Woerden (1956) method was used to determine the new times of minima and their corresponding errors for our observations. The obtained times of minima are listed in Table 2 in line with the literature; their uncertainty, epoch and $O-C$ values computed with the linear light elements in equation (1), type of minima ("pri" for primary and "sec" for secondary minimum), observational method ("ccd" for charge-coupled device observations) are also listed; the references are given in the last column.

When we performed a linear $O-C$ fit to all the primary and secondary minimum times given in Table 2 by using the unweighted least squares method, we found that the $O-C$ differences between the observed and the calculated times of minima regarding to the primary minimum behave in opposite phases

---

[3] IRAF is distributed by the National Optical Observatories, operated by the Association of Universities for research in Astronomy, Inc., under cooperative agreement with the National Science Foundation.

[4] https://astroutils.astronomy.osu.edu/time/index.html.

TABLE 1

JOURNAL OF SPECTROSCOPIC OBSERVATIONS[*]

No	Date (YYYYMMDD)	Julian Date (HJD)	Exp. Time (s)	S/N	Orbital Phase
1	20170516	2457890.3826	3000	40	0.178
2	20170606	2457911.4226	3000	40	0.746
3	20170611	2457916.4894	3000	110	0.365
4	20170612	2457917.5082	3000	110	0.489
5	20170622	2457927.4824	3000	40	0.706
6	20170702	2457937.4004	3000	110	0.917
7	20170703	2457938.4406	3000	50	0.044
8	20170704	2457939.5348	3000	100	0.177
9	20170709	2457944.4475	3000	100	0.777
10	20170711	2457946.4449	3000	135	0.021
11	20170719	2457954.4968	3000	100	0.003
12	20170720	2457955.3306	3000	110	0.105
13	20170723	2457958.4583	4200	140	0.487
14	20170802	2457968.3904	3000	140	0.699
15	20170918	2458015.3474	6600	50	0.430
16	20170920	2458017.3004	6000	50	0.669
17	20170928	2458025.2668	7200	40	0.641
18	20171011	2458038.2554	6000	50	0.226
19	20180828	2458359.3891	3000	110	0.421
20	20180829	2458360.3098	3000	110	0.533
21	20180913	2458375.3204	3000	70	0.365
22	20180917	2458379.3137	3000	80	0.853
23	20180918	2458380.3664	3000	110	0.981
24	20180919	2458381.3540	3000	100	0.102
25	20180922	2458384.2969	3000	110	0.461
26	20181002	2458394.3723	3000	40	0.691
27	20181003	2458395.3006	3000	40	0.804
28	20181005	2458397.2865	3000	140	0.046
29	20181007	2458399.2858	3000	125	0.290

[*] S/N ratio refers to the wavelength region around 5500 Å.

compared to those of the secondary minima. Then we applied the unweighted least squares fits to the primary and secondary eclipsing times separately and obtained the new linear ephemerides as follows (numbers in parentheses indicate errors in the last digit, and E is the number of cycles):

$$MinI(HJD) = 2448048.752(7) + 8.193314(6) \times E, \tag{1}$$

$$MinII(HJD) = 2448052.398(7) + 8.193316(7) \times E. \tag{2}$$

This result is a clear sign that the system shows apsidal motion. Therefore, we decided to perform an apsidal motion analysis using the times of minima (except for 2453177.7065 due to its large deviation from the expected location in the $O-C$ diagram) given in Table 2. To model the observed $O-C$s we used the equation given by Giménez & Bastero (1995) (equation 15 in their paper). We applied a differential correction method to represent the corrections to the input values of the parameters, which are selected as adjustable, and used the unweighted least squares method to obtain them. Unfortunately, when we selected all five parameters as adjustable, we were unable to get a convergent solution. The main reason for this may be that the range covered by the times of minima available is short compared to the apsidal period of the system.

In order to reduce the number of the adjustable parameters and thus obtain an acceptable solution, we decided to determine the orbital eccentricity from the shape of the system's LC. In a LC of an eccentric eclipsing binary system, $e\cos w$ and $e\sin w$, the combinations of orbital eccentricity (e) with the longitude (w) of the periastron, are related with the amount of displacement of the secondary minimum with respect to the primary minimum and with the durations of the minima, respectively.

TABLE 2

TIMES OF MINIMA OF V990 HER

JD (Hel.) 2400000+	Error	E	$O-C$	Type	Method	Reference
48048.7550		0.0	0.0030	pri	ccd	Otero et al. (2006)
48052.401		0.5000	-0.4477	sec	ccd	Otero et al. (2006)
53177.7065*	0.0016	626.0	-0.0601	pri	ccd	Zakrzewski,B. (SuperWASP) unpublished
53746.7457	0.0024	695.5	-0.4477	sec	ccd	Zakrzewski,B. (ASAS-3) unpublished
53751.2885	0.0027	696.0	-0.0100	pri	ccd	Zakrzewski,B. (ASAS-3)unpublished
57192.4960	0.001	1116.0	0.0056	pri	ccd	This study (MASCARA)
57212.5300	0.002	1118.5	-0.4437	sec	ccd	This study (MASCARA)
57253.4970	0.001	1123.5	-0.4433	sec	ccd	This study (MASCARA)
58249.4300	0.010	1245.0	0.0021	pri	ccd	This study (AUT25)
58290.4000	0.01	1250.0	0.0055	pri	ccd	This study (AUT25)
58634.5000	0.01	1292.0	-0.0137	pri	ccd	This study (AUT25)
58646.3500	0.01	1293.5	-0.4537	sec	ccd	This study (AUT25)
59011.4045	0.0005	1338.0	-0.0016	pri	ccd	This study (TESS)
59019.5977	0.0006	1339.0	-0.0017	pri	ccd	This study (TESS)
59023.2540	0.001	1339.5	-0.4421	sec	ccd	This study (TESS)

*Not used in the apsidal motion analysis.

For relatively small eccentricities, these relationships are given as $e\cos w = \pi\delta/(1+\csc^2 i)$ and $e\sin w = (D_2-D_1)/(D_2+D_1)$, where δ is the amount of displacement of the secondary minimum with respect to the primary minimum, i is the orbital inclination and D_1 and D_2 are the duration of the primary and secondary minimum, respectively. As a result, from the LCs (see Figure 7) of the system we obtained the values $e\cos w = -0.0867$ and $e\sin w = -0.0899$ which yield the orbital eccentricity as $e = 0.125$.

We managed to obtain a solution by keeping this value of eccentricity constant. The results are given in Table 3 associated with their internal errors. In Table 3, the parameters T_0 , P, e, w_0 and $\dot{w}$ denote the initial epoch, orbital period, eccentricity, longitude of the periastron point at the initial epoch, and apsidal motion rate, respectively. The observed $O-C$ variations (symbols) of V990 Her are shown in Figure 1 concerning the theoretical curves (solid lines) computed with the apsidal motion elements given in Table 3.

According to the results given in Table 3, V990 Her has an apsidal motion with a period of $U = 14683 \pm 2936$ years. Due to the relatively long apsidal period compared with the time span of about 30 years which is covered by the observations, the apsidal motion parameters have larger errors. Therefore, the results given in Table 3 should be considered as a preliminary ones. Thus, for V990 Her more observations, which will be performed in the future, are essential.

TABLE 3

APSIDAL MOTION PARAMETERS OF V990 HER

Parameter	Value	Error
T_0 (HJD)	2448048.513	0.004
P (days)	8.193315	0.000003
e	0.125	(fixed)
w_0 (deg)	226.2	0.8
$\dot{w}$ (deg cycle^{-1})	0.00055	0.00011

3.2. *Spectroscopic Orbital Parameters*

MgII, SiII, FeI, FeII and HI lines can be clearly seen in the spectrum of V990 Her. RVs were obtained from the orders containing the relatively sharp lines of MgII (4481Å), FeI (4957Å), FeI (5616Å) and HI (6563Å). The studied regions are shown in Figure 2. From top to bottom along the y-axis in Figure 2, the normalized spectra are plotted in accordance with the decreasing HJD times given in Table 1.

Gaussian profiles were applied to the central parts of the lines to measure the RVs and then a barrycentric correction was applied to correct the RVs. Measured RVs were listed in Appendices A,

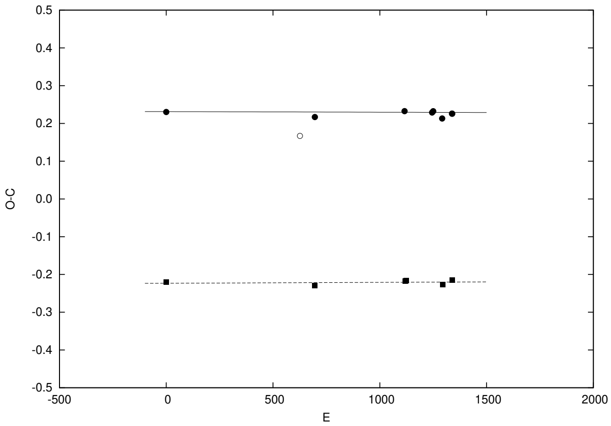

Fig. 1. The $O - C$ variations of V990 Her. Circles and squares represent primary and secondary minima, respectively. The open circle represents the minimum time which is not used in the analysis. Solid and dashed lines are for the theoretical model given in Table 3.

B, C and D. The least squares method has been applied to fit the RV equation to the measured RVs. We used the orbital period derived in equation (1) and fixed it during the iterations. The measured RVs and fitted curves (solid red lines) are shown in Figure 3 for each selected line separately. The spectroscopic orbital parameters, such as the longitude of the periastron, ω, orbital eccentricity, e, mass ratio, $q = K_1/K_2$ and velocity semi-amplitude of the components, $K_{1,2}$, were obtained from different lines and their arithmetic mean values are given in Table 4.

3.3. *Photometric Elements*

The previously mentioned three photometric data sets obtained in VRI bands were used for the photometric analysis of V990 Her to determine the photometric elements of the system and the light contributions of the components at different phases, which were used to model the component spectra in § 3.4 and § 3.5. The LC solutions were performed with the program PHOEBE 1.0 (Prša & Zwitter 2005), which is an extension of the WD program (Wilson & Devinney 1971).

The improved light elements given in equation (1) were used in the LCs analysis. The effective temperature of V990 Her was given as $T_{\rm eff} = 7514$ K by McDonald et al. (2012). However, we obtained a more reliable temperature for the primary component as $T_{\rm eff1} = 8000$ K directly from the spectrum of the system (see § 3.5). The temperature for the primary component $T_{\rm eff1}$, the improved period given in § 3.1, the eccentricity e, and the mass ratio q given in Table 4 were fixed during the LC solution. Convergence was allowed for the orbital inclination i, the longitude of the periastron point ω, the dimensionless surface potentials of the components Ω_1 and Ω_2, the effective temperature of the secondary component $T_{\rm eff,2}$, and the relative monochromatic luminosity of the primary component $l_1/l_{\rm tot}$. The bolometric albedos $A_{1,2}$ and gravitational darkening coefficients $g_{1,2}$ were adopted as 1.0, as suggested for early-type stars. The bolometric limb-darkening coefficients $x_{\rm bol1,2}$ were computed automatically by PHOEBE 1.0 with the internal tables of the programme which were generated according to the models given by van Hamme (1993). The results of the solution are listed in Table 5.

TABLE 4

PRELIMINARY ORBITAL PARAMETERS OF V990 HER

Element	Value
ω (deg)	191.8 ± 0.7
e	0.09 ± 0.02
K_1 (km s^{-1})	76.8 ± 0.1
K_2 (km s^{-1})	87.1 ± 0.1
$q = K_1/K_2$	0.88 ± 0.01
V_γ (km s^{-1})	-32.6 ± 3.5
$a \sin i$ ($R_\odot$)	26.4 ± 1.0

3.4. *Disentangling the Components Spectrum*

One of the advantages of having numerous spectra taken at different phases is that they allow to obtain the spectrum of the components separately. Thus, we used the KOREL program provided by Hadrava (1995) which needs approximate orbital elements and the light contributions of the components at the phases in which the individual spectrum were taken. The orbital parameters and light contributions of the components obtained in § 3.2 and § 3.3 were used as initial values for the KOREL solution. The orbital period P given in equation (1) was used and fixed during the iterations. The KOREL solution gives the RVs (see Table 6) of the components and the orbital parameters (see Table 7) of the binary system. The KOREL solution agrees very well with those obtained from individual lines (see Table 4). The disentangled spectra in the H$_\alpha$ region for both components can be seen in Figure 4.

3.5. *Atmosphere Modelling*

We have a spectrum of the system in the middle of the secondary minimum of the LC where $\approx$ 45

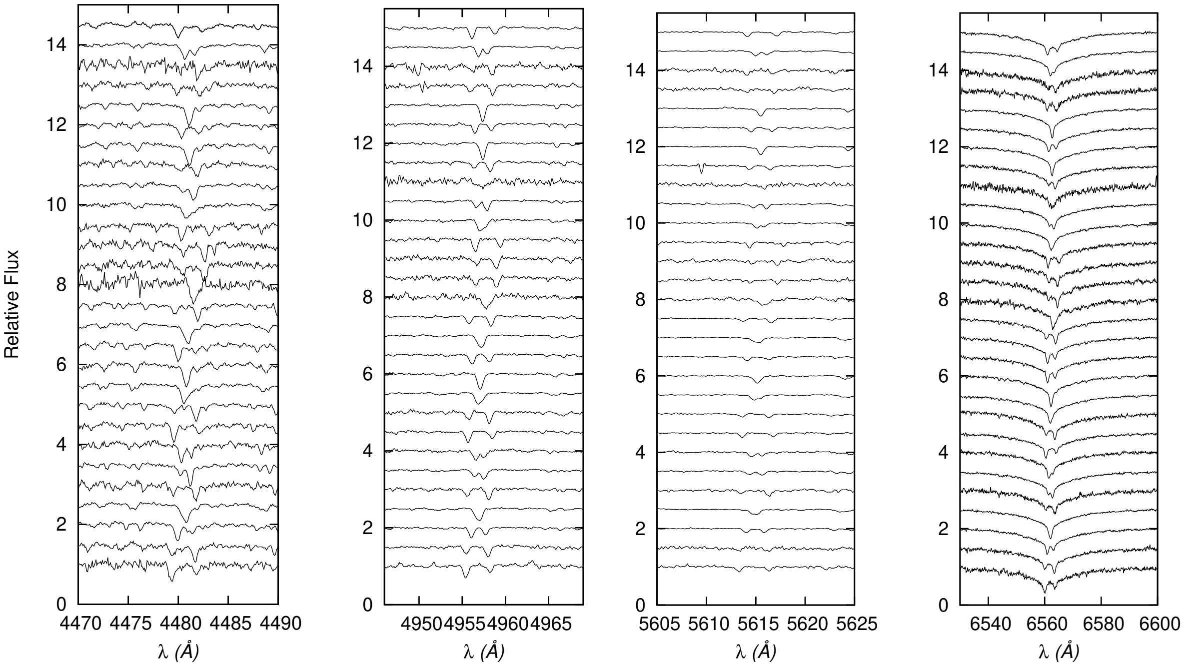

Fig. 2. Analyzed spectral lines. From top to bottom along the y-axis, the normalized spectra are plotted in accordance with the decreasing HJD times given in Table 1 in each panel.

TABLE 5

THE LIGHT CURVE MODEL OF V990 HER

Element	Primary	System	Secondary
P (d)		8.193314 (fixed)	
$PhaseShift$		-0.0278 ± 0.0001	
q		0.88 (fixed)	
e		0.09(fixed)	
w (rad)		3.50 ± 0.01	
i (°)		85.48 ± 0.03	
$T_{\rm eff}$ (K)	8000 (fixed)		7544 ± 27
Ω	13.91 ± 0.08		11.92 ± 0.06
$x_{\rm bol}$	0.198		0.199
$y_{\rm bol}$	0.549		0.547
$l/l_{(1+2)}$ V band	0.526 ± 0.004		0.474 ± 0.004
$l/l_{(1+2)}$ R band	0.514 ± 0.004		0.486 ± 0.004
$l/l_{(1+2)}$ I band	0.504 ± 0.004		0.496 ± 0.004
$r_{\rm mean}$	0.0772 ± 0.0004		0.0818 ± 0.0004
χ^2		0.777	

percent of the light of the secondary component is eclipsed. When the similar physical properties of the components (see Table 5) are taken into consideration, it can be regarded as a useful spectrum for a temperature estimation of the primary component.

We know that the components are not early type since there are no He I lines in the composite or disentangled spectra, which means that their temperature is no higher than ≈ 10000 K, and therefore, the local thermodynamic equilibrium assumption could be used to construct the atmosphere models. ATLAS9 atmosphere models computed by Castelli & Kurucz (2004) and SYNTHE program of Kurucz (1993) were used for the generation of the atmospheric models

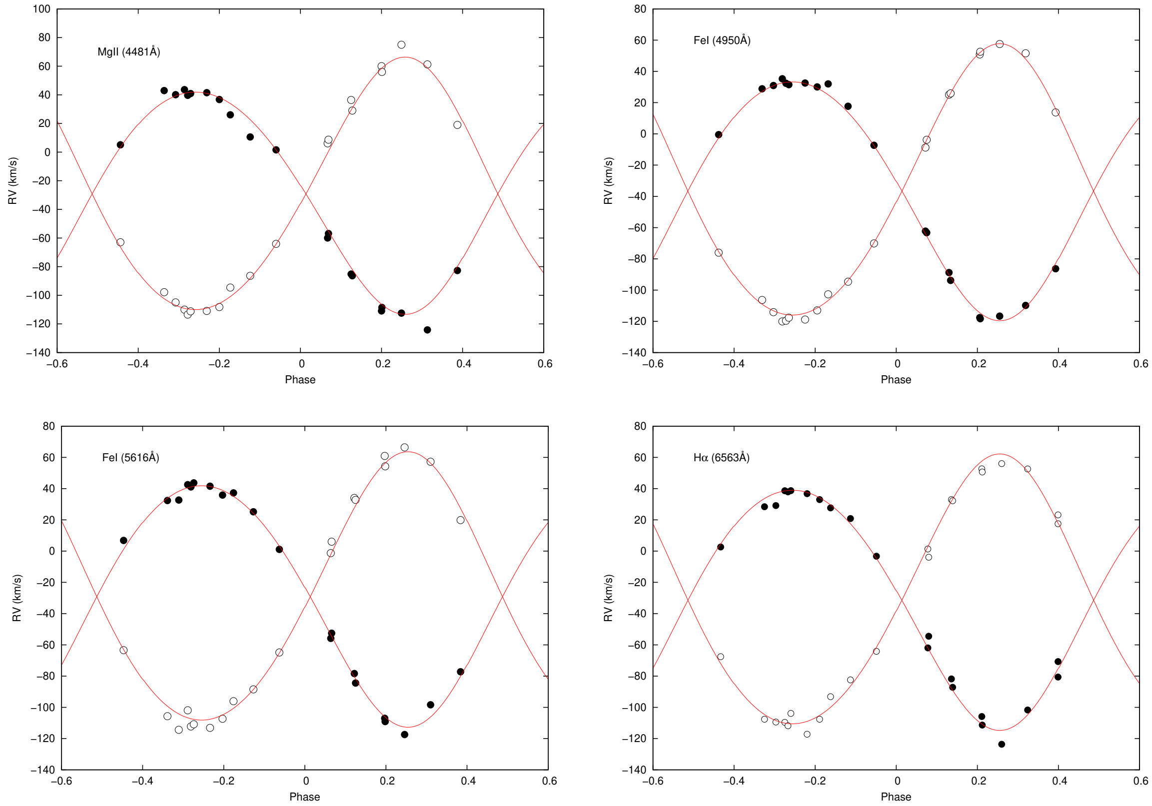

Fig. 3. RVs observations (symbols) and fitted models (red lines) for different spectral lines. Black dots and circles denote the primary and secondary components. The color figure can be viewed online.

and the synthetic spectra for the components. In the ATLAS9 code, Z=0.03 and $\xi = 2$ km s^{-1} were assumed for the metallicity and micro turbulence velocity, respectively. This method has been applied to the wavelength regions where the dominant lines reside. In Figure 5, the observational data and the synthetic spectra are given for four different wavelength regions as examples.

The atmospheric model parameters of the primary component, such as the temperature, T_{eff1}=8000 ± 200 K, the surface gravity, $\log g_1 = 4.0 \pm 0.1$ and the rotational velocity v_{rot1}=28 ± 5 km s^{-1} were determined.

Moreover, we have a spectrum at orbital phase $\phi = 0.0$. Using a similar approach, the atmospheric model parameters of the secondary component were estimated as T_{eff2}=7500±200 K, log g_2=4.0±0.1 and v_{rot2}=25±5 km s^{-1}. At three different orbital phases ($\phi = 0.699$, 0.533, 0.290), the synthetic spectra of the components were combined using their light contributions and their specific RVs. The observed spectra taken at the indicated maximum phases and the combined theoretical spectra are shown together in Figure 6.

3.6. *Simultaneous Radial Velocity and Light Curves Solution*

The RVs of the components obtained from the KOREL solution and the multi-colour LCs of the system were analyzed simultaneously with PHOEBE 1.0. The initial orbital parameters were used from the averaged values given in Tables 4 and 7. We used the improved light elements given in equation (1). The orbital period P and the effective temperature of the primary component T_{eff1} were fixed as in § 3.3, the other orbital and photometric parameters were all adjusted in the analyses.

The results of the simultaneous solution are listed in Table 8. The observed LCs in *VRI* bands and the radial velocity curves (RVCs) of the components are shown along with the theoretical models in Figure 7. The Roche geometry of V990 Her at phases ϕ=0.0, 0.25 and 0.45 can be seen in Figure 8.

TABLE 6

ADOPTED RVS OF THE COMPONENTS OF V990 HER

No	HJD (+2400000)	Phase	Primary RV km s^{-1}	$(O-C)_1$ km s^{-1}	Secondary RV km s^{-1}	$(O-C)_2$ km s^{-1}
1	57890.3826	0.178	-113.42	-4.06	51.26	-5.99
2	57911.4226	0.746	32.72	-5.56	-119.83	-9.04
3	57916.4894	0.365	-84.21	-4.91	14.56	-8.48
4	57917.5082	0.489	-	-	-	-
5	57927.4824	0.706	38.85	-0.81	-112.49	-0.13
6	57937.4004	0.917	-2.22	1.07	-65.03	-1.55
7	57938.4406	0.044	-62.92	-3.32	1.15	0.55
8	57939.5348	0.177	-111.31	-2.14	51.65	-5.38
9	57944.4475	0.777	38.67	3.79	-107.78	-0.85
10	57946.4449	0.021	-	-	-	-
11	57954.4968	0.003	-	-	-	-
12	57955.3306	0.105	-85.53	1.04	32.20	0.88
13	57958.4583	0.487	-	-	-	-
14	57968.3904	0.699	43.63	4.10	-107.86	4.35
15	58015.3474	0.430	-	-	-	-
16	58017.3004	0.669	63.50	25.82	-83.33	26.77
17	58025.2668	0.641	57.11	22.97	-103.97	2.10
18	58038.2554	0.226	-77.16	37.56	86.45	23.10
19	58359.3891	0.421	-	-	-	-
20	58360.3098	0.533	2.17	-1.44	-71.89	-0.57
21	58375.3204	0.365	-	-	-	-
22	58379.3137	0.853	20.40	2.04	-89.44	-1.31
23	58380.3664	0.981	-	-	-	-
24	58381.3540	0.102	-83.37	1.92	32.56	2.71
25	58384.2969	0.461	-	-	-	-
26	58394.3723	0.691	39.51	0.27	-110.91	0.97
27	58395.3006	0.804	29.90	-0.34	-100.61	1.02
28	58397.2865	0.046	-58.81	2.11	8.22	6.12
29	58399.2858	0.290	-113.89	-6.95	45.34	-9.15

TABLE 7

ORBITAL PARAMETERS OF V990 HER DERIVED FROM KOREL SOLUTION

Element	Value
T_{per} (days)	2457883.010 ± 0.003
ω (deg)	200.7 ± 0.3
e	0.085 ± 0.008
K_1 (km s^{-1})	77.2 ± 0.4
K_2 (km s^{-1})	87.9 ± 0.6
$q = K_1/K_2$	0.880 ± 0.002

4. RESULTS

4.1. *Physical Properties and Evolutionary Status*

Using the parameters given in Tables 7 and 8, the astrophysical parameters of the components and the distance of V990 Her were derived and are given in Table 9. The masses of the components (2.01±0.07 $M_\odot$ and 1.83±0.03 $M_\odot$) correspond to main sequence stars of spectral type between A3-A5 (Straizys & Kuriliene 1981). The evolution status of the components according to the $T_{\rm eff}$ and log L values given in Table 9 is shown in Figure 9 along with the theoretical evolutionary tracks taken from Bressan et al. (2012). The isochrone in Figure 9 was taken from Girardi et al. (2000).

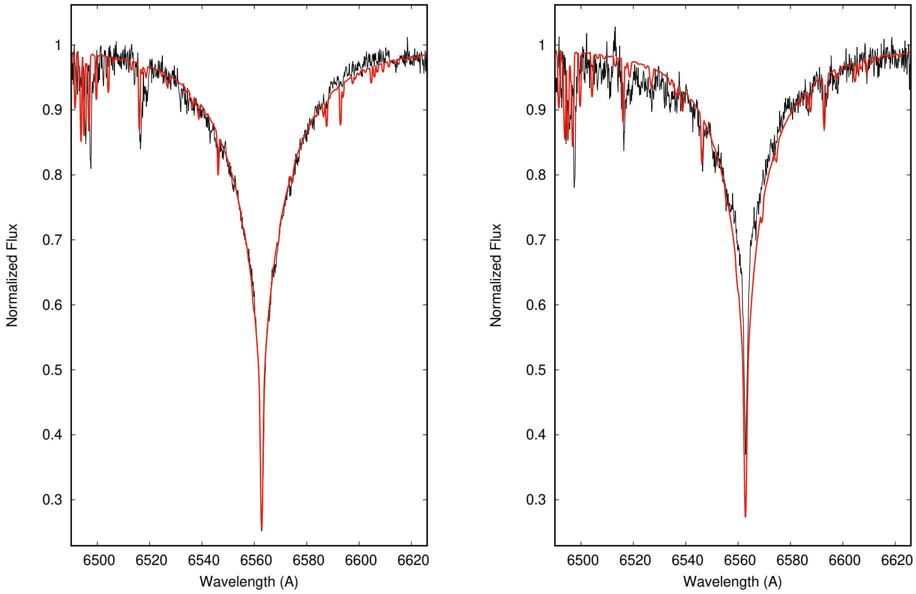

Fig. 4. Disentangled spectra in H_α region for the primary (left panel) and the secondary (right panel) components of V990 Her obtained from KOREL solution. The red solid lines represent the synthetic spectra calculated in § 3.5. The color figure can be viewed online.

TABLE 8

THE SIMULTANEOUS SOLUTION OF RVCS AND LCS OF V990 HER

Element	Primary	System	Secondary
P (d)		8.193314 (fixed)	
$PhaseShift$		-0.0278 ± 0.0001	
a ($R_\odot$)		26.8 ± 0.2	
q		0.912 ± 0.005	
V_γ (km s^{-1})		-31.8 ± 0.3	
e		0.089 ± 0.001	
w ($^\circ$)		198 ± 1	
i ($^\circ$)		85.46 ± 0.03	
$T_{\rm eff}$ (K)	8000 (fixed)		7570 ± 31
Ω	13.06 ± 0.07		12.72 ± 0.05
$x_{\rm bol}$	0.198		0.199
$y_{\rm bol}$	0.549		0.547
$l/l_{(1+2)}$ V band	0.575 ± 0.006		0.425
$l/l_{(1+2)}$ R band	0.564 ± 0.005		0.436
$l/l_{(1+2)}$ I band	0.554 ± 0.006		0.447
$r_{\rm mean}$	0.0828 ± 0.0005		0.0792 ± 0.0004
χ^2		0.800	

Bolometric corrections (BC) for the primary and secondary components were calculated as 0.027 and 0.034 mag using $T_{\rm eff}$–BC tables of Flower (1996). The bolometric magnitudes $M_{\rm bol}$ given in Table 9 and BCs were used to derive the absolute magnitudes of the components as $M_{\rm V1} = 1^m.60 \pm 0.11$ and $M_{\rm V2} = 1^m.93 \pm 0.12$, respectively. By using the $V_J = V_T - 0.09 \times (B_T - V_T)$ relation and Tycho magnitudes ($B_T = 7^m.950$, $V_T = 7^m.710$) given by Esa (1997), we derived the total visual magnitude of the

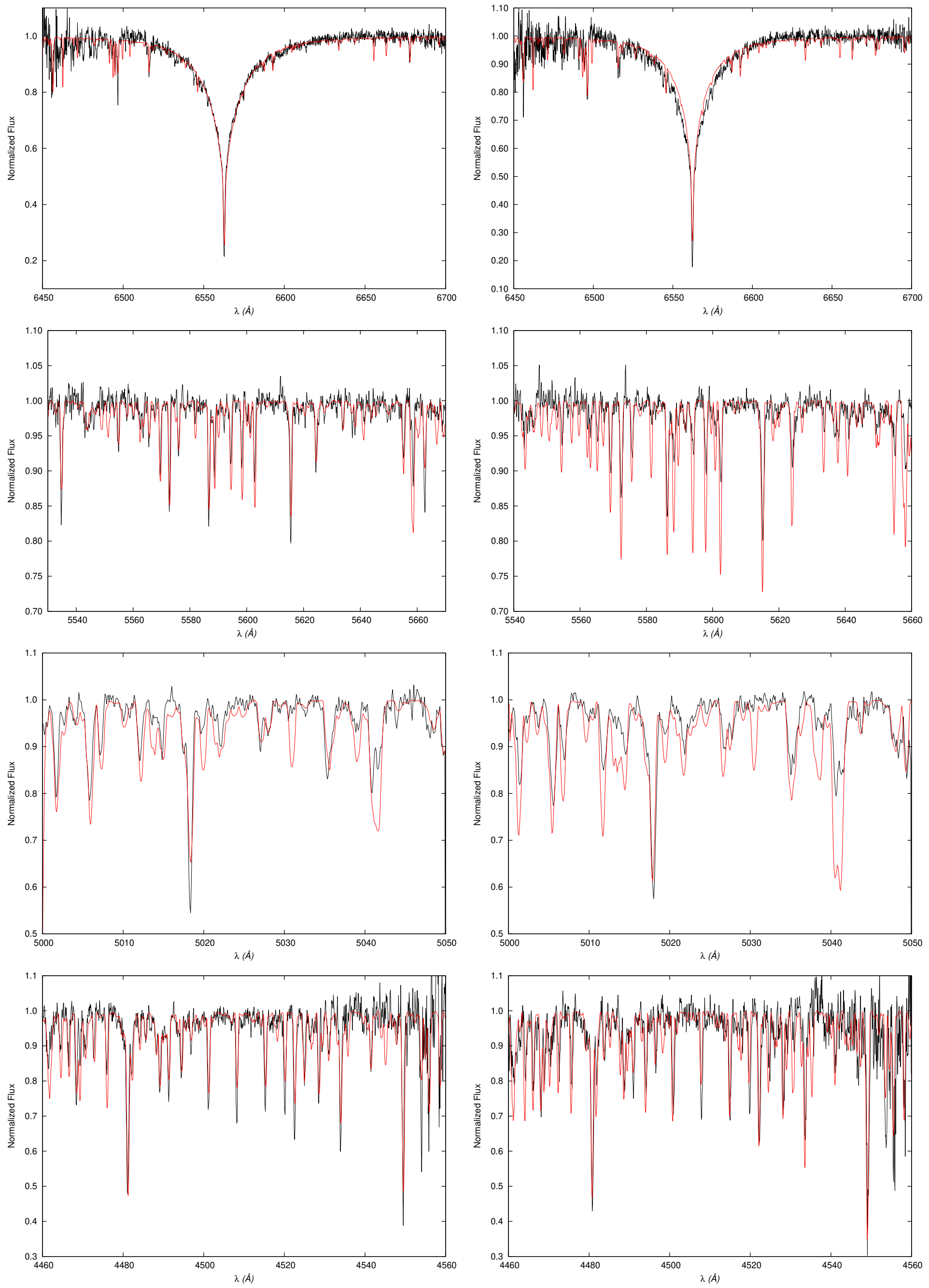

Fig. 5. The observed spectra taken during the secondary (left panel) and primary (right panel) minimum. The synthetic models are shown with red solid lines. The color figure can be viewed online.

system as $m_{\rm V} = 7^{m}.688$. To obtain the $E(B-V)$ color excess and the distance of the system we used the total $u'g'r'i'z'$ magnitudes of the system given by Pickles & Depagne (2010) in the following transformation relationships of Smith et al. (2002):

$$V = g' - 0.55(g' - r') - 0.03, \tag{3}$$

$$(V - R_C) = 0.59(g' - r') + (0.11), \tag{4}$$

$$(R - I)_C = 1.00(r' - i') + (0.21) \text{for} (r' - i') < 0.95. \tag{5}$$

Using the light contribution of the components given in Table 8 together with the $I_{\rm C}$ magnitudes of the system estimated by equations 3-5 and the

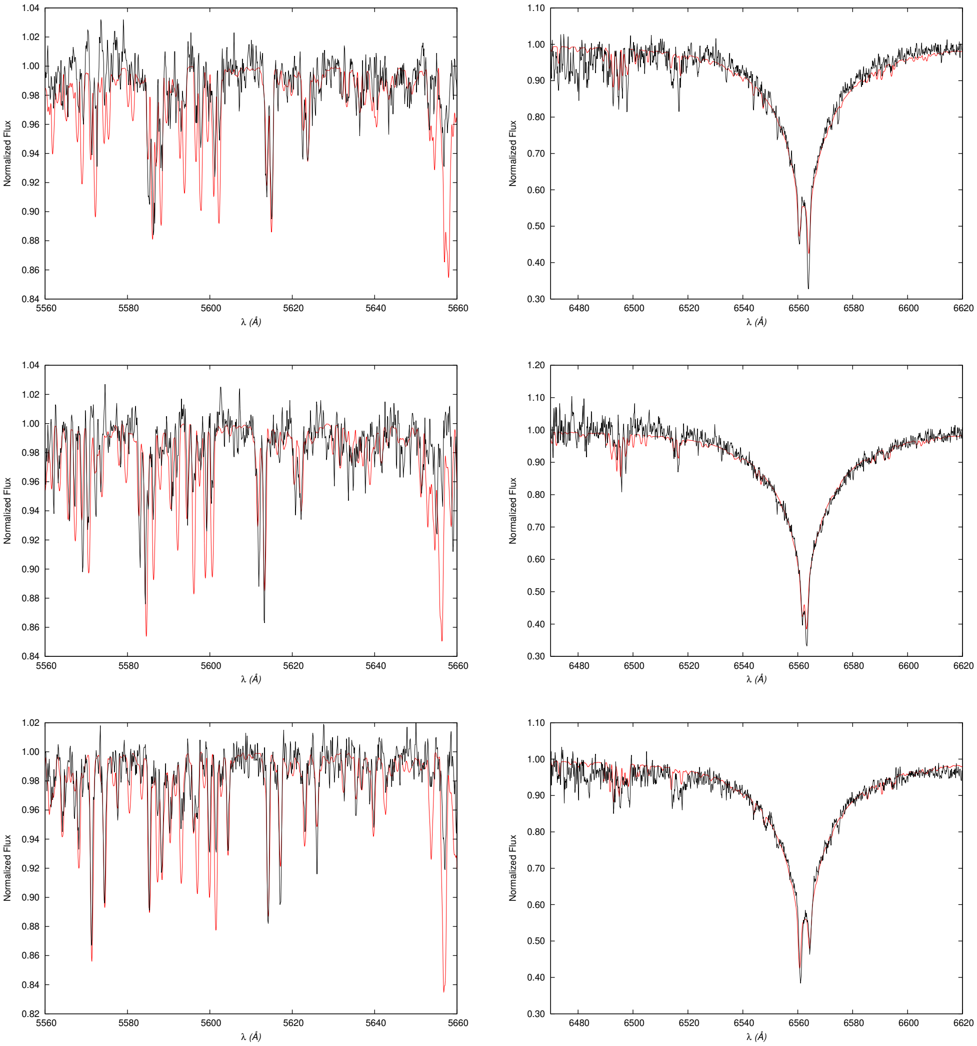

Fig. 6. The composite synthetic models (red solid lines) fitted to the observed spectra around FeI (5616Å) and HI (6563Å) lines. Each row refers to orbital phases at $\phi = 0.699$ (upper panels), 0.533 (middle panels) and 0.290 (bottom panels). The color figure can be viewed online.

$(B-V)-(V-I_{\rm C})$ tables given by Cousins (1981), we obtained the $(B-V)$ colors as 0.185 and 0.250 mag for the primary and secondary components, respectively. For the unreddened $(B-V)_0$ colors of the components we used the $T_{\rm eff}$–$(B-V)_0$ tables of Flower (1996) and obtained the values of $(B-V)_0$ as 0.162 and 0.234 mag, which correspond to $E(B-V)$ values of 0.023 and 0.017 mag for the primary and secondary components, respectively. Thus, we adopted an average color excess of $E(B-V) = 0.020$ mag and as a result we obtained the distance of the system as $d = 212 \pm 21$ pc. Alternatively, an $E(B-V) = 0^m.066$ value estimated from stilism maps given by Kervella et al. (2019) corresponds to a distance of $d = 198 \pm 19$ pc. However, our photometric distance value matches better the value of 235 pc given by Gaia which corresponds to a parallax of $\mu = 4.25 \pm 0.08$ mas (Gaia Collaboration et al. 2016; Lindegren et al. 2021) within the given uncertainty box.

4.2. *Apsidal Motion and Internal Structure Constant*

To test the observed preliminary results concerning the apsidal motion of V990 Her given in § 3.1, we can use the results of previous section. As is known, the total apsidal motion in a binary system occurs mainly for two contributions: (1) a classical part which is due to tidal interactions of the oblate components, and (2) a relativistic contribution which is a direct result of the General Relativity Theory.

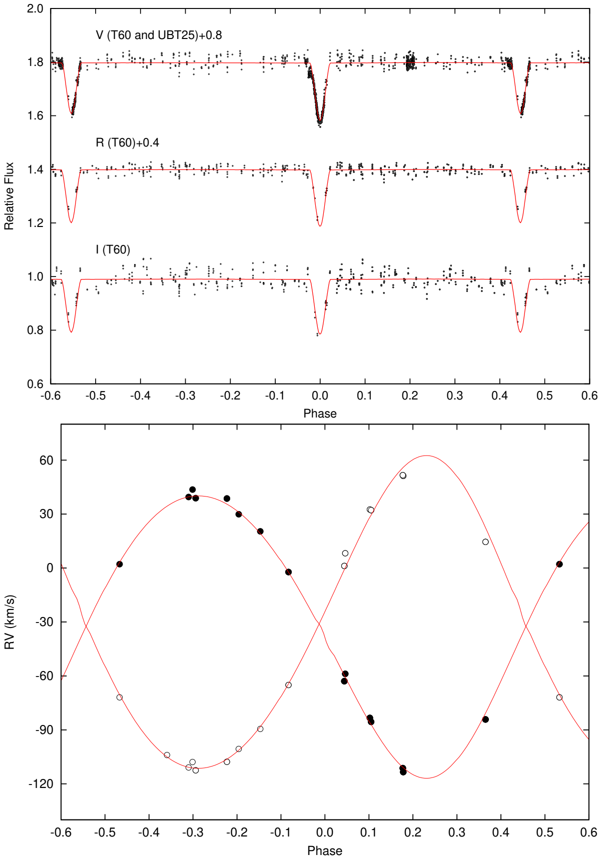

Fig. 7. The theoretical representations of the observed LCs of the system in VRI bands (upper panel) and the observed RVCs of the components (lower panel). The V and R band LCs are shifted 0.8 and 0.4 mag, respectively, for a better illustration. The color figure can be viewed online.

TABLE 9

THE BASIC PROPERTIES OF V990 HER

Element	Unit	Primary	Secondary
M	$M_\odot$	2.01±0.07	1.83±0.03
R	$R_\odot$	2.22±0.02	2.12±0.01
$T_{\rm eff}$	K	8000±200	7570±200
$\log L$	$L_\odot$	1.25±0.04	1.12±0.05
$M_{\rm bol}$	mag	1.6±0.1	2.0±0.1
$\log\, g$	cgs	4.06±0.01	4.04±0.01
V_{rot}	km s^{-1}	28±5	25±5
V_{syn}	km s^{-1}	13.6±0.1	13.1±0.1
d	pc	212±21	

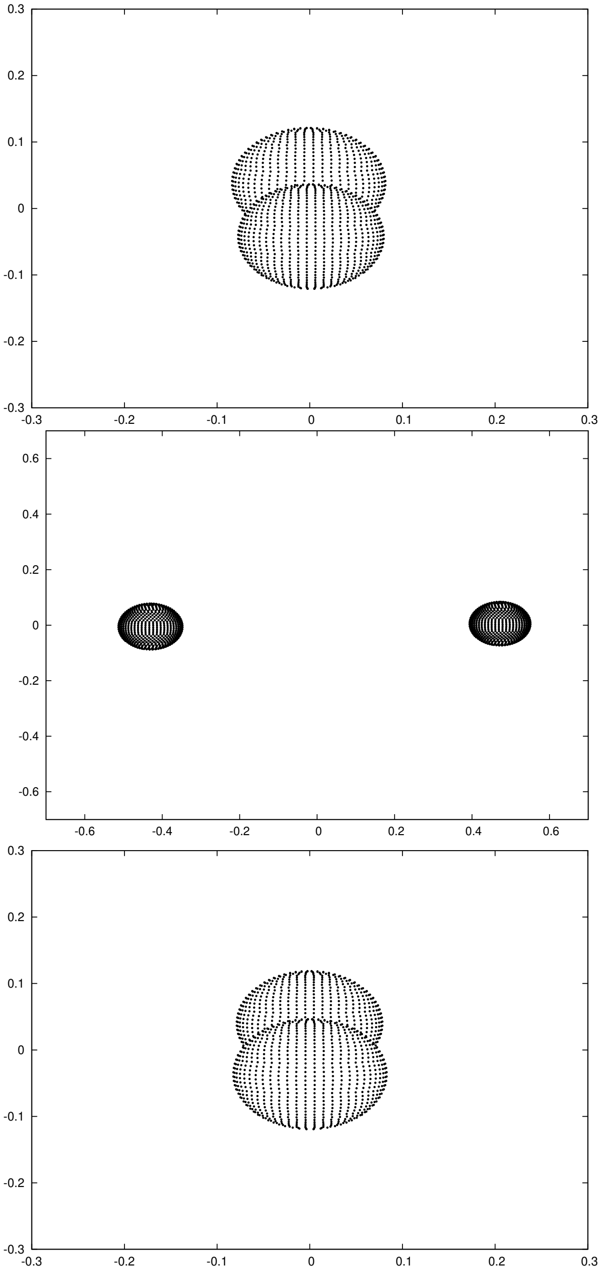

Fig. 8. The Roche geometry of V990 Her at the phases $\phi = 0.00$ (upper panel), $\phi = 0.25$ (middle panel) and $\phi = 0.45$ (lower panel).

The relativistic contribution $\dot{w}_{rel}$ (in degrees per orbital cycle) to total apsidal motion is given by (see Giménez 1985):

$$\dot{w}_{rel} = 5.45 \times 10^{-4} \frac{1}{1-e^2} \left(\frac{m_1 + m_2}{P} \right)^{2/3}, \quad (6)$$

which was first derived by Levi-Civita (1937). Here, $m_{1,2}$ are the masses of the components in units of solar mass, e is the orbital eccentricity and P is the orbital period in units of days. By using the related parameters given in Tables 3 and 9 we obtained $\dot{w}_{rel} = 0^{\circ}.00033$ cycle^{-1} and so $\dot{w}_{cl} = 0^{\circ}.00022$ cycle^{-1}.

On the other hand, the relation for the classical part of the apsidal motion rate was given by Kopal (1978) as follows

$$\frac{\dot{w}_{cl}}{360} = c_{21}k_{21} + c_{22}k_{22}, \tag{7}$$

where k_{2i} (i=1, 2) are internal structure constants (ISCs) of the components, while c_{2i} are as follows

$$c_{2i} = \left[\left(\frac{w_i}{w_k}\right)^2 \left(1 + \frac{m_{3-i}}{m_i}\right) f(e) + 15\frac{m_{3-i}}{m_i} g(e)\right] (R_i/a)^5 \,. \tag{8}$$

Here R_i/a and w_i/w_k are the relative radii and and rotational angular velocity for the corresponding component, respectively, $w_k = \frac{2\pi}{P}$ is the orbital (Keplerian) angular velocity and P is the orbital period of the system. The f and g functions of the orbital eccentricity e are given by

$$f(e) = (1 - e^2)^{-2}, \tag{9}$$

$$g(e) = (1 - e^2)^{-5}(1 + 1,5e^2 + 0,125e^4). \tag{10}$$

Using the apsidal and absolute parameters given in Tables 3 and 9 we obtained the observed average ISC for the system as $\overline{k}_2 = 0.0035 \pm 0.0008$.

To obtain the theoretical ISCs of the components we used the stellar models given by Claret & Gimenez (1992), which assume X=0.649, Z=0.03 and take mass loss and core overshooting into account. By the interpolation we obtained log L=1.30 and $1.13L_{\odot}$, $T_{\rm eff}$=8222 and $7621K$, $Age = 5.72 \times 10^8$ and 7.89×10^8 years and $k_2 = 0.0032$ and 0.0031 for the primary and secondary components, respectively. These results correspond to a value of $\overline{k}_2(theo) = 0.0032$ and $\dot{w}_{cl}(theo) = 0^{\circ}.00019$ cycle^{-1}. Consequently, the theoretical value of the total apsidal motion rate is obtained as $\dot{w}(theo) = 0^{\circ}.00052$ cycle^{-1}. On the other hand, by taking the weighted average of the ages of the components with the corresponding c_i we obtained the age of the system as 6.74×10^8 years.

5. DISCUSSION

The absolute parameters of the eccentric binary V990 Her has been obtained with a good precision; ≤1 per cent for masses and radii. This allowed us to see the evolutionary status of the system. The system consists of two early A-type main-sequence stars with an age of 6.3×10^8 years estimated by isochrone fitting, which is compatible with 6.74×10^8 years obtained from the apsidal motion analysis. The circularization and synchronization time scales were computed as 1.5×10^8 and 7.6×10^{10} years according to Zahn (Zahn 1977). The averaged age of the system is larger than the circularization and smaller than the synchronization time scales, which explains the fast rotation speed of the components.

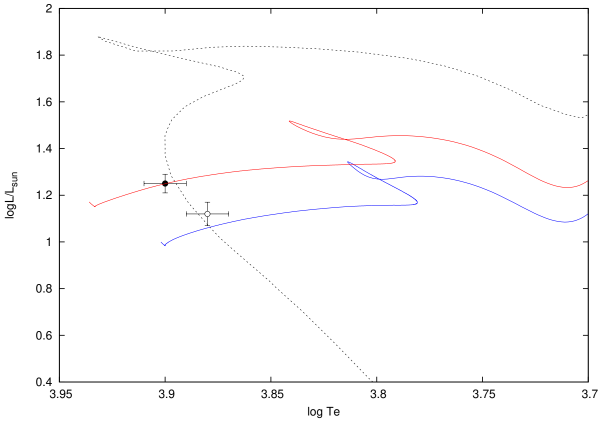

Fig. 9. Comparison of components with evolution models (Black dot and circle represent the primary and secondary components, red and blue solid lines indicates evolution models for $Z = 0.03$ for a $2.00M_{\odot}$ and $1.825M_{\odot}$ star individually). Black dashed line represents isochrone corresponds 6.3×10^8 yrs for $Z = 0.03$. The color figure can be viewed online.

Different $E(B-V)$ color excess values of $0^m.166$ (Jayasinghe et al. 2018), $0^m.11$ (Gontcharov & Mosenkov 2017) and $0^m.066$ (Kervella et al. 2019) are also available in the literature. According to these values, we estimated the distance of the system as 172 ± 17, 186 ± 18 and 198 ± 19 pc, respectively. Our photometric distance ($d = 212 \pm 21$ pc), estimated in § 4.1, is closer to the one given by Gaia than the distances determined using the above color excesses.

The apsidal motion in V990 Her puts it into a special place and allows us to estimate the structure of the component stars. However, the time span of the available data we have is a very small portion (≈ 0.2%) of the apsidal cycle. This situation creates problems in the apsidal motion analysis of the system and makes it difficult to determine the apsidal motion rate and orbital eccentricity together. For now, based on our findings we can say that the orbital eccentricity of the system has a value between 0.09 and 0.13. More accurate results can be obtained with more observations to be made in the future. Lastly, the apsidal motion of V990 Her has a period of about 14700 years and is predominantly (60%) due to relativity.

The research of EK was supported with the fellowship of BİDEP-2218 Post-Doctoral Research Fellowship Programme of The Scientific and Technological Research Council of Turkey (TÜBİTAK). We thank TÜBİTAK National Observatory for partial support in using T60 telescope with project number 18BT60-1327. We thank Akdeniz University, Space Sciences and Technologies Department for granting telescope time for UBT60 and AUT25 telescopes. We would like to thank Assoc. Prof. Mustafa Caner for reviewing the language of the article and making suggestions. It is a pleasure to record here our thanks to referee for her/his valuable comments and suggestions. This work has made use of data from the European Space Agency (ESA) mission *Gaia* (https://www.cosmos.esa.int/gaia), processed by the *Gaia* Data Processing and Analysis Consortium (DPAC, https://www.cosmos.esa.int/web/gaia/dpac/consortium). Funding for the DPAC has been provided by national institutions, in particular the institutions participating in the *Gaia* Multilateral Agreement. In this research, we benefited from the use of the SIMBAD database and the VizieR service operated at CDS, Strasbourg, France; and the NASA's Astrophysics Data System Bibliographic Service. We acknowledge the use of TESS High Level Science Products (HLSP) produced by the Quick-Look Pipeline (QLP) at the TESS Science Office at MIT, which are publicly available from the Mikulski Archive for Space Telescopes (MAST). Funding for the TESS mission is provided by NASA's Science Mission directorate.

APPENDIX A. RADIAL MEASURED FROM MgII (4481.13Å)

No	Time (HJD) (+2400000)	Phase	RV_{pri} km s^{-1}	eRV_{pri}	RV_{sec} km s^{-1}	eRV_{sec}
1	57890.3826	0.17819	-108.49	1.26	56.00	1.80
2	57911.4226	0.74614	41.53	1.15	-110.89	0.39
3	57916.4894	0.36455	-82.72	10.86	18.99	2.88
4	57917.5082	0.48889	-21.62	2.19	-	-
5	57927.4824	0.70625	40.92	1.92	-111.20	0.62
6	57937.4004	0.91675	1.59	4.25	-64.10	4.02
7	57938.4406	0.04371	-59.96	0.08	6.12	0.19
8	57939.5348	0.17726	-110.89	0.41	60.00	3.53
9	57944.4475	0.77685	36.74	0.48	-108.18	0.52
10	57946.4449	0.02064	-	-	-44.75	2.20
11	57954.4968	0.00338	-	-	-31.85	0.50
12	57955.3306	0.10514	-86.31	0.23	29.01	1.44
13	57958.4583	0.48688	-22.08	2.41	-	-
14	57968.3904	0.69910	39.67	0.34	-113.48	0.19
15	58015.3474	0.43024	-30.26	1.67	-	-
16	58017.3004	0.66860	40.08	4.93	-104.93	6.02
17	58025.2668	0.64091	42.99	3.21	-97.84	0.20
18	58038.2554	0.22618	-112.45	3.80	75.00	1.59
19	58359.3891	0.42077	-40.57	5.14	-	-
20	58360.3098	0.53315	5.07	0.10	-62.93	0.43
21	58375.3204	0.36521	-	-	-	-
22	58379.3137	0.85258	10.56	27.31	-86.40	1.34
23	58380.3664	0.98107	-	-	-25.82	0.56
24	58381.3540	0.10161	-85.17	11.40	36.38	0.91
25	58384.2969	0.46079	-27.83	0.35	-	-
26	58394.3723	0.69050	43.64	0.21	-110.00	1.16
27	58395.3006	0.80380	26.02	6.82	-94.60	10.76
28	58397.2865	0.04618	-56.89	0.24	8.67	2.10
29	58399.2858	0.29019	-124.13	38.11	61.24	1.43

APPENDIX B. RVs MEASURED FROM FeI (4957.59Å)

No	Time (HJD) (+2400000)	Phase	RV_{pri} km s^{-1}	eRV_{pri}	RV_{sec} km s^{-1}	eRV_{sec}
1	57890.3826	0.17819	-118.29	2.06	52.60	0.97
2	57911.4226	0.74614	32.55	0.79	-118.86	1.15
3	57916.4894	0.36455	-86.34	1.11	13.73	1.02
4	57917.5082	0.48889	-32.50	2.46	-	-
5	57927.4824	0.70625	31.50	0.23	-117.69	1.28
6	57937.4004	0.91675	-7.28	1.02	-70.12	0.32
7	57938.4406	0.04371	-62.26	1.16	-8.76	1.67
8	57939.5348	0.17726	-117.61	0.68	50.84	0.59
9	57944.4475	0.77685	30.04	0.55	-113.01	2.26
10	57946.4449	0.02064	-	-	-45.42	3.14
11	57954.4968	0.00338	-	-	-37.40	0.24
12	57955.3306	0.10514	-93.81	1.26	25.91	1.38
13	57958.4583	0.48688	-32.73	1.90	-	-
14	57968.3904	0.69910	32.42	1.00	-119.61	1.20
15	58015.3474	0.43024	-41.34	1.05	-	-
16	58017.3004	0.66860	30.95	1.38	-114.16	2.28
17	58025.2668	0.64091	28.89	2.63	-106.35	1.36
18	58038.2554	0.22618	-116.67	1.37	57.50	0.75
19	58359.3891	0.42077	-49.35	2.78	-	-
20	58360.3098	0.53315	-0.49	1.25	-76.03	1.63
21	58375.3204	0.36521	-	-	-	-
22	58379.3137	0.85258	17.70	0.34	-94.66	1.87
23	58380.3664	0.98107	-	-	-33.01	0.35
24	58381.3540	0.10161	-88.77	0.70	25.08	0.87
25	58384.2969	0.46079	-34.77	0.61	-	-
26	58394.3723	0.69050	35.27	0.33	-120.04	3.05
27	58395.3006	0.80380	31.99	1.37	-102.69	4.17
28	58397.2865	0.04618	-63.24	0.13	-3.75	0.58
29	58399.2858	0.29019	-109.79	0.34	51.62	0.75

APPENDIX C. RVs MEASURED FROM FeI (5615.64Å)

No	Time (HJD) (+2400000)	Phase	RV_{pri} km s^{-1}	eRV_{pri}	RV_{sec} km s^{-1}	eRV_{sec}
1	57890.3826	0.17819	-109.10	1.38	54.27	1.41
2	57911.4226	0.74614	41.54	2.41	-113.12	4.36
3	57916.4894	0.36455	-77.21	0.13	19.85	0.54
4	57917.5082	0.48889	-19.13	5.37	-	-
5	57927.4824	0.70625	43.71	2.79	-110.86	0.61
6	57937.4004	0.91675	1.13	1.58	-64.91	2.58
7	57938.4406	0.04371	-55.86	0.91	-1.26	0.36
8	57939.5348	0.17726	-107.00	0.05	60.96	1.23
9	57944.4475	0.77685	35.90	0.13	-107.32	1.57
10	57946.4449	0.02064	-	-	-20.40	0.49
11	57954.4968	0.00338	-	-	-31.26	1.15
12	57955.3306	0.10514	-84.44	1.80	32.79	2.35
13	57958.4583	0.48688	-28.89	1.10	-	-
14	57968.3904	0.69910	41.09	0.45	-112.25	0.05
15	58015.3474	0.43024	-44.84	3.02	-	-
16	58017.3004	0.66860	32.70	31.86	-114.36	0.98
17	58025.2668	0.64091	32.42	0.32	-105.70	1.92
18	58038.2554	0.22618	-117.41	0.94	66.41	0.73
19	58359.3891	0.42077	-43.17	0.16	-	-
20	58360.3098	0.53315	6.84	0.54	-63.41	0.27
21	58375.3204	0.36521	-	-	-	-
22	58379.3137	0.85258	25.18	0.29	-88.52	1.56
23	58380.3664	0.98107	-	-	-25.86	0.48
24	58381.3540	0.10161	-78.36	0.25	34.04	2.18
25	58384.2969	0.46079	-25.95	1.13	-	-
26	58394.3723	0.69050	42.53	6.13	-101.88	4.49
27	58395.3006	0.80380	37.28	24.73	-96.06	9.58
28	58397.2865	0.04618	-52.55	0.54	6.05	0.20
29	58399.2858	0.29019	-98.37	0.77	57.20	2.44

APPENDIX D. RVs MEASURED FROM HI (6562.79Å)

No	Time (HJD) (+2400000)	Phase	RV_{pri} km s^{-1}	eRV_{pri}	RV_{sec} km s^{-1}	eRV_{sec}
1	57890.3826	0.17819	-111.34	2.24	50.65	2.07
2	57911.4226	0.74614	36.79	1.16	-117.24	2.17
3	57916.4894	0.36455	-80.59	2.66	23.18	4.54
4	57917.5082	0.48889	-28.70	0.71	-	-
5	57927.4824	0.70625	38.73	2.35	-103.90	6.91
6	57937.4004	0.91675	-3.24	0.75	-64.17	1.30
7	57938.4406	0.04371	-61.95	1.64	1.37	0.68
8	57939.5348	0.17726	-105.89	8.05	52.67	4.79
9	57944.4475	0.77685	33.00	1.13	-107.61	1.60
10	57946.4449	0.02064	-	-	-39.90	1.13
11	57954.4968	0.00338	-	-	-31.83	0.44
12	57955.3306	0.10514	-87.17	0.12	32.26	0.88
13	57958.4583	0.48688	-27.62	1.97	-	-
14	57968.3904	0.69910	37.92	0.31	-111.79	1.05
15	58015.3474	0.43024	-47.93	3.27	-	-
16	58017.3004	0.66860	29.16	2.61	-109.43	11.90
17	58025.2668	0.64091	28.44	4.96	-107.64	1.94
18	58038.2554	0.22618	-123.64	0.12	56.01	2.88
19	58359.3891	0.42077	-38.60	2.26	-	-
20	58360.3098	0.53315	2.67	0.43	-67.58	1.20
21	58375.3204	0.36521	-70.70	20.16	17.51	31.75
22	58379.3137	0.85258	20.87	0.63	-82.44	0.28
23	58380.3664	0.98107	-	-	-29.16	0.33
24	58381.3540	0.10161	-81.79	1.36	33.02	0.30
25	58384.2969	0.46079	-27.06	0.96	-	-
26	58394.3723	0.69050	38.68	3.70	-109.63	1.22
27	58395.3006	0.80380	27.69	0.45	-93.17	2.33
28	58397.2865	0.04618	-54.51	0.25	-3.93	1.20
29	58399.2858	0.29019	-101.71	0.05	52.61	0.48

REFERENCES

Avvakumova, E. A., Malkov, O. Y., & Kniazev, A. Y. 2013, AN, 334, 860

Bakış, V., Eker, Z., Sarı, O., Yücel, G., & Sonbaş, E. 2020, MNRAS, 496, 2605

Bressan, A., Marigo, P., Girardi, L., et al. 2012, MNRAS, 427, 127

Burggraaff, O., Talens, G. J. J., Spronck, J., et al. 2018, A&A, 617, 32

Cannon, A. J. & Pickering, E. C. 1993, VizieR Online Data Catalog: III/135A

Castelli, F. & Kurucz, R. L. 2004, arXiv Astrophysics e-prints, astro-ph/0405087

Claret, A. & Gimenez, A. 1992, A&AS, 96, 255

Cousins, A. W. J. 1981, SAAOC, 6, 4

Eastman, J., Siverd, R., & Gaudi, B. S. 2010, PASP, 122, 935

ESA. 1997, The Hipparcos and Tycho Catalogues, ESA SP-1200

Flower, P. J. 1996, ApJ, 469, 355

Gaia Collaboration, Prusti, T., de Bruijne, J. H. J., et al. 2016, A&A, 595, 1

Giménez, A. 1985, ApJ, 297, 405

Giménez, A. & Bastero, M. 1995, Ap&SS, 226, 99

Girardi, L., Bressan, A., Bertelli, G., & Chiosi, C. 2000, A&AS, 141, 371

Gontcharov, G. A. & Mosenkov, A. V. 2017, MNRAS, 472, 3805

Hadrava, P. 1995, A&AS, 114, 393

Huang, C. X., Vanderburg, A., Pál, A., et al. 2020, RNAAS, 4, 204

Jayasinghe, T., Kochanek, C. S., Stanek, K. Z., et al. 2018, MNRAS, 477, 3145

Kazarovets, E. V., Samus, N. N., Durlevich, O. V., et al. 1999, IBVS, 4659, 1

Kervella, P., Arenou, F., Mignard, F., & Thévenin, F. 2019, A&A, 623, 72

Kopal, Z. 1978, Dynamics of close binary systems (Dordrecht: Astrophysics and Space Science Library, Springer)

Kreiner, J. M. 2004, AcA, 54, 207

Kurucz, R. L. 1993, SYNTHE Spectrum Synthesis Programs and Line Data (Cambridge, MA: Smithsonian Astrophysical Observatory)

Kwee, K. K. & van Woerden, H. 1956, BAN, 12, 327

Levi-Civita, T. 1937, Am. J. Math., 59, 255

Lindegren, L., Klioner, S. A., Hernández, J., et al. 2021, A&A, 649, A2

McDonald, I., Zijlstra, A. A., & Boyer, M. L. 2012, MNRAS, 427, 343

Otero, S. A., Wils, P., Hoogeveen, G., & Dubovsky, P. A. 2006, IBVS, 5681, 1

Pickles, A. & Depagne, É. 2010, PASP, 122, 1437

Pojmanski, G. & Maciejewski, G. 2004, AcA, 54, 153

Prša, A. & Zwitter, T. 2005, ApJ, 628, 426

Smith, J. A., Tucker, D. L., Kent, S., et al. 2002, AJ, 123, 2121

Straizys, V. & Kuriliene, G. 1981, Ap&SS, 80, 353

Talens, G. J. J., Spronck, J. F. P., Lesage, A.-L., et al. 2017, A&A, 601, 11

van Hamme, W. 1993, AJ, 106, 2096

Wilson, R. E. & Devinney, E. J. 1971, ApJ, 166, 605

Zahn, J.-P. 1977, A&A, 57, 383

H. Bakiş, V. Bakiş, and E. Kiran: Department of Space Sciences and Technologies, Faculty of Science, Akdeniz University, 07058, Antalya, Turkey (evrimkiran@akdeniz.edu.tr).

Ö. L. Değirmenci: Department of Astronomy and Space Sciences, Faculty of Science, Ege University, 35100, Bornova - İzmir, Turkey.

Revista Mexicana de Astronomía y Astrofísica, **57**, 381–389 (2021)

https://doi.org/10.22201/ia.01851101p.2021.57.02.10

STUDY OF AN INTERMEDIATE AGE OPEN CLUSTER IC 1434 USING GROUND-BASED IMAGING AND GAIA DR2 ASTROMETRY

Y. H. M. Hendy[1] and D. Bisht[2]

Received November 21 2020; accepted June 11 2021

ABSTRACT

We present a detailed photometric and kinematical analysis of the poorly studied open cluster IC 1434 using CCD VRI, APASS, and Gaia DR2 database for the first time. By determining the membership probability of stars we identify the 238 most probable members with a probability higher than 60% by using proper motion and parallax data as taken from the Gaia DR2 catalog. The mean proper motion of the cluster is obtained as $\mu_x = -3.89 \pm 0.19$ and $\mu_y = -3.34 \pm 0.19$ mas yr^{-1} in both the directions of right ascension and declination. The radial distribution of member stars provides the cluster extent as 7.6 arcmin. We estimate the interstellar reddening $E(B-V)$ as 0.34 mag using the transformation equations from the literature. We obtain the values of cluster age and distance as 631 ± 73 Myr and 3.2 ± 0.1 kpc.

RESUMEN

Presentamos un estudio fotométrico y cinemático detallado del cúmulo IC 1434 utilizando por primera vez CCD VRI, APASS, y la base de datos Gaia DR2. Mediante el análisis de los movimientos propios y las paralajes del catálogo Gaia DR2 identificamos los 238 miembros más probables del cúmulo, con una probabilidad mayor que 60%. Encontramos que el movimiento propio medio del cúmulo es $\mu_x = -3.89 \pm 0.19$ and $\mu_y = -3.34 \pm 0.19$ mas yr^{-1} en ascensión recta y declinación. La distribución radial de las estrellas miembros muestra que la extensión del cúmulo es 7.6 minutos de arco. Estimamos un enrojecimiento interestelar de $E(B-V) = 0.34$ mag mediante las ecuaciones de transformación de la literatura. Obtuvimos una edad para el cúmulo de 631 ± 73 millones de años y una distancia de 3.2 ± 0.1 kpc.

Key Words: astrometry — Hertzsprung-Russell and colour-magnitude diagrams — open clusters and associations: individual: IC 1434

1. INTRODUCTION

Open clusters (OCs) are important tools to probe the Galactic disk properties (see, e.g., Friel 1995). OCs are very advantageous to interpret many queries regarding the assessment of chemical abundance gradients in the disk (see, e.g., Twarog, Ashman & Anthony-Twarog 1997; Chen, Hou & Wang 2003), Galactic structure and evolution (e.g., Janes & Adler 1982; Janes & Phelps 1994), interactions between thin and thick disks (e.g., Sandage 1988), as well as the theories of stellar formation and evolution (e.g., Meynet, Mermilliod & Maeder 1993; Phelps & Janes 1993). It's not an easy task to segregate cluster members from field stars considering that OCs are generally projected against the Galactic disc stars. The second data release (DR2) (Gaia Collaboration et al. 2016a) contains 1.7 billion sources and was made public on 2018 April 24 (Jordi et al. 2010; Gaia Collaboration et al. 2016a,b; Salgado et al. 2017). The Gaia DR2 data contains photometric magnitudes in three bands (G, G_{BP}, and G_{RP}) and astrometric data at the sub-milliarcsecond level along with the parallax (Gaia Collaboration et al. 2018a). Gaia data have been used recently by many authors to

---

[1] Astronomy Department, National Research Institute of Astronomy and Geophysics (NRIAG), Helwan, Cairo, Egypt.

[2] Key Laboratory for Researches in Galaxies and Cosmology, University of Science and Technology of China, Chinese Academy of Sciences, Hefei, Anhui, 230026, China.

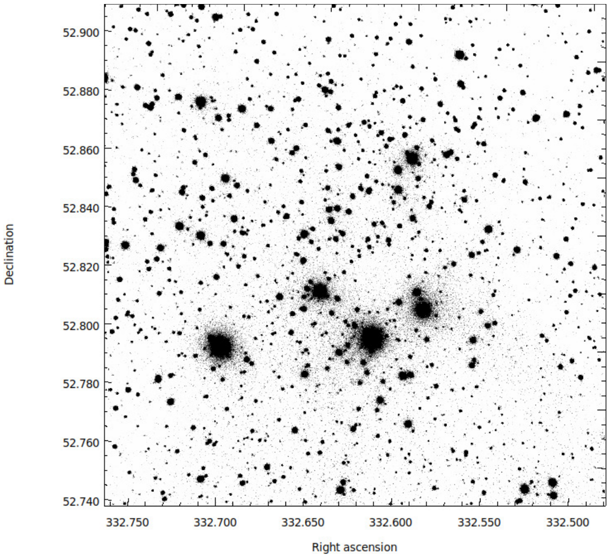

Fig. 1. Finding chart of the stars in the field of IC 1434. Filled circles of different sizes represent the brightness of the stars. The smallest size denotes stars of $V \approx 20$ mag.

estimate the membership probability of stars lying towards the cluster regions (Cantat-Gaudin et al. 2018; Gao 2018; Rangwal et al. 2019; Bisht et al. (2019, 2020a, 2020b)).

The open cluster IC 1434 ($\alpha_{2000} = 22^h10^m30^s$, $\delta_{2000} = 52°50'00''$; l=99°.937, b=-2°.700) is located in the second Galactic quadrant. Tadross (2009) analyzed this object using 2MASS and NOMAD data sets. He obtained the age, the interstellar reddening $E(B-V)$, and the distance of this object as 0.32 Gyr, 0.66 mag, and 3035 ± 140 pc, respectively. In this paper, our main goal is to accomplish a deep and precise analysis of an intermediate-age open cluster IC 1434 using CCD VRI, APASS, and Gaia DR2 data.

The layout of the paper is as follows. A brief description of data used, data reduction, and calibration are described in § 2. § 3 deals with the study of proper motion and determination of membership probability of stars. The derivation of structural properties and of fundamental parameters using the most probable cluster members is carried out in § 4. The conclusions are presented in § 5.

2. OBSERVATIONS AND CALIBRATION OF CCD DATA

The VRI CCD photometric observations of IC 1434 were carried out using the 74-inch Kottamia astronomical observatory (KAO) of NRIAG in Egypt. Images were collected using a $2k \times 2k$ CCD system. The observations were taken at the Newtonian focus with a field area of $10' \times 10'$ and a pixel scale of $0''.305$ pixel^{-1} on 8th November 2013. The read-out noise was 3.9 e$^-$/pixel. Observations were organized in several short exposures with the air mass ranges of 1.32-1.62 in each of the filters, as described in Table 1. All CCD frames were observed with two amplifiers, which were treated for overscan, bias, and flat field corrections using an IRAF's code written by one of the authors (Y.H.M. Hendy, see Tadross et al. 2018). To perform the photometry, we used a DAOPHOT package on IRAF (Stetson 1987, 1992). The data reduction procedure was explained by Bisht et al. (2019). The identification chart for IC 1434 based on our V-band observations is shown in Figure 1.

TABLE 1

LOG OF OBSERVATIONS, WITH DATES AND EXPOSURE TIMES FOR EACH PASSBAND

Band	Exposure Time (seconds)	Date
V	120×3, 60×1	8th November 2013
R	120×2, 60×1	”
I	120×3, 60×1	”

To obtain the instrumental magnitudes of stars in the observed field, we used the point spread function of Stetson (1987). We transformed the pixel coordinates (X and Y) into right ascension and declination using the astrometry website (https://nova.astrometry.net/).

To transform the VRI instrumental magnitudes into Johnson and Kron-Cousin standard magnitudes, we used the photometric data available in the V-band from Maciejewski & Niedzielski (2008) and in the RI-bands from the USNO-B1.0 catalog (Monet et al. 2003).

The transformation equations for converting the instrumental magnitude in to standard magnitude, are as follows:

$$\begin{aligned} V &= V_{ins} - (0.14 \pm 0.039)(V-R) + 21.18 \pm 0.031, \\ V-R &= (1.06 \pm 0.035)(V-R)_{ins} + 0.56 \pm 0.022, \\ V-I &= (0.90 \pm 0.036)(V-I)_{ins} + 0.85 \pm 0.027 \ . \end{aligned}$$

The respective errors in zero points and color coefficients are ≈0.03 mag shown in the above transformation equations. The internal errors derived from DAOPHOT are plotted against V magnitude in Figure 2. This figure shows that the average photometric errors are ≤ 0.02 mag at $V \approx 18^{th}$ mag, and ≤ 0.1 mag at $V \approx 19^{th}$ mag.

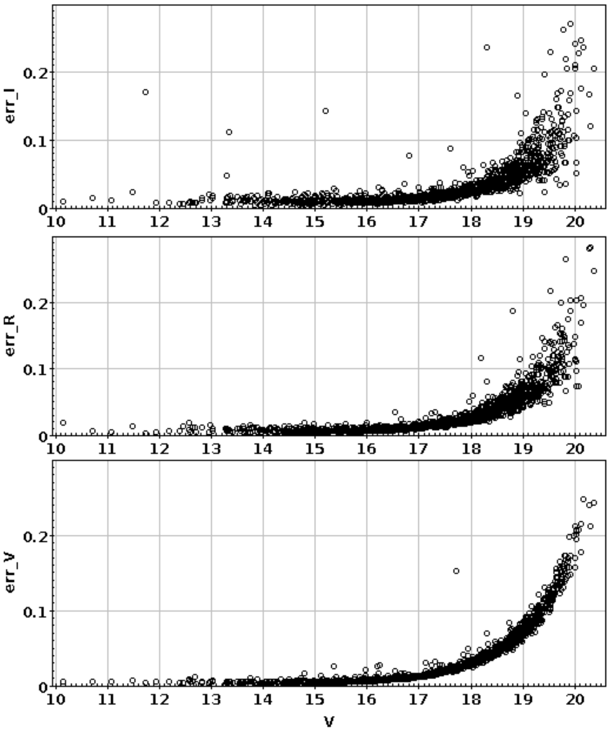

Fig. 2. Photometric errors in the V, R, and I bands against V magnitude.

To compare the photometry, we have cross-identified the stars in our observed data with the American Association of Variable Star Observers (AAVSO) Photometric All-Sky Survey (APASS) DR9 catalog. We have assumed that stars are accurately matched if the difference in position is less than 1 arcsec and, in this way, we have found 32 common stars. The APASS survey is cataloged in five filters B, V, g, r, and i. The range of magnitude in the V band is from 7 to 17 mag (Heden & Munari 2014). The DR9 catalog covers almost about 99 % of the sky (Heden et al. 2016). To obtain the Cousins I band using the Sloan ri photometric bands from the APASS catalog ($I_{APASS} = i - (0.337 \pm 0.191)$ $(r-i)-(0.370 \pm .041)$), we have adopted the method given by Tadross & Hendy (2016).

The difference indicates that present V and $(V-I)$ measurements are in fair agreement with those of stars given in the APASS catalog. The comparable difference is found as 0.07 in the V band and 0.08 in $(V-I)$ as shown in Figure 3.

2.1. *Gaia DR2*

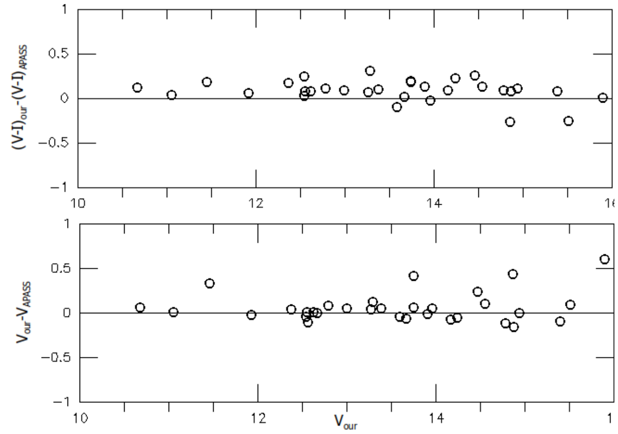

Fig. 3. Differences between measurements presented in the APASS catalog and this study for the V magnitude and $(V-I)$ colors. A zero difference is indicated by the solid line.

The Gaia DR2 (Gaia Collaboration et al. 2018b) database within a 20′ radius of the cluster is used for the astrometric analysis. These data consist of positions on the sky (α, δ), parallaxes and proper motions $(\mu_\alpha \cos\delta, \mu_\delta)$ with a limiting magnitude of $G = 21$ mag. The errors in photometric magnitudes (G, G_{BP}, and G_{RP}) versus G mag are shown in Figure 4. In this figure, we find the mean errors in the G band are ≈ 0.01 mag while the mean errors in the G_{BP} and G_{RP} bands are ≈ 0.1 mag at 20 mag. The proper motions with their respective errors are plotted against G magnitude in Figure 5. The uncertainties in the corresponding proper motion components are ≈ 0.06 mas yr^{-1} (for $G \leq 15$ mag), ≈ 0.2 mas yr^{-1} (for $G \approx 17$ mag), and ≈ 1.2 mas yr^{-1} (for $G \approx 20$ mag).

3. PROPER MOTION STUDY AND MEMBERSHIP PROBABILITIES OF STARS

The proper motion of a cluster is a change in its angular position with time as seen from the center of mass of the Solar System. Proper motions play an influential role to eliminate non-members from the cluster's main sequence (Yadav et al. 2013; Bisht et al. 2020a). We have cross-matched our observational data in VRI bands and data from the Gaia DR2 catalog. A circle of 0.6 mas/yr around the cluster center in the VPD characterizes our membership criteria as shown in Figure 6. The chosen radius in the VPD is a compromise between losing members with poor proper motions and including field stars.

The OCs are highly contaminated by a large number of foreground/background stars especially towards the fainter end of the main sequence. Vasilevskis et al. (1958) have set up a mathematical model to obtain membership probabilities of stars

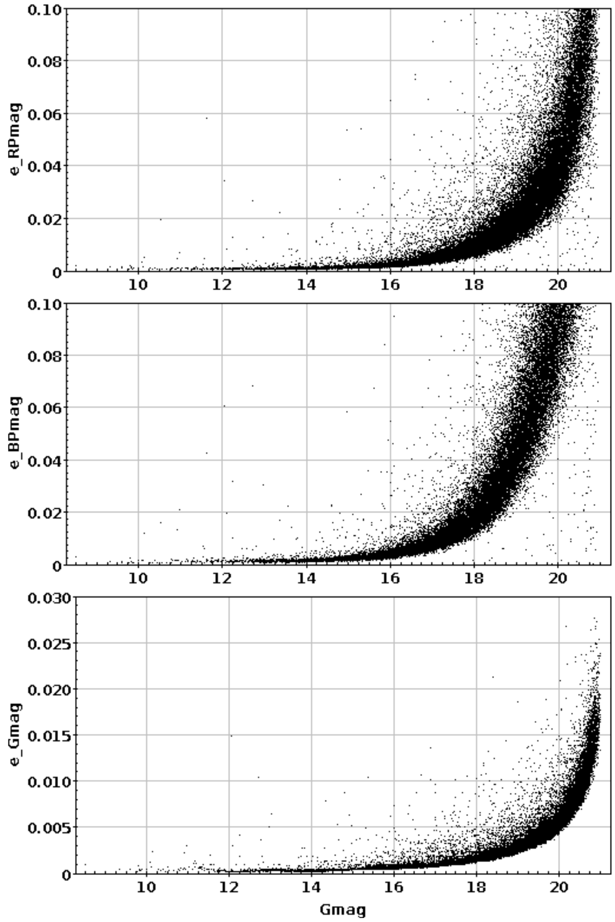

Fig. 4. Photometric errors in the Gaia bands (G, BP, and RP) against G magnitude.

using proper motion data. A revised technique was developed by Stetson (1980) and Zhao & He (1990) to check the membership of stars in OCs based on proper motions. To find the membership probability of stars towards the region of IC 1434, we have adopted the criteria of Kharchenko et al. (2004). This method has been previously used by Bisht et al. (2018) for OCs Teutsch 10 and Teutsch 25. Hendy (2018) used this method for the open cluster FSR 814. The kinematical probability of stars is expressed as:

$$P_k = e^{\left[-0.25\left(\frac{(\mu x-\overline{\mu x})^2}{\sigma_x^2}+\frac{(\mu y-\overline{\mu y})^2}{\sigma_y^2}\right)\right]},$$

where $\sigma_x^2 = \sigma_{\mu_x}^2 + \sigma_{\overline{\mu_x}}^2$ and $\sigma_y^2 = \sigma_{\mu_y}^2 + \sigma_{\overline{\mu_y}}^2$. Here μ_x and μ_y are the proper motion of a particular star, while σ_{μ_x} and σ_{μ_y} are the corresponding errors. The $\overline{\mu_x}$ and $\overline{\mu_y}$ are the mean values of the proper motions, while $\sigma_{\overline{\mu_x}}$ and $\sigma_{\overline{\mu_y}}$ are their corresponding standard deviations. Using the above method, we identified possible members of IC1434 if their membership probability was higher than 60% which can be seen in Figure 7.

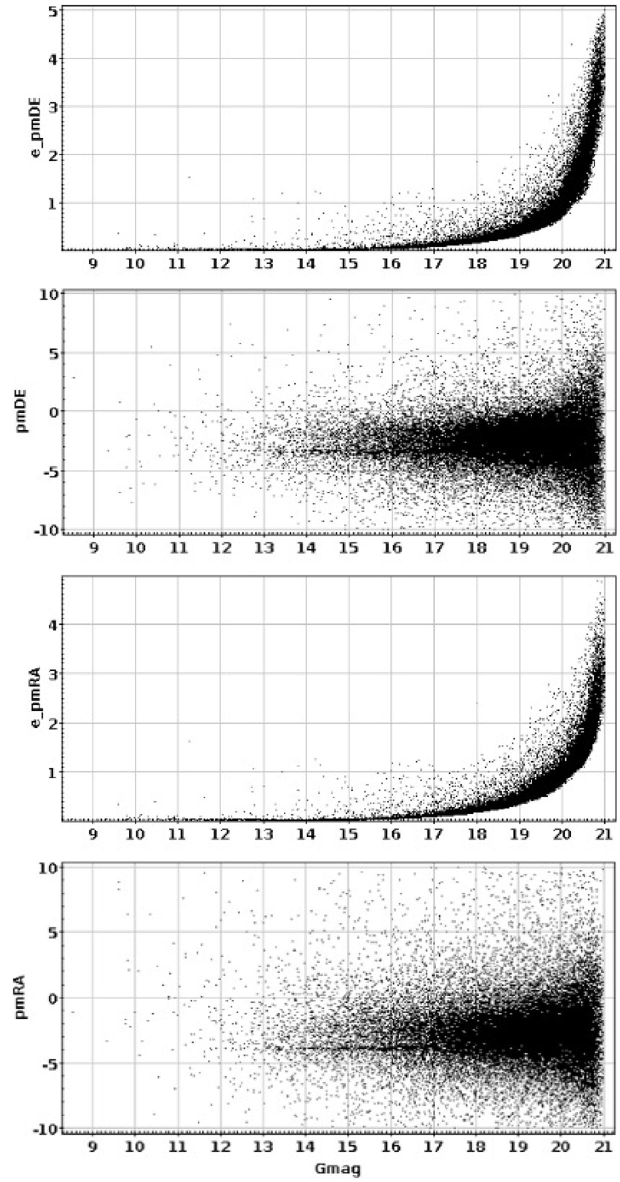

Fig. 5. Plot of proper motions and their errors versus G magnitude.

We used only probable cluster members to estimate the mean value of proper motions and parallax of IC 1434. We fitted Gaussian profile to the construct histograms shown in Figure 8. We obtained the mean-proper motion of IC 1434 as -3.89 ± 0.19 and -3.34 ± 0.19 mas yr^{-1} in RA and DEC directions, respectively. We determined the mean value

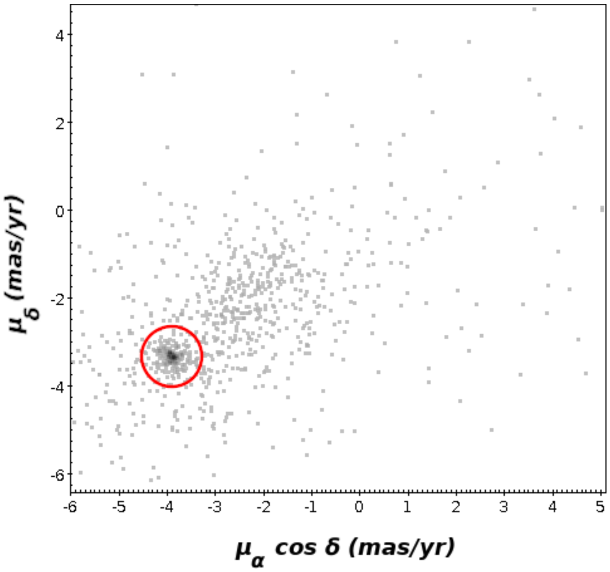

Fig. 6. Vector point diagram. The circle defines the cluster region of IC 1434 within a radius of 0.6 mas/yr. The color figure can be viewed online.

of the parallax as 0.30 ± 0.11 mas. Our findings are very close to the values given by Cantat-Gaudin et al. (2018).

Finally, we considered a star as a most probable member if it lies within a 0.6 mas/yr radius in the VPD, having a membership probability higher than 60% and a parallax within 3σ from the mean parallax of the cluster IC 1434. In Figure 9, we plot the proper motions and parallax distribution of the most probable members (denoted by red dots) and of all observed stars (denoted by gray dots) against G magnitude. In this figure, the horizontal solid line indicates the mean value of the proper motions and parallaxes.

4. STRUCTURAL PROPERTIES OF IC 1434

4.1. *Spatial Structure: Radial Density Profile*

The accuracy of the central coordinates is very important for the reliable estimation of the cluster's main fundamental parameters (e.g., age, distance, reddening, etc.). We applied a star-count technique to obtain the center coordinates towards the area of IC 1434. The resulting histograms in both the RA and DEC directions are shown in the left panel of Figure 10. The Gaussian curve-fitting at the central zones provided the center coordinates as $\alpha = 332.612 \pm 0.06$ deg ($22^h10^m26.8^s$) and $\delta = 52.84 \pm 0.04$ deg ($52°50'24''$). These estimated values are in very good agreement with the values given by Dias et al. (2002) and Cantat-Gaudin et al. (2018).

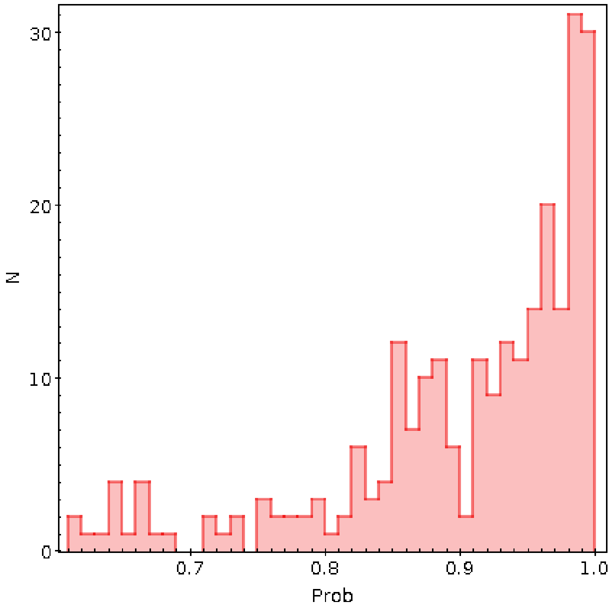

Fig. 7. Membership probability histogram of stars for IC 1434. We considered stars with a probability ≥ 0.6 as cluster members. The color figure can be viewed online.

TABLE 2

STRUCTURAL PARAMETERS OF IC 1434*

Name	f_0	f_b	R_c	c	δ_c
IC 1434	23.70±3.49	8.78±0.21	1.25±0.19	0.78	3.7

*Background and central densities are given in units of stars per arcmin^2. Core radius (r_c) is given in arcmin.

The radial density profile (RDP) is plotted in Figure 11 to estimate the radius of the cluster. We divided the observed area of IC 1434 into several concentric rings. The number density, R_i, in the ith zone is determined by using the formula $R_i = \frac{N_i}{A_i}$, where N_i is the number of stars and A_i is the area of the ith zone. This RDP flattens at $R \approx 7.6$ arcmin and begins to merge with the background density, as clearly shown in the right panel of Figure 11. Therefore, we consider 7.6 arcmin as the cluster radius. A smooth continuous line represents the fitted King (1962) profile:

$$f(r) = f_{bg} + \frac{f_0}{1 + (r/r_c)^2}$$

where r_c, f_0, and f_{bg} are the core radius, central density, and the background density level, respectively. By fitting the King model to RDP, we estimated the structural parameters of IC 1434 and list them in Table 2.

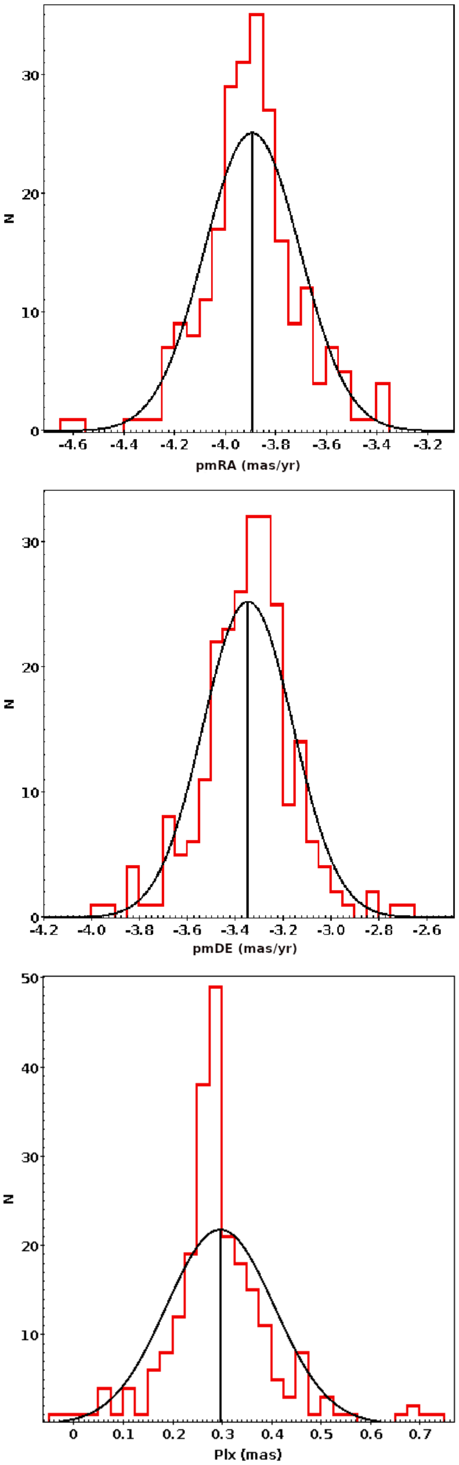

Fig. 8. Histogram to determine the mean values of proper motions in RA and DEC (top and middle panels). Histogram to find the mean parallax (bottom panel). The Gaussian function fits to the central bins provide the mean values in proper motion and parallax shown in each panel. The color figure can be viewed online.

We estimated the concentration parameter using equation $c = \log\left(\frac{r_{lim}}{r_c}\right)$, as given by Peterson & King 1975). In the present study, the concentration parameter was found to be 0.78 for IC 1434. Maciejewski & Niedzielski (2007) reported that R_{lim} may vary for individual clusters from $2R_c$ to $7R_c$. The estimated value of R_{lim} ($\approx 6.1R_c$) shows a fair agreement with the Maciejewski & Niedzielski (2007) value. We obtained the density contrast parameter ($\delta_c = 1+[f_0/f_{bg}]$) for IC 1434 as 3.7. It is lower than the range $7 \leq \delta_c \leq 23$ derived by Bonatto & Bica (2009). This demonstrates that IC 1434 is a sparse cluster.

4.2. *Age and Distance Estimation Using the CMD*

Age and distance are important parameters to trace the structure and chemical evolution of the Milky Way Galaxy using OCs (Friel & Janes 1993). The (G, $BP-RP$), and (V, $V-I$) color magnitude diagrams (CMDs) are shown in Figure 12. In this figure, filled dots stand for the most probable cluster members with membership probability $\geq 60\%$ while open circles stand for the ones matched with the catalog of Cantat-Gaudin et al. (2018). The age of IC 1434 was estimated by fitting the theoretical isochrones of Marigo et al. (2017) with a metallicity of $Z = 0.0152$ to the CMDs, as shown in Figure 12. In this figure, we used the isochrones of different ages, log(age) = 8.75, 8.80 and 8.85. We found the best global fit at log(age)=8.80, which corresponds to a cluster age of 631 ± 73 Myr.

Our estimated value of the color-excess in the Gaia bands $E(BP-RP)$ is 0.43 mag from the isochrone fitting to the CMD's. We calculated the interstellar reddening $E(B-V)$ as 0.34 mag using the transformation equations ($E(B-V)$= 0.785 $E(BP-RP)$) as taken from Abdelaziz et al. (2020). The distance modulus ($m - M_G$=12.51 mag) of IC 1434 provides the heliocentric distance as 3.2 ± 0.1 kpc. Our estimated values of $E(B-V)$ and distance modulus are in fair agreement with the values $E(B-V) = 0.49$ and $m - M_G$=12.43 obtained by Angelo et al. (2020).

We obtained the Galactocentric distance as 9.4 ± 0.1 kpc by assuming an 8.3 kpc distance of the Sun to the Galactic center. The Galactocentric coordinates are estimated as $X_\odot = -0.55 \pm 0.04$ kpc, $Y_\odot = 3.1 \pm 0.2$ kpc and $Z_\odot = -0.15 \pm 0.010$ kpc. The estimated values of the Galactocentric coordinates are very close to the values obtained by Cantat-Gaudin et al. (2018).

We also checked the distance of IC 1434 using the parallax of stars from the Gaia DR2 cat-

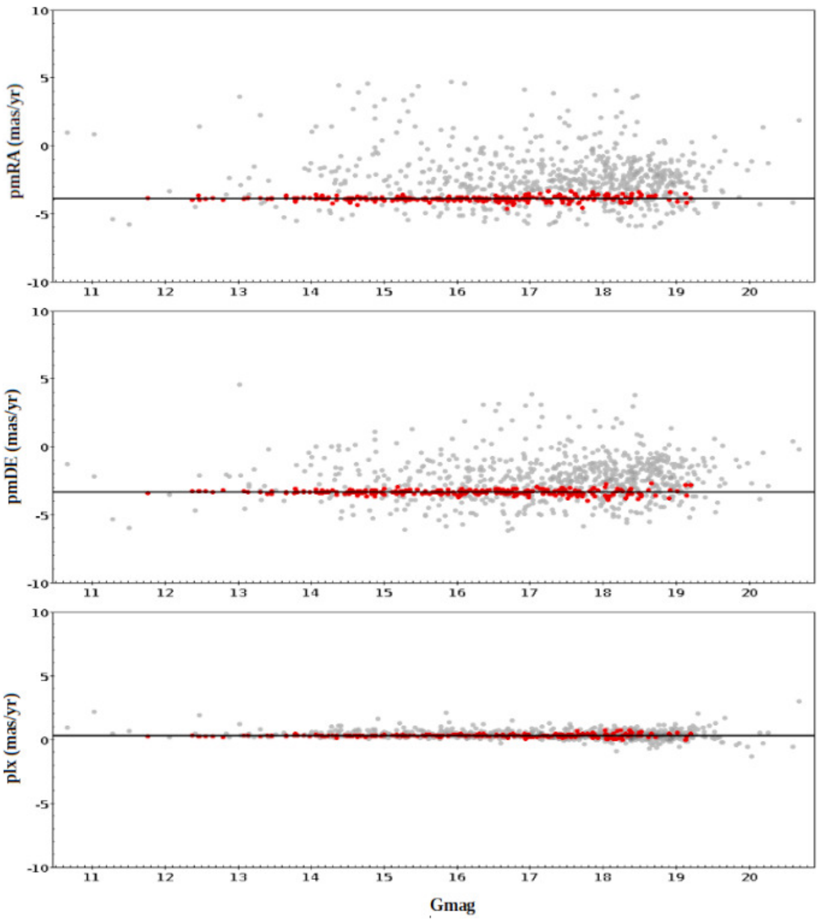

Fig. 9. Proper motion components and parallax distribution of most probable members (red dots) and all stars (gray dots) against *G* band magnitude. The horizontal line indicates the mean value of proper motion and parallax. The color figure can be viewed online.

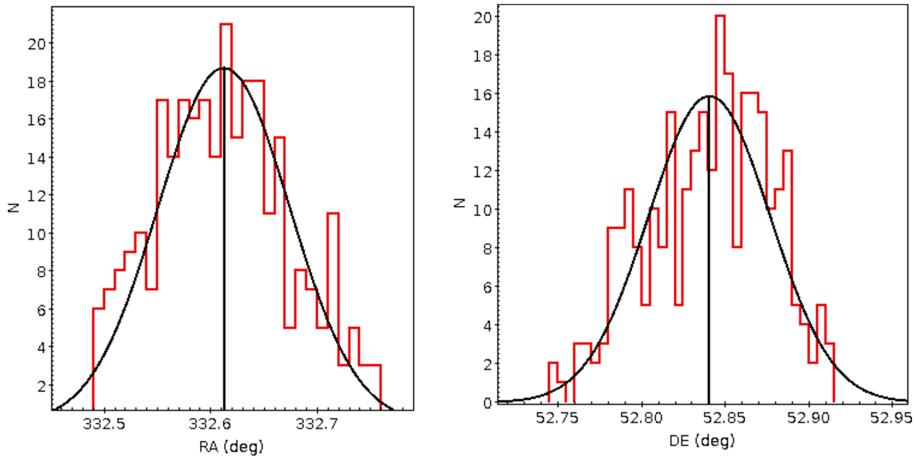

Fig. 10. Profiles of stellar counts across cluster IC 1434. Gaussian fits have been applied. The center of symmetry about the peaks of right ascension and declination is taken to be the position of the cluster center. The color figure can be viewed online.

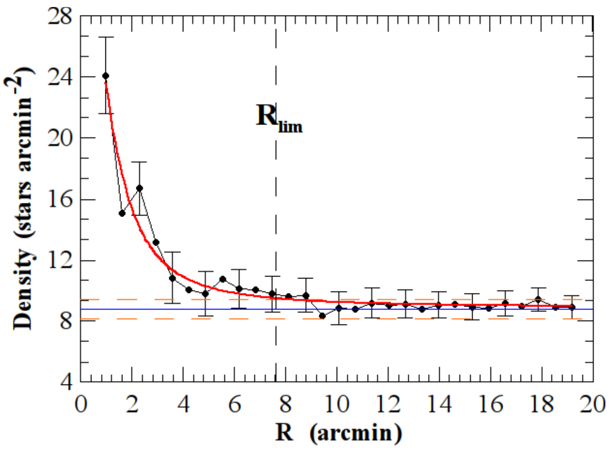

Fig. 11. Surface density distribution of the cluster IC 1434. Errors are determined from sampling statistics $\frac{1}{\sqrt{N}}$, where N is the number of stars used in the density estimation at that point. The smooth line represents the fitted profile whereas the dotted line shows the background density level. Long and short dash lines represent the errors in the background density. The color figure can be viewed online.

alog. We found the distance of this object to be 3.3 kpc, which is very close to our estimation from the isochrone fitting method. Angelo et al. (2020), Cantat-Gaudin (2020), Kharchenko et al. (2013), and Tadross (2009) have determined distance values for IC 1434 of 3.1, 3.3, 3.2, and 3.0 kpc, respectively. Our derived value of the distance is in good agreement with Angelo et al. (2020), Cantat-Gaudin (2020), and Kharchenko et al. (2013). The distance estimation of IC 1434 by Tadross (2009) is based on 2MASS and NOMAD data. Our obtained value of the distance is more precise than that of Tadross (2009) because our estimation is based on good quality optical data along with the high precision Gaia DR2 astrometry.

5. CONCLUSIONS

We presented a photometric and kinematic study of the poorly studied open cluster IC 1434 using CCD VRI and Gaia DR2 data. We estimated the membership probabilities of stars towards the region of IC 1434 and found 238 members with a membership probability $\geq 60\%$. We used those probable members to derive the fundamental parameters. The main results of the current investigation are as follows:

- The updated cluster center coordinates are estimated as: $\alpha = 332.612 \pm 0.06$ deg ($22^h 10^m 26.8^s$) and $\delta = 52.84 \pm 0.04$ deg ($52°50'24''$) using the most probable cluster members. The cluster radius is obtained as 7.6 arcmin using the radial density profile.

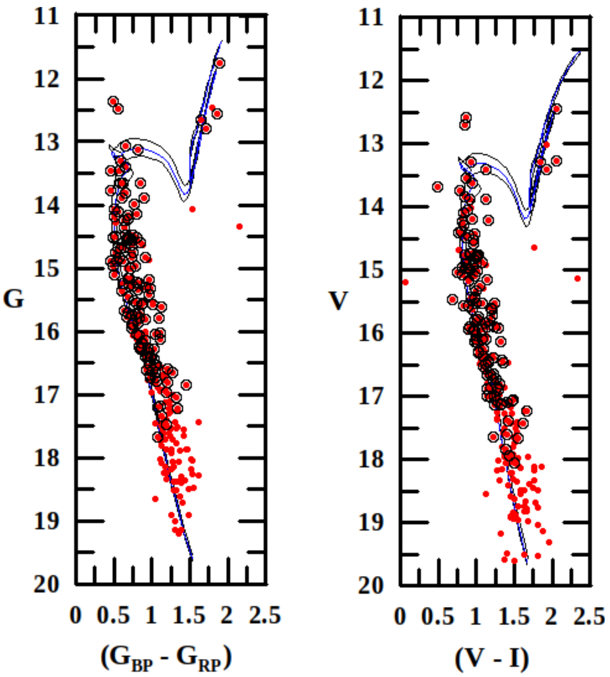

Fig. 12. Isochrone fitting to the CMDs. The curves are the solar metallicity isochrones taken from Marigo et al. (2017) for log(age) = 8.75, 8.80, and 8.85. The filled and open circles are our 238 members and the 127 members of Cantat-Gaudin et al. (2018), respectively. The color figure can be viewed online.

- On the basis of the vector point diagram and membership probability estimation of stars, we identified 238 most probable cluster members for IC 1434. The mean PM of the cluster is estimated as -3.89 ± 0.19 and -3.34 ± 0.19 mas yr^{-1} in the RA and DEC directions, respectively.

- The distance to the cluster IC 1434 is determined as 3.2 ± 0.1 kpc. This value is well supported by the distance estimated using the mean parallax, 3.3 kpc. The age is estimated as 631 ± 73 Myr by comparing the cluster CMD with the theoretical isochrone given by Marigo et al. (2017) with $Z = 0.0152$.

The authors are thankful to the anonymous referee for useful comments, which improved the contents of the paper significantly. This work is supported by the IMHOTEP collaboration program No. 42088ZK between Egypt and France. D. Bisht is supported by the Natural Science Foundation of China (NSFC-11590782, NSFC-11421303). This work made use of data from the European Space Agency (ESA) mission Gaia (https://www.cosmos.esa.int/gaia), processed by the Gaia Data Processing and Analysis Consortium (DPAC, https://www.cosmos.esa.int/web/gaia/dpac/consortium). Funding for the DPAC has been provided by national institutions, in particular the institutions participating in the Gaia Multilateral Agreement. This work made use of TOPCAT (http://www.starlink.ac.uk/topcat). It was developed mostly in the UK within various UK and Euro-VO projects (Starlink, AstroGrid, VOTech, AIDA, GAVO, GENIUS, DPAC) and under PPARC and STFC grants. Its underlying table processing facilities were provided by the related packages STIL and STILTS. This research made use of the Vizier catalogue access tool, CDS, Aladin Sky Atlas developed at CDS, Strasbourg Observatory, France. This work made use of data from the American Association of Variable Star Observers (AAVSO) Photometric All-Sky Survey (APASS) DR9 catalog.

REFERENCES

Abdelaziz, A. E., Hendy, Y. H. M., Shokry, A., et al. 2020, RMxAA, 56, 245

Angelo, M. S., Santos, J. F. C., & Corradi, W. J. B. 2020, MNRAS, 493, 3473

Bisht, D., Ganesh, S., Yadav, R. K. S., et al. 2018, AdSpR, 61, 517

Bisht, D., Yadav, R. K. S., Ganesh, S., et al. 2019, MNRAS, 482, 1471B

Bisht, D., Zhu, Q., Yadav, R. K. S., et al. 2020a, MNRAS, 494, 607-623

Bisht, D., Elsanhoury, W. H., Zhu, Q., et al. 2020b, AJ, 160, 119B

Bonatto, C. & Bica, E. 2009, MNRAS, 397, 1915

Cantat-Gaudin, T., Jordi, C., Vallenari, A., et al. 2018, A&A, 618, 93

Cantat-Gaudin, T., Anders, F., & Castro-Ginard, A. 2020, A&A, 640, 1

Chen, L., Hou, J. L., & Wang, J. J. 2003, AJ, 125, 1397

Dias, W. S., Alessi, B. S., Moitinho, A, et al. 2002, A&A, 389, 873

Friel, E. D. & Janes, K. A. 1993, A&A, 267, 75

Friel, E. D. 1995, ARA&A, 33, 381F

Gaia Collaboration, Prusti, T, de Bruijne, et al. 2016a, A&A, 595, 1

Gaia Collaboration, Brown, A. G. A., Vallenari, A., et al. 2016b, A&A, 595, 2

Gaia Collaboration, Babusiaux, C., van Leeuwen, F., et al. 2018a, A&A, 616, 10

Gaia Collaboration, Brown, A. G. A., Vallenari, A., et al., 2018b, A&A, 616, 17

Gao, X.-h. 2018, PASP, 130, 124101

Henden, A. & Munari, U. 2014, CoSka, 43, 518

Henden, A. A., Templeton, M., Terrell, D., et al. 2016, VizieR Online Data Catalog: II/336

Hendy, Y. H. M. 2018, NRIAG Journal of Astronomy and Geophysics, 7, 180

Janes, K. & Adler, D. 1982, ApJS, 49, 425

Janes, K. A. & Phelps, R. L. 1994, AJ, 108, 1773

Jordi, C., Gebran, M., Carrasco, J. M., et al. 2010, A&A, 523, 48

Kharchenko, N. V., Piskunov, A. E., Röser, S., Schilbach, E., & Scholz, R.-D. 2004, AN, 325, 740

Kharchenko, N. V., Piskunov, A. E., Schilbach, E., Röser, S., & Scholz, R.-D. 2013, A&A, 558, 53

King, I. 1962, AJ, 67, 471

Maciejewski, G. & Niedzielski, A. 2007, A&A, 467, 1065

_________. 2008, AN, 329, 602

Marigo, P., Girardi, L., Bressan, A., et al. 2017, ApJ, 835, 77

Meynet, G., Mermilliod, J.-C., & Maeder, A. 1993, A&AS, 98, 477

Monet, D. G., Levine, S. E., Canzian, B., et al. 2003, AJ, 125, 984

Peterson, C. J. & King, I. R. 1975, AJ, 80, 427

Phelps, R. L. & Janes, K. A. 1993, AJ, 106, 1870

Rangwal, G., Yadav, R. K. S., Durgapal, A., Bisht, D., & Nardiello, D. 2019, MNRAS, 490, 1383

Salgado, J., González-Núñez, J., Gutiérrez-Sánchez, R., et al. 2017, A&C, 21, 22

Salpeter, E. E. 1955, ApJ, 121, 161

Sandage, A. 1988, BAAS, 20, 1037

Spitzer, L. J. & Hart, M. M. 1971, ApJ, 164, 399

Stetson, P. B. 1980, AJ, 85, 387

_________. 1987, PASP, 99, 191

_________. 1992, ASPC 25, Astronomical Data Analysis Software and Systems, ed. D. M. Warrall, Ch. Biemesderfer, & J. I. Barnes, 297

Tadross, A. L. 2009, New Astronomy, 14, 200

Tadross, A. L. & Hendy, Y. H. M. 2016, JKAS, 49, 53

Tadross, A. L., Bendary, R., Hendy, Y., & Bonaltu, Ch. 2018, AN, 339, 698

Twarog, B. A., Ashman, K. M., & Anthony-Twarog, B. J. 1997, AJ, 114, 2556

Vasilevskis, S., Klemola, A., & Preston, G. 1958, AJ, 63, 387

Yadav, R. K. S., Sariya, D. P., & Sagar, R. 2013, MNRAS, 430, 3350

Zhao, J. L. & He, Y. P. 1990, A&A, 237, 54

D. Bisht: Key Laboratory for Researches in Galaxies and Cosmology, University of Science and Technology of China, Chinese Academy of Sciences, Hefei, Anhui, 230026, China (dbisht@ustc.edu.cn).

Y. H. M. Hendy: Astronomy Department, National Research Institute of Astronomy and Geophysics (NRIAG), Helwan, Cairo, Egypt (y.h.m.hendy@gmail.com).

Revista Mexicana de Astronomía y Astrofísica, **57**, 391–397 (2021)

https://doi.org/10.22201/ia.01851101p.2021.57.02.11

STAR FORMATION HISTORIES OF BRIGHTEST CLUSTER GALAXIES WITH INTERMEDIATE CENTRAL AGES

J. Umanzor and M. L. Talavera

Universidad Nacional Autónoma de Honduras, Facultad de Ciencias Espaciales, Departamento de Astronomía y Astrofísica.

Received February 16 2021; accepted July 14 2021

ABSTRACT

This work is devoted to the study of the star formation histories (SFHs) of the brightest cluster galaxies (BCGs) with intermediate central ages (from 5 to 10 Gyr), to confirm if BCGs with these ages represent different accretion histories or simply a stochastic effect. The sample is composed of 6 BCGs with intermediate central ages and 3 BCGs with old central ages (> 12 Gyr) as comparison galaxies. The galaxies were observed with the integrated field spectrograph VIMOS installed in the Very Large Telescope (VLT). The SFHs were obtained with the full spectrum fitting technique using the star population code STARLIGHT. The BCGs of intermediate central age analyzed formed almost 100 % of their stars at $z > 2$ and their SFHs are similar to the SFHs of BCGs of old central ages and elliptical galaxies of similar mass ($\mathrm{M_{Dyn}} > 10^{11}\, M_{\odot}$); therefore, these BCGs do not represent different SFHs.

RESUMEN

Este trabajo está dedicado al estudio de las historias de formación estelar (HFE) de BCGs (brightest cluster galaxies) con edades centrales intermedias (de 5 a 10 Ga), para confirmar si BCGs con estas edades representan historias de acreción distintas o si es simplemente un efecto estocástico. La muestra está compuesta de 6 BCGs con edades intermedias y 3 BCGs con edades centrales viejas (> 12 Ga) como galaxias de comparación. Las galaxias se observaron con el espectrógrafo de campo integrado VIMOS instalado en el VLT (Very Large Telescope). Las HFE se obtuvieron con la técnica de ajuste de todo el espectro usando el código de poblaciones estelares STARLIGHT. Las BCGs de edades centrales intermedias analizadas formaron casi el 100 % de sus estrellas a $z > 2$ y sus HFE son similares a las HFE de BCGs de edades centrales viejas y de galaxias elípticas de masa similar ($\mathrm{M_{Din}} > 10^{11}\, M_{\odot}$); por tanto, estas BCGs no representan HFE distintas.

Key Words: galaxies: clusters: general — galaxies: elliptical and lenticular, cD — galaxies: evolution — galaxies: formation — galaxies: star formation

1. INTRODUCTION

Brightest cluster galaxies (BCGs) are the largest and most luminous galaxies in the Universe, generally very close to the space and kinematic center of galaxy clusters. At first BCGs appear to be giant elliptical galaxies. However, they have unique properties (shallower surface brightness profiles, high speed scattering, relatively high luminosities and masses), and their special formation environment makes them different from giant elliptical galaxies. The following formation theories have been proposed to explain the origin of BCGs: cooling flows (Silk 1976; Cowie & Binney 1977; Fabian 1994), galactic cannibalism (Ostriker & Tremaine 1975; White 1976; Malumuth & Richstone 1984; Merritt 1985) and two-phase (De Lucia & Blaizot 2007; Naab et al. 2009; Laporte et al. 2013). However, when these theories were tested in different cosmological settings, not all of them gave realistic results.

The first studies of BCGs focused on their high luminosities. BCGs are typically 10 times more luminous than normal elliptical galaxies (Sandage & Hardy 1973; Schombert 1986), with absolute magnitudes between −21.5 to −23.5 in the V band. Other studies found that the luminosities of BCGs are too high to be simply the brightest member of a standard luminosity function (Schechter & Peebles 1976) of elliptical galaxies (e.g. Tremaine & Richstone 1977; Dressler 1978; Bernstein & Bhavsar 2001).

BCGs have usually been classified into two morphological types, cD galaxies that have faint and extended stellar halos and giant ellipticals, without an envelope. This is based on the morphology shown by BCGs in the optical range and their colors in the optical and near infrared, which suggest relatively old stellar populations and little ongoing star formation activity (Dubinski 1998; Tonini et al. 2012; Bai et al. 2014; Zhao et al. 2015). However, they distinguish themselves from the typical cluster elliptical galaxy by their relatively large masses ($\approx 10^{13}\,M_{\odot}$, Katayama et al. (2003)) and luminosities, and by shallower surface brightness profiles and central velocity dispersions of $300 - 400\,\mathrm{km\ s^{-1}}$ (Oemler 1976; Schombert 1986; Dubinski 1998; Edwards et al. 2020). Von der Linden et al. (2007) found BCGs to have a higher dynamical-to-stellar mass ratio, indicating that they contained a larger fraction of dark matter compared to a sample of non-BCG galaxies. Also, the BCGs often show double or multiple nuclei (Schneider et al. 1983; Laine et al. 2003).

By using integral field unit (IFU) spectroscopy Oliva-Altamirano et al. (2015) performed an analysis of the stellar populations of 9 BCGs at $z < 0.1$. They showed that BCGs have high central metallicity, flat metallicity gradients and ages in a wide range of 5 to 15 Gyr. They also found that 67 % (6/9) of BCGs have intermediate central ages (5 Gyr < age < 10 Gyr) suggesting a history of active accretion (star formation up to $z \approx 1$) and 33 % (3/9) have old central ages (age > 11 Gyr) reflecting that they have not had star formation since $z \approx 2$. The stellar population measurements come from the luminosity-weighed distribution and are sensitive to the brightest and youngest populations of the stars in the galaxy (e.g. Trager & Somerville 2009).

Hydrodynamic simulations of early type galaxies (ETGs) in environments less dense than those typically found around BCGs predict that more massive galaxies are older than less massive galaxies, such that at masses $> 10^{10.5}\,M_{\odot}$ the galaxies are older than 10 Gyr (Naab et al. 2014; Peeples et al. 2014; Hirschmann et al. 2013) and show passive evolution from $z \approx 2$.

The SFH is a function that describes how the rate of star formation varies over cosmic time until the moment of observation. The SFH in galaxies is one of the most important parameters to constrain cosmological models, the formation and evolution of galaxies and the star formation theories. Knowledge of SFH is important for the development of various topics in the evolution of galaxies, such as chemical enrichment, interactions between galaxies as dissipators of star formation, and the role played by stellar dynamics and the self-propagation of star formation. In particular, the SFH of BCGs provide information about their formation conditions in the early universe and also about the mechanism by which star formation shuts down.

In this work, the SFH of BCGs of intermediate and old central ages are inferred using the sample of BCGs from Oliva-Altamirano et al. (2015). The SFH were obtained with the whole spectrum fitting technique using the stellar population code STARLIGHT (Cid Fernandes et al. 2005). We investigated whether BCGs with intermediate central ages have different accretion histories, or whether it is simply a stochastic effect. The outline of this paper is as follows. In § 2 we describe observations, data reduction and spectrum fitting. We present the results in § 3. These are later discussed in § 4. For the analysis of the results we adopt the ΛCDM cosmology with $\Omega_M = 0.27$ and $H_o = 70\,\mathrm{Km\ s^{-1}\ Mpc^{-1}}$.

2. METHODOLOGY

2.1. *Observations*

The observations of the BCGs were carried out using an IFU. An IFU is an instrument that divides the field of view into many spaxels (cells or spatial pixels). In astronomy, IFUs are used to study large objects such as nebulae, galaxies or a crowded cluster of stars or galaxies in one shot, using a technique known as integral field spectroscopy. In this method, the signal from each spaxel in the field of view is fed into a spectrograph, which generates a spectrum for each individual spaxel. With all the resulting spectra, a data cube is formed, which contains everything in the 2D field of view, in addition to the third dimension obtained by the spectrograph.

The sample is composed of 6 BCGs with intermediate central ages and 3 BCGs with old central ages (See Table 1). The ages were calculated by a stellar population analysis (Olivia-Altamirano et al. 2015). The BCGs are part of the C4 Cluster Catalog (Miller et al. 2005) from the Third Data Release (DR3) from the Sloan Digital Sky Survey (SDSS; York et al. 2000). BCGs were observed with the VLT using the VIMOS spectrograph (Le Fèvre et al.

TABLE 1

BCGS OF INTERMEDIATE AND OLD CENTRAL AGES

BCGs [a] (SDSS-C4-DR3)	R_e [b] [″]	z [b]	log M_{Dyn} [b, c] [$M_\odot$]	Age [d] [Gyr]	Merging? [d]
Intermediate age					
1027	6.98	0.090	11.79	8.9	y
1042	7.22	0.094	11.83	6.4	n
1048	5.17	0.077	11.59	7.1	y
1066	4.95	0.083	11.62	5.8	y
1261	5.76	0.037	11.32	8.8	n
2039	8.82	0.082	11.86	9.6	n
Old age					
1050	8.43	0.072	11.78	16.4	n
2001	5.84	0.041	11.38	12.6	n
2086	4.83	0.083	11.60	13.2	y

[a] We use the same nomenclature as Jimmy et al. (2013) and Oliva-Altamirano et al. (2015), i.e. we present each cluster by the last four digits of the SDSS flag, rather than the SSDS-C4-DR3 number.

[b] Jimmy et al. (2013).

[c] The dynamical mass was calculated using the standard equation given in Cappellari et al. (2006).

[d] Oliva-Altamirano et al. (2015).

2003). VIMOS was used in IFU mode with the high-resolution blue grism, which has a spectral resolution of 0.51 Å pixel^{-1}. The galaxies observed with the instruments mentioned above have a spatial sampling of 0.″67 pixel^{-1} and a field of view of 27″ × 27″. The observations were made in two parts: from April to August 2008 (Prog. ID 381.B-0728) and from April to July 2011 (ID 087.B-0366), during dark nights with an average seeing of 0.″9.

2.2. *Data Reduction*

The reduction of the IFU data was done first using the VIMOS code (Izzo et al. 2004). This code generates the calibration files (master bias, arc spectrum, flat field, fiber identification, etc.) and extracts the science spectrum in every fiber of every image. The VIMOS field of view is made up of four quadrants and the VIMOS code reduces each quadrant separately. Second, an IDL routine is used to mask the bad fibers, subtract the sky in each of the quadrants of the science images, and then combine the quadrants to form a data cube. More details on the observations and data reduction can be found in Jimmy et al. (2013) and Oliva-Altamirano et al. (2015).

2.3. *Spectrum Fitting*

After generating the data cube for each galaxy we used the PYTHON code of Oliva-Altamirano et al. (2015) to obtain the spectrum of the center of each BCG. This code divides each galaxy into rings and then the spaxels (spectrum of a region of the field of view) of each ring are stacked to obtain one spectrum per ring. The code identifies the rings following the total flow, therefore the shape of the rings is not circular but rather defined by the morphology of the galaxy. The spectrum of each spaxel of each galaxy was run at the wavelength of the rest frame before being stacked using the speed calculated with the program pPXF (Penalized Pixel Fitting) of Emsellem et al. (2007). pPXF fits stellar pattern libraries to the characteristic absorption lines of the BCG spectra, giving the recession rates of the spectral lines.

The left panel of Figure 1 shows the annular distribution of BCG 2039. The right panel is the flux-collapsed VIMOS image. The annuli are 0.2, 0.48, 0.77 and 1.0 R_e in each galaxy. The central aperture has been defined as 0.2 ± 0.03 R_e. In Table 1, we show R_e for each galaxy. BCG 1027 has $z = 0.09$ and $R_e = 6.''98$; for this galaxy R_e corresponds to ≈ 13 kpc.

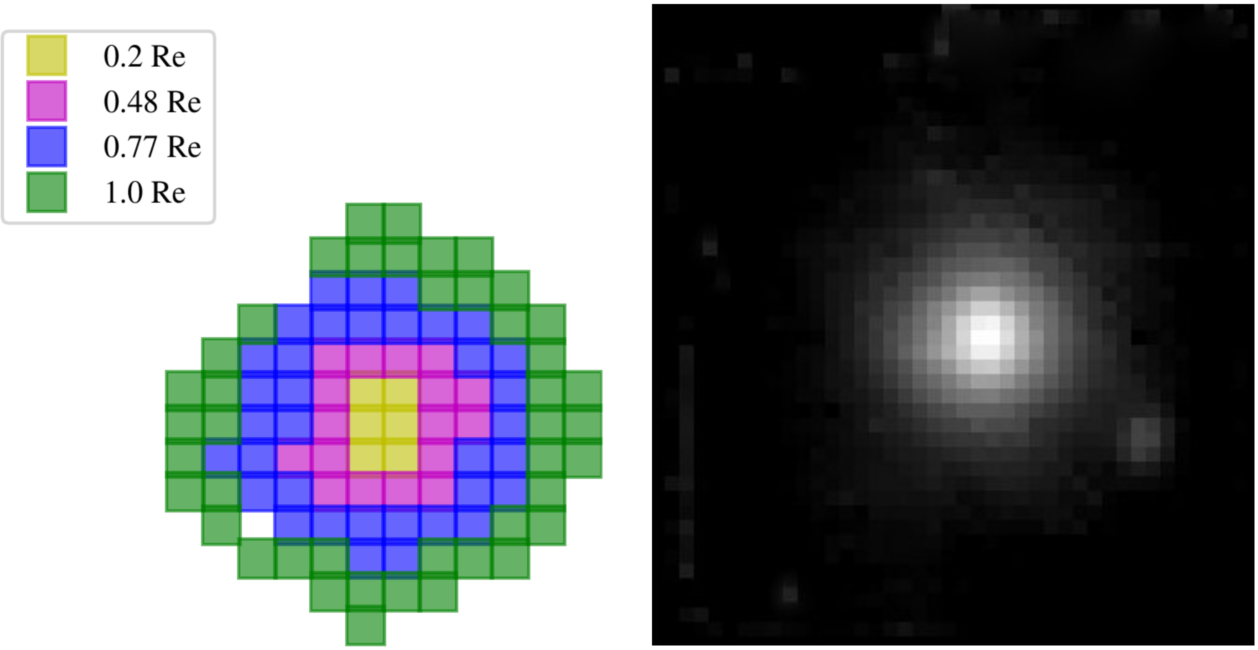

Fig. 1. Left Panel: The annular distribution of BCG 2039. The central annulus, corresponds to the aperture 0.2±0.03 R_e. The annuli all extend to 1 R_e. Right Panel: The flux-collapsed VIMOS image BCG 2039. The color figure can be viewed online.

Finally, with the STARLIGHT code, the SFHs of the BCGs were determined. STARLIGHT is a synthesis code for stellar populations. The method is based on fitting the observed spectrum of the galaxy as a linear combination of spectra of simple stellar populations. The adjustment is carried out through the techniques of simulated annealing, Metropolis and Markov Chain Monte Carlo. STARLIGHT fits an observed spectrum with a combination of $N_\star$ simple stellar populations from the evolutionary synthesis models of Bruzual and Charlot (2003). In this work we use a base that contains $N_\star$=45 spectra of 3 different metallicities ($Z = 0.2,\ 1.0,\ 2.5\,Z_\odot$) and 15 ages between 1 Myr and 13 Gyr. The stellar extinction is modeled by the extinction law of Cardelli et al. (1989) with $RV = 3.1$.

Figures 2 and 3 illustrate the spectrum fits obtained for BCGs. The upper left panel shows the observed spectrum (black line) and the model (red line). The lower left panel shows the residual spectrum (observed − model). The histograms in the right panel show the SFHs as % of the light fraction at 4020 Å(upper) and as % of the mass fraction (lower) both decomposed into 15 ages and 3 metallicities. Some of the derived properties are shown in the upper right: χ^2_λ is the fit χ^2 divided by the number of λ's used in the fit; adev is the mean relative difference between the model and observed spectrum; S/N is the signal to noise ratio in the region centered at $\lambda = 5000$ Å.

3. RESULTS

In this section we use the integrated spectrum fit with an aperture of 0.2 ± 0.03 R_e to investigate the SFHs of 6 BCGs (SDSS-C4-DR3 1027, SDSS-C4-DR3 1042, SDSS-C4-DR3 1048, SDSS-C4-DR3 1066, SDSS-C4-DR3 1261 and SDSS-C4-DR3 2039) of intermediate central ages. In addition, the fits of 3 BCGs (SDSS-C4-DR3 1050, SDSS-C4-DR3 2001 and SDSS-C4-DR3 2086) of old central ages are inferred.

Since a composite stellar population can be seen as the sum of simple stellar populations (Bruzual & Charlot 2003), the SFH of a stellar population can be understood as the fraction of stellar mass produced as a function of time in the form of simple stellar populations. Therefore, the mass fraction μ_j provided by STARLIGHT plotted as function of the simple stellar populations ages can be considered as direct proxy for the output SFH (Citro et al. 2016).

In Figure 4 the SFHs of BCGs of intermediate central ages are shown. The SFHs of these galaxies are formed with few stellar populations of different ages (less than 4). 83 % (5/6) of the BCGs (1027, 1048, 1066, 1261 and 2039) of intermediate

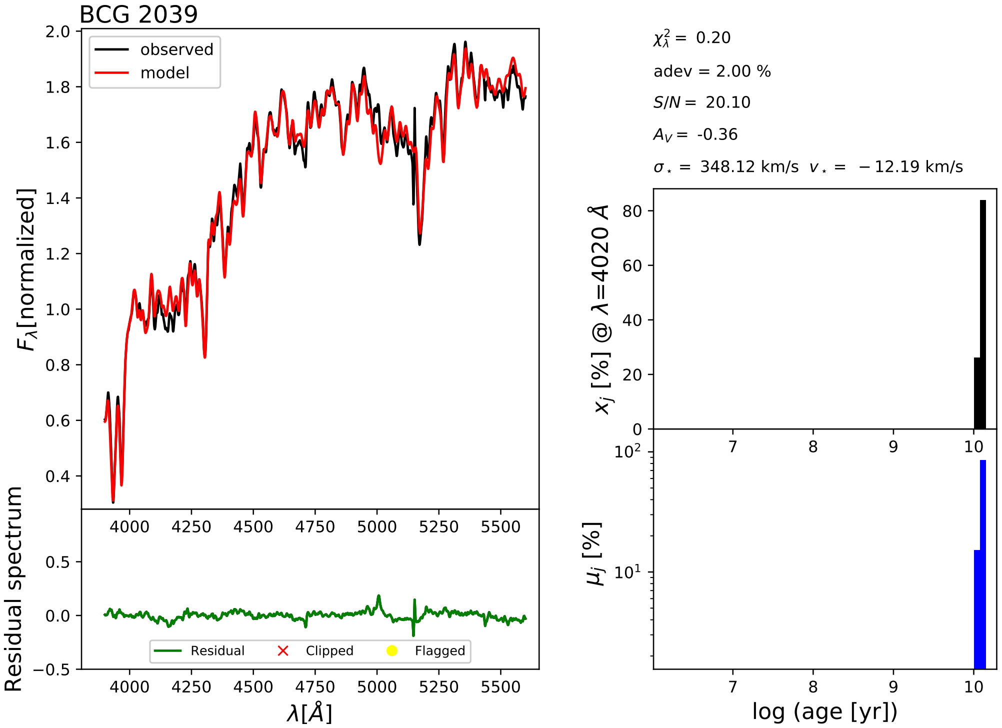

Fig. 2. Spectral synthesis of an intermediate age BCG. Top left: Observed (black line) and model (red line). Bottom left: residual spectrum (green line). Right: Flux (top) and mass (bottom) fractions as a function of age. Some of the derived properties are listed in the top right: χ^2_λ is the reduced χ^2, adev is is the mean relative difference between model and observed spectra and S/N refers to the region around $\lambda = 5000$ Å. The color figure can be viewed online.

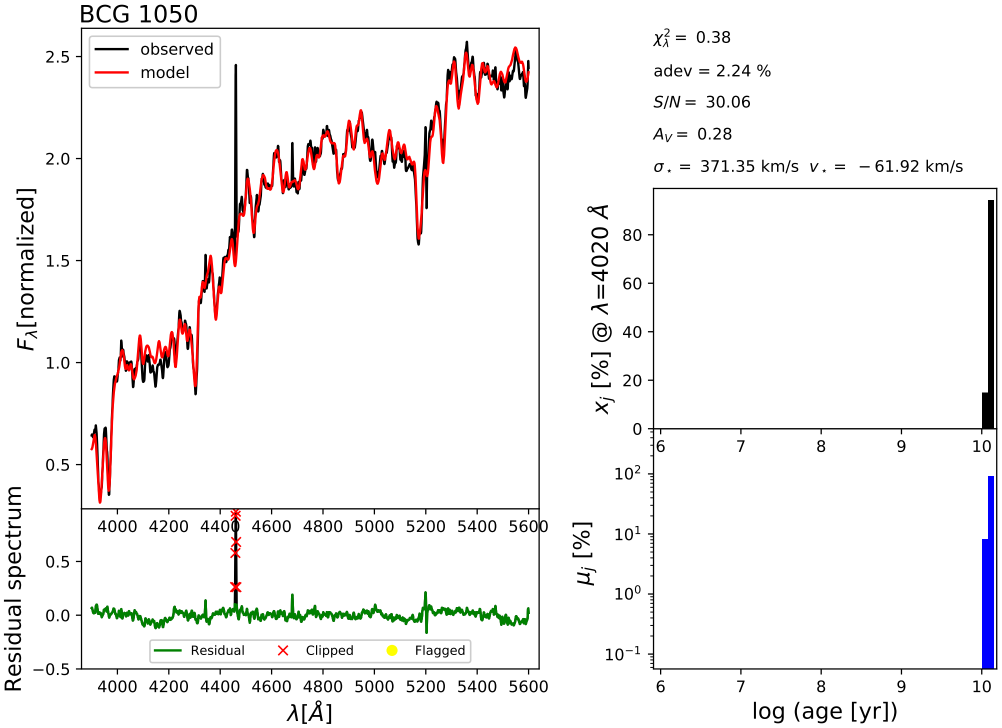

Fig. 3. As Figure 2, but for an old age BCG. The color figure can be viewed online.

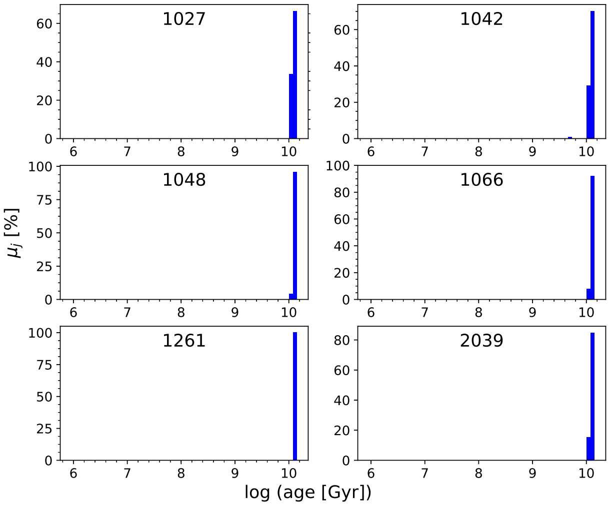

Fig. 4. Star formation histories of BCGs of intermediate central ages. The mass fraction μ_j (obtained by a spectrum fit with STARLIGHT) as a function of logarithm of age. The color figure can be viewed online.

central ages formed 100 % of their stars at $z > 2$. The BCG 1042 shows an incipient star formation at $z < 2$ (less than 1 % in mass). 100 % (3/3) of the BCGs (1050, 2001 and 2086) of old central ages are established with only two stellar populations at $z > 2$ (see Figure 5).

4. DISCUSSION

In this work, we inferred the SFHs of a sample of BCGs at $z < 0.1$ with the objective of determining if these BCGs of intermediate central ages have different accretion histories or if it is only a random effect.

The SFHs found agree with the expectations for elliptical galaxies. These galaxies formed their stars in the early stages of the Universe ($z > 2$) and do not show recent star formation. Most of the SFHs of BCGs were fitted with only two stellar populations of different ages, and no more than four according to the results of the work of Groenewald & Loubser (2014).

The SFHs of BCGs of intermediate central ages (Figure 4) and old ages (Figure 5) inferred in this work are similar. According to Citro et al. (2016), passive and high mass ETGs ($\log(\mathrm{M_{Dyn}}) > 11.25\,M_{\odot}$), ages between approximately $10 - 13$ Gyr and z from 0.06 to 0.08 have SFH similar to those found in our BCGs. McDermid et al. (2015) inferred the SFHs of ETGs from the ATLAS$^{\mathrm{3D}}$ survey of mass between $11.5 < \log(\mathrm{M_{Dyn}})\,[M_{\odot}] < 12$ and found that 90 % of their stars were formed in the first 3 Gyr ($z \approx 2$).

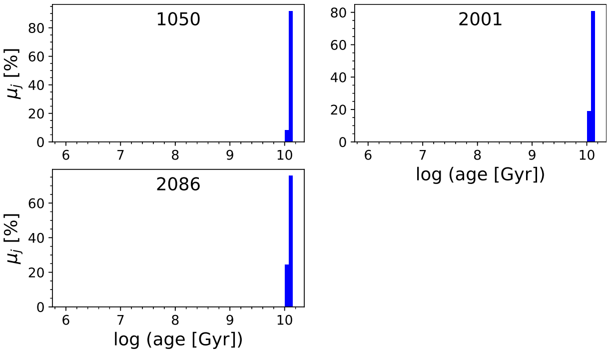

Fig. 5. Star formation histories of BCGs of old central ages. As Figure 4. The color figure can be viewed online.

The results obtained in this work (SFHs showing star formation at $z > 2$) and Oliva-Altamirano et al. (2015) (high central metallicities and shallow flat metallicity gradients) indicate that the formation and evolution of the BGGs of intermediate ages probably occur through the two-phase scenario. Star formation dominates the mass increase of BCGs at $z > 2$ and dry mergers dominate the mass assembly at $z < 1$. Jimmy et al. (2013) found that 50 % (3/6) of the BCGs of intermediate central ages in our study have experienced recent or ongoing mergers.

Our results are in agreement with semi-analytical models (De Lucia & Blaizot 2007) and hydrodynamic simulations (Ragone-Figueroa et al. 2018), which propose that star formation in BCGs occurs at $z > 2$. Then the BCGs are assembled by dry fusions without significant star formation. These authors disagree on the stellar mass growth rate. Ragone-Figueroa et al. (2018) found a growth rate of 1.3 at 30 kpc and 1.6 at 50 kpc, which is significantly lower (≈ 3) than the one proposed by De Lucia & Blaizot (2007).

The two-phase scenario is supported by several observational studies that have measured the stellar mass growth rate mostly for values less than $z \approx 1$ (e.g. Lidman et al. 2012; Lin et al. 2013; Bellstedt et al. 2016; Zhang et al. 2016). Lidman et al. (2012) showed that BCGs grow by a factor of 1.8 for z between 0.2 and 0.9. Lin et al. (2013) found a similar growth, such that the stellar mass of BCGs increases by a factor of 2.3 from $z \approx 1.4$. Zhang et al. (2016) showed a mass growth of by a factor of $z \approx 2$ from $z \approx 1.2$.

Recently, Edwards et al. (2020) investigated the formation and evolution of local BCGs. They determined stellar populations and dynamics from galaxy core through the outskirts and into the intracluster light. Their results are consistent with the idea that the BCG core and inner regions formed quickly and long ago. The outer regions and intracluster light formed more recently, and are continuing to assemble through minor merging.

Based on the above, we conclude that the intermediate central ages of these BCGs do not represent distinct SFHs.

The authors are grateful to Paola Oliva Altamirano and Sarah Brough for comments that led to improvement of this article and data for this research. We thank the STARLIGHT project supported by the Brazilian agencies CNPq, CAPES and FAPESP and by the Frace-Brazilian CAPES/cofecub program.

REFERENCES

Bai, L., Yee, H. K. C., Yan, R., et al. 2014, ApJ, 789, 134
Bellstedt, S., Lidman, C., Muzzin, A., et al. 2016, MNRAS, 460, 2862
Bernstein, J. P. & Bhavsar, S. P. 2001, MNRAS, 322, 625
Bruzual, G. & Charlot, S. 2003, MNRAS, 344, 1000
Cappellari, M., Bacon, R., Bureau, M., et al. 2006, MNRAS, 366, 1126
Cardelli, J. A., Clayton, G. C., & Mathis, J. S. 1989, ApJ, 345, 245
Cid Fernandes, R., Mateus, A., Sodré, L., Stasińska, G., & Gomes, J. M. 2005, MNRAS, 358, 363
Citro, A., Pozzetti, L., Moresco, M., & Cimatti, A. 2016, A&A, 592, A19
Cowie, L. L. & Binney, J. 1977, ApJ, 215, 723
De Lucia, G. & Blaizot, J. 2007, MNRAS, 375, 2
Dressler, A. 1978, ApJ, 223, 765
Dubinski, J. 1998, ApJ, 502, 141
Edwards, L. O. V., Salinas, M., Stanley, S., et al. 2020, MNRAS, 491, 2617
Emsellem, E., Cappellari, M., Krajnović, D., et al. 2007, MNRAS, 379, 401
Fabian, A. C. 1994, ARA&A, 32, 277
Groenewald, D. N. & Loubser, S. I. 2014, MNRAS, 444, 808
Hirschmann, M., Naab, T., Davé, R., et al. 2013, MNRAS, 436, 2929
Izzo, C., Kornweibel, N., McKay, D., et al. 2004, Msngr, 117, 33
Jimmy, T. K.-V., Brough, S., Gebhardt, K., et al. 2013, ApJ, 778, 171
Katayama, H., Hayashida, K., Takahara, F., & Fujita, Y. 2003, ApJ, 585, 687
Laine, S., van der Marel, R. P., Lauer, T. R., et al. 2003, AJ, 125, 478
Laporte, C. F. P., White, S. D. M., Naab, T., & Gao, L. 2013, MNRAS, 435, 901
Le Fèvre, O., Saisse, M., Mancini, D., et al. 2003, SPIE, 4841, 1670
Lidman, C., Suherli, J., Muzzin, A., et al. 2012, MNRAS, 427, 550
Lin, Y.-T., Brodwin, M., Gonzalez, A. H., et al. 2013, ApJ, 771, 61
Malumuth, E. M., & Richstone, D. O. 1984, ApJ, 276, 413
McDermid, R. M., Alatalo, K., Blitz, L., et al. 2015, MNRAS, 448, 3484
Merritt, D. 1985, ApJ, 289, 18
Miller, C. J., Nichol, R. C., Reichart, D., et al. 2005, AJ, 130, 968
Naab, T., Johansson, P. H., & Ostriker, J. P. 2009, ApJ, 699, L178
Naab, T., Oser, L., Emsellem, E., et al. 2014, MNRAS, 444, 3357
Oemler, A., Jr. 1976, ApJ, 209, 693
Oliva-Altamirano, P., Brough, S., Jimmy, T. K.-V., et al. 2015, MNRAS, 449, 3347
Ostriker, J. P. & Tremaine, S. D. 1975, ApJ, 202, L113
Peeples, M. S., Werk, J. K., Tumlinson, J., et al. 2014, ApJ, 786, 54
Ragone-Figueroa, C., Granato, G. L., Ferraro, M. E., et al. 2018, MNRAS, 479, 1125
Sandage, A. & Hardy, E. 1973, ApJ, 183, 743
Schechter, P. L. & Peebles, P. J. E. 1976, ApJ, 209, 670
Schneider, D. P., Gunn, J. E., & Hoessel, J. G. 1983, ApJ, 264, 337
Schombert, J. M. 1986, ApJS, 60, 603
Silk, J. 1976, ApJ, 208, 646
Tonini, C., Bernyk, M., Croton, D., Maraston, C., & Thomas, D. 2012, ApJ, 759, 43
Trager, S. C. & Somerville, R. S. 2009, MNRAS, 395, 608
Tremaine, S. D. & Richstone, D. O. 1977, ApJ, 212, 311
Von der Linden, A., Best, P. N., Kauffmann, G., & White, S. D. M. 2007, MNRAS, 379, 867
White, S. D. M. 1976, MNRAS, 174, 19
York, D. G., Adelman, J., Anderson, J. E., Jr., et al. 2000, AJ, 120, 1579
Zhang, Y., Miller, C., McKay, T., et al. 2016, ApJ, 816, 98
Zhao, D., Aragon-Salamanca, A., & Conselice, C. J. 2015, VizieR Online Data Catalog, 744

M. L. Talavera and J. Umanzor: Universidad Nacional Autónoma de Honduras, Facultad de Ciencias Espaciales, Departamento de Astronomía y Astrofísica, Edificio K1, Bulevar Suyapa, Tegucigalpa, Honduras, C.A. (martha.talavera, jesus.umanzor@unah.edu.hn).

Revista Mexicana de Astronomía y Astrofísica, **57**, 399–405 (2021)

https://doi.org/10.22201/ia.01851101p.2021.57.02.12

MASS RATIOS OF LONG-PERIOD BINARY STARS RESOLVED IN PRECISION ASTROMETRY CATALOGS OF TWO EPOCHS

Valeri V. Makarov

U.S. Naval Observatory, Washington, DC, USA.

Received February 16 2021; accepted July 14 2021

ABSTRACT

Mass ratios of widely separated, long-period, resolved binary stars can be directly estimated from the available data in major space astrometry catalogs, such as the ESA's Hipparcos and Gaia mission results. The method is based on the universal principle of inertial motion of the system's center of mass in the absence of external forces, and is independent of any assumptions about the physical parameters or stellar models. The application is limited by the precision of input astrometric data, the orbital period and distance to the system, and possible presence of other attractors in the vicinity, such as in triple systems. A generalization of this technique to triples is proposed, as well as approaches to estimation of uncertainties. The known long-period binary HIP 473 AB is discussed as an application example, for which a $m_2/m_1 = 0.996^{+0.026}_{-0.026}$ is obtained.

RESUMEN

Los cocientes de masas de las binarias abiertas, de largo período, pueden estimarse directamente a partir de datos precisos de los catálogos astrométricos más importantes, como el Hipparcos de ESA, y los catálogos de la misión Gaia. El método se basa en el principio del movimiento inercial del centro de masa del sistema en ausencia de fuerzas externas, y es independiente de suposiciones sobre parámetros físicos o modelos estelares. Su aplicación está limitada por la precisión de los datos astrométricos, el período orbital y la distancia al sistema, así como por la posible presencia de otros atractores, como en los sistemas triples. Se propone una generalización del método a sistemas triples, y se discuten maneras de estimar las incertidumbres. Se estudia como ejemplo la bien conocida binaria de largo período HIP 473 AB, para la cual se obtiene un cociente $m_2/m_1 = 0.996^{+0.026}_{-0.026}$.

Key Words: astrometry — binaries: visual — stars: fundamental parameters

1. INTRODUCTION

The majority of stars in the Galaxy have masses less than the solar mass. Almost half of the regular solar type field stars are also components of binary or multiple gravitationally bound systems (Tokovinin 2014). A binary star's orbit and ephemerides are described by seven orbital parameters (elements). From the astrometric point of view, an additional five parameters representing the position at a given epoch, proper motion, and parallax of the barycenter are required to completely characterize the absolute location of the components on the celestial sphere at a given time. The most important elements for astrophysical investigations are the size (semimajor axis), the period, and the eccentricity. The former two yield the total mass of the binary via Kepler's third law. But the distribution of masses between the components often remains unknown, because the barycenter is not directly available from astrometric observations. In some rare cases, the mass ratio can be directly inferred from spectroscopic radial velocity measurements for double-lined spectroscopic binaries (SB2) of similar brightness, which limits this method mostly to pairs of similar masses. When a good astrometric orbit, which is differential for resolved pairs, is also available for an SB2, accurate individual component masses can be obtained, providing valuable and still rare data for astrophysics. Furthermore, detached eclipsing binaries have a special status because not only precise individual masses but also physical dimensions can be obtained (Torres et al. 2010) and stellar evolution theory can be put to test, with the number of suitable objects counting in dozens.

Wide binaries with periods longer than 100 yr are harder to characterize, even if they are resolved in general astrometric catalogs. Both astrometric and spectroscopic observations should be decades long to produce robust orbital solutions and mass ratio estimates. Techniques have been proposed to statistically estimate or constrain some of the essential parameters. For example, the relative velocity of components can be used to estimate the eccentricity (Tokovinin 2020). Apart from the traditional position measurements, astrometric catalogs provide information about the apparent acceleration of stars, which can be used to detect previously unknown binary systems from the observed change of their proper motions (Wielen et al. 1999) and, in some cases, to set constraints on the masses of unresolved companions (Makarov & Kaplan 2005). Apparent angular accelerations were introduced into the basic astrometric model for the first time in the Hipparcos main mission. As a detection tool for new binaries they proved partially successful, as some of them could not be confirmed by high-resolution and spectroscopic follow-up observations, but more sophisticated statistical analysis can produce more efficient selections of candidates (Fontanive et al. 2019). Physical accelerations can also be used to estimate component masses in several specific cases when combined with astrometric acceleration data, epoch position measurements, and spectroscopic radial velocity observations (Brandt et al. 2019).

The goal of this paper is to demonstrate that accurate mass ratios can be derived for resolved long-period binary stars from precision astrometry at two separate epochs, e.g., from the data in the Hipparcos (ESA 1997) and Gaia EDR3 (Gaia Collaboration et al. 2021) catalogs, for potentially thousands of objects. No astrophysical assumptions or additional data are needed for this method, and only the absolute positions are required from the first-epoch catalog. As a side product, the proper motion of the system's barycenter is obtained, which can be used in kinematic studies of binary members of nearby open clusters, for example. The main conditions of applicability are that the orbital period should be much longer than the duration of each astrometric mission, which is about 4 years for the considered example, and that the system should be close enough to produce measurable changes in the apparent orbital motion of the components. The method is presented in § 2. Its specific application is described on the example of a known nearby multiple star HIP 473 in § 3. Realistic estimation of the resulting mass ratio error (uncertainty), taking into account the full variance-covariance matrix of the input data, is essential, and a Monte Carlo-based technique is described in § 4. § 5 describes a generalization of this method to triple systems, in which case mass ratios of two components can be directly computed, or approximately estimated using a weighted generalized least-squares adjustment within the Jacobi coordinates paradigm. The prospects of applying this new method to extensive surveys and space astrometry catalogs are discussed in § 6, as well as possible caveats related to the required absolute character of the utilized astrometric data.

2. MASS RATIOS FROM ASTROMETRY

Let a binary star system with two components $i = 1, 2$ have position unit-vectors $\boldsymbol{r}_{ij}$ in two astrometric catalogs, $j = 1, 2$, at epochs t_1 and t_2. If $\boldsymbol{r}_{0j}$ is the mean position of the barycenter at these epochs, the vectors $\boldsymbol{\rho}_{ij} = \boldsymbol{r}_{ij} - \boldsymbol{r}_{0j}$ represent the angular separations of the components, which are, to a very good approximation, equal to the projected orbital radii[1]. The projection onto the tangent plane preserves the center of mass definition, so that

$$m_1 \boldsymbol{\rho}_{1j} + m_2 \boldsymbol{\rho}_{2j} = 0, \tag{1}$$

where m_i is the mass of the ith component. The barycenter's proper motion

$$\boldsymbol{\mu}_0 = \frac{\boldsymbol{r}_{02} - \boldsymbol{r}_{01}}{\Delta t}, \tag{2}$$

where Δt is the epoch difference $t_2 - t_1$, is assumed to be constant in time, which is also a good approximation for realistic epoch differences. The projected orbital motion of component i at epoch j is

$$\boldsymbol{\psi}_{ij} = \boldsymbol{\mu}_{ij} - \boldsymbol{\mu}_0, \tag{3}$$

where $\boldsymbol{\mu}_{ij}$ is the observed proper motion. From differentiating equation 1 in time, we can see that

$$m_1 \boldsymbol{\psi}_{1j} + m_2 \boldsymbol{\psi}_{2j} = 0. \tag{4}$$

---

[1] The small difference caused by the the curvature of the celestial sphere and the non-orthogonality of these vectors to $\boldsymbol{r}_{0j}$ can be safely neglected.

Dividing this equation by m_1 and introducing $q = m_2/m_1$ one obtains

$$\boldsymbol{\mu}_0 = \frac{\boldsymbol{\mu}_{1j} + q\boldsymbol{\mu}_{2j}}{1+q}. \tag{5}$$

Taking the difference of equations 1 between the two epochs, dividing it by m_1, and substituting equation 5 results in

$$\boldsymbol{r}_{12} - \boldsymbol{r}_{11} + q(\boldsymbol{r}_{22} - \boldsymbol{r}_{21}) = (\boldsymbol{\mu}_{1j} + q\boldsymbol{\mu}_{2j})\Delta t. \tag{6}$$

All the terms in this equations are known from observation except q, which makes an overdetermined system of up to four condition equations with one unknown. Unfortunately, the proper motions of visual binaries in the Hipparcos catalog, which is used as the first-epoch catalog, are too unreliable to be used with this method (Makarov 2020), so that only $j = 2$ can be used, leaving two condition equations. Introducing the long-term apparent motion of the component $\boldsymbol{\nu}_i = (\boldsymbol{r}_{i2} - \boldsymbol{r}_{i1})/\Delta t$, the exact solutions for q can be written as

$$q = \frac{\boldsymbol{\mu}_{12} - \boldsymbol{\nu}_1}{\boldsymbol{\nu}_2 - \boldsymbol{\mu}_{22}}. \tag{7}$$

Note that we have not made any assumptions about the masses of component in this derivation, and the estimated q can be negative. The vectors in the numerator and denominator are not parallel because of observational errors, which effectively leads to two equations when their coordinate projections are considered. The two emerging estimates of q can be averaged with weights; however, as we will see in the example of HIP 473, one of the projections can be practically useless when the orbital acceleration is almost aligned with the other coordinate direction. It is simpler to use the ratio of the norms of the two calculated vectors:

$$q = \frac{\|\boldsymbol{\mu}_{12} - \boldsymbol{\nu}_1\|}{\|\boldsymbol{\nu}_2 - \boldsymbol{\mu}_{22}\|}. \tag{8}$$

Alternatively, a more complex approach can be considered, involving projections of the two observed vectors onto a common unit vector, which minimizes the variance of q from the combined contribution of the corresponding error ellipses. The degree of misalignment, which is defined as

$$\eta = \arccos\left(\boldsymbol{v}_1 \cdot \boldsymbol{v}_2 / (\|\boldsymbol{v}_1\|\,\|\boldsymbol{v}_2\|)\right), \tag{9}$$

where $\boldsymbol{v}_1$ and $\boldsymbol{v}_2$ are the vectors in the numerator and denominator of equation 7, is a useful diagnostic of the reliability of estimation.

3. APPLICATION TO THE WIDE BINARY SYSTEM HIP 473

The long-period binary star HIP 473 = HD 38 = WDS 00057+4549 is one of the better studied systems due to its proximity and brightness. It consists of two well-separated ($\rho = 6.041''$) late-type dwarfs A and B of spectral types K6V and M0.5V (Joy & Abt 1974; Keenan & McNeil 1989; Tamazian et al. 2006). Earlier spectroscopic observations suggested twin component of the same spectral type M0 (Anosova et al. 1987). Kiyaeva et al. (2001) used multiple photographic position measurements, as well as previously available radial velocity estimates from Tokovinin (1990), to produce a first reliable orbital solution for the inner pair, as well as preliminary estimates for the orbit of a distant physical tertiary known as component F in the WDS. The latter has only a very short segment available from astrometric observations due to its very long period. The method of *Apparent Motion Parameters* specially designed by Kiselev (1989); Kiselev & Kiyaeva (1980) for such poorly constrained solutions was employed, which required the knowledge of the center of mass for the AB pair. Kiyaeva et al. (2001) assumed equal masses for the A and B companions, which was a guess based on the spectroscopic and photometric similarity of these stars (cf. Luck 2017; Cvetković et al. 2019). For the inner pair, they estimated a semimajor axis $a = 6.21 \pm 0.77''$, a period $P = 509.65 \pm 96.99$ yr, and an eccentricity $e = 0.22 \pm 0.04$. Their assumption about the relative masses of these components allowed them to draw interesting conclusions about the relative inclination of the inner and outer orbits. The estimated total mass $1.4\,M_\odot$, on the other hand, appears to be higher than what the spectral type would suggest. The primary star HD 38 was already included in the first edition of the *Catalog of Chromospherically Active Binary Stars* by Strassmeier et al. (1988). The signs of chromospheric activity in M dwarfs, such as Hα emission lines and detectable X-ray radiation, are often related to rapid rotation fueled by a close orbiting companion. More recent radial velocity measurements indicate that both A and B companions may be binary systems (Sperauskas et al. 2016), which would make the entire system at least quintuple. Owing to its brightness and relatively wide separation, the AB pair has been vigorously pursued with speckle and direct imaging CCD camera astrometry (Mason et al. 2007; Cvetković et al. 2011; Mason et al. 2012; Hartkopf & Mason 2015) aiming at a better characterization of its orbit and component masses. Despite this effort and many decades of observation, there is some ambiguity about the orbit. A much shorter-period orbit with a higher eccentricity was proposed by Izmailov (2019): $P = 370.7\,\mathrm{yr}$, $e = 0.48$. Consequently, the total mass for this version is substantially smaller, yielding a mass of $\approx 0.6\,M_\odot$ for each component, when equally divided. There is no observational information about the mass ratio. Potentially, this parameter can be estimated from the gradient of individual radial velocities, which requires a similarly persistent multi-year spectroscopic campaign. It can also be obtained from equation 8 using publicly available astrometric data from the Hipparcos and Gaia EDR3 catalogs.

We begin by extracting the RA and Dec coordinates for both components at the corresponding mean epochs 1991.25 and 2016. The separation barely changed in the intervening 24.75 years, but the relative orientation did change because of the orbital motion by approximately 10° in position angle. These coordinates are used to compute the long-term proper motions vectors $\boldsymbol{\nu}_1$ and $\boldsymbol{\nu}_2$. They happen to differ from the short-term proper motions taken directly from Gaia EDR3 by several mas yr^{-1}, which is a large multiple of their formal errors. The high signal-to-noise ratio hints at an accurate determination (§4). Indeed, the orbital signal for both components exceeds 5 mas yr^{-1} in the declination coordinate, which is much greater than the formal errors. The computation of q by equation 8 is straightforward resulting in $q = 0.996$. The measure of misalignment η (equation 9) caused by the astrometric errors is comfortably small at 2.5° .

Binaries with near-twin components, such as the HIP 473 AB system, are more amenable to the proposed astrometric estimation of q because the observed signal is more equally distributed between the components in equation 8. Numerous systems with small q values are harder to process because the signal in the numerator becomes too small compared to the expectation of observational error. Apart from the misalignment parameter η, a useful quantity to filter out unreliable solutions is the empirical signal-to-noise (SNR) parameter, which can be calculated as $\mathrm{SNR} = \sqrt{\boldsymbol{v}_1'\,\boldsymbol{C}_1^{-1}\,\boldsymbol{v}_1}$. On the other hand, low-mass companions are often much fainter than the primaries, and the quality of Hipparcos astrometry quickly deteriorates for magnitudes approaching the sensitivity limit $H_p \approx 11$ mag.

4. ESTIMATION OF UNCERTAINTIES

The estimated mass ratio is the ratio of two random variables (equation 8) derived from the astrometric data in two separate catalogs. Given the complete variance-covariance matrices of the astrometric parameters, it is possible to analytically estimate the resulting variance of q in the large signal-to-noise approximation, because the numerator and denominator are assumed to be statistically independent[2]. A more general and reliable approach, which is presented in this section, utilizes Monte Carlo simulations and confidence interval estimation. It is valid in the low signal-to-noise regime too, providing an additional indication of problematic cases. The greatest weakness of both techniques is the underlying assumption of Gaussian-distributed noise in the input data.

The five astrometric parameters for a regular solution are indexed 1 through 5 in this order: right ascension coordinate, declination coordinate, parallax, proper motion in right ascension, proper motion in declination. The associated covariance matrix $\boldsymbol{C}$ is a 5×5 symmetric matrix that can be reconstructed from the 5 formal standard errors and 10 correlation coefficients given in the catalog. For the first-epoch catalog (Hipparcos), we only need the position covariances from the block in the intersection of 1st and 2nd rows and 1st and 2nd columns, which is denoted as $(1,2;1,2)$ here. The second-epoch catalog (Gaia) contributes three 2×2 blocks, namely, the position covariance $(1,2;1,2)$, the proper motion covariance $(4,5;4,5)$, and the off-diagonal position – proper motion covariance $(1,2;4,5)$. The total covariance of vector v_i is then

$$\begin{aligned}\boldsymbol{Cov}[v_i] =&\boldsymbol{C}_{i1(1,2;1,2)}\Delta t^{-2} + \boldsymbol{C}_{i2(1,2;1,2)}\Delta t^{-2} + \\ &\boldsymbol{C}_{i2(4,5;4,5)} - 2\boldsymbol{C}_{i2(1,2;4,5)}\Delta t^{-1}.\end{aligned} \tag{10}$$

For the HIP 473 binary, I computed these covariances from the data in the *Double and Multiple System Annex* (DMSA) of the Hipparcos catalog and the Gaia EDR3 catalog. DMSA does not provide the correlations $\boldsymbol{C}_{i1(1;2)}$, so I used the correlation coefficient from the main catalog for the primary component (A), which is -0.05, and assumed the same value for the B component. For each component, 2000 random $\mathcal{N}(0,1)$-distributed 2-vectors were generated. If $\boldsymbol{p}$ is one of such vectors, a single randomly generated realization of $\boldsymbol{v}_i$ with Gaussian additive er-

---

[2] In truth, the astrometric data for nearby stars in a space mission astrometric catalog are always positively correlated because of the common attitude and calibration unknowns in the condition equations. Since the global normal equations are not available, these correlations are not accurately known, and are usually neglected.

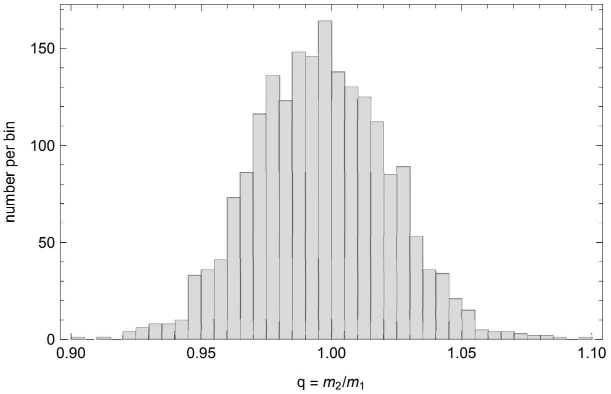

Fig. 1. Monte Carlo simulated distribution of the mass ratio q for the binary star HIP 473 with nominal astrometric parameters and variance-covariance matrices from the Hipparcos DMSA and Gaia EDR3. 2000 random trials were computed for each of the two components.

rors is $\boldsymbol{v}_i + \boldsymbol{Cov}[v_i]^{1/2} \cdot \boldsymbol{p}^3$. Each of these realizations results in a randomly dispersed q by equation 8.

Figure 1 shows the histogram of 2000 Monte Carlo estimates of q for HIP 473 with astrometry from Hipparcos and Gaia EDR3. The sampled distribution is bell-shaped and fairly symmetric with a well-defined core. The standard deviation errors on the negative and positive sides can be estimated directly from the 0.1573 and 0.8427 quantiles of the sampled distribution, which are not necessarily equal in absolute value. The result for this binary star is $q = 0.996^{+0.026}_{-0.026}$. Alternatively, we deduce from the 0.01 quantile that $q > 0.935$ with a 99% confidence given the data in Hipparcos and Gaia EDR3. The major part of the uncertainty comes from the position errors of the Hipparcos catalog.

5. GENERALIZATION FOR TRIPLE STARS

The orbital motion of isolated hierarchical triple star systems is long-term non-Keplerian, with the trajectories subject to secular changes of sometimes drastic character, including flips of inner orbit orientation and reversal of orbital spin (Naoz et al. 2013). On time scales of one orbital revolution and shorter, however, the inner and outer trajectories can be well approximated with Kepler's orbits of fixed elements. Within this approximation, the paradigm of Jacobi coordinates simplifies the consideration of relative orbital motion. We consider a mathematical center of mass of the inner pair components 1 and 2, which is located at $\boldsymbol{r}_0$. This point is involved in orbital motion with the tertiary at $\boldsymbol{r}_3$ around the barycenter of the entire triple system at $\boldsymbol{r}_{\rm B}$ as if there were a physical body of mass $m_1 + m_2$. For the proper motions, we can write

$$m_3\, \bar{\boldsymbol{\mu}}_3 + (m_1 + m_2)\, \bar{\boldsymbol{\mu}}_0 = 0, \qquad (11)$$

where $\bar{\boldsymbol{\mu}}_3$ and $\bar{\boldsymbol{\mu}}_0$ are the proper motion parts caused by the projected orbital motion, and index j defining the epoch of observation is dropped for brevity. Like in a two-body problem, the actual or "observed" proper motions are

$$\begin{aligned} \boldsymbol{\mu}_3 &= \boldsymbol{\mu}_{\rm B} + \bar{\boldsymbol{\mu}}_3, \\ \boldsymbol{\mu}_0 &= \boldsymbol{\mu}_{\rm B} + \bar{\boldsymbol{\mu}}_0, \end{aligned} \qquad (12)$$

where index B denotes the current center of mass of the entire system. Within the Jacobi coordinates paradigm, the observed components of the inner pair are

$$\begin{aligned} \boldsymbol{\mu}_1 &= \boldsymbol{\mu}_0 + \bar{\boldsymbol{\mu}}_1, \\ \boldsymbol{\mu}_2 &= \boldsymbol{\mu}_0 + \bar{\boldsymbol{\mu}}_2, \end{aligned} \qquad (13)$$

with the orbital components still obeying the local inertial motion condition

$$m_1 \bar{\boldsymbol{\mu}}_1 + m_2 \bar{\boldsymbol{\mu}}_2 = 0. \qquad (14)$$

This leads to the general equation

$$m_1 \boldsymbol{\mu}_1 + m_2 \boldsymbol{\mu}_2 + m_3 \boldsymbol{\mu}_3 = (m_1 + m_2 + m_3) \boldsymbol{\mu}_{\rm B}, \quad (15)$$

despite the vectors connecting 0 with 3 and 1 with 2 being possibly not coplanar. This can also be derived by differentiating the position equation in time:

$$m_1 \boldsymbol{r}_{1j} + m_2 \boldsymbol{r}_{2j} + m_3 \boldsymbol{r}_{3j} = (m_1 + m_2 + m_3) \boldsymbol{r}_{j{\rm B}}. \quad (16)$$

Taking the difference between epochs 1 and 2 results in

$$m_1 \boldsymbol{\nu}_1 + m_2 \boldsymbol{\nu}_2 + m_3 \boldsymbol{\nu}_3 = (m_1 + m_2 + m_3) \boldsymbol{\mu}_{\rm B}, \quad (17)$$

where we assumed that the system's barycenter moves along a linear trajectory in space with a constant velocity. Eliminating the unknown barycenter proper motion in equations 15 and 17 leads to the final condition equations

$$q_2(\boldsymbol{\nu}_2 - \boldsymbol{\mu}_2) + q_3(\boldsymbol{\nu}_3 - \boldsymbol{\mu}_3) = -(\boldsymbol{\nu}_1 - \boldsymbol{\mu}_1). \qquad (18)$$

There are two unknowns, $q_2 = m_2/m_1$ and $q_3 = m_3/m_1$, and two equations, so an explicit solution is available. This would neglect the uncertainties of the vectors both in the condition and the

---

[3] The matrix square root of $\boldsymbol{x}$ is computed by functions `sqrtm(x)` in MATLAB or `MatrixPower[x, 1/2]` in Mathematica.

right-hand part of the equations. Alternatively, a generalized least-squares solution can be applied utilizing the known covariances. This can be technically realized as a least-squares solution with a left-multiplied non-diagonal weight matrix $\boldsymbol{\Omega}^{-1}$, which is the inverted sum of all three individual covariance matrices, $\boldsymbol{\Omega} = \boldsymbol{C}_1 + \boldsymbol{C}_2 + \boldsymbol{C}_3$, each computed by equation 10. The solution is then $[q_2, q_3]' = (\boldsymbol{X}' \boldsymbol{\Omega}^{-1} \boldsymbol{X})^{-1} \boldsymbol{X}' \boldsymbol{\Omega}^{-1} \boldsymbol{y}$, where $\boldsymbol{X}$ is the design matrix and $\boldsymbol{y}$ the right-hand part of condition equations 18. The main limitation of this method comes from the fact that the components of $\boldsymbol{\nu}_3 - \boldsymbol{\mu}_3$ appear in the denominator of the explicit solution. The orbital motion of tertiary stars may be so slow that only the nearest hierarchical systems are suitable for this analysis. On the other hand, a weak signal for the tertiary allows one to ignore the apparent acceleration of the inner pair due to its presence, and to apply the algorithm for isolated binary systems.

6. DISCUSSION AND FUTURE WORK

The proposed method of mass ratio estimation for resolved binary stars requires only precision astrometric positions from two separate epochs and proper motions from one epoch. It is free of any astrophysical assumptions or models about the physical parameters of the component stars. It should be emphasized, however, that the astrometric data need to be *absolute*, not differential. In other words, the components' positions and proper motions should be referenced to a well-established, non-rotating celestial reference frame. This brings up the issue of reference frame consistency between the available astrometric solutions. The most obvious application is the Hipparcos-Gaia pair, now separated by 24.75 years. The alignment of these important optical frames remains an open issue. Gaia DR2 and Hipparcos have a statistically significant misalignment, which emerges when Gaia positions of brighter stars are transferred to 1991.25 and compared with Hipparcos mean positions (Makarov & Berghea 2019). Based on archival VLBI astrometry of 26 selected radio stars (which are optically bright), Lindegren (2020) concluded that the Gaia DR2 proper motion field includes a rigid spin of approximately 0.1 mas yr^{-1} for brighter stars only. Therefore, the global spin of the Gaia EDR3 frame was technically adjusted by a similar amount via a specific instrument calibration parameter for brighter stars ($G < 13$ mag, Lindegren et al. 2020). If the origin of this systematic error is correctly identified, this ad hoc correction should remove the estimation bias of q. There remains a possibility that the discrepancy comes in part from a misalignment of the Hipparcos frame, or Gaia EDR3 frame, or both, with respect to a common inertial reference frame. Even though the systematic error is practically equal for the two components of a binary system, it comes with a different sign with respect to the true orbital signal $\nu_i - \mu_i$, and the impact may be significant. For example, the estimated misalignment of the Gaia frame by 1.4 mas results in a perturbation in the components' orbital signal of up to 57 μas yr^{-1}, which can be critical for nearby long-period pairs such as HIP 473. Further progress and performance improvement depends on our ability to evaluate and correct the remaining orientation misalignments and spins of the optical reference frames.

Resolved triple systems can be processed as well providing both mass ratios for the companions. Unresolved and unrecognized triples, on the other hand, are a threat to the proposed method because the observed proper motions are perturbed by the orbital motion of the close binaries. The effective perturbation is not always easy to estimate even for known single-lined spectroscopic orbits, as the photocenter effect is magnitude- and color-dependent. If the orbital period of the inner pair is shorter than the mission length (about 4 years), the perturbation may be significantly averaged out, so that the estimated mass ratio may still be of value. The inner orbital perturbation tends to statistically increase the norm of the proper motion difference. If the primary (more massive component) is a tight binary, this perturbation mostly increases the estimated q, sometimes resulting in values much exceeding 1. On the contrary, unresolved orbital motion of the secondary would decrease the estimated mass ratio, leading to an excess of systems with nearly zero q. The proposed SNR parameter is not helpful in such cases, but the misalignment angle η remains an efficient tool for vetting perturbed and unreliable solution. Therefore, this method can be used to identify hidden hierarchical triples among resolved double stars.

The method of astrometric mass ratio determination described in this paper requires absolute positions of components at two epochs separated by a significant fraction of the orbital period, plus a proper motion from one of the epochs. This points to the Hipparcos-Gaia combination as the most obvious source of data. Numerous differential observations with speckle cameras, adaptive optics imaging, or long-base interferometry cannot be used, unfortunately, unless they are "absolutized" by direct or indirect reference to a well-established realization of the inertial celestial frame. For example, HST images of fainter binaries can be reprocessed using the

Gaia sources in the field of view as astrometric reference. VLBI measurements of double radio sources are mostly obtained in the phase-reference regime and are anchored to the nearby ICRF calibrators. Furthermore, this method can be trivially generalized for three separate epochs of position astrometry without the need for precision proper motions.

Accurate mass ratio estimation requires a sufficiently high signal-to-noise ratio. The main contribution to the estimation uncertainty for the HIP 473 AB pair, used as an example in this paper, comes from the formal errors of Hipparcos positions. This cannot be improved, and the application is currently limited to nearby systems and binaries with orbital periods within a few hundred years. For a circular face-on orbit with a period much longer than the epoch difference ($\Delta t << P$), the total proper motion change can be estimated as

$$\Delta\mu \approx (2\pi)^2 M^{\frac{1}{3}} \varpi \Delta t P^{-\frac{4}{3}}. \qquad (19)$$

We also note that binaries with near twins are favourable for this method, because the $\Delta\mu$ signal is more evenly distributed between the companions. Among the future plans, the proposed Gaia-NIR space astrometry mission holds the best promise (Hobbs et al. 2019; McArthur et al. 2019). Having two epochs of absolute astrometry at the Gaia's level of accuracy separated by 25–30 years will lead to the characterization of millions of fainter and more distant binaries.

REFERENCES

Anosova, Z. P., Berdnik, E. V., & Romanenko, L. G. 1987, ATsir, 1517, 1

Brandt, T. D., Dupuy, T. J., & Bowler, B. P. 2019, AJ, 158, 140

Cvetković, Z., Pavlović, R., Damljanović, G., & Boeva, S. 2011, AJ, 142, 73

Cvetković, Z., Pavlović, R., & Boeva, S. 2019, AJ, 158, 215

ESA 1997, ESA Special Publication, 1200

Fontanive, C., Mužić, K., Bonavita, M., & Biller, B. 2019, MNRAS, 490, 1120

Gaia Collaboration, Brown, A. G. A., Vallenari, A., et al. 2021, A&A, 649, A1, doi: 10.1051/0004-6361/202039657

Hartkopf, W. I. & Mason, B. D. 2015, AJ, 150, 136

Hobbs, D., Brown, A., Høg, E., et al. 2019, arXiv:1907.12535

Izmailov, I. S. 2019, AstL, 45, 301

Joy A. H. & Abt H. A. 1974, ApJS, 28, 1

Keenan P. C. & McNeil R. C. 1989, ApJS, 71, 245

Kiselev, A. A. & Kiyaeva, O. V. 1980, Azh, 57, 1227

Kiselev, A. A. 1989, Theoretical foundations of photographic astrometry (Moskva, USSR)

Kiyaeva, O. V., Kiselev, A. A., Polyakov, E. V., & Rafa'Skii, V. B. 2001, AstL, 27, 391

Lindegren, L. 2020, A&A, 633, 1

Lindegren, L., Klioner, S. A., Hernández, J., et al. 2020, arXiv:2012.03380

Luck, R. E. 2017, AJ, 153, 21

Makarov, V. V. & Kaplan, G. H. 2005, AJ, 129, 2420

Makarov, V. & Berghea, C. 2019, 53rd ESLAB Symposium: The Gaia Universe, 2019gaia.confE. (Noordwijk, The Nethelands), 25

Makarov, V. V. 2020, AJ, 160, 284

Mason, B. D., Hartkopf, W. I., Wycoff, G. L., & Wieder, G. 2007, AJ, 134, 1671

Mason, B. D., Hartkopf, W. I., & Friedman, E. A. 2012, AJ, 143, 124

McArthur, B., Hobbs, D., Høg, E., et al. 2019, BAAS, 51, 118

Naoz, S., Farr, W. M., Lithwick, Y., Rasio, F. A., & Teyssandier, J. 2013, MNRAS, 431, 2155

Sperauskas, J., Bartašiūtė, S., Boyle, R. P., et al. 2016, A&A, 596, 116

Strassmeier, K. G., Hall, D. S., Zeilik, M., et al. 1988, A&AS, 72, 291

Tamazian, V. S., Docobo, J. A., Melikian, N. D., & Karapetian, A. A. 2006, PASP, 118, 814

Tokovinin, A. A. 1990, Catalogue of stellar radial velocities. Catalogue of proper motions (Moskva, USSR: Izdatel'stvo Moskovskogo Universiteta)

Tokovinin, A. 2014, AJ, 147, 87

Tokovinin, A. & Kiyaeva, O. 2016, MNRAS, 456, 2070

Tokovinin, A. 2020, MNRAS, 496, 987

Torres, G., Andersen, J., & Giménez, A. 2010, A&ARv, 18, 67

Wielen, R., Dettbarn, C., Jahreiß, H., Lenhardt, H., & Schwan, H. 1999, A&A, 346, 675

Valeri V. Makarov: U.S. Naval Observatory, 3450 Massachusetts Ave., Washington, DC 20392-5420, USA (valeri.makarov@gmail.com).

Revista Mexicana de Astronomía y Astrofísica, **57**, 407–418 (2021)

https://doi.org/10.22201/ia.01851101p.2021.57.02.13

STABILITY ANALYSIS OF RELATIVISTIC POLYTROPES

Abdel-Naby S. Saad[1,2], Mohamed I. Nouh[2], Ashraf A. Shaker[2], and Tarek M. Kamel[2]

Received March 29 2021; accepted July 23 2021

ABSTRACT

We study the relativistic self-gravitating, hydrostatic spheres with a polytropic equation of state, considering structures with the polytropic indices $n = 1(0.5)3$ and illustrate the results for the relativistic parameters $\sigma = 0 - 0.75$. We determine the critical relativistic parameter at which the mass of the polytrope has a maximum value and represents the first mode of radial instability. For $n = 1(0.5)2.5$, stable relativistic polytropes occur for σ less than the critical values $0.42, 0.20, 0.10$, and 0.04, respectively, while unstable relativistic polytropes are obtained when σ is greater than the same values. When $n = 3.0$ and $\sigma > 0.5$, energetically unstable solutions occur. The results of critical values are in full agreement with those evaluated by several authors. Comparisons between analytical and numerical solutions of the given relativistic functions provide a maximum relative error of order 10^{-3}.

RESUMEN

Estudiamos esferas hidrostáticas, autogravitantes y relativistas, con una ecuación de estado politrópica, considerando estructuras con índices politrópicos $n = 1(0.5)3$, e ilustramos los resultados para parámetros relativistas $\sigma = 0 - 0.75$. Determinamos el parámetro relativista crítico, para el cual la masa del politropo alcanza un valor máximo y representa el primer modo de inestabilidad radial. Con $n = 1(0.5)2.5$ encontramos politropos relativistas estables para σ menor que los valores críticos $0.42, 0.20, 0.10$, y 0.04, respectivamente. Se obtienen politropos relativistas inestables para valores mayores de σ. Cuando $n = 3.0$ y $\sigma > 0.5$ encontramos soluciones energéticamente inestables. Los resutados sobre los valores críticos concuerdan muy bien con los de otros autores. Al comparar las soluciones analíticas y numéricas de las funciones relativistas estudiadas se encuentran errores relativos máximos del orden de 10^{-3}.

Key Words: methods: analytical — methods: numerical — stars: interiors

1. INTRODUCTION

Polytropic models could be considered simple models of stellar structure, and we have all of the equations needed to make more sophisticated stellar models by solving the equations of stellar structure. However, there is a need to ask whether the calculated models provide stable spherically symmetric models.

Several authors have investigated the stability of the polytropic models. Bonnor (1958) found that self-gravitating, polytropic spheres with $n = 3$ were inconditionally stable to radial perturbations. For the first time, Chandrasekhar (1964) provided the radial stability equation. Earlier methods used to examine the stability of polytropic stars are listed in Bardeen et al. (1966). More recently, the stability of polytropes with different polytropic indices was described by Horedt (2013) and Raga et al. (2020).

In stellar structures such as white dwarfs, neutron stars, black holes and supermassive stars, and in star clusters, relativistic effects play a significant role (Sen and Roy 1954, Sharma 1988). Tooper (1964) performed a relativistic analysis of the polytropic equation of state and derived the non-relativistic Lane-Emden equation from two nonlinear differential equations (Tolman-Oppenheimer, TOV). The problem of the stability of relativistic stars has long been investigated in the literature, for example, by

---

[1] Department of Mathematics, Deanship of Educational Services, Qassim University, Buraidah, Saudi Arabia.

[2] Astronomy Department, National Research Institute of Astronomy and Geophysics(NRIAG), 11421 Helwan, Cairo, Egypt.

Zeldovich and Novikov (1978), Shapiro and Teukolsky (1984), Takatsuka and Tamagaki (1993), Casalbuoni and Nardulli (2004), Khalilov (2002), Isayev (2015), Chu et al. (2015).

In the present paper, we examine the stability of the relativistic polytrope for different polytropic indices. An analytical solution to the TOV equation is introduced, which provides the physical parameters of the relativistic polytrope. We investigate the critical values of the relativistic parameter for which the onset of the radial instability occurs. The structure of the paper is as follows: § 2 is devoted to the formulation of the TOV equation. In § 3 we give a brief description of the analytical method used to solve the TOV equation. § 4 deals with the obtained results. The conclusion is outlined in § 5.

2. THE EQUATION OF HYDROSTATIC EQUILIBRIUM

The interior of a symmetric star can be described in a spherical coordinate system (r, ϑ, φ) by the standard form of the metric (Tolman 1939, Landu & Lifshitz 1975)

$$ds^2 = e^{\nu} c^2 dt^2 - e^{\lambda} dr^2 - r^2 d\vartheta^2 - r^2 \sin^2\vartheta d\varphi^2, \quad (1)$$

where ν and λ are functions of radius r. As for a fluid star, the components of the energy momentum tensor corresponding to the above metric are given by

$$T_0^0 = \rho c^2 e^{\nu}, \;\; T_1^1 = P e^{\lambda}, \;\; T_2^2 = P r^2, \;\; T_3^3 = P r^2 \sin^2\vartheta, \quad (2)$$

where ρ, P and c are the mass density, pressure, and speed of light, respectively. The time-independent gravitational equations for the line element equation (1) and the energy momentum tensor are

$$e^{-\lambda}\left(\frac{1}{r}\frac{d\nu}{dr} + \frac{1}{r^2}\right) - \frac{1}{r^2} = \frac{8\pi G}{c^4} P, \quad (3)$$

$$e^{-\lambda}\left(\frac{1}{r}\frac{d\lambda}{dr} - \frac{1}{r^2}\right) + \frac{1}{r^2} = \frac{8\pi G}{c^4} \rho c^2, \quad (4)$$

$$\frac{dP}{dr} = -\frac{1}{2}(P + \rho c^2)\frac{d\nu}{dr}, \quad (5)$$

where $G = 6.67 \times 10^{-8} g^{-1}\ \mathrm{cm}^3\ \mathrm{s}^{-2}$ is the Newtonian gravitational constant. Equations (3), (4), and (5) together with the equation of state $\rho = \rho(P)$ represent the hydrostatic equilibrium for an isotropic general relativistic fluid sphere and can be solved to get λ, ν, P and ρ as functions of r. For hydrostatic equilibrium stars, the Tolman-Oppenheimer-Volkoff (TOV) general relativity equation obtained by solving Einstein's field equations has the form

$$\frac{dP}{dr} = -\frac{G\,\varepsilon(r)\,m(r)}{c^2\,r^2}\left[1 + \frac{P(r)}{\varepsilon(r)}\right]\left[1 + \frac{4\,\pi r^3\,P(r)}{m(r)\,c^2}\right] \left[1 - \frac{2G\,m(r)}{c^2\,r}\right]^{-1}, \quad (6)$$

where

$$m(r) = \int_0^r 4\pi\rho(r) r^2 dr,$$

is the gravitational mass interior to radius r and $\varepsilon(r)$ is the internal energy density.

Equation (6) is an extension of the Newtonian formalism with a relativistic correction. The equation of state for a polytropic star is $P = K\rho^{1+\frac{1}{n}}$, where n is the polytropic index. Tooper (1964) has shown that the TOV equation together with the mass conservation equation have the form

$$\xi^2 \frac{d\theta}{d\xi}\frac{1 - 2\sigma\,(n+1)\upsilon/\xi}{1 + \sigma\,\theta} + \upsilon + \sigma\,\xi\,\theta\frac{d\upsilon}{d\xi} = 0, \quad (7)$$

and

$$\frac{d\upsilon}{d\xi} = \xi^2\theta^n, \quad (8)$$

with the initial conditions

$$\theta(0) = 1, \qquad \upsilon(0) = 0, \quad (9)$$

where

$$\theta = \rho/\rho_c, \quad \xi = rA, \quad \upsilon = \frac{A^3 m(r)}{4\pi\rho_c},$$
$$A = \left(\frac{4\pi G\rho_c}{\sigma(n+1)c^2}\right)^{1/2}, \; \sigma = \frac{P_c}{\rho_c\,c^2} = \frac{K{\rho_c}^{1/n}}{c^2}, \quad (10)$$

σ is the relativistic parameter that can be related to the sound velocity in the fluid, because the sound velocity is given by ${\upsilon_s}^2 = \frac{dP}{d\rho}$ in an adiabatic expression. In equations (10) θ, ξ and υ are dimensionless parameters, while A is a constant.

If the pressure is much smaller than the energy density at the center of a star (i.e. σ tends to zero), then equation (7) reduces to

$$\xi^2\frac{d\theta}{d\xi} + \upsilon = 0. \quad (11)$$

Equation (8) together with equation (11) reproduce the well-known Lane-Emden equation for Newtonian polytropic stars

$$\frac{1}{\xi^2}\frac{d}{d\xi}\left(\xi^2\frac{d\theta}{d\xi}\right) + \theta^n = 0. \quad (12)$$

When n tends to zero, we obtain the case of incompressible matter, for which the analytic solutions are possible in both relativistic and nonrelativistic cases. The nonrelativistic Lane-Emden equation has an analytical solution in closed form only for $n = 0,\ 1$ and 5. However, this is not possible for the relativistic equation, and numerical integrations must be performed (Tooper 1964; Bludman 1973; Ferrari et al. 2007).

3. ANALYTICAL SOLUTIONS OF THE RELATIVISTIC EQUATIONS

Nouh (2004), Nouh and Saad (2013) introduced a new analytical solution of equations (7-8) applying the Euler-Abel transformation (Demodovich & Maron, 1973) and then a Pade approximation to the Euler-Abel transformed series (Appendix B) to accelerate the convergence of the power series solutions.

In this paper, we analyze the gravitational stability of polytropic fluid spheres based on the analytical solution of the TOV equations that have already been given by Nouh and Saad (2013). We consider the cases of polytropic index $n = 3.0, 2.5, 2.0, 1.5$, and 1.0 for $\sigma < n/(n+1)$.

The analytical solution has the form:

$$\theta(\xi) = 1 + \sum_{k=1}^{\infty} a_k \xi^{2k}, \tag{13}$$

where

$$\begin{aligned} a_{k+1} =& \frac{\sigma}{2(k+1)}(2(n+1)\gamma_{k-1} - \eta_k - \beta_k + \sigma\zeta_k) - \\ & \frac{\alpha_k}{2(k+1)(2k+3)}, \quad k \geq 1, \\ \gamma_{k-1} =& \sum_{i=0}^{k-1} f_i g_{k-i-1}, \quad \eta_k = \sum_{i=0}^{k} a_i g_{k-i}, \\ \beta_k =& \sum_{i=0}^{k} a_i \alpha_{k-i}, \quad \zeta_k = \sum_{i=0}^{k} a_i \beta_{k-i}, \\ f_i =& 2(i+1)a_{i+1},\ g_i = \frac{\alpha_i}{(2i+3)},\ \gamma_k = \sum_{i=0}^{k} f_i g_{k-i}, \\ \alpha_k =& \frac{1}{k a_0} \sum_{i=1}^{k} (ni - k + i) a_i \alpha_{k-i}, \quad k \geq 1, \\ \alpha_0 =& a_0^n, \text{ and } a_0 = 1. \end{aligned} \tag{14}$$

From equations (10), for some values of n, σ and ρ_c we can determine K, and obtain the radius R and the mass $M(R)$ from

$$R = A^{-1}\xi_1 = \left[\frac{c^2}{4\pi G}(n+1)\sigma^{(1-n)}\left(\frac{K}{c^2}\right)^n\right]^{1/2} \xi_1, \tag{15}$$

$$M = \frac{4\pi\rho_c}{A^3}\nu(\xi_1) = \left[\frac{1}{4\pi}\left(\frac{(n+1)c^2}{G}\right)^3\left(\frac{K}{c^2}\right)^n\right]^{1/2} \tilde{M}, \tag{16}$$

$$\tilde{M} \equiv \sigma^{(3-n)/2}\ \nu(\xi_1). \tag{17}$$

ξ_1 is the first zero of the Lane-Emden function $\theta(\xi)$; equation (8), can be written in the form

$$\upsilon(\xi_1) = \sum_{k=0}^{\infty} \frac{\alpha_k}{(2k+3)}\ {\xi_1}^{2k+3}\ . \tag{18}$$

The power series solution, equation (13), converges rapidly for values of the polytropic index $n \leq 2$ and the error between analytical and numerical solutions is of order 10^{-4}. For $n > 2$, the series solution utilized gives a slow convergence, and the calculation of the stellar mass from equations (16) and (17) indicates a larger error. The physical range for a convergent power series can be extended with a change of the independent variable. Transformations by changing the independent variable are utilized to improve and accelerate the series convergence in equation (18) for $n > 2$ (Pasucal 1977, Saad 2004):

$$x = 6 * \left\{\left(1 + \frac{1}{3}\xi^2\right)\right\}^{1/2}. \tag{19}$$

4. RESULTS

The results evaluated by the use of equations in § 3 are utilized here to analyze the stability of relativistic polytropes for various values of the general relativity parameter σ and polytropic index n. The numerical results obtained are tabulated in Appendix A for $n = 1(0.5)$ to 3.0 and a range of values of σ. Comparisons of the analytical solutions of equation (1) and $\tilde{M}(\sigma)$ to the numerical method are given in Tables 5 to 9. Table 10 shows the critical values of $\tilde{M}(\sigma)$ due to relativistic effects for different polytropic indices.

In Figures 1 to 5 we plot $\tilde{M}$, equation (17), as a function of the index n and the relativistic effect σ. The figures show an increase of $\tilde{M}$ (consequently an increase of the stellar mass M) with σ up to some maximum values (say, σ_{CR}). It is worth mentioning that the critical value σ_{CR} marks

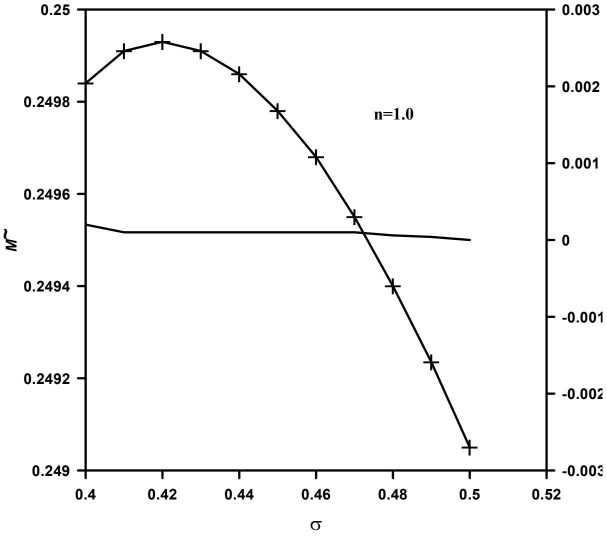

Fig. 1. $\tilde{M}(\sigma)$ for $n = 1$, and $\sigma_{CR} \approx 0.42$. Stable relativistic polytropes occur for $\sigma < 0.42$, while unstable models occur when $\sigma > 0.42$. Comparison of analytical and numerical results provides errors of order 10^{-4}.

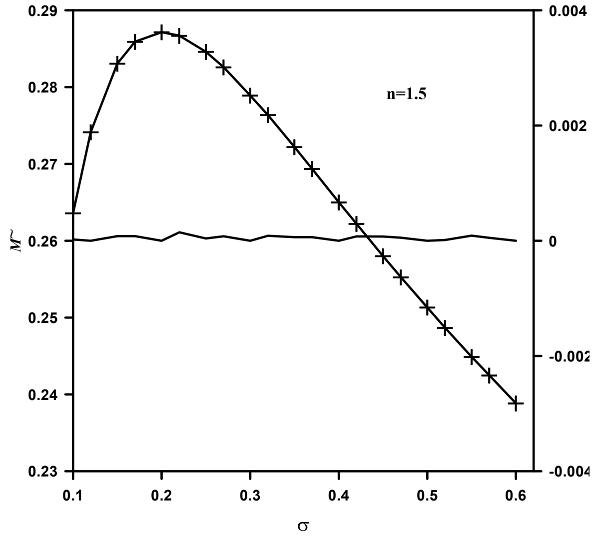

Fig. 2. $\tilde{M}(\sigma)$ for $n = 1.5$, and $\sigma_{CR} \approx 0.2$. Stable relativistic polytropes occur for $\sigma < 0.2$, while unstable models occur when $\sigma > 0.2$. Comparison of analytical and numerical results provides errors of order 10^{-5}.

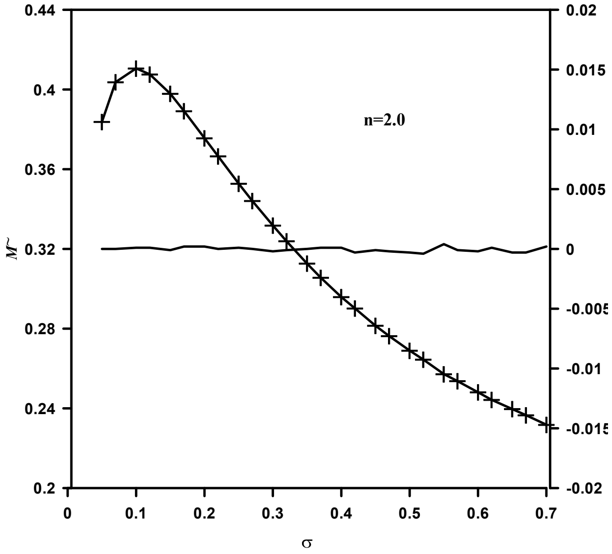

Fig. 3. $\tilde{M}(\sigma)$ for $n = 2$, and $\sigma_{CR} \approx 0.1$. Stable relativistic polytropes occur for $\sigma < 0.1$, while unstable models occur when $\sigma > 0.1$. Comparison of analytical and numerical results provides errors of order 10^{-4}.

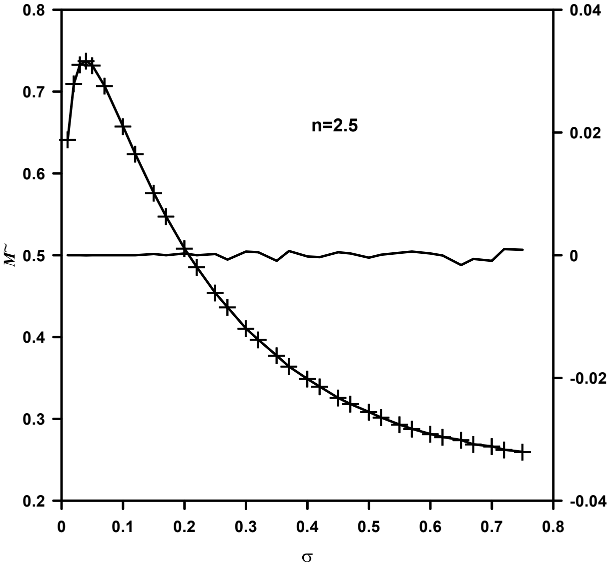

Fig. 4. $\tilde{M}(\sigma)$ for $n = 2.5$, and $\sigma_{CR} \approx 0.04$. Stable relativistic polytropes occur for $\sigma < 0.04$, while unstable models occur when $\sigma > 0.04$. Comparison of analytical and numerical results provides errors of order 10^{-4}.

the onset of the first mode of radial instability. For the case $n = 1.0$, Figure 1 shows that the critical value $\sigma_{CR} = 0.42$, and the relativistic polytropes are stable for $\sigma < 0.42$. In Figures 2, 3, and 4 we observe critical values of the general relativity index $\sigma_{CR} = 0.2$, $\sigma_{CR} = 0.1$ and $\sigma_{CR} = 0.04$ for the cases $n = 1.5$, $n = 2.0$ and $n = 2.5$ respectively. In Figure 5 where $n = 3.0$, $\tilde{M}$ has a maximum at $\sigma_{CR} = 0$ which marks the onset of the first mode of instability, while the minimum value at $\sigma_{CR} = 0.53$ marks the onset of the next mode of nonradial instability. In this case, equation (17) reduces to $\tilde{M} \equiv \nu(\xi_1)$. We

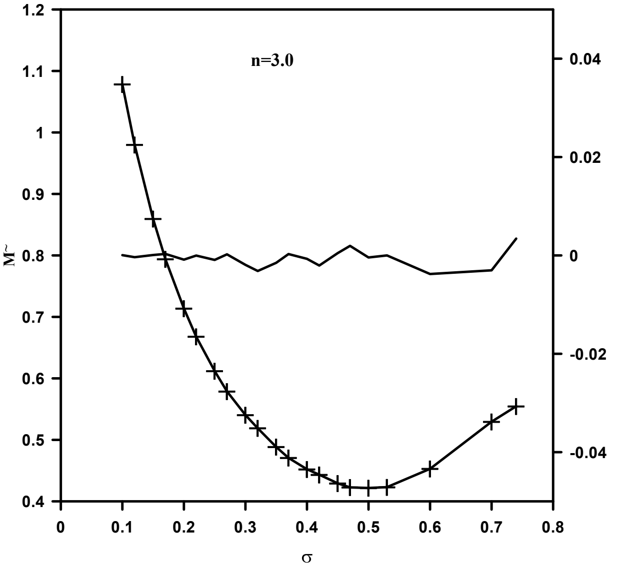

Fig. 5. For $n = 3.0$, $\tilde{M}$ has a maximum at $\sigma_{CR} = 0$ which marks the onset of the first mode of instability, while the minimum at $\sigma_{CR} \approx 0.53$ marks the onset of the next mode of nonradial instability. Comparison of analytical and numerical results provides errors of order 10^{-3}.

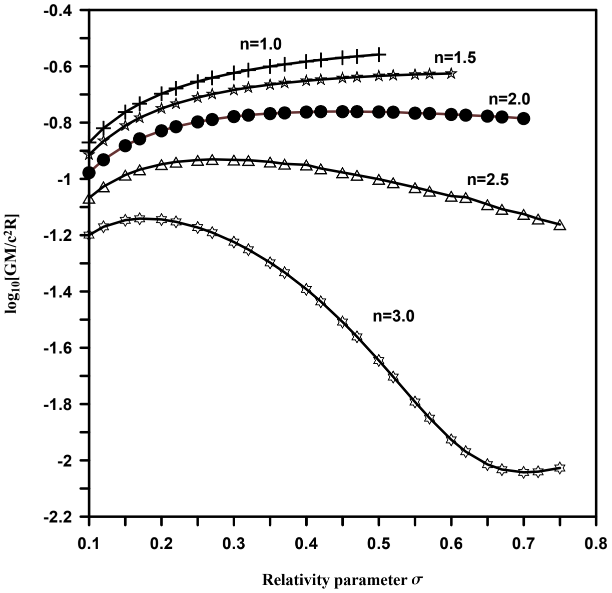

Fig. 6. The logarithmic ratio of the gravitational radius to the coordinate radius, as a function of the relativistic parameter σ, for different values of the polytropic index n.

conclude that for $\sigma_{CR} > 0.5$ the relativistic polytropic models are energetically unstable.

The study of the stability of polytropes is useful for determining some physical properties, such as the maximum mass limit, and illustrates how the stellar mass increases or decreases due to the effects of general relativity. For a given mass, radius, and a polytropic index n, Figure 6 of the mass-radius relation can be used to determine the internal structure of a polytrope. This means that each value of a relativistic parameter σ corresponds to a certain internal structure. We can see from Figure 6 that one pair of mass and radius corresponds to two different values of σ. For the case of a polytropic index $n = 3.0$, the logarithmic function $\log_{10}[\sigma\ (n+1)v(\xi_1)/\xi_1)] = -2.03$ has two values of $\sigma \simeq 0.67$ and $\sigma \simeq 0.75$. Then we have two spherical polytropic configurations of the same mass and radius, but with different internal structures. When $n = 2.0$, the logarithmic function $\log_{10}[\sigma\ (n+1)v(\xi_1)/\xi_1)] = -0.76$ has two values of $\sigma \simeq 0.42$ and $\sigma \simeq 0.47$. Such information reflects the importance of relativistic solutions.

Table 1 gives the limits of the mass-radius relations; for example, if the polytropic index $n = 1.0 GM/c^2\overline{R} \leq 0.214$, then the gravitational radius $2GM/c^2$ is at most 43% of the invariant(physical) radius $\overline{R}$. When the polytropic index $n = 3.0\ GM/c^2\overline{R} \leq 0.072$, then the gravitational radius 2GM/c^2 is at most 14.5% of the invariant radius $\overline{R}$, which is very small compared to the limit value when $n = 1.0$.

The results of all critical values obtained in this paper for different polytropic indices are in full agreement with those evaluated by several authors such as Tooper(1964), Bludman(1973), and Araujo & Chirenti (2011). These critical values σ_{CR} and $\tilde{M}(\sigma)$ together with various indices n are given in Table 10 (Appendix A). It is shown that the spherical polytrope of index $n = 3.0$ and $\sigma > 0.5$ is energetically unstable.

The mass-radius relation (Tooper 1964) has the form:

$$\frac{GM}{c^2\overline{R}} = \frac{\sigma\ (n+1)v(\xi_1)}{\overline{\xi_1}}, \tag{20}$$

where $\overline{R}$ defines the physical radius (invariant radius) of the sphere and $\overline{\xi_1} = A\overline{R}$ can be obtained by integrating the equation

$$\overline{\xi_1} = \int_0^{\xi_1} \left(1 - 2\sigma\ (n+1)v(\xi)/\xi\right)^{-1/2} d\xi. \tag{21}$$

The mass-radius relation is useful for determining the surface redshift. It gives the ratio of the gravitational radius $2GM/c^2$ to the invariant radius $\overline{R}$ when n and σ are known. Rewrite equation (20) in

TABLE 1

LIMITS OF THE MASS-RADIUS RELATIONS

n	Max. value of $\log_{10}[\sigma\ (n+1)v(\xi_1)/\overline{\xi_1}]$	Limit ratio of $GM/c^2\overline{R}$	Limit ratio of GM/c^2R
1.0	−0.670	0.214	0.277
1.5	−0.769	0.170	0.237
2.0	−0.885	0.130	0.174
2.5	−1.022	0.095	0.117
3.0	−1.201	0.0633	0.072

terms of numerical values for solar mass and solar radius and take logarithms of both sides of the resulting equation (Tooper, 1964). Then using the solutions introduced in § 3, we plotted the logarithmic ratio of gravitational radius to a geometrical radius as a function of the relativistic parameter for different values of the polytropic index n (see Figure 6). Table 1 gives the limits of the mass-radius relations for different polytropic index n.

5. SERIES CONVERGENCE

The power series solution of the relativistic problem without using any acceleration techniques is very limited. Tables 2, 3, and 4 show the radius of convergence ξ_1 of the power series solution $({}_1)$ of equation (13) and the relative error (ε) before performing any acceleration. For the polytropic indices $n = 1.0$ and $n = 1.5$, the series is rapidly convergent. However, beyond these values, the power series solution is either slowly convergent or divergent. Note that the relative error ($\varepsilon = |\xi_1\,(An) - \xi_1\,(Num)|\,/\xi_1\,(Num)$) increases gradually with relativistic effect σ and polytropic index n. This in turn results in a small physical range for the convergent power series solutions, and may produce inaccurate physical parameters of the relativistic polytropes.

The fourth order Runge-Kutta method was used for the performance of the numerical solution of the relativistic TOV equation. Analytical and numerical calculations were done using the Mathematica package, version 11.2.

To extend the physical radii of the convergent power series solutions, a combination of the two techniques for Euler-Abel transformation and Padé approximation (Nouh 2004; Nouh & Saad 2013) were utilized. Tables 5 to 9 (Appendix A) show comparisons between numerical and analytical results. It is worth noting that the power series solutions are rapidly convergent for polytropic indices $n = 1(0.5)3.0$ and provide a maximum relative error of order 10^{-3}.

TABLE 2

RADII OF CONVERGENCE OF $\theta(\xi)$ AND RELATIVE ERROR FOR $n = 1.0$

σ	$\xi_1(N)$	$\xi_1(A)$	ε: relative error
0.1	2.5990	2.5990	0.0
0.2	2.2770	2.2765	0.000219635
0.3	2.0641	2.0637	0.000193827
0.4	1.9132	1.9111	0.001098844
0.5	1.8008	1.8862	0.045276217

TABLE 3

RADII OF CONVERGENCE OF $\theta(\xi)$ AND RELATIVE ERROR FOR $n = 1.5$

σ	$\xi_1(N)$	$\xi_1(A)$	ε: relative error
0.1	3.0384	3.0730	0.011259356
0.2	2.6993	2.6025	0.037195005
0.3	2.4930	2.4281	0.026728718
0.4	2.3610	2.2648	0.042476157
0.5	2.2749	2.0644	0.101966673
0.6	2.2192	1.8340	0.210032715

TABLE 4

RADII OF CONVERGENCE OF $\theta(\xi)$ AND RELATIVE ERROR FOR $n = 2.0$

σ	$\xi_1(N)$	$\xi_1(A)$	ε: relative error
0.1	3.6989	3.4259	0.07968709
0.2	3.3983	2.5632	0.325803683
0.3	3.2711	2.5577	0.278922469
0.4	3.2473	1.9503	0.665025893
0.5	3.2967	1.9836	0.661978221
0.6	3.3986	1.7686	0.92163293
0.67	3.4982	1.6556	1.112949988

6. CONCLUSION

In the present paper, we study the stability properties of the relativistic polytrope. We analyze for various polytropic indices the stability of the relativistic polytrope. An analytic solution is applied to the TOV equation that provides us with relativistic polytropic physical parameters. For each polytropic index, we test the critical values of the relativistic parameter at which the radial instability started. It is shown that for a given mass, radius and polytropic index n, the internal structure of a polytropic fluid sphere can be determined as a function of the relativistic parameter σ. For $n = 1(0.5)2.5$, stable relativistic polytropes occur for σ less than the critical values $0.42, 0.20, 0.10$, and 0.04, respectively, while unstable relativistic polytropes are obtained when the relativistic parameter σ is greater than the same values. When $n = 3.0$ and $\sigma > 0.5$, energetically unstable solutions occur.

We thank the referee for his/her valuable comments which improved the paper.

APPENDIX A: NUMERICAL RESULTS

In the following tables, we list the numerical results obtained for different polytropic indices. The designation of the columns are as follows:

1. σ: is the relativistic parameter.
2. ξ_1: is the first zero of the Emden function.
3. $\nu(\xi_1)_{Num}$: is the numerical solution of the relativistic function.
4. $\nu(\xi_1)_{An}$: is the analytical solution of the relativistic function.
5. $\tilde{M}(\sigma)_{Num}$: is a parameter analog to the mass of the polytrope computed numerically.
6. $\tilde{M}(\sigma)_{An}$: is a parameter analog to the mass of the polytrope computed analytically.
7. $\Delta\nu(\xi_1)_{Num}$: is the difference between the analytical and the numerical values of the function.
8. $\Delta\tilde{M}(\sigma)_{An}$: is the difference between the analytical and the numerical values.
9. $\sigma_{critical}$: is the critical value of the fractional parameter at which instability started.

TABLE 5

COMPARISONS BETWEEN ANALYTICAL AND NUMERICAL SOLUTIONS OF THE RELATIVISTIC FUNCTIONS (1) AND $\tilde{M}(\sigma)$ FOR $n = 1.0$

σ	ξ_1	$\nu(\xi_1)_{Num}$	$\nu(\xi_1)_{An}$	$\tilde{M}(\sigma)_{Num}$	$\tilde{M}(\sigma)_{An}$	$\Delta\nu(\xi_1)_{Num}$	$\Delta\tilde{M}(\sigma)_{An}$
0.0	3.1415	3.1416	3.1416	0.0	0.0	0.0	0.0
0.10	2.5990	1.7514	1.7514	0.1751	0.1751	0.0	0.0
0.12	2.5221	1.5922	1.5922	0.1911	0.1911	0.0	0.0
0.15	2.4198	1.3941	1.3941	0.2091	0.2091	0.0	0.0
0.17	2.3590	1.2834	1.2835	0.2182	0.2182	0.0001	0.0
0.20	2.2770	1.1426	1.1426	0.2285	0.2285	0.0	0.0
0.22	2.2278	1.0624	1.0624	0.2337	0.2337	0.0	0.0
0.25	2.1607	0.9585	0.9585	0.2396	0.2396	0.0	0.0
0.27	2.1200	0.8983	0.8981	0.2425	0.2425	0.0002	0.0
0.30	2.0641	0.8192	0.8190	0.2457	0.2457	0.0002	0.0
0.32	2.0299	0.7727	0.7728	0.2473	0.2473	-0.0001	0.0
0.35	1.9827	0.7109	0.7109	0.2488	0.2488	0.0	0.0
0.37	1.9536	0.6742	0.6742	0.2495	0.2495	0.0	0.0
0.40	1.9132	0.6249	0.6250	0.2500	0.2500	0.0001	0.0
0.42	1.8882	0.5954	0.5954	0.2501	0.2501	0.0	0.0
0.45	1.8531	0.5553	0.5554	0.2499	0.2499	0.0001	0.0
0.47	1.8314	0.5311	0.5310	0.2496	0.2496	0.0001	0.0
0.50	1.8008	0.4981	0.4981	0.2491	0.2491	0.0	0.0

TABLE 6

COMPARISONS BETWEEN ANALYTICAL AND NUMERICAL SOLUTIONS OF THE RELATIVISTIC FUNCTIONS (1) AND $\tilde{M}(\sigma)$ FOR $n = 1.5$

σ	ξ_1	$\nu(\xi_1)_{Num}$	$\nu(\xi_1)_{An}$	$\tilde{M}(\sigma)_{Num}$	$\tilde{M}(\sigma)_{An}$	$\Delta\tilde{M}(\sigma)_{An}$
0.0	3.6537	2.7141	2.7141	0.0	0.0	0.0
0.10	3.0384	1.4823	1.4822	0.263592	0.263569	2.3E-05
0.12	2.9552	1.3446	1.3446	0.274153	0.274151	2E-06
0.15	2.8464	1.1744	1.1741	0.283069	0.282987	8.2E-05
0.17	2.783	1.08	1.08	0.285922	0.285841	8.1E-05
0.20	2.6993	0.9602	0.9602	0.287166	0.287166	0.0
0.22	2.65	0.8925	0.8921	0.286706	0.286558	0.000148
0.25	2.5843	0.805	0.8049	0.284609	0.284568	4.1E-05
0.27	2.5453	0.7545	0.7543	0.282603	0.282524	7.9E-05
0.30	2.493	0.6881	0.6881	0.278913	0.278913	0.0
0.32	2.4619	0.6496	0.6494	0.27638	0.276292	8.8E-05
0.35	2.42	0.5982	0.5981	0.272214	0.272151	6.3E-05
0.37	2.3949	0.5678	0.5677	0.269366	0.269303	6.3E-05
0.40	2.361	0.5269	0.5269	0.265018	0.265018	0.0
0.42	2.3407	0.5026	0.5025	0.262221	0.262144	7.7E-05
0.45	2.3134	0.4696	0.4695	0.258014	0.25794	7.4E-05
0.47	2.297	0.4497	0.4496	0.25527	0.255216	5.4E-05
0.50	2.2749	0.4227	0.4227	0.251326	0.251326	0.0
0.52	2.2617	0.4061	0.4061	0.248669	0.248655	1.4E-05
0.55	2.2439	0.3835	0.3833	0.244906	0.244817	8.9E-05
0.57	2.2333	0.3696	0.3696	0.242484	0.242432	5.2E-05
0.60	2.2192	0.3504	0.3504	0.238846	0.238846	0.0

TABLE 7

COMPARISONS BETWEEN ANALYTICAL AND NUMERICAL SOLUTIONS OF THE RELATIVISTIC FUNCTIONS (1) AND $\tilde{M}(\sigma)$ FOR $n = 2.0$

σ	ξ_1	$\nu(\xi_1)_{Num}$	$\nu(\xi_1)_{An}$	$\tilde{M}(\sigma)_{Num}$	$\tilde{M}(\sigma)_{An}$	$\Delta\tilde{M}(\sigma)_{An}$
0.0	4.3531	2.411	2.411	0.0	0.0	0.0
0.05	3.9617	1.7165	1.7162	0.3838	0.3838	0.0
0.07	3.8443	1.5258	1.5258	0.4037	0.4037	0.0
0.10	3.6989	1.2987	1.2983	0.4107	0.4106	0.0001
0.12	3.6191	1.1769	1.1766	0.4077	0.4076	0.0001
0.15	3.5198	1.0272	1.0274	0.3978	0.3979	-0.0001
0.17	3.4653	0.9445	0.9440	0.3894	0.3892	0.0002
0.20	3.3983	0.8403	0.8399	0.3758	0.3756	0.0002
0.22	3.3619	0.7814	0.7815	0.3665	0.3665	0.0
0.25	3.3186	0.7058	0.7056	0.3529	0.3528	0.0001
0.27	3.2962	0.6623	0.6622	0.3441	0.3441	0.0
0.30	3.2711	0.6055	0.6057	0.3316	0.3318	-0.0002
0.32	3.2595	0.5723	0.5725	0.3238	0.3239	-0.0001
0.35	3.2491	0.5285	0.5285	0.3127	0.3127	0.0
0.37	3.2463	0.5026	0.5024	0.3057	0.3056	0.0001
0.40	3.2473	0.4680	0.4678	0.2960	0.2959	0.0001
0.42	3.2526	0.4474	0.4478	0.2899	0.2902	-0.0003
0.45	3.2644	0.4195	0.4196	0.2814	0.2815	-0.0001
0.47	3.2754	0.4028	0.4030	0.2761	0.2763	-0.0002
0.50	3.2967	0.3800	0.3804	0.2687	0.2690	-0.0003
0.52	3.3128	0.3662	0.3668	0.2641	0.2645	-0.0004
0.55	3.3416	0.3474	0.3468	0.2576	0.2572	0.0004
0.57	3.3632	0.3359	0.3360	0.2536	0.2537	-0.0001
0.60	3.3986	0.3201	0.3202	0.2479	0.2481	-0.0002
0.62	3.4253	0.3104	0.3103	0.2444	0.2443	0.0001
0.65	3.4678	0.2970	0.2973	0.2394	0.2397	-0.0003
0.67	3.4982	0.2887	0.2891	0.2363	0.2366	-0.0003

TABLE 8

COMPARISONS BETWEEN ANALYTICAL AND NUMERICAL SOLUTIONS OF THE RELATIVISTIC FUNCTIONS (1) AND $\tilde{M}(\sigma)$ FOR $n = 2.5$

σ	ξ_1	$\nu(\xi_1)_{Num}$	$\nu(\xi_1)_{An}$	$\tilde{M}(\sigma)_{Num}$	$\tilde{M}(\sigma)_{An}$	$\Delta\tilde{M}(\sigma)_{An}$
0.0	5.3552	2.1872	2.1872	0.0	0.0	0.0
0.01	5.2623	2.0281	2.0281	0.641341	0.641341	0.0
0.02	5.1793	1.88702	1.88702	0.709633	0.709632	0.0
0.03	5.1052	1.76134	1.76131	0.733034	0.7033021	1.3E-05
0.04	5.0393	1.648899	1.648930	0.737410	0.737424	-1.4E-05
0.05	4.9809	1.5479	1.548019	0.7320	0.732013	0.0
0.07	4.8841	1.3744	1.374359	0.7069	0.706927	0.0
0.10	4.7819	1.1692	1.169269	0.6575	0.657528	0.0
0.12	4.7383	1.0599	1.059908	0.6238	0.623826	0.0
0.15	4.7044	0.9261	0.925878	0.5764	0.576204	0.0002
0.17	4.7006	0.8527	0.852617	0.5475	0.547477	0.0
0.20	4.7206	0.7606	0.760086	0.5086	0.508299	0.0003
0.22	4.7498	0.7088	0.708902	0.4855	0.485503	0.0
0.25	4.8163	0.6426	0.642273	0.4544	0.454155	0.0002
0.27	4.8753	0.6048	0.605615	0.4359	0.436554	-0.0007
0.30	4.9855	0.5556	0.554771	0.4112	0.410576	0.0006
0.32	5.0734	0.5271	0.527703	0.3964	0.396896	0.0005
0.35	5.2273	0.4896	0.490730	0.3766	0.377450	-0.0009
0.37	5.3450	0.4677	0.466891	0.3648	0.364138	0.0007
0.40	5.5448	0.438571	0.444662	0.348782	0.348982	-0.0002
0.42	5.6943	0.4214	0.421721	0.3392	0.339499	-0.0003
0.45	5.9440	0.3984	0.397734	0.3263	0.325758	0.0005
0.47	6.1284	0.3847	0.384457	0.3186	0.318326	0.0003
0.50	6.4335	0.3664	0.366915	0.3081	0.308537	-0.0004
0.52	6.6569	0.3555	0.355406	0.3019	0.301804	0.0001
0.55	7.0239	0.3408	0.340363	0.2935	0.293112	0.0004
0.57	7.2910	0.3320	0.331352	0.2885	0.287911	0.0006
0.60	7.7273	0.3202	0.319843	0.2818	0.281497	0.0003
0.62	8.0423	0.3131	0.319070	0.277851	0.277888	-3.7E-05
0.65	8.5563	0.3036	0.305345	0.2726	0.274169	-0.0016
0.67	8.9257	0.2980	0.297274	0.2696	0.268953	-0.0006
0.70	9.5224	0.2905	0.291442	0.2657	0.266579	-0.0009
0.72	9.9494	0.2860	0.284817	0.2634	0.2623610	0.001

TABLE 9

COMPARISONS BETWEEN ANALYTICAL AND NUMERICAL SOLUTIONS OF THE RELATIVISTIC FUNCTIONS (1) AND $\tilde{M}(\sigma)$ FOR $n = 3.0$.

σ	ξ_1	$\nu(\xi_1)_{Num}$	$\nu(\xi_1)_{An}$	$\tilde{M}(\sigma)_{Num}$	$\tilde{M}(\sigma)_{An}$	$\Delta\tilde{M}(\sigma)_{An}$
0.0	6.8968	2.01824	2.01824	2.01824	2.01824	0.0
0.05	6.7074	1.42463	1.42463	1.42463	1.42463	0.0
0.07	6.7206	1.26543	1.26542	1.26543	1.26542	1.0E-05
0.10	6.8258	1.07845	1.07837	1.07845	1.07837	8.0E-05
0.12	6.9521	0.979601	0.979949	0.979601	0.979949	- 0.0003
0.15	7.2285	0.85958	0.859491	0.85958	0.859491	9.0E-05
0.17	7.4751	0.794229	0.793908	0.794229	0.793908	0.0003
0.20	7.9508	0.713042	0.713880	0.713042	0.713880	-0.0008
0.22	8.3481	0.667954	0.667963	0.667954	0.667963	-1.0E-05
0.25	9.0894	0.611096	0.612004	0.611096	0.612004	-0.0009
0.27	9.6994	0.579159	0.578934	0.579159	0.578934	0.0002
0.30	10.8327	0.538631	0.540522	0.538631	0.540522	-0.0018
0.32	11.7690	0.515833	0.519000	0.515833	0.519000	-0.003
0.35	13.5271	0.487068	0.488563	0.487068	0.488563	-0.001
0.37	15.0007	0.471124	0.470841	0.471124	0.470841	0.0003
0.40	17.8197	0.451585	0.452268	0.451585	0.452268	-0.0007
0.42	20.2306	0.441299	0.443341	0.441299	0.443341	-0.002
0.45	24.9438	0.429831	0.429350	0.429831	0.429350	0.0005
0.47	29.0538	0.424822	0.422867	0.424822	0.422867	0.0020
0.50	37.2058	0.421395	0.421807	0.421395	0.421807	-0.0004
0.53	48.5317	0.423168	0.418075	0.423168	0.418075	0.0051
0.60	91.0723	0.449319	0.453089	0.449319	0.453089	-0.004
0.70	162.5832	0.526621	0.529641	0.526621	0.529641	-0.003
0.74	177.9357	0.558153	0.554724	0.558153	0.554724	0.003
0.75	180.4379	0.565394	0.541169	0.565394	0.541169	0.0242

TABLE 10

THE CRITICAL VALUES σ_{CR} CORRESPONDING $\tilde{M}(\sigma)$ FOR VARIOUS INDICES N

n	ξ_1	$\sigma_{critical}$	$\tilde{M}(\sigma)$
1.0	1.8882	0.42	0.249930
1.5	2.6993	0.20	0.287166
2.0	3.6989	0.10	0.410546
2.5	5.0393	0.04	0.737424
3.0	6.8968	0.0	2.01824
3.0	48.5317	0.53	0.416203

APPENDIX B. THE SERIES ACCELERATION TECHNIQUE

To accelerate the convergence of the series solution of equation 13, we followed the scheme developed by Nouh (2004). As the first step of this scheme, the alternating series is accelerated by Euler–Abel transformation (Demodovich & Maron 1973).
Let us write

$$\theta(\xi) = a_0 + \xi\phi(\xi), \tag{22}$$

where

$$\phi(\xi) = \sum_{k=0}^{\infty} a_k \xi^{k-1} = \sum_{k=1}^{\infty} a_{k+1}\xi^k; \tag{23}$$

then

$$(1-\xi)\phi(\xi) = \sum_{k=0}^{\infty} a_{k+1}\xi^k - \sum_{k=1}^{\infty} a_k\xi^k = a_0 + \sum_{k=0}^{\infty} \Delta a_k \xi^k, \tag{24}$$

where $\Delta a_k = a_{k+1} - a_k, k = 0, 1, 2, ...$ are finite differences of the first order of the coefficients a_k. Applying the Euler-Abel transformation to the power series $\sum_{k=0}^{\infty} \Delta a_k \xi^k$, $\boldsymbol{p}$ times, and after some manipulations we obtain

$$\sum_{k=0}^{\infty} a_k\xi^k = \sum_{i=0}^{\infty} \Delta^i a_0 \frac{\xi^i}{(1-\xi)^{i+1}} + \left(\frac{\xi}{1-\xi}\right)^p \sum_{k=0}^{\infty} \Delta^p a_k \xi^k, \tag{25}$$

where $\Delta^0 a_0 = a_0$. Equation (25) becomes meaningless when $\xi = 1$, so, by setting $\xi = -t$, we obtain the Euler-Abel transformed series as

$$\theta E_n(t) = \sum_{k=0}^{\infty} \Delta^i a_0 \frac{t^i}{(1-t)^{i+1}} + \left(\frac{t}{1-t}\right)^p \sum_{k=0}^{\infty} \Delta^p[(-1)^k a_k] t^k. \tag{26}$$

Returning to the earlier variable, ξ, we obtain

$$\theta E_n(\xi) = \sum_{i=0}^{p-1} (-1)^i \Delta^i a_0 \frac{\xi_i}{(1+\xi)^i} + \left(\frac{\xi}{1+\xi}\right)^p \sum_{k=0}^{\infty} (-1)^{k+p} [\Delta^p a_k] \xi_k, \tag{27}$$

where

$$\Delta^p a_k = \Delta^{p-1} a_{k+1} - \Delta^{p-1} a_k.$$

Any order difference $\Delta^p a_k$ can be written as a linear combination

$$\Delta^p a_k = \sum_{i=0}^{p} (-1)^{p-i} \begin{pmatrix} p \\ i \end{pmatrix} a_{k+1},$$

where

$$\begin{pmatrix} p \\ i \end{pmatrix} = \frac{p!}{i!(p-i)!}.$$

The second step is to apply Padé approximation to the Euler-Abel transformed series, equation 27.

REFERENCES

Araujo, F. M. & Chirenti, C. B. M. H. 2011, arXiv:1102.2393

Bardeen, J. M., Thorne, K. S., & Meltzer, D. W. 1966, ApJ, 145, 505

Bludman, S. A. 1973, ApJ, 183, 637

Bonnor, W. B. 1958, MNRAS, 118, 523

Casalbuoni, R. & Nardulli, G. 2004, RvMP, 76, 263

Chandrasekhar, S. 1964, ApJ, 140, 417

Chu, P. Ch., Wang, X., Chen, L. W., & Huang, M. 2015, PhRvD, 91, 3003

Demidovich, B. P. & Maron, I. A. 1973, Computational Mathematics, 519.4, D4

Ferrari, L., Estrela, G., & Malheiro, M. 2007, IJMPE, 16, 2834

Horedt, G. P. 2004, Polytropes-Applications in Astrophysics and Related Fields, Astrophysics and Space Science Library 306 (Dordrecht: Springer)

Horedt, G. P. 2013, ApJ, 773, 131

Isayev, A. A. 2015, PhRvC, 91, 5208

Khalilov, V. R. 2002, PhRvD, 65, 6001

Landau, L. D. & Lifshitz, E. M. 1975, The classical theory of fields (2nd ed; Reading, MA: Addison-Wesley Publishing Co.)

Nouh, M. I. 2004, NewA, 9, 467

Nouh, M. I. & Saad, A. S. 2013, International Review of Physics, 7(1), 16

Pascual, P. 1977, A&A, 60, 161

Raga, A. C., Osorio-Caballero, J. A., Chan, R. S., et al. 2020, RMxAA, 56, 55

Saad, A. S. 2004, AN, 325, 733

Sen, N. R. & Roy, T. C. 1954, ZA, 34, 84

Shapiro, S. L. & Teukolsky, S. A. 1983, Black-holes, white dwarfs and neutron stars: the physics of compact objects (New York, NY: Wiley)

Sharma, J. P. 1988, ApJ, 329, 232

Takatsuka, T. & Tamagaki, R. 1993, PthPS, 112, 27

Tolman, R. C. 1939, PhRv, 55, 364

Tooper, R. F. 1964, ApJ, 140, 434

Zeldovich, Y. B. & Novikov, I. D. 1978, Relativistic Astrophysics, Vol. I: Stars and relativity (Chicago, IL: University of Chicago Press)

Tarek M. Kamel, Mohamed I. Nouh, Abdel-Naby S. Saad, and Ashraf A. Shaker: Astronomy Department, National Research Institute of Astronomy and Geophysics(NRIAG), 11421 Helwan, Cairo, Egypt.

Abdel-Naby S. Saad: Department of Mathematics, Deanship of Educational Services, Qassim University, Buraidah, Saudi Arabia (saad6511@gmail.com).

Revista Mexicana de Astronomía y Astrofísica, **57**, 419–431 (2021)

https://doi.org/10.22201/ia.01851101p.2021.57.02.14

A STUDY OF THE SX PHE STAR BL CAM[1]

J. H. Peña[2,3,4], J. D. Paredes[2,5], D. S. Piña[2,4], H. Huepa[3], and J. Guillen[4]

Received November 10 2020; accepted August 2 2021

ABSTRACT

We determined the physical parameters of the SX Phe star BL Cam from newly available times of maximum light and other times from the literature, as well as from $uvby-\beta$ photoelectric photometry. From our analysis we found that this star is a binary system. The mass of the companion star was calculated in term of the mass of the primary star and the orbital angle. For this star we determined a metallicity [Fe/H] of -1.2 ± 0.3.

RESUMEN

Determinamos los parámetros físicos de la estrella tipo SX Phe BL Cam a partir de nuevos tiempos de máximo observados y otros de la literatura, así como de fotometría fotoeléctrica $uvby-\beta$. Con nuestro análisis encontramos que esta estrella es un sistema binario. Calculamos la masa de la estrella compañera en términos de la masa de la estrella primaria y el ángulo orbital. Para esta estrella hemos determinado una composición química [Fe/H] de -1.2 ± 0.3.

Key Words: binaries: eclipsing — stars: individual: BL Cam — stars: variables: Scuti

1. INTRODUCTION

In their article on BL Cam and DY Peg, two SX Phe stars, Blake et al. (2000) reported that Hintz et al. (1997) on studying the rate of period change for BL Cam found that over an observational baseline of 30 years, BL Cam had exhibited a steady period change with no sudden jumps. However, they found that the light curve of BL Cam was exhibiting periodic amplitude variations of up to 0.2 magnitude. Such behavior was unexpected and had not been previously reported.

The most recent study of BL Cam (= 2MASS J03471987+6322422, Gaia DR2 487276688415703040, GD 428 in Simbad) is that of Zong et al. (2019) with observations from 2014 to 2018. They determined that the period content of BL Cam was dominated by a frequency of 25.5790 (3) c/d and its two harmonics, plus an independent frequency of 25.247 (2) c/d, a non-radial mode frequency detected from the data in 2014. With a O−C analysis of their times of maxima from the literature they determined a periodic change which, if caused by the light-time travel effect (LTTE), made BL Cam a binary system. Besides, they did not find evidence of the triple system suggested by previous authors.

We must remark that despite high quality space missions like TESS and the analysis of their data on A-F stars (Antoci et al. 2019), observational programs that have enough time series data to study the rate of period change must be developed, which is a task not possible to perform with TESS observations.

The Observatorio Astronómico Nacional de Tonantzintla (TNT) finds itself in an analogous situation to that described by Blake et al. (2000) referring to York University Observatory, since they are both located near large metropolitan areas. This restricts the types of research projects that can be conducted to those not requiring absolute photometry. Given the occasional large gaps in observational coverage of HADS and SX Phoenicis stars that have hindered the study of their period changes for several years, we have carried out a long-term monitoring program for such variables. Here we report our observations of BL Cam obtained as part of this program conducted by the staff and students of the Observational As-

---

[1] Based on observations collected at the Tonantzintla and San Pedro Mártir Observatories, México.

[2] Instituto de Astronomía, Universidad Nacional Autónoma de México, Cd. México, México.

[3] Observatorio Astronómico Nacional, Tonantzintla Puebla, UNAM, México.

[4] Facultad de Ciencias, Universidad Nacional Autónoma de México, México.

[5] Facultad de Ciencias, Universidad Central de Venezuela, Venezuela.

TABLE 1

LOG OF OBSERVING SEASONS AND NEW TIMES OF MAXIMA OF BL CAM

Date yr/month/day	Observers/Reductors	Npoints	Time span day	Nmax	Tmax (HJD-2458000) day	Observatory
20/01/1112	hh,ESAOBELA20/hh,jdp	122	0.0960	3	860.7052	TNT
					860.7448	
					860.7842	
20/01/1213	hh,ESAOBELA20/hh,jdp	162	0.1396	3	861.7247	TNT
					861.7641	
					861.8022	
20/01/1314	hh,ESAOBELA20/hh,jdp	116	0.0880	3	862.7415	TNT
					862.7804	
					862.8204	
20/01/1415	hh,ESAOBELA20/hh,jdp	151	0.1230	3	863.7182	TNT
					863.7599	
					863.7959	
20/01/1617	hh,ESAOBELA20/hh,jdp	117	0.0906	2	865.7510	TNT
					865.7905	
20/01/1718	hh,ESAOBELA20/hh,jdp	146	0.1187	2	866.7287	TNT
					866.7684	
20/02/2425	dsp/dsp,jdp	40	0.0819	2	904.6927	SPM
					904.7318	

Notes: dsp, Piña D. S.; hh, Huepa H.; jdp Paredes, J. D.; ESAOBELA20: Carrasco, L.; Vargas, C., Martínez, G., Castellanos, M., Mejía, N., Buenfil, G., Vásquez, F., Martínez, B., León, A., Beato, M. & Paredes, J. D.

tronomy courses of the National University of Mexico at TNT. These observations have been supported with $uvby-\beta$ photometry from the Observatorio Astronómico Nacional de San Pedro Mártir (SPM), México.

The purpose the present paper is to describe the procedure to acquire the new times of maximum, observations and reduction. With the new times of maximum and those found in the literature we analyzed them with an *O-C* procedure. The residuals derived utilizing the ephemerides values of Zhou et al. (1999) are congruent with a physical explanation, and suggested a periodic function, so we analyzed them with Period04. This package provided the orbital parameters assuming a binary system. The physical parameters are determined from $uvby-\beta$ photoelectric photometry and the unreddening procedure of Nissen (1988). The unreddened values were compared with the grids of Castelli & Kurucz (2006).

A brief summary of the contents of each section is the following: a description of the observations and data reduction is presented; period determination was done by the O−C procedure studying the proposed ephemerides. Our conclusion is that the star behaviour is explained if we assume a binary system, and so we determined the orbital elements and mass of the companion star; to conclude, we determined from $uvby-\beta$ photometry, its metallicity, surface gravity and effective temperature.

2. OBSERVATIONS AND DATA REDUCTION

Although some of the times of maximum light of this star have been reported elsewhere (Peña et al., 2021), here we present new times of maxima and the procedure followed to acquire the data. The observations were done at both the Observatorio Astronómico Nacional of San Pedro Mártir and Tonantzintla, in México. Table 1 presents the log of observations, as well as the new times of maximum light.

A 10-inch Meade telescope equipped with an Andor Apogy CCD camera was utilized at the TNT Observatory. There were around 11,000 counts with an integration time of 1 min, enough to secure high precision. The reduction work was done with AstroImageJ (Collins & Kielkopf 2013) Period determination. This software is relatively easy to use and besides being free, it works satisfactorily on the most common computing platforms. For the CCD photometry two reference stars were utilized in a differential photometry mode. The results were obtained from the difference $V_{\rm variable}-V_{\rm reference}$ and the scatter was calculated from the difference $V_{\rm reference1}-V_{\rm reference2}$. Light curves were also obtained. The new times of maximum light are listed in Table 1.

TABLE 2

COMPILATION OF THE LITERATURE

Reference	T_0	Period (day)	A	σ
Berg77	2,443,125.80476	0.0390883		
McNamara78	2,443,125.8048	0.03909760		0.0011
Hintz97	2,443,125.8042	0.03909773	6.153×10^{-13}	0.00068
Zhou99	2,443,125.8041	0.03909771	3.5728×10^{-13}	0.0013
Conidis13	2,443,125.8026	0.039097911	2.86×10^{-13}	0.0045
Zong19	2,443,125.7748	0.0390980385	-2×10^{-13}	0.0015

Notes. Berg77: Berg & Duther (1977); McNamara78: McNamara & Feltz (1978); Hintz97: Hintz et al. (1997); Zhou99: Zhou et al. (1999); Conidis13: Conidis & Delaney (2013); Zong19: Zong et al. (2019).
Notes: Compilation of the literature that presented ephemerides equations with the data available during their analysis.

3. O−C ANALYSIS

3.1. *O−C*

Before calculating the coefficients of the ephemeris equation, we studied the existing literature related to BL Cam. Several authors have carried out studies of the O−C behavior of this particular object and developed models. When these models were constructed, they were built with the data available to them based on the length of their observation time. However, they often differ in the interpretation of the data.

Hintz et al. (1997) presented a thorough study of this star concluding that BL Cam is a double-mode variable with a primary period of 0.0391 day, with evidence that the fundamental period had increased by 0.009 s in the previous 20 years. Their determined variation differs from that of McNamara and Feltz (1978) who proposed a linear variation. They found that the best fit to the data was given by equation (1), and concluded that the period had changed by 0.009 s in the last 20 years:

$$HJD_{max} = 2443125.8048 + 0.03909760(E). \qquad (1)$$

It was Hintz et al. (1997) who decided that this star had an increasing period and Blake et al. (2000) corroborated this assertion. Using their observations those authors proposed that the amplitude of the star's light curve is modulated and that the physical cause may be tied to the fact that the star is known to exhibit the features of double-mode pulsation. However, works such as Wolf et al. (2002) could not confirm the results of Hintz et al. (2000) implying that the star had a constant increasing pulsational period. Their conclusion, as expected, was that this star deserved continuous monitoring. One year later Kim et al. (2003) found that the parabolic period variation had recently reversed.

In view of the discrepancies among the different authors, we did a follow-up of the literature that contained ephemerides equations with the data available at that epoch. Most of the ephemerides equations have been calculated utilizing equation 2, in which P is the period, in days; β is the rate of the variation; Z, is the zero point; B is the amplitude; Ω, the frequency and α, the phase. These ephemerides elements are presented in Table 2.

$$\begin{aligned} HJD_{max} =& T_0 + PE + \frac{1}{2}\beta E^2 + Z + \\ & \sum_{i=1}^{n} B_i \sin\left[2\pi\left(\omega_i E + \alpha_i\right)\right] \end{aligned} \qquad (2)$$

with $A = \frac{1}{2}\beta$.

In Table 3, we list the author and the year of publication in Column one, Columns two and three show the initial and final dates of the data they analyzed, Column four shows the time span they considered, in years; the next column shows the number of points in their analysis consisting of the points they obtained combined with those of the literature at that time; the last column lists the number of points each author observed. The behavior of their O−C analysis is shown schematically in Figure 1.

For our analysis we collected a total of 520 times of maximum light from the literature and our observations. To these data we added those of VizieR to get 1985 data points, some of which were duplicated. Removing these repeated values, we got a total of 1606 data points. The elapsed time of observations is from 2443125.8046 to 2458904.7320 for a time span of 15778 days, or forty-three years, a considerable length of time.

The starting point for our O−C analysis was that provided by Zhou et al. (1999), who utilized the ephemerides listed in equation 1 proposed by McNamara et al.(1978). As a first stage, we reproduced what Zhou et al. (1999) obtained in their O−C resid-

TABLE 3

CHRONOLOGY OF THE COMPILATION

Reference	(HJD - 2400000)$_{Initial}$	(HJD - 2400000)$_{final}$	Δt(years)	N(T_{max})	N(observed)
Hintz97	43125.8046	50151.7268	19	69	39
Zhou99	43125.8046	50447.1520	20	136	58
Kim03	43125.8046	52272.1994	25	249	104
Fauvaud06	43125.8046	53478.4921	28	415	105
Conidis13	43125.8046	55635.6073	34	1465	73
Zong19	43125.8046	58413.3119	41	1583	123

Notes: Chronology of the compilation of times of maximum by several authors. The time span and number of points in the database employed in the literature are presented.

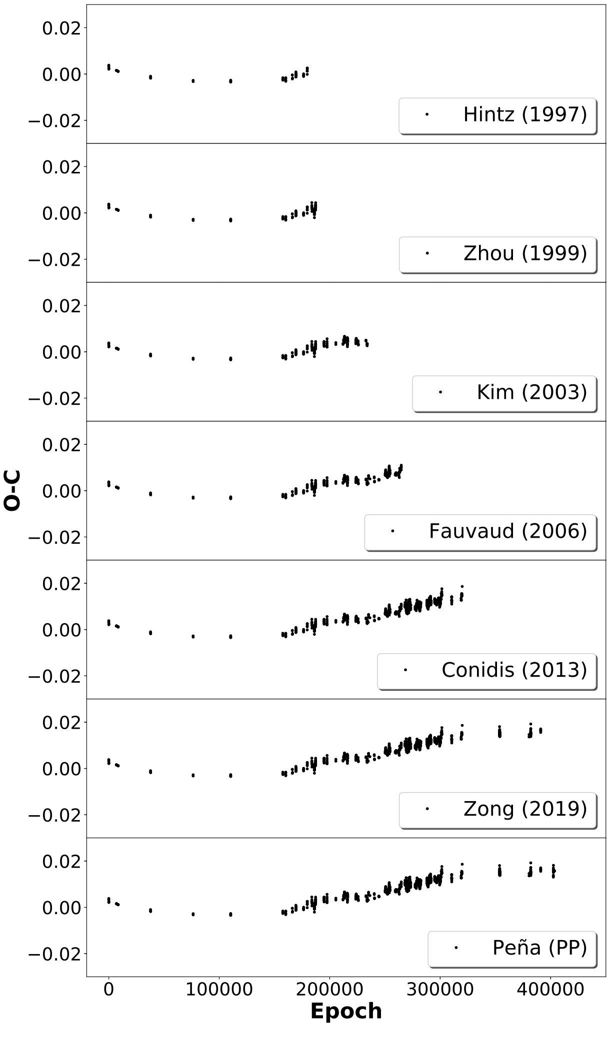

Fig. 1. O−C diagrams calculated with data from different authors (see main text) employing the ephemeris given by Zhou et al. 1999.

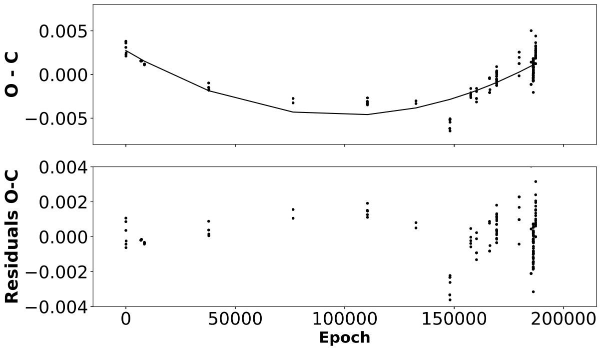

Fig. 2. Behaviour of the data points of Zhou et al. (1999) calculated reproducing their results: Top, the logically inferred parabolic behavior interpretation. Bottom, the O−C residuals calculated both linearly and quadratically. The plots use their own time span.

uals with their 136 times of maximum light, in which we can see that the parabolic behavior interpretation was logically inferred (see Figure 2). It is important to mention that they report a change in rate of 7.1457×10^{-13}day/cycle.

We have extended the time basis with the new values of T_{max} determined in January and February, 2020 for a total of 1606 times of maximum light and a time basis of twenty three years elapsed since the Zhou et al. (1999) study, increasing the accuracy of the ephemerides elements, T_0 and P given by Zhou et al. (1999). We followed the prescription provided by Zong et al. (2019) who calculated the number of elapsed cycles adjusting a linear fit to the times of maximum number of cycles presented in Figure 3 in the XY plane with X, the number of cycles and Y the times of maximum light. The newly determined values for T_0 and P are given in equation 3:

$$HJD = 2443125.7938(2) + 0.0390979132(9) \times E. \tag{3}$$

With these new determined values we calculated the new O−C values represented in Figure 4, analogous to those presented by Zong et al. (2019) in their Figure 5.

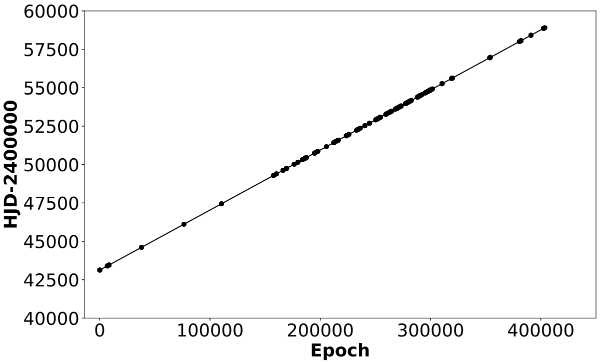

Fig. 3. Graphic representation of the linear equation 3 originally calculated by Zhou et al. (1999) that includes the new ephemerides elements with an extended time basis of 23 years. The new determined values are $T_0 = 2443125.7938(2)$ d and $P = 0.0390979132(9)$ d/cycle.

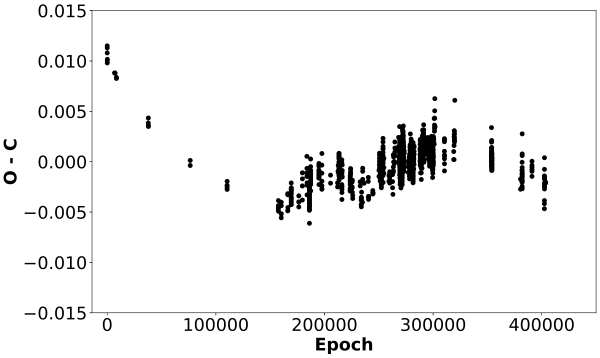

Fig. 4. O−C residuals of the 1606 data points with the new ephemerides equation deduced by a linear fit. This resembles equation 3 in Zong et al. (2019).

However, they arbitrarily discarded all O−C data points with E less than 150000 cycles because they showed an unexplained behaviour. Given the analogous results we obtained from Zong et al. (2019), we could have proceeded in the same fashion but, we preferred to consider all the O−C elements in the ephemerides procedure in Zhou et al. (1999).

Zong et al. (2019) carried out an exhaustive analysis of the O−C residuals. Their origin was based on the work of Fu et al. (2008) who suggested that the main period of BL Cam might have undergone an abrupt change. This change was studied by Fauvaud et al. (2010) and by Conidis & Delaney (2013) who suggested that the change of the main period might be caused by a third body explained by a cubic curve adjustement shown in their Figure 5, which is presented here in Figure 4.

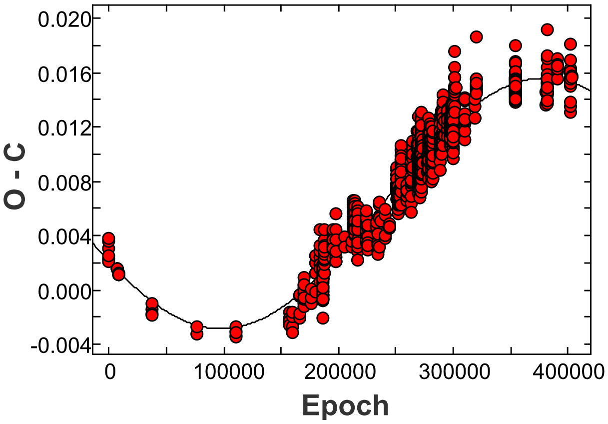

Fig. 5. Behavior of the O−C residuals for the whole sample of the 1606 data points with the ephemerides elements listed in equation 2 of Zhou et al. (1999) as a function of cycles. The color figure can be viewed online.

However, the model proposed by Zhou et al. (1999) shows that the main frequency derived in the O−C analysis is quite consistent with the fundamental frequency decomposed by Fourier transforms which explains all the times of maxima. Following this approach, we utilized Zhou et al.'s (1999) equation and considered the number of cycles and the O−C for the extended time basis all the elements, including those below an E of 150000 which Zong et al. (2019) had discarded. The smooth variation presented in Figure 5 was obtained if a sinusoid was assumed. If we only take the time span employed in Zhou et al (1999) into account, the logical deduction would be a parabolic behavior. This parabolic assumption was also assumed by Fauvaud et al. (2006) although their time basis was not long enough to reach a different conclusion, but when the elapsed time was extended, a sinusoidal variation can be seen.

Due to the fact that a sinusoid can be considered, in Figure 5 we calculated the variation parameters through a fit obtained with Period04, a canonical procedure utilized for short period variable stars (Lenz & Breger, 2005). Period04 is a computer program especially dedicated to the statistical analysis of large astronomical time series containing gaps. The program offers tools to extract the individual frequencies from the multiperiodic content of time series and provides a flexible interface to perform

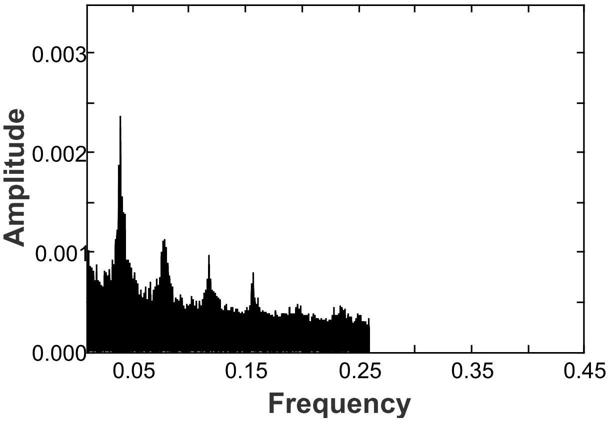

Fig. 6. Periodogram of the O−C residuals. The main peak is at 1.78×10^{-6} cycle/day.

TABLE 4

COEFFICIENTS DERIVED WITH PERIOD04

Parameter	Values	Uncertainty
Ω_1	178×10^{-8}	2×10^{-8}
B_1	923×10^{-5}	8×10^{-5}
α_1	576×10^{-3}	2×10^{-3}
Z	64×10^{-4}	1×10^{-4}

multiple-frequency fits. The Fourier analysis in Period04 is based on a discrete Fourier transform algorithm.

This fit to a sinusoid is shown in the Figure 5 by the continuous line, which explains those points discarded by Zong et al. (2019) and the newly observed points in 2020. The output of Period04 is presented by the following equation 4, with the numerical values presented in Table 4. It is shown schematically in Figure 6.

$$O - C = Z + \sum_{i=1}^{n} B_i \sin(2\pi(\Omega_i E + \alpha_i)). \quad (4)$$

With an extended time span it becomes evident that the conclusion reached previously was partial because it was obtained based on the limited time span at that time. Now, we postulate a sinusoidal behavior that could be explained by the presence of another unseen companion star and the light travel time effect (LTTE). Due to the above, we adjusted the equation:

$$(O - C) = a_0 + \sum_{i=1}^{2} \left[a_i \cos(iwE) + b_i \sin(iwE)\right], \quad (5)$$

to determine the optimized parameters for the equation to get the best fit to the data, we utilized the algorithm of Levenberg-Marquardt. As initial parameters we considered a_0 equal to $2Z$ and $w = 2\pi\Omega_1$. To the remaining coefficients we assigned zero values. The obtained optimized parameters and their standard deviations are presented in Table 5 for a frequency of $w = (122 \pm 2) \times 10^{-7}$ (1/d). This new analysis provides an orbital period of the star with a result of $P_{orb} = 55.2$ years. This postulation will be tested with continuous monitoring of this star over the next 12 years when the 55.2 years period that we predict will be completed. The results are shown in Figure 7.

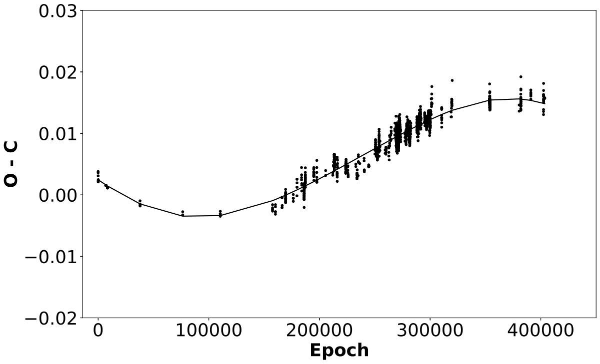

Fig. 7. New fit obtained utilizing Fourier series considering equation 5 and the Fourier coefficients listed in Table 5.

TABLE 5

FOURIER COEFFICIENTS

	[Values]$\times 10^{-4}$	[Uncertainty]$\times 10^{-4}$
a_0	59	1
a_1	-29	3
a_2	-5	1
b_1	-91	2
b_2	-5	2

Subtracting the calculated fit, we obtained the results presented in Figure 8. No clear evidence of another frequency exists as Fauvaud et al. (2010) and Conidis et al. (2013) proposed, but from our analysis it cannot be discarded due to the lack of observations in the cycle intervals between [0, 142000] and [330000, 382000] which makes the analysis difficult. Calculating the standard deviation of the residuals we get $\sigma = 0.0012$, less than that obtained by Zhou et al. (1999), Conidis et al. (2013) and Zong et al. (2019). This supports the sinusoidal behavior shown in the O−C diagram of Figure 7.

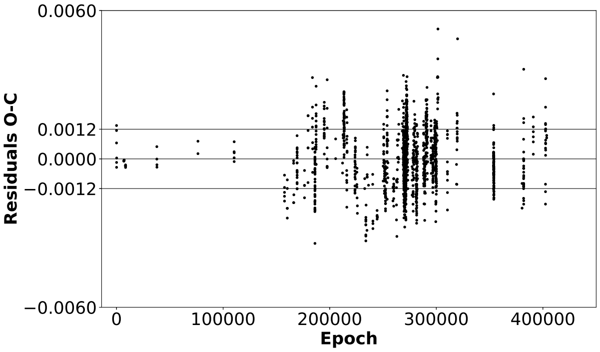

Fig. 8. Residuals after the Fourier series fit shown in Figure 7. The central horizontal line represents the mean value and the other extreme lines the standard deviation of the residuals.

TABLE 6

PARAMETERS OF THE COMPANION STAR OF BL CAM

Orbital Parameter	Value
$e^{'}$	0.15
$w^{'}$	281.76
$A^{'}\sin(i^{'})$	1.65
P_{orb}	55.2

3.2. *Determination of Orbital Parameters and Mass of the Companion Star*

Carrying out an analysis of a binary system such as that developed by Zong et al. (2019), it is possible to determine the parameters of the companion star utilizing the formulae 6, 7 and 8 proposed by Borkovits et al. (1996), which are function of the Fourier coefficients.

$$e^{'} = 2\sqrt{\frac{a_2^2 + b_2^2}{a_1^2 + b_1^2}}, \tag{6}$$

$$w^{'} = \arctan\left(\frac{(b_1^2 - a_1^2)b_2 + 2a_1a_2b_1}{(a_1^2 - b_1^2)a_2 + 2a_1b_1b_2}\right), \tag{7}$$

$$A_i^{'}\sin(i^{'}) = c\sqrt{a_1^2 + b_1^2}, \tag{8}$$

where a_0 is shown in equation 5; $a_{1,2}$; $b_{1,2}$ are the Fourier coefficients. These are listed in Table 5. $A^{'}$ denotes the semi-major axis. $i^{'}$,$e^{'}$ y $w^{'}$ are the elements of the orbit of the companion, c is the speed of light in astronomical units per day.

TABLE 7

MASS OF THE COMPANION AS A FUNCTION OF THE ANGLE

Angle	Semi-major axis	Mass
20	4.8	0.42
25	3.9	0.32
30	3.3	0.27
40	2.6	0.20
50	2.2	0.16
60	1.9	0.14
70	1.8	0.13
80	1.7	0.12

Then, we followed Borkovits & Heged*ü*s (1996) for the determination of the mass of the companion star.

Considering a three body system, Borkovits & Heged*ü*s (1996) present equation 11 in their paper as a solution which we used, adapting it to a binary system in which BL Cam orbits around another unseen star and the encountered variations in the O−C are provoked by the LTTE. This follows a prescription first employed by Fu et al. (2008). Combining them, equation 9 provides the mass function in terms of the orbital parameters.

Substituting the above-mentioned values listed in Table 6 calculated in this work in the mass function equation given in equation 9, it is possible to calculate the mass of the companion. Considering the mass of BL Cam as $m_1 = 0.99$ from McNamara (1997), we calculated the mass m_2 for different angles $i^{'}$, shown in Table 7, determining the roots of the polynomial given in the equations:

$$f(m) = \frac{(A^{'}\sin(i^{'}))^3}{P_{orb}^2} = \frac{(m_2\sin(i^{'}))^3}{(m_1 + m_2)^2} = 0.00148, \tag{9}$$

$$\sin(i^{'})^3 m_2^3 - f_{(m)}m_2^2 - 2f_{(m)}m_1m_2 - f_{(m)}m_1 = 0. \tag{10}$$

Being a cubic equation, it has three solutions. In each case we considered as a solution the real root. The other two are imaginary roots without physical interpretation. The mass of the companion star as a function of the inclination angle is shown in Table 7.

The behavior of mass as a function of angle is shown in Figure 9. Given the obtained values we can say that we are dealing with a M-type star.

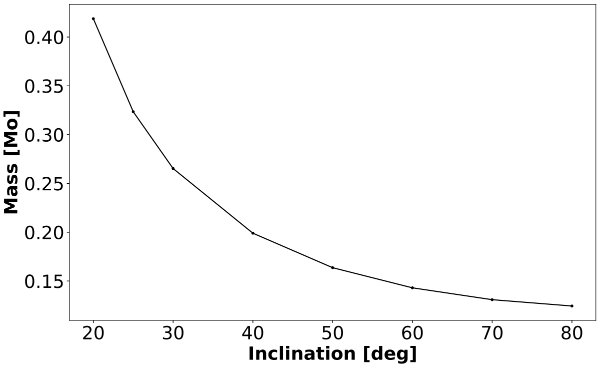

Fig. 9. Mass of the companion as a function of the angle.

3.3. *Period Determination Conclusions*

Despite having been determined to be a variable star many years ago, the variability of the SX Phe star BL Cam has been described with several interpretations as more information has been gathered. Considering the interpretation of this century only, we highlight the following studies.

Kim et al. (2003) found that the parabolic period variation had recently reversed. They also determined five frequencies for BL Cam using Fourier analysis. They stated that in order to confirm the periodic variation of the O−C values, BL Cam should be observed for at least 10 more years.

Rodriguez et al. (2007) reported that their results confirmed the existence of multi-periodicity in this star. In addition to the main frequency f_0=25.5769 c/d and its harmonics $2f_0$ and $3f_0$, with stable amplitude, a secondary frequency f_1 exists in the region 31-32 c/d with variable amplitude.

A more recent article, that of Fauvaud et al. (2010), states that the short-term O−C variation, if interpreted as a light travel-time effect, is indicative of a massive stellar component (0.46 to 1 $M_\odot$) with a short period orbit (144.2 d), within a distance of 0.7 AU from the primary and encourage more observations to confirm the long-term O−C variations. If they were also caused by a light travel-time effect, they could be interpreted in terms of a third component, in this case probably a brown dwarf star ($\geq$ 0.03$M_\odot$), orbiting in 3400 d at a distance of 4.5 AU from the primary.

Conidis and Delaney (2013) found a more accurate period of 0.039097912(1) days, and presented an updated linear ephemeris. This newly presented linear ephemeris was used to calculate revised O−C values, which were fitted with a parabolic curve to measure the rate of change of the pulsation period. Although the parabolic fit has a physical interpretation, it is noted that a cubic fit more appropriately describes the behavior of the O−C diagram, but they concluded that this assumes the O−C diagram is best represented by a quadratic fit. This has been shown to be a poor assumption, since a cubic polynomial is a better representation of the O−C diagram. This, according to them, is problematic since the physical meaning of the third order term cannot be explained physically.

The most recent paper, that of Zong et al. (2019) did not find evidence of a triple system as stated by Fu et al. (2008). Fauvaud et al. (2010) performed a triple system analysis of the O−C diagram. However, the determination of the second companion's parameters was not successful. The residuals of fitting the O−C curve implied that BL Cam might be a binary system in an eccentric orbit with a period of 14.01 (9) yr. The companion might be a brown dwarf.

In this study, with an extended time basis of 15779 days or 403578.6 cycles, we performed an O−C analysis and found that the residuals do not conform to the parabolic variation proposed by other authors but rather present a sinusoidal variation with a period of 60 years.

In our analysis we do not need to invoke multi-periodicity as was previously proposed, nor a parabolic behavior. Instead, with only one stable period, using Period04, we adjusted the 1606 times of maximum light shown in Figure 5. Our final fit is obtained using equation 5 and is presented in Figure 7; its residuals are shown in Figure 8.

Considering the obtained results of the present work, and taking into account the residuals in the σ interval presented in Figure 8, this paper has shed light on the nature of BL Cam. Before we consider that it might be a triple system, as Fauvaud1 (2010) proposed, continuous monitoring of the star is mandatory.

4. PHYSICAL PARAMETERS

In this section, we consider $uvby-\beta$ photometry to determine some physical parameters. With this photometric system it is possible to determine reddening and unreddened values via the procdure proposed by Nissen (1988). The accuracy of our photometry is evaluated by three methods. From these we determined the metallicity [Fe/H] and by comparing the unreddened indexes c_0 and $(b-y)_0$ with the Castelli & Kurucz (2006) models effective temperature and surface gravity were estimated.

TABLE 8

MEAN PHOTOMETRIC VALUES AND STANDARD DEVIATIONS OF THE STANDARD STARS OF THE 2020 SEASON

ID	V	$(b-y)$	m_1	c_1	β	σV	$\sigma(b-y)$	σm_1	σc_1	$\sigma\beta$	N
HD114710	4.233	0.365	0.195	0.340	2.600	0.004	0.003	0.002	0.006	0.014	5
HD111812	4.944	0.429	0.204	0.406	2.589	0.044	0.003	0.004	0.005	0.016	5
HD28355	5.000	0.113	0.240	0.890	2.847	0.010	0.003	0.003	0.007	0.016	5
HD69897	5.117	0.314	0.148	0.383	2.630	0.010	0.002	0.002	0.005	0.013	8
HD115383	5.176	0.369	0.190	0.390	2.615	0.005	0.003	0.003	0.003	0.015	5
HD154029	5.255	0.002	0.174	1.098	2.871	0.021	0.002	0.004	0.008	0.012	5
HD157214	5.374	0.395	0.178	0.318	2.571	0.008	0.003	0.004	0.006	0.015	5
HD76398	5.427	0.085	0.208	0.971	2.852	0.007	0.003	0.003	0.006	0.010	8
HD178233	5.497	0.174	0.193	0.737	2.755	0.015	0.003	0.003	0.006	0.013	5
HD23324	5.638	-0.008	0.089	0.639	2.751	0.008	0.002	0.001	0.002	0.013	4
HD26462	5.695	0.234	0.170	0.590	2.723	0.014	0.003	0.003	0.009	0.016	5
HD24357	5.951	0.227	0.167	0.605	2.724	0.008	0.002	0.001	0.003	0.018	4
HD32147	6.218	0.614	0.639	0.248	2.552	0.022	0.001	0.004	0.008	0.018	5
HD122563	6.236	0.633	0.103	0.474	2.526	0.063	0.004	0.004	0.007	0.013	5
HD137778	7.573	0.538	0.453	0.292	2.567	0.017	0.004	0.006	0.011	0.012	5
HD125455	7.579	0.502	0.366	0.299	2.555	0.013	0.003	0.004	0.008	0.014	5
HD36003	7.636	0.641	0.663	0.200	2.521	0.021	0.002	0.002	0.011	0.016	5
HD154363	7.698	0.666	0.635	0.167	2.488	0.008	0.002	0.004	0.008	0.014	5
HD21197	7.846	0.667	0.731	0.152	2.537	0.011	0.002	0.006	0.011	0.012	4
HD117243	8.352	0.408	0.205	0.405	2.610	0.016	0.004	0.004	0.006	0.010	5
Mean						0.016	0.003	0.003	0.007	0.014	103
Stnd. Dev.						0.014	0.001	0.001	0.003	0.002	

The $uvby-\beta$ photometric system has the advantage that reddening and unreddened colors can be determined from the photometry and the proper calibrations. One of the pioneer works in this matter was that of Crawford and collaborators. Later, in 1988, Nissen (1988) extended the sample of clusters to thirteen and developed empirical calibrations which determined the intrinsic color index $(b-y)_0$ in terms of the other color indexes and β utilizing as reference the Hyades. Nissen's (1988) procedure is applicable for A and F type stars. For F type stars ($2.59 \leq \beta \leq 2.72$) the intrinsic color index $(b-y)_0$ is calculated by the expression:

$$(b-y)_0 = K + 1.11\Delta\beta + 2.7\Delta\beta - 0.05\delta c_0 - (0.1+3.6\Delta\beta)\delta m_0. \quad (11)$$

4.1. *Data Acquisition and Reduction at SPM*

At the SPM Observatory the observational, as well as the reduction procedures, have been employed since 1986 and have been described many times. A recent detailed description of the methodology can be found in Peña and Martinez (2014).

The star BL Cam was observed in $uvby-\beta$ photometry in February, 2020. The season covered five nights during which BL Cam was observed on two. Over all the nights of observation the following procedure was used: each measurement consisted of five ten-second integrations of the star and three ten-second integrations of the sky simultaneously for the *uvby* filters and almost simultaneous for the narrow and wide filters that define Hβ.

The accuracy of our observation was evaluated by three numerical procedures: (i) the accuracy of each point; (ii) a comparison of the observed standard stars with those values in the literature, and (iii) a comparison of the observed standard stars obtained in each night throughout the whole season.

In the first case, the accuracy is a direct result of the star counts. Although BL Cam is a faint star for our telescope-spectrophotometer system we obtained in the five ten-seconds integrations, enough counts to calculate the errors for the u, b, v, and y filters that define the $uvby-\beta$ photoelectric photometry, equal to (18491, 53040, 68053, 24413), respectively, which translated into uncertainties of (0.0074, 0.0043, 0.0038, 0.0064) magnitudes.

For the second criterion we reduced each night separately calculating the transformation coefficients and the difference in magnitude between the obtained values and the values reported in the literature for each night. To calculate the final photo-

TABLE 9

MEAN VALUES AND STANDARD DEVIATIONS

Season	B	D	F	J	H	I	L
2020 Feb	0.0743	0.9814	1.0758	0.0431	1.051	0.1893	-1.3529
$<\sigma>$	0.0303	0.0019	0.0037	0.0023	0.0054	0.0106	0.0139

Notes: Mean values and standard deviations $<\sigma>$ of the transformation coefficients obtained for the seasons.

metric values we averaged the nightly coefficients and the differences with the literature. With the obtained photometric values we reduced the data as described in Peña & Martínez (2014). What must be noted here are the transformation coefficients for the observed season (Table 9). This led to the obtainment of the final photometric values. The season errors were evaluated using the observed standard stars with those employed from the literature. These uncertainties were calculated through the differences in magnitude and colors for (V, $(b-y)$, m_1, c_1 and Hβ) which are (0.035, 0.008, 0.011, 0.011, 0.012) for the 2020 season.

For the final numerical evaluation of the accuracy we considered all the standard stars on each night in the whole season, for a total of 118 points in *uvby* and 106 points in Hβ, of the standard stars. For each star we calculated its mean value as well as the standard deviation. This provides a numerical evaluation of our uncertainties considering the whole season, as well as the goodness of the season. The obtained results are presented in Table 8 with the ID of the star in Column 1. Columns two to six present the magnitude and color indexes (V, $(b-y)$, m_1, c_1 and Hβ) and Columns seven to eleven, their corresponding standard deviations; the last column lists N, the number of data points of each star in the season. The mean values of the season with the standard deviations are shown in the last two lines. With the exception of the star HD122563 the standard deviation of all the standard stars is on the order of thousandths in the V magnitude. For this reason, HD122563 may be a new variable star since it is similar to HD 115520, which was discovered to be a new δ Scuti variable by Peña et al. (2007).

4.2. *Metallicity (*[Fe/H]*) Determination Through* $uvby-\beta$ *Observations*

Nissen (1988) also proposed equations to determine metal abundance (for stars of F spectral type). The metal abundance [Fe/H] is given by Nissen (1988) through the equation:

$$[\mathrm{Fe/H}] = -(10.5 + 50(\beta - 2.626))\delta m_0 + 0.12\ . \quad (12)$$

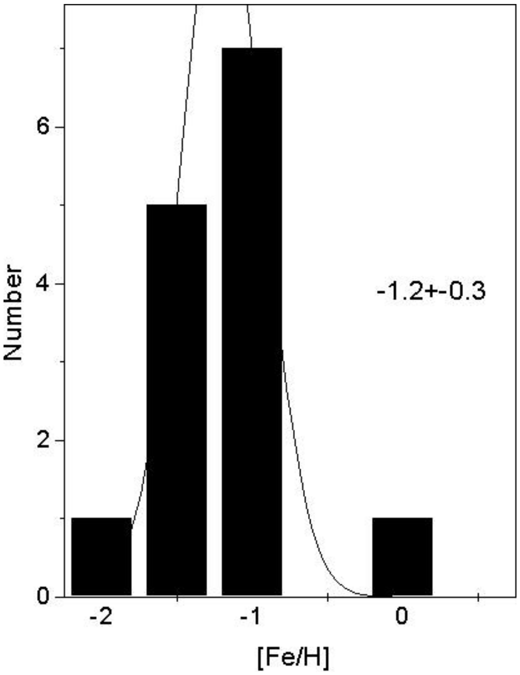

Fig. 10. Distribution of metallicity when the star goes through an F type stage.

We applied Nissen's (1988) prescription (described in detail in Peña & Martínez 2014) to the $uvby-\beta$ photometric values presented in Table 10 arranged by decreasing β, and we determined the reddening, the unreddened indexes $(b-y)_0$, m_0, c_0, as well as the metallicity when the star passes through an F type stage. The metallicity values distribution is presented in Figure 10 which shows the histogram of all the values. As can be seen the mean value is -1.2 ± 0.3. The continuous line is a Gaussian fit.

A comparison between the unreddened indexes c_0 and $(b-y)_0$ was obtained for the star with the Castelli & Kurucz (2006) models which are based on ATLAS9 model atmospheres. This allowed us to determine the effective temperature T_e and the surface gravity $\log g$ (Figure 11). The effective temperature varies between 7250 K and 8000 K, whereas the surface gravity is around $\log g = 3.5$. Table 10 lists these values. Column 1 shows the HJD, Column 2 to 5 the unreddened indexes and β.

TABLE 10

TIME, MAGNITUDE, COLOR INDEXES AND β OF BL CAM

HJD(-2458000)	V	$(b-y)$	m_1	c_1	β
904.6674	13.121	0.483	-0.075	0.973	2.824
904.6690	13.151	0.425	-0.005	0.801	2.784
904.6719	13.177	0.409	0.013	0.816	2.679
904.6735	13.196	0.433	-0.021	0.858	2.665
904.6767	13.230	0.404	-0.004	0.878	2.702
904.6785	13.216	0.394	0.016	0.798	2.785
904.6814	13.187	0.380	0.040	0.829	2.643
904.6828	13.153	0.375	0.038	0.795	2.863
904.6857	13.041	0.409	0.008	0.845	2.794
904.6872	13.004	0.374	0.023	0.912	2.838
904.6898	12.949	0.352	0.047	0.996	2.830
904.6914	12.947	0.326	0.077	0.957	2.643
904.6939	12.932	0.342	0.047	0.993	2.713
904.6956	12.978	0.306	0.103	0.933	2.834
904.6982	12.982	0.390	0.016	0.909	2.804
904.7001	13.269	0.331	0.004	0.913	2.888
904.7024	13.100	0.375	0.017	0.915	2.774
904.7039	13.121	0.361	0.087	0.897	2.809
904.7069	13.142	0.417	-0.022	0.904	2.788
904.7085	13.208	0.362	0.046	0.886	2.763
904.7130	13.203	0.440	-0.059	0.860	2.804
904.7145	13.195	0.410	0.057	0.745	2.781
904.7171	13.172	0.444	-0.023	0.775	2.934
904.7187	13.171	0.420	0.019	0.786	2.915
904.7202	13.179	0.374	0.058	0.835	2.782
904.7217	13.156	0.436	-0.060	0.828	2.881
904.7241	13.123	0.342	0.075	0.849	2.719
904.7257	13.046	0.363	0.054	0.844	2.901
904.7281	12.966	0.344	0.079	0.809	2.893
904.7295	12.974	0.312	0.080	0.887	2.824
904.7336	12.953	0.336	0.072	0.976	
904.7354	12.975	0.369	-0.022	1.013	2.805
904.7370	12.983	0.402	-0.026	0.976	2.716
904.7384	13.024	0.347	0.095	0.848	2.746
904.7408	13.060	0.373	0.065	0.857	2.778
904.7423	13.113	0.360	0.052	0.871	2.766
904.7439	13.123	0.409	-0.016	0.911	2.759
904.7453	13.141	0.393	0.012	0.888	2.635
904.7478	13.182	0.398	0.006	0.916	2.681
904.7493	13.159	0.438	0.011	0.820	2.623
906.6732	13.278	0.382	0.073	0.854	2.842
906.6754	13.247	0.357	0.125	0.856	2.835
906.6771	13.143	0.386	0.025	0.800	2.717
906.6908	12.968	0.314	0.087	0.894	2.819
906.6922	12.994	0.340	0.054	0.908	2.778
906.6937	13.059	0.334	0.089	1.015	2.817
906.7193	13.067	0.333	0.088	0.871	2.903
906.7208	12.999	0.320	0.076	0.953	2.777
906.7223	13.011	0.294	0.071	0.959	2.907
906.7315	12.985	0.356	0.003	1.037	2.865
906.7331	13.003	0.369	0.019	0.947	2.827

Table 10. Continued

HJD(-2458000)	V	$(b-y)$	m_1	c_1	β
906.7345	13.076	0.302	0.168	0.826	2.654
906.7438	13.176	0.365	0.078	0.830	2.782
906.7452	13.168	0.394	0.027	0.859	2.834
906.7467	13.208	0.380	0.050	0.832	2.771
906.7501	13.211	0.385	0.022	0.854	2.817
906.7516	13.195	0.388	0.030	0.824	2.834
906.7530	13.185	0.399	0.042	0.795	2.697
904.7478	13.182	0.398	0.006	0.916	2.681
904.6719	13.177	0.409	0.013	0.816	2.679
904.6735	13.196	0.433	-.021	0.858	2.665
906.7345	13.076	0.302	0.168	0.826	2.654
904.6814	13.187	0.380	0.040	0.829	2.643
904.6914	12.947	0.326	0.077	0.957	2.643
904.7453	13.141	0.393	0.012	0.888	2.635
904.7493	13.159	0.438	0.011	0.820	2.623
904.7336	12.953	0.336	0.072	0.976	

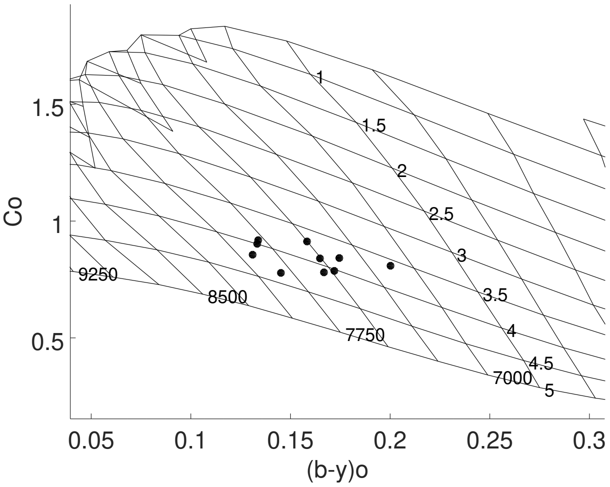

Fig. 11. Unreddened color indexes on the Castelli & Kurucz (2006) grids.

Subsequent columns present metallicity, effective temperature from the theoretical relation reported by Rodriguez (1989) based on a relation from Petersen & Jorgensen (1972, hereinafter P&J72) $Te = 6850 + 1250 \times (\beta - 2.684)/0.144$ for each value and averaged, and suface gravity. The averaged temperature along the phase interval of 0.3 to 0.8 is 7682 ± 503 K.

4.3. *Physical Parameters Conclusions*

Most of the papers devoted to BL Cam have emphasised its pulsational nature and few have tried to determine its physical parameters. In this paper, we were able to unredden the color indexes and determine the reddening and the metallicity

TABLE 11

COLOR INDEXES & PHYSICAL PARAMETERS OF BL CAM AS A FUNCTION OF PHASE

HJD - 2458900.0	$(b-y)_0$	m_0	c_0	β	[Fe/H]	$Te[K]$	$\log g$	Phase
6.7315	0.067	0.090	0.979	2.865		8421	3.9	0.54
4.6828	0.093	0.123	0.739	2.863		8403	4.7	0.14
6.6732	0.104	0.156	0.798	2.842		8221	4.3	0.05
4.6872	0.102	0.105	0.858	2.838		8186	4.1	0.26
6.6754	0.110	0.199	0.807	2.835		8160	4.3	0.11
4.6956	0.103	0.164	0.892	2.834		8152	4.0	0.47
6.7452	0.110	0.112	0.802	2.834		8152	4.3	0.89
6.7516	0.114	0.112	0.769	2.834		8152	4.4	0.06
4.6898	0.100	0.123	0.946	2.830		8117	3.8	0.32
6.7331	0.107	0.097	0.895	2.827		8091	3.9	0.58
4.6674	0.107	0.038	0.898	2.824		8065	3.8	0.75
4.7295	0.116	0.139	0.848	2.824		8065	4.1	0.34
6.6908	0.119	0.145	0.855	2.819		8021	4.1	0.50
6.6937	0.109	0.157	0.970	2.817		8004	3.6	0.58
6.7501	0.125	0.100	0.802	2.817		8004	4.2	0.02
4.7039	0.127	0.157	0.850	2.809		7935	4.0	0.68
4.7354	0.119	0.053	0.963	2.805		7900	3.6	0.49
4.6982	0.130	0.094	0.857	2.804		7891	3.9	0.54
4.7130	0.135	0.033	0.799	2.804		7891	4.1	0.91
4.6857	0.144	0.087	0.792	2.794		7804	4.1	0.22
4.7069	0.143	0.060	0.849	2.788		7752	3.8	0.76
4.6785	0.156	0.087	0.750	2.785		7726	4.2	0.03
4.6690	0.157	0.075	0.747	2.784		7718	4.1	0.79
4.7202	0.155	0.124	0.791	2.782		7700	4.0	0.10
6.7438	0.155	0.141	0.788	2.782		7700	4.0	0.86
4.7145	0.165	0.131	0.696	2.781		7692	4.3	0.95
4.7408	0.156	0.130	0.814	2.778		7665	3.9	0.63
6.6922	0.151	0.111	0.870	2.778		7665	3.7	0.54
6.7208	0.147	0.128	0.918	2.777		7657	3.6	0.27
4.7024	0.153	0.084	0.871	2.774		7631	3.7	0.64
6.7467	0.164	0.115	0.789	2.771		7605	3.9	0.93
4.7423	0.164	0.111	0.832	2.766		7561	3.8	0.67
4.7085	0.165	0.105	0.847	2.763		7535	3.7	0.80
4.7439	0.166	0.057	0.862	2.759		7501	3.6	0.70
4.7384	0.182	0.144	0.815	2.746		7388	3.7	0.56
4.7241	0.200	0.118	0.821	2.719	-0.775	7153	3.4	0.20
6.6771	0.200	0.081	0.763	2.717	-1.314	7136	3.6	0.15
4.7370	0.187	0.039	0.933	2.716	-1.939	7127	2.9	0.53
4.6939	0.194	0.091	0.963	2.713	-1.121	7101	2.8	0.43
4.6767	0.203	0.056	0.838	2.702	-1.539	7006	3.1	0.99
6.7530	0.217	0.096	0.759	2.697	-0.937	6962	3.4	0.09
4.7478	0.217	0.060	0.880	2.681	-1.334	6823	2.8	0.81
4.6719	0.225	0.068	0.779	2.679	-1.221	6806	3.1	0.86
4.6735	0.226	0.041	0.817	2.665	-1.518	6685	2.8	0.90
4.6814	0.257	0.077	0.804	2.643	-1.068	6494	2.7	0.11
4.6914	0.259	0.097	0.944	2.643	-0.837	6494	2.3	0.36
4.7453	0.252	0.054	0.860	2.635	-1.322	6424	2.5	0.74
4.7493	0.268	0.062	0.786	2.623	-1.244	6320	2.6	0.84
Average					-1.244	7598		
σ					0.315	555		

with $uvby - \beta$ photoelectric photometry and the well-calibrated equations of Nissen (1988). Locating these indexes on the grids of Castelli & Kurucz (2006) we determined the effective temperature and surface gravity of the star along its cycle of pulsation.

5. CONCLUSIONS

In the present study we have demonstrated that BL Cam is pulsating with one stable varying period whose O−C residuals show a sinusoidal pattern compatible with a light-travel time effect.

We have shown that the evolution of the ephemerides of the different authors were natural and correct given the shortness of the available data at their times. With a longer time basis we have shown that the long term variation is due to a binary system.

For the determination of the physical parameters some authors mentioned the need to acquire data in $uvby - \beta$, a need that we were able to satisfy. New observations in $uvby - \beta$ and CCD photometry were carried out at the San Pedro Mártir and Tonantzintla observatories, respectively, on the SX Phe star BL Cam.

The appropriate model of Castelli & Kurucz (2006) provided the physical characteristics of the star: effective temperature (T_e) and surface gravity ($\log g$), once the metallicity had been determined. The effective temperature was also calculated through the theoretical relation (P&J72). The numerical values obtained by both methods gave similar results within the error bars, and gave a good idea of the behavior of the star.

We would like to thank the staff of the OAN at SPM and Tonantzintla and E. D. Orozco for their assistance in securing the observations. This work was partially supported by PAPIIT IN106615, IG100620 and PAPIME PE113016. Proofreading was done by J. Miller. F. Ruiz assisted us in the computing and B. Juárez for the bibliographic help. All the students thank the IA for allotting the telescope time. Special thanks to A. Rentería and F. Martínez for discussions. This paper has been improved by the comments and suggestion made by an anonymous referee. We have made use of the Simbad databases operated at CDS, Strasbourg, France and NASA ADS Astronomy Query Form.

REFERENCES

Antoci, V., Cunha, M. S., Bowman, D. M., et al. 2019, MNRAS, 490, 4040

Berg, R. A. & Duther, J. G. 1977, ApJ, 215, 25

Blake, R. M., Khosravani, H., & Delaney, P. A. 2000, JRASC, 94, 124

Borkovits, T. & Hegedus, T. 1996, A&AS, 120, 63

Castelli, F. & Kurucz, R. L. 2006, A&A, 454, 333

Collins, K. & Kielkopf, J. 2013, AstroImageJ: ImageJ for Astronomy, Astrophysics Source Code Library, record ascl:1309.001

Conidis, G. J. & Delaney, P. A. 2013, PASP, 125, 639

Fauvaud, S., Rodríguez, E., Zhou, A. Y. et al. 2006, A&A, 451, 999

Fauvaud, S., Sareyan, J.-P., Ribas, I., et al. 2010, A&A, 515, 39

Fu, J.-N., Zhang, Ch., Marak, K., et al. 2008, ChJAA, 8, 237

Hintz, E. G., Joner, M. D., McNamara, D. H., Nelson, K., & Moody W. 1997, PASP, 109, 15

Kim, C., Jeon, Y.-B., & Kim, S.-L. 2003, PASP, 115, 755

Lenz, P. & Breger, M. 2005, CoAst, 146, 53

McNamara, D. 1997, PASP, 109, 1221

McNamara, D. H. & Feltz, K. A., Jr. 1978, PASP, 90, 275

Nissen, P. 1988, A&A, 199, 146

Peña, J. H., Sareyan, P., Cervantes-Sodi, B., et al. 2007, RMxAA, 43, 217

Peña, J. H. & Martínez, A. 2014, RMxAA, 50, 119

Peña, J. H., Huepa, H., Piña, D. S., et al. 2021, RMxAA, 57, 241

Rodríguez, E., 1989, Tesis Doctoral, Universidad de Granada, Spain

Rodríguez, E., Fauvaud, S., Farrell, J. A., et al. 2007, A&A, 471, 255

Wolf, M., Crlikova, M., Basta, M., et al. 2002, IBVS, 5317, 1

Zong, P., Esamdin, A., Fu, J. N., et al. 2019, PASP, 131, 4202

Zhou, A.-Y, Rodríguez, E., Jiang, S.-Y., Rolland, A., & Costa, V. 1999, MNRAS, 308, 631

J. Guillen, J. H. Peña, and D. S. Piña: Facultad de Ciencias, Universidad Nacional Autónoma de México, México.

H. Huepa and J. H. Peña: Observatorio Astronómico Nacional, Tonantzintla Puebla, UNAM, México.

J. D. Paredes: Facultad de Ciencias, Universidad Central de Venezuela, Venezuela.

J. D. Paredes, J. H. Peña, and D. S. Piña: Instituto de Astronomía, Universidad Nacional Autónoma de México, Apdo. Postal 70-264, Cd. de México, México (jhpena@astro.unam.mx).

Revista Mexicana de Astronomía y Astrofísica, **57**, 433–444 (2021)

https://doi.org/10.22201/ia.01851101p.2021.57.02.15

INTERPRETATION OF OPTICAL AND IR LIGHT CURVES FOR TRANSITIONAL DISK CANDIDATES IN NGC 2264 USING THE EXTINCTED STELLAR RADIATION AND THE EMISSION OF OPTICALLY THIN DUST INSIDE THE HOLE

E. Nagel[1], F. Gutiérrez-Canales[1], S. Morales-Gutiérrez[1], and A. P. Sousa[2]

Received May 10 2021; accepted August 6 2021

ABSTRACT

In the stellar forming region NGC 2264 there are objects catalogued as hosting a transitional disk according to spectrum modeling. Four members of this set have optical and infrared light curves coming from the *CoRoT* and *Spitzer* telescopes. In this work, we try to simultaneously explain the light curves using the extinction of the stellar radiation and the emission of the dust inside the hole of a transitional disk. For the object Mon-296, we were successful. However, for Mon-314, and Mon-433 our evidence suggests that they host a pre-transitional disk. For Mon-1308 a new spectrum fitting using the 3D radiative transfer code Hyperion allows us to conclude that this object hosts a full disk instead of a transitional disk. This is in accord to previous work on Mon-1308 and with the fact that we cannot find a fit for the light curves using only the contribution of the dust inside the hole of a transitional disk.

RESUMEN

En la región de formación estelar NGC 2264 se encuentran objetos catalogados como anfitriones de discos transicionales según los modelos del espectro. Para cuatro de sus miembros se tienen curvas de luz en el óptico y en el infrarrojo provenientes de los telescopios CoRot y Spitzer. Tratamos de explicar ambas curvas de luz simultáneamente usando la extinción de la radiación estelar y la emisión del polvo dentro del agujero de un disco transicional. Para el objeto Mon-296 fuimos exitosos pero nuestra evidencia indica un disco pre-transicional para Mon-314 y Mon-433. Un nuevo ajuste del espectro con el código 3D de transferencia radiativa Hyperion nos permite concluir que Mon-1308 tiene un disco completo en lugar de un disco transicional. Esto coincide con trabajo previo sobre Mon-138 y con el hecho de no haber encontrado un ajuste de las curvas de luz a partir del uso exclusivo de la contribución del polvo dentro del agujero de un disco transicional.

Key Words: dust, extinction — protoplanetary disks — stars: pre-main-sequence

1. INTRODUCTION

Spectral and photometric variability of young stellar objects (YSOs) is the usual outcome of multiwavelength campaigns (Stauffer et al. 2014, 2015, 2016; Cody et al. 2014; Morales-Calderón et al. 2011). For young stars in NGC 2264, Stauffer et al. (2014) extract the accretion burst dominated light curves (lcs), Stauffer et al. (2015) show the short-duration periodic flux dips in the lcs and Stauffer et al. (2016) present the stochastically varying lcs. Cody et al. (2014) extract optical and infrared (IR) lcs from the *Spitzer* and *CoRoT* telescopes for 162 classical T Tauri stars (CTTSs) where flux variations are clearly detected. They catalog them into seven distinct classes describing multiple origins of young star variability: circumstellar obscuration events, hot spots, accretion bursts and structural changes in the inner disk. Focusing at 3.6 and 4.5μm, lcs of hundreds

---

[1] Departamento de Astronomía, Universidad de Guanajuato, México.

[2] Institut de Planétologie et d'Astrophysique de Grenoble, Université Grenoble Alpes, France.

of objects in the Orion Nebula Cluster, Morales-Calderón et al. (2011) found variability that can be interpreted by processes occurring in the disk, like density structures intermittently blocking our line of sight. From this and other studies is extracted the label "dippers" for the objects showing changes in the flux that can be explained by circumstellar material crossing the line of sight directed towards the object. Bouvier et al. (1999) refer to the prototypical dipper AA Tau interpreting the lcs by asymmetries at the inner edge of the dusty disk where a magnetically induced warp is formed. This object showed a sudden dimming in 2011 that can be interpreted as the extinction produced by an overdense region orbiting around the star (Bouvier et al. 2013). Alencar et al. (2010) use observations of the *CoRoT* telescope to search for AA Tau type like objects in NGC 2264. They conclude that the dipper objects are common because the frequency is ≈ 30 to 40% in YSOs with dusty disks.

Identification of dippers (Rodriguez et al. 2017) and its interpretation locating material in the innermost regions of the disk (Bodman et al. 2017; Nagel & Bouvier 2020) is a key issue to characterize the interaction of the magnetosphere and the disk. We need a reasonable amount of material in the accretion streams to account for the dipper behavior (Bodman et al. 2017). However, the weak accretion signatures of the transitional disks (TDs) in the sample of dippers in Ansdell et al. (2016) is enough to interpret the variability of the lcs with the extinction of the material in the innermost part of the disk, which is interacting with the magnetospheric lines.

Ansdell et al. (2016) interpret the lcs of the ten objects in their sample using three different mechanisms: occulting inner disk warps, vortices caused by the Rossby wave instability (RWI) and transiting circumstellar clumps. Warps require the presence of material in the innermost region of the circumstellar environment, which is revealed by strong accretion signatures. The RWI is responsible for forming non-axisymmetric structures (Lovelace & Romanova 2014) as vortices (Meheut et al. 2010), which explain shallow, short-duration and periodic dippers in the Ansdell et al. (2016)'sample. Transiting circumstellar clumps can explain the lc of the evolved disk in EPIC 205519771 because the lc is aperiodic and the accretion signatures are weak. The few days timescale for the variations in any of these objects leads to assume that any mechanism requires material in the innermost circumstellar zones. The interpretation of lcs with low periodicity indicates that the explanation should include the effects of the highly dynamic environment close to the star. For different campaigns, in a subsample of dippers studied by McGinnis et al. (2015) there is a change between unstable and stable accretion regimes (Blinova et al. 2016), affecting the mass accretion rate towards the star, $\dot{M}$ (Kulkarni & Romanova 2008), and in this way shaping the behavior of the lcs.

The concept of pre-transitional (PTDs) and TDs has a recent presence in the discussion of YSOs. Using sub-millimeter observations, Andrews et al. (2011a) observed 12 TDs with cavities in the range from 15 to 73 AU. Espaillat et al. (2010, 2011) favor its existence modeling the SEDs including the presence of an inner disk component and emission of dust coming from the gap or hole. From this modeling, Espaillat et al. (2010) catalogued LkCa 15, UX TauA, and ROX44 as hosting PTDs, but GM Aur and DM Taos hosting TDs. The modeling requires some optically thin dust in the hole of the disk associated for GM Aur but for DM Tau the hole is empty of grains, as previously interpreted by Calvet et al. (2005). The variability of PTDs is interpreted in the sample of Espaillat et al. (2011) by changes of $\approx 20\%$ in the inner disk wall height which they associate to a warp. For the TD in GM Aur, the variability between two campaigns is explained by changes in the inner edge height of the disk at 23 AU from 2.9 to 3.2 AU. The absence of variability for DM Tau is interpreted using the absence of dust within the hole of its TD as an argument to justify the non-existence of a mechanism to explain the variability occurring at this timescale. For GM Aur, the model by Ingleby et al. (2015) requires changes in $\dot{M}$ associated to inhomogeneities in the inner disk as the process explaining ultraviolet, optical and near-infrared (near-IR) observations. Nagel et al. (2017) also model this object, but using the intermittent formation of a sublimation wall associated to accumulation of matter as the physical mechanism to explain variability in the SpeX spectrum. Both analyses point out the multiplicity of ways to explain this kind of objects but restrict the structures formed in the inner region as the relevant aspect to focus on.

In YSOs, one way to interpret optical and infrared lcs is by means of the dust in the disks surrounding them. In many cases, along with the lcs, their spectral energy distributions (SEDs) are the only sources of information for them; thus, when images are not available, the physical characteristics of these systems should be only interpreted by modeling their fluxes, or using selection criteria defined by different ranges in some phometric colors and spectral indices (Fang et al. 2009; Merín et al. 2010; Cieza et al. 2010; Muzerolle et al. 2010).

Help to choose an adequate structure around each object comes from the distinction between a full and a TD shown as a different signature in the SED but also its effect on the optical lc. During the last years, using the available new facilities, images of TDs are obtained for a few systems. These images show that the structure is complex, presenting vortices and spirals as in the TD HD 135344B (Muto et al. 2012; van der Marel et al. 2016) with a bias towards large cavities (van der Marel et al. 2018). The formation of spirals is justified with a spiral density wave theory in Muto et al. (2012). Note that the stellar radiation produces a puffed up inner rim that occults some disk regions from this radiation, clearly changing the radial temperature profile and affecting the formation of structures (Dullemond & Monnier 2010). Flaherty et al. (2012) explain the observed variability in the IR range with changes in the inner disk structure, i.e. scale height fluctuations. We summarize this by saying that a physically correct model should be able to explain many sources of information: photometry, spectra and images. These ideas highlight the importance of being able to identify which kind of disk we are dealing with. However, due to the difficulty to achieve enough spatial resolution to obtain images for many of the objects, even in close stellar forming regions, the interpretation leads to degeneracy; thus at most we can find models consistent with the observations.

In this work, we focus on TDs; the interpretation of the information coming from the *Spitzer Space Telescope* and other facilities allows the astronomy community to be confident that TDs are out there (Espaillat et al. 2007, 2008, 2014). Surveys of objects allow a characterization; for instance, the observed $\dot{M}$ estimated using the UV excesses caused by the magnetospheric streams falling towards the stellar surface can be explained when these estimates are compared with the value for $\dot{M}$ of classical T Tauri stars (Najita et al. 2007, 2015). The disk mass ($M_{\rm d}$) is correlated with $\dot{M}$ either in full disks (Manara et al. 2016) or in TDs (Owen & Clarke 2012; Najita et al. 2015). This lead us to conclude that an estimated $\dot{M}$ using detected UV excesses in TDs is a key piece of information to guarantee the presence of gas in the hole (Manara et al. 2014). The dust attached to it is responsible to shape lcs by extinction of the stellar radiation. The analysis of lcs by Ansdell et al. (2016) point out occulting inner disk warps and transiting circumstellar clumps as possible processes explaining the observations. For the TD candidates analyzed in our work, a non-zero $\dot{M}$ guarantees that there is gas in the inner region of the disk. Assuming that the dust is attached to the gas, the previous mechanism, or any other that uses dust in the innermost region of the disk either as optically thin inside the cavity in a TD or as an optically thick dusty ring in the PTD case, are plausible scenarios to explain the lcs.

It is usually assumed that the star is not variable in the timescale of the physical processes included to model the lc variability, such that the asymmetry of the dust distribution leads to the features observed. The main contributor to the optical emission is the star. This means that the depth of the signal in the optical lc is given by the amount of dust eclipsing the star. A reservoir of optically thin dust prone to extinct the star is found in the inner hole of TDs.

Specifically, we focus on the sample of TD candidates in the NGC 2264 stellar forming region presented in Sousa et al. (2019). From this sample we choose the objects that have contemporaneous optical and infrared (IR) lcs from *CoRoT* and *Spitzer*, respectively (McGinnis et al. 2015), in order to check the effect on the lcs caused by the material in the disk hole. These objects are Mon-296, Mon-314, Mon-433 and Mon-1308. We focus the study on the YSO Mon-1308 because for this system, we have two different scenarios proposed. The first one is analysed in Nagel & Bouvier (2019) where they simultaneously explain *CoRoT* and *Spitzer* lcs using a full disk as the optically thick structure responsible for the shape of the optical lc, because it occults sections of the stellar surface; also, it is responsible for the shape of the IR lc using the disk emission. The second one is presented in Sousa et al. (2019) where they modeled the SED of a sample of objects using 3 possible cases: a full disk, no disk, and a TD. For Mon-1308, their best fit is a TD with a 20.18 AU hole, which is completely different from the full disk structure required in Nagel & Bouvier (2019). The aim of this work is to complement the analysis in Nagel & Bouvier (2019), which searched for an explanation of the optical and IR lcs of Mon-1308 using a full disk; instead, we extend the analysis using a TD.

As a complementary analysis, we repeat the steps applied to Mon-1308 for the other 3 TD candidates that also share contemporaneous IR and optical lcs. From the whole set, we point out differences in the tuning of the modeling required to look for the interpretation of the lcs of systems that have a range of hole sizes spanning from 0.12 AU to 20.18 AU. In the analysis, we should not forget that not all the lcs are

TABLE 1

OBSERVED PARAMETERS

Object	$R_\star(R_\odot)$	$M_\star(M_\odot)$	$T_\star$(K)	$\dot{M}_{\rm min}$[a]	$\dot{M}_{\rm obs}$[a]	$\dot{M}_{\rm max}$[a]	$R_{\rm H}$(AU)
Mon-296	1.71	1.42	4950		1.73		0.12
Mon-314	1.35	0.29	3360	5.75	5.75	13.5	3.58
Mon-433	0.99	0.44	3680	1.38	2.04	2.51	7.39
Mon-1308	1.59	0.63	3920	5.62	8.51	28.8	20.18

[a] All the $\dot{M}$ are given in units of $10^{-9}\,M_\odot{\rm yr}^{-1}$.

TABLE 2

COROT LIGHT CURVES PERIODS FOR THE 2008 AND 2011 CAMPAIGN

Object	P(days), 2008 campaign	P(days), 2011 campaign
Mon-296	2.51	3.91
Mon-314	—	3.38
Mon-433	—	—
Mon-1308	6.45	6.68

periodic and not always there is a high resemblance between the IR and the optical lcs.

In § 2 we present the details of the sample studied; in § 3 the model is explained, in § 4 the modeled lc for the 4 objects studied is presented and finally, in § 5 and § 6, the discussion and conclusions are shown.

2. SAMPLE OF OBJECTS STUDIED

The objects studied belong to the sample of McGinnis et al. (2015) for objects having AA-Tau like and variable extinction dominated lcs and to the sample of TD candidates in Sousa et al. (2019). The hypothesis for this set of objects is that the dust inside the hole is relevant to explain both the lcs in the optical and in the IR. The objects are: Mon-296, Mon-314, Mon-433, and Mon-1308. The hole size $R_{\rm H}$, the stellar mass $M_\star$, the stellar radius $R_\star$, the stellar temperature $T_\star$, the minimum $\dot{M}_{\rm min}$, the maximum $\dot{M}_{\rm max}$ and the observed disk mass accretion rate $\dot{M}_{\rm obs}$ are presented in Table 1; unless otherwise mentioned, these parameters come from Venuti et al. (2014). The mass accretion rate comes from two estimates: (u-g) and (u-r) color excesses modeling. $\dot{M}_{\rm obs}$ is taken from the first estimate. $\dot{M}_{\rm min}$ and $\dot{M}_{\rm max}$ are the minimum and maximum values from both estimates, including the errors. Notice that the range of R_H spans from 0.12 AU in Mon-296 to 20.18 AU in Mon-1308, a difference of more than two orders of magnitude, allowing to analyse the effect of this parameter in the lcs.

The analysis of the periodicity of the lcs for the objects in the sample was done by Cody et al. (2014) using as a starting point the auto correlation function (ACF) defined and used to calculate the rotational period for a sample of M dwarfs by McQuillan et al. (2013). Applied to a time series, the maximum of the ACF gives the time elapsed between two points for which the signal is the most correlated. In order to confirm that the selected period really corresponds to the main period of the data, Cody et al. (2014) compute a Fourier transform periodogram and search for peaks within 15% of the frequency associated to the period obtained. From this analysis, the objects in our sample show the periods given in Table 2.

Two of the systems show a clear periodicity in their *CoRoT* lcs (Mon-296, Mon-1308). A structure explaining this can be a fixed warp in the inner section of the disk that is repeated periodically along the line of sight. The lc for Mon-314 has a low-probability periodicity in the 2011 epoch and is non periodic in the 2008 epoch, which indicates that the physical mechanism shaping the lc is not long-lived. Thus, a warp may or may not be the cause to explain the 2011 epoch lc. For Mon-433, both epochs the lc is not periodic. Thus, the shape cannot be described with a stable warp. However, looking at the lc, there is a clear sequence of peaks and valleys, such that the occulting structures are locally periodic (they are moving at the Keplerian velocity according to their location) but the dominant one is not always the same, meaning that the period is changing. Also from the lc we can conclude that the timescale of the variability is a few days, indicating that the structures are located close to the inner edge of the disk. The shaping of this region is given by the interaction of the disk with the stellar magnetic

TABLE 3

OBSERVED AMPLITUDES FOR THE LCS

Object	$\Delta mag_{\rm obs}$[a]	$\Delta mag_{\rm IR,obs}$[b]
Mon-296	$0.2 - 0.7$	< 0.1
Mon-314	$0.1 - 0.15$	$0.1 - 0.15$
Mon-433	$0.2 - 0.4$	$0.2 - 0.4$
Mon-1308	$0.2 - 0.4$	$0.2 - 0.4$

[a] Values from the *CoRoT* Telescope.

[b] Values from the *Spitzer* Telescope.

field lines (Romanova et al. 2013; Nagel & Bouvier 2020).

Another aspect to be pointed out is the resemblance or not of the *CoRoT* and *Spitzer* lcs: for Mon-296 both lcs are completely different, for Mon-314 and Mon-433 there is a resemblance between both lcs and, finally, for Mon-1308, the resemblance is remarkable. A high resemblance between the lcs suggests a strong connection between the mechanisms explaining them.

The observational values that we aim to model are the amplitudes for the optical (Δmag_{obs}) and the IR lcs ($\Delta mag_{\rm IR,obs}$). These values are given in data of the *CoRoT* and *Spitzer* telescopes extracted by McGinnis et al. (2015) and included in Table 3. $\Delta mag_{\rm obs}$ from the *CoRoT* Telescope and $\Delta mag_{\rm IR,obs}$ are taken from the *Spitzer* telescope. The *Spitzer* photometric data include values for wavelengths of 3.6 and 4.5μm. Because the behavior is similar in both wavelengths we choose 3.6μm for the analysis.

3. MODELING

For the modeling of the optical lc for each object, we modify the code used in Nagel & Bouvier (2019) to include the extinction by dust in a disk hole where the contribution of an optically thick region is neglected. We include also the emission of the dust located in the hole in order to consistently calculate the modeled IR lc. As mentioned, the lcs are completely shaped by the spatial dust distribution which is given by the gas density; the gas (and dust) is inwards limited by the magnetospheric radius, $R_{\rm mag}$, which is assumed to equal the Keplerian radius ($R_{\rm k}$) at the period extracted from the optical lcs and outwards limited by the hole radius ($R_{\rm H}$) given in Sousa et al. (2019). The optically thin material is distributed according to the gas density ρ, which depends on the azimuthal angle ϕ and the vertical coordinate z, and is given by

$$\rho = A\cos(\frac{\phi-\phi_0}{2})e^{-z/H_H}(1-\beta\frac{R}{R_H}), \qquad (1)$$

where $\phi = \phi_0$ is the location where the maximum density is found and the factor 1/2 allows to have only one maximum in the ϕ range. The value for ϕ_0 is chosen such that at $phase = 0.5$ (center of the plotted lc) the maximum density (and the minimum optical flux) is located along a line of sight towards the star. This density peak is responsible for periodically occulting the star, as required to interpret the optical lc. The argument inside the exponential simply models a natural concentration tendency towards the midplane of the disk. We do not assume that the hole material has reached vertical hydrostatic equilibrium. The scale height $H_{\rm H}$ represents a width of the accreting stream in the hole, which we fix as $H_{\rm H} = 0.1R_{\rm H}$, a value typical of the disk scale height at the location where the material "falls" to the hole from a stationary disk in vertical hydrostatic equilibrium. Because the velocity in the stream is much larger than the accreting velocity in the disk, the density in the hole is lower, as required to get an optically thin environment. As the timescales between disk and hole are different, it is safe to assume that in the hole, the vertical equilibrium is not reached. In any case, the exact shape of the functional form of ρ is irrelevant to the main conclusions presented in this work, because the amplitude of the optical lc is mainly given by the density maximum, whose order of magnitude is given by $\dot{M}$ and not by the functional form of ρ.

The free parameter β models the radial concentration of dust/gas: $\beta = 0$ corresponds to a homogeneous distribution, and $\beta = 1$ indicates that the material is concentrated towards the inner edge of the hole. Note that this latter case is close to what one expects for a structure moving at the observed periodicity ($3-10$ days) for the sample of objects, where R_k is located in the inner region. We do not include a detailed analysis of dust sublimation. Even for the $\beta = 1$ case, most of the region responsible to shape the lcs is beyond the magnetospheric radius, which is the lower limit for the grid used. The constant coefficient A is calculated assuming two facts; first, that all the material being incorporated into the hole (at R_H) arrives at the star in the free-fall time given by $t_{\rm ff} = \frac{R_{\rm H}}{v_{\rm ff}}$ where

$$v_{\rm ff} = \sqrt{\frac{2GM_\star}{R_\star}}\sqrt{1-\frac{R_\star}{R_{\rm H}}} \qquad (2)$$

is the free-fall velocity; second, that $\dot{M}$ resulting of this process is equal to the observed value, $\dot{M}_{\rm obs}$.

Note that the dust located in the gas distributed as in equation 1 is responsible to shape the IR lc. In fully optically thin stellar surroundings, the IR photometric variability is small because the dust grain emission is not extincted or blocked. However, in the system configuration there are grains occulted behind the star. For Mon-296, whose hole is small, the fractional area representing this occultation ($f_{\rm A} = \frac{\pi R_\star^2}{\pi R_{\rm H}^2 \cos i}$) amounts to 0.009 such that the blocking of this fraction of the emission corresponds to $\Delta mag_{\rm IR} \approx -2.5 \log 10(1 - f_{\rm A}) \approx 0.01$, which is of the order of magnitude of $\Delta mag_{\rm IR,obs}$, as can be seen in Table 3. For Mon-314,433 and 1308 the variability coming from this geometrical occultation is 3 to 4 orders of magnitude smaller than for Mon-296. This means that for the 3 objects the dust extinction is relevant to search for a physical configuration to explain $\Delta mag_{\rm IR,obs}$.

We assume that all the material in the hole is moving at the same rotational velocity. However, this is not true. The expected orbit for each accreting particle is a spiral, because at $R_{\rm H}$ and $R_{\rm k}$ the orbital Keplerian periods in a circular trajectory are ≈ 4000 days and 6.45 days, respectively, which can be compared to $t_{\rm ff} = 89$ days, where the parameters for Mon-1308 are used. In other words, during the free-fall, the particle orbits several times around the star before it arrives at the surface. The assumption of a dynamical model will locally change the dust distribution, but to fit $\Delta mag_{\rm obs}$ the most important parameter is the maximum surface density along the line of sight. The maximum is calculated using ρ, and this latter will not change appreciably using a detailed model.

4. RESULTS

The fitting of $\Delta mag_{\rm obs}$ and $\Delta mag_{\rm IR,obs}$ is done using two free parameters: β and the dust to gas ratio ζ. The latter is parameterized by α where $\zeta = \alpha\zeta_{\rm typ}$ and $\zeta_{\rm typ} = 0.01$ is assumed as typical for protoplanetary disks. According to the model, the value $\beta = 1$ corresponds to the configuration with the largest concentration of material close to the star which, as mentioned in § 3, is a physically expected configuration. For this reason, the fiducial model is defined by $\alpha = 1$ and $\beta = 1$.

For each object, $\dot{M}_{\rm obs}$ is given as in Table 1 and H_H is fixed to $H_{\rm H} = 0.1R_{\rm H}$. We note that there is a degeneracy between $\dot{M}$ and ζ because if both parameters increase/decrease then the amount of dust increases/decreases keeping the shape of the spatial distribution of material. We decided to fix $\dot{M}$ at $\dot{M}_{\rm obs}$ because it is consistent with the estimates based on observations, and therefore we interpret the model according to changes in ζ (α). The value for $\Delta mag_{\rm IR}$ is assigned to the maximum magnitude change for the 3.6μm *Spitzer* band. Note that the behavior for the 4.5μm band is similar, as can be seen in the *Spitzer* observations shown in McGinnis et al. (2015) for the set of objects studied here.

We find models consistent with the observed range of $\Delta mag_{\rm obs}$ and $\Delta mag_{\rm IR,obs}$ using a grid in the ranges of α and β given by $[0.1, 10]$ and $[0, 1]$, respectively. In Table 4, we present the parameters for the representative consistent models found in § 4.1,§ 4.2,§ 4.3, and § 4.4. The first column corresponds to the object name, the second column to α, and the third to β. The next three columns are associated to the optical lc; the minimum flux of the star, $F_{\rm min,opt}$, the maximum flux of the star, $F_{\rm max,opt}$ and Δmag. The final three columns are associated to the IR lc; the minimum total flux of the star plus disk, $F_{\rm min,IR}$, the maximum total flux of star plus disk, $F_{\rm max,IR}$ and $\Delta mag_{\rm IR}$. All the fluxes are given in units of $10^{-12}\,{\rm erg\,cm^{-2}\,s^{-1}}$.

4.1. *Mon-1308*

For both $\Delta mag_{\rm obs}$ and $\Delta mag_{\rm IR,obs}$ the range is $[0.2, 0.4]$. A fit for $\Delta mag_{\rm obs}$ is found when $\alpha = 5$ (with $0.8 < \beta < 1$), $\alpha = 7$ (with $0 < \beta < 1$) and $\alpha = 10$ (with $0 < \beta < 0.8$). Due to the grid of models, we run models for $\alpha = 5, 7$ and 10 but not for intermediate values; however other models with values of α between 5 and 10 are also inside the range for $\Delta mag_{\rm obs}$. For these models $\Delta mag_{\rm IR} < 10^{-4}$ which is 3 orders of magnitude lower than required for a reasonable fit. The parameters for the models with $\beta = 1$ are shown in Table 4.

In order to favor these models, either the dust to gas mass ratio should be higher than expected in a typical disk, or $\dot{M}$ should be outside the observational estimates. In any case, even if this can be achieved, only $\Delta mag_{\rm obs}$ can be explained; the fitting of $\Delta mag_{\rm IR,obs}$ is left to another physical mechanism.

IR photometric variability is not expected in an optically thin stationary system because all the emitting material contributes to the IR lc. However, this is not true if there is extinction and occultation; namely the dust extincts and the star occults the dust behind it. Including both mechanisms, the model variability in the IR is small compared to the one in the optical. The previous result, and the fact that for Mon-1308, $\Delta mag_{\rm obs} \approx \Delta mag_{\rm IR,obs}$, explains

TABLE 4

PARAMETERS FOR REPRESENTATIVE MODELS

Object	α	β	$F^a_{\rm min,opt}$	$F^a_{\rm max,opt}$	Δmag	$F^a_{\rm min,IR}$	$F^a_{\rm max,IR}$	$\Delta mag_{\rm IR}$
Mon-296	1	1	47.7	57.6	0.226	5.30	5.35	1.05×10^{-2}
Mon-296	10	0.5	30.3	55.0	0.719	8.01	8.33	4.37×10^{-2}
Mon-314	0.5	0.7	3.267	3.60	0.107	1.610	1.619	5.68×10^{-3}
Mon-314	0.7	1	3.265	3.60	0.107	1.612	1.620	5.58×10^{-3}
Mon-433	—	—	—	—	—	—	—	—
Mon-433	—	—	—	—	—	—	—	—
Mon-1308	5	1	10.8	14.1	0.284	2.94800	2.94812	4.29×10^{-5}
Mon-1308	7	1	9.79	14.1	0.398	2.94803	2.94819	5.98×10^{-5}

[a] All the fluxes are given in units of $10^{-12}\,{\rm erg\,cm^{-2}\,s^{-1}}$.

our inability to consistently model IR and optical lcs using optically thin material in the hole of a TD.

The last analysis leads us to conclude that instead of a TD, a possible configuration to simultaneously explain both the optical and the IR lcs is a PTD. In spite of the classification of Sung et al. (2009) where Mon-1308 is catalogued as a TD due to the amount of dust in the inner disk, we try to interpret this object as a PTD. For the modeling of Mon-1308 in Nagel & Bouvier (2019) required an optically thick warp located at $R_{\rm mag}$, meaning that the remaining emission should be associated to the disk outside the warp. Nagel & Bouvier (2019) do not explicitly characterize the shape of the disk but in accordance with the analysis given here, the thick warp plays the role of the inner disk of the PTD.

Taken together, the previous discussion should be connected to the SED fitting code used in Sousa et al. (2019) which only includes the dust emission outside an empty hole. In the model presented here, the dust emission should come from an optically thin hole and the outer disk. We point out that in our model the variability is completely associated to the dust distribution inside the hole. In the case of a PTD, the observed emission should be interpreted as coming from both an inner, an outer disk, and the dusty gap. A follow-up goal is to find a SED fit consistent with the model described in Nagel & Bouvier (2019), where the innermost structure is a sublimation wall covering a small radial range.

The optical flux from our TD model lies between the $F_{\rm min,opt}$ and $F_{\rm max,opt}$ values given in Table 4. These values are consistent with the SED fitting in Nagel & Bouvier (2019). For Mon-1308, the model presented in Nagel & Bouvier (2019) shows that the flux at 4.5μm coming from the full disk, namely $F_{\rm disk,4.5}$ is similar to the flux at 4.5μm coming from the star, namely $F_{\star,4.5}$ which is around half the observed flux, namely $F_{\rm obs,4.5}$. In Table 4 the range of fluxes modeled at 3.6μm is presented, lying between the values $F_{\rm min,IR}$ and $F_{\rm max,IR}$. These values are consistent with $F_{\rm disk,4.5}+F_{\star,4.5}$. In the model by Sousa et al. (2019), $F_{\star,4.5} \approx F_{\rm obs,4.5}$, because there is a negligible contribution of any part of the disk. We note that in their model, $T_\star$ (a free parameter) is 1091 K higher than the values estimated in Venuti et al. (2014), allowing us to suggest that a new model including an inner disk and a star with a lower $T_\star$ as the main contributors in the near-IR is reasonable. Besides, note that in McGinnis et al. (2015), $F_{\rm disk,4.5}/F_{\star,4.5} = 0.7$ meaning that there is a clear contribution of material around the star. This suggests that PTD or full disks are configurations likely to explain this excess.

In order to pursue this further, we find a new synthetic SED using the Python-based fitting code Sedfitter (Robitaille 2017) based on the 3D dust continuum radiative transfer code Hyperion, an open-source parallelized three-dimensional dust continuum radiative transfer code by Robitaille (2011), which was used for the modeling in Sousa et al. (2019). This code is composed of modular sets with components that can include a stellar photosphere, a disk, an envelope, and ambipolar cavities. For Mon-1308, we used two sets of models. Model 1 is composed of a stellar photosphere and a passive disk, Model 2 includes a stellar photosphere, a passive disk, and a possible inner hole. The Hyperion SED model includes only a passive disk, and does not consider disk heating due to accretion. The input parameters of the Hyperion Sedfitter are a range of Av, the distance from the Sun, the fluxes, and the

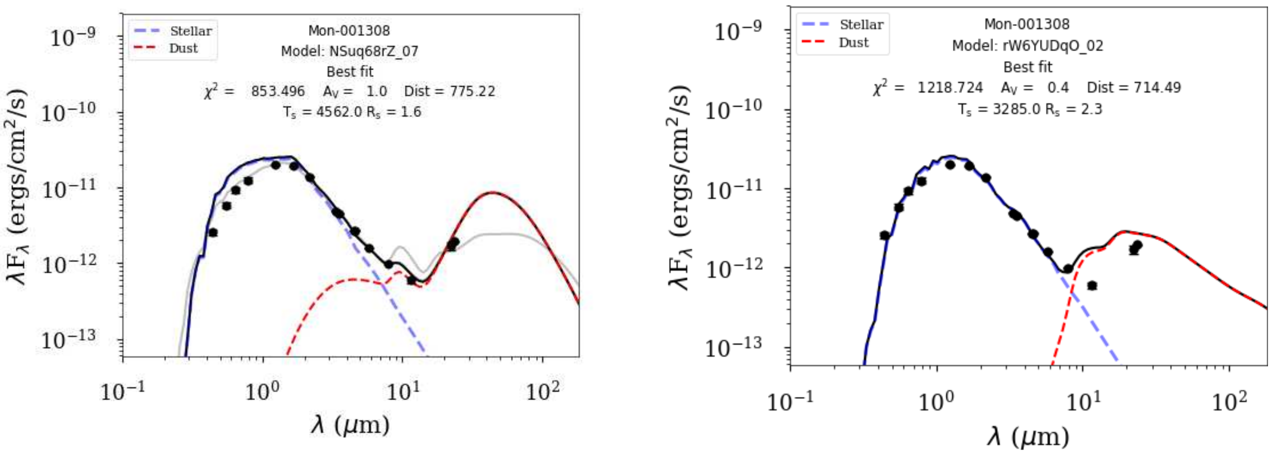

Fig. 1. Two new SED fits for Mon-1308 using the 3D dust continuum radiative transfer code Hyperion. The SED on the left corresponds to the best fit using a stellar photosphere and a full disk. The SED on the right corresponds to the best fit using a stellar photosphere and a disk with an inner hole (TD). The plot includes the values for the fitted parameters. The emission comes from the star (blue line), and a full-disk or TD (red line). The total flux is shown as a black line. The color figure can be viewed online.

uncertainties. The input fluxes use $UBVRcIc$ optical photometry from Rebull et al. (2002), near-IR photometry JHKs from 2MASS, *IRAC* (Fazio et al. 2004) and MIPS (Rieke et al. 2004) magnitudes from *Spitzer* satellite, and *WISE* observations at 3.4, 4.6, 12.0, and 22 μm (Wright et al. 2010). We used the distance estimated from parallax data obtained from the *Gaia* second release (Gaia Collaboration et al. 2016, 2018).

This code does not have a setup for a PTD; thus, we are not able to test this scenario. For the new fit, we remove the SDSS magnitudes because we realized that they are not as trustworthy compared to $UBVRI$ data. The magnitudes are input parameters in the code. Besides, using a different $A_{\rm v}$ range from Sousa et al. (2019); we find a new fit for the data with a full disk model with more consistent $T_\star$ and inclination i values. Instead of $A_{\rm v} = 0.2$, $T_\star = 5011$K and $i = 86.4°$, the new values are $A_{\rm v} = 1$, $T_\star = 4562$K and $i = 60.99°$. We try to fit the observational data using a TD but the i obtained is $i = 18.8°$, a value not consistent with the variability observed in the lcs which requires dusty structures that intermittently block the stellar radiation only present in a high-i configuration. As a secondary argument, against the TD model $\chi^2 = 1218.724$ compared to $\chi^2 = 853.496$ for the full-disk case. Both new fits are shown in Figure 1.

Summarizing, there are three important facts. The first one is that our modeling of the lcs is unsuccessful; thus, the presence of dust in the inner hole (a TD) is not consistent with this part of the observations. The second fact is that the PTD scenario cannot be tested. The third is that the new fitting of the SED suggest that a full disk in Mon-1308 is reasonable. Our conclusion is that a full disk could be a possible option for this object.

4.2. *Mon-433*

For both, $\Delta mag_{\rm obs}$ and $\Delta mag_{\rm IR,obs}$, the range is $[0.2, 0.4]$. A fit for $\Delta mag_{\rm obs}$ is not found for the ranges of α and β studied ($0.1 < \alpha < 10$,$0 < \beta < 1$). For these models $\Delta mag < 0.1$ which is not consistent with the observations. We require an increase of more than one order of magnitude in $\dot{M}$ or in the dust to gas ratio to explain $\Delta mag_{\rm obs}$, but in any case we are unable to interpret $\Delta mag_{\rm IR,obs}$. The larger observational estimate of $\dot{M}$ is only 1.23 times the value used for the modeling. Thus, the evidence leads us to conclude that the optically thin material in the hole is not enough to interpret the lcs in the optical and in the IR.

In Table 2 we show that the periodicity analysis done in Cody et al. (2014) indicates that there is no clearly defined period for the *CoRoT* lc of Mon-433. This is summarized in McGinnis et al. (2015), where they catalogued the *CoRoT* light curve in 2011 as aperiodic. However, over a timescale of around 5 to 10 days, there is a sequence of peaks and valleys that indicates that underneath it there is some periodic physical structure as the one presented in this work. Around this main periodic structure there

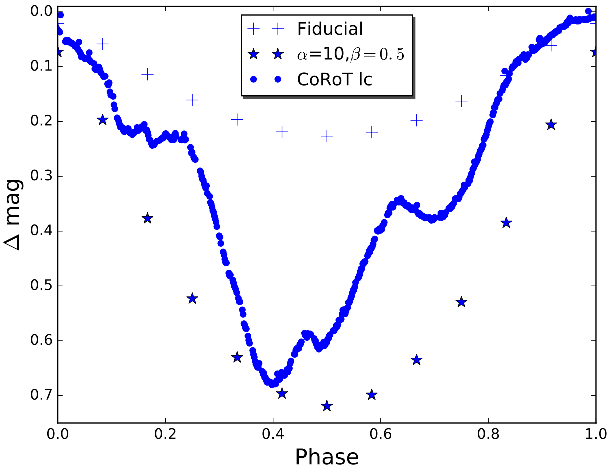

Fig. 2. Two models for the optical lc of Mon-296. The first model is shown with plus signs, corresponding to the fiducial: $\alpha = 1$ and $\beta = 1$. The second model is represented with stars, corresponding to $\alpha = 10$ and $\beta = 0.5$. The points show a representative section of the *CoRoT* lc in the 2011 Campaign. The color figure can be viewed online.

is another set of minor structures located at different places with different periods which shape the observed light curve. This evidence leads us to a physically reasonable test of this model. As in Mon-1308, for Mon-433 a PTD includes a structure responsible to add another component for the extinction in order to explain the observations. We are unable to test this using the SEDfitter code based on Hyperion because it does not have a setup for a PTD, just for full disks and TDs.

4.3. *Mon-314*

For both $\Delta mag_{\rm obs}$ and $\Delta mag_{\rm IR,obs}$, the range is $[0.1, 0.15]$. A fit for $\Delta mag_{\rm obs}$ is found when $\alpha = 0.3$ (and $0 < \beta < 0.4$), $\alpha = 0.5$ (and $0.1 < \beta < 0.7$) and $\alpha = 0.7$ (and $0.4 < \beta < 1$). Due to the grid of models, we run models for $\alpha = 0.3, 0.5$ and 0.7 but not for intermediate values; however, other models with values of α between 0.3 and 0.7 are also inside the range of $\Delta mag_{\rm obs}$. For these models $\Delta mag_{\rm IR} < 10^{-2}$ which is one order of magnitude lower than required for a reasonable fit. The optical flux from the model lies between the $F_{\rm min,opt}$ and $F_{\rm max,opt}$, values given in Table 4. In Table 4 the range of fluxes modeled at 3.6μm is presented, spanning between $F_{\rm min,IR}$ and $F_{\rm max,IR}$. These values are consistent with the modeling in Sousa et al. (2019). Note that the values for α imply that the dust-to-gas ratio is lower than typical for protoplanetary disks. However, we think that the models are physically reasonable to explain $\Delta mag_{\rm obs}$ but their inability to explain $\Delta mag_{\rm IR,obs}$ led us to look for another configuration.

As the objects Mon-1308 and Mon-433, Mon-314 also satisfy $\Delta mag \approx \Delta mag_{\rm IR}$, the analyses developed in § 4.1 are valid here. Table 4 shows some parameters from the modeling of two cases explaining $\Delta mag_{\rm obs}$.

Note that McGinnis et al. (2015) do not find a stable period in the lc. However, it is clear that the physical mechanism repeats itself, because within a temporal range a sequence of peaks and valleys is clearly seen in the lc. Thus, it is valid to try a periodical model to fit the photometric data. As for Mon-433, a likely model for Mon-314 is a PTD.

4.4. *Mon-296*

For $\Delta mag_{\rm obs}$ and $\Delta mag_{\rm IR,obs}$, the range is $[0.2, 0.7]$ and $[0, 0.1]$, respectively. A fit for $\Delta mag_{\rm obs}$ is found when $\alpha = 0.7$ (and $0 < \beta < 0.3$), $\alpha = 1$ (and $0 < \beta < 1$), $\alpha = 3$ (and $0 < \beta < 1$), $\alpha = 5$ (and $0 < \beta < 0.8$), $\alpha = 7$ (and $0 < \beta < 0.7$) and $\alpha = 10$ (and $0 < \beta < 0.5$). Due to the grid of models, we run models for $\alpha = 0.7, 1, 3, 5, 7$ and 10 but not for intermediate values; however other models with values of α between 0.7 and 10 are also inside the range for $\Delta mag_{\rm obs}$. For these models $\Delta mag_{\rm IR}$ is between 1.05×10^{-2} and 4.37×10^{-2} which is an order of magnitude lower than required for a reasonable fit. The optical flux coming from the model lies between the $F_{\rm min,opt}$ and $F_{\rm max,opt}$, values given in Table 4. These values are consistent with the SED fitting in Sousa et al. (2019).

For Mon-314, Mon-433, and Mon-1308, $\Delta mag_{\rm IR}$ is between two and three orders of magnitude lower than $\Delta mag_{\rm IR,obs}$. For the fiducial model for Mon-296, $\Delta mag = 0.226$ and $\Delta mag_{\rm IR} = 0.01$. This is the only system for which the fiducial model is consistent with $\Delta mag_{\rm obs}$. For a 10 times more massive hole ($\alpha = 10$) with $\beta = 0.5$, both values increase to: $\Delta mag = 0.719$ and $\Delta mag_{\rm IR} = 0.0437$, the last value is consistent with the observed IR lc. The modeled lcs corresponding to the previous cases are presented in Figure 2 for the optical and in Figure 3 for the IR. Also in the figures we include a section of the *CoRoT* and *Spitzer* lcs for Campaign 2011. An increase of the dust abundance and/or $\dot{M}$ is required to explain the lcs within the framework of this modeling. Another possibility is that the material in the hole is not completely thin but coexists with partial or completely optically thick structures, like streams that connect the outer disk with the star.

In Table 4 the ranges of the total flux modeled at 3.6μm for the fiducial and the massive model are

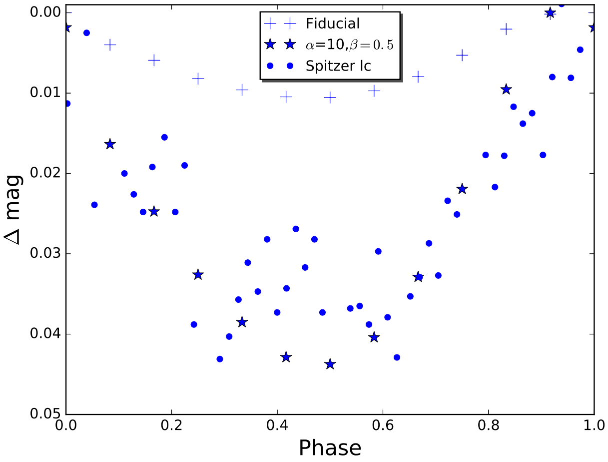

Fig. 3. Two models for the IR lc of Mon-296. The first model is shown with plus signs, corresponding to the fiducial: $\alpha = 1$ and $\beta = 1$. The second model is represented with stars, corresponding to $\alpha = 10$ and $\beta = 0.5$. The points show a representative section of the *Spitzer* lc in the 2011 Campaign. The color figure can be viewed online.

presented, spanning between $F_{\rm min,IR}$ and $F_{\rm max,IR}$. In the models for the optical, the total flux range lies between $F_{\rm min,opt}$ and $F_{\rm max,opt}$. These values are consistent with the modeling in Sousa et al. (2019). If we extract the contribution of the stellar flux in the optical and in the IR then $F_\star \approx 5 \times 10^{-11}$ and $F_{\star,\rm IR} \approx 5 \times 10^{-12}$, which are consistent with the SED presented in Sousa et al. (2019). In the fiducial case, the IR flux of the material in the hole is $F_{\rm IR} \approx 5 \times 10^{-13}$, which is one order of magnitude lower than the flux associated to the optically thick disk required for the modeling using the SED fitting code based in Hyperion (Sousa et al. 2019). However, the hole material for the massive model produces a flux given by $F_{\rm IR} \approx 3.29 \times 10^{-12}$, where $F_{\rm IR}/F_{\star,IR} = 0.7$, just a factor of two lower than the observational estimate of 1.6 for 4.5μm in McGinnis et al. (2015). The value for $F_{\rm IR}$ is estimated as the excess above the photospheric template used to calculate $F_{\star,\rm IR}$. This means that in the latter case the flux of the material in the hole does noticeably affect the SED fitting. But it is still necessary to explain the lcs in both the optical and the IR.

An estimate of the surface density required to calculate the extinction is done using the constant parameter A in equation 1, such that the largest value corresponds to Mon-296. This explains the existence of many models consistent with $\Delta mag_{\rm obs}$. Also, among our set of objects, this is the only one satisfying $\Delta mag >> \Delta mag_{\rm IR}$, resulting in the emission and occultation caused by a small optically thin hole to be consistent either with the SED as shown in Sousa et al. (2019) or the *CoRoT* and *Spitzer* lcs presented in McGinnis et al. (2015). Note that the optically thick disk outside the hole can produce occultations for inclinations larger than $a\tan(R_{\rm H}/H_{\rm H}) = 84.29°$, meaning that for this object the occultation structure is located inside the hole. For the other objects, occultations caused by the outer edge of the hole are not relevant according to the evidence iof the lcs, namely, the variability timescale is associated to their inner regions.

5. DISCUSSION

For Mon-1308, the presence of a small optically thick inner disk is required in order to simultaneously explain the optical and IR lcs, because in this case both lcs have a strong resemblance, and hence the physical region shaping both is the same. As noted in § 4.1, we are able to explain the optical lc with the material concentrated at the inner edge of the disk. However, in order to fit the IR lc, an increase in the amount of dust by several orders of magnitude is required, which is not physically correct.

Because it is not possible to find a physically correct modeling for the optical and IR lcs for Mon-314 and Mon-433, we suggest that these two systems require a small optically thick disk in the innermost regions responsible to shape both lcs. This is consistent with the LkCa 15 TD because it has a 50 AU wide cavity (Andrews et al. 2011b), and also a photometric variability with a very small period, which implies a disk-like structure located very close to the star (Alencar et al. 2018).

For Mon-296, the $R_{\rm k}$ consistent with the stellar rotational period P is less than $R_{\rm H}$; thus the material responsible to shape the periodic optical lc is inside the optically thin environment. For this object, $R_{\rm k} = 0.054$ AU and $R_{\rm H} = 0.12$ AU, such that $R_{\rm ovr} = 0.086$ AU is inside this range. $R_{\rm ovr}$ is the location of the outer vertical resonance, which results from the analysis of the propagation of small-amplitude waves in the disk. Here, the study of out-of-plane gravity modes implies the excitation at this radius of bending waves. This analysis results from the linearization of the equations of motion for the fluid in the disk, where the external force is calculated with the stellar magnetic field, which is moving at the stellar rotational velocity (Romanova et al. 2013). The bending wave rotates at the stellar rotational velocity. Thus it is a structure likely to explain periodicity with the period corresponding to this velocity. Note that a value of $\beta = 0.9$ means that 66% of the material is moving at the velocity required to have a periodic feature with a period P. However, the model explaining $\Delta mag_{\rm obs}$ corresponds to $\beta = 0.5$ implying that not all the dust is distributed in a region where the material is rotating with period P. It is important to mention that the modeled optical and IR lcs evolve with the same periodicity, but for Mon-296 there is no clear resemblance between the observed lcs. This leads to an interpretation where the actual dust distribution is not completely described by the density ρ given in equation 1. This ρ works as the backbone of the actual structure, where the multiple features expected in a highly dynamical environment near the stellar magnetosphere are important to explain the details of the lcs.

Optically thin dust emission does not depend on the lc phase; thus, the low amplitude magnitude shown in the *Spitzer* lc for Mon-296 is consistent with this fact; note that at many different times the IR magnitude is constant. The small value for R_H means that an optically thick disk is close enough to the star to have an adequate temperature to contribute in the IR, as can be seen in Sousa et al. (2019). This is important because the physical configuration for the model presented here results in similar shapes for the optical and IR lcs, which is contrary to the observations. Thus, we can argue that an optically thick disk flux contribution changing with phase is relevant as a second mechanism to fully interpret the IR variability.

6. CONCLUSIONS

1.- For Mon-314 and Mon-1308, $\Delta mag \approx \Delta mag_{\rm IR}$ but the model predicts $\Delta mag >> \Delta mag_{\rm IR}$. Thus, we are able to model $\Delta mag_{\rm obs}$ but not to consistently model $\Delta mag_{\rm IR,obs}$. Using the grid of models defined within the range $0.1 < \alpha < 10$ and $0 < \beta < 1$, we cannot find a consistent model for Mon-433. Mon-296 is the only system where $\Delta mag >> \Delta mag_{\rm IR}$; hence this is the only object that can be modeled using the optically thin material inside the disk.

2.- The density in a small optically thin hole (≈tenths of AU) is large enough to explain typical amplitudes (≈tenths) of the optical lc produced by dust extinction of the stellar spectrum. Using the observed stellar and disk parameters, Mon-296 can be explained with the fiducial model ($\alpha = 1$ and $\beta = 1$). This value of β corresponds to material concentrated at the inner edge of the hole, a fact consistent with the small period of the variability, which locates the extinct material very close to the star.

3.- Neither the extinction in the IR caused by the hole material nor the stellar occultations contribute noticeably to $\Delta mag_{\rm IR}$, ending with a very low value. Note that as $R_{\rm H}$ increases, the fraction of material occulted by the star decreases, and therefore its contribution to $\Delta mag_{\rm IR}$ also decreases. Thus, Mon-296 is the object that contributes the most to $\Delta mag_{\rm IR}$, as can be seen in the modeling.

4.- The extinction is given by the surface density along the line of sight. The largest value corresponds to Mon-296, resulting in the largest contribution to $\Delta mag_{\rm IR}$. Thus, along with the smallest $R_{\rm H}$ as mentioned in the previous item, both facts lead to the largest non-negligible value of $\Delta mag_{\rm IR}$ for Mon-296.

5.- According to the modeling, Mon-314, and Mon-433 require an optically thick inner disk to interpret the lcs. We suggest that instead of hosting a TD they host a PTD. The existence of this structure helps to increase the magnitude amplitude for the IR lcs, as required to interpret the observations. In order to pursue this idea, SED modeling presented by Sousa et al. (2019) should include a small optically thick inner disk. Note that a disk of small size is enough to produce the occultations required to explain $\Delta mag_{\rm obs}$ without noticeably changing the fitting by Sousa et al. (2019).

6.- Using the tool Sedfitter based on Hyperion, a new SED fitting is found for Mon-1308. The new fit favors a full-disk instead of a TD. This is consistent with the modeling of the lcs by Nagel & Bouvier (2019) and with our inability to explain the lcs using optically thin material in the hole. We do not have the tools to test the PTD scenario, but it is also a possible scenario for Mon 1308. Our final remark is that we cannot rely on a SED fitting alone. An analysis of lcs in the optical and in the IR may give us relevant information to cast doubt on this preliminary result. Indeed, revisiting Mon-1308 led us to conclude that the most probable configuration for this object is a full-disk.

REFERENCES

Alencar, S. H. P., Teixeira, P. S., Guimarães, M. M., et al. 2010, A&A, 519, 88, DOI: 10.1051/004-6361/201014184

Alencar, S. H. P., Bouvier, J., Donati, J.-F., et al. 2018, A&A, 620, 195, DOI: 10.1051/004-6361/201834263

Andrews, S. M., Wilner, D. J., Espaillat, C., et al. 2011, ApJ, 732, 42, DOI: 10.1088/0004-637X/732/1/42

Andrews, S. M., Rosenfeld, K. A., Wilner, D. J., & Bremer, M. 2011, ApJ, 742, 5, DOI: 10.1088/2041-8205/742/1/L5

Ansdell, M., Gaidos, E., Rappaport, S. A., et al. 2016, ApJ, 816, 69, DOI: 10.3847/0004-637X/816/2/69

Blinova, A. A., Romanova, M. M., & Lovelace, R. V. E. 2016, MNRAS, 459, 2354, DOI: 10.1093/mnras/stw786

Bodman, E. H. L., Quillen, A. C., Ansdell, M., et al. 2017, MNRAS, 470, 202, DOI: 10.1093/mnras/stx1034

Bouvier, J., Chelli, A., Allain, S., et al. 1999, A&A, 349, 619

Bouvier, J., Grankin, K., Ellerbroek, L. E., Bouy, H., & Barrado,D. 2013, A&A, 557, 77, DOI: 10.1051/004-6361/201321389

Calvet, N., D'Alessio, P., Watson, D. M., et al. 2005, ApJ, 630, 185, DOI: 10.1086/491652

Cieza, L. A., Schreiber, M. R., Romero, G. A., et al. 2010, ApJ, 712, 925, DOI: 10.1088/0004-637X/712/2/925

Cody, A. M., Stauffer, J., Baglin, A., et al. 2014, AJ, 147, 82, DOI: 10.1088/0004-6256/147/4/82

Dullemond, C. P., & Monnier, J. D. 2010, ARA&A, 48, 205, DOI: 10.1146/annurev-astro-081309-130932

Espaillat, C., Calvet, N., D'Alessio, P., et al. 2007, ApJ, 670, 135, DOI: 10.1086/524360

Espaillat, C., Muzerolle, J., Hernández, J., et al. 2008, ApJ, 689, 145, DOI: 10.1086/595869

Espaillat, C., D'Alessio, P., Hernández, J., et al. 2010, ApJ, 717, 441, DOI: 10.1088/0004-637X/717/1/441

Espaillat, C., Furlan, E., D'Alessio, P., et al. 2011, ApJ, 728, 49, DOI: 10.1088/0004-637X/728/1/49

Espaillat, C., Muzerolle, J., Najita, J., et al. 2014, in Protostars and Planets VI, ed. H. Beuther, R. S. Klessen, C. P. Dullemond, & T. Henning (Tuczon, AZ: UAP), 497, DOI: 10.2458/azu_uapress_9780816531240-ch022

Fang, M., van Boekel, R., Wang, W., et al. 2009, A&A, 504, 461, DOI: 10.1051/0004-6361/200912468

Fazio, G. G., Hora, J. L., Allen, L. E., et al. 2004, ApJS, 154, 10, DOI: 10.1086/422843

Flaherty, K. M., Muzerolle, J., Rieke, G., et al. 2012, ApJ, 748, 71, DOI: 10.1088/0004-637X/748/1/71

Gaia Collaboration, et al. 2016, A&A, 595, 1, DOI: 10.1051/004-6361/201629272

Gaia Collaboration, et al. 2018, A&A, 616, 1, DOI: 10.1051/004-6361/201833051

Ingleby, L., Espaillat, C., Calvet, N., et al. 2015, ApJ, 805, 149, DOI: 10.1088/0004-637X/805/2/149

Kulkarni, A. K., & Romanova, M. M. 2008, MNRAS, 386, 673, DOI: 10.1111/j.1365-2966.2008.13094

Lovelace, R. V. E., & Romanova, M. M. 2014, FIDyR, 46, 1401, DOI: 10.1088/0169-5983/46/4/041401

Manara, C. F., Testi, L., Natta, A., et al. 2014, A&A, 568, 18, DOI: 10.1051/0004-6361/201323318

Manara, C. F., Rosotti, G., Testi, L., et al. 2016, A&A, 591, 3, DOI: 10.1051/0004-6361/201628549

McGinnis, P. T., Alencar, S. H. P., Guimarães, M. M., et al. 2015, A&A, 577, 11, DOI: 10.1051/0004-6361/201425475

McQuillan, A., Aigrain, S., & Mazeh, T. 2013, MNRAS, 432, 1203, DOI: 10.1093/mnras/stt536

Meheut, H., Casse, F., Varniere, P., & Tagger, M. 2010, A&A, 516, 31, DOI: 10.1051/0004-6361/201014000

Merín, B., Brown, J. M., Oliveira, I., et al. 2010, ApJ, 718, 1200, DOI: 10.1088/0004-637X/718/2/1200

Morales-Calderón, M., Stauffer, J. R., Hillenbrand, L. A., et al. 2011, ApJ, 733, 50, DOI: 10.1088/0004-637X/733/1/50

Muto, T., Grady, C. A., Hashimoto, J., et al. 2012, ApJ, 748, 22, DOI: 10.1088/2041-8205/748/2/L22

Muzerolle, J., Allen, L. E., Megeath, S. T., Hernández, J. & Gutermuth, R. A. 2010, ApJ, 708, 1107, DOI: 10.1088/0004-637X/708/2/1107

Nagel, E., álvarez-Meraz, R., & Rendón, F. 2017, RMxAA, 53, 227

Nagel, E. & Bouvier, J. 2019, A&A, 625, 45, DOI: 10.1051/004-6361/201833979

_________. 2020, A&A, 643, 157, DOI: 10.1051/0004-6361/202038594

Najita, J. R., Strom, S. E., & Muzerolle, J. 2007, MNRAS, 378, 369, DOI: 10.1111/j.1365-2966.2007.11793.x

Najita, J. R., Andrews, S. M., & Muzerolle, J. 2015, MNRAS, 450, 3559, DOI: 10.1093/mnras/stv839

Owen, J. E. & Clarke, C. J. 2012, MNRAS, 426, 96, DOI: 10.111/j.1745-3933.2012.01334.x

Rebull, L. M., Makidon, R. B., Strom, S. E., et al. 2002, AJ, 123, 1528, DOI: 10.1086/338904

Rieke, G. H., Young, E. T., Engelbracht, C. W., et al. 2004, ApJS, 154, 25, DOI: 10.1086/422717

Robitaille, T. P. 2011, A&A, 536, 79, DOI: 10.1051/0004-6361/201117150

_________. 2017, A&A, 600, 11, DOI: 10.1051/0004-6361/201425486

Rodríguez, J. E., Ansdell, M., Oelkers, R. J., et al. 2017, ApJ, 848, 97, DOI: 10.3847/1538-4357/aa8c78

Romanova, M. M., Ustyugova, G. V., Koldova, A. V., & Lovelace, R. V. E. 2013, MNRAS, 430, 699, DOI: 10.1093/mnras/sts670

Sousa, A. P., Alencar, S. H. P., Rebull, L. M., et al. 2019, A&A, 629, 67, DOI: 10.1051/0004-6361/201935563

Stauffer, J., Cody, A. M., Baglin, A., et al. 2014, AJ, 147, 83, DOI: 10.1088/0004-6256/147/4/83

Stauffer, J., Cody, A. M., McGinnis, P., et al. 2015, AJ, 149, 130, DOI: 10.1088/0004-6256/149/4/130

Stauffer, J., Cody, A. M., Rebull, L., et al. 2016, AJ, 151, 60, DOI: 10.3847/0004-6256/151/3160

Sung, H., Stauffer, J. R., & Bessell, M. S. 2009, AJ, 138, 1116, DOI: 10.1088/0004-6256/138/4/1116

van der Marel, N., Cazzoletti, P., Pinilla, P., & Garufi, A. 2016, ApJ, 832, 178, DOI: 10.3847/0004-637X/832/2/178

van der Marel, N., Williams, J. P., Ansdell, M., et al. 2018, ApJ, 854, 177, DOI: 10.3847/1538-4357/aaaa6b

Venuti, L., Bouvier, J., Flaccomio, E., et al. 2014, A&A, 570, 82, DOI: 10.1051/0004-6361/201423776

Wright, E. L., Eisenhardt, P. R. M., Mainzer, A. K., et al. 2010, AJ, 140, 1868, DOI: 10.1088/0004-6256/140/6/1868

Fernando Gutiérrez-Canales, Sebastián Morales-Gutiérrez, and Erick Nagel: Departamento de Astronomía, Universidad de Guanajuato, Callejón de Jalisco S/N, 36240 Guanajuato, Guanajuato, México (e.nagel@ugto.mx).

Alana P. Sousa: Université Grenoble Alpes, IPAG, F-38000 Grenoble, France.

Revista Mexicana de Astronomía y Astrofísica, **57**, 445–457 (2021)

https://doi.org/10.22201/ia.01851101p.2021.57.02.16

A SURVEY ON EXTENSIONS OF THE PURE GRAVITY SWING-BY MANEUVER

A. F. S. Ferreira[1], R. V. de Moraes[1,2], A. F. B. A. Prado[2,3], O. C. Winter[1], and V. M. Gomes[1]

Received March 30 2021; accepted August 13 2021

ABSTRACT

The present paper surveys the more recent techniques related to the swing-by maneuver, where a spacecraft changes its energy and angular momentum by passing close to celestial bodies. It is focused on the literature related to extensions of this maneuver, with emphasis in the powered version, where an impulse is applied to the spacecraft near the closest approach. Several mathematical models are considered, including the patched-conics approximation for analytical studies, and the restricted three-body problem for the numerical simulations. The main goal is to show the models and the main conclusions available in the literature for those maneuvers. Some key results are shown to discuss important aspects of this maneuver, including the analysis of the energy variation of the spacecraft, the behavior of the trajectories and other applications.

RESUMEN

Presentamos una reseña de los resultados recientes sobre la maniobra de columpio, en la cual una nave espacial cambia su energía y momento angular al pasar cerca de un cuerpo celeste. Nos concentramos en la literatura sobre las extensiones de esta maniobra, con énfasis en la versión con potencia aplicada, en la cual se le impone a la nave un impulso durante el máximo acercamiento. Se consideran varios modelos matemáticos, incluyendo la aproximación de la cónica parcial para estudios analíticos y el problema restringido de los tres cuerpos para las simulaciones numéricas. Nuestro objetivo principal es mostrar los modelos y las conclusiones disponibles en la literatura para estas maniobras. Con los principales resultados discutimos aspectos interesantes de la maniobra, incluyendo el análisis de la variación de la energía de la nave y el comportamiento de las trayectorias.

Key Words: celestial mechanics — methods: numerical — minor planets, asteroids: general — space vehicles — surveys

1. INTRODUCTION

Missions to distant planets, asteroids and comets have been planned and performed frequently by space agencies around the world. A significant and important issue for the development of these missions is the high fuel consumption required by those missions. It is well known that the cost to send a spacecraft to space is high and one of the most expensive parts of the mission is the large amount of fuel necessary to send materials to space. Therefore, to minimize this cost is a fundamental problem in astrodynamics. The well-known bi-impulsive Hohmann transfer (Hohmann 1925) is a major and first step into this problem, studying the minimum fuel consumption to transfer a spacecraft between two co-planar circular orbits. This maneuver shows that a transfer ellipse tangential to both the initial and final orbits is the solution that gives the minimum increments of velocities. After that, Hoelker & Silber (1959) and Shternfeld (1959) showed that the tri-impulsive bi-elliptic transfer is more economical to transfer a spacecraft between two coplanar circular orbits, if the radius of the external orbit divided by the radius of the interior orbit is larger than 11.93875. Those are the first solutions to the prob-

---

[1] São Paulo State University - FEG-UNESP, Brazil.
[2] National Institute for Space Research - INPE, Brazil.
[3] University of Russia - RUDN University, Russia.

lem of minimizing fuel consumption in space maneuvers, which will later include gravity assisted maneuvers.

After that, several, alternatives of maneuvers with minimum fuel consumption appeared in the literature, showing extensions of those two important bi-impulsive transfers. Some examples are found in Edelbaum (1959), Roth (1965), Jezewski & Rozendaal (1968), Jin & Melton (1991) and Prussing (1992). To reduce even more the fuel expenditure, it is also possible to consider low thrusts, where a small force is applied to the spacecraft for a relatively long time. The advantage of this approach is the high specific impulses of those thrusts, which can generate large increments of velocity with a small mass of fuel consumed. Good examples are shown in Lawden (1953), Lawden (1954), Sukhanov & Prado (2001), Casalino & Colasurdo (2007), Ozimek & Howell (2010), Zhang et al. (2015), Carvalho et al. (2016) and Fernandes & Carvalho (2018). A particularly interesting example is shown in Qi & Ruiter (2020). A method to obtain preliminary continuous thrust powered swing-by (PSB) orbits was constructed considering a series of discrete optimal single impulsive PSBs. Using these initial guesses, optimal continuous thrust PSB orbits were designed by using optimal control problem techniques. Another good example is available in Konstantinov & Thein (2017), which simplifies the problem using a method which allows us to avoid the difficulties of solving the optimization problem of the interplanetary trajectory of a spacecraft propelled by electric power using a sequence of swing-bys.

Considering those advances in the swing-by techniques, the present paper has the goal of making a complete survey, covering all the options available for mission designers. Some of the main models are briefly explained and the pertinent literature is indicated for more details. Particular importance is given to the powered version of this maneuver, where an impulse is combined with the close approach. The different mathematical models used to solve this problem are also showed and key results are discussed, in particular in terms of the energy variations of the spacecraft. Several important applications are described, also indicating the appropriate literature.

The following sections describe the history and mathematics behind the pure gravity swing-by maneuver, when only the gravity of the body is considered in maneuver, and the powered swing-by (PSB), when propulsion is applied to the probe to improve the maneuver. In § 2, the history and applications of the pure gravity maneuver in space missions are presented, as well as an introduction on the extension of the pure gravity maneuver to the powered swing-by maneuver. § 3 shows the mathematical model of the pure maneuver, including the "patched conics approach" for an analytical study and the "circular and elliptical restricted three-body problem" for numerical simulations, in addition to the analytical equations that show the effect of the maneuver. Throughout the work the historical context is cited. § 4 presents the different types of powered extensions available in the literature. § 5 shows a detailed description of the powered swing-by maneuver, focusing on the mathematical and geometric presentation of the problem, in addition to the historical description, and presenting a summary of the analyzes available in the literature. Finally, § 6 talks about captures of the spacecraft.

2. THE PURE GRAVITY SWING-BY MANEUVER

To reduce even more the fuel consumption in orbital maneuvers, a new concept appeared in the literature of space missions, the swing-by maneuver. Negri & Prado (2020) show a historical description of the early years of this maneuver, considering the pure gravity maneuver. In this sense, the present paper is a continuation of Negri & Prado (2020), showing some of the later advances and generalizations of this technique, covering all the options available for mission designers. Particular importance is given, in this work, to the powered version of this maneuver, where an impulse is combined with the close approach. Some of the main models are briefly explained and the pertinent literature is indicated for more details.

In terms of practical applications, Minovitch, in 1961, wrote an important document (Minovitch 1961), where he showed the basic physics involved in this close approach maneuver when applied to spacecraft trajectories, and the possibility of using this technique to send a spacecraft out of the Solar System with a much smaller fuel consumption, when compared to maneuvers made exclusively based in propulsion systems. A detailed description of the research developed by Minovitch is shown in Dowling et al. (1990) and Dowling et al. (1991). Looking at real missions that already used this technique, it is possible to find several examples. Flandro (1966) showed a detailed plan for the Voyager mission, which was composed by two spacecraft that made a series of close approaches to several planets of the

Solar System to gain energy for the trip. The calculations were made based on the equations developed by Minovitch (1961), and it was possible to verify the efficiency of this maneuver in a grand tour of the Solar System. It was one of the most important interplanetary missions that would not have been possible without the use of close approaches to the planets visited. Several other missions used passages by the planets of the Solar System to increase their energy, so helping the spacecraft to complete the goals of the mission. Some examples are shown in Farquhar & Dunham (1981) and Farquhar et al. (1985). Another good example is the Galileo mission, which used pure gravity swing-by maneuvers to gain energy, as shown in D'Amario et al. (1981), D'Amario et al. (1982) and Byrnes & D'Amario (1982). This same concept was also used in the Messenger and Bepi-Colombo missions, which were two missions directed to the planet Mercury (McNutt et al. 2004, 2006; Grard 2006), but in this case the goal was to reduce the two-body energy Sun-spacecraft. Those possibilities will be explained later in the present paper.

One of the good descriptions of this maneuver available in the literature is shown in Broucke (1988). It is a paper presenting the basic celestial mechanics of the pure gravity assisted maneuver. A few books also mention this problem, but usually very quickly, like Ruppe (1967), Opik (1976) and Kaplan (1976).

Looking for extensions of this pure gravity based maneuver, the concept of "powered swing-by maneuver" appeared in the literature, which is a combination of a pure gravity swing-by, which depends only on the gravity field of the celestial body approached and the geometry of the passage, with the application of an impulse in the spacecraft at some point inside the sphere of influence of the body involved in the maneuver. The use of this maneuver is an important option when the energy obtained from the pure gravity swing-by maneuver is not enough to complete a given mission. It gives new options to the mission design and can enable missions that could not be achieved without this technique. The best choice for the geometry can give higher energy variations to the spacecraft and, consequently, more velocity after it leaves the system. If the objective is to remove energy to insert the spacecraft in orbit around a celestial body, this type of maneuver is also efficient. There are studies that analyze the best geometry for this maneuver and the effects of the parameters related to it, which are described in some detail later. When considering elliptical systems (which increases the accuracy of the results, in particular when the planets Mars and Mercury are involved, because they have larger eccentricities) it is necessary to use two more parameters to describe the maneuver, both of them related to the geometry of the primaries: the eccentricity of their orbits and the true anomaly of the secondary body in its orbit around the primary at the moment of closest approach.

To show that the powered swing-by maneuver can benefit some missions, it is necessary to make a detailed comparison between maneuvers performed with the impulse applied near the close approach of the spacecraft around the celestial body and maneuvers performed with the impulse applied after the spacecraft leaves the sphere of influence of the body. This point is shown in Striepe & Braun (1991) in a mission from Earth to Mars making a powered swing-by in Venus. Following that, Prado (1996) made a detailed and general analysis of this maneuver for circular systems, to verify its efficiency. The author considered the situation where the impulse is applied to the spacecraft at the moment when it passes through the periapsis of its orbit, as well as the situation where the impulse is applied at a point outside the sphere of influence of the secondary body. The results showed that, in many circumstances, to apply the impulse at the periapsis has advantages in terms of getting extra gains of energy from the impulsive maneuver. This study was followed by Casalino et al. (1999a), which extended this maneuver for the situation where the application of the impulse is not made at the periapsis of the orbit of the secondary body. The next step was to consider this problem when the impulse is applied in the periapsis of the close approach trajectory in systems with elliptical orbits for the primaries, thus studying the effects of the eccentricity of the primaries on the maneuver. It was done in Prado (1997), Ferreira et al. (2017) and Ferreira et al. (2018a). It is important to study those systems, because elliptical systems are numerous in space, and important celestial bodies, like the planets Mars and Mercury, are among them, and they have been used for swing-by maneuvers. The results showed that the eccentricity gives strong effects in the maneuver.

Taking into account those considerations, this review has the goal of presenting a more detailed discussion of some of the main extensions of the swing-by maneuver, including the key conclusions available in the literature. Before going in detail into this maneuver, an introduction to the work related to the unpowered version of the maneuver is also made, to explain the most important aspects of this technique and some lines of research related to them. The reader interested in more details about this history should look at Negri & Prado (2020).

3. MATHEMATICAL MODELS FOR THE PURE GRAVITY SWING-BY MANEUVERS

Analytical and numerical studies are available in the literature regarding the pure gravity swing-by maneuver, and both approaches will be summarized next. Analytical studies are based on the "patched-conics" model and numerical studies derive from the use of the restricted three-body problem (RTBP) for the circular and elliptic case (Szebehely 1967).

3.1. *"Patched-Conics" Approach*

The "patched-conics" approach (Bate et al. 1971) is a method for simplifying the calculation of trajectories that employs the concept of the sphere of influence of a celestial body. The approximation is made by dividing the space into several parts and then assigning a sphere of influence to each body of the system.

When the spacecraft is within the sphere of influence of a body, only the effect of the gravitational force of this body is considered, regardless of the size of the bodies. The effects of the forces coming from the other bodies of the system are neglected and the spacecraft follows a Keplerian orbit. For a swing-by maneuver the sequence is the following (Broucke 1988):

- The spacecraft (M_3) initially comes from an orbit around the main body of the system (M_1). At this phase of the motion only the gravitational force of M_1 acts on M_3, and the effect of the gravity of the secondary body (M_2) is neglected;
- When M_3 reaches a certain distance from M_2, its gravity starts to dominate the motion of the spacecraft, and the effect of M_1 can be neglected, so the gravity of the secondary body (M_2) is assumed to be the only force acting in the motion of M_3;
- Then, the spacecraft escapes from M_2 and goes again toward the main body. The gravity of M_1 is then assumed to be the only force acting in the spacecraft again.

This method reduces the more complex three-body problem to a sequence of two-body problems, for which the solutions are the usual conic sections (Keplerian orbits).

3.2. *Circular and Elliptical Restricted Three Body Problem*

The "three-body problem" is the simplest particular case, and perhaps the most popular one, of the N-body problem. It is a non-integrable problem so, in general, there is no analytical solution, but for some mass values and initial conditions there are periodic or quasi-periodic solutions. This is the case of the "restricted three-body problem", that can be circular or elliptical. In this version, there is a larger body, called M_1, which is the primary body of the system. It is followed by the secondary body M_2, the second largest in mass, and the problem studies the motion of a massless body M_3, which can be a spacecraft that orbits the system formed by the other two bodies.

The circular restricted three-body problem (CRTBP) (Szebehely 1967; Murray & Dermott 2000; Valtonen & Karttunen 2006; Pourtakdoust & Sayanjali 2014; Zotos 2015; Qian et al. 2016) assumes that M_1 and M_2 are in circular orbits around the common center of mass of the system. In this review, the motion is always limited to the orbital plane of the primaries. The mass of M_1 is given by $1-\mu$, with $\mu = \frac{m_2}{(m_1+m_2)}$ the mass parameter of the system. m_1 and m_2 are the masses of the bodies M_1 and M_2, respectively. These choices are compatible with the canonical system of units, which is a system where the total mass of the system is one; the unit of distances is the semi-major axis (a) of the orbit of the primaries; the gravitational constant is one; and the unit of time is defined such that the orbital period of the primaries is 2π (Szebehely 1967).

For the elliptical restricted three-body problem (ERTBP), the bodies M_1 and M_2 are moving in elliptical orbits around their common center of mass (Szebehely 1967; Murray & Dermott 2000; Valtonen & Karttunen 2006; Szebehely & Giacaglia 1964). From basic celestial mechanics, it is known that the distance between M_1 and M_2 is given by $d = \frac{a(1-e^2)}{(1+e\cos\nu)}$, where a is the semi-major axis, e is the eccentricity of the orbit of the primaries and ν is the true anomaly of the secondary body. The equations of motion (equation 1) are integrated in time and the mathematical model can be built using a reference system with the origin fixed in the center of mass of the bodies

$$\ddot{x} = -\frac{(1-\mu)(x-x_1)}{r_1^3} - \frac{\mu(x-x_2)}{r_2^3},$$

$$\ddot{y} = -\frac{(1-\mu)(y-y_1)}{r_1^3} - \frac{\mu(y-y_2)}{r_2^3}. \tag{1}$$

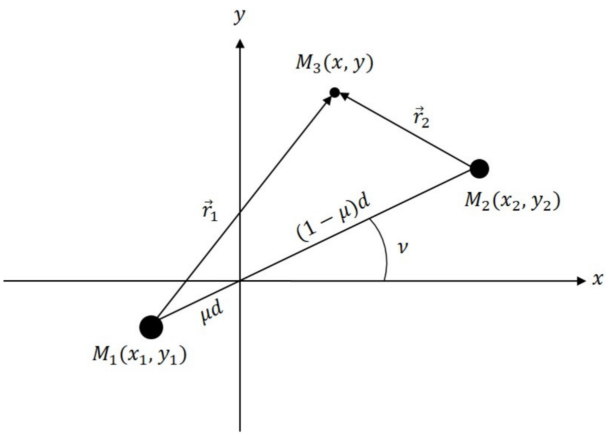

Fig. 1. Geometry of the restricted three-body problem.

In those equations, $r_1 = \sqrt{(x-x_1)^2 + (y-y_1)^2}$ represents the distance between M_1 and the spacecraft; $r_2 = \sqrt{(x-x_2)^2 + (y-y_2)^2}$ the distance between M_2 and the spacecraft; (x, y) the position of the spacecraft; (x_1, y_1) and (x_2, y_2) the positions of M_1 and M_2, respectively, as shown in Figure 1.

In contrast to the patched-conics model, simulations in the CRTBP and ERTBP consider the influence of the two massive bodies on the spacecraft at all times. There are no analytical solutions, but the numerical approach generates more accurate results than the "patched conics" approach.

3.3. *Analytical Equations to Measure the Effects of the Pure Gravity Swing-by Maneuver*

After reviewing those basic concepts, it is time to look in more detail at the pure gravity swing-by maneuver. Broucke (1988) presented a theoretical exposition of the celestial mechanics and the fundamental principles of the gravity-assisted maneuver, or pure gravity swing-by. It started from references that investigated this maneuver before, like Deerwester (1966); Hiller (1969); Longman (1970); Hollenbeck (1975); Diehl & Myers (1987) and Diehl et al. (1987). The most common goal of this maneuver is to give energy to the spacecraft to follow its journey, but there are also some researches showing maneuvers ending in captures by the secondary body of the system after a close approach (Helton 1972; Cline 1979; Nock & Upholf 1979).

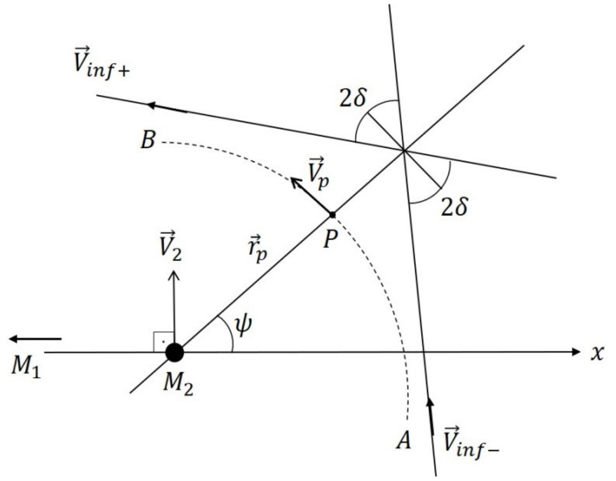

Fig. 2. Geometry of the pure gravity swing-by (adapted from Broucke (1988)).

Broucke (1988) derived analytically, from the patched-conics approach, the geometric results of the maneuver, which was basically obtained from the rotation of the velocity vector of the spacecraft at the time of close approach. He also calculated the variations in energy and angular momentum of the spacecraft with respect to the primary body of the system. Besides that, he made numerical integrations based on the restricted three-body problem, to get more accurate trajectories.

The maneuver is realized around the less massive primary of the system and the variations are measured with respect to the main body of the system. The system has circular orbits, angular velocity ω and planar motion.

Figure 2 is an adaptation based on Broucke (1988). The spacecraft comes from a Keplerian two-body orbit with main body (M_1), passes close to the secondary body (M_2), and is affected by the gravity of this body, which causes a rotation of the velocity vector of the spacecraft. Then, it moves away from the secondary body to a new Keplerian two-body orbit around M_1. The angle of curvature of the velocity vector is 2δ for the whole maneuver; $\vec{V}_{inf-}$ is the approach velocity of the spacecraft relative to M_2; $\vec{V}_{inf+}$ is the escape velocity relative to M_2; ψ is the angle of approach; $\vec{r}_p$ is the radius of the periapsis and $\vec{V}_2$ the velocity of M_2 around the center of mass of the system, which makes an angle of 90 deg with the x-axis. From this geometry Broucke derived equations 2-4 for the variations of velocity, energy and angular momentum of the pure gravity maneuver

$$\Delta V = 2V_{inf-} \sin\delta, \tag{2}$$

$$\Delta E = -2V_2 V_{inf-} \sin\delta \sin\psi, \tag{3}$$

$$\Delta C = -2\omega V_2 V_{inf-} \sin\delta \sin\psi. \tag{4}$$

Examining the formula for ΔE, an analysis of the configuration of the gains and losses of energy due to the maneuver can be made (Broucke 1988). If $0 < \psi < 180\,\mathrm{deg}$, the periapsis of the orbit of the spacecraft is in front of M_2 and there are losses of energy due to gravity. Missions like Mariner 10, Messenger and BepiColombo (McNutt et al. 2004, 2006; Grard 2006; NASA 1999-2012, 2021; Dunne & Burgess 1978; Jehn et al. 2008) used the pure gravity swing-by to remove energy from the spacecraft to insert it into orbit. On the opposite side, if $180 < \psi < 360\,\mathrm{deg}$, the periapsis of the orbit of the spacecraft is behind M_2 and the spacecraft gains energy due to the gravity of the secondary body. Broucke (1988) also included a classification of the types of orbits resulting from the gravity assisted maneuver, obtained from numerical explorations of the problem using the restricted three-body problem.

An analytical equation to show the variation of energy of the spacecraft in a pure gravity elliptic swing-by maneuver was derived in Ferreira et al. (2018b). It is shown in equation 5 below. It extends the literature by expanding analytical studies based in the patched-conics approach to elliptical orbits. In this equation, "a" is the semi-major axis of the orbit of the primaries, "e" is the eccentricity of this orbit, μ the mass parameter of the system, V_{inf} the velocity of approach of the spacecraft when getting closer to M_2, ν the true anomaly of M_2 when the close approach occurs, ψ is the angle of approach and $\beta = \cos^{-1}(-\frac{V_r}{V_2})$, with V_r the radial velocity of M_2, and V_2 the magnitude of the velocity of M_2 with respect to M_1

$$\Delta E = 2V_{inf}\sqrt{(1-\mu)\left(\frac{2}{\frac{a(1-e^2)}{1+e\cos\nu}} - \frac{1}{a}\right)}\sin\delta\cos(\psi+\beta). \tag{5}$$

Equation 5 shows that the energy variation is dependent on the angle between the velocity of M_2 around the center of mass and the axis connecting the primaries ($180° - \beta$). The angular momentum variation is also obtained (equation 6), and it is shown that it is directly dependent on the distance between the bodies $d = \frac{a(1-e^2)}{(1+e\cos\nu)}$, but not on the angle β

$$\Delta C = -2\frac{a(1-e^2)}{1+e\cos\nu}V_{inf}\sin\delta\sin\psi. \tag{6}$$

This same reference (Ferreira et al. 2018b) identified the configurations of maximum gains and losses of energy due to the gravity effect of the secondary body. It concluded that maneuvers with energy loss occur when $90 < \psi + \beta < 270\,\mathrm{deg}$, with maximum loss at $\psi + \beta = 180\,\mathrm{deg}$. The region of gains of energy is $-90 < \psi + \beta < 90\,\mathrm{deg}$, with maximum in $\psi + \beta = 0\,\mathrm{deg}$ or $\psi + \beta = 360\,\mathrm{deg}$. The effect of the swing-by in the energy variation is zero when $\psi + \beta = 90\,\mathrm{deg}$ or $\psi + \beta = 270\,\mathrm{deg}$. Numerical simulations validated the equations presented in the paper. It was also shown that the variation of velocity in the elliptic maneuver does not depend on the orbit of the secondary body. It remains the same as that obtained from the circular maneuver.

Regarding differences in the results obtained from the two-and restricted three-body dynamics in the pure gravity maneuver, there are also some comparisons available in the literature measuring the effects of the analytical approximations on the results for a swing-by maneuver. Good examples are Campagnola et al. (2012); Negri et al. (2017) and Negri et al. (2019), which show the errors made by the patched-conics approach in different aspects, including those errors as a function of the mass parameter of the system.

Several other applications of this type of maneuver exist, like the use of the inner planets of the Solar System to send a spacecraft to the Sun, considered in Sukhanov (1999); or a mission leaving and returning to the Earth with an intermediate swing-by with the Moon (Gagg Filho & Fernandes 2018). A graphical method to solve this problem is developed in Strange & Longuski (2002). Some references also studied the problem of multiple swing-by maneuvers, like (Dunham & Davis 1985; Marsh & Howell 1988; Ross & Scheeres 2007; Jerg et al. 2009; Vasile & Campagnola 2009; Kloster et al. 2011). Swing-by with a cloud of particles was also studied, like in Gomes & Prado (2008, 2010); Gomes et al. (2013); Formiga et al. (2018). Other studies showed the flyby transfers between Sun Earth Moon libration point orbits with different energies in the Sun Earth Moon restricted four-body problem, like in Qi et al. (2017). There are also some researches considering the particular case of orbits for a spacecraft travelling around the Sun and perturbed by Jupiter, even when the spacecraft does not enter the sphere of influence of the planet (Carusi et al. 1982; Greenberg et al. 1988; Carusi et al. 1990, 1995).

Swing-bys are also considered in the "endgame problem", whose goal is to minimize the energy required to insert a spacecraft around a celestial body at the end of a multi-body mission (Woolley & Scheeres 2009; Campagnola & Russell 2010a,b). A dynamical system approach, using the RTBP as the mathematical model, is also used to study the pure gravity swing-by maneuvers in Koon et al. (2000, 2001, 2002, 2008); Howell et al. (2001); Anderson (2005); Belbruno et al. (2008); Anderson & Lo (2010, 2011) and Qi & Ruiter (2018a).

4. EXTENSIONS OF THE PURE GRAVITY MANEUVER

Another version of the family of the close approach maneuver available in the literature is the one where the atmosphere of a planet is used to change the trajectory of the spacecraft, which is a type of transition to the powered maneuver, since the atmosphere acts like a continuous propulsion applied to the spacecraft during the atmospheric flight. It is the so called "aero-gravity assisted maneuver". Several papers exist covering this topic. Some of them are more generic, trying to understand the whole effect of the atmosphere and the shape of the spacecraft, like McRonald & Randolph (1992); Lohar et al. (1994); Elices (1995); Lohar (1996); Bonfiglio et al. (2000); Armellin et al. (2006, 2007) and Prado & Broucke (1995). There are also studies concentrated on the atmosphere of the Earth, which has more accurate models available for its density distribution, like Gomes et al. (2013, 2016) and Piñeros & Prado (2017). Another main line of research includes atmospheres of planets and focuses on interplanetary trajectories using the atmosphere of an intermediate planet, like in Gillespie & Ross (1967); Lewis & McRonald (1992); Randolph & McRonald (1992); Sims et al. (1995, 2000); Lohar et al. (1997); Lavagna et al. (2005); Murcia et al. (2018a,b).

The literature also considers space maneuvers that include a combination of low thrust and a close approach by a celestial body, in two separate steps. Examples are shown in Casalino et al. (1999b); McConaghy et al. (2003) and Okutsu et al. (2016).

Applications of the gravity-assisted maneuvers also exist linked to the gravitational capture maneuver (Belbruno 1987, 1990, 1994; Yamakawa 1992; Yamakawa et al. 1992, 1993; Belbruno & Miller 1993; Machuy et al. 2007), where one or more swing-bys are performed to help the capture of a spacecraft by a celestial body.

5. THE POWERED SWING-BY MANEUVER

As already explained, the powered swing-by maneuver is a technique where the spacecraft approaches a celestial body and uses the gravity of this body to modify its trajectory, but the maneuver is combined with an impulse applied to the spacecraft by a propulsive system. It is a more complex maneuver when compared to the pure gravity "swing-by" maneuver, where the only forces acting in the motion of the spacecraft are the gravity fields of the celestial bodies involved. The impulse can be applied in different locations of the trajectory of the spacecraft and in different directions, but always inside the sphere of influence of the celestial body. In this way, the main objective of these researches is to study the effects of different geometries and characteristics of the impulse in the variations of the energy of the spacecraft, in particular in finding the locations of the points and directions of the impulses that gives maximum and minimum variations of energy.

This particular maneuver is also an extension of the pure gravity maneuver, and the main goal of the present paper is to review and to describe it in more detail. The study made by Broucke (1988) was later expanded by adding an impulse to the spacecraft during the maneuver, at the time of the close approach (Prado 1996). This impulse is free to vary its magnitude and direction. A set of analytical equations is derived which calculate the increment in velocity, energy and angular momentum of the spacecraft after the combined maneuver, similarly to the ones available in Broucke (1988), but with the presence of the impulse (Ferreira et al. 2018a). The most important ones are shown in equations (7-10), which give the variations of velocity and energy.

The velocity variation is given by $\Delta\vec{V} = \vec{V}_o - \vec{V}_i$, being $\vec{V}_i = \vec{V}_{inf-} + \vec{V}_2$ the approach velocity and $\vec{V}_o = \vec{V}_{inf+} + \vec{V}_2$ the departure velocity of the spacecraft, both with respect to M_1. Soon, $\Delta V = \sqrt{(V_{inf+x} + V_{inf-x})^2 + (V_{inf+y} + V_{inf-y})^2}$, obtained from the components of $\vec{V}_{inf-}$ and $\vec{V}_{inf+}$, which are given by equations 7.

$$\begin{aligned} V_{inf-x} &= -V_{inf-}\sin(\psi-\delta), \\ V_{inf-y} &= V_{inf-}\cos(\psi-\delta), \\ V_{inf+x} &= -V_{inf+}\sin(\psi-\delta+\Theta), \\ V_{inf+y} &= V_{inf+}\cos(\psi-\delta+\Theta), \end{aligned} \tag{7}$$

where $\Theta = \delta - f_0 + f_{lim} + 90$ deg is the total deflection angle of the impulsive maneuver derived in Ferreira et al. (2018a); f_0 is the angle between the radius of the periapsis ($\vec{r}_p$) of the initial maneuver and the new radius of the periapsis ($\vec{r}_{p+}$) obtained after the application of the impulse; f_{lim} is the true anomaly of the asymptotes of the second orbit of the spacecraft, after the impulse is applied; and the other variables have already been defined in Figure 1, § 3.

$$\Delta V = \sqrt{V_{inf-}^2 + V_{inf+}^2 - 2V_{inf-}V_{inf+}\cos\Theta}. \tag{8}$$

For the energy variation we have $\Delta E = \frac{1}{2}(\vec{V}_o^2 - \vec{V}_i^2)$, with $\vec{V}_o$ and $\vec{V}_i$ being already defined, and the components of $\vec{V}_2$ given by $\vec{V}_2 = (-V_2 \cos\beta, V_2 \sin\beta)$, where $180\,\mathrm{deg} - \beta$ is the angle between $\vec{V}_2$ and the $M_1 - M_2$ line. The complete mathematical and geometric explanation of these equations is given in Ferreira et al. (2018a).

$$\Delta E = \frac{1}{2}\Big(V_{inf+}^2 - V_{inf-}^2 - 2V_2V_{inf-}\sin(\beta - \delta + \psi) + 2V_2V_{inf+}\sin(\beta - \delta + \Theta + \psi)\Big). \tag{9}$$

This paper also shows the efficiency of the powered swing-by maneuver, which is defined as the amount of extra energy that is obtained by the spacecraft when the impulse is applied at the moment of closest approach, if compared to a maneuver where an impulse, with the same magnitude, is applied after the spacecraft leaves the sphere of influence of M_2. The analysis was performed according to the gravitational parameter of the secondary body (μ), periapsis radius (r_p), orientation of the swing-by maneuver (ψ) and approach velocity (V_{inf-}). The reason for the positive efficiency of this maneuver is that when the impulse is applied at the periapsis and using different initial conditions, with variations in the magnitude and direction of the impulse, the energy variations due to the gravitational part of the maneuver can be changed, which means that optimal situations can be found. It happens because the orbit changes instantly when the impulse is applied, so its geometry of approach is different, including a new periapsis distance and a new angle of approach, which not only change the results of the impulsive part of the maneuver, but also the effects of the gravitational contribution of the maneuver.

Results were obtained based in the two-body and in the restricted three-body problem models, using the same variables and initial conditions as Broucke (1988), namely, the angle of approach (ψ) equals to 90 degrees (condition of maximum loss of energy) and 270 degrees (condition of maximum gain of energy). The results showed that the maximum transfer of velocity and energy to the spacecraft occurs around $\alpha = -20$ degrees, where α is the angle between the impulse and the velocity of the spacecraft, while the minimum occurs for extreme values of α (around ± 180) degrees. This occurs for the cases of gains of energy, considering $\psi = 270$ degrees. For losses of energy ($\psi = 90$) degrees the maximum transfer is around $\alpha = 20$ degrees. A comparison between the models (two and restricted three body problems) showed that the errors are smaller than 10%.

A more detailed study of the powered swing-by maneuver with the impulse applied at the periapsis of the orbit of the spacecraft around the Moon was later made by (Ferreira et al. 2015), presenting a study of the maximum gains and losses of energy. Also shown in more detail were the situations where there are captures and collisions of the spacecraft with the Moon, a point that analytical approximations are not able to make. In addition to the analysis of the results, empirical equations were obtained that give the maximum and minimum variations of energy, as well as an analysis of the effect of the periapsis distance in the maneuver.

Another version of this maneuver can be made by giving freedom to the application point of the impulse. Casalino et al. (1999a) showed this more flexible maneuver, where a constraint on the periapsis altitude replaces the fixed point where the impulse is applied, so leaving the location of the application point of the impulse as a free parameter. They modeled the problem using the patched-conics approach and showed that the gains or losses of energy have some peculiarities and need to be addressed with some differences in the approach used to solve the problem. The main conclusion is that it is possible to get some extra energy by making an optimized choice of this parameter.

Following this paper, Ferreira et al. (2017) and Silva et al. (2013) made numerical mappings of the energy gains, also considering the position of the application of the impulse as a free parameter, which is used to control the maneuver. Having the magnitude and direction of the impulse as variables, this study extended the research on this problem by analyzing different positions within the sphere of influence of the secondary body to apply the impulse. This new variable of control is an angle θ, measured from the periapsis line, and it defines the position for the application of the impulse. This variable must be selected such that the application point of the impulse is always inside the sphere of influence of the secondary body. As examples, different initial conditions were considered for the Earth-Moon and Sun-Jupiter systems. A superficial look at this problem suggests that the best place to apply the impulse is when the spacecraft passes by the periapsis of its orbit, because it is the point of maximum velocity, which increases the energy transfer from the impulsive maneuver to the spacecraft. However, these researches showed that, for the circular case, this is not true, and some deviations in the direction of the impulse and in the point of the application of the impulse can increase the energy gains of the combined maneuver.

As a natural sequence of those researches, the problem of powered swing-by was extended to systems where the primaries are in elliptical orbits (Prado 1997; Ferreira et al. 2017, 2018a,b; Qi & Ruiter 2018a,b). This is interesting from the academic point of view, to learn the effects of the eccentricity of the primaries in this maneuver, as well as from the engineering side, because there are several systems with considerable eccentricity in the Solar System. Good examples are Mars, which has an eccentricity of 0.093, and Mercury, with an eccentricity of 0.2056. Both of those planets have been considered many times for swing-by maneuvers (McNutt et al. 2004, 2006; Grard 2006; NASA 1999-2012, 2021; Dunne & Burgess 1978; Jehn et al. 2008; Hollister & Prussing 1966).

The physical reasons for the better results in terms of larger variations of energy in elliptical systems are the well-known facts that the velocity of a celestial body in an elliptic orbit is not constant, and that the larger the eccentricity, the smaller the distance between the primary bodies at the periapsis, for a fixed semi-major axis. This means that there will be an important influence of the eccentricity of the orbits on the results, considering that the energy of the spacecraft (with respect to the main body) before and after the maneuver is proportional to those parameters.

Another study of this type of maneuver was made by Qi & Ruiter (2018b), where the optimal two-impulsive strategy for the powered swing-by maneuver was investigated and compared with the one-impulse case. They considered the ERTBP, with both the location and direction of the impulsive maneuver as free parameters. Numerical results showed that the swing-by epoch and the phase angle of the periapsis influence only the value of the energy variation. Other parameters influence also the capture and collision regions. For example, the increase of the magnitude of the impulsive maneuver extends these regions. However, the effect of the eccentricity of the incoming orbit is opposite to that of the impulsive maneuver. The increase of the periapsis distance enlarges the capture regions and shrinks the collision regions.

One problem that appears in this type of maneuver is the existence of errors in the magnitude and direction of the applied impulse. This problem is addressed in Ferreira et al. (2019); they show under which conditions the maneuver is still efficient, even in the presence of those errors. The literature also shows that it is possible to combine a close approach with impulsive and low thrust maneuvers (Gao et al. 2019) for a mission to the Earth's Trojan asteroid 2010TK7, which was defined as the main target for a mission that has the goal of passing by several asteroids. The multiple flyby sequence mission for asteroid explorations was proposed, and the orbit of the spacecraft was optimized for that purpose. Low-thrust and impulsive maneuvers were combined, respectively, to design the trajectories for this mission. The main goal was to reduce the fuel consumption.

Another form of powered swing-by maneuver is the one where a tether is involved. Yamasaki (2018) considers the situation where two spacecraft are linked to each other by a tether. When the tether is cut, one satellite accelerates, while the other one decelerates. This is equivalent to a propulsive maneuver that does not require additional propellant consumption, and benefits from the combination of a close approach and an impulsive maneuver.

6. CAPTURES RESULTING FROM THE MANEUVER

From the studies of the swing-by maneuver, it is well known that one of the consequences of its use is the capture or collision of the spacecraft by the secondary body. The impulsive maneuver can increase those occurrences, because the spacecraft can be directed to the body close enough to be captured or to collide with its surface. Some specific characteristics of the geometry generate these results, which basically come from the reduction of the energy that causes the spacecraft to slow down and, consequently, the orbital curvature to increases and to tend to approach the body.

According to Broucke (1988), the selection of the periapsis to be located such that $\psi = 90$ degrees with respect to the secondary body favors the use of the gravity effect in the reduction of the energy of the spacecraft, since this geometry causes the spacecraft to pass in front of the body, and so it is decelerated due to the gravity of M_2. It is shown that captures and collisions occur, usually, for extreme values of α, when the spacecraft is stopped and sent towards M_2 (Ferreira et al. 2017).

Still related to captures, a flyby approach and capture method for uncontrolled spacecraft capture was developed (Matsumoto et al. 2003). The basic ideas come from the gravity-assisted maneuver and the bi-elliptic transfer orbit. The results show that a smaller time of flight results in smaller savings in energy. Swing-by in the Galilean satellites to capture a spacecraft into the orbit of Jupiter by combining gravity assisted maneuvers and solar electric propulsion was also analyzed in the literature (Landau et al. 2010), as well as a method for capturing a Near-Earth-Asteroid (NEA) using a lunar flyby to reduce the energy required by the capture (Gong & Li 2015). Planetary captures were considered in terms of astronautical activities (MacDonald & McInnes 2005), as well as astronomy (Agnor & Hamilton 2006; Nesvorny et al. 2007). They used gravity assists to understand captures of natural bodies, like moons and asteroids.

Very recent applications of powered swing-by maneuvers can be also seen in Yang et al. (2019) and Pan & Hou (2020). Yang et al. (2019) develop a powered gravity-assist maneuver based on the pseudostate theory. Using this tool, it is possible to solve the gravity-assist segments using the restricted three-body problem to model the dynamical system. Pan & Hou (2020) study transfers from orbits around the co-linear equilibrium point L_2 to orbits around the equilibrium triangular point L_4, considering the Earth-Moon system. They start by using the simplified circular planar restricted three body problem model for the Earth-Moon system. Two types of low-energy transfer orbits are considered. Type-I uses planar Lyapunov orbits and powered lunar gravity assist, while type-II uses two tangential maneuvers, the first one at the departure and the second one at the nominal orbit.

7. CONCLUSIONS

This paper made a survey of the swing-by maneuver, showing many options available for this maneuver, as well as citing articles available in the literature on the subject. The main focus was to show more recent versions of this maneuver, which appeared in the literature after the well-known pure gravity maneuver. Initially, a historical and mathematical review of the pure gravity maneuver was made, as well as the exposition of a large list of real applications of the swing-by maneuver in space missions. The survey then explored the context of the extensions of this type of maneuver. Particular attention was given to the powered maneuver. However, different types of the propulsion studied were also presented, such as atmospheric drag, tethers, continuous propulsion, among others.

The powered swing-by combines the gravity of the body with the application of an impulse on the spacecraft, whose position of application in the orbit can vary. The best choice for the geometry can give larger energy variations to the spacecraft and, consequently, a larger velocity after it leaves the system, or can simply change the orbit within the same system. If the objective is to remove energy to insert the spacecraft in orbit around a celestial body, this type of maneuver is also efficient. The results of the various works presented showed the best configuration of the geometry and parameters of the initial orbit, in addition to the maneuver efficiency, the effect of possible errors in the assignment of parameters, the several models available to study this problem, like the patched-conics for analytical approximation and the restricted three-body problem models, in the circular and elliptic versions, for numerical studies. The text also highlighted the importance of the powered maneuver, because this is a good option when the energy obtained from the pure gravity swing-by maneuver is not enough to complete a given mission. It provides new options to the mission design, and can make possible missions that could not be achieved without this technique.

In the last section, this work presented a historical note of works that focused on the study of captures of the spacecraft occurring due to the swing-by maneuver, and described the favorable geometry for this type of event.

Finally, this survey aimed to gather a large amount of different studies on the swing-by maneuver and its extensions available in the literature. Several key results were shown, as well as mathematical and geometrical descriptions obtained from these works.

The authors wish to express their appreciation for the support provided by Grants 305210/2018-1 from the National Council for Scientific and Technological Development (CNPq); Grants 2016/24561-0, 2016/23542-1 from São Paulo Research Foundation (FAPESP) and the financial support from the Coordination for the Improvement of Higher Education Personnel (CAPES).

REFERENCES

Agnor, C. B. & Hamilton, D. P. 2006, Natur, 441, 192, DOI: 10.1038/nature04792

Anderson, R. L. 2005, Low thrust trajectory design for resonant flybys and captures using invariant manifolds (Ph.D. Thesis, University of Colorado at Boulder)

Anderson, R. L. & Lo, M. W. 2010, JGCD, 33, 1899, DOI: 10.2514/1.45060

_________. 2011, JAnSc, 58, 167, DOI: 10.1007/BF03321164

Armellin, R., Lavagna, M., & Ercoli-Finzi, A. 2006, CeMDA, 95, 391, DOI: 10.1007/s10569-0006-9024-y

Armellin, R., Lavagna, M., Starkey, R. P., & Lewis, M. J. 2007, JSpRo, 44, 1051, DOI: 10.2514/1.28713

Bate, R. R., Mueller, D. D., & White, J. E. 1971, Fundamentals of astrodynamics (New York, N. Y.: Dover)

Belbruno, E. 1987, AIAA, 87

_________. 1992, AIAA, 90

_________. 1994, JBIS, 47, 73

Belbruno, E. A. & Miller, J. K. S. 1993, JGCD, 16, 770, DOI: 10.2514-3.21079

Belbruno, E., Topputo, F., & Gidea, M. 2008, AdSpR, 42, 1330, DOI: 10.1016/j.asr.2008.01.018

Bonfiglio, E. P., Longuski, J. M., & Vinh, N. X. 2000, JSpRo, 37, 768, DOI: 10.2514/2.3649

Broucke, R. A. 1988, AIAA/AAS Astrodynamics Conference, (Minneapolis, MN) 88

Byrnes, D. V. & D'Amario, L. A. 1982, AIAA/AAS Astrodynamics Conference, (San Diego, CA) 82

Campagnola, S. & Russell, R. P. 2010a, JGCD, 33, 463, DOI: 10.2514/1.44258

_________. 2010b, JGCD, 33, 476, DOI: 10.2514/1.44290

Campgnola, S., Skerrit, P., & Russel, R. P. 2012, CeMDA, 113, 343, DOI: 10.1007/s10569-012-9427-x

Carusi, A., Kresák, L., & Valsecchi, G. B. 1995, EM&P, 68, 71, DOI: 10.1007/BF00671499

Carusi, A., Valsecchi, G. B., & Greenberg, R. 1990, CeMDA, 49, 111, DOI: 10.1007/BF00050709

Carusi, A., Kresák, L., & Valsecchi, G. B. 1982, BAICz, 33, 141

Carvalho, F. D. C., Fernandes, S. S., & de Moraes, R. V. 2016, Comp. & Appl. Math, 35, 907, DOI: 10.1007/s40314-016-0325-9

Casalino, L. & Colasurdo, G. 2007, JGCD, 30, 1504, DOI: 10.2514/1.28694

Casalino, L., Colasurdo, G., & Pastrone, D. 1999a, JGCD, 22, 156, DOI: 10.2514/2.4362

_________. 1999b, JGCD, 22, 637, DOI: 10.2514/2.4451

Cline, J. K. 1979, CeMec, 19, 405, DOI: 10.1007/BF01231017

D'Amario, L. A., Byrnes, D. V., & Stanford, R. H. 1981, JGCD, 4, 591, DOI: 10.2514/3.56115

_________. 1982, JGCD, 5, 465, DOI: 10.2514/3.56194

Deerwester, J. M. 1966, JSpRo, 3, 1564, DOI: 10.2514/3.28707

Diehl, R. & Myers, M. R. 1987, Gravity-Assist Trajectories to the Outer Solar System JPL, D-4677

Diehl, R., Belbruno, E., Bender, D., et al. 1987, AAS/AIAA Astrodynamics Conference, 65-695

Dowling, R. L., Kosmann, W. J., Minovitch, M. A., & Ridenoure, R. W. 1990, 41th Congress of the IAF (Dresden, GDR, 6-12 Oct)

_________. 41th Congress of the IAF (Dresden, GDR, 6-12 Oct.)

Dunham, D. & Davis, S. 1985, JAnSc, 33, 275, DOI: 10.2514/6.1984-1978

Dunne, J. A. & Burgess, E. 1978, NASSP, 424

Edelbaum, T. N. 1959, ARS Journal, 29, 864

Elices, T. 1995, JSpRo, 32, 921, DOI: 10.2514/3.26707

Farquhar, R. W. & Dunham, D. W. 1981, JGC, 4, 192

Farquhar, R. W., Muhonen, D., & Church, L. C. 1985, JAnSc, 33, 235

Fernandes, S. S., Carvalho, F. D. C., & Romao, J. V. B. 2018, RMxAA, 54, 111

Ferreira, A. F. S., Prado, A. F. B. A., & Winter, O. C. 2015, AdSpR, 56, 252, DOI: 10.1016/j.asr.2015.04.016

_________. 2017, Nonli. Dyn., 89, 791, DOI: 10.1007/s11071-017-3485-2

Ferreira, A. F. S., Moraes, R. V., Prado, A. F. B. A., & Winter, O. C. 2019, JGCD, 42, 2246, DOI: 10.2514/1.G004187

Ferreira, A. F. S., Prado, A. F. B. A., Winter, O. C., & Santos, D. P. S. 2017, AdSpR, 59, 2071, DOI: 10.1016/j.asr.2017.01.033

_________. 2018a, Ap&SS, 363, 145, DOI: 10.1007/s10509-018-3362-6

_________. 2018b, Ap&SS, 363, 24, DOI: 10.1007/s10509-017-3242-5

Flandro, G. 1966, AsAc, 12, 329, available in http://www.gravityassist.com/IAF2/Ref.%202-123.pdf

Formiga, J. K., Gomes, V. M., & Moraes, R. V. 2018, Comp. & Ap. Math., 33, 371, DOI: 10.1007/s40314-017-0443-z

Gagg Filho, L. A. & Fernandes, S. S. 2018, AcAau, 151, 228, DOI: 10.1016/j.actaastro.2018.06.006

Gao, Y., Lu, X., Peng, Y., Xu, B., & Zhao, T. 2019, AdSpR, 63, 432, DOI: 10.1016/j.asr.2018.08.047

Gillespie, R. W. & Ross, S. 1967, JSpRo, 4, 170, DOI: 10.2514/3.28830

Gomes, V. M. & Prado, A. F. B. A. 2008, WSEAS Transactions on Applied and Theoretical Mechanics, 3, 869

_________. 2010, WSEAS Trans Math., 9, 811

Gomes, V. M., Prado, A. F. B. A., & Golebiewska, J. 2013, Sci World J., 1, DOI: 10.1155/2013/489645

Gomes, V. M., Formiga, J. K. S., & Moraes, R. V. 2013, Math. Prob. Eng., 1, DOI: 10.1155/2013/468624

Gomes, V. M., Piñeros, J. O. M., Prado, A. F. B. A., & Golebiewska, J. 2016, Comp. & Ap. Math., 35, 817, DOI: 10.1007/s40314-015-0256-x

Gong, S. & Li, J. 2015, AdSpR, 56, 848, DOI: 10.1016/j.asr.2015.05.020

Grard, R. 2006, AdSpR, 38, 563, DOI: 10.1016/j.asr.2006.06.015

Greenberg, R., Carusi, A., & Valsecchi, G. B. 1988, Icar, 75, 1, DOI: 10.1016/0019-1035(88)90125-X

Helton, M. R. 1972, Gravitational Capture Characteristics of the Jupiter Ganymede System (Master Thesis, UCLA)

Hiller, H. 1969, JBIS, 22, 60

Hoelker, R. F. & Silber, R. 1959, The bi-elliptic transfer between circular coplanar orbits, Alabama: Army Ballistic Missile Agency Redstone Arsenal, (DA Tech Memo 2-59)

Hohmann, W. 1925, Die Erreichbarkeit der Himmelskörper (München und Berlin: Druck und Verlag

R. Oldenburg)

Hollenbeck, G. R. 1975, AAS/AIAA Astrodynamics Conference on the Exploration of the Outer Planets

Hollister, W. M. & Prussing, J. E. 1966, AsAc, 12, 169

Howell, K. C., Marchand, B. G., & Lo, M. W. 2001, JAnSc, 49, 539, DOI: 10.1007/BF03546223

Jehn, R., Companys, V., Corral, C., García Yárnoz, D., & Sánchez, N. 2008, AdSpR, 42, 1364, DOI: 10.1016/j.asr.2008.01.011

Jerg, S., Junge, O., & Ross, S. D. 2009, CNSNS, 14, 4168, DOI: 10.1016/j.cnsns.2008.12.009

Jezewski, D. J. & Rozendaal, H. L. 1968, AIAAJ, 6, 2160, DOI: 10.2514/3.4949

Jin, H. & Melton, R. G. 1991, AAS/AIAA Spaceflight Mechanics Meeting, 91

Kaplan, M. H. 1976, Modern Spacecraft Dynamics & Control (New York, NY: John Wiley & Sons)

Kloster, K. W., Petropoulos, A. E., & Longuski, J. M. 2011, AcAau, 68, 931, DOI: 10.1016/j.actaastro.2010.08.041

Konstantinov, M. S. & Thein, M. 2017, AcAau, 136, 297, DOI: 10.1016/j.actaastro.2017.02.018

Koon, W. S., Lo, M. W., Marsden, J. E., & Ross, S. D. 2002, Celestial Mechanics: Dedicated to Donald Saari for His 60th Birthday, ed. A. Chencier, R. Cushman, C. Robinson, & Z. J. Xia (Euanston, IL: Northwestern University), DOI: 10.1090/conm/292/04919

Koon, W. S., Lo, M. W., Marsden, J. E., & Ross, S. D. 2000, Chaos, 10, 427, DOI: 10.1063/1.166509

_________. 2001, CeMDA, 81, 63, DOI: 10.1023/A:1013359120468

_________. 2008, Dynamical Systems, the Three-Body Problem and Space Mission Design (Marsden Books)

Landau, D., Strange, N., & Lam, T. 2010, AAS/AIAA Spaceflight Mechanics Conference, Paper AAS 10-169

Lavagna, M., Povoleri, A., & Finzi, A. E. 2005, AcAau, 57, 498, DOI: 10.1016/j.actaastro.2005.03.052

Lawden, D. F. 1953, ARS Journal, 23, 360, DOI: 10.2514/8.4642

_________. 1954, JBIS, 13, 87

Lewis, M. J. & McRonald, A. D. 1992, JSpRo, 29, 653, DOI: 10.2514/3.11506

Lohar, F. A., Misra, A. K., & Mateescu, D. 1996, AcAau, 38, 445, DOI: 10.1016/0094-5765(96)00017-3

Lohar, F. A., Mateescu, D., & Misra, A. K. 1994, AcAau, 32, 89, DOI: 10.1016/0094-5765(94)90059-0

_________. 1997, JSpRo, 34, 16, DOI: 10.2514/2.3186

Longman, R. W. & Schneider, A. M. 1970, JSpRo, 7, 570, DOI: 10.2514/3.29992

MacDonald, M. & McInnes, C. 2005, JGCD, 28, 365, DOI: 10.2514/1.11866

Machuy, A. L., Prado A. F. B. A., & Stuchi, T. J. 2007, AdSpR, 40, 118, DOI: 10.1016/j.asr.2007.02.069

Marsh, S. M. & Howell, K. C. 1988, Double Lunar Swing by Trajectory Design, AIAA paper 88-4289

Matsumoto, S., Dubowsky, S., Jacobsen, S., & Ohkami, Y. 2003, AIAA Guidance, Navigation, and Control Conference, 5745, DOI: https://doi.org/10.2514/6.2003-5745

McConaghy, T., Debban, T. J., Petropulos, A. E., & Longuski, J. M. 2003, JSpRo, 40, 380, DOI: 10.2514/2.3973

McNutt Jr., R. L., Solomon, S. C., Gold, R. E., & Leary, J. C. 2006, AdSpR, 38, 564, DOI: 10.1016/j.asr.2005.05.044

McNutt Jr., R. L., Solomon, S. C., Grard, R., Novara, M., & Mukai, T. 2004, AdSpR, 33, 2126, DOI: 10.1016/S0273-1177(03)00439-3

McRonald, A. D. & Randolph, J. E. 1992, JSpRo, 29, 216, DOI: 10.2514/3.26337

Minovitch, M. A. 1961, Pasadena: JPL, 47 (JPL Tec. Memo 312-130, Aug. 23)

Murcia, J. O. P., Prado, A. F. B. A., & Gomes, V. M. 2018a, RMxAA, 54, 143

_________. 2018b, RMxAA, 54, 485

Murray, C. D. & Dermott, S. F. 2000, Solar System Dynamics (Cambridge, UK: CUP), DOI: https://doi.org/10.1017/CB09781139174817

NASA 1999-2012, “Messenger Trajectory Developed by JHU/APL”, available at http://messenger.jhuapl.edu/themission

NASA 2021, “Nasa Space Science Data Coordinate Archive: Mariner 10”, available at: https://nssdc.gsfc.nasa.gov/nmc/spacecraftDisplay.do?id=1973-085A

Negri, R. B. & Prado, A. F. B. A. 2020, Journal of the Brazilian Society of Mechanical Sciences and Engineering, 42, 406, DOI: https://doi.org/10.1007/s40430-020-02489-x

Negri, R. B., Prado, A. F. B. A., & Sukhanov, A. 2017, CeMDA, 129, 269, DOI: 10.1007/s10569-017-9779-3

Negri, R. B., Sukhanov, A., & Prado, A. F. B. A. 2019, AdSpR, 64, 42, DOI: 10.1016/j.asr.2019.04.002

Nesvorný, D., Vokrouhlický, D. & Morbidelli, A. 2007, AJ, 133, 1962

Nock, K. T. & Upholf, C. W. 1979, AAS/AIAA paper 79-165

Okutsu, M., Yam, C. H., & Longuski, J. M. 2016, AIAA Paper 2006-6745

Öpik, E. J. 1976, Interplanetary Encounters: Close-range gravitational interactions (Amsterdam: Elsevier Scientific Publishing)

Ozimek, M. T. & Howell, K. C. 2010, JGCD, 33, 533, DOI: 10.2514/1.43179

Pan, S. S. & Hou, X. Y. 2020, AdSpR, 65, 2878, DOI: 10.1016/j.asr.2020.03.022

Piñeros, J. O. M. & Prado, A. F. B. A. 2017, Ap&SS, 362, 120, DOI: 10.1007/s10509-017-3097-9

Pourtakdoust, S. H. & Sayanjali, M. 2014, Nonlinear Dyn., 76, 955

Prado, A. F. B. A. 1996, JGCD, 19, 1142, DOI: 10.2514/3.21756

_________. 1997, JGCD, 20, 797, DOI: 10.2514/2.4115

Prado, A.F.B.A. & Broucke, R. 1995, AcAau, 36, 285, DOI: 10.1016/0094-5765(95)00114-X

Prussing, J. E. 1992, JGCD, 15, 1037, DOI: 10.2514/3.20941

Qi, Y. & Ruiter, A. 2018a, MNRAS, 478, 1392, DOI: 10.1093/mnras/sty1155

_________. 2018b, MNRAS, 481, 4621

_________. 2020, JGCD, 43, 111, DOI: 10.2514/1.G004358

Qi, Y., Xu, S., & Qi, R. A. 2017, MNRAS, 468, 2265, DOI: 10.1093/mnras/stx505

Qian, Y. J., Zhang, W., Yang, X. D., & Yao, M. H. 2016, Nonlinear Dyn., 85, 463

Randolph, J. E. & McRonald, A. D. 1992, JSpRo, 29, 223, DOI: 10.2514/3.26338

Ross, S. D. & Scheeres, D. J. 2007, SJADS, 6, 576, DOI: 10.1137/060663374

Roth, H. L. 1965, No. Aerospace corp. el. Segundo ca. el. Segundo technical operations (TDR-469 (5540-10)-5)

Ruppe, H. O. 1967, Introduction to Astronautics, Vol. 2 (New York, NY: Academic Press)

Shternfeld, A. 1959, Soviet Space Science: The Russian Story of Artificial Satellites (New York, NY: Basic Books Inc)

Silva, A. F., Prado, A. F. B. A., & Winter, O. C. 2013b, JPhCS, 465, 012001, DOI:10.1088/1742-6596/465/1/012001

Sims, J. A., Longuski, J. M., & Patel, M. R. 1995, AcAau, 35, 297, DOI: 10.1016/0094-5765(94)00195-R

_________. 2000, JSpRo, 37, 49, DOI: 10.2514/2.3525

Strange, N. J. & Longuski, J. M. 2002, JSpRo, 39, 9, DOI: 10.2514/2.3800

Striepe, S. A. & Braun, R. D. 1991, J. Astronaut. Sci., 39, 299

Sukhanov, A. A. 1999, AcAau, 45, 177, DOI: 10.1016/S0094-5765(99)00135-6

Sukhanov, A. A. & Prado, A. F. B. A. 2001, JGCD, 24, 723, DOI: 10.2514/2.4772

Szebehely, V. 1967, Theory of Orbits. The restricted problem of three bodies (New York, NY: Academic Press)

Szebehely, V. & Giacaglia, G. E. O. 1964, AJ, 69, 230, DOI: 10.1086/109261

Valtonen, M. & Karttunen, H. 2006, The Three-Body Problem (Cambridge, UK: CUP)

Vasile, M. & Campagnola, S. 2009, JBIS, 62, 15

Woolley, R. C. & Scheeres, D. J. 2009, Advances in the Astronautical Sciences, 135, 1245

Yamakawa, H. 1992, On Earth-Moon Transfer Trajectory with Gravitational Capture (PhD. Thesis, University of Tokyo)

Yamakawa, H., Kawaguchi, J., Ishii, N., & Matsuo, H. A. 1992, AAS/AIAA Spaceflight Mechanics Meeting, AAS Paper 92-186

_________. 1993, AAS/AIAA Astrodynamics Specialist Conference, AAS Paper 93-633

Yamasaki, T., Bando, M., & Hokamoto, S. 2018, AcAau, 142, 212, DOI: 10.1016/j.actaastro.2017.11.002

Yang, B., Yang, H., & Li, S. 2019, AcA, 165, 139

Zhang, Ch., Topputo, F., Bernelli-Zazzera, F., & Zhao, Y. 2015, JGCD, 38, 1501, DOI: 10.2514/1.G001080

Zotos, E. E. 2015, Nonlinear Dynamics, 82, 1233, DOI: 10.1007/s11071-015-2229-4

Rodolpho V. de Moraes: National Institute for Space Research - INPE, CEP 12227-010, São José dos Campos - SP, Brazil (rodolpho.vilhena@gmail.com).

Alessandra F. S. Ferreira: Department of Mathematics - São Paulo State University (FEG-UNESP), CEP 12516-410, Campus of Guaratinguetá - SP, Brazil (alessandra.ferraz@unesp.br).

Antonio F. B. A. Prado: Volunteer Professor at Peoples' Friendship University of Russia (RUDN University), CEP 117198, Moscow, Russian Federation (antonio.prado@inpe.br).

Revista Mexicana de Astronomía y Astrofísica, **57**, 459–465 (2021)

AUTHOR INDEX

La *Revista Mexicana de Astronomía y Astrofísica*, fundada en 1974, publica trabajos originales de investigación en todas las ramas de la astronomía, astrofísica y temas vinculados a éstas. Se editan dos números por año y su distribución es gratuita a todas las instituciones relacionadas con los campos cubiertos por esta revista.

La política editorial de la *RMxAA* consiste en enviar a arbitrar los artículos recibidos a especialistas en el campo. Los interesados en publicar en nuestra revista deberán enviar por correo electrónico, a la dirección `rmaa@astro.unam.mx`, la versión completa de su artículo en formato PostScript o PDF y el archivo LaTeX. Estos archivos deberán ir acompañados de una carta de presentación. Todos los trabajos deben ser preparados en inglés usando la versión más reciente del macro en LaTeX de la *RMxAA* "rmaa.cls" (disponible en https://www.irya.unam.mx/rmaa/). Se requiere un "Abstract" no mayor que 12 líneas, y un "Resumen" en español (este último podrá ser provisto por los editores de ser necesario); también se incluirán de 1 a 6 palabras clave ("Keywords") de la lista de las revistas astronómicas internacionales. Se requiere que cada tabla incluida en el texto esté numerada y con título; las figuras deberán estar en formato PostScript (.ps) o PostScript encapsulado (.eps), estar numeradas y con leyenda explicativa. Se requiere que cada tabla y figura estén mencionadas en el texto. El estilo de las referencias sigue las normas astronómicas internacionales recientes. Para mayor información sobre el estilo de la *RMxAA* se puede consultar el archivo de ejemplo que viene incluido en los macros. La publicación es gratuita para los autores.

En 1995 se inició la Serie de Conferencias de la *Revista Mexicana de Astronomía y Astrofísica*, dedicada a la publicación de las memorias de reuniones astrónomicas efectuadas en México y en otros países del continente. Hasta 1994 las memorias de reuniones astronómicas de la región se publicaron como volúmenes especiales de la *RMxAA*.

Las condiciones de publicación de cada volumen de las memorias de conferencias serán el resultado de un convenio establecido entre la *RMxAC* y los organizadores de cada evento. Los detalles de la publicación, que incluyen fechas y extensión de los textos, serán anunciados por los editores de cada conferencia. Las contribuciones extensas estarán en inglés con un resumen en español (o portugués en caso de las Reuniones regionales). Los resúmenes de las reuniones que no son temáticas tendrán una extensión máxima de 300 palabras incluyendo título, autores y afiliación; serán exclusivamente en inglés. Los macros LaTeX para las memorias se encuentran en http://www.astroscu.unam.mx/~rmaa. Todas las contribuciones y resúmenes deberán estar en estos formatos.

Se concede permiso a los autores de artículos y libros científi-cos para citar trabajos publicados en la *RMxAA* y en la *RMxAC* siempre y cuando se dé la referencia completa. También se permite la reproducción de figuras y tablas bajo las mismas condiciones.

La *RMxAA* aparece indexada en Current Contents, Science Citation Index, Astronomy and Astrophysics Abstracts, Physics Briefs, Publicaciones Científicas en América Latina, Astronomy and Astrophysics Monthly Index, PERIODICA, RedALyC, Latindex y SciELO.

The *Revista Mexicana de Astronomía y Astrofísica*, founded in 1974, publishes original research papers in all branches of astronomy, astrophysics and closely related fields. Two numbers per year are issued and are distributed free of charge to all institutions engaged in the fields covered by the *RMxAA*.

All papers received by the *RMxAA* are sent to a specialist in the field for refereeing. Authors interested in publishing in the *RMxAA* should send their papers to the e-mail address `rmaa@astro.unam.mx`, in PostScript or PDF format, along with the LaTeX file. A submission letter should also be sent. Papers should be prepared in English, using the most recent version of the *RMxAA* LaTeX document class "rmaa.cls" (available from https://www.irya.unam.mx/rmaa/). An "Abstract" of at most 12 lines is required, as well as a "Resumen" in Spanish. The latter can be provided by the Editors, if necessary. A total of six or fewer "Keywords", taken from the lists of international astronomical journals should be included. Tables should be numbered and include a title. Figures should be submitted in PostScript (.ps) or Encapsulated PostScript (.eps) format, should be numbered, and should include a caption. Both tables and figures should be mentioned in the text. The style of the references follows recent international astronomical usage. For more information about the style norms of *RMxAA* please consult the example included in the LaTeX package. Publication in *RMxAA* is free of charge to authors.

The Conference Series of *Revista Mexicana de Astronomía y Astrofísica* was founded in 1995 to publish the proceedings of astronomical meetings held in Mexico and other countries throughout the continent. Until 1994 such proceedings had been published as special issues of *Revista Mexicana de Astronomía y Astrofísica*.

Conditions of publication of proceedings of each conference will be the result of a mutual agreement between the *RMxAC* and the organizing committee. Details of publication, including length of papers, will be announced by the editors of each event. The extensive contributions should be in English, and should include an abstract in Spanish (or Portuguese for regional meetings). The abstracts of non-thematic meetings should not exceed 300 words including title, authors, and affiliation; they should be exclusively in English. The LaTeX templates specially prepared for proceedings can be obtained at http://www.astroscu.unam.mx/~rmaa; all papers should be submitted in this format.

Authors of scientific papers and books may quote articles published both in *RMxAA* and *RMxAC* provided that a complete reference to the source is given. Reproduction of figures and tables is also permitted on the same basis.

The *RMxAA* is indexed in Current Contents, Science Citation Index, Astronomy and Astrophysics Abstracts, Physics Briefs, Publicaciones Científicas en América Latina, Astronomy and Astrophysics Monthly Index, PERIODICA, RedALyC, Latindex, and SciELO.